europhysics
conference
abstracts

17th EPS Conference on

Controlled Fusion and Plasma Heating

Amsterdam, 25-29 June 1990

Editors: G. Briffod, Adri Nijsen-Vis, F.C. Schüller

Contributed Papers
Part III

Published by: European Physical Society

ies Editor: Prof. K. Bethge, Frankfurt/M.

naging Editor: G. Thomas, Geneva

VOLUME 14 B Part III

XVII FUSION AMSTERDAM 1990

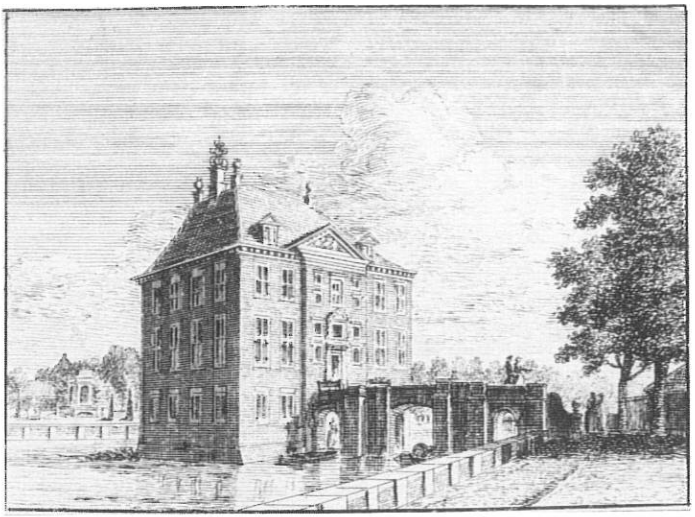

't Huis Rynhuizen.

17th
FUSION
AMSTERDAM
1990

E
F
G
H

17th European Conference on

Controlled Fusion and Plasma Heating

Amsterdam, 25-29 June 1990

Editors: G. Briffod, Adri Nijsen-Vis, F.C. Schüller

Contributed Papers
Part III

EUROPHYSICS CONFERENCE ABSTRACTS is published by the
European Physical Society, © 1990

PREFACE

The 17th European Conference on Controlled Fusion and Plasma Heating was held in Amsterdam, the Netherlands, from the 25th to the 29th of June 1990 by the Plasma Physics Division of the European Physical Society (EPS).

The Conference has been organized by the FOM-Instituut voor Plasmafysica Rijnhuizen, which is part of the Foundation for Fundamental Research on Matter (Stichting Fundamenteel Onderzoek der Materie). FOM is supported by the Dutch Research Organization NWO and Euratom.

The Conference has been sponsored by the Koninklijke Nederlandse Academie van Wetenschappen (KNAW) and by the Foundation Physica.

The programme, format and schedule of the Conference are determined by the International Programme Committee appointed by the Plasma Physics Division of the EPS.

The programme included 18 invited lectures; from the contributed papers 24 were selected for oral presentation and 470 for poster presentation.

This 4-volume publication is published in the Europhysics Conference Abstract Series and contains all accepted contributed papers received in due time by the organizers. The 4-page extended abstracts were reproduced photographically using the manuscripts submitted by the authors. The invited papers will be published in a special issue of the journal "Plasma Physics and Controlled Fusion" and sent free of charge to each registered participant.

The editors would like to acknowledge the skillful and dedicated support given by Laura van Veenendaal - van Uden, Rosa Tenge - Tjon A Tham and Cora de Bruijne in preparing the manuscripts for reproduction in these four volumes.

May 1990

The Editors

INTERNATIONAL PROGRAMME COMMITTEE

G. Briffod, Chairman, CEN, Grenoble, France
K. Appert, CRPP, Lausanne, Switzerland
R. Balescu, Université Libre de Bruxelles, Belgium
F. De Marco, Euratom-ENEA, Frascati, Italy
C. Gormezano, JET Joint Undertaking, Abingdon, United Kingdom
L. Laurent, Association Euratom-CEN, St. Paul-lez-Durance, France
S. Ortolani, Association Euratom-CNR, Padova, Italy
D.D. Ryutov, Academy of Sciences, Novosibirsk, USSR
F.C. Schüller, FOM-Rijnhuizen, Nieuwegein, The Netherlands
S.E. Segre, Euratom-ENEA, Frascati, Italy
P.E. Stott, JET Joint Undertaking, Abingdon, United Kingdom
H. Wobig, Max-Planck-Institut für Plasmaphysik, Garching bei München, FRG

LOCAL ORGANIZING COMMITTEE

M.J. van der Wiel, Chairman, FOM-Rijnhuizen, Nieuwegein
F.C. Schüller, Vice-Chairman, FOM-Rijnhuizen, Nieuwegein
A. Nijsen-Vis, Scientific Secretary, FOM-Rijnhuizen, Nieuwegein
J.T. van den Hout, Treasurer, FOM-Rijnhuizen, Nieuwegein
A.J.H. Donné, FOM-Rijnhuizen, Nieuwegein
N.J. Lopes Cardozo, FOM-Rijnhuizen, Nieuwegein
J. Rem, FOM-Rijnhuizen, Nieuwegein
H. Hopman, FOM-AMOLF, Amsterdam
D.C. Schram, Technical University, Eindhoven

CONTENTS

Part I	- A	TOKAMAKS	
	A1	Tokamaks, General	I-1 – I-101
	A2	Scaling Laws	I-102 – I-149
	A3	Determination of Transport Coefficients	I-150 – I-198
	A4	Fluctuations	I-199 – I-214
	A5	Results Pellet Injection	I-215 – I-246
	A6	H-Mode	I-247 – I-302
	A7	MHD Phenomena	I-303 – I-414
	A8	Vertical Instabilities	I-415 – I-430
Part II	- B	STELLARATORS	
	B1	Experiments	II-431 – II-487
	B2	Theory	II-488 – II-532
	- C	ALTERNATIVE MAGNETIC CONFINEMENT SCHEMES	
	C1	Reversed Field Pinches	II-533 – II-588
	C2	Other Magnetic Confinement Schemes	II-589 – II-666
	- D	MAGNETIC CONFINEMENT THEORY AND MODELLING	
	D1	Magnetic Confinement Theory	II-667 – II-776
	D2	Modelling	II-777 – II-860
	D3	General Theory	II-861 – II-973
Part III	- E	HEATING BY NEUTRAL BEAM INJECTION	III-974 – III-986
	- F	RF HEATING	
	F1	Ion Cyclotron Resonance Heating	III-987 – III-1071
	F2	Electron Cyclotron Resonance Heating	III-1072 – III-1136
	F3	Lower Hybrid Heating	III-1137 – III-1189
	- G	CURRENT DRIVE AND PROFILE CONTROL	
	G1	Electron Cyclotron Current Drive	III-1190 – III-1238
	G2	Lower Hybrid Current Drive	III-1239 – III-1294
	G3	Others	III-1295 – III-1340
	- H	IMPURITY AND EDGE PHYSICS	III-1341 – III-1483
PART IV	- I	DIAGNOSTICS	
	I1	Results	IV-1484 – IV-1611
	I2	Technique/New Method	IV-1612 – IV-1724
	- J	BASIC COLLISIONLESS PLASMA PHYSICS	IV-1725 – IV-1851
	- K	INERTIAL CONFINEMENT FUSION	IV-1852 – IV-1883

PAPER IDENTIFICATION

All contributed papers are listed with their title and responsible author. In those cases where no author was underlined the first author mentioned was taken. The day of the poster presentation of each paper, followed by the number of the poster board, is given under the title in the list of contributed papers. The four poster sessions will be held on:

Monday afternoon indicated as Mo,
Tuesday afternoon indicated as Tu,
Thursday afternoon indicated as Th,
Friday afternoon indicated as Fr.

The poster boards are numbered from 1 to 130. From the 494 contributed papers, 24 were selected for oral presentation. The authors of those orally presented papers were requested to give also a poster presentation. Most of them confirmed that they were prepared to do so.

TITLE LIST OF CONTRIBUTED PAPERS

A. TOKAMAKS

D-D neutron production from JET plasmas.
First author: G. Sadler et al.
Mo 1 A 1 I-1

Peaked profiles in low q high current limiter plasmas in JET.
First author: P.J. Lomas et al.
Mo 2 A 2 I-5

The fusion performance of JET limiter plasmas using Be coated graphite and solid Be surfaces.
First author: T.T.C. Jones et al.
Mo 3 A 3 I-9

The role of various loss channels in the ion energy balance in T-10.
First author: E.L. Berezovskij et al.
Mo 4 A 4 I-13

First experiments and numerical simulation of a plasma column compression in high field tokamak.
First author: E.A. Azizov et al.
Mo 5 A 5 I-14

A study of poloidal and toroidal rotation in the TJ-1 ohmically heated tokamak.
First author: B.G. Zurro et al.
Mo 6 A 6 I-18

Runaway electron fluctuations studies in TJ-I.
First author: L. Rodríguez et al.
Mo 7 A 7 I-22

Particle and impurity confinement in helium discharges in the Texas Experimental Tokamak (TEXT).
First author: W.L. Rowan et al.
Mo 8 A 8 I-26

The first Mexican small tokamak.
First author: L. Meléndez-Lugo et al.
Mo 9 A 9 I-30

The confinement improvement modes in JIPP T-11U.
First author: Y. Hamada et al.
Mo 10 A 10 I-34

Measurements of fluctuations and space potential profiles in the Texas Experimental Tokamak (TEXT).
First author: P.M. Schoch et al.
Mo 11 A 11 I-38

Test of ITG-mode marginal stability in TFTR.
First author: M.C. Zarnstorff et al.
Mo 12 **A12*** I-42

Perturbative transport studies of neutral beam heated TFTR plasmas using carbon pellet injection.
First author: R.A. Hulse et al.
Mo 13 A 13 I-46

Measurements of radial profiles of transport parameters of HE^2 on TFTR.
First author: E.J. Synakowski et al.
Mo 14 A 14 I-50

T_e profile invariance under transient conditions on ASDEX.
First author: H.D. Murmann et al.
Tu 1 A 15 I-54

The isotope dependence of confinement in ASDEX: Part 2.
First author: F. Wagner et al.
Tu 2 A 16 I-58

Demixing of impurities and hydrogen as deduced from Z_{eff} profiles in the boronized ASDEX.
First author: K.H. Steuer et al.
Tu 3 A 17 I-62

Confinement studies in sawtooth-free ohmic discharges.
First author: U. Stroth et al.
Tu 4 A 18 I-66

Modifications of density profile and particle transport in ASDEX during lower hybrid heating and current drive.
First author: O. Gehre et al.
Tu 5 A 19 I-70

Particle transport studies on TCA using the dynamic response of the effective mass.
First author: Th. Dudok de Wit et al.
Tu 6 A 21 I-74

Transition to high density discharges through hard gas puffing.
First author: Z.A. Pietrzyk et al.
Tu 7 A 22 I-78

Current penetration measurements in TUMAN-3 by active charge exchange diagnostics.
First author: V.I. Afanasiev et al.
Tu 8 A 23 I-82

* This paper will also be presented orally on Friday 29 June at 9.40 hrs.

Ohmic discharges in TORE SUPRA - Marfes and detached plasmas.
First author: J.C. Vallet et al.
Tu 9 A 24 I-86

Toroidal plasma rotation in JET.
First author: H.P.L. de Esch et al.
Tu 10 A 25 I-90

ELM-free H-mode with CO- and CTR-neutral injection in ASDEX.
First author: F. Ryter et al.
Tu 11 **A26*** I-94

A regime showing anomalous triton burnup in JET.
First author: S. Conroy et al.
Tu 12 A 27 I-98

Scaling from JET to CIT and ITER-like devices using dimensionless parameters.
First author: J. Sheffield
Mo 15 A 28 I-102

Extrapolation of the high performance JET plasmas to D-T operation.
First author: J.G. Cordey et al.
Mo 16 A 29 I-106

Global H-mode scalings based on JET and ASDEX data.
First author: O. Kardaun et al.
Mo 17 A 30 I-110

Transport studies in high recycling neutral beam heated discharges on TFTR.
First author: D.W. Johnson et al.
Mo 18 A 31 I-114

Energy confinement scaling laws for FT ohmic plasma.
First author: G. Bracco et al.
Mo 19 A 32 I-118

Profile consistency coupled with MHD equilibrium extended to non stationary plasma conditions.
First author: M. Roccella et al.
Mo 20 A 33 I-122

Scaling dimensionally similar tokamak discharges to ignition.
First author: R.E. Waltz et al.
Mo 21 A 34 I-126

Transport code simulations of IGNITOR..
First author: M.F. Turner et al.
Mo 22 A 35 I-130

* This paper will also be presented orally on Tuesday 26 June at 14.30 hrs.

A physics perspective on CIT.
First author: R.J. Goldston et al.
Mo 23 A 36 I-134

Burn threshold for fusion plasmas with helium accumulation.
First author: B.D. Fried et al.
Mo 24 A 37 I-138

Heating profile and sawtooth effects on energy confinement in elongated tokamak plasmas.
First author: J.D. Callen et al.
Mo 25 A 38 I-142

The scaling of confinement with major radius in TFTR.
First author: L.R. Grisham et al.
Mo 26 A 39 I-146

Coupling of plasma particle diffusion and heat flow in TEXT.
First author: D.L. Brower et al.
Th 1 A 40 I-150

Sawtooth heat pulse propagation and electron heat conductivity in HL-1.
First author: Gancheng GUO et al.
Th 2 A 41 I-154

Evidence of coupling of thermal and particle transport from heat and density pulse measurements at JET.
First author: G.M.D. Hogeweij et al.
Th 3 A 42 I-158

Determination of local transport coefficients by heat flux analysis and comparisons with theoretical models.
First author: B. Balet et al.
Th 4 A 43 I-162

Dynamic response of plasma energy and broad-band magnetic fluctuations to additional heating in JET.
First author: C. Nardone et al.
Th 5 A 44 I-166

Analysis of heat pulse propagation in plasmas using Fourier methods.
First author: A. Jacchia et al.
Th 6 A 45 I-170

Particle and thermal transport in TEXT from perturbation experiments.
First author: K.W. Gentle et al.
Th 7 A 46 I-174

Investigation of coupled energy and particle transport.
First author: M. Cox et al.
Th 8 A 47 I-178

Is the ion confinement improving in ASDEX H-mode discharges?
First author: O. Gruber et al.
Th 9 A 48 I-182

Momentum transport studies on ASDEX.
First author: A. Kallenbach et al.
Th 10 A 49 I-183

Dynamic response analysis as a tool for investigating transport mechanisms.
First author: Th. Dudok de Wit et al.
Th 11 A 50 I-187

Heat and density pulse propagation in ASDEX.
First author: L. Giannone et al.
Th 12 A 51 I-151

Study of the electron heat pulse propagation from ECRH on T-10.
First author: A.A. Bagdasarov et al.
Th 13 A 52 I-195

Dimensionality analysis of chaotic density fluctuations in tokamak.
First author: F.C. Schüller et al.
Fr 1 A 53 I-199

Density fluctuation measurements via reflectometry on DIII-D during L- and H-mode operation.
First author: E.J. Doyle et al.
Fr 2 A 54 I-203

Investigation of density fluctuations in the ASDEX tokamak via collective laser scattering.
First author: E. Holzhauer et al.
Fr 3 A 55 I-207

Fluctuations and transport in DITE.
First author: G. Vayakis et al.
Fr 4 A 56 I-211

Online density feedback on ASDEX for pellet-refuelled discharges.
First author: R. Loch et al.
Fr 5 A 57 I-215

Simultaneous evolution of temperature and density perturbations following pellet injection in JET.
First author: J.R. Martin-Solis et al.
Fr 6 A 58 I-219

Impurity behavior in pellet-fuelled plasma of JT-60.
First author: T. Sugie et al.
Fr 7 A 59 I-223

Fast cooling phenomena with ice pellet injection in JIPP T-IIU tokamak.
First author: K.N. Sato et al.
Fr 8 A 60 I-227

The pellet trajectory toroidal deflection in T-10.
First author: A.A. Bagdasarov et al.
Fr 9 A 61 I-231

Scaling of experimentally determined pellet penetration depths on ASDEX.
First author: R. Loch et al.
Fr 10 A 62 I-235

Repetitive pellet injection combined with ion cyclotron resonance heating in ASDEX.
First author: J.-M. Noterdaeme et al.
Fr 11 **A63*** I-239

Evolution of pellet clouds and cloud structures in magnetically confined plasmas.
First author: L.L. Lengyel et al.
Fr 12 A 64 I-243

Transport of impurities during H-mode pulses in JET.
First author: L. Lauro Taroni et al.
Tu 13 A 65 I-247

Particle and heat deposition in the X-point region at JET.
First author: D.P. O'Brien et al.
Tu 14 **A66**** I-251

ICRH produced H-modes in the JET tokamak.
First author: V.P. Bhatnagar et al.
Tu 15 **A67***** I-255

The compatibility of the JET H-mode with other regimes of improved performance.
First author: A. Tanga et al.
Tu 16 A 68 I-259

Radiation asymmetries and H-modes.
First author: N. Gottardi et al.
Tu 17 A 69 I-263

Electric field profile of plasmas with improved confinement in JFT-2M tokamak.
First author: K. Ida et al.
Tu 18 A 70 I-267

---

* This paper will also be presented orally on Tuesday 26 June at 14.10 hrs.
** This paper will also be presented orally on Tuesday 26 June at 13.30 hrs.
*** This paper will also be presented orally on Tuesday 26 June at 13.50 hrs.

Comparison of thermal and angular momentum transport in neutral beam-heated hot-ion H- and L-mode discharges in DIII-D.
First author: K.H. Burrell et al.
Tu 19 A 71 I-271

The effects of carbonization on the confinement properties of the DIII-D H-mode.
First author: D.P. Schissel et al.
Tu 20 A 72 I-275

Physics of the L to H transition in DIII-D.
First author: H. Matsumoto et al.
Tu 21 A 73 I-279

Transport properties of high β_{pol} PBX-M plasmas.
First author: B. LeBlanc et al.
Tu 22 A 74 I-283

H-mode behaviour induced by edge polarization in TEXTOR.
First author: R.R. Weynants et al.
Tu 23 A 75 I-287

ELMS as triggered and as triggering relaxation phenomena in ASDEX.
First author: O. Klüber et al.
Tu 24 A 76 I-291

Long-pulse heating in ASDEX L- and H-mode discharges.
First author: O. Vollmer et al.
Tu 25 A 77 I-295

Ohmic H-mode in "TUMAN-3" tokamak.
First author: S.V. Lebedev et al.
Tu 26 A 78 I-299

Runaway electron production during major disruptions in TORE SUPRA.
First author: G. Martin et al.
Th 14 A 79 I-303

Runaway relaxation oscillation on HL-1 tokamak.
First author: Xuantong DING et al.
Th 15 A 80 I-307

Energy loss in a major disruption and MHD instabilities at low q in the HL-1 tokamak.
First author: Qingdi GAO
Th 16 A 81 I-311

MHD-Perturbations in T-10.
First author: P.V. Savrukhin et al.
Th 17 A 82 I-315

Sawtooth modulated density fluctuations in the central plasma region of NBI-heated discharges in TEXTOR.
First author: M. Jadoul et al.
Th 18 A 83 I-319

High-beta regimes in JET.
First author: P. Smeulders et al.
Th 19 **A 84*** I-323

Sawtooth stabilisation by fast ions: comparison between theory and experiments.
First author: F. Porcelli et al.
Th 20 A 85 I-327

JET neutron emission profiles and fast ion redistribution from sawteeth.
First author: F.B. Marcus et al.
Th 21 **A 86**** I-331

The detailed topology of the m=1 instability in the JET sawtooth collapse.
First author: S.W. Wolfe et al.
Th 22 A 87 I-335

Density limits in JET with beryllium.
First author: C.G. Lowry et al.
Th 23 A 88 I-339

Faraday rotation measurements on JET, and the change in the safety factor profile during a sawtooth collapse.
First author: J. O'Rourke et al.
Th 24 A 89 I-343

Sawtooth triggered disruptions at the density limit on DITE.
First author: G.M. Fishpool et al.
Th 25 A 90 I-347

Electromagnetic interactions between plasmas and vacuum vessel during disruptions in the Hitachi tokamak HT-2.
First author: M. Abe et al.
Th 26 A 91 I-351

Asymmetric effects of an l -1 external helical coil on the sawtooth amplitude on Tokoloshe tokamak.
First author: D.E. Roberts et al.
Th 27 A 92 I-355

* This paper will also be presented orally on Friday 29 June at 9.00 hrs.
** This paper will also be presented orally on Friday 29 June at 9.20 hrs.

Measurement of ohmic tokamak momentum confinement times from controlled locking and unlocking of tearing modes.
First author: D.E. Roberts et al.
Fr 13 A 93 I-359

The characteristics of low-q discharges on HT-6B tokamak.
First author: Guoxiang LI et al.
Fr 14 A 94 I-363

Profiles and MHD activities in PBX-M tokamak.
First author: H. Takahashi et al.
Fr 15 A 95 I-367

The beta limit in the DIII-D tokamak.
First author: J.R. Ferron et al.
Fr 16 A 96 I-371

MHD characteristics and edge plasma stability during periods of ELM activity in PBX-M.
First author: S.M. Kaye et al.
Fr 17 A 97 I-375

Resonant magnetic perturbations and disruption studies on COMPASS-C.
First author: A.W. Morris et al.
Fr 18 A 98 I-379

Stabilisation of sawtooth oscillations by trapped energetic particles in TEXTOR.
First author: J. Ongena et al.
Fr 19 A 99 I-383

Production of high poloidal beta equilibria limited by an inboard separatrix in TFTR.
First author: S.A. Sabbagh et al.
Fr 20 A 100 I-387

Soft-X-ray tomography of sawteeth and m=1 modes on ASDEX.
First author: R. Büchse et al.
Fr 21 A 101 I-391

Density limit in ASDEX under clean plasma conditions.
First author: A. Stäbler et al.
Fr 22 A 102 I-395

Theoretical analysis of high-beta JET shots.
First author: T.C. Hender et al.
Fr 23 A 103 I-399

Analysis of the energy heat quench during a disruption in TEXTOR.
First author: K.H. Finken et al.
Fr 24 A 104 I-403

Enhanced turbulence during the energy quench of disruptions.
First author: G.J.J. Remkes et al.
Fr 25 A 105 I-407

High density mode in "TUMAN-3" tokamak.
First author: L.G. Askinasi et al.
Fr 26 A 106 I-411

Nonlinear vertical displacement instability of elongated plasma in tokamak and its stabilization.
First author: Guoyang YU et al.
Th 28 A 107 I-415

Vertical instabilities in JET.
First author: P. Noll et al.
Th 29 A 108 I-419

Scaling of poloidal currents during rapid vertical displacement events.
First author: G.W. Pacher et al.
Th 30 A 109 I-423

Experiments at high elongations in DIII-D.
First author: E.A. Lazarus et al.
Th 31 A 110 I-427

B. STELLARATORS

Electron cyclotron radiation (ECR) asymmetry measurements at 2 ω_{He} in the L-2 stellarator.
First author: D.K. Akulina
Th 55 B 1 II-431

Confinement studies of ECRH plasmas in a toroidal heliac.
First author: G.D. Conway et al.
Th 56 B 2 II-435

Measurements of the fast ion distribution during neutral beam injection and ion cyclotron heating in ATF.
First author: M.R. Wade et al.
Th 57 B 3 II-439

Bootstrap current studies in the Advanced Toroidal Facility.
First author: M. Murakami et al.
Th 58 **B 4*** II-443

Impurity transport in ATF and the effect of controlled impurity injection.
First author: L.D. Horton et al.
Th 59 B 5 II-447

Transport study on ECH- and NBI- heated plasmas in the low-aspect-ratio helical system CHS.
First author: H. Iguchi et al.
Th 60 B 6 II-451

Cleanup and improvement of operational performance of ATF by chromium and titanium gettering.
First author: R.C. Isler et al.
Th 61 B 7 II-455

Confinement and stability on Heliotron E plasma.
First author: K. Kondo et al.
Th 62 B 8 II-459

Efficiency of electron-cyclotron plasma heating in the L-2 stellarator.
First author: Eh.D. Andryukhina et al.
Fr 49 B 9 II-463

Ray tracing during ECRH by X-wave on the second harmonic of ω_{ce} in L-2 stellarator.
First author: K.M. Likin et al.
Fr 50 B 10 II-467

Particle transport and recycling studies on the W VII-AS stellarator.
First author: F. Sardei et al.
Fr 51 B 11 II-471

* This paper will also be presented orally on Tuesday 26 June at 14.50 hrs.

H_α-spectroscopy on WVII-AS.
First author: A. Dodhy et al.
Fr 52 B 12 II-475

Results from X-ray measurements on the Wendelstein W7-AS stellarator.
First author: A. Weller et al.
Fr 53 B 13 II-479

First results with neutral injection into W VII-AS stellarator.
First author: W. Ott et al.
Fr 54 B 14 II-483

Statistical analysis of electron heat conduction on W7-AS.
First author: G. Kühner et al.
Fr 48 B 15 II-484

Two-ion ICRH heating in the flexible heliac TJ-II.
First author: J.F. Miramar Blázquez
Th 63 B 16 II-488

Influence of TJ-II flexibility upon ECRH.
First author: F. Castejón et al.
Th 64 B 17 II-489

Ideal interchange stability boundaries for stellarator configurations.
First author: L. García
Th 65 B 18 II-493

Self-stabilization of ideal modes in a heliac.
First author: C. Alejaldre et al.
Th 66 **B 19*** II-497

Determination of Boozer magnetic coordinates.
First author: A. López Fraguas et al.
Th 67 B 20 II-501

Bootstrap currents in heliac TJ-II configurations.
First author: A. Rodríguez Yunta et al.
Th 68 B 21 II-505

Equilibrium and stability of high ι TJ-II configurations.
First author: A. López Fraguas et al.
Fr 55 B 22 II-509

A general theory of LMFP neoclassical transport in stellarators.
First author: C.D. Beidler
Fr 56 B 23 II-513

* This paper will also be presented orally on Tuesday 26 June at 15.10 hrs.

On the edge structure of the W VII-AS stellarator.
First author: F. Rau et al.
Fr 57 B 24 II-517

Physics studies for the H-1 heliac.
First author: B.D. Blackwell et al.
Fr 58 B 25 II-521

Study of plasma equilibrium currents in an 1=3 torsatron.
First author: V.N. Kalyuzhnyj et al.
Fr 59 B 26 II-525

Impurity flux reversal in 1=2 torsatrons using RF heating.
First author: D.L. Grekov et al.
Fr 60 B 27 II-529

C. ALTERNATIVE MAGNETIC CONFINEMENT SCHEMES

Ion temperature measurements on the ETA-BETA II RFP.
First author: L. Carraro et al.
Tu 53 **C 1*** II-533

Carbon emission measurements on the RFP ETA-BETA II.
First author: M.E. Puiatti et al.
Tu 54 C 2 II-537

Shell gap modification and limiter insertion in the REPUTE-1 RFP.
First author: S. Shinohara et al.
Tu 55 C 3 II-541

Observations of high energy electrons in TPE-1RM15 reversed field pinch.
First author: Y. Yagi et al.
Tu 56 C 4 II-545

Coherent soft X-ray oscillations and magnetic flux regeneration in the REPUTE-1 RFP.
First author: Y. Shimazu et al.
Tu 57 C 5 II-549

Impurity ion temperature and rotational velocity observations in the HBTX1C RFP.
First author: R.A. Bamford et al.
Tu 58 C 6 II-553

Ion heating and confinement in the HBTX1C Reversed Field Pinch.
First author: P.G. Carolan et al.
Tu 59 **C 7**** II-557

Ion power loss in the HBTX1C Reversed Field Pinch.
First author: K.J. Gibson et al.
Th 69 C 8 II-561

RFP plasma resistance following laser ablation of carbon.
First author: B. Alper et al.
Th 70 C 9 II-565

Particle confinement in the HBTX1C Reversed Field Pinch.
First author: M.J. Walsh et al.
Th 71 C 10 II-569

High current density toroidal pinch discharges with weak toroidal fields.
First author: J.R. Drake et al.
Th 72 C 11 II-573

* This paper will also be presented orally on Thursday 28 June at 13.30 hrs.
** This paper will also be presented orally on Thursday 28 June at 13.50 hrs.

Relaxation, reconnection and the MHD dynamo.
First author: D.A. Kitson et al.
Th 73 C 12 II-577

Magnetic and electrostatic fluctuation measurements on the ZT-40M reversed field pinch.
First author: K.F. Schoenberg et al.
Th 74 C 13 II-581

Finite element analysis of helically symmetric equilibria.
First author: T. Honma et al.
Th 75 C 14 II-585

MHD stability of a plasma with anisotropic component in the rippled magnetic field.
First author: V.V. Arsenin
Tu 60 C 15 II-589

Hot electron plasmas instabilities in open traps OGRA-4 and OGRA-4K.
First author: M.I. Belavin et al.
Tu 61 C 16 II-593

Self organization of wave coupling at SK/CG-1 machine and conceptual design of SK/CG-2.
First author: S. Sinman et al.
Tu 62 C 17 II-597

FRC: TC-I machine results.
First author: M. Machida et al.
Tu 63 C 18 II-601

Study of an FRC with n=1 external perturbations.
First author: B.A. Nelson et al.
Tu 64 C 19 II-605

Optimization of pulse plasma production in Z-pinch systems.
First author: L.I. Rudakov et al.
Tu 65 C 20 II 609

Extrap L-1 experimental stability.
First author: J. Scheffel et al.
Tu 66 C 21 II-610

Dense plasma heating in a mirror trap during injection of 100 kJ microsecond electron beam.
First author: A.V. Burdakov et al.
Th 76 C 22 II-614

On possibility of creating MHD-stable plasma distribution in axisymmetric paraxial mirror.
First author: S.V. Kuz'min et al.
Th 77 C 23 II-618

Magnetic and Langmuir probe measurements in the SPHEX spheromak.
First author: D.A. Kitson et al.
Th 78 C 24 II-622

Magnetic field configuration of FBX-II spherical torus.
First author: M. Irie et al.
Th 79 C 25 II-626

Correlation between magnetic tearing and X-ray emission in coaxial discharges.
First author: H.M. Soliman et al.
Th 80 C 26 II-630

Specific operational modes of high-current pinch discharges.
First author: M. Sadowski et al.
Th 81 C 27 II-634

Field-reversed configurations: a search for a viable reactor option.
First author: M. Heindler et al.
Th 82 C 28 II-638

Self-similar dynamics of fiber initiated high-density Z-pinch.
First author: M.A. Liberman et al.
Fr 61 C 29 II-639

Improved understanding of current drive and confinement in spheromaks.
First author: R.M. Mayo et al.
Fr 62 C 30 II-643

Diffusion-driven currents in a Z-pinch.
First author: B. Lehnert
Fr 63 C 31 II-647

Passage of powerful current pulses through plasma layer.
First author: L.E. Aranchuk et al.
Fr 64 C 32 II-651

New spectroscopic results from EXTRAP-T1 plasma.
First author: J.H. Brzozowski et al.
Fr 65 C 33 II-655

Compression, heating and fusion in dynamic pinches stabilized by an axial magnetic field.
First author: M.A. Liberman et al.
Fr 66 C 34 II-659

The dense Z-pinch project at Imperial College.
First author: M.G. Haines et al.
Fr 67 C 35 II-663

D. MAGNETIC CONFINEMENT THEORY AND MODELLING

Turbulent drift of electrons across a magnetic field: the effect of an average electric field.
First author: M.B. Isichenko et al.
Tu 98 D 1 II-667

Anomal diffusion in plasmas across the magnetic field in approaching of strong turbulence.
First author: A.B. Arutiunov et al.
Tu 99 D 2 II-671

Average magnetic surfaces in TBR-1 tokamak.
First author: S.J. de Camargo et al.
Tu 100 D 3 II-675

Suppressing effect of electrostatic waves on drift wave instability.
First author: Yongxiang YIN
Tu 101 D 4 II-679

Drift dissipative instabilities in a two electron temperature plasma.
First author: M. Bose et al.
Tu 102 D 5 II-684

Effects of ripple losses on fusion alpha particle distributions.
First author: G. Kamelander
Tu 103 D 6 II-685

Stationary spectra of short-wave low-frequency fluctuations in a finite-beta plasma.
First author: P.P. Sosenko et al.
Tu 104 D 7 II-686

The effect of magnetic field perturbations on the numerically derived diffusion coefficient for the fast alpha particles.
First author: E. Bittoni et al.
Tu 105 D 8 II-687

On diffusion of magnetic field lines.
First author: D.F. Düchs et al.
Tu 106 D 9 II-691

Toroidal ion temperature gradient driven weak turbulence.
First author: N. Mattor et al.
Tu 107 **D 10*** II-695

On self-consistent distribution function of high-energy alpha particles in axisymmetric tokamak.
First author: V.A. Yavorskij et al.
Tu 108 D 11 II-699

* This paper will also be presented orally on Thursday 28 June at 14.10 hrs.

Magnetic island self-sustainment by finite Larmor radius effect.
First author: M. Hugon et al.
Tu 109 D 12 II-703

The long wavelength limit of the ion-temperature gradient mode in tokamak plasmas.
First author: F. Romanelli et al.
Tu 110 D 13 II-707

Solitary vortex solution of nonlinear η_i-mode equations.
First author: F. Romanelli et al.
Tu 111 D 14 II-711

Neoclassical transport calculations for "linear" MHD equilibria.
First author: H. Werthmann et al.
Tu 112 D 15 II-715

Diffusion of ions in presence of nearly overlapping magnetic islands.
First author: J.T. Mendonça et al.
Th 93 D 16 II-719

Toroidal η_i-mode turbulence with collisional trapped electron effects.
First author: A. Jarmén et al.
Th 94 D 17 II-723

The anomalous resistivity in the neutral sheet of the magnetotail.
Guilding center theory in the reversed magnetic geometry.
First author: Jian-lin MU et al.
Th 95 D 18 II-727

Specific edge effects on turbulence behaviour.
First author: L. Laurent et al.
Th 96 D 19 II-728

Ripple induced stochastic diffusion of trapped particles in tokamak reactors.
First author: J-P. Roubin et al.
Th 97 D 20 II-732

Microtearing modes.
First author: X. Garbet et al.
Th 98 D 21 II-736

Modelling of improved confinements in tokamaks.
First author: S.I. Itoh et al.
Th 99 D 22 II-740

The effect of the radial electric field on the L-H mode transition.
First author: M. Tendler et al.
Th 100 D 23 II-744

A fast method for simulating α-particle orbits in tokamaks.
First author: W.D. D'haeseleer
Th 101 D 24 II-748

The neoclassical effects on resistive MHD modes in general toroidal geometry.
First author: Duk-in Choi et al.
Th 102 D 25 II-752

Low frequency electrostatic instabilities in a toroidal plasma with a hot ion beam.
First author: M. Liljeström
Th 103 D 26 II-756

Radiation-induced η_e-modes.
First author: P.K. Shukla et al.
Th 104 D 27 II-760

Ionization and charge exchange effects on dissipative drift modes in an edge tokamak plasma.
First author: D.K. Morozov et al.
Th 105 D 28 II-764

Equilibrium beta limit and alpha-particle containment in stellarators as a function of their aspect ratio.
First author: F. Alladio et al.
Th 106 D 29 II-765

Collisionless two-fluid theory of toroidal η_i stability.
First author: J.P. Mondt et al.
Th 107 D 30 II-769

Modelling of transport in stochastic magnetic field regions.
First author: M.A. Hellberg et al.
Th 108 D 31 II-773

Simplified models for radiational losses calculation in a tokamak plasma.
First author: A.B. Arutiunov et al.
Tu 113 D 32 II-777

Physical accuracy estimate of global energy confinement scaling laws for tokamaks.
First author: A.N. Chudnovskij et al.
Tu 114 D 33 II-781

Transport model of canonic profiles for ion and electron temperatures in tokamaks.
First author: Yu.N. Dnestrovskij et al.
Tu 115 D 34 II-785

Plasma periphery influence on plasma core confinement under auxiliary heating.
First author: S.I. Krasheninnikov et al.
Tu 116 D 35 II-789

Current density and energy transport in high temperature plasmas.
First author: B. Coppi et al.
Tu 117 D 36 II-793

Unified physical scaling laws for tokamak confinement.
First author: J.P. Christiansen et al.
Tu 118 D 37 II-797

Assessment of transport models on the basis of JET ohmic and L-mode discharges.
First author: Ch. Sack et al.
Tu 119 D 38 II-801

A quantitative assessment of ∇T_i-driven turbulence theory based on JET experimental data.
First author: F. Tibone et al.
Tu 120 D 39 II-805

Transport of scrape-off layer plasma in toroidal helical system.
First author: K. Itoh et al.
Tu 121 D 40 II-809

Sensitivity of ignition conditions to plasma parameters for a compact tokamak.
First author: G. Cenacchi et al.
Tu 122 D 41 II-813

Studies of burn control for ITER/NET.
First author: H. Persson et al.
Tu 123 D 42 II-817

On tearing mode stabilization by local current density perturbations.
First author: E. Westerhof
Fr 97 **D 43*** II-821

Implementation of scaling laws in 1-1/2-d transport codes and applications to the ignition spherical torus.
First author: A. Nicolai et al.
Fr 98 D 44 II-825

Simulation of density profile peaking and energy and particle transport in the IOC regime.
First author: G. Becker
Fr 99 D 45 II-829

Unified χ_e scaling for the ohmic, L and intermediate regimes of ASDEX.
First author: G. Becker
Fr 100 D 46 II-833

Changes in the density profile due to the m=2 tearing mode in ASDEX.
First author: M.E. Manso et al.
Fr 101 D 47 II-837

Determination of off-diagonal transport coefficients from particle and power balance analysis.
First author: O. Gruber et al.
Fr 102 **D 48**** II-841

* This paper will also be presented orally on Thursday 28 June at 14.50 hrs.
** This paper will also be presented orally on Thursday 28 June at 15.10 hrs.

Thermal bifurcation and stability of an edge diverted plasma.
First author: H. Capes et al.
Fr 103 D 49 II-845

On bootstrap current enhancement by anomalous electron-electron collisions.
First author: A. Nocentini
Fr 104 D 50 II-849

Direct derivation of neoclassical viscosity coefficients in tokamaks.
First author: J.D. Callen et al.
Fr 105 D 51 II-853

Tokamak density profiles associated with vanishing entropy production.
First author: E. Minardi
Fr 106 D 52 II-857

Discrete Alfvén waves in cylindrical plasma: arbitrary beta and magnetic twist.
First author: H. Shigueoka et al.
Th 109 D 53 II-861

Three wave interactions in dissipative systems.
First author: J. Teichmann et al.
Th 110 D 54 II-864

Stationary states with incompressible mass flow in ideal MHD.
First author: U. Gebhardt et al.
Th 111 D 55 II-868

Determination of the plasma current density profile in a tokamak from magnetic and polarimetric measurements.
First author: J. Blum et al.
Th 112 **D 56*** II-872

New evaluation of the fusion cross-sections.
First author: H.-S. Bosch et al.
Th 113 D 57 II-873

The relaxation in two temperature plasma.
First author: I.F. Potapenko et al.
Th 114 D 58 II-877

A multiple timescale derivative expansion method applied to the Fokker-Planck equation for the description of plasma relaxation and turbulent transport.
First author: J.W. Edenstrasser
Th 115 D 59 II-881

Equilibria and dynamics of a fusion reactor plasma.
First author: H. Wilhelmsson
Th 116 D 60 II-885

* This paper will also be presented orally on Thursday 28 June at 14.30 hrs.

Numerical simulation of the internal kink m = 1 in tokamak.
First author: H. Baty et al.
Th 117 D 61 II-889

Thermal plasma core instability.
First author: A.B. Arutiunov et al.
Th 118 D 62 II-893

Numerical simulation of the tearing-mode in tokamak with non-circular cross section. New approach to study nonlinear evolution of resistive helical modes.
First author: Yu.N. Dnestrovskij et al.
Th 119 D 63 II-894

Stabilisation of drift-tearing modes at the breakdown of the constant-ψ approximation.
First author: F. Porcelli et al.
Th 120 D 64 II-898

On the existence of a Benard-like convective instability in the sawtooth evolution.
First author: F. Spineanu et al.
Th 121 D 65 II-902

Global, resistive stability analysis in axisymmetric systems.
First author: A. Bondeson et al.
Th 122 D 66 II-906

Alpha-particle driven MHD instabilities in ignited tokamaks.
First author: C.Z. Cheng
Th 123 D 67 II-910

To the question of adiabatic R-compression in tokamak.
First author: N.N. Gorelenkov et al.
Th 124 D 68 II-914

Magnetic field structure at the onset of sawtooth relaxations.
First author: J.T. Mendonça et al.
Fr 107 D 69 II-918

The m = 1 internal kink mode in a rotating tokamak plasma with anisotropic pressure.
First author: H.J. de Blank
Fr 108 D 70 II-919

Interaction of resonant magnetic perturbations with rotating plasmas.
First author: T.C. Hender et al.
Fr 109 D 71 II-923

The effect of the plasma shape on the accessibility of the second stability regime.
First author: Oh Jin KWON et al.
Fr 110 D 72 II-927

Global ideal MHD stability of 3D plasmas with pseudo-vacuum treatment for free-boundary modes.
First author: U. Schwenn et al.
Fr 111 D 73 II-931

Transition between resistive kink and Kadomtsev reconnection.
First author: K. Lerbinger et al.
Fr 112 D 74 II-935

Tearing mode stabilization by energetic trapped ions.
First author: D. Edery et al.
Fr 113 D 75 II-938

Asymptotic theory of the non-linearly saturated m = 1 mode in tokamaks with q(0) < 1.
First author: A. Thyagaraja et al.
Fr 114 D 76 II-942

Large gyroradius m = 1 Alfvén modes and energetic particles.
First author: T.J. Schep et al.
Fr 115 D 77 II-946

Tearing modes in high-S plasmas.
First author: A. Voge
Fr 116 D 78 II-950

Influence of triangularity and profiles on ideal-MHD beta limits for NET.
First author: C.G. Schultz et al.
Fr 117 D 79 II-954

Influence of an X-point and its poloidal location on the ideal MHD stability of a quasi-circular tokamak.
First author: A. Roy et al.
Fr 118 D 80 II-958

Simulation of MHD activity during density limit disruptions in JET.
First author: R. Parker et al.
Fr 119 D 81 II-962

Effect of sheared toroidal plasma flows on equilibrium and stability of tokamaks.
First author: A. Sen et al.
Fr 120 D 82 II-966

Alpha containment, heating, and stability in the IGNITEX experiment.
First author: R. Carrera et al.
Fr 121 D 83 II-970

E. HEATING BY NEUTRAL BEAM INJECTION

A one dimensional volume ion source model.
First author: D.J. Mynors
Mo 72 E 1 III-974

Surface effects in D^- ion sources for neutral beam injection.
First author: R.M.A. Heeren et al.
Mo 73 E 2 III-978

Present status of the design of a DC low-pressure, high-yield D^- source.
First author: W.B. Kunkel et al.
Mo 74 E 3 III-979

Cascade arc hydrogen source for plasma neutralizers.
First author: D.C. Schram et al.
Mo 75 E 4 III-983

F. RF HEATING

Trapped and passing ion transport in ICRH tokamak plasmas.
First author: M.V. Osipenko et al.
Mo 44 F 1 III-987

Automic FMS mode tracking during ICRH in TO-2 tokamak.
First author: I.A. Kovan et al.
Mo 45 F 2 III-991

Studies of mode conversion physics for waves in the ion cyclotron range of frequences.
First author: G.J. Morales et al.
Mo 46 F 3 III-995

Ballistic-wave analysis of gyroresonant heating.
First author: A.N. Kaufman et al.
Mo 47 F 4 III-999

Edge absorption of fast wave due to Alfvén resonance and wave nonlinearity in ICRH.
First author: J.A. Heikkinen et al.
Mo 48 F 5 III-1003

D-He^3 fusion yield in higher harmonic ICRF heated plasma.
First author: M. Yamagiwa et al.
Mo 49 F 6 III-1007

Theoretical analysis of higher harmonic ICRF heating in JT-60.
First author: K. Hamamatsu et al.
Mo 50 F 7 III-1011

^{3}He-D fusion studies and α-particle simulations using MeV ions created by ICRH in the JET tokamak.
First author: D.F.H. Start et al.
Mo 51 **F 8*** III-1015

Fast ion orbit effects in high power ICRH modulation experiments in the JET tokamak.
First author: D.F.H. Start et al.
Mo 52 F 9 III-1019

Analysis of ICRF coupling and heating in CIT and JET.
First author: J.E. Scharer et al.
Mo 53 F 10 III-1023

Studies on the distribution function of minority ions under ICRF wave heating.
First author: Duk-in Choi et al.
Mo 54 F 11 III-1027

* This paper will also be presented orally on Monday 25 June at 13.45 hrs.

Parasitic coupling of the fringing fields of an ion-Bernstein wave antenna.
First author: S.C. Chiu et al.
Tu 42 F 12 III-1031

Mode coupling between I.C.R.F. waves propagating outside the $\underline{B}$-$\nabla\underline{B}$ plane.
First author: B.M. Harvey et al.
Tu 43 F 13 III-1035

An analysis of ridged waveguide for plasma heating by using integral equation method.
First author: T. Honma et al.
Tu 44 F 14 III-1039

Study of the neutron yield behaviour in ICRH and NBI heated discharges on TEXTOR.
First author: G.Van Wassenhove et al.
Tu 45 F 15 III-1040

Eigenfunctions of the anisotropic quasilinear Fokker-Planck equation.
First author: D. Lebeau et al.
Tu 46 F 16 III-1044

ICRF heating up to the 4.5 MW level on TFTR.
First author: J.E. Stevens et al.
Tu 47 **F 17*** III-1048

ICRF hydrogen minority heating in the boronized ASDEX tokamak.
First author: F. Ryter et al.
Tu 48 F 18 III-1052

Induction of parallel electric fields at the plasma edge during ICRF heating.
First author: M. Brambilla et al.
Tu 49 F 19 III-1056

Ion-cyclotron absorption of fast magnetosonic waves by cold minority ions in an open trap.
First author: V.E. Moyseenko et al.
Tu 50 F 20 III-1060

RF plasma heating in the gas-dynamics mirror trap.
First author: I.F. Potapenko et al.
Tu 51 F 21 III-1064

Experimental study of strong nonlinear wave phenomena during ICRH on TEXTOR.
First author: R.Van Nieuwenhove et al.
Tu 52 F 22 III-1068

Some features of ECRH in inhomogeneous magnetic fields.
First author: V.A. Zhil'tsov et al.
Mo 55 F 23 III-1072

* This paper will also be presented orally on Monday 25 June at 14.05 hrs.

Observation of "H"-like phenomena at the beginning phase of ECR-heating on T-10.
First author: A.V. Sushkov et al.
Mo 56 F 24 III-1076

Reasons for averaged electron-density limitation - Experimental study in T-10 and simulation.
First author: V.V. Alikaev et al.
Mo 57 F 25 III-1080

Optimization of break-down and of initial stage of discharge with ECH in T-10.
First author: V.V. Alikaev et al.
Mo 58 F 26 III-1084

Nonlinear heating by a spatially localized electron cyclotron wave.
First author: D. Farina et al.
Mo 59 F 27 III-1088

Power absorption and energy confinement during LH injection in ASDEX.
First author: R. Bartiromo et al.
Mo 60 F 28 III-1092

Scattering and localizability of ECH power in CIT.
First author: G.R. Smith
Mo 61 F 29 III-1096

Combined electron cyclotron ray tracing and transport code studies in the Compact Ignition Tokamak.
First author: M. Porkolab et al.
Mo 62 F 30 III-1100

Stochastic electron energy diffusion in electron cyclotron heating.
First author: R. Pozzoli et al.
Mo 63 F 31 III-1104

Calculated power deposition profiles during ECRH on the FTU tokamak.
First author: S. Cirant et al.
Th 47 F 32 III-1108

Microwave breakdown of the neutral gas around the EC resonance in high power transmission lines for ECRH.
First author: L. Argenti et al.
Th 48 F 33 III-1112

Ray tracing study of the second electron cyclotron harmonic wave absorption and current drive.
First author: S. Pešić et al.
Th 49 F 34 III-1116

High power mode-purity measurements on the 60 GHz transmission line for ECRH on RTP.

First author: A.G.A. Verhoeven et al.
Th 50 F 35 III-1117

ECRH sustained breakdown plasmas in RTP.
First author: R.W. Polman et al.
Th 51 F 36 III-1121

The electron temperature behaviour study in FT-I tokamak plasma heated by the ordinary and extraordinary ECRH waves.
First author: M.Yu. Kantor et al.
Th 52 F 37 III-1125

Electron-cyclotron heating in NET using the ordinary mode at down-shifted frequency.
First author: G. Giruzzi et al.
Th 53 F 38 III-1129

Recent electron cyclotron heating results on TEXT.
First author: B. Richards et al.
Th 54 F 39 III-1133

RF Alfvén wave heating of a high-beta plasma column.
First author: F.L. Ribe et al.
Mo 64 F 40 III-1137

Generation of fast magnetosonic waves in a mirror trap.
First author: A.G. Elfimov et al.
Mo 65 F 41 III-1141

Nonlinear transformation of Alfvén waves in a hot plasma.
First author: V.P. Minenko et al.
Mo 66 F 42 III-1145

Experimental studies of kenetic Alfvén waves on CT-6B tokamak.
First author: Daming ZHANG et al.
Mo 67 F 43 III-1149

Electron absorption of fast magnetosonic waves by TTMP in JET.
First author: F. Rimini et al.
Mo 68 F 44 III-1150

Ion Bernstein wave experiments and preliminary observations of Alfvén wave resonance in tokamak KT-5B.
First author: W. LIU et al.
Mo 69 F 45 III-1154

Edge-plasma heating via parasitic-torsional-mode excitation by Faraday-shielded ion-Bernstein-wave antennas.
First author: S. Puri
Mo 70 F 46 III-1158

Propagation absorption and particle dynamics of ion-Bernstein wave in tokamaks.
First author: A. Cardinali et al.
Mo 71 F 47 III-1159

Modelling of the interaction of energetic ions with lower hybrid waves on JET.
First author: E. Barbato
Fr 41 F 48 III-1163

Probe measurements of lower-hybrid wavenumber spectra in the ASDEX edge plasma.
First author: M. Krämer et al.
Fr 42 F 49 III-1167

Transition from electron- to ion-interaction of LH-waves in ASDEX.
First author: H.-U. Fahrbach et al.
Fr 43 F 50 III-1171

Alfvén wave heating in ASDEX.
First author: G.G. Borg et al.
Fr 44 F 51 III-1175

An experimental study of Alfvén wave heating using electrostatically shielded antennas in TCA.
First author: G.G. Borg et al.
Fr 45 F 52 III-1179

Acceleration of beam ions in simultaneous injection of NB and LH wave on JT-60.
First author: M. Nemoto et al.
Fr 46 F 53 III-1183

Stochastic heating of charged particles by two modes of plasma oscillations.
First author: V.S. Krivitaky et al.
Fr 47 F 54 III-1187

G. CURRENT DRIVE AND PROFILE CONTROL

On the filling of the "spectral gap" by particles in the process of a driven current generation.
First author: S.I. Popel et al.
Mo 76 G 1 III-1190

The effect of the induced RF current density profile during lower-hybrid current drive on the evolution of the q profile and sawteeth stabilization.
First author: M. Shoucri et al.
Mo 77 G 2 III-1191

The 3.7 GHz lower hybrid current drive system for the tokamak de Varennes.
First author: A. Hubbard et al.
Mo 78 G 3 III-1195

Effect of quasi-linear distortions on the LH-wave current drive in a reactor-tokamak.
First author: V.S Belikov et al.
Mo 79 G 4 III-1199

Parametric decay instabilities studies in ASDEX.
First author: V. Pericoli Ridolfini et al.
Mo 80 G 5 III-1203

Quasilinear theory for spatially delimited wave patterns.
First author: E. Canobbio et al.
Mo 81 G 6 III-1207

Parametric study on lower hybrid current drive efficiency for next step devices.
First author: H. Takase et al.
Tu 67 G 7 III-1211

Combined operation of pellet injection and lower hybrid current drive on ASDEX.
First author: F.X. Söldner et al.
Tu 68 G 8 III-1215

Transport effects on current drive efficiency and localisation.
First author: M. Cox et al.
Tu 69 G 9 III-1219

M=2 mode limit on lower hybrid current drive in ASDEX.
First author: H. Zohm et al.
Tu 70 G 10 III-1223

Evaporation rate of an hydrogen pellet in presence of fast electrons.
First author: B. Pégourié et al.
Tu 71 G 11 III-1227

Lower hybrid wave experiments in TORE SUPRA.
First author: M. Goniche et al.
Tu 72 G 12 III-1231

Modelling of plasma current ramp-up by lower hybrid waves: comparison with experiments and application to NET.
First author: J.G. Wégrowe et al.
Tu 73 G 13 III-1235

Numerical studies of an electron cyclotron current drive efficiency and the role of trapped particles.
First author: Yu.N. Dnestrovskij et al.
Mo 82 G 14 III-1239

Impact of source power spectrum on ECRH current drive efficiency.
First author: A.G. Shishkin et al.
Mo 83 G 15 III-1243

Electron cyclotron current drive and tearing mode stabilization in ITER.
First author: L.K. Kuznetsova et al.
Mo 84 G 16 III-1247

Three-dimensional Fokker-Planck analysis on RF current drive in tokamaks.
First author: A. Fukuyama et al.
Mo 85 G 17 III-1251

Linear evaluation of current drive in TJ-II.
First author: F. Castejón et al.
Mo 86 G 18 III-1255

Electron cyclotron current drive experiments on DIII-D.
First author: R.A. James et al.
Mo 87 G 19 III-1259

Investigation of electron cyclotron emission in the ASDEX tokamak during lower hybrid current drive and heating.
First author: K. Wira et al.
Mo 88 G 20 III-1263

Electron cyclotron current drive for $\omega < \omega_c$.
First author: A.C. Riviere et al.
Tu 74 G 21 III-1267

Current drive experiments at the electron cyclotron frequency.
First author: V. Erckmann et al.
Tu 75 **G 22*** III-1271

Non-inductive currents in W VII-AS: experimental results and theoretical modelling.
First author: U. Gasparino et al.
Tu 76 G 23 III-1275

Current drive by electron-cyclotron and fast waves in DIII-D.
First author: G. Giruzzi et al.
Tu 77 G 24 III-1279

* This paper will also be presented orally on Monday 25 June at 14.25 hrs.

Lower hybrid current drive in DITE.
First author: B. Lloyd et al.
Tu 78 **G 25*** III-1283

Coupling of the 2 x 24 waveguide grill at 2.45 GHz in ASDEX.
First author: F. Leuterer et al.
Tu 79 G 26 III-1287

Lower hybrid current drive efficiency at 2.45 GHz in ASDEX.
First author: F. Leuterer et al.
Tu 80 G 27 III-1291

Simulation of fast waves current drive by multi-loop antennae in ITER.
First author: V.L. Vdovin et al.
Mo 89 G 28 III-1295

A 1-2/2 D Eulerian Vlasov code for the numerical simulation of beat current drive in a magnetized plasma.
First author: M. Shoucri et al.
Mo 90 G 29 III-1299

High frequency current drive by nonlinear wave-wave interactions.
First author: S.J. Karttunen et al.
Mo 91 G 30 III-1303

Possibility of ion current drive by RF helicity injection.
First author: K. Hamamatsu et al.
Mo 92 G 31 III-1307

Development of fast-wave ICRF current drive systems at ORNL.
First author: R.H. Goulding et al.
Mo 93 G 32 III-1311

Current drive via Landau damping of kinetic Alfvén wave in toroidal geometry.
First author: A.G. Elfimov et al.
Mo 94 G 33 III-1315

RF current drive by a standing Alfvén wave in the R-O device as a possible effect of RF helicity injection.
First author: A.G. Kirov et al.
Mo 95 G 34 III-1319

Profile control with lower hybrid waves on ASDEX.
First author: F.X. Söldner et al.
Tu 81 **G 35**** III-1323

Tearing mode stabilization by local current density profiling in tokamak.
First author: M.P. Gryaznevich et al.
Tu 82 G 36 III-1327

* This paper will also be presented orally on Monday 25 June at 14.45 hrs.
** This paper will also be presented orally on Monday 25 June at 15.05 hrs.

Surface wave antenna for excitation of travelling fast magnetosonic or ion Bernstein waves in plasma.
First author: A.V. Longinov et al.
Tu 83 G 37 III-1331

Hard X-ray emission during 2.45 GHz LH experiments on ASDEX.
First author: A.A. Tuccillo et al.
Tu 84 G 38 III-1335

Neutral beam current drive with balanced injection.
First author: D. Eckhartt
Tu 85 G 39 III-1336

Absorption characteristics of 200 MHz fast wave in JFT-2M tokamak.
First author: Y. Uesugi et al.
Tu 86 G 40 III-1340

H. IMPURITY AND EDGE PHYSICS

Special phenomena of edge density fluctuations in HL-1 tokamak.
First author: Qingwei YANG et al.
Mo 96 H 1 III-1341

Influence of neutral injection inhomogeneity on tokamak edge plasma.
First author: M.Z. Tokar'
Mo 97 H 2 III-1345

Influence of the helical resonant fields on the plasma edge of TBR-1 tokamak.
First author: I.L. Caldas et al.
Mo 98 H 3 III-1349

Edge fluctuation studies in ATF.
First author: C. Hidalgo et al.
Mo 99 H 4 III-1353

Effect of limiter composition on Z_{eff} and recycling in JET.
First author: J.P. Coad et al.
Mo 100 **H 5*** III-1357

Charge exchange spectroscopy measurements of light impurity behaviour in the JET beryllium phase.
First author: H. Weisen et al.
Mo 101 H 6 III-1361

Retention of gaseous (Ar, He) impurities in the JET X-point configuration.
First author: G. Janeschitz et al.
Mo 102 H 7 III-1365

Modelling impurity control in the JET pumped divertor.
First author: R. Simonini et al.
Mo 103 H 8 III-1369

Scrape-off layer parameters at JET during density limit discharges.
First author: S. Clement et al.
Mo 104 H 9 III-1373

Temperatures and densities in the JET plasma boundary deduced from deuterium and beryllium spectra.

First author: M.F. Stamp et al.
Mo 105 H 10 III-1377

Formation of detached plasmas during high power discharges in JET.
First author: G.M. McCracken et al.
Mo 106 H 11 III-1381

* This paper will also be presented orally on Friday 29 June at 11.00 hrs.

An investigation into high ion temperatures in the JET plasma boundary.
First author: S.K. Erents et al.
Mo 107 H 12 III-1385

Edge plasma behaviour in the FT tokamak.
First author: V. Pericoli Ridolfini
Mo 108 **H 13*** III-1389

Scrape-off layer based model for the disruptive tokamak density limit and implications for next-generation tokamaks.
First author: K. Borrass
Mo 109 H 14 III-1393

Simulation of edge plasma and divertor conditions in NET/ITER.
First author: H.D. Pacher et al.
Mo 110 H 15 III-1397

Collector probe measurements of impurity fluxes in TEXTOR with molybdenum and graphite limiters.
First author: M. Rubel et al.
Mo 111 H 16 III-1401

Electron excitation coefficients for the continuous spectrum of deuterium.
First author: B.M. Jelenković et al.
Mo 112 H 17 III-1405

3d-Monte Carlo modelling of the neutral gas transport in pump limiters.
First author: A. Nicolai
Mo 113 H 18 III-1409

Radiation from impurities in JET limiter plasmas during the C and Be phases.
First author: K.D. Lawson et al.
Mo 114 H 19 III-1413

Modelling of carbon in the TFTR edge plasma.
First author: B.J. Braams et al.
Fr 68 H 20 III-1417

First-wall behavior in TFTR.
First author: C.S. Pitcher et al.
Fr 69 H 21 III-1419

Multi-species impurity accumulation phenomena in ASDEX.
First author: G. Fussmann et al.
Fr 70 H 22 III-1423

Power flow and electric current asymmetries in the ASDEX SOL.
First author: N. Tsois et al.
Fr 71 H 23 III-1427

* This paper will also be presented orally on Friday 29 June at 11.20 hrs.

Determination of impurity transport coefficients by sinusoidal modulated gas puffing.
First author: K. Krieger et al.
Fr 72 H 24 III-1431

Impurity transport and production in lower hybrid discharges in ASDEX.
First author: R. De Angelis
Fr 73 H 25 III-1435

Plasma edge behavior on the way to and at the density limit.
First author: K. McCormick et al.
Fr 74 H 26 III-1439

Thermoelectric currents in the scrape-off layer.
First author: R. Chodura
Fr 75 H 27 III-1443

Influence of plasma-neutral interactions on ALT-II pump limiter performance during NI heating at TEXTOR.
First author: R.A. Moyer et al.
Fr 76 H 28 III-1447

An analytical model for neutral and charged particles in closed pump limiter.
First author: M.Z. Tokar'
Fr 77 H 29 III-1448

Ergodized edge experiments in JFT-2M tokamak.
First author: T. Shoji et al.
Fr 78 H 30 III-1452

Edge turbulence and its possible suppression by velocity shear in TEXT.
First author: Ch.P. Ritz et al.
Fr 79 H 31 III-1456

A comparison of fluctuations and transport in the scrape-off layer of a limiter [TEXT] and divertor tokamak [ASDEX].
First author: R.D. Bengtson et al.
Fr 80 H 32 III-1460

Structure of density fluctuations in the edge plasma of ASDEX.
First author: A. Rudyj et al.
Fr 81 H 33 III-1464

Evaluation of neutral gas flux measurements in the ASDEX-divertor with respect to divertor-geometry and recycling.
First author: D. Meisel et al.
Fr 82 H 34 III-1468

A study of impurity transport in the TEXTOR plasma boundary.
First author: S.J. Fielding et al.
Fr 83 H 35 III-1472

Effects of boronisation on the plasma parameters in TCA.
First author: B. Joye et al.
Fr 84 H 36 III-1476

Pump limiter influence on the helium discharge parameters in TUMAN-3 tokamak.
First author: V.I. Afanasiev et al.
Fr 85 H 37 III-1480

I. DIAGNOSTICS

Tokamak T-10 soft X-ray imaging diagnostic.
First author: P.V. Savrukhin et al.
Mo 27 I 1 IV-1484

Measurement of neutral deuterium fluxes on T-10 periphery.
First author: E.L. Berezovskij et al.
Mo 28 I 2 IV-1488

Density fluctuation measurements on ATF using a two-frequency reflectometer.
First author: E. Anabitarte et al.
Mo 29 I 3 IV-1492

Measurements of deuteron density profiles in JET.
First author: W. Mandl et al.
Mo 30 I 4 IV-1496

First measurements of electron density profiles on JET with a multichannel reflectometer.
First author: R. Prentice et al.
Mo 31 **I 5*** IV-1500

A method for the determination of the total internal magnetic field in JET.
First author: L. Porte et al.
Mo 32 I 6 IV-1504

Current profile measurement using neutral He beam in JT-60 tokamak.
First author: H. Takeuchi et al.
Mo 33 I 7 IV-1508

Real time profiling of total radiation in the TJ-1 tokamak by a fluorescent detector.
First author: B.G. Zurro et al.
Mo 34 I 8 IV-1512

Ion temperature determination from neutron rate measurements during deuterium injection.
First author: B. Wolle et al.
Mo 35 I 9 IV-1516

Absolute determination of high neutron yields for ASDEX.
First author: R. Bätzner et al.
Mo 36 I 10 IV-1520

Plasma diagnostics in infrared and far-infrared range for Heliotron E.
First author: K. Kondo et al.
Mo 37 I 11 IV-1524

* This paper will also be presented orally on Friday 29 June at 10.00 hrs.

Neutral beam probe diagnostic at TEXTOR.
First author: E.P. Barbian et al.
Mo 38 I 12 IV-1528

Visible bremsstrahlung measurements on TEXTOR for the determination of Z_{eff} under different discharge and heating conditions.
First author: J. Ongena et al.
Mo 39 I 13 IV-1532

Electron density propagation on magnetic surface in T-10 during pellet injection.
First author: N.L. Vasin et al.
Mo 40 I 14 IV-1536

Measurements of ion cyclotron emission and ICRF-driven waves in TFTR.
First author: G.J. Greene et al.
Mo 41 I 15 IV-1540

Density fluctuation measurements from microwave scattering on TFTR.
First author: R. Nazikian et al.
Mo 42 I 16 IV-1544

Influence of neutron scattering on measured TFTR neutron profiles.
First author: J.D. Strachan et al.
Mo 43 I 17 IV-1548

Edge density X-mode reflectometry of RF-heated plasmas on ASDEX.
First author: R. Schubert et al.
Th 32 I 18 IV-1552

Measurement of poloidal rotation on ASDEX.
First author: J.V. Hofmann et al.
Th 33 I 19 IV-1556

Localized density measurements on ASDEX using microwave reflectometry.
First author: M.E. Manso et al.
Th 34 I 20 IV-1560

Tangential soft X-ray/VUV tomography on COMPASS-C.
First author: R.D. Durst et al.
Th 35 I 21 IV-1564

A new probe to determine the Mach number of plasma flow in a magnetized plasma.
First author: K. Höthker et al.
Th 36 I 22 IV-1568

Reflectometry observations of density fluctuations in Wendelstein VII-AS stellarator.
First author: J. Sanchez et al.
Th 37 I 24 IV-1572

On density and temperature fluctuations observed by ECE diagnostics in Wendelstein VII-AS stellarator.
First author: H.J. Hartfuss et al.
Th 38 I 25 IV-1576

Fast scanning fiber-multiplexer used for plasma-edge visible spectroscopy on TORE SUPRA.
First author: W.R. Hess et al.
Th 39 I 26 IV-1580

Fusion profile measurement on TORE SUPRA.
First author: G. Martin et al.
Th 40 I 27 IV-1584

First density fluctuations observations by CO_2 scattering in TORE SUPRA.
First author: C. Laviron et al.
Th 41 I 28 IV-1588

Turbulence studies in TJ-1 tokamak by microwave reflectometry.
First author: J. Sanchez et al.
Th 42 I 29 IV-1592

X-mode broadband reflectometric density profile measurements on DIII-D.
First author: E.J. Doyle et al.
Th 43 I 30 IV-1596

Strongly non-maxwellian electron velocity distributions observed with Thomson scattering at the TORTUR tokamak.
First author: C.J. Barth et al.
Th 44 I 31 IV-1600

Microturbulence studies on DIII-D via far infrared heterodyne scattering.
First author: R. Philipona et al.
Th 45 I 32 IV-1604

Ion temperature measurements at JET.
First author: H.W. Morsi et al.
Th 46 I 33 IV-1608

A simple and sensitive instrument for plasma electron temperature determination.
First author: Yu.V. Gott et al.
Tu 27 I 34 IV-1612

Determination of poloidal fields by the pecularities of elliptically polarised probe wave in tokamak.
First author: Yu.N. Dnestrovskij et al.
Tu 28 I 35 IV-1616

Space-time tomography problem for plasma diagnostic.
First author: Yu.N. Dnestrovskij et al.
Tu 29 I 36 IV-1620

Electron and ion tagging diagnostic for high temperature plasmas.
First author: F. Skiff et al.
Tu 30 I 37 IV-1624

Transient internal probe diagnostic.
First author: E.J. Leenstra et al.
Tu 31 I 38 IV-1628

On the possibility of laser diagnostics of anisotropically superheated electrons in magnetic fusion systems.
First author: A.B. Kukushkin
Tu 32 I 39 IV-1632

Collective scattering spectra with anisotropic distributions of fast ions and alpha particles.
First author: U. Tartari et al.
Tu 33 I 40 IV-1636

Feasibility study of bulk ion temperature measurement on JET by means of a collective scattering of a gyrotron radiation.
First author: F. Orsitto
Tu 34 I 41 IV-1640

On the possibilities of spectroscopic measurements of various electric fields and related plasma parameters for tokamak conditions.
First author: E. Oks
Tu 35 I 42 IV-1644

Modelling of non-thermal electron cyclotron emission during ECRH.
First author: V. Tribaldos et al.
Tu 36 I 43 IV-1648

Physics studies of compact ignition plasmas using neutron measurements.
First author: G. Gorini et al.
Tu 37 I 44 IV-1652

The multi-channel interferometer/polarimeter for the RTP tokamak.
First author: A.C.A.P.van Lammeren et al.
Tu 38 I 45 IV-1656

Application of function parametrization to the analysis of polarimetry and interferometry data at TEXTOR.
First author: B.Ph.van Milligen et al.
Tu 39 I 46 IV-1660

Feasibility of alpha particle diagnostics for the active phase of JET, using Charge Exchange Recombination Spectroscopy.
First author: G.J. Frieling et al.
Tu 40 I 47 IV-1664

Polarization rotation and ion Thomson scattering.
First author: D.A. Boyd
Tu 41 I 48 IV-1668

A possible electric field measurement by a molecular hydrogen beam.
First author: W. Herrmann
Fr 27 I 49 IV-1672

The limitations of measurements of the local wavenumber.
First author: A. Carlson et al.
Fr 28 I 50 IV-1676

Ion temperature measurements in the TCA tokamak by collective Thomson scattering.
First author: M. Siegrist et al.
Fr 29 I 51 IV-1680

Thomson scattering diagnostics development in FT-I tokamak for the electron temperature temporal variation measurements.
First author: M.Yu. Kantor et al.
Fr 30 I 52 IV-1684

In-beam study of $^{9}Be(\alpha\, n_1\, \gamma)^{12}C$ reaction, promising as fast alpha-particle diagnostics in tokamak plasmas.
First author: V.G. Kiptilyj et al.
Fr 31 I 53 IV-1688

A high resolution LIDAR-Thomson scattering system for JET.
First author: H. Fajemirokun et al.
Fr 32 I 54 IV-1692

Localization of fluctuation measurement by wave scattering close to a cut off layer.
First author: X.L. Zou et al.
Fr 33 I 55 IV-1693

Polarization of hard X rays, a contribution to the measurement of the non-thermal electron distribution function (L.H.C.D.).
First author: M. Hesse et al.
Fr 34 I 56 IV-1697

The Thomson scattering systems of TORE SUPRA. First results.
First author: J. Lasalle et al.
Fr 35 I 57 IV-1701

Differential electron-cyclotron wave transmission for investigation of a lower-hybrid fast tail in the reactor regime.
First author: R.L. Meyer et al.
Fr 36 I 58 IV-1705

Diagnostic potentialities of electron cyclotron waves in L.H. current drive experiments.
First author: G. Ramponi et al.
Fr 37 I 59 IV-1709

Feasibility of diagnostic of JET LHCD plasmas by means of X-ray crystal spectroscopy.
First author: F. Bombarda et al.
Fr 38 I 60 IV-1713

The JET time of flight neutral particle analyser.
First author: G. Bracco et al.
Fr 39 I 61 IV-1717

Project of magnetic fluctuation measurement by cross polarization scattering in the TORE SUPRA tokamak.
First author: M. Paume et al.

Fr 40 I 62 IV-1721

J. BASIC COLLISIONLESS PLASMA PHYSICS

To the theory of Jupiter's decametric S-emission.
First author: A.G. Boyev et al.
Mo 115 J 1 IV-1725

On a gas-dynamic description of scattering of a rapid electron cloud in a plasma.
First author: V.N. Mel'nik
Mo 116 J 2 IV-1729

Nonequilibrium spectra forming for relativistic electrons interacting with MHD-turbulence.
First author: A.E. Kochanov
Mo 117 J 3 IV-1733

Resonant absorption of MHD bulk waves via surface modes.
First author: V.K. Okretic et al.
Mo 118 J 4 IV-1737

Nonlinear transparency of underdense plasma layer under the effect of intense circularly-polarized electromagnetic wave.
First author: V.V. Demchenko
Mo 119 J 5 IV-1741

Formation and equilibrium of an electron plasma in a small aspect ratio torus.
First author: Puravi Zaveri et al.
Mo 120 J 6 IV-1745

Formation of vortices in a toroidal plasma.
First author: A.K. Singh et al.
Mo 121 J 7 IV-1749

Arbitrary-amplitude electron-acoustic solitons in a two electron component plasma.
First author: R.L. Mace et al.
Mo 122 J 8 IV-1750

The obliquely propagating electron-acoustic instability
First author: M.A. Hellberg et al.
Mo 123 J 9 IV-1754

Generation of extraordinary mode radiation by an electrostatic pump in a two electron temperature plasma.
First author: S. Guha et al.
Mo 124 J 10 IV-1758

Propagation of electromagnetic waves in a modulated density plasma.
First author: M. Lontano et al.
Mo 125 **J 11*** IV-1762

* This paper will also be presented orally on Monday 25 June at 16.00 hrs.

Laser wakefield acceleration in an external magnetic field.
First author: P.K. Shukla
Mo 126 J 12 IV-1766

Radiative energy transport in thermonuclear plasmas.
First author: S. Puri
Tu 87 J 13 IV-1770

Nonlinear excitation of P-polarized surface wave in anisotropic plasma layer.
First author: Sh.M. Khalil et al.
Tu 88 J 14 IV-1774

Non-linear coupling of drift modes in a quadrupole.
First author: J.A. Elliott et al.
Tu 89 J 15 IV-1778

A two-dimensional collisionless model of the single-ended Q-machine.
First author: S. Kuhn et al.
Tu 90 J 16 IV-1782

Ion-acoustic eigenmodes in a collisionless bounded plasma.
First author: S. Kuhn et al.
Tu 91 J 17 IV-1786

Plasma heating by a strong multimode laser field.
First author: R. Daniele et al.
Tu 92 J 18 IV-1790

Turbulence and fluctuation induced transport in a double plasma device.
First author: M.J. Alport et al.
Tu 93 J 19 IV-1794

Resonant four-wave mixing and phase conjugation in an unmagnetized plasma.
First author: N.C. Luhmann, Jr. et al.
Tu 94 J 20 IV-1798

Kinetic vortices in magnetized plasmas.
First author: A.G. Sitenko et al.
Tu 95 J 21 IV-1802

Electron-cyclotron waves in non-maxwellian, relativistic plasmas.
First author: F. Moser et al.
Tu 96 J 22 IV-1803

Ion cyclotron wave excitation by double resonance parametric coupling.
First author: A. Fasoli et al.
Tu 97 J 23 IV-1807

Ion wave excitation for the study of wave-induced transport.
First author: T.N. Good et al.
Fr 86 J 24 IV-1811

The sheath formation near an electron absorbing boundary.
First author: N. Jelić et al.
Fr 87 J 25 IV-1815

Kinetic description of nonequilibrium plasma fluctuations.
First author: O.D. Kocherga
Fr 88 J 26 IV-1819

On the role of anomalous resistivity in a dynamics of plasma switching.
First author: A.S. Kingsep et al.
Fr 89 J 27 IV-1820

Kinetic theory on Alfvén solitions in collisional plasmas.
First author: Chuan-Hong PAN et al.
Fr 90 J 28 IV-1824

Ion-acoustic rarefactive soliton in two-electron temperature plasma.
First author: V.K. Sayal et al.
Fr 91 J 29 IV-1828

Relativistic dispersion functions for anisotropic plasmas.
First author: M. Bornatici
Fr 92 J 30 IV-1832

Boundary Larmor radius effects.
First author: Jin LI et al.
Fr 93 J 31 IV-1836

Numerical solution of the Vlasov-Maxwell system in the heavy-ion fusion problems.
First author: O.V. Batishchev et al.
Fr 94 J 32 IV-1840

Nonstationary self-action of electromagnetic wave beams in the beat accelerator.
First author: L.A. Abramyan et al.
Fr 95 J 33 IV-1844

Self-interaction of the magnetohydrodynamic surface waves at the plasma-metal boundary.
First author: N.A. Azarenkov et al.
Fr 96 J 34 IV-1848

K. INERTIAL CONFINEMENT FUSION

Detection of SRS produced electron plasma waves by the use of enhanced Thomson scattering.
First author: E.J. Leenstra
Th 83 K 1 IV-1852

Measurements of mass ablation rate and ablation pressure in planar layered targets.
First author: F. Dahmani et al.
Th 84 K 2 IV-1856

Heavy-ion driver design for indirect-drive implosion experiments.
First author: R.C. Arnold et al.
Th 85 K 3 IV-1860

Nova Program at LLNL.
First author: D. Correll et al.
Th 86 K 4 IV-1861

Study of instabilities in long scalelength plasmas with and without laser beam smoothing techniques.
First author: O. Willi et al.
Th 87 K 5 IV-1864

Hydrodynamic behavior of the plasma ablation in laser-irradiated planar targets.
First author: D.P. Singh et al.
Th 88 K 6 IV-1867

Experimental studies on the mechanism of Mach wave generation.
First author: V. Palleschi et al.
Th 89 K 7 IV-1871

Evaluating KrF lasers for ICF applications.
First author: D.C. Cartwright et al.
Th 90 K 8 IV-1875

Second harmonic: a versatile diagnostic for laser interaction with underdense plasmas.
First author: D. Giulietti et al.
Th 91 K 9 IV-1876

Excitation of sound by electromagnetic pulse in a dense semi-infinite non-isothermal collisional plasma.
First author: V.I. Muratov et al.
Th 92 K 10 IV-1880

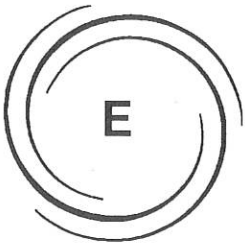

HEATING BY NEUTRAL BEAM INJECTION

A ONE DIMENSIONAL VOLUME ION SOURCE MODEL

D.J Mynors

University of Oxford, Dept. of Engineering Science,
Parks Road, Oxford.
Work carried out with the support of the
Euratom/UKAEA Fusion Association.

INTRODUCTION

With projects such as NET and ITER demanding high energy neutral beams for injection to provide current drive and possibly plasma heating, the low neutralisation efficiency of D^+ ions has resulted in the need to develop further an effective D^- ion source. Of the two main categories of ion source, surface plasma sources and volume ion sources, volume ion sources with magnetic filters are at present favoured for use in neutral injection systems.

The construction of a computer model of such a discharge should enhance the understanding of the processes involved, and so enable experimentalists to optimise the source construction and operation.

Previous attempts at ion source modelling have been described by Glasser and Smith[1] along with their own time dependent model.

Although the projects mentioned above require deuterium as their fuel the model described here will be based on hydrogen.

EXPERIMENTAL CONFIGURATION MODELLED

The volume ion source modelled, the layout shown in figure 1, has a cross sectional area of 550mm x 310mm and a depth of 210mm. At the back of the source there are 24 filaments which produce the ionising electrons. The filaments protrude 70mm into the source. The virtual transverse magnetic filter field, displayed in figure 2, is produced by re-orientating some of the wall magnets used for confinement. The purpose of this magnetic filter in a H^- ion source is to enhance the production of negative ions by cooling the plasma electrons down from approximately 5eV at the back of the source to less than 1eV near the extraction plane.

SETTING UP THE MODEL

The model is one dimensional and independent of time.

The region of the source that has been modelled is between the end of the filaments and the extraction plane, along a line through the centre of the source. The discharge was assumed to contain only ionising electrons, the resultant H^+ ions, plasma electrons and a background of stationary isothermal hydrogen molecules.

Each of the charged species was represented as a fluid, using the first three moments of the gyroaveraged Boltzmann equation. The equations used for each species were a modified version of those derived by Zawaideh[2] et al.

Continuity

$$n\frac{dV}{dx} + V\frac{dn}{dx} = S$$

Momentum

$$mnV\frac{dV}{dx} = \pm neE - n\frac{dT}{dx} - T\frac{dn}{dx} - mVS + R$$

Energy

$$Vn\frac{dT}{dx} + VT\frac{dn}{dx} = -3nT\frac{dV}{dx} + ST^s + mV^2 + Q$$

S Source of species
R Inter fluid friction including background gas
Q Inter fluid equipartition including background gas
T^S Temperature which source produced

These equations are for plasma transport parallel to a magnetic field and so provided no means of modelling the magnetic filter within the source. To overcome this the momentum equation has been re-written to include the expanded Lorentz term $ne(E_x + V_y \times B_z)$ in the place of the electric field term neE_x. The procedure used by Zawaideh et al. in deriving their equations was not followed when including the $V_y \times B_z$ term, so statements made about adiabatic invariants and small drift limits in their original paper may no longer be valid in the equations used here.

The y directional drift velocity has now been introduced into a supposedly one dimensional set of equations. The method used by Chapman and Cowling[3] to calculate the perpendicular diffusion coefficient was extended to the full momentum equations, after applying assumptions of zero y dimensional electric field and gradients, expressions for V_y for each species were obtained. V_y appears proportional to B_z as expected for classical transport.

Having made the assumption of zero y directional electric field no restraints are placed on the values of V_y[4]. This was overcome by imposing a maximum value of V_y for the plasma electrons equal to the sound speed, defined below, such that depending on the filter size and shape the transport across the filter changes from B^2 to a B dependence.

To solve the equations the plasma electrons and H^+ fluids were assumed to have the same number densities and drift velocities. The momentum equations for these two fluids were then summed to removed the electric field from the calculation. On rearranging the equations into a solvable form there were seven first order differential equations; these were then solved simultaneously using a variable step fourth order Kutter-Merson method.

i Initial boundary conditions

The starting point for the model, at the end of the filaments, was assumed to be a point of symmetry with drift velocities, density gradients and temperature gradients set equal to zero. The three energy equations, combined with the continuity equations, at x=0 produced simultaneous equations which were solved in conjunction with the zero dimensional source model[5] and provided the initial temperatures for each charged species. The hydrogen molecules were assumed to have a constant temperature of 0.13 eV.

ii Final boundary conditions

The final boundary condition for the plasma electrons and H^+ fluids was taken to be the adiabatic sound speed

$$C_s = \sqrt{\left(\frac{\gamma_e T_e + \gamma_+ T_+}{m_e + m_+}\right)}$$

Which was calculated from the assumption of one degree of freedom for each species. This boundary condition coincided with the singularity encountered on solving the equations. The ionising electron fluid equations were solved until their temperature was of the same order as the plasma electron temperature.

RESULTS

Figures 3 and 4 show a comparisons between the theoretical results and those obtained using Langmuir probes. It is obvious that the energy dissipation calculations are not as representative as the density calculations appear to be. Figures 5 and 6 show the predicted plasma drift velocity and H^+ ion temperature. Calculations for the ionising electrons predicted the following initial conditions

Operating conditions	Temperature	Density
1000A 100V 12mT	22.1eV	$1.2 \times 10^{18} m^{-3}$
500A 100V 10mT	20.8eV	$7.5 \times 10^{17} m^{-3}$
370A 100V 10mT	20.2eV	$5.5 \times 10^{17} m^{-3}$

The ionising electrons were included in the calculations for a few centimetres, before termination.

1 A.H Glasser and K.Smith, Comput.Phy. Commun. **54** 409 (1989)
2 E.Zawaideh,F.Najmabadi and R.W Conn
Phys. Fluids **29** 463 (1986)
3 S.Chapman and T.G Cowling
Mathematical Theory of Nonuniform Gases
(Cambridge U.P.,Cambridge, 1953).
4 A.A Temeev ICPIG X1X (1989)
5 M.B Hopkins and W.G Graham Vacuum **36** 873 (1986)

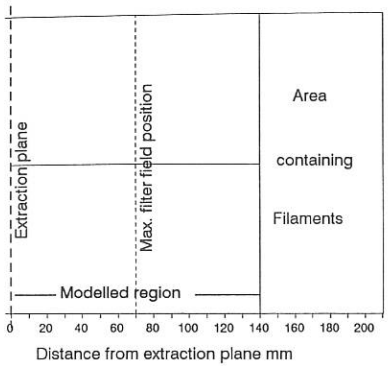

Figure 1 Source layout

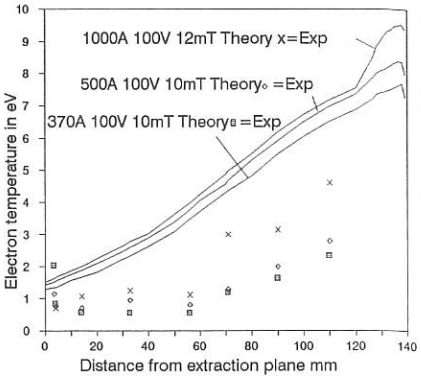

Figure 3 Electron temperature

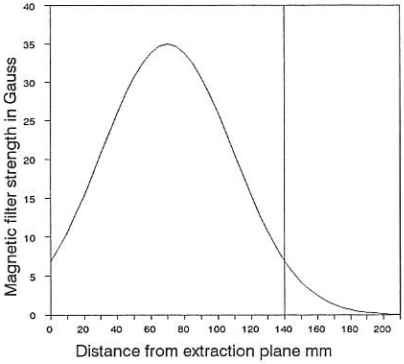

Figure 2 Magnetic filter

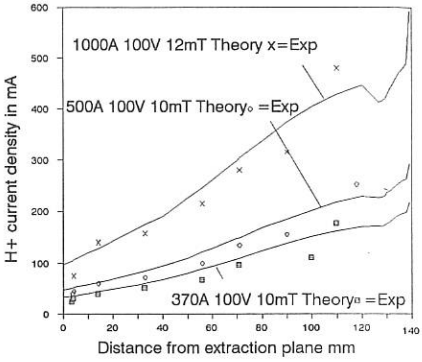

Figure 4 H+ current density

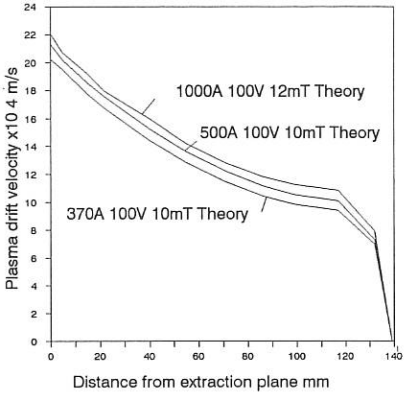

Figure 5 Drift velocity

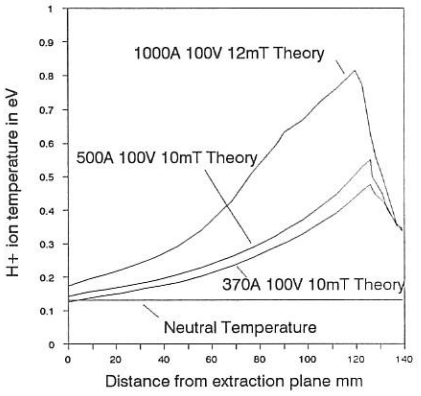

Figure 6 H+ ion temperature

SURFACE EFFECTS IN D⁻ ION SOURCES FOR NEUTRAL BEAM INJECTION

R.M.A. Heeren, D. Ciric, S. Yagura, H.J. Hopman and A.W. Kleyn

FOM-Institute for Atomic- and Molecular physics, Kruislaan 407, 1098 SJ Amsterdam.

The production of D^- ions inside a bucket ion source is commonly attributed to dissociative attachment of slow electrons to vibrationally excited deuterium molecules inside the plasma. Recent experiments have shown that also processes taking place at the wall of the source play an important role in the formation of D^- ions. Two of the processes which are currently being investigated are the dissociative recombination of deuterium ions and direct D^- formation on a low workfunction surface. [1], [2] and [3] For this purpose an existing bucket ion source has been modified in order to be able to change the surface to volume ratio. The effect of this surface to volume ratio on the negative ion formation will be presented. Moreover, the effects of seeding the source with barium, leading to a low work-function wall coverage, are currently being studied in detail. First experiments of this kind will also be discussed.

[1] C.F.A. van Os, P.W. van Amersfoort and J. Los, J. Appl. Phys. 64 (1988) 3863
[2] M. Bacal and D.A. Skinner, Comments At. Mol. Phys., Vol. 23, 6, (1990), 283
[3] J.R. Hiskes and A.M. Karo, AIP Conf. Proc. 111, 125, (1984)

PRESENT STATUS OF THE DESIGN OF A DC LOW-PRESSURE, HIGH-YIELD D^- SOURCE

C.F.A. van Os, K.N. Leung, A.F. Lietzke, J.W. Stearns, and W.B. Kunkel

Lawrence Berkeley Laboratory, University of California, Berkeley, USA.

The development of negative-ion sources is required for high energy (> 500 keV/u) Neutral Beam Injection (NBI) in future TOKAMAK experiments. Two schemes to produce negative ions are under development: volume production and surface conversion. The first method is based on the extraction of H^- or D^- ions formed in the bulk of a plasma (e.g. by dissociative attachment of electrons to vibrationally excited molecules). In the second method, the negative ions are produced via electron attachment while interacting with a negatively-biased, low work-function electrode (converter) immersed in a hydrogen or deuterium discharge.

Adequate volume production requires high molecule density and hence, a relatively high source filling pressure ($\geq$ 10 mTorr). This produces a high gas load for the accelerator column and premature stripping of the negative ions. The suppression of plasma electrons (extracted simultaneously with the negative ions) is also troublesome. Surface conversion which requires no molecular content in the plasma, allows the source filling pressure to be substantially lower (< 2 mTorr). In addition, negative ions produced at the converter surface are accelerated in the plasma sheath and are "self-extracted". Furthermore, these more-energetic negative ions make magnetic suppression of plasma electrons less problematic. Unfortunately, the transverse energy of the negative ions is higher.

This paper presents, an overview of ongoing experimental work at LBL to develop a reliable surface conversion source. The design criteria are; low source-filling pressure, low gas flow, dc operation and complete electron suppression at a delivered D^- current of 100 mA. This research effort can be subdivided into two areas: A study of the consequences of the type of plasma generator on the performance of the converter, and investigation of a full scale surface conversion source to define the operational characteristics. Earlier experiments at LBL have shown that a surface conversion source, delivering of the order of 1 A of negative ions, with a source pressure of 1 mTorr, is feasible.[1] The design was based on a cesiated molybdenum converter which introduced voltage holding problems in the accelerator structure. Recent experiments at the FOM (Fundamenteel Onderzoek der Materie) Institute for Atomic and Molecular Physics in Amsterdam, have demonstrated that a pure barium metal converter is capable of producing negative ions with a similar efficiency as a cesiated-molybdenum converter.[2,3] With this approach, the voltage holding problems are greatly reduced.

The work at LBL is focussed on the production of D^- ions for application to ITER, however, hydrogen is also used, since more experimental results are available for comparison. A schematic diagram of one of the experimental arrangements is shown in the insert of Fig. 1. It consists of a shielded converter support structure immersed in a multicusp plasma generator. The source geometry has been described elsewhere.[4] The system is operated with a 1 mm diameter tungsten filament mounted on a coaxial feedthrough. Behind the exit opening is a movable Faraday cup, which is equipped with a small mass spectrometer.

This arrangement is used for both hydrogen and deuterium to measure the negative ion yield as a function of the converter current, with a converter potential of -310 V and source filling pressure of 1 mTorr. These results are plotted in Fig. 4, and are discussed later. After installing a permanent magnet filter between the filament and the converter a remarkably different scaling of the negative ion yield versus converter current is observed. The negative ion yield is more or less proportional to the converter current with an unfiltered plasma, while the relationship is greater than linear for a filtered plasma. Details of this comparison can be found in Ref. 5 where this difference is attributed to *a difference in electron temperature and primary electron content of the discharge*. Fig. 1 also shows a typical mass-spectrum of the "self-extracted" negative ions, obtained for a converter potential of -170 V. It is found that *the oxygen contamination of the surface decreases the H^- yield*, however, this contamination could be reduced by argon discharge cleaning.

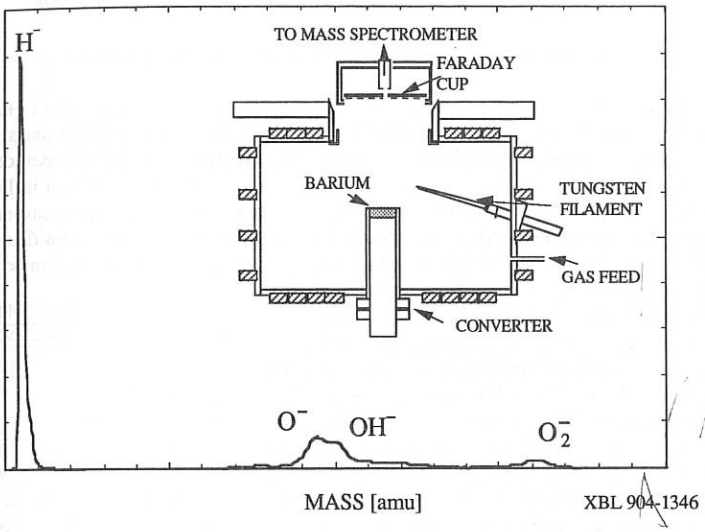

Fig. 1 The negative ion mass spectra. Shown in the insert is the schematic experimental arrangement. The converter is 5 cm^2 and made out of barium.

Fig. 2 shows the schematic configuration of the full scale surface conversion source. The deuterium plasma is generated by 8 tungsten filaments and confined by means of a permanent-magnet cage. The converter consists of a water-cooled copper disk upon which barium is deposited under high vacuum conditions. The converter is round (Ø = 6 cm) with a curved surface (R = 20 cm) to geometrically focus the negative ions formed at the surface. For the results presented here, the "self-extracted" negative ion current is collected near the focal point of the converter after passing through a 5 cm diameter exit aperture. This aperture has a positively biased insert and a transverse magnetic field (400 G-cm) to suppress most of the plasma ions and electrons.

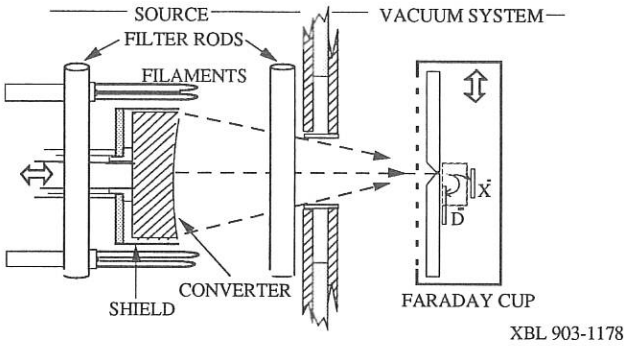

Fig. 2 The schematic arrangement of the source. X^- represent the impurity negative ions.

The negative ion current is measured with a large-area, movable, biased (+20 V) and screened (-45 V) Faraday cup. A small portion of the beam enters a small mass separator, which provides us an estimate of the impurity negative-ion content of the 'self-extracted' beam[6] and a measurement of the beam profile. A beam profile for D^- ions is shown in Fig. 3 for a converter potential of - 590 V. From this profile we estimate that the average transverse energy of the surface produced negative ions is around 7 eV. The negative ion yields for deuterium and hydrogen are plotted in Fig. 4 for low power levels (maximum converter current < 3 A). The impurity content for these measurments was less than 3 % for deuterium and less than 1.2 % for hydrogen.

The data of FOM is obtained with a barium converter of 12 cm^2 see Ref. 2 and the data of Culham is measured with a 3.14 cm^2 barium converter.[7] This graph illustrates an overall agreement in the observed H^- ion yields for this range of converter current densities. However,a remarkable difference is observed when one compares the D^- yield with the H^- yield. At present this behaviour is believed to be related to a higher impurity content and/or higher barium ion density in the deuterium discharge because of the higher sputtering rate of the converter. Both mechanism can cause for a reduction of the negative ion yield and will become more severe for higher arc power.

The highest yield achieved for DC operation at this time : 72 mA of D^- for a converter current of 5.6 A and voltage of -560 V. The source filling pressure is 1.3 mTorr, with a gas flow of 22 sccm, and the discharge current is 180 A at -70 V. The transverse

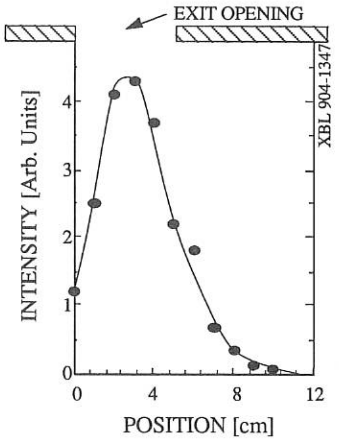

Fig. 3 D^- beam profile for a converter potential of 590 V.

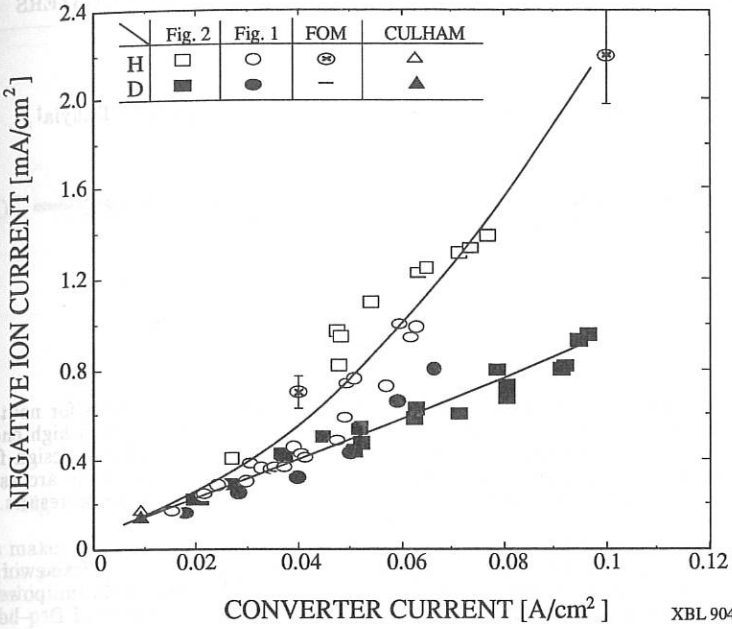

Fig. 4 Compilation of measured negative ion current densities, for hydrogen (open symbols) and for deuterium (closed sysmbols), versus converter current densities at LBL, FOM and Culham. The converter potential in all cases is ≈ 300 V and the source filling pressure 1 mTorr. Lines are drawn to guide the eye.

temperature of the beam estimated from the beam profile close to the focal point of the converter is less than 10 eV. The impurity content less than 3 %.

Daignostics are being set-up to measure i) the barium ion density in the discharge via spectrosopy, and ii) the work-function of the converter surface via photo emmission. This work was supported by the Director, Office of Energy Research, Office of Fusion Energy, Development and Technology Division, of the U.S. Department of Energy under contract No. DE-AC03-76SF00098

References

1 J.W. Kwan et al., Rev. Sci. Instrum. **57**, 831 (1986).
2 C.F.A. van Os, P.W. van Amersfoort and J. Los, J. Appl. Phys. **64**, 3863 (1988).
3 C.F.A. van Os, C. Leguijt, A.W. Kleyn and J. Los, SPIE's Symposium on Innovative Science and Technology (1061), 15-20 Jan 1989, Los Angeles, USA.
4 K.W. Ehlers and K.N. Leung, Appl. Phys. Lett. **38**, 287 (1981).
5 C.F.A. van Os, K.N. Leung, and W.B. Kunkel, submitted to Appl. Phys. Lett.
6 K.N. Leung and K.W. Ehlers, Rev. Sci. Instrum. **53**, 803 (1982).
7 C.F.A. van Os, A.W. Kleyn, L.M. Lea, A.J.T. Holmes, and P.W. van Amersfoort, Rev. Sci. Instrum. **60**, 539 (1989)

CASCADE ARC HYDROGEN SOURCE FOR PLASMA NEUTRALIZERS

D.C. Schram, P.M. Vallinga*, H.J. Hopman+, F.J. de Hoog, R.P. Dahyia‡, M.J. de Graaf, J.J. Beulens

Department of Physics, Eindhoven University of Technology
P.O. Box 513, NL–5600 MB Eindhoven

*KSEPL, Rijswijk
+NET–Team, München, BRD
‡Centre of Energy Studies, IIT, New Delhi, India

Abstract
Thermal plasmas offer a good possibility to obtain intense particle sources for neutralizers [1]. The principle is to produce a plasma at high pressure, since then a high energy efficiency and ionization degree can be reached. In this paper a conceptual design for a plasma neutralizer is presented and detailed numerical data on the cascade arc as the plasma source is given. Where available, these are verified with experimental results.

Introduction
In the present paper a new effective plasma source is discussed in the framework of neutralization of negative ion beams. Injection of 50 MW neutral beam power is considered in the next generation of tokamaks and plasma neutralization of D^- –beams could offer a significant gain in efficiency compared to the traditional gas neutralization. In a plasma neutralizer the electrons are most effective to strip the negative ion of its electron. Since the electron affinity of D^- is low (0.75 eV), a low electron temperature will suffice. Electric and magnetic fields have to be small to avoid degradation of the incoming beam brightness. Therefore a quiescent plasma with no currents and only buckettype magnetic fields for confinement will be the best line of approach. This requires effective plasma sources, which pair high ionization degree with low neutral flux and low power consumption. Similar demands are found in the field of plasma surface modification : here also a flux of particles (preferably ions) is needed with a low power flux and thus power consumption. For carbon and silicon deposition a cascade arc plasma source has been developed. In this paper, this source will be discussed for argon and hydrogen in the neutralizer context.

Neutralizer Concept
First, demands will be discussed shortly. The design of the neutralizer is as scetched in Fig. 1. A volume with dimensions 2.2x0.4x0.4 m (HxLxW) is filled with plasma from m sources at two sides with fluence Φ_i. The plasma will diffuse freely outwards with an anomaly factor of 4 compared to classical diffusion. In a buckettype confined geometry with a passive currentfree plasma in which no electric and magnetic fields exist this assumption seems to be conservative but needs experimental verification. The optimum target thickness depends slightly on the attainable ionization degree [2]. For an ionization degree $\alpha \sim 0.4$ a value of $n_eL \sim 2\ 10^{19}/m^2$ is optimum. The ambipolar diffusion time of deuterium atoms for the neutralization volume can be estimated as

$$\tau_{da} \simeq n_e L^2 \left(1 + \frac{1}{\alpha}\right) 2.5\ 10^{-23}\ \hat{T}^{-0.6},$$

in which n_eL is the effective target thickness, $\alpha = n_e/n_g$ the ionization degree and $\hat{T}$ the

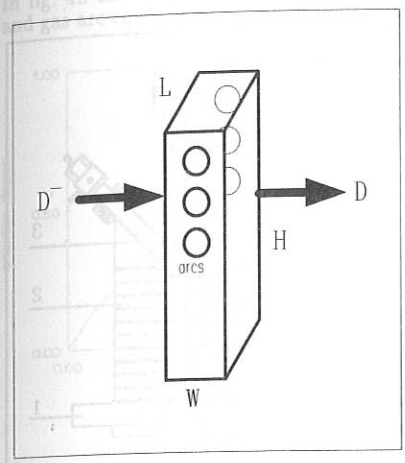

Fig. 1 plasmaneutralizer concept

temperature in eV. With this value and an anomaly factor of 4, a transversal dimension of 0.4 m and an electrontemperature of 0.5 eV we obtain

$$\tau_d = \tfrac{1}{4}\tau_{da} = 2 \cdot 10^{19} \cdot 0.4 \cdot (1.25) \cdot 2.5 \cdot 10^{-23} \cdot 1.5 \simeq 3\ 10^{-4}\,s$$

This is only a few acoustic transit times, so it seems a very realistic estimation. The fluence of m plasma sources should compensate the losses in the neutralizer according to $n_e(LxWxH)/\tau_d \simeq m\Phi_e$. With electron fluences of $\Phi_e = 5\ 10^{21}/s$ the number of sources should be 10.

Using hydrogen or deuterium in the plasma source the estimated consumed power for such a unit (including the power consumed by the pumps) is 600 kW. This compares favourably with the saved power because of the gain in efficiency (20%) of 50 MW. With argon feeding the diffuse losses in the neutralization volume are appreciable lower and no possibility of recombination exists. This makes the alternative of an argon plasma neutralizer attractive.

At this point the problem of creating a power saving plasma neutralizer in a quiescent recombining current free mode is essentially a problem of designing an effective and very bright particle source. Extensive work has been done on cascaded arc argon plasmas, both theoretical and experimental. Here we present a quasi–two–dimensional model. This model has been adapted for hydrogen and deuterium, and numerical data on these are also given.

Model

To describe the plasma, a model for a strongly flowing cascaded arc by Beulens [3] is used. In the approach adopted in this model the plasma is treated as a two–phase medium, which consists of heavy particles (neutral atoms and ions) and electrons. The model is developed for the predictions of a strongly flowing monoatomic cascade arc plasma. The flow is assumed to be compressible and strongly non–isothermal. The argon plasma is considered as singly ionized, locally quasi–neutral ($n_e \simeq n_i$) with local temperature non–equilibrium ($T_e \neq T_h$). Influence of wall friction is included. For the full description of this two–phase flow one needs to solve the mass, momentum and energy equations for both phases. However, due to the small electron mass, their momentum is neglected in comparison with the heavy particle momentum. Therefore a two–phase flow character is kept only with respect to the heavy particle and electron temperatures which are assumed to be different and described by separate energy equations. Ohmic heat input is consumed by electrons, which in frequent collisions heat and ionize the heavy particles.

The Cascade Arc

The cascade arc (Fig. 2) consists basically of an anode (1), a stack of insulated copper plates (2) and three cathodes (3). These components are all water cooled. The cathodes are 1 mm diameter tungsten thorium tips for currents up to 30 A per cathode. The cascade plates have an inner bore of 4 mm and a thickness of 5 mm. Typical operation conditions are a gas flow of 100 scc/sec and an arc current of 10 Amps per cathode. The

plasma has a temperature of about 1 eV. The pressure in the arc channel is between 0.1 and 1 bar. The thermal plasma is allowed to expand supersonically, through a hole in the anode plate of 4 mm diameter, into a vacuum vessel. Here the pressure is typical 1 Torr. The thought behind the cascaded arc is to constrict the plasma in the channel thermically, as the gas is cooled by the wall. This gives a very stable plasma.

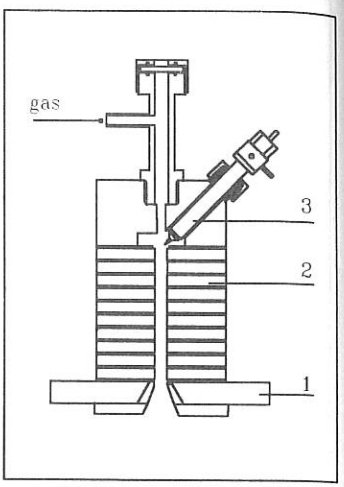

Fig. 2 cascade arc

Argon Neutralizer

We present results on the following conditions: arc current 50 A, flow = 200 scc/sec. For these settings experimental data by Kroesen [4] are available. Fig. 3a gives the ionization degree of the plasma. It appears to be approximately linear with the axial position. Fig. 3b shows the axial profile of electron and gas (heavy particle) temperatures. As can be seen, the electron temperature is nearly constant over the arc. The gas temperature relaxes towards the electron temperature but a noticeable temperature difference remains. Due to the expansion and acceleration of the plasma, temperature decreases at the end of the arc. There is good agreement between model and experiment.

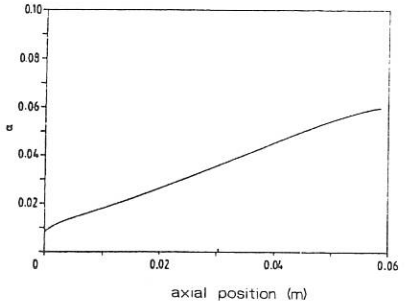

Fig. 3a axial profile of ionization degree

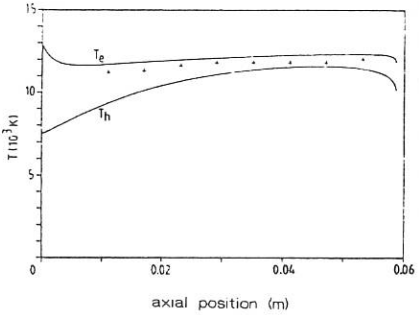

Fig. 3b electron and gas temperature. The + represent experimental data

Hydrogen or deuterium neutralizer

Calculations have been done on both hydrogen and deuterium. No significant differences between these two were found for ionization degree and plasma temperatures. This can be explained by the fact that ionization and dissociation are dominant in the energy balance. Ionization degree and temperatures are given for a gas flow of 100 scc/sec and a current of 95A. The arc lenght is in this case 11.8 cm. This longer arc gives a higher degree of ionization, at these plasma conditions $\alpha > 80\%$ at the end of the arc (fig. 4a).

In fig. 4b can be seen that, unlike the argon arc, within 1 cm temperatures of electrons and gas are equal. This is due to the much smaller mass of hydrogen.

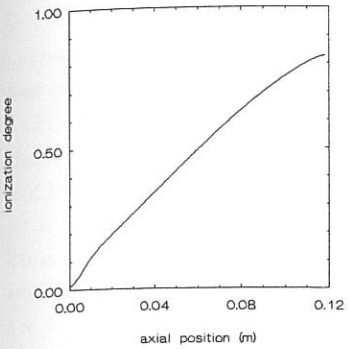

Fig. 4a ionization degree

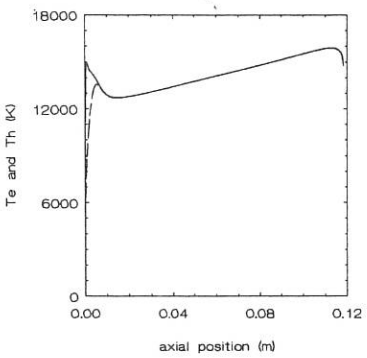

Fig. 4b electron (solid curve) and gas temperature

Concluding Remarks

According to Vallinga [1] the electron fluences from the presented cascade arc settings are $\Phi_e = 2\ 10^{20}$ for argon,

$\Phi_e = 4.8\ 10^{21}$ for deuterium,

so the calculations predict that when operated on deuterium, the electron fluence demands for a plasma neutralizer can be met with a cascade arc source at the presented settings. The argon source shows a much lower ionization degree than the deuterium source and seems less appropriate. However, this result was obtained with both a lower current (50 A for argon) and a shorter arc. As the ionization degree is almost proportional to the arc lenght, future work needs to be done on this.

Finally, we conclude that plasma neutralizers promise an effective method for neutralization of D^- –beams with an efficiency of approximately 80% compared to 60% for the traditional gas neutralizer.

References

[1] P.M. Vallinga, Cascaded arcs for plasma neutralizers, NET, internal report NET/88–145

[2] K.H. Berkner, R.V. Pyle, S.E. Savas and K.R. Stalder, Proc. 2–nd Int. Symp. on Production and Neutralization of Negative Hydrogen Ions and Beams, Brookhaven National Laboratory,BNL Report 51304, Upton NY USA(1980), p.291

[3] J.J. Beulens, G.M.W. Kroesen, H. de Regt, P.M. Vallinga and D.C. Schram, 9th Int. Symp. on Plasma Chem. (ISPC–9), Pugnochioso, Italy (1989)

[4] G.M.W. Kroesen, Ph. D. Thesis, Eindhoven University of Technology, The Netherlands (1986)

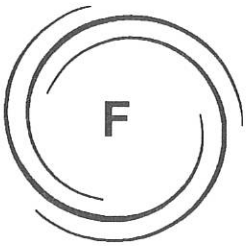

RF HEATING

F1

F1 ION CYCLOTRON RESONANCE HEATING

TRAPPED AND PASSING ION TRANSPORT IN ICRH TOKAMAK PLASMAS

M. V. Osipenko, R. V. Shurygin

I. V. Kurchatov Institute of Atomic Energy, Moscow, USSR

Nowdays most optimistic prognoses to attain thermonuclear parameters in tokamak are connected with the application of ICRF heating method as an additional heating. The experimental data analysis supports wide recognition of the inherent influence of ICRF waves injection on the tokamak plasmas transport properties. It is the aim of this study the consistent development of evolutionary quasihydrodynamic equations to describe particle, momentum and energy transport in the collisionless ICR heated plasmas. To do this we'll follow the procedure developed in [1,2] which based on Hamiltonian formalism and quasilinear diffusion equation in action $\vec{J}=(P,J,M)$ - angle $\vec{\theta}=(\varphi,\theta,\theta_g)$ variables

$$\frac{\partial f_o(\vec{J})}{\partial t} = \frac{\partial}{\partial \vec{J}} D \frac{\partial f_o(\vec{J})}{\partial \vec{J}} \qquad (1)$$

where $D=\sum_l \vec{l}\vec{l} |\delta H_l|^2 \pi\delta(l\vec{\Omega}-\omega)$ is the resonant diffusion tensor in action space. Tokamak magnetic field can be written in terms of flux coordinates (α,β,ζ) as $\vec{B}= \vec{B}_t+\vec{B}_p = \nabla\alpha\times\nabla\beta+\nabla\zeta\times\nabla\psi$, where $\alpha=B_o r^2/2$, β and ζ are poloidal and toroidal angles respectively, $\psi(\alpha)=\int \frac{d\alpha}{q(\alpha)}$ poloidal flux, $q=rB_t/RB_p$, r and $R=R_o+r\cos\beta$ - minor and major tori radii. Taking into account $\varepsilon=r/R << 1$ so that $B_p<<B_t$ henceforth we use $B\approx B_o(1-\varepsilon\cos\beta)$.

Hamiltonian of particle motion in tokamak magnetic field is given by $H_o=mv_\parallel^2/2+m\mu B$, $\mu=v_\perp^2/2B$; actions are defined by $P=mv_\parallel R - \frac{e}{c}\psi(\alpha)$, $J=\frac{e}{c}\oint \frac{d\beta}{2\pi}\alpha(\beta,\vec{J})$, $M=mv_\perp^2/2\Omega$, where $\Omega=eB/mc$. Frequencies $\Omega_\varphi=\partial H_o/\partial P$ and $\Omega_\theta=\partial H_o/\partial J$ so as φ,θ canonical angles expressions were calculated in [2]. To study ICRH probleme expressions for $\Omega_g=\partial H_o/\partial M$ and θ_g are necessary in case of untrapped ("u", $1<\kappa<\infty$) and trapped ("t" $0<\kappa<1$) particles respectively:

$$\Omega_g^u=\Omega_o(1-\varepsilon\langle\cos\beta\rangle_u), \quad \langle\cos\beta\rangle_u=2\kappa^2(\mathcal{E}(\bar{\kappa})/\mathcal{K}(\bar{\kappa})-1)+1,$$
$$\theta_g^u=\eta+\lambda_u \mathcal{Z}(y_u,\bar{\kappa}), \qquad (2)$$

$$\Omega_g^t=\Omega_o(1-\varepsilon\langle\cos\beta\rangle_t),\quad \langle\cos\beta\rangle_t=2\mathcal{E}(\kappa)/\mathcal{K}(\kappa)-1,$$
$$\theta_g^t=\eta+\lambda_t\mathcal{Z}(y_t,\kappa), \tag{3}$$

where $\kappa^2=[H_o-m\mu B_o(1-\varepsilon)]/2\varepsilon m\mu B_o$, $\bar\kappa=1/\kappa$, $\mathcal{E}(\kappa)$ and $\mathcal{K}(\kappa)$ are complete elliptic integrals, $\mathcal{Z}(y,\kappa)$ - Jacoby function, $\lambda_u=4\sigma\varepsilon\kappa qR\Omega_o/u_o$, $\lambda_t=4\varepsilon qR\Omega_o/u_o$, $y_u=\mathcal{K}(\bar\kappa)\theta^u/\pi$, $y_t=2\mathcal{K}(\kappa)\theta^t/\pi$, $u_o=2\sqrt{\varepsilon\mu B_o}$, $\sigma=\pm1$, $\eta=\int\Omega dt$ - gyrophase, $\Omega_o=eB_o/mc$.

In presence of waves Hamiltonian is : $H=H_o(\vec J)+\delta H(\vec J,\vec\theta)$. Using $\Phi=0$ calibration we have $\vec E=-\frac{1}{c}\frac{\partial\vec A}{\partial t}=i\frac{\omega}{c}\vec A$. Thus, $\delta H=-\frac{e}{c}\vec v\vec A=i\frac{e}{\omega}\vec v\vec E$, which for the wave field of the form $\vec E=(E_r,E_\perp,E_\parallel)\exp[i(k_\perp r+\frac{k_\perp v_\perp}{\Omega_o}\sin\eta+L\zeta-N\beta-\omega t)]$ and $\vec v_\perp=v_\perp(\vec e_r\cos\eta-\vec e_\perp\sin\eta)$ becomes $\delta H=i\frac{e}{\omega}[v_\parallel E_\parallel+v_\perp(E_r\cos\eta-E_\perp\sin\eta)]\exp(i\Delta)$, where $\Delta=k_\perp r-\omega t+k_\perp\rho\sin\eta+L\zeta-N\beta$. To proceed futher, we need to know Fourier transform of the perturbed Hamiltonian in $\vec\theta$ angles: $\delta H=\sum_{\vec l}\delta H_{\vec l}\exp(i\vec l\vec\theta)$, $\vec l=(l,-n,l_g)$, $\delta H_{\vec l}=\oint\frac{d\vec\theta}{(2\pi)^3}\delta H\exp[-i\vec l\vec\theta]$. Assuming $E_\parallel\ll E_r,E_\perp$ and using $\sin\frac{\beta^t}{2}=\kappa sn(y_t,\kappa)$ $\varphi^t\approx\zeta^t-q\beta^t$, $\sin\frac{\beta^u}{2}=sn(y_u,\bar\kappa)$, $\varphi^u\approx\zeta^u-q(\beta^u-\theta^u)$, [2], so as (2),(3) gives

$$|\delta H_{\vec l}|^2_{u,t}=\frac{c^2}{\omega^2}\frac{v_\perp^2}{2}|E_+J_{l_g-1}(k_\perp\rho)+E_-J_{l_g+1}(k_\perp\rho)|^2\delta_{l_L}|I_{u,t}|^2, \tag{4}$$

where $E_\pm=(E_r\pm iE_\perp)/2$, $J_l(x)$ is the Bessel function,

$$I_u=\frac{1}{2\mathcal{K}(\bar\kappa)}\int_0^{4\mathcal{K}(\kappa)}\exp(i[\gamma\arcsin(sny_u)]-\lambda_u\mathcal{Z}(y_u)+\frac{n\pi}{\mathcal{K}(\bar\kappa)}y_u])dy_u, \tag{5}$$
$$I_t=\frac{1}{4\mathcal{K}(\kappa)}\int_0^{2\mathcal{K}(\kappa)}\exp(i[\gamma\arcsin(\kappa sny_t)]-\lambda_t\mathcal{Z}(y_t)+\frac{n}{\mathcal{K}(\kappa)}y_t])dy_t, \tag{6}$$

$\gamma=2k_\parallel qR$, $k_\parallel=(Lq-N)/qR$. Exact calculation of integrals $I_{u,t}$ is not trivial, but if $\lambda_{u,t}\gg1$ and $\lambda_{u,t}\gg\gamma$ (which corresponds spectrum limitation $k_\parallel\ll\varepsilon/\rho$) then stationary phase method is applicable to obtain

$$|I_u|^2=\frac{\pi}{2\mathcal{K}(\bar\kappa)}\frac{1}{2\pi}\left|\frac{\langle\cos\beta\rangle_u}{qR\,k_n^u}\right|,\quad |I_t|^2=\frac{|\langle\cos\beta\rangle_t|}{16qR|k_n^t|[\kappa^2-1/2]^{1/2}\mathcal{K}(\kappa)}, \tag{7}$$

here $k_n^u=\frac{lq-n}{qR}$, $k_n^t=\frac{n}{2qR}$, and the resonance condition $l\Omega_\varphi-n\Omega_\theta+l_g\Omega_g=\omega$ have been used with $\Omega_\theta^u=\sigma(\kappa u_o/qR)(\pi/2\mathcal{K}(\bar\kappa))$, $\Omega_\varphi^u=q\Omega_\theta^u$, $\Omega_\theta^t=\sigma(u_o/2qR)(\pi/2\mathcal{K}(\kappa))$, $\Omega_\varphi^t\approx0$.

According to [2] the time evolution of some quantity

χ averaged over distribution function $\bar{\chi}=\int d^3v f_o \chi$ and over constant-α magnetic surface $\langle\bar{\chi}\rangle = (V')^{-1}\oint d\alpha d\beta d\zeta \left[\sqrt{g}\bar{\chi}\delta(\alpha-\bar{\alpha})\right.$, where f satisfies Eq.(1), can be described by a radially lokal transport law

$$\frac{\partial\langle\chi\rangle}{\partial t} - \langle\frac{\partial\bar{\chi}}{\partial t}\rangle + \frac{1}{r}\frac{d}{dr} r\, \Gamma[\chi] = U[\chi], \qquad (8)$$

here, $\Gamma = \sum_i \Gamma_i$, $U = \sum_i U_i$,

$$\Gamma_i[\chi] = -\oint \frac{d\vec{J}}{m^3 V' r_o B_o} D_o \vec{I}\frac{\partial f}{\partial \vec{J}} \circ \oint d^3\vec{\theta}\ \chi\ a_i\ \delta(\alpha-\bar{\alpha}), \qquad (9)$$

$$U_i[\chi] = -\oint \frac{d\vec{J}}{m^3 V'} D_o \vec{I}\frac{\partial f}{\partial \vec{J}} \circ \oint d^3\vec{\theta}\ \vec{I}\frac{\partial \chi}{\partial \vec{J}}\ \delta(\alpha-\bar{\alpha}), \qquad (10)$$

where $a_i = \vec{I}\frac{\partial\alpha}{\partial\vec{J}}$, $\alpha=\alpha(\vec{J},\vec{\theta})$ - particle orbit, $\bar{\alpha}$ marks magnetic surface. Trajectory of particle in explicit form is determind by P=const condition with the expansion: $\psi(\alpha) \approx \psi(\alpha_o)+(\alpha-\alpha_o)\partial\psi/\partial\alpha$, where α_o, is defined by $P=mRKu_o - e\psi(\alpha_o)/c$ for passing particles and $P=-e\psi(\alpha_o)/c$ for trapped particles. Then a passing orbit is described by $\alpha = \alpha_o + mcqR(v_\parallel - \sigma K u_o)/e$, where $v_\parallel = \sigma u_o[\kappa^2 - \sin^2\beta/2]^{1/2} = \sigma K u_o \mathrm{dn}(y_u,\bar{\kappa})$, and trapped particle orbit is $\alpha=\alpha_o+mcqRv_\parallel/e$, where $v_\parallel = K u_o \mathrm{cn}(y_t,\kappa)$.

Chosing $\chi = 1,\ mv_\parallel,\ mv^2/2$, we obtain quasilinear set of equations in a familiar form: $\partial_t N + \nabla\Gamma = 0$, $\partial_t(mNV_\parallel) + \nabla\Pi = R_\parallel$, $\partial_t(3NT/2) + \nabla Q = P$, where $\nabla = \frac{1}{r}\partial_r r$, Γ,Π and Q are particle, momentum and energy radial quasilinear fluxes, P - heating power, $R_\parallel$ - toroidal force. To consider ICR heated tokamak plasmas with $l_g=1$, $\omega=\Omega_o$ we take near-Maxwellian distribution function $f_o = f_o[\alpha_o(\vec{J}), H_o(\vec{J})] = N_o(\alpha_o)\left(\frac{m}{2\pi T(\alpha_o)}\right)^{3/2}\exp\{-H_o/T(\alpha_o)\}$. In this case $\vec{I}\frac{\partial f}{\partial\vec{J}}\circ = \vec{I}\vec{\Omega}\frac{\partial f}{\partial H_o}\circ + \vec{I}\frac{\partial\alpha_o}{\partial\vec{J}}\frac{\partial f}{\partial\alpha_o}\circ$.

Taking into account $\rho_p/r \ll 1$, $\rho_p = v_T/\Omega_p$, $\alpha\approx\alpha_o$ and using (8), it is easy to obtain $\vec{I}\frac{\partial\alpha_o}{\partial\vec{J}}\frac{\partial f_o}{\partial\alpha_o} \approx \frac{c}{e}\frac{\omega}{T} f_o G_n$, where $G_n = Lq - \frac{rq\omega}{Ku_o} + (Lq\frac{rq\omega}{Ku_o})\frac{\rho^2}{2r^2}A_o$, $A_o = A_1 + \frac{H}{T}A_2$, $A_1 = \frac{N_o'}{N_o} - \frac{3}{2}\frac{T'}{T}$, $A_2 = \frac{T'}{T}$, $\rho = v_T/\Omega_o$.

Thus, with $d^3J = \sum_\sigma \frac{m^3 R u_o}{2\varepsilon B_o}\left(\frac{2K(\bar{\kappa})}{\pi}\right) du_o d\kappa d\alpha_o$, $\sigma=\pm1$ (where

relations $dP=dH/|\omega_\varphi|$, $dM=\frac{m^2c}{e}d\mu$, $dJ\approx\frac{c}{e}d\alpha_o$, $dH=mu_o^2\kappa d\kappa$, $d\mu=u_o du_o/2\varepsilon B_{o_\infty}$ have been used) Eq.(12) becomes:

$$\begin{pmatrix}\Gamma_n\\ \Pi_n\\ Q_n\end{pmatrix}=\frac{\pi^2\omega c}{\varepsilon r e B_o T_o}\sum\int_0^\infty u_o^2 du_o\int_1^\infty d\kappa\left(\frac{2\mathcal{K}(\bar\kappa)}{\pi}\right)^2|\delta H|^2\delta(\omega-\vec l\vec\Omega)f_o G_n\int d\alpha_o\delta(\alpha_o-\bar\alpha)\begin{pmatrix}1\\ mv_\parallel\\ H_o\end{pmatrix}.$$

Finally, completing the integration and n-summation yields the fluxes connected with passing ions:

$$\Gamma=-\frac{N_o v_E^2}{\omega\varepsilon r}\left\{Lq+\frac{(Lq\rho)^2}{2r}\left(\frac{N_o'}{N_o}+\frac{T'}{T}\right)+\frac{r q^2}{2(2\varepsilon)^{1/2}}\frac{N_o'}{N_o}\right\}, \qquad (11)$$

$$\frac{Q}{T}=-\frac{N_o v_E^2}{\omega\varepsilon r}\left\{\frac{5}{2}Lq+\frac{5}{4}\frac{(Lq\rho)^2}{r}\left(\frac{N_o'}{N_o}+2\frac{T'}{T}\right)+\frac{3 r q^2}{4(2\varepsilon)^{1/2}}\left(\frac{N_o'}{N_o}+\frac{T'}{T}\right)\right\}, \qquad (12)$$

$$\Pi=mN_o v_E^2\left(\frac{q}{\varepsilon}\right)\left\{1+\frac{Lq\rho^2}{r}\left(\frac{N_o'}{N_o}+\frac{T'}{T}\right)\right\}, \qquad v_E=\frac{c|E_+|}{B}. \qquad (13)$$

In the same way Eq.(13) gives

$$P=\frac{mN_o v_E^2\omega}{\varepsilon}\left\{1+\frac{Lq\rho^2}{r}\left(\frac{N_o'}{N_o}+\frac{T'}{T}\right)\right\},$$

$$R_\parallel=-\frac{mN_o v_E^2}{r}\left\{L+\frac{L^2 q\rho^2}{2r}\left(\frac{N_o'}{N_o}+\frac{T'}{T}\right)+\frac{rq}{2(2\varepsilon)^{1/2}}\frac{N_o'}{N_o}\right\}. \qquad (14)$$

We assumed here: $\varepsilon<<1$ and $|E_+|^2J_o^2(k_\perp\rho)>>|E_-|^2J_2^2(k_\perp\rho)$.

Analogous calculations for trapped particles show that contribution of passing ions in quasilinear transport exceeds in $(\varepsilon)^{1/2}$ times the trapped ion contribution. As can be seen from (11)-(14) passing ion fluxes consist of convective term proportional to $k_\zeta=L/R$, so as diffusive term proportional to k_ζ^2 and diffusive term independent on k_ζ except $E_+^2(k_\zeta)$. There are inward convective fluxes if the spectrum is asymmetric in k_ζ and the wave expands in the direction of toroidal magnetic field. For the symmetric spectrym transport is determined by the diffusive part of fluxes.

1. Kayfman A. N. (1972) Phys. Fluids, **15**, 1063.
2. Mahajan S. M., Hazeltine R. D., Hitchcoch D. A. (1983) Phys. Fluids, **26**, 1164.
3. Chen L., Vaclavik J., Hammett G. W. (1988) Nucl. Fusion, **28**, 389.

AUTOMATIC FMS MODE TRACKING DURING ICRH ON TO-2 TOKAMAK

Kovan I.A., Kovrov P.E., Monakhov I.A.

Kurchatov Institute of Atomic Energy, Moscow, USSR

The interest to the problem of the fast magnetosonic (FMS) mode tracking is induced by consideration of the ITER ICRF current drive scenario, based on excitation of the low frequency FMS waves ($f \leqslant 20$ MHz) and relatively weak electron damping [1,2]. Existence of the eigenmode cavity resonances for certain values of plasma concentration under these conditions can strongly modify the antenna radiation resistance and RF input power and require special measures for the mode tracking [3,4].

A new simple mechanism of the FMS eigenmode tracking due to the automatic plasma density stabilization was discovered during ICRH experiments on TO-2 tokamak. The effect is based on recycling intensification caused by energetic particles accelerated in resonant field of the FMS wave. Due to the rare eigenmode spectrum of the small size low density TO-2 plasma the neighbouring FMS resonances don't overlap even in the case of relatively strong damping. Accordingly the FMS wave conversion to the ion Bernstein wave (IBW) near the ion-ion hybride resonance layer was used as the main damping mechanism in ICRH experiments, making it possible to study the electron heating during the eigenmode tracking.

The TO-2 device is the tokamak with two toroidal divertors. The dimensions of the racetrack vacuum chamber are: the minor radius a=18 cm, the radius of toroidal sections R=60 cm, the length of linear sections L=72 cm. During the ICRH experiments the separatrix radius exceeded the radius of the limiter (a_p=14.5 cm). The main parameters of the Ohmic stage of the limiter discharge: B_T =1.2 T, I_p = 40 KA, $U_p \simeq$ 3 V, $Z_{eff} \simeq$ 1.4, $\bar{n}_e = 1 \div 2 \cdot 10^{13}$ cm^{-3}, $T_{eo} \simeq$ 380 eV, $T_{io} \simeq$ 140 eV. The poloidal 1/3 turn loop antenna was placed at the low magnetic field side of the tokamak. The graphite protection of the antenna electrostatic shield played the role of the main limiter. The 500 KW RF generator tuned to 17.3 MHz with the pulse duration 30 ms was used.

In order to realize the central electron heating in the wave conversion regime the 15-20% hydrogen admixture was added to the D-plasma. Because of the narrowness of the internal evanescence region and the low value of the FMSW to IBW conversion coefficient in the TO-2 conditions the FMS wave propagation revealed multi-pass character and the toroidal resonator eigenmodes were observed. The quality factor of the resonances was about $Q \simeq 40 \div 50$. The exitation of the eigenmode was accompanied by a significant increase of RF fields and the antenna radiation resistance. Figure 1 shows evolution of the

signal of the magnetic probe measuring the toroidal component of the RF field H_z near the chamber wall, the RF power P_{RF} delivered to the plasma and the flux J_{CX} of the 1 KeV neutral particles. In case of arbitrary density variations the time of the eigenmode existence was very short comparatively with the generator pulse duration, so the mean power input to the plasma was low and the central electron temperature increase didn't exceed 90 eV.

A new method of automatic plasma density stabilization which needs no special equipment was used for the eigenmode tracking. It is based on the recycling intensification due to the wall and limiter bombardment by RF accelerated fast particles. The flux of the particles accelerated in the ion-cyclotron layer strongly depends on the RF field amplitude hence the stimulated gassing appreciably increases during the eigenmode resonance excitation. In previous ICRF experiments on TO-2 [5] the correlation between the RF field amplitude, the high-energy neutral particles flux (see also Fig.1) and the ion density in the scrape-off layer have been demonstrated. Because the eigenmode excitation for the given frequency and magnetic field depends mainly on the plasma density the RF field-recycling correlation can be used as a feedback mechanism for the automatic density stabilization during the cavity resonance build-up. For this purpose the RF generator should be turned on during the plasma density fall. As the density corresponding to certain eigenmode excitation is achieved, the intensified recycling prevents the further density drop and vice versa any accidental density increase leads to the off-resonance conditions and little additional gas influx. Evidently this process is possible only if the rate of the initial density fall doesn't exceed the ultimate rate of the RF stimulated gas influx from the wall. The latter depends on the wall conditions and on the maximum amplitude of the RF field, so for a given rate of the initial density fall the mode tracking occurs beginning with a certain antenna voltage.

The automatic density stabilization was realized on TO-2 tokamak for the r=1 m=1 l=9 FMS eigenmode with a corresponding line averaged density $\bar{n}_e=1.5\cdot10^{13}$ cm^{-3} for the total RF pulse duration (Fig.3). The nighbouring eigenmodes were also easily tracked after a little change of the initial density fall rate. Figure 2 shows the same characteristics as Fig.1 for the case of the mode tracking (the second successive mode tracking is depicted). It can be seen that high values of RF field and input power were constantly maintained during the RF pulse.

The discovered mode tracking mechanism was utilized for the effective RF power input $P_{RF}\simeq200$ KW to the plasma during ICRF heating in the wave conversion regime. Figure 4 demonstrates the evolution of some parameters of the discharge with ICRF

heating in case of the eigenmode tracking and in case of the successive separate eigenmode excitation (the latter is acieved by faster initial density fall) for equivalent antenna voltages: I_p - the discharge current, $\langle T_{eo} \rangle$ -the time-averaged central electron temperature, I_{fb} - the current of the horizontal plasma position feedback regulator , P_{rad} - the power of radiation losses. The electron temperature was measured by means of the X-ray spectrometer with Si(Li) detector , the registration energy range was 1.8÷10 KeV and resolution 240 eV. The second registration time interval coincided with the RF generator pulse. ICRF heating with automatic FMS eigenmode tracking resulted in time-averaged electron temperature increase from $\langle T_{eo} \rangle$ = 380 eV to $\langle T_{eo} \rangle$=1.1 KeV. The electron heating efficiency was about $\eta \simeq 4.5 \div 5.0 \cdot 10^{13}$ eV·cm^{-3}/KW. The central ion temperature increased on 40 eV without noticeable energy spectrum distortion. The behaviour of I_{fb} signal on Fig.4 can be explained by the plasma stored energy increase. The power of radiation energy losses varied proportionally to the total input power. The effective plasma charge Z_{eff} evaluated according to integral soft X-ray signal variation has not changed significantly during the ICRF heating. The use of graphite limiters on TO-2 turned to be a very efficient measure to provide central electron heating the in wave conversion regime as it was previosly reported (e.g.[6]).

ACKNOWLEDGMENTS

The authors wish to express their gratitude to Dr. N.V.Ivanov for helpful discussions and to the TO-2 group for active assitance in the experiment.

REFERENCES

[1] Ehst D.A., Batchelor D.B., Jaeger E.F. et.al., ITER Meeting on CD/Heating Modellig, Garching, June 1989.
[2] Vdovin V.L., Fedorov S.V., Dmitrieva M.V., ITER Meeting on CD/Heating Modellig, Garching, August 1989.
[3] Ivanov N.V., Kovan I.A., Los' E.V., Sov.J. Pis'ma Zh.E.T.P., 1971, 14, 212.
[4] Colestock P.L., Hosea J.C., Jobes F.C., Heating in Toroidal Plasmas CEC, Pergamon Press, 1978, v.2, p.217.
[5] Artemenkov L.I., Vukolov K.Y., Gott Y.V. et. al., Proc. 15th Eur. Conf. on Cont. Fusion and Plasma Heating, Dubrovnik, 1988, Part 3, p.702.
[6] Equipe TFR, Plasma Phys. and Contr. Fusion,1984,26,№1A,165.

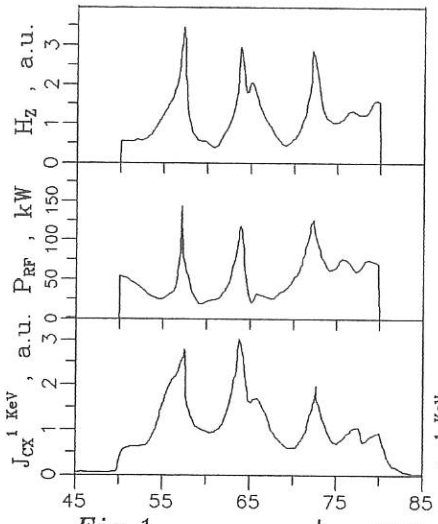

Fig.1

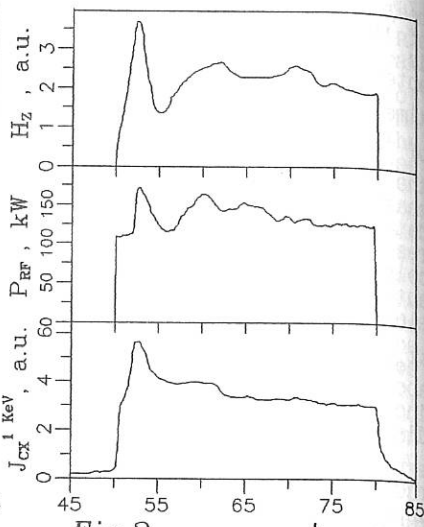

Fig.2

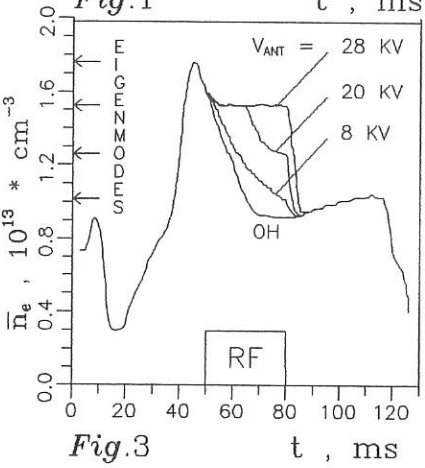

Fig.3

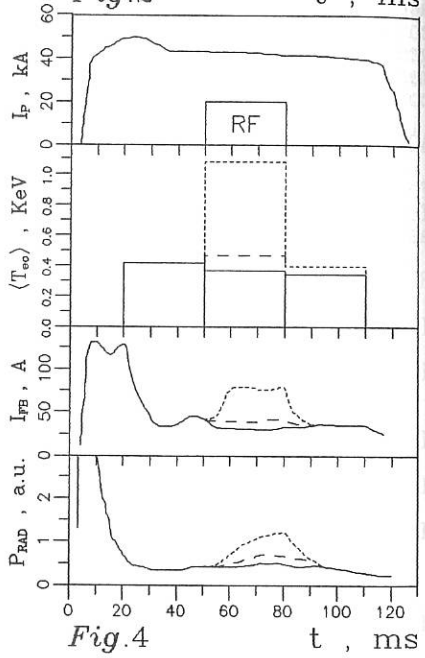

Fig.4

——— without ICRH →
– – – ICRH multimode
..... ICRH mode tracking

STUDIES OF MODE CONVERSION PHYSICS FOR WAVES IN THE ION CYCLOTRON RANGE OF FREQUENCIES

H. Romero and G. J. Morales

Physics Department
University of California at Los Angeles
Los Angeles, CA 90024-1547 USA

I. INTRODUCTION

Mode conversion processes are central to the analysis of heating by waves in the ion cyclotron range of frequencies (ICRF). In particular, the problem of mode conversion from a long wavelength fast Alfven wave to a short wavelength electrostatic wave (i.e., the direct mode conversion problem) has received considerable attention. The objective of the present work is to complement previous studies of ICRF mode conversion physics by investigating the following: i) the inverse mode conversion problem, i.e., mode conversion from an Ion Bernstein wave to a fast Alfven wave, ii) effects of low frequency density fluctuations on the absorption efficiency, and iii) the consequences of nonlinear density depletion of heated ions. A system of equations which is self-adjoint in the absence of dissipation is used in these investigations.

II. MODEL EQUATIONS

A kinetic formulation of ICRF wave propagation and absorption which includes the effects of gradients in the equilibrium plasma was developed in Refs. [1,2]. A wave differential operator is obtained assuming the smallness of $k_\perp\rho$ and ρ/L where ρ denotes the ion gyroradius, $k_\perp$ the local wavenumber, and L the scale length of the equilibrium quantities. The perturbed distribution function is solved to second order in $k_\perp\rho$. In Ref. [2], it is shown that in order for the system of equations to be self-adjoint, the equilibrium distribution function must include terms of second order in the quantity ρ/L. The resulting wave equation can be written in the form:

$$\frac{d}{dx}\left[\underline{\underline{A}}\,(x)\,\frac{d\vec{E}}{dx}\right] + \underline{\underline{B}}\,(x)\,\frac{d\vec{E}}{dx} + \frac{d}{dx}\left[\underline{\underline{B}}\,(x)\vec{E}\right] + \underline{\underline{C}}\,(x)\,\vec{E} = 0 \ . \qquad (1)$$

The matrices **A**, **B**, **C** can be found in Ref. [2], where it is also shown that Eq. (1) is self-adjoint in the absence of dissipation. This results in an energy conservation equation which relates the power absorbed by the plasma and the incident, reflected, transmitted and mode converted fluxes. The specific form of the energy conservation equation can also be found in Ref. [2].

III. INVERSE MODE CONVERSION

Using Eq.(1), we investigate the physics of inverse mode conversion for conditions corresponding to ICRF heating in tokamaks. We assume that an

electrostatic ion Bernstein wave (IBW) approaches the resonance layer from the high magnetic field region. A reflected IBW or a mode converted fast Alfven wave can carry energy away from the resonance layer towards the high field region. On the low magnetic field side, the only propagating mode is a fast Alfven wave. Cyclotron damping takes place in the vicinity of the ion resonance layer. The results are compared against those corresponding to the following two direct cases: i) a fast Alfven wave incident from the low magnetic field side, and ii) a fast Alfven wave incident from the high magnetic field side.

Figure 1 summarizes our principal observation concerning the inverse mode conversion process, namely, the reciprocity of the fast to IBW and IBW to fast wave mode conversion coefficients. Figure 1 shows the ratio of the two mode conversion coefficients as a function of the parallel wavenumber. It is assumed that the fast Alfven wave is incident from the high magnetic field region. For reference, the ratio of the power absorbed by the minority species in each of these cases is also shown. Although Fig. 1 shows the reciprocity between the mode conversion coefficients for a fast wave incident from the high field side, this result is also found for the case of fast wave incidence from the low magnetic field side and for a variety of plasma conditions. We conclude that the reciprocity of these two mode conversion coefficients is a rigorous result for ICRF heating of tokamak plasmas, even in the presence of strong cyclotron absorption.

IV. EFFECTS OF DENSITY FLUCTUATIONS

It is well known that the ICRF ion heating efficiency depends critically on the ratio of ion densities. Hence, it is of interest to determine what modifications arise when density fluctuations in the minority species and/or bulk plasma are present. We have investigated this problem using Eq. (1). In addition, to facilitate analytical treatment, we have also investigated this problem using an approximation to Eq. (1), i.e., a Budden-type of equation,

$$\frac{d^2\psi(x)}{dx^2} + \left\{ \frac{x - w + 2\omega\varepsilon \sin(k_N x + \theta)}{x + 3w\varepsilon \sin(k_N x + \theta)} \right\} \psi(x) = 0 \quad , \tag{2}$$

where the density fluctuations have been assumed to be sinusoidal with amplitude ε, and wavenumber (normalized to the Alfven wavenumber) k_N, and phase θ_N. In the absence of fluctuations, the resonance is located at $x = 0$ and the cutoff is located at $x = w = 0.25\, k_A L\eta$, where k_A is the Alfven wavenumber, L is the gradient scale length of the magnetic field, and η is the minority concentration.

Four important physical effects are embodied in Eq. (2): i) modulation of the Alfven wavenumber leading to backscattering, ii) modulation of the distance between the resonance and cutoff points leading to enhanced or decreased reflection depending on the phase, iii) modification of the spatial structure of the resonance region affecting the absorption efficiency, and iv) the appearance of a regime of multiple resonances. This last effect has important consequences for the case of incidence from the high field region since it affects the form of the resonance first encountered by the incident wave.

To illustrate the response of the system, we mention only the case of fluctuations in the minority species and wave incidence from the high field side. Figure 2 considers the case $w = 3$, and $\varepsilon = 5\%$. The following features are observed. For k_N less than $2\, k_A$, no reflection is possible. Strong backscattering occurs in the interval

$2k_A < k_N < 8k_A$. The reflection coefficient increases in this regime from 0% to 75%. As k_N increases further, a multiple resonance (i.e., two different positions where the ion-ion hybrid resonance is satisfied) develops leading to strong absorption. As the noise wavenumber is increased beyond the range shown in Fig. 2, the absorption efficiency of the multiple resonance decreases, and backscattering dominates again.

For low field incidence, the effect of incoherent density fluctuations is to increase the absorption. We find an absorption coefficient > 80% for fluctuation amplitudes of 60% in the minority species. This correspond to bulk plasma fluctuations on the order of 5%.

V. Nonlinear Density Depletion

A consequence of ICRF heating is the acceleration of the resonant (minority) species in the direction perpendicular to the confining magnetic field. This causes the heated particles to become trapped in banana orbits. The net effect is the transport of minority particles, a process which we model in this paper by assuming that the minority density depletion is directly proportional to the power absorbed from the ICRF wave: $n'(x) = n(x)\{1 - \alpha[p(x) - p_T]\}$, where n is the density before the ICRF is applied, n' is the density after the minority species has been heated, p(x) is the local power absorbed by the minority species, p_T the threshold power below which no depletion takes place, and α is the efficiency with which depletion takes place.

The numerical results are obtained as follows. An initial density profile is assumed and the local ICRF power deposition profile is calculated. The updated density profile n' is evaluated and this allows the calculation of a new power deposition profile. Parameters appropriate to fundamental minority heating in the JET tokamak are used for a plasma composed of hydrogen and deuterium with hydrogen being 5% of the electron density. Our principal observation is the decrease in the reflection coefficient (by more than 50%), and the corresponding increase in the absorption. The reduction in the reflection arises because the location of the ion-ion hybrid resonance becomes closer to that of the minority cyclotron resonance, thus reducing the tunneling distance.

Acknowledgement: This work is sponsored by the U.S. Department of Energy.

References

1. H. Romero and J.E. Scharer, Nucl. Fusion, 27, 363 (1987).
2. H. Romero and G. J. Morales, Phys Fluids B 1, 1805 (1989).

Fig. 1. Test of reciprocity between inverse and direct mode conversion as a function of parallel wavenumber. M_B^- is the mode conversion coefficient into IBW for an incident fast wave from high field, and M_f^- is the mode conversion coefficient into a fast wave for IBW incident from high field. Dashed and dotted curves show asymmetry of minority absorption P_H, and fast wave transmission T_f between the two cases. Parameters correspond to JET.

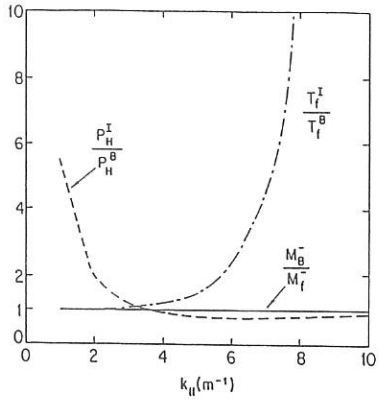

Fig. 2. Dependence of absorption and reflection (squared) coefficients on the scaled noise wavenumber $k = k_N/k_A$. Solid curves are numerical results and dashed curve is WKB scattering prediction. For $k > 8$, the ion-ion hybrid resonance occurs at two different spatial positions and strong absorption overcomes backscattering.

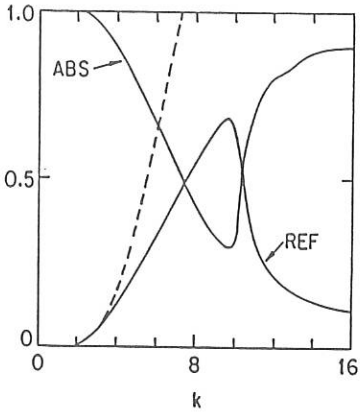

BALLISTIC-WAVE ANALYSIS OF GYRORESONANT HEATING

A.N. KAUFMAN, D.R. COOK, H. YE

Lawrence Berkeley Laboratory, Berkeley, CA 94720, USA

Plasma waves have traditionally been associated with electromagnetic fields. Accordingly, the standard approach to wave propagation has involved the derivation of a dielectric tensor, upon elimination of the linear plasma response to an electromagnetic perturbation. In the neighborhood of a local gyroresonance $\omega \approx \ell\Omega(x)$ (ω =fixed wave frequency, gyrofrequency $\Omega \equiv eB_0/mc$, ℓ = integer), the (non-Hermitian) dielectric tensor becomes rapidly varying in space, so that eikonal methods have failed. This difficulty is avoided by the introduction of **gyroresonant ballistic waves** (GBW), which represent the propagation of linear perturbations of the Vlasov distribution in the **absence** of electromagnetic perturbations. For a slab model of a nonuniform background magnetic field $\mathbf{B}_0 = \hat{z}B_0(x)$, the dispersion relation of a GBW is $\omega = \ell\Omega(x) + k_z v_z$. We recognize this as the local gyroresonance condition, equating the Doppler-shifted frequency $\omega - k_z v_z$ to a multiple ℓ of the local gyrofrequency. (For simplicity, we ignore unperturbed cross-field drift.) The Hamilton ray equations, $\dot{x} = \partial\omega/\partial k_x = 0$, $\dot{z} = \partial\omega/\partial k_z = v_z$, $\dot{k}_x = -\partial\omega/\partial x = -\ell\, d\Omega/dx \equiv -\Omega'$, $\dot{k}_z = -\partial\omega/\partial z = 0$. Thus a GBW propagates in k_x-space, but not in x-space. [Think of a wave-packet in x-z space, whose envelope moves at v_z along $\mathbf{B}_0$. The wave fronts within the packet (with phase velocity ω/k) rotate as $\mathbf{k}$ evolves.] Taking $\ell = 1$, $\Omega' > 0$, we see that the ray trajectory in (x,k_x) space is a vertical line [see Fig. 1] at constant $x(v_z)$. Expanding $\Omega(x)$ about $x = 0$ [chosen so that $\Omega(0) = \omega$], we have $\Omega(x) = \omega + x\Omega'$, and $x(v_z) = -k_z v_z/\Omega'$.

Let the unperturbed (normalized) v_z-distribution be $g(v_z)$. There is thus a **continuum** of GBW rays (for fixed ω, k_z), all propagating downward in k_x-space at the common velocity $-\Omega'$. These GBW can be excited by a linear conversion process. In this paper, we study their excitation by a **magnetosonic wave** (MSW), carried by a (cold) majority (M) ion species. For simplicity, we set $k_y = 0$ and let $k_z << k_x$, so that the magnetosonic wave has the dispersion relation $\omega = \pm k_x c_A$. Ignoring the spatial variation of c_A, we see that the MSW rays are the two horizontal trajectories, at $k_x = \pm\omega/c_A$.

The GBW studied here represent a minority (m) species, with $n_m/n_M << 1$. We consider the non-degenerate case, $\Omega_m \neq \ell\Omega_M$ for all ℓ. Our methods apply equally to other gyroresonant processes, such as second-harmonic absorption (ℓ=2); thus our results are **universal** for slab models. The process of linear conversion is evident from Fig. 1, exhibiting two **crossings** in ray phase space (x, k_x). **After** the two crossings, the set of GBW is to be analyzed to extract the embedded **collective** mode, the **minority Bernstein wave**. What remains is interpreted as gyroresonant **absorption.**

The interpretation of absorption as linear conversion to ballistic waves was introduced by Friedland and Goldner [1] for the case of parallel propagation. This was a natural outgrowth of Friedland's Reduction Algorithm (FRA) [2], a radically new approach to plasma wave phenomena. The basic idea of FRA is that, for a background state with slow spatial

variation, the coefficients of the coupled equations for the components of the wave field should enjoy this same slowly-varying property: one must never divide by a coefficient which passes through zero in order to reduce the number of field components. Thus, in FRA, one never has resonance **denominators**; rather, there appear resonance **coefficients**, interpreted as dispersion functions of waves. Here, these waves are ballistic; what is novel about them is their primary propagation in k_X-space [3]. The recognition that the gyroresonance absorption process was in reality a **two-step** linear conversion evolved in a series of papers by Bers, Cairns, Fuchs, Lashmore-Davies, and co-workers. They showed that the electromagnetic waves could best be understood as rays in the phase space (x,k_X). In our work, we have extended those ideas to the GBW.

Our analysis of this process is based on the existence of **three** small parameters, which are taken to be of the **same** order. The first, ε_W, is the **weak-coupling** parameter, which represents the interaction strength of the GBW with the MSW. For the case of minority resonance, which we treat in detail here, ε_W is essentially the ratio of minority density to majority density: $\varepsilon_W \equiv (1/4)(\omega_m^2/\omega_M^2)(\Omega_M/\Omega_m - 1)^2$. The second, ε_L, is the **eikonal** parameter, representing the spatial nonuniformity of the background magnetic field. In our problem, $\varepsilon_L \equiv (k_o L)^{-1} << 1$, where $k_o \equiv \omega/c_A$ is the MSW wave number, and $L \equiv \Omega/\Omega'$ is the magnetic scale length. The third, $\varepsilon_D \equiv k_z v_m/\omega << 1$, is the **Doppler** parameter, representing the spread in the resonance due to the (rms) thermal spread v_m of the v_z - distribution of the minority species. By taking these three small parameters to be of the same order, we are led to two order-one parameters, their ratios: $\eta \equiv \varepsilon_W/\varepsilon_L$, $\kappa \equiv \varepsilon_D/\varepsilon_L = k_z L(v_m/c_A)$. It has been known for some decades that the **transmission** coefficient T (ratio of transmitted to incident wave energy flux) depends only on η: $T(\eta) = \exp(-2\pi\eta)$. The new result of our work is that the reflection coefficient $R = (1-T)^2\Phi$ depends only on T and on the **phasing** function Φ; while Φ in turn depends **only** on κ, being **independent** of η: $\Phi(\kappa) = \exp(-4\kappa^2)$. [This dependence of Φ on κ is for Maxwellian $g(v_z)$.]

We first study the **phases** of the wave fields in order to obtain Φ, and then their amplitudes. (This analysis was stimulated by R.A. Cairns' unpublished derivation of $R(\eta,\kappa)$, based on phasing of the magnetosonic waves only.) For an eikonal wave in the standard (one-dimensional) x-representation, the GBW field $j(x;v_z)$ is proportional to the phase factor $\exp i\theta(x;v_z)$, with $k_x(x) = \partial\theta/\partial x$. Correspondingly, in the k_X-representation, obtained by Fourier transformation and the method of stationary-phase, the wave field $j(k_X;v_z)$ has the phase factor $\exp i\tilde{\theta}(k_X;v_z)$, with $x(k_X) = -\partial\tilde{\theta}/\partial k_X$. The two phase functions, $\theta(x)$ and $\tilde{\theta}(k_X)$, are Legendre transforms of each other: $\tilde{\theta}(k_x) = \theta(x) - k_x x$, because $d\tilde{\theta} \equiv -x dk_x = k_x dx - d(k_x x) = d(\theta - k_x x)$. We first consider the phase of **each** GBW at its creation point I [see Fig. (1)]. We have, for each v_z, $\tilde{\theta}_I(v_z) \equiv \tilde{\theta}(k_x = k_o; v_z) = \theta[x(v_z)] - k_o x(v_z)$. The GBW created at $x(v_z)$ inherits the phase $\theta(x)$ of the incident magnetosonic wave which converts to it; relative to x=0, the latter is given by $\theta_{inc}(x) = \int(o,x)k_x dx = k_o x$. On substituting, we see that the GBW phases $\tilde{\theta}_I(v_z)$ all vanish at their creation, so they are exactly **in phase** at $k_x = +k_o$, where they are created. In propagation from their first conversion point, I, to their second, II, the phase change is $\Delta\tilde{\theta}(v_z) \equiv \tilde{\theta}_{II}(v_z) - \tilde{\theta}_I(v_z) = -\int(I,II)x dk_x = -x(v_x)[k_x(II) - k_x(I)] = +2k_o x(v_z)$, since $k_x(II) = -k_o$, $k_x(I) = +k_o$. Thus, for each v_z, the phase factor at II is $\exp i\tilde{\theta}_{II}(v_z) = \exp i\Delta\tilde{\theta}(v_z) = \exp i2k_o x(v_z)$. The reflected MSW phase is obtained by superposing the converted contribution of each GBW. First we transform from $\tilde{\theta}_{II}(v_z)$ to $\theta_{II}(v_z)$, at $k_z = -k_o$:

$\theta_{II}(v_z) = \tilde{\theta}_{II}(v_z) + k_x x(v_z) = 2k_o x(v_z) + (-k_o)x(v_z) = k_o x(v_z)$. Then we propagate the (reflected) magnetosonic wave from $x(v_z)$ to the reference point $x=0$, obtaining the phase contribution from each GBW: $\theta_{refl}(v_z) \equiv \theta_{II}(v_z) + \int[0, x(v_z)]k_x\, dx = k_o x(v_z)$ $+(-k_o)[-x(v_z)] = 2k_o x(v_z)$. We then superpose the contributions of all v_z, weighted by $g(v_z)$, to obtain the effect of phasing on the reflected wave field: $\Phi \equiv |<\exp i2k_o x(v_z)>|^2$.

For the relation of R to T, we recapitulate the amplitude arguments of earlier work. At the first conversion I, the set of GBW carries the fraction 1-T of the wave energy flux; at the second conversion II, again the fraction 1-T is converted, now from the GBW to the reflected wave. Hence, R is proportional to $(1-T)^2$.

We now turn to an FRA derivation of the coupled equations for the GBW and MSW. The minority species is treated as cold-fluid in the plane perpendicular to $\mathbf{B}_o$, and kinetic in the parallel direction. Their linearized **perpendicular** momentum equation is thus $-i(\omega - k_z v_z)u(v_z) = (e/m)(E + u \times B_o / c)$. Taking the **left-circular** components, denoted u, E_L, we have $[\omega - k_z v_z - \Omega_m(x)]\, u(x; v_z) = (ie/m)E_L(x)$.

For the magnetosonic waves, we use the cold-fluid model for the majority, with $E_z \to 0$ following from $\omega << \omega_e, \Omega_e$. The minority does not appear in the dielectric tensor, but rather as a driving current $<j>(x) \equiv \int dv_z\, g(v_z) j(x; v_z)$, with $j(x; v_z) \equiv n_m e_m u(x; v_z)$. The equation for the vector potential $A(x) \equiv E_L/(i\omega)$ is $D_A(k_x)A(x) = -<j>(x)$, where $D_A(k_x) \equiv 2(\omega_M^2/4\pi)(\Omega_M - \Omega_m)^{-2}(\omega^2 - k_x^2 c_A^2)$. We ignore the weak x-dependence, while k_x is the operator $-i\partial/\partial x$. The last factor can be approximated as $-2k_o c_A^2 (k_x - k_o)$ for the incident MSW, and as $2k_o c_A^2 [k_x - (-k_o)]$ for the reflected MSW.

Returning to the GBW equation, we write it as $D_j(x; v_z) j(x; v_z) = -A(x)$, where $D_j(x; v_z) = 4\pi\Omega'[x(v_z) - x]/\omega_m^2 \omega$. This set of two coupled equations is **Hermitian**; it follows [4] that the transmission coefficient T is the **same** for each conversion **point** and conversion **direction**: $T = \exp(-2\pi\eta)$, $\eta = \{D_j, D_A\}^{-1}$, in terms of the Poisson Bracket of the respective dispersion functions: $\{D_j, D_A\} = (\partial D_j/\partial x)(\partial D_A/\partial k_x) \equiv \varepsilon_L/\varepsilon_W$.

In conclusion, we have used FRA and the phasing of GBW to obtain a simple analytic expression for the wave reflection coefficient associated with gyroresonance crossing. The analysis used here for minority resonance applies as well to second-harmonic resonance [3], with $\varepsilon_W \equiv (1/4)(v_M^2/c_A^2)$, and $\varepsilon_D \equiv k_z v_M/\omega$. The success of these methods leads us to anticipate that more realistic two- or three-dimensional configurations are amenable to this approach.

References

[1] L. Friedland and G. Goldner, Phys. Fluids **29**, 4073 (1986).

[2] L. Friedland and A.N. Kaufman, Phys. Fluids **30**, 3050 (1987).

[3] H. Ye and A.N. Kaufman, Phys. Rev. Lett. **60**, 1642 (1988); **61**, 2762 (1988).

[4] E.R. Tracy and A.N. Kaufman, Phys. Rev. Lett. **64**, 1621 (1990); A.N. Kaufman and L. Friedland, Phys. Lett. **123A**, 387 (1987); L. Friedland, G. Goldner, and A.N. Kaufman, Phys. Rev. Lett. **58**, 1392 (1987).

This work was supported by the U.S. Department of Energy under Contract No. DE-AC03-76SF00098.

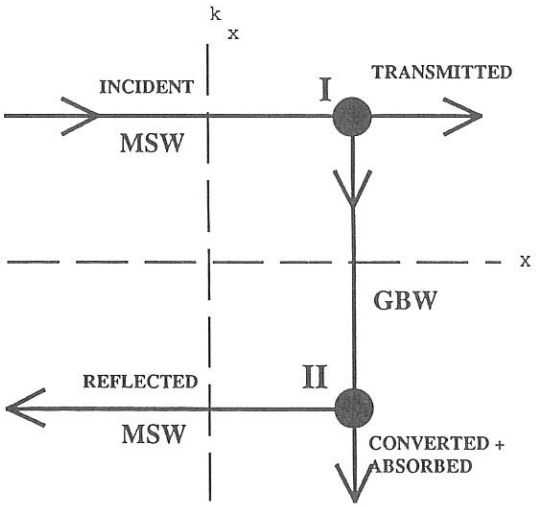

Figure 1. [Low-field incidence] In ray phase space (x,k_x), an incident magnetosonic wave (MSW), at $k_x = k_0 \equiv \omega/c_A$, linearly converts (at I) to one of a continuum of gyroresonant ballistic waves (GBW). Each GBW propagates downward in k_x at constant $x(v_z)$. When its k_x crosses $k_x = -k_0$ (at II), it linearly converts to the reflected MSW. The set of GBW contains the collective minority Bernstein wave, which propagates away; the residuum represents gyroresonant absorption.

EDGE ABSORPTION OF FAST WAVE DUE TO ALFVÉN RESONANCE AND WAVE NONLINEARITY IN ICRH

J.A. Heikkinen, T. Hellsten+, M.J. Alava* and T.J.H. Pättikangas*

Technical Research Centre of Finland, Nuclear Engineering Laboratory, P.O.Box 169, SF-00181 Helsinki, Finland
+Royal Institute of Technology, Plasma Physics and Fusion Research, S- 10044, Stockholm, Sweden
*Helsinki University of Technology, Department of Technical Physics, Rakentajanaukio 2C, SF-02150 Espoo, Finland.

Abstract: Mode conversion of the fast wave into a slow wave at the Alfvén resonance during ICRH in tokamaks is analysed for two important heating schemes: (^{3}He)D minority heating and heating at first harmonic of tritium in DT-plasma. A simple analytical formula is presented which is used to estimate the converted power. This formula is compared with numerical computations. The effects of wall reflection, finite electron inertia and finite temperature are discussed. We also estimate the edge absorption caused by a resonant parametric decay of the fast wave in front of the antenna.

Alfvén resonance: For some ICRH scenarios in small aspect ratio tokamaks the cyclotron frequency of the majority ions will at the high field side exceed the frequency of the launched wave. In such cases the magnetosonic wave aimed to heat the centre of the plasma can undergo mode conversion into an Alfvén wave at the plasma boundary on the high field side. In the cold plasma limit and neglecting electron inertia, i.e. by letting $\mid P \mid \rightarrow \infty$, one obtains an equation [1]

$$E_y'' + \frac{(S - n_z^2)^2 - D^2}{S - n_z^2} E_y = 0. \tag{1}$$

Here S, D and P are the dielectric tensor elements according to the Stix's notation and n_z is the parallel refractive index of the radiation while the prime denotes derivation with respect to x, the radial coordinate. All the lengths are normalised to c/ω where c is the speed of the light and ω is the angular frequency of the radiation. The poloidal refractive index is assumed to be zero. By integrating the derivative of the real part of the Poynting flux across the Alfvén resonance at $S = n_z^2$ we obtain for the fraction ΔI of the Poynting flux I which is absorbed at the Alfvén resonance

$$\Delta I = -\int_{-d}^{d} I' dx = \pi \frac{D_0^2}{\mid S' \mid} \mid E_y \mid^2, \tag{2}$$

where E_y, D_0 and S' are calculated at the resonance. We note that the expression in Eq.(2) shows the expected similarity with the result by Karney et al. [2] obtained for the conversion fraction $C = \Delta I/I$ in a one-ion component plasma. In the general case one obtains $C = 4.97(D_0^2/\mid S' \mid)[\mid S' \mid /(S'^2 - D'^2)]^{1/3}$. For practical applications, Eq.(2) is more useful because of the possible reflection of the fast wave from the inner wall which is not included in the derivation of the Karney estimate. The presence of the wall makes the wave field to decrease in the evanescent region near the plasma boundary faster than in the absence of the wall.

One can improve the Karney treatment with matched asymptotic expansion by requiring that the evanescent solution vanishes at the wall. In this way and following the derivation presented in ref. [2] we get

$$C = \frac{\Delta I}{I} = 4.97 \frac{D_0^2}{\mid S' \mid} \left(\frac{\mid S' \mid}{S'^2 - D'^2} \right)^{1/3} \frac{[1 - \sqrt{3} Ai(L_w/h)/Bi(L_w/h)]^2}{1 + Ai(L_w/h)^2/Bi(L_w/h)^2} \tag{3}$$

for the conversion fraction in the presence of reflection. Here L_w, which is normalised to c/ω, is the distance between the Alfvén resonance and the wall. The incoming (+) and reflected (−) fast wave on the high density side are taken to be of the form $Ai(x/h) \pm iBi(x/h)$, where $Ai(z)$ and $Bi(z)$ are the solutions of the Airy equation $E_y'' - zE_y = 0$ (the coefficient of E_y in Eq.(1) is linearised) and $h = [\mid S' \mid /(S'^2 - D'^2)]^{1/3}$. On the low density side near the wall the evanescent waves are taken to be of the form $Ai(x/h)$ and $Bi(x/h)$. From Eq.(3) we see directly that $C \to 0$ as $L_w \to 0$ i.e. $E_y \to 0$ according to the estimate of Eq.(2) while C approaches the Karney estimate as L_w increases. Note that the estimate in Eq.(3) is valid at $D_0^2/\mid S' \mid^{4/3} << 1$, i.e. at small C.

Fig.1 shows the conversion C as a function of a, the distance between the wall and the right boundary through which we let the transmitted fast wave and converted slow wave to propagate out. We have $L_w c/\omega = d + a$, where d is the distance between the right boundary and Alfvén resonance. C is computed numerically from full wave equations [3] including finite temperature, finite electron inertia and gradients of the background plasma. An exponential density profile $1.6 \times 10^{19} \exp(-x(\mathrm{cm})/1.176)\mathrm{m}^{-3}$ for $0 < x < L$ and constant for $x > L$ with $B = 5.5\mathrm{T}$, $\omega = 2.1 \times 10^8 \mathrm{s}^{-1}$ and $n_z = 8$ are assumed simulating the edge plasma near the inner wall in JET for (^{3}He)D minority heating scheme with 5% helium concentration. In this case $d = 1.5\mathrm{cm}$, $D_0 = 49$, and $\mid S' \mid = 7873$. The estimate of Eq.(3) is found to describe well the functional dependence of C on a. At large a, C saturates as expected due to the decrease of the wall reflection. The numerical values are larger by a factor of two, approximatively, which was found to be due to the boundary conditions and the linearisation of S and D applied in the derivation of Eq.(3). On the other hand it was found that the numerical results agree with the estimate in Eq.(2). Finite electron inertia effects were discovered to be important at small n_z and at steep gradients where the estimate in Eq.(2) still gave the correct scaling but its magnitude could deviate even by a factor of two from the correct result. This was tested by letting $P \to \infty$ in the numerical program. Fig. 2 shows C as a function of n_z for the case of Fig. 1 with $a = 2\mathrm{cm}$ and $a = 80\mathrm{cm}$. Note that C is larger at larger n_z for

this case because of the n_z dependence of D_0 in the estimate in Eq.(2). In Fig. 3 we show C as a function of n_z for the case of first harmonic heating of tritium in DT-plasma. A density profile $10^{19}[1-x(\mathrm{cm})/20]\mathrm{m}^{-3}$ with the wall at $x = 20$ cm is chosen with $T = 500$ eV. The magnetic field dependence $5.15\mathrm{T}\times R/(R-x(\mathrm{m}))$ with $R = 2$ m is assumed. Here C is maximised for small n_z because of the n_z dependence of D_0. Note that D_0 here is particularly sensitive to the magnetic field while in the case of Figs. 1 and 2 it was the density that dominated due to the different location of the Alfvén resonance in these two cases. Because of the large conversion in the case of Fig. 3 at small n_z the estimate in Eq.(3) was not found to be reliable but instead the results agreed well with the estimate in Eq.(2).

Resonant parametric decay: The nonlinear decay of the fast wave into two ion Bernstein waves is observed in various tokamaks but no correlation between the edge modification and the presence of the decay has yet been found. In a recent study [4] the nonresonant decay of the fast wave was analysed in detail in a realistic edge plasma environment. It was concluded that relatively large fields in excess of 200 V/cm are needed for a nonnegligible nonlinear power absorption. We have repeated a corresponding analysis for the resonant decay of the fast wave into two ion Bernstein waves for pertinent heating schemes. Fig. 4 shows the amplification in resonant growth of the decay waves in the case of (H)DT minority heating. The amplification has been calculated from the theory outlined in ref. [5]. Convective losses of the decay waves are determined from the radial phase mismatch due to the temperature inhomogeneity. It is found that fast wave fields larger than 100 V/cm are sufficient for a strong instability at the relevant temperature region. This field level is easily exceeded in present experiments. We note that power absorption can be much larger in the resonant decay than in the nonresonant decay [4].

Conclusions: Simple analytical estimates for the power conversion in Alfvén resonance during ICRH have been derived which include the effects of fast wave reflection from the wall. A good agreement with numerical predictions is found. The conversion is strongest for weak local density gradient, high density and for resonances lying far away from the wall. Its dependence on parallel wavenumber turns out to be sensitive to the ion composition and to the exact location of the resonance. In the 2T-D heating scheme C may amount to 90% for small n_z while in (^{3}He)D minority scheme it remains below 20%. The possibility of a localised resonant decay of the fast wave into ion Bernstein waves near the Faraday screens is pointed out which may amount to a nonnegligible power conversion in spite of convective losses.

References

[1] Stix, T.H. et al., in "Handbook of Plasma Physics", Vol.I, 1983, Ch.2.4.
[2] Karney, C.F.F. et al., Pl. Phys. and Contr. Fus. **30**(1988)149.
[3] Brambilla, M., Nuclear Fusion **28**(1988)549.
[4] Heikkinen, J.A. et al., Nuclear Fusion **29**(1989)1307.
[5] Härms, K.D. et al., Nuclear Fusion **14**(1974)657.

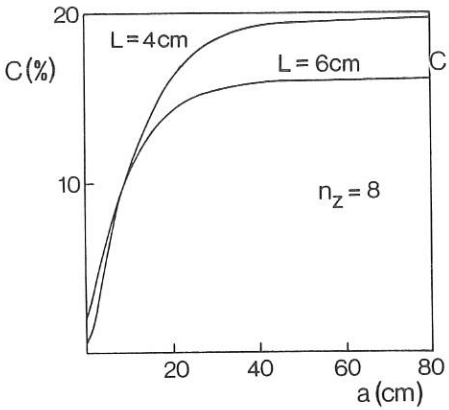

Fig. 1 The mode conversion fraction C as a function of a for D(^{3}He) plasma with 5% helium concentration.

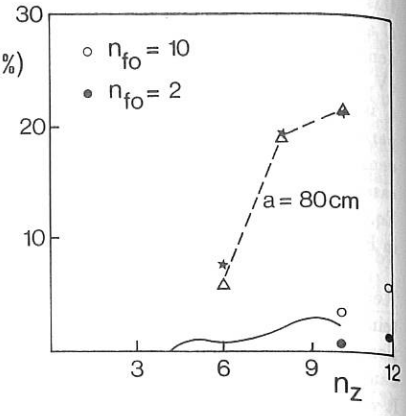

Fig. 2 C as a function of n_z for the case of Fig.1 with $a = 2$ cm and $L = 4$ cm (solid line). A few results with predetermined $n_{0x} = 10$ and 2 (o) are shown for higher n_z. The result with $a = 80$cm (Δ) is also depicted together with the prediction of the estimate of Eq.(2) ($\star$).

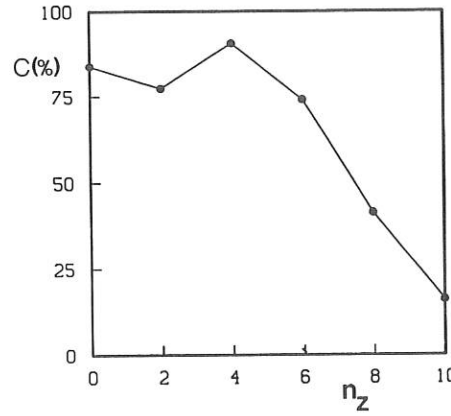

Fig. 3 C as a function of n_z for D-T plasma with first harmonic heating of tritium. $\omega = 2.1 \times 10^8$ s^{-1}.

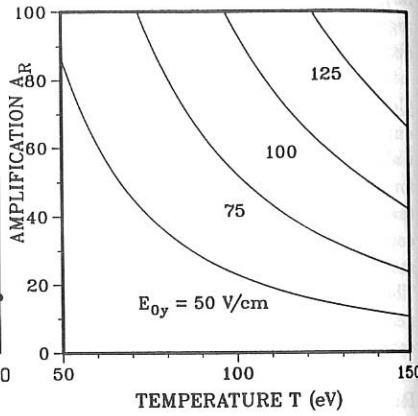

Fig. 4 A for an exponential growth $\exp(A)$ for the amplitudes of the resonant modes in the decay of the fast wave to ion Bernstein waves ($\omega_1 \sim \Omega_D, \omega_2 \sim 2\Omega_T$) in (H)DT plasma with 5% H concentration as a function of temperature for various pump wave fields. The pump wave frequency 41.8 MHz with $B = 2.24$ T and $N = 10^{18}\mathrm{m}^{-3}$ is assumed

D-He^3 FUSION YIELD IN HIGHER HARMONIC ICRF HEATED PLASMA

M. Yamagiwa, H. Kimura, T. Takizuka and T. Fujii

Naka Fusion Research Establishment
Japan Atomic Energy Research Institute
Naka-machi, Naka-gun, Ibaraki-ken 311-01, Japan

Abstract

The D-He^3 fusion output power for the higher harmonic ICRF heating of He^3 beams is investigated. The fusion power multiplication factor, Q_{RF}, in the high He^3 concentration ($n_{He^3}/n_e > \sim 5\times10^{-2}$) can become larger than that for the fundamental heating. The empirical scaling for Q_{RF} in the fourth harmonic ICRF heating is also presented.

Introduction

The fusion reactivity can be enhanced by the presence of a non-Maxwellian ion tail. The JET experiments [1] in the (He^3)D minority scheme produced the fusion power of ~60 kW with the RF power of ~12 MW. Good agreement was found between the measured values of the fusion yield and ones calculated by using Fokker-Planck and global wave codes [2]. In JT-60 experiments, remarkable beam acceleration has been observed during the third harmonic ICRF heating in combination with NBI heating. It is confirmed that the beam acceleration occurs in the plasma core [3]. In this paper, the D-He^3 fusion output power for the higher harmonic ICRF heating of He^3 beams is investigated. The fusion power multiplication factor is estimated on the basis of the local Fokker-Planck calculation. Comparison is made with the case of the fundamental heating.

Modelling

In the present calculation, the fourth harmonic heating of He^3 beams is considered for avoiding wave absorption by a small component of hydrogens(H) which may be present in a plasma. The third harmonic resonance of He^3 coincides with the second harmonic resonance of H. When $\omega=2\omega_{cHe^3}(R_0)$, wave absorption via the fundamental resonance of H in a stronger magnetic field region, $B(R=3/4\ R_0)=4/3\ B(R_0)$, may also be serious to the efficient wave coupling with He^3. The fusion power enhancement by the fundamental heating of He^3 beams is examined for comparison.

The ion velocity distribution function is calculated semi-analytically by use of a Fokker-Planck equation combined with beam source and quasi-linear RF

diffusion terms [4]. The fusion power multiplication factor, $Q_{RF}=P_F/P_{IC}$, is estimated on the basis of local power absorption near the plasma center. Here, P_F is the fusion output power due to the D-He^3 reaction and P_{IC} the ICRF power. The wave parameters are determined from the cold plasma dispersion relation [5]. In order to derive the ratio of the circularly polarized amplitudes of the RF electric field, $|E_-|/|E_+|$, for $\omega=\omega_{cHe^3}$, the hot plasma dielectric tensor [6] is applied. The He^3 beam is injected with the injection energy of 100 keV and the injection power density of 0.25 MW/m^3. We study the cases of the cyclotron harmonic number of N=4 and N=1 for the same toroidal magnetic field of 3 T.

Results and Discussion

Figure 1 shows typical energy spectra of He^3(solid line), D(thin solid line), He^4(dashed line), and H(dash-dotted line) in the case of (a) N=4 and (b) N=1. The background plasma temperature, T, is 10 keV, the electron density, n_e, is 5×10^{19} m^{-3}, the He^3 concentration, n_{He^3}/n_e, is 5×10^{-2}, and the absorbed RF power density, p_{rf}, is 0.5 MW/m^3. The parallel wave number is chosen as $N_{//}=1$ for (a) N=4 and $N_{//}=10$ for (b) N=1. Values of $|E_-|/|E_+|$ are (a) 1.5 and (b) 15.2. The ion tail in the fundamental heating is extended to the higher energy region because of the large value of $|E_-|/|E_+|$ than that in the fourth harmonic heating. However, the fusion yields of these cases are on the same level, as is shown later.

Figures 2 and 3 show the dependence of Q_{RF} on p_{rf} for N=4 and N=1, respectively. The plasma parameters are as follows; T=10 keV, (a) $n_e=5\times10^{19}$ m^{-3} and (b) $n_e=10^{20}$ m^{-3}, and $n_{He^3}/n_e=5\times10^{-3}$ (dashed line), 10^{-2} (solid line), 5×10^{-2} (dotted line), and 10^{-1} (dash-dotted line). In the low He^3 concentration, we can see the ranges of p_{rf}, where the values of Q_{RF} decrease sharply with p_{rf} (dashed and solid lines in Fig.2 and Fig.3a, and dashed line in Fig.3b). This is due to the excessive acceleration of the high energy ions (beyond the maximum in the D-He^3 cross section, $E_{He^3}\sim750$ keV) and to the depletion of the low energy part of the distribution function. Unless the depletion of the low energy part occurs, Q_{RF} for N=4 is almost independent of p_{rf}. The values of Q_{RF} for N=4 can be larger than those for N=1 in the high $n_{He^3}/n_e(>\sim5\times10^{-2})$ regime.

Figure 4 indicates the $N_{//}$ dependence of Q_{RF} as a function of p_{rf} for T=10 keV, $n_e=5\times10^{19}$ m^{-3}, and $n_{He^3}/n_e=5\times10^{-2}$. The N=4 cases are depicted by dashed lines and the N=1 cases by solid lines. The values of Q_{RF} for N=4 decrease with $N_{//}$. This is because the increase of $|E_-|/|E_+|$ with increasing $N_{//}$ leads to the excessive acceleration. For $N_{//}^2\leq O(1)$, $|E_-|/|E_+|$ is almost independent of $N_{//}$. On the other hand, in the case of N=1, $|E_-|/|E_+|$ becomes significantly large for $N_{//}\ll\sim n_{He^3}/n_e\cdot c/v_t$ ($\sim$20 in this case), where c is the speed of light and v_t the thermal speed of He^3. Then, the value of Q_{RF} becomes small for low $N_{//}$.

Figure 5 shows the relation between Q_{RF} and n_{He^3}/n_e for N=4. The cases of $n_e=5\times10^{19}$ m^{-3} (open symbols), 10^{20} m^{-3} (closed symbols) and T=5 keV (triangles), 10 keV (circles) are plotted for p_{rf}=0.5 MW/m^3 and $N_{//}$=1. The following empirical scaling (solid lines) for Q_{RF} can be deduced from the figure;

$$Q_{RF} \sim 0.055 \left(\frac{T}{10[\mathrm{keV}]}\right) \left(\frac{n_e}{10^{20}[\mathrm{m}^{-3}]}\right)^{4/3} \left(1 - 2.7\frac{n_{He^3}}{n_e}\right).$$

This scaling is applicable to a relatively wide range of local RF power density and/or RF deposition radius, under condition that the He^3 concentration is in the range of $\sim 0.01 \leq n_{He^3}/n_e \leq \sim 0.2$ and that the value of $N_{//}^2$ is at most on the order of unity. In the present calculation, the distribution function can be deformed significantly owing to the RF-induced diffusion. The TCT effect due to the RF-extended tail becomes much stronger than that due to the beam-induced tail. Therefore, the above scaling is also expected to be weakly dependent on the beam power density, except for the cases of low p_{rf} and of high injection energy. Combined NBI and ICRF heating is, however, seemed to be useful in the sense that plasma-antenna coupling is improved by the beam-induced tail component.

References

[1] BOYD D.A. et al. (1989) Nucl. Fusion **29**, 593.
[2] ERIKSSON L.-G. et al. (1989) Nucl. Fusion **29**, 87.
[3] UEHARA K. and KIMURA H. (1989) Radio Frequency Power in Plasma, Proc. 8th Top. Conf., Irvine, CA, 1989, American Institute of Physics, New York.
[4] YAMAGIWA M., TAKIZUKA T. and KISHIMOTO Y. (1987) Nucl. Fusion **27**, 1773.
[5] YAMAGIWA M. and TAKIZUKA T. (1988) Nucl. Fusion **28**, 2241.
[6] ADAM J. (1987) Plasma Phys. Contr. Fusion **29**, 443.

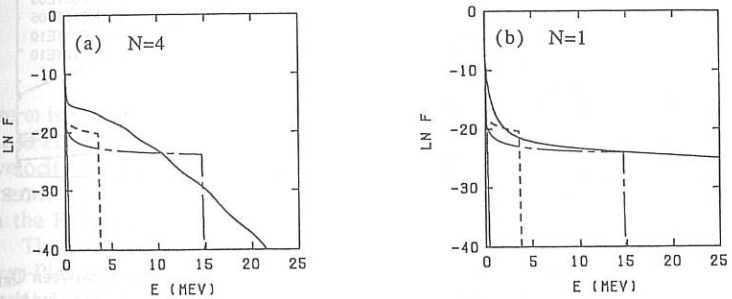

Fig.1 Energy spectra of He^3 (solid line), D (thin solid line), He^4 (dashed line), and H (dash-dotted line) in cases of (a) N=4 and (b) N=1.

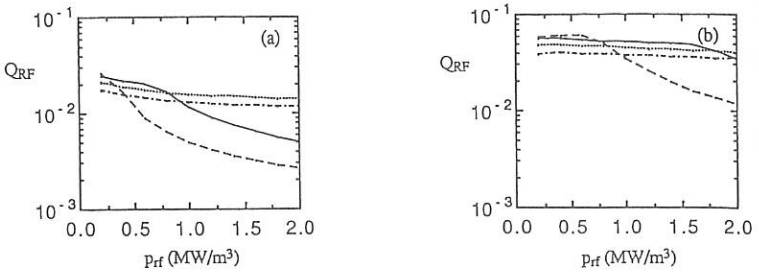

Fig.2 Dependence of Q_{RF} on p_{rf} for N=4. Parameters are (a) $n_e=5\times10^{19}$ m^{-3} and (b) $n_e=10^{20}$ m^{-3}, and $n_{He^3}/n_e=5\times10^{-3}$ (dashed line), 10^{-2} (solid line), 5×10^{-2} (dotted line), and 10^{-1} (dash-dotted line).

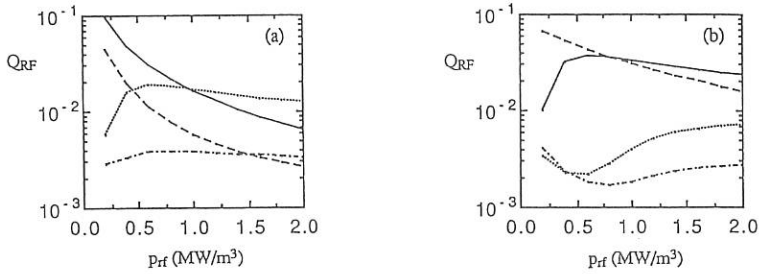

Fig.3 Dependence of Q_{RF} on p_{rf} for N=1. Parameters are the same as those of Fig.2.

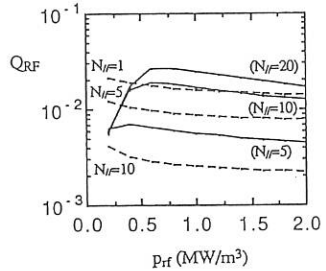

Fig.4 $N_{//}$ dependence of Q_{RF} as a function of p_{rf} for N=4 (dashed lines) and N=1 (solid lines).

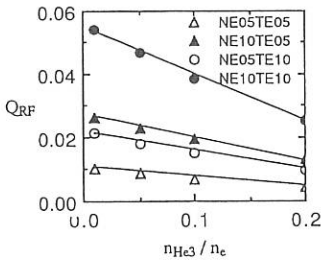

Fig.5 Relation between Q_{RF} and n_{He^3}/n_e for N=4. Solid lines indicate the empirical scaling.

THEORETICAL ANALYSIS OF HIGHER HARMONIC ICRF HEATING IN JT-60

K. Hamamatsu, H. Kimura, T. Fujii, K. Tobita, M. Nemoto, M. Azumi and A. Fukuyama*.

Japan Atomic Energy Institute, Naka Fusion Research Establishment
Naka-machi, Naka-gun, Ibaraki, 311-02.
*Faculty of Engineering, Okayama University, Okayama, 700, Japan.

I. Introduction The second and third harmonic ICRF heating experiments have been carried out with neutral beam injection in JT-60. The plasma is composed of pure hydrogen or mixture of hydrogen and helium. The RF frequency is chosen to be the second or third cyclotron resonance of hydrogen. The hydrogen neutral beam is injection to the plasma. Fast ions are observed in the charge exchange neutral spectrum in both cases of second and third harmonic resonance heating.

As for the second resonance heating combined with NBI, the theoretical model has been developed [1] and applied to the experimental results [2]. We extend this model into the higher harmonic ICRH heating. The global wave structure and acceleration of high energy particles are numerically calculated in a self-consistent manner.

II. Theoretical Model Our model consists of two parts. The first part is the description of ICRH wave propagation and absorption in a real space. The second part is the description of the deformation of the velocity distribution caused by NBI and ICRF heating.

The wave field is described in the one dimensional slab model [3] in which the in homogeneties in the direction of the major radius (x-direction) are kept. The profiles of density and temperature are given as a parabolic function of x. The wave equation is written as

$$\nabla \times \nabla \times E - \frac{\omega^2}{c^2} = i\omega\mu_0 (\Sigma J_j + J^A) \qquad (1)$$

where ω is the RF angular frequency, J^A is the antenna current and J_j is the induced current by the j-th species. In the calculation of the conductivity tensor, the velocity distribution of hydrogen is assumed to be bi-Maxwellian, whose temperatures are determined by the velocity moment of distribution obtained from the Fokker-Planck equation.

The velocity distribution function of hydrogen is obtained by solving the Tokker-Planck equation. On each magnetic surface, we take the O-th order moment of the Legandre expansion of velocity distribution function, f, and obtain

$$\frac{\partial f}{\partial t} = C(f) + S_{NBI} + Q_{RF}(f) + L_p(f) \ , \qquad (2)$$

where C is the Coulomb collision term, S_{NBI} is a source term of NBI, $Q_{RF}$is an RF heating term, L_p is a particle loss term. S_{NBI} is obtained by the pencil beam model and L_p is determined to keep a steady state, i.e., $\partial f/\partial t = 0$. Q_{RF} includes the $(\ell\text{-}1)$-th order Bessel function $J_{\ell-1}(k_\perp v_\perp)$, where ℓ is the harmonic number, $k_\perp$ is a perpendicular wave vector and $v_\perp$ is the velocity perpendicular to the magnetic field. Q_{RF} also contains an unknown factor, which is determined by solving self-consistently Eq. (1) and (2), i.e., $\langle E^* \cdot J \rangle = 4\pi \int dv^2 \frac{1}{2} mv^2 Q_{RF}(f)$. To combine the solutions of the wave equation and the Fokker-Planck equation, we must calculate the RF power deposition averaged over magnetic surface and solve Eq. (2) on each magnetic surface. To save a CPU time, however, the Fokke-Planck equation is solved at the cyclotron resonance point (x=0) where the magnetic axis (r=0) locates. We assume that the RF power deposition is localized near the magnetic axis: $r \leq L_A$. L_A is the poloidal length of antenna. The temperature and density of high energy ions are also assumed to be similar.

III. Wave Propagation We apply this model to the regime of the JT60 plasma. Plasma parameters are R = 3.07m, a = 0.9m, $n_{eo} = 0.34 \times 10^{19}$ m^{-3}, $T_{eo} = T_{Ho} = 2.5$ keV, $\omega/2\pi$ = 131 MHz. A toroidal magnetic field is chosen in order to place the resonance layer on the magnetic axis, i.e., $B_T \cong 4.3T$ for the second harmonic resonance and $B_T \cong 2.86T$ for the third one. Two antennas, which have the phase difference with 180° in the toroidal direction, is arranged in the low field side of the torus.

Figure 1 (a) shows the radial profile of electric field, Ey, and (b) shows the power deposition profile of the combined NBI and the second harmonic ICRF heating. The launched RF power is 0.8 MW and the applied NBI power is about 8 MW and beam energy is 65 keV. This result includes the fast ions of NBI and accelerated ions due to ICRF heating. Even thought the high energy ions do not exist, the damping rate of second harmonic ICRF wave is large enough to suppress the cavity resonance. As for the propagation of second harmonic ICRF waves in this plasma regime, the contribution of high energy ions is not so important.

In the case of the third resonance heating, the high energy ions play a more important role than the second resonance case. Figure 2 shows the radial profile of Ey and the power deposition profile of the ICRF alone heating. We do not take high energy ions into account in Fig. 2. This is able to be regarded as the moment the RF power is switched on. A standing wave is excited and many reflections occur on both the plasma surface: $x = \pm 0.9$ m. The input power is absorbed by hydrogen near the cyclotron resonance layer: $x \simeq 0$. The condition of electron Landau damping is not satisfied so much. The absorbed power by electrons, however, amounts to 10% of the input power because of the weak

absorption of hydrogen. Figure 3 shows the stationary state after the acceleration of high energy ions. Incoming wave propagates from the low field side antenna. The standing wave ratio of Ey becomes small compared with Fig. 2. The main part of input RF power is absorbed by high energy ions: more than 97%. The electron absorbed power becomes negligibly small: less than 1%. The extension of the power absorption region is due to the RF power deposition averaged over the magnetic surface.

IV. Tail Acceleration The differences between the heated plasma by the second resonance and by the third one are in the temperature and density of tail ions. In the second resonance case, the density increment of fast ions due to ICRF heating is about 8.8% whether NB is injected or not. The incremental tail temperatures are $\Delta T_{tail}^{2nd} \cong 54$ keV for the ICRF alone heating and $\Delta T_{tail}^{2nd+NB} \cong 20$ keV for the combined NBI heating. When the third resonance heating is carried out, the density increment is about 4.7% whether NBI or not. As for the tail temperature, $\Delta T_{tail}^{3rd} = 150$ keV and $\Delta T_{tail}^{3rd+NB} = 47$ keV. The third resonance heating accelerates higher energy ions than the second one. The production rate of fast ions is smaller than the second resonance heating. This is caused by the difference of the quasi-linear diffusion coefficient. The tail temperature decreases with the increase of the NBI power. Because, the NBI heating is regarded as the lower energy particle source compared with ICRH heating.

IV. Conclusion and Discussion In both cases of the second and third harmonic resonance heating with NBI, the wave propagation, power absorption and acceleration of fast ions are numerically analyzed using the self-consistent model. Although the damping rate of the third harmonic resonance is weak, the wave power is mainly absorbed by hydrogen due to the acceleration of fast ions. The incremental tail energy by third resonance heating is greater than that of second resonance heating.

In this article, we assumed the stationary state and that the RF power deposition is localized near the magnetic axis. When the standing wave is excited, the RF power is absorbed in the whole poloidal cross section due to the two dimensional analysis. The RF power density is reduced and temporal growth of fast ions will be delayed. The problems in connection with time evolution will have to be further investigation.

References

1. K. Hamamatsu, et al., Nucl. Fusion 29, 147 (1989)

2. T. Fujii, et al., Proc. of 15th Europ. Conf. on Cont. Fusion and Plasma Physics. Dubrovnik Vol. 12B, Pt.2, 766 (1988).

3. A. Fukuyama, et. al., Nucl. Fusion 23, 1005 (1983).

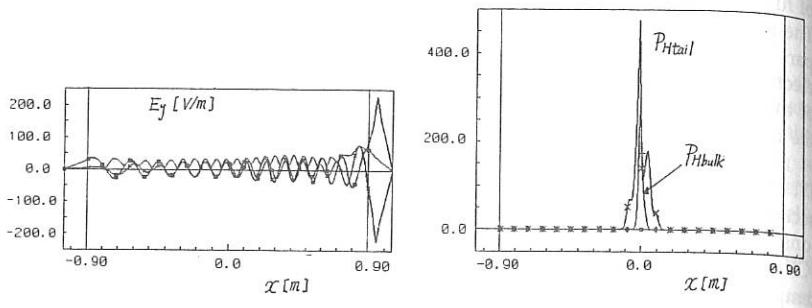

Fig.1. Radial profiles of Ey and power deposition. 2nd harmonic ICRF + NBI heating

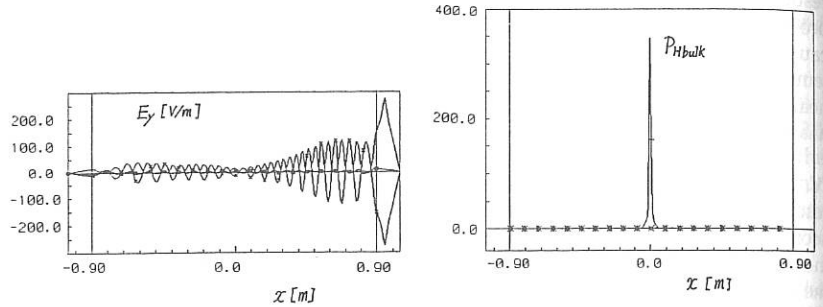

Fig. 2. Radial profiles of Ey and power deposition. 3rd harmonic ICRF heating before tail acceleration.

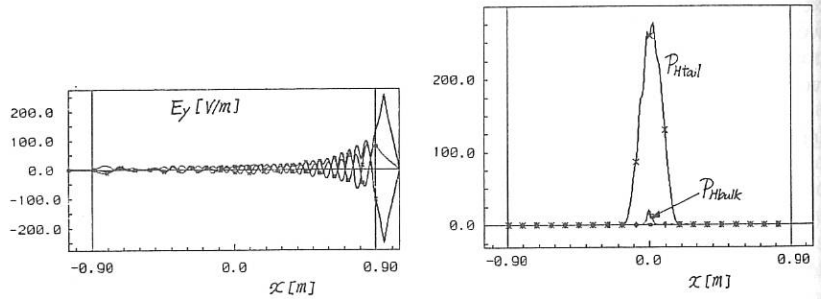

Fig. 3. Radial profiles of Ey and power deposition. 3rd harmonic ICRF heating after tail acceleration.

^{3}HE–D FUSION STUDIES AND α–PARTICLE SIMULATIONS USING MEV IONS CREATED BY ICRH IN THE JET TOKAMAK.

D F H Start, V P Bhatnagar, M Bures, D J Campbell, J P Christiansen, J G Cordey, W G F Core, G A Cottrell, L–G Eriksson, T Hellsten[1], J Jacquinot, O N Jarvis, P Lallia, P J Lomas, C Lowry, P Nielsen, J O'Rourke, F Rimini, G Sadler, A Tanga, P R Thomas, K Thomsen, B Tubbing, P van Belle, and J A Wesson.

JET Joint Undertaking, Abingdon, Oxon, OX14 3EA, UK
[1]Royal Institute of Technology S–10044, Stockholm, Sweden.

1. INTRODUCTION Non–thermal fusion reactions driven by ICRH could reduce the power required to reach ignition in a reactor. The reaction $^3He + D \rightarrow {}^4He(3.6MeV) + p(14.7MeV)$ has been produced in JET by (^{3}He)D minority ICRH and the results of the initial experiments have been reported in a previous paper[1]. Those experiments, with carbon coated walls and limiters achieved a fusion power of 60kW and found that the central deuterium density was only about 38% of the electron density. This damaging dilution was overcome in the present experiments by beryllium gettering of the torus. The reactivity has been increased to 100kW and a Q value ($Q \equiv P_{fus}/P_{rf}$) of 1% has been achieved. The ability of ICRH to generate energetic ions provides a good opportunity to study aspects of α–particle behaviour prior to D–T operation. A crucial question is whether the full α–particle heating can be utilised or whether tokamak reactors will suffer from α–particle losses with the concomitant increased power loading of the first wall. The criterion for maximum α–particle heating is that the confinement time exceeds the slowing down time τ_s, and this implies a particle diffusivity less than $a^2/4\tau_s$ where 'a' is the minor radius. Values of $a^2/4\tau_s$ for the next step devices are expected to be close to $2m^2/s$[2]. In JET, $a^2/4\tau_s$ can be as low as $0.7m^2/s$ so that, if the slowing down is demonstrably classical in these cases, then efficient α–particle heating in reactors can be anticipated with some confidence.

^{3}HE–D FUSION EXPERIMENTS. The ^{3}He–D reaction produced by ^{3}He minority ICRH has been measured by detecting the 16.6 MeV γ–rays from the weak $^3He + D \rightarrow {}^5Li + \gamma$ branch. The experiments were conducted after beryllium gettering of the vessel and used the following discharge parameters; $I_p = 3MA$, $B_t = (3.0 - 3.4)T$, $n_e(0) \simeq 4x10^{19}m^{-3}$, and $P_{rf} \leq 14MW$. Most of the data were recorded with the ICRF resonance placed close to the magnetic axis but a scan of the resonance position in major radius was also made in an attempt to optimise the fusion reactivity. The results for the central resonance position are shown in fig 1, together with the results of the previous series of experiments in the carbon coated vessel [1]. With the beryllium coating the reaction rate is generally twice that with carbon walls and limiters and reaches a maximum value close to 100kW of fusion power. The maximum Q value, as defined by $Q = P_{fus}/P_{rf}$, was about 1% as shown in fig 2. The results have been compared with theoretical predictions based on the Stix model[3] for the minority distribution function.This model calculates the fusion reactivity on each flux surface assuming a Gaussian power deposition profile of width $\simeq$ 0.2m and that 65% of the input power is coupled to the ions. The latter is consistent with both RF modulation experiments [4] and the observed fast ion energy contents (see also ref 1). The model simulates the measured reactivities provided the deuterium density is taken to be 70% of the electron density. This value is about twice that obtained from analysis of the data with the carbon coated vessel and is a result of the lower impurity level afforded by the Be gettering. The higher concentration of deuterium is consistent with the lower

$Z_{eff} \simeq 2.5$ compared with $Z_{eff} \simeq 3.5$ for the previous series.

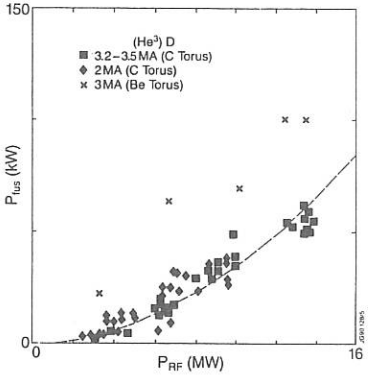

Fig 1. ^3He-D fusion power versus P_{rf}.

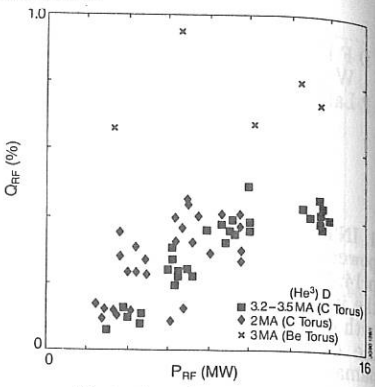

Fig 2. Q–value versus P_{rf}

The modelling shows that at the highest power levels the ^{3}He ions in the plasma centre have energies substantially greater than that (0.5MeV) at which the fusion cross section peaks. This over–heating of the minority ions can be reduced by moving the resonance off–axis in order to reduce the power density and optimise the reaction rate. A search for this effect was carried out and the results are shown in fig 3.

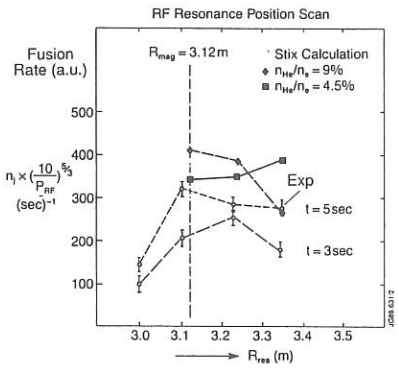

Fig. 3. γ–ray yield versus R_{res}.

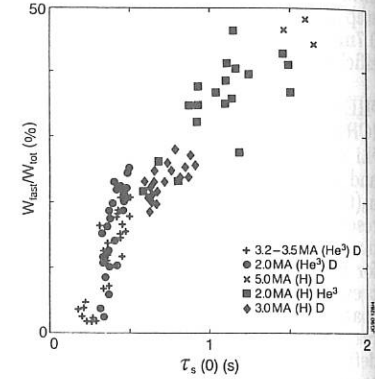

Fig. 4. W_f/W_{tot} versus $\tau_s(0)$.

As the resonance is moved up to 0.2m towards the low field side the γ–ray intensity remains constant and no increase in the γ–ray count rate is seen. The reason for this lack of enhancement is, according to the Stix calculations, due to insufficient energy in the ^{3}He ions. In these discharges the RF power was between 8MW and 10MW and the ^{3}He concentration was approximately 9% of the electron density. For such conditions the ^{3}He tail temperature in the plasma centre was calculated to be only

1MeV for the central resonance case. The Stix code predictions are also shown in fig 3.

With the resonance placed on the high field side the γ–ray emission falls by a factor of 2.5. This is due to the fact that the high field side of the magnetic axis is shielded from the detector which views vertically downwards. The reduced count rate is consistent with the assumption that most of the reacting ions are on trapped orbits which turn at the resonance layer. These ions spend typically 60% of their time behind the shielding for a resonance radius of 3.0m.

ALPHA–PARTICLE SIMULATION STUDIES. The objective of these studies was to test for classical slowing down of the fast ions by comparing the measured fast ion energy content with the predictions of the Stix code described above. The data were taken from Monster sawtooth discharges with on–axis ICRH and the plasma parameters covered a wide range: I_p=(2–5)MA, B_t=(2.0–3.4)T, $n_e(0)$=(2–6)x$10^{19}m^{-3}$, central electron temperature $T_e(0)$ = (4–12)keV and $P_{rf} \leq$ 14MW. The fast ion energy content was deduced from the energy measurements given by the diamagnetic loop (W_{dia}) and Shafranov shift (W_{mhd}). The fast ion energy content is given by $W_f = 1.33(W_{dia} - W_{mhd})$ and the total energy content is obtained from the expression $W_{tot} = 0.33(W_{dia} + 2W_{mhd})$. The maximum value of W_f was 2.5 MJ which was achieved during a Monster sawtooth in a 5MA discharge and represented nearly 50% of the total energy content as shown in fig. 4. In this figure the ratio W_f/W_{tot} is plotted against the central slowing down time $\tau_s(0)$; the fast ion energy content can be written as $W_f = kP_{rf}\tau_s(0)/2$ where k is a form factor accounting for the effects on τ_s of the radial profiles of n_e and T_e. We can also define an effective slowing down time as $\tau_{eff} = 2W_f/P_{rf}$ and fig 5 shows a plot of τ_{eff} against $\tau_s(0)$.

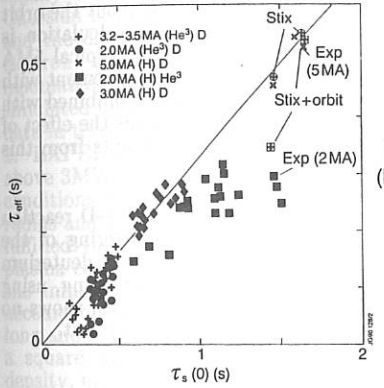

Fig 5. Effective slowing down time versus central slowing down time $\tau_s(0)$.

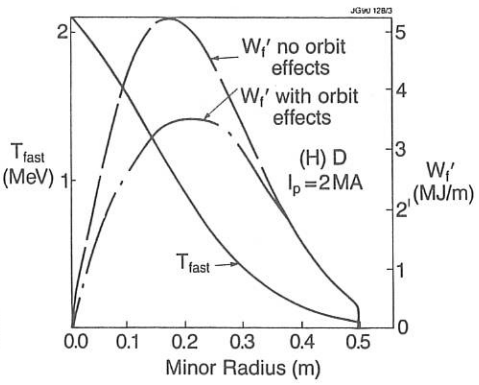

Fig 6. Model fast ion tail temperature and energy content for I_p = 2MA and $\tau_s(0)$ =1.5s.

Most of the data show a similar ratio of $\tau_{eff}/\tau_s(0)$ and these cases are well represented by the Stix model. However, as the central slowing down time becomes greater that 1 sec, the values of τ_{eff} for the 2MA data depart from the linear relation with $\tau_s(0)$. There is no deviation for the 5MA data and comparable values of $\tau_s(0)$.

This dependence of the deviation on plasma current suggests that the effect is

connected with the orbit sizes of the fast ions. For example protons with energies of several MeV can follow large D–shaped orbits in the poloidal plane which pass through the plasma centre and also allow access to the cool plasma periphery. In the case of the 2MA results with $\tau_s(0) = 1.5$s the Stix calculation gives a tail temperature of 2MeV in the plasma centre (see fig 6). Trapped ions of this energy, and which have their turning points at the resonance, follow D–shaped orbits with a diameter of about 0.4m. At this distance from the plasma centre the slowing down time is a factor of two less than $\tau_s(0)$. An estimate of the effect of the orbit on the average slowing down time has been made using a semi–analytic model. The collisional power loss during a bounce time, τ_b, is $\Delta P = \Delta W_f/\tau_b = \tau_b^{-1}\int 2W_f/\tau_s \, dt$. The bounce average slowing down time $<\tau_s>$ is defined by $\Delta P = 2W_f/<\tau_s>$ so that we obtain the expression

$$<\tau>^{-1} = \int_{r_{min}}^{r_{max}} \frac{1}{\tau_s(r)} \frac{1}{v_r} dr \Big/ \int_{r_{min}}^{r_{max}} \frac{1}{v_r} dr$$

where r is the minor radius, r_{min} and r_{max} are the radial extremities of the orbit and v_r is the radial velocity. Analytic expressions for $v_r(r)$ are obtained from narrow orbit theory for the low energy ions on banana orbits and from the model by Stringer [5] for the D–shaped orbits. The principal difference is that the radial velocity for the D–shaped orbits is asymmetric about the mean radius $r_m = (r_{max} + r_{min})/2$ whereas it is symmetric for the banana orbits. Thus the energetic ions spend proportionately more time in the cooler plasma regions which produces significant deviation of $<\tau_s>$ from $\tau_s(r_m)$. This is not the case for the normal banana orbits for which $<\tau_s> \simeq \tau_s(r_m)$. The correction produced by the D–shaped orbits can be seen in fig 6 which shows the radial profiles of fast ion energy content, dW_f/dr, calculated both with and without the orbit effect for one of the 2MA discharges. The value of $<\tau_s>$ from this calculation is plotted in fig 5 and is within 20% of the measured value of τ_{eff}. For a typical 5MA case the orbit correction amounts to only a 3% decrease in τ_{eff} in good agreement with the measurement. Recently this calculation of the orbit effects has been combined with the Stix code to produce a self–consistent model; in the initial calculations the effect of $<\tau_s>$ on the tail temperature was not taken into account. The first results from this code agree remarkably well with the initial calculations.

SUMMARY. Non–thermal ICRF driven fusion experiments using the ^{3}He–D reaction have achieved 100kW of fusion power in JET following beryllium gettering of the vessel. The results agree well with theoretical modelling which indicates a deuterium density of about 70% of the electron density. Simulation of α–particle heating, using MeV ions created by ICRH in mhd–quiescent Monster sawtooth discharges, shows no evidence for anomalous losses when the orbit effects on τ_s are taken into account.

REFERENCES.

1) D A Boyd et al., Nuclear Fusion 29(1989)593.
2) J G Cordey, 7th Euro. Tokamak Programme Workshop, Heathrow, UK 1988.
3) T H Stix, Nuclear Fusion 29(1989)593.
4) D F H Start et al.,Proc. of the 12th IAEA Conf on Plasma Phys. and Contr. Nucl. Fusion Research, Nice 1988, Vol 1, p 593
5) T E Stringer, Plasma Physics 16(1974)651.

FAST ION ORBIT EFFECTS IN HIGH POWER ICRH MODULATION EXPERIMENTS IN THE JET TOKAMAK

D F H Start, M P Evrard[1], V P Bhatnagar, M Bures, D J Campbell, W G F Core, G A Cottrell, M Cox[2], L–G Eriksson, N Gottardi, H Hamnen[3], T Hellsten[4], M A Kovanen[5], H Lean[2], J Jacquinot, M R O'Brien[2], J O'Rourke, P R Thomas, and U Willen[3]

JET Joint Undertaking, Abingdon, Oxon, OX14 3EA, UK
[1]LPP–ERM/KMS EUR–EB Association, 1040, Belgium.
[2]Culham Laboratory,Abingdon, Oxon. OX14 3DB, UK.
[3]Chalmers University, Gothenburg, Sweden.
[4]Royal Institute of Technology S–10044, Stockholm, Sweden.
[6]Lappeenranta University of Technology, Finland.

1. INTRODUCTION The discovery of 'Monster' sawteeth in JET has provided the opportunity to perform ICRH thermal wave measurements which are uncompromised by the locking of sawteeth to the RF modulation frequency [1]. The aim of such studies is to measure the electron heat diffusivity, χ_e, and the electron heating profiles. Modulated ICRH experiments have been carried out in JET using on–axis heating with both ^{3}He and hydrogen minority ions. The results with 5% ^{3}He concentration gave $1.5<\chi_e(m^2/s)<3$ and have been reported previously [2]. Those data could be readily interpreted in terms of a simple heat diffusion model containing on–axis Gaussian heating profiles for both the collisional electron heating by the minority ions and the direct heating due to mode conversion, transit time magnetic pumping and electron Landau damping. Experiments with lower minority density produced modulated electron temperature profiles which were hollow and which cannot be simulated by such a simple model. In this paper we propose an interpretation of these data in terms of the response of the energetic minority ions to modulated RF.

2. EXPERIMENTAL CONDITIONS AND RESULTS For coupled power levels above 3MW, ICRH produces Monster sawteeth in JET over a wide range of discharge conditions. Important requirements are power deposition inside the sawtooth inversion radius and a value of the safety factor, q_{cyl}, greater than 3.3. The present experiments fulfilled these criteria and were performed with an RF frequency of 32 MHz. The plasma current was either 2 MA or 3 MA and the toroidal field was chosen to position the minority ion fundamental resonance close to the magnetic axis, having taken account of paramagnetism and finite β effects. The RF power pulse was typically 5 sec long and consisted of a steady component of between 5MW and 10 MW together with a square wave modulation of about 25% relative amplitude. The central electron density, $n_e(0)$, was in the range 3.0×10^{19} m^{-3} to 3.8×10^{19} m^{-3} during the heating.

The electron temperature profile was measured in the equatorial plane using an ECE grating polychromator. The amplitude and phase of the electron temperature perturbation, $*T_e$, at the fundamental modulation frequency, ω, was obtained by Fourier analysis of both the ECE signals and the RF power. The pressure variation caused a modulation of the Shafranov shift by typically 3 mm which produced a spurious component in $*T_e$ of up to 40eV. The data were corrected for this effect.

The plasma energy content measurements from the diamagnetic loop (E_{dia}) and the equilibrium analysis (E_{mhd}) were also modulated. The total modulated plasma energy content ($*E_{tot}$) was then obtained from $*E_{tot} = (*E_{dia} + 2*E_{mhd})/3$. Since the global energy confinement time, τ_g, satisfies $\omega\tau_g>>1$ the absorbed modulated RF power ($*P_{abs}$) in the bulk plasma is given by $*P_{abs} = \omega*E_{tot}$.

2.1 (^{3}He)D ICRH with 2% Minority Concentration. These experiments were carried out with a plasma current of 3.1MA and a toroidal field of 3.16T. The RF power was modulated at 4Hz between 8MW and 12MW.The minority ions were injected into the discharge as a 1 sec pulse of ^{3}He gas before the RF heating. The subsequent rise in $n_e(0)$ gave an estimate of 2% for the ^{3}He concentration relative to the electron density. The ICRH resonance layer intersected the median plane at R=3.09m, which is close to the magnetic axis at R_o=3.13±0.10m. The effect of the ICRH on T_e at a major radius

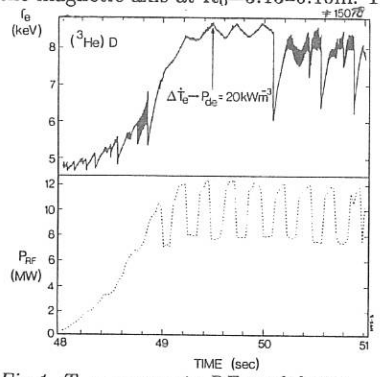

Fig 1. T_e response to RF modulation.

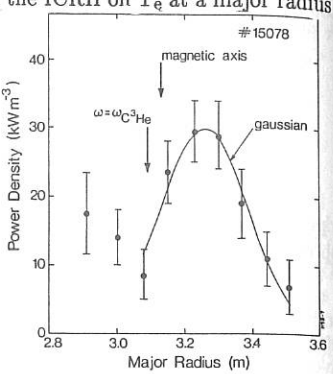

Fig 2. Direct electron heating profile.

of 3.25m is shown in fig 1. A Monster sawtooth appears at 48.9 sec and lasts for 1.2 sec. The triangular T_e modulation has a peak–to–peak value of 0.3 keV compared with a steady component of 8.5 keV. The discontinuity in the time derivative of the temperature, coincident with the power level switching, reveals the presence of direct electron heating. The direct heating power density, $*P_{de}$, can be calculated from the discontinuity [2] and the result is shown in fig 2. The solid line is a Gaussian fit to the data outside R = 3.0m. The Gaussian is slightly off–axis and has a maximum power density of 30 kW/m^3. From this profile we estimate that the direct heating is about 10–15% of the coupled RF power. The total power absorbed in the bulk of the plasma is 82±11% of the coupled power, as obtained from $*E_{dia}$ and $*E_{mhd}$.

The results of Fourier analysis of T_e are shown in fig 3 and fig 4. The maximum amplitude of $*T_e$ at 4Hz is 140eV at about 0.2m minor radius. On–axis, the amplitude is only 60eV. Such a hollow profile would indicate off–axis absorption even though the resonance layer intersects the median plane centrally. On the other hand, the phase delay shows a minimum on–axis which suggests that the power deposition is central. Central power deposition is also supported by the 16 Hz modulation results in fig 3.

2.2 (H)^{3}He Minority ICRH Experiments. Studies with hydrogen minority ions were made in ^{3}He discharges with I_p=2 MA and B_t=2.18T. The power was modulated at 5Hz between 3.8MW and 6.4MW and the fraction of the couple power deposited in the bulk plasma was 85±10%. In these experiments the hydrogen density was deduced indirectly from a) the ratio of hydrogen to deuterium from the neutral particle analysers and b) the influx rate of deuterium from the vessel walls and limiters. These data suggest that n_h/n_e is about 2%. The amplitude profile of $*T_e$ is hollow, as in the case with 2% ^{3}He minority. However, the central minimum is much less deep than that in fig 3. A further difference is that the minimum in the phase coincides with the amplitude maximum. The direct heating profile was difficult to determine due to a low

signal to noise ratio, but the maximum was estimated to be 28±8kW/m³ at R = 3.23m.

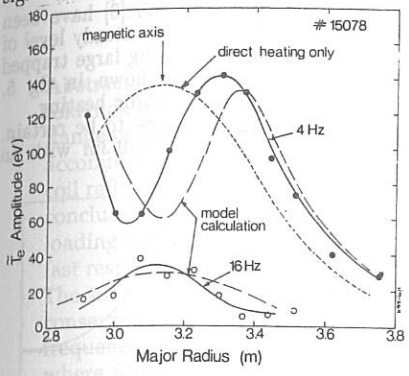

Fig 3. Amplitude profile of $*T_e$ *modulation.*

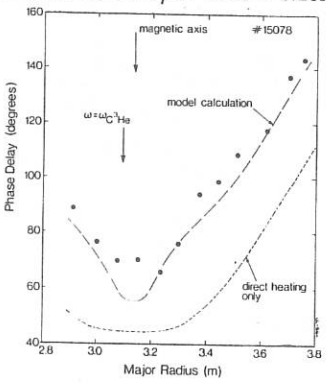

Fig 4. Phase profile of $*T_e$ *modulation.*

3. DISCUSSION. The interpretation of the above results is based on the one dimensional heat diffusion equation in cylindrical geometry for T_e, namely,

$$\frac{3}{2}\frac{\partial}{\partial t}(n_e T_e) = \frac{1}{r}\frac{\partial}{\partial r}(r n_e \chi_e \frac{\partial T_e}{\partial r}) + P_{ed} + P_{em} \qquad (1)$$

The electron heating power density profiles, $P_{ed}(r)$ and $P_{em}(r)$, are the direct and minority heating, respectively. Each component is taken as a Gaussian profile with the minority heating being modulated in both amplitude and width;–

$$P_{em} = \frac{P_{ab}}{2\pi^2 R W^2}(1 - F_d)(1 + \alpha c)\, e^{-r^2/W^2(1+\beta c)^2} \qquad (2)$$

In eq(2) P_{ab} is the steady absorbed power level, W is the width of the minority heating profile, F_d is the fraction of power absorbed directly, and $c \equiv \cos(\omega t - \theta)$. The minority heating is assumed to be on–axis. The phase delay, θ, due to the slowing down time of the minority ions, is given by $\tan\theta = \omega\tau_e$. The value of θ was close to $\pi/2$ for all cases. Equation (1) was solved numerically with $n_e\chi_e$ kept constant.

The width modulation provides a depletion of the heating power in the centre so that there is a sign reversal between the on–axis and off–axis minority heating. This feature appears to be the key element in simulating the hollow temperature profiles. The previous modulation experiments [2] can be fitted with $\chi_e \simeq 2m^2/s$, $\alpha = -0.047$ and $\beta = 0.0$ (i.e. no width modulation). However, for the 2% ^{3}He minority case, the $*T_e$ profiles cannot be reproduced with $\beta = 0.0$. The difficulty is illustrated by the calculated $*T_e$ modulation for the off–axis direct heating alone. Using χ_e=2m²/s and the Gaussian fit to the direct heating profile (fig 2), we obtain a centrally peaked $*T_e$ profile as shown in fig 3. Moving the centre of the heating out to 0.25m and decreasing the width from 0.2m to 0.15m, to reduce the central power deposition to the limit of compatibility with the data, still produces a peaked profile. A slightly hollow profile can be achieved if χ_e is reduced tenfold inside a radius of 0.25m, but then the phase has a minimum at 0.25m and increases towards the axis.

The profiles can be simulated for $\chi_e = 2m^2/s$, W = 0.18m, $\alpha = -0.037$ and $\beta = 0.029$ as shown in fig 3 and fig 4. The direct heating was again the fitted data. The values of α and β are kept consistent with the modulated absorbed power amplitude

which sets the constraint $\alpha + 2\beta = 0.02$ for pulse 15078. The model also gives reasonable fits to the phase and amplitude profiles of the hydrogen minority case.

Monte Carlo ICRH orbit calculations using the HECTOR code[3] have been carried out to test for depletion of the central minority heating. With a steady level of RF power there is certainly a density depletion due to the ions following large trapped orbits as the energy increases. An example for pulse 15078 is shown in fig 5. Preliminary calculations with modulated power indicate antiphase electron heating ($\theta = -\pi/2$) in the centre but the statistical fluctuations are too large to be certain. However, modulated heating, with $\theta = \pi/2$, is clearly seen at r = 0.3m with an amplitude close to that required by the transport model.

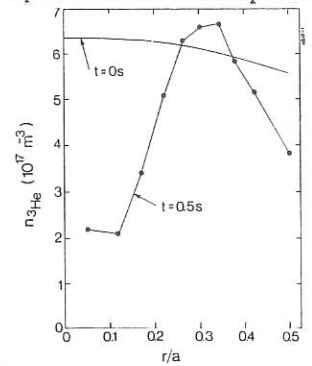

Fig 5. Depletion of ^{3}He ions by RF heating.

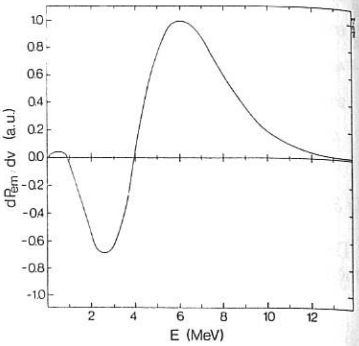

Fig 6. d^*P_{em}/dv versus minority energy.

An antiphase component has also been seen in Fokker–Planck calculations [4] and an example is shown in fig 6. The 2MeV particles heat the electrons with $\theta = -\pi/2$ whereas $\theta = \pi/2$ for the 7MeV ions. At these energies, trapped ions passing through the centre follow large D–shaped orbits which allow access to the cool outer regions of the plasma. This affects the slowing down and has been modelled by reducing τ_e with increasing energy in a way consistent with the orbit widths and the T_e and n_e profiles. However, the density modifications due to the orbits are not accounted for and these will tend to reduce the power transfered from the more energetic minority ions.

SUMMARY. The hollow $^*T_e$ profiles obtained in the low minority density cases seem to reveal some interesting aspects of fast ion physics. The key element in the interpretation is the on–axis sign reversal of the modulated power flowing from the minority to the electrons. This has been modelled by modulating the width of the minority heating but could also be due to central depletion of the fast ions (by orbit effects) or an intrinsic feature of their distribution function.

ACKNOWLEDGEMENTS. It is a pleasure to thank the JET operating team and the diagnostics groups for their assistance with these experiments.

REFERENCES.

1) D J Gambier et al., Nuclear Fusion, 30(1989)23.
2) D F H Start et al., Proc. of the 12th IAEA Conf on Plasma Phys. and Contr. Nucl. Fusion Research, Nice 1988 Vol 1 p593.
3) M A Kovanen and W G F Core, private communication.
4) L–G Eriksson and U Willen, JET report JET–IR(89)16.

Analysis of ICRF Coupling and Heating in CIT and JET

J.E. Scharer, N.T. Lam and R.S. Sund
Electrical and Computer Engineering Department
University of Wisconsin, Madison, USA 53706

Abstract -- We study the effects of an L- to H- mode transition in a tokamak on the coupling of fast wave launchers in the Ion Cyclotron Range of Frequencies. Waveguides or coils can readily be accommodated within the formalism. We calculate the waveguide or coil reflection coefficient for conditions appropriate to CIT. It is concluded that an L-to H-mode transition can impose substantial loading variations on the launcher system which can be handled by a fast response matching system similar to that successfully used on JET. The subject of linear wave propagation and its associated power conservation in a slab geometry for waves in the ion cyclotron range of frequencies is treated. The development is applicable to instances where full-wave effects such as reflection, mode-conversion, and absorption may be important. The local power conservation relation follows from a definition of local power absorption and a companion general expression for kinetic flux based on basic principles. These expressions are evaluated to second order in a numerical code, and results are presented for several cases. For fundamental minority ^{3}He and second harmonic absorption in machines comparable to JET, fast wave launching in CIT is discussed.

I. Calculation of Plasma Coupling - In this paper, we consider the effects of the L- to H-mode transition on launchers designed for fast wave heating of tokamaks, specifically CIT [1]. For analytical simplicity, the launcher is taken as a dielectric-filled rectangular waveguide. We also consider the plasma as one-dimensional and cold. This approximation is valid in our case, since the fast wave is the dominant power-coupling mode. The launcher configuration is arranged such that x = radial direction; y = poloidal direction; z = toroidal direction. In the waveguide, the transverse fields can be written as linear combinations of TE and TM modes.

In the slab model, the plasma transverse fields can be Fourier-analysed and continuity of E_T and H_T at the interface (x = 0) and mode orthogonality yield the following system of equations for A_l and B_l : $A_l - B_l = \Sigma_m L_{lm} (A_m + B_m)$, where

$$L_{lm} = \frac{1}{4\pi^2} \frac{\int \bar{H}_l^* (\bar{k}) \bullet \bar{\bar{Y}} \bullet \bar{E}_m (\bar{k}) dk_y dk_z}{D_l^w \int | \bar{H}_l(y,z) |^2 dydz}, \qquad (1)$$

Following Bers and Theilhaber [2], we have introduced the plasma surface admittance tensor $\bar{\bar{Y}}$ defined as $\bar{H}_T^p (k_y,k_z,0) = \bar{\bar{Y}} \bullet \bar{E}_T^p (k_y,k_z,0)$ where we assume that $\bar{\bar{Y}}$ depends only on the local edge plasma

parameters. We calculate the slow wave fields by solving the full set of wave equations, while the fast wave fields are computed from a reduced set obtained by setting $E_z = 0$. Explicitly, it can be written as

$$\frac{1}{k_0}\frac{dE_y^p}{dx} = -\frac{n_y D}{S - n_z^2} E_y^p + i\left[1 - \frac{n_y^2}{S - n_z^2}\right] H_z^p$$

$$\frac{1}{k_0}\frac{dH_z^p}{dx} = i\left[S - n_z^2 - \frac{D^2}{S - n_z^2}\right] E_y^p + \frac{n_y D}{S - n_z^2}, \qquad (2)$$

where $k_0 = \omega/c$; $n_y = k_y/k_0$; $n_z = k_z/k_0$ and S, D, P = dielectric tensor elements for the cold plasma. Since only this mode can propagate in the waveguide, we anticipate that the dominant admittance element for the calculation of the reflection coefficient is $Y_{zy} \simeq H_z^f / E_y^f$ corresponding to the incident TE_{10} mode. Thus we need only deal with the system of differential equations for the fast wave given above. Assuming that no reflections occur from deep inside the plasma, the system of differential equations (2) has been solved numerically [3] by a Runge-Kutta algorithm.

II. Power Conservation and Wave Heating in the Plasma Core -- Our work is distinct in providing fundamental definitions of local power absorption and kinetic flux. The total power absorbed by all the particles passing through $\bar{r}$ is obtained [4] by an integration over v.

$$P(\bar{r}) = \int d^3v \; < q\bar{E}(\bar{r}',t') \cdot \bar{v}' f_1^*(\bar{r}',\bar{v}',t') > \qquad (3)$$

where $< >$ denotes the time-average over t' and the star indicates the complex conjugate. Kinetic flux is the flux of energy carried by the coherent oscillation of plasma particles. The amount of energy being transferred between the particles and the wave at time t' is given by

$$\Phi = \Re e\,(E(r', t') \cdot v')\,\Re e\, f_1(r', v', t') =$$

$$\frac{1}{4}\left[e^{-i(kz - \omega^* t)} e^{i(kv_{\|} - \omega^*)\tau} \sum_n a_n^* e^{in\omega_0 \tau} + c.c.\right]$$

$$\times \left[e^{i(kz - \omega t)} e = i(kv_{\|} - \omega)\tau \sum_m \frac{b_m e^{-im\omega_0 \tau}}{i\Delta_m} + c.c.\right] \qquad (4)$$

where $\tau = t - t'$ and $\Delta_m = \omega - kv_{\|} - m\omega_0$. The total energy gained or lost by the particles since a time τ seconds before t until t is $\int_0^t \Phi(\tau')\, d\tau'$. Φ contains a **secular** part which is independent of τ which we designate as $< \Phi >_\tau$. We have previously identified $< \Phi >_\tau$ giving rise to the power absorption density P. The total kinetic flux is then simply $S_k = \int d^3v\, v \left\langle \int_0^\infty (\Phi - <\Phi>_\tau)\, d\tau \right\rangle_t$. The result for evaluation of the total kinetic flux is

$$S_k = \frac{1}{2}\Re e \lim_{\gamma \to 0} \int d^3v \frac{v}{\omega_0} \sum_{n\,m} \frac{1}{n - m} \frac{a_n^* b_m}{\Delta_m} \qquad (n \neq m) \qquad (5)$$

The evaluation of the kinetic flux terms in Eq. (5) to third order is carried out in the same manner as that for local power absorption. A

computer code, XWAVE, has been written which solves the wave equation for a fast wave incident from either the high or low magnetic field side of the mode conversion zone or for a Bernstein wave incident from the high-field side. It also computes the local power absorption profile for each particle species and the power flux.

III. Results -- We consider coupling for a CIT-like plasma with the following parameters: major radius R = 210 cm, minor radius a = 65 cm; B_0 = 10.0 T; 1-1 D-T plasma with $n_{D0} = n_{T0} = 2.0 \times 10^{14}$ cm^{-3} and the percentage of ^{3}He = 5% of the total electron density. We divide the density profile into an exponential variation from the launcher to the separatrix: exp[(a - x) / scl] with scl = 5 cm; a shifted Gaussian variation and a plateau region to the plasma center. For CIT parameters, we have chosen the separatrix density gradient as 6×10^{12} cm^{-4} for the L-mode and as 6×10^{13} cm^{-4} for the H-mode scaled from recent experiments. The waveguide has a width of 30 cm and is filled with a dielectric of $\varepsilon_r = 81$. It is placed 5 cm away from the separatrix. [The heating is at the fundamental frequency of ^{3}He f = 95 MHz (Z_w = 51.7Ω).] Table I lists the power reflection coefficient $|\Gamma|^2$ and plasma impedance for various waveguide heights for the L and H-modes.

Figures 1 and 2 show Re(Y_{zy}) vs. k_y and k_z for the L- and H-mode, respectively. The shorter evanescence lengths in the H-mode account for the wider spectrum in Y_{yz}. However, the magnitude of Re(Y_{zy}) is significantly reduced. This is in accord with the significant increase of the power reflection coefficient in the H-mode (7% in the L-mode vs. 37% in the H-mode for a 2:1 waveguide). We suggest that the variation in launcher loading during the L to H mode transition in CIT can be handled by stub tuners and frequency tuning of a moderate bandwidth RF amplifier, as has been demonstrated on JET [5].

The amounts of wave reflection, integrated absorption by species over the ±20 cm resonance region, transmission, and mode conversion from the incident fast mode to the Bernstein mode are evaluated and shown on Fig. 3 as a function of the wave number vector, $k_{||}$, parallel to the magnetic field for JET parameters corresponding to 5% ^{3}He, 90% D with $n_e = 5 \times 10^{13}$/cm and B_0 = 3.45 T on axis at a fundamental ^{3}He resonance. Note that the ^{3}He absorption peaks at a value of 45% of the incident power at a $k_{||}$ value of 6 m^{-1} with a corresponding value of about 5.5% of the power absorbed by the electrons via Landau and transit-time damping.

The fast wave, low field incidence 5% minority ^{3}He case in a 45%-45% deuterium-tritium plasma with parameters comparable to CIT is illustrated in Fig. 4. Our CIT parameters correspond to those in Fig. 1 except that $n_{^3He} = 2 \times 10^{13}$/cm^3 and T = 20 keV. Note that the ^{3}He single pass absorption of 65% peaks at a high $k_{||}$of 18 m^{-1}. The associated electron absorption is 12% and the tritium absorbs 4% of the incident fast wave power from the low field side for a 20 cm absorption width near the core of the plasma. One also notes that a substantial fast

wave reflection (>40%) from the helium cyclotron resonance occurs for lower (<10 m^{-1}) values of $k_{\|}$.

TABLE I, $|\Gamma|^2$ and Z_p for various waveguide heights in the L and H-modes

	H (cm)	$\|\Gamma\|^2$	Z_p (Ω)
L-mode	20.0	0.02	68.6 + j 3.3
	15.0	0.07	82.1 + j 16.6
	10.0	0.19	98.5 + j 49.6
H-mode	20.0	0.31	54.4 + j 70.3
	15.0	0.37	52.1 + j 77.3
	10.0	0.51	41.5 + j 93.1

IV. ACKNOWLEDGEMENTS

This work is supported by DOE grant #FG-02-86ER53218.

[1] CIT Conceptual Design Review, PPPL, Jan. 1988.
[2] A. Bers and K. Theilhaber, Nucl. Fusion 23 (1983) 41-48.
[3] N.T. Lam and J.E. Scharer, to be published in Fusion Engineering and Design.
[4] B.D. McVey, R.S. Sund and J.E. Scharer, Phys. Rev., 55, 507 (1985).
[5] G. Bosia et al., 15th Symposium on Fusion Technology, (Utrecht, 1988) pp 459-463.

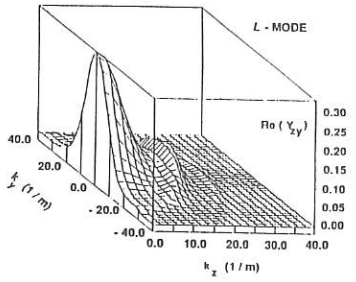

Figure 1

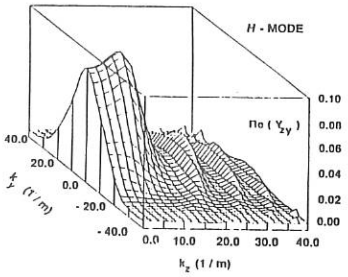

Figure 2

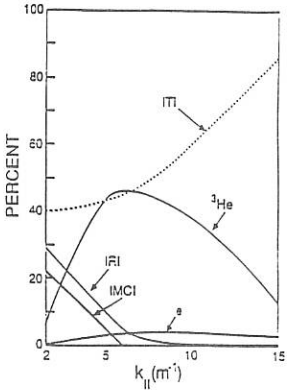

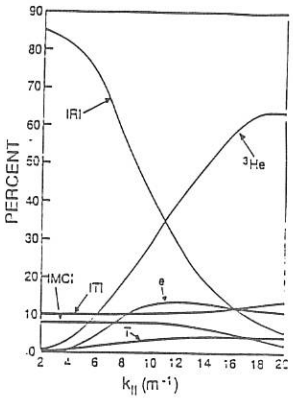

Studies on the distribution function of minority ions under ICRF wave heating

Chong-Han Park, Wook-Hee Koh, Duk-In Choi and *C. S. Chang*

Department of Physics
Korea Advanced Institute of Science and Technology
P.O.Box 150, Cheongyangni, Seoul, Korea

Introduction An analytical representation of the resonant ion velocity distribution in two dimensional velocity space would greatly facilitate understanding the experimental results as well as relating them to the analytical theory. However the analytical approach for the study of the ICRF heating is difficult to treat and majority of existing works are numerical approaches. In this paper the bounce averaged quasilinear kinetic equation of the form $\{C\}f_0^{(0)} + \{Q\}f_0^{(0)} = 0$ is solved numerically by finite element method (FEM) to obtain the minority ion distribution function driven by ICRF wave at the fundamental harmonic. A reasonably simple and accurate analytical expression which can well represent the numerical solution is then obtained.

Derivation of the resonant ion distribution function The lowest-order distribution function $f_0^{(0)}$ can be determined from

$$\frac{1}{v^2}\frac{\partial}{\partial v}[a_1\frac{\partial f_0^{(0)}}{\partial v} + a_2\frac{\partial f_0^{(0)}}{\partial \xi_m} + a_3 f_0^{(0)}] + \frac{1}{\xi_m}\frac{\partial}{\partial \xi_m}[b_1\frac{\partial f_0^{(0)}}{\partial v} + b_2\frac{\partial f_0^{(0)}}{\partial \xi_m}] = 0, \tag{1}$$

where

$$a_1 = \frac{D_b}{\Gamma_t n_e} + \langle\frac{Bv}{B_m|v_\parallel|}\rangle_\theta v[Z_{eff}G(\frac{v}{v_i}) + G(\frac{v}{v_e})], \quad a_2 = \frac{D_b}{\Gamma_t n_e}\frac{\xi_m^2 - \xi_0^2}{v\xi_m},$$

$$a_3 = \langle\frac{Bv}{B_m|v_\parallel|}\rangle_\theta M_t v^2[Z_{eff}G(\frac{v}{v_i})/T_i + G(\frac{v}{v_e})/T_e], \quad b_1 = -\frac{D_b}{\Gamma_t n_e}\frac{\xi_m^2 - \xi_0^2}{v^3},$$

$$b_2 = \frac{1}{2\Gamma_t n_e}(\nu_{ti} + \nu_{te})\frac{1-\xi_m^2}{\xi_m}\langle\frac{B_m|v_\parallel|}{Bv}\rangle_\theta + \frac{D_b}{\Gamma_t n_e}\frac{(\xi_m^2 - \xi_0^2)^2}{v^4\xi_m},$$

$$D_b = D_b^*\frac{(v^2 - v_{\parallel res}^2)\sqrt{1-\xi_0^2}}{\sqrt{\xi_m^2 - \xi_0^2 + (\Delta\xi_D)^2}}H(\xi_m^2 - \xi_0^2 + (\Delta\xi_D)^2), \quad D_b^* = (\frac{z_t ec}{2M_t B}|E_+|^2\frac{R}{r|\sin\theta|})_{res},$$

$$v_{\parallel res} = \pm\frac{v}{\sqrt{1-\xi_0^2}}\{\sqrt{\xi_m^2 - \xi_0^2 + (\Delta\xi_D)^2} + \Delta\xi_D\}, \quad \Delta\xi_D = \frac{k_\parallel v}{2\Omega_m}(1-\xi_m^2)\sqrt{1-\xi_0^2},$$

$$\xi_0^2 = 1 - \frac{B_m}{B_R}, \quad Z_{eff} \equiv \frac{n_i z_i^2}{n_e}, \quad \Gamma_t = \frac{4\pi z_t^2 e^4(\ln\Lambda)}{M_t^2}, \quad \nu_{ti} = \frac{\Gamma_t n_i z_i^2}{v^3}[\Phi(\frac{v}{v_i}) - G(\frac{v}{v_i})],$$

$$\langle\frac{Bv}{B_m|v_\parallel|}\rangle_\theta = \begin{cases} \frac{2}{\pi}\frac{1}{|\xi_m|}K(\xi_t^2/\xi_m^2), & \xi_m^2 > \xi_t^2, \\ \frac{2}{\pi}\frac{1}{\xi_t}K(\xi_m^2/\xi_t^2), & \xi_m^2 < \xi_t^2, \end{cases}$$

$$\langle \frac{B_m|v_{\|}|}{Bv} \rangle_\theta = \begin{cases} \frac{2}{\pi}|\xi_m| E(\xi_t^2/\xi_m^2), & \xi_m^2 > \xi_t^2, \\ \frac{2}{\pi}\xi_t[E(\xi_m^2/\xi_t^2) - (1 - \frac{\xi_m^2}{\xi_t^2})K(\xi_m^2/\xi_t^2)], & \xi_m^2 < \xi_t^2. \end{cases}$$

Here $\xi_m = v_{\|m}/v$ and 'm' means the midplane. The Heaviside step function H means that $\{Q\}$ is zero for trapped particles which never reach the resonance position. ξ_0 is the pitch angle of particles whose banana tips lie in the un-Doppler-shifted resonance layer where $\omega = \Omega$. $\Delta\xi_D$ is the amount of resonance broadening in pitch angle and $\Delta\xi_D \ll 1$, since $k_{\|}v \ll \Omega_m$ for ions. We note here singularities may occur whenever the argument of the square root in D_b is zero; however these singularities are known to be integrable (when averaged over any finite region in pitch angle) leading to finite power absorption [1]. Φ is the error function and G is the Chandrasekhar function. E and K are the complete elliptic integrals and $\xi_t = \sqrt{2\lambda}$, where ξ_t is the pitch angle at the trapped-passing boundary and λ is the inverse aspect ratio.

The governing Eq. (1) has been solved numerically by the finite element method. To illustrate our calculations we choose one representative case - a tokamak plasma with the following plasma parameters [2]: $R = 3m, a = 1.2m$, T_i=7 keV, T_e= 8 keV, B=3.45 T , $k_{\|}$= 0.05 cm^{-1}, $n_e = 6\times10^{13}$cm^{-3}, $Z_{eff} = 2$, $n_H/n_D = 0.05$ and $(n_H+n_D)/n_e = 0.8$, where majority ions are deutrons and minority ions are hydrogens. In Fig. 1(a) we plot the constant $f_0^{(0)}(v,\xi_m)$ contours of numerical solutions. At low energies $f_0^{(0)}$ is isotropic in pitch angle, while at high energies it is sharply peaked around ξ_0 as expected, where we let $\xi_0 = 0.454$. Comparison of Fig. 1(a) with Kerbel and McCoy's result [3] shows that they have the same characteristics in both energy and pitch angle profiles.

We have obtained a reasonably simple and accurate analytical solution ,which is given by

$$f_0^{(0)}(v,\xi_m) = f_{Max} + f_{tail}, \tag{2}$$

where

$$\begin{aligned} f_{Max} &= n_0 r_l [\frac{1}{\pi v_l^2}]^{3/2} \exp[-\frac{v^2}{v_l^2}] \\ f_{tail} &= n_0 r_t [\frac{\alpha}{2\pi\sqrt{\pi}\Gamma(\frac{\beta+3}{\alpha})}] \frac{1}{(v_t v_0)^{3/2}} \\ &\quad (\frac{v}{v_t})^{\beta+3/2} \exp[-(v/v_t)^\alpha] \frac{\sum_{\sigma=\pm1} \exp[-(v/v_0)^3(\xi_m - \sigma\xi_0)^2]}{\sum_{\sigma=\pm1} \Phi((1-\sigma\xi_0)(v/v_0)^{3/2})} \end{aligned}$$

with the help of Table 1. f_{Max} is the isotropic low temperature Maxwellian component, and f_{tail} is the anisotropic tail component which vanishes at zero energy. n_0 is the minority ion density in the midplane velocity space. r_j represents the fraction of j-th component with $j = l$ for low temperature and $j = t$ for tail component respectively. Here the Γ is the Gamma function. v_l is the thermal speed of low temperature particles and v_t used here is a parameter for fitting. To describe the thermal speed of the non-Maxwellian tail the average kinetic energy should be used.

We used the least square method to determine the five fitting parameters: α, β, r_l, v_l and v_t ($r_t = 1 - r_l$). An example of the fitting of f^{iso} is shown in Fig. 2 and there the fitting is very satisfactory in both low and high energy regions, where $f^{iso} \equiv (\int d\xi_m)^{-1}$

	$\kappa = 20$	$\kappa = 40$	$\kappa = 60$	$\kappa = 80$
r_l	0.41	0.16	0.11	0.07
v_l/v_i	1.50	1.68	1.87	2.03
v_t/v_i	2.05×10^{-3}	3.26×10^{-3}	4.13×10^{-3}	4.67×10^{-3}
α	0.4			
β	6			
v_0/v_c	0.9			

Table 1: The fitting parameters for different κ values, where $\kappa \equiv D_b^* \tau_{te} M_t / T_e$. v_i is the thermal speed of majority ions ,i.e., $v_i = (2T_i/M_i)^{1/2}$. v_c is the critical ion-electron slowing down speed, where $v_c = (3\pi^{1/2} M_e / 4M_i)^{1/3} v_e$.

$\int d\xi_m f_0^{(0)}(v, \xi_m)$. In Table 1 the fitting parameters are given for different levels of ICRF power. For high power, r_l is very small ,i.e., most of resonant minority ions are in tail part. A notable point in this part of numerical study is that the exponents α and β stay constants for wide range of power levels and also for wide range of the plasma parameters. The reason behind is under investigation.

v_0 is determined by trial and errors. The value of v_0 thus obtained stays fairly constant for wide range of power levels; however it is rather sensitive function of other plasma parameters such as T_e, T_i, M_i, M_t and Z_{eff}. In Fig. 1(b) we plot the constant $f_0^{(0)}(v, \xi_m)$ contours of our analytical solution of Eq. (2). Comparison of Fig. 1(b) with Fig. 1(a) shows that the analytical and the numerical solution are qualitatively consistent with each other. The valid region of our analytical solution seems to cover the whole velocity space and it may be considered as a unified analytical form for the whole ICRF heated minority ions. This is to be compared with other analytical results which are either one dimensional [4] or applicable to the tail species only [5].

Discussions

The flux surface averaged power density $\langle P \rangle$, which is the average power per unit volume delivered to the resonant minority ions on a magnetic surface by the applied ICRF wave, is given by

$$\langle P \rangle \simeq \kappa \frac{8\sqrt{\pi} z_t^2 e^4 (\ln\Lambda) n_e n_0}{3 M_t v_e}, \quad n_0 \simeq \frac{\langle n_H \rangle}{(2 - \xi_t) r_l + (2\xi_0/\xi_t) r_t}, \tag{3}$$

where $\langle n_H \rangle$ is the flux surface averaged minority ion density. Thus for the plasma parameters employed in this paper and choosing the value of Coulomb logarithm($\ln\Lambda$) to be 20, $\kappa = 40$ corresponds to $\langle P \rangle \simeq 0.32$ watts/cm^3.

Using our analytical solution Eq. (2) we can calculate the particle flux Γ_ρ and the heat flux q_ρ. The power transferred to the bulk plasma through the Coulomb collison with minority ions can also be computed. These calculations are under investigation and will be reported elsewhere.

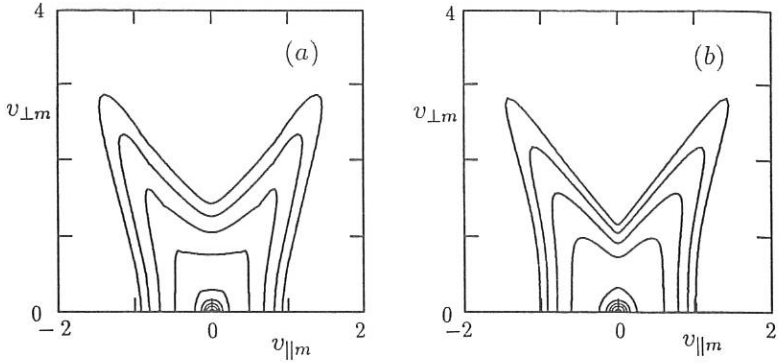

Fig. 1. Constant $f_0^{(0)}$ contours of the ICRF-heated minority ions in two dimensional velocity space with $\kappa = 40$. $v_{\perp m}$ and $v_{\|m}$ are normalized by $10^9 cm/s$. (a) Numerical solution (b) Analytical solution

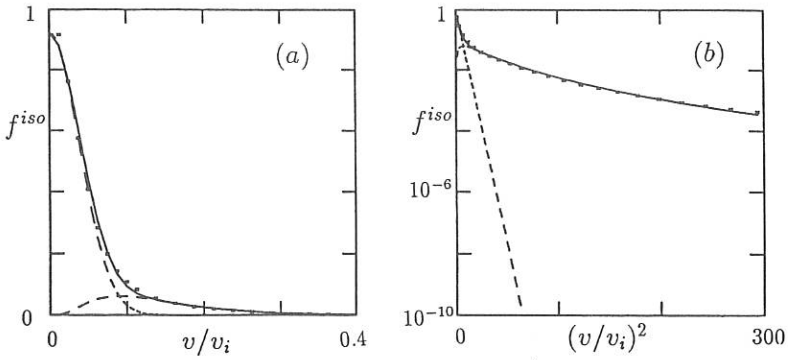

Fig. 2. Example of fitting f^{iso} as a sum of two species of f_{Max} and f^{iso}_{tail} for (a)low energy and (b)high energy range. The crossed points are f^{iso} of numerical solution. The dashed lines are f_{Max} and f^{iso}_{tail}, where f^{iso}_{tail} vanishes at v =0, and the solid line is $f_{Max} + f^{iso}_{tail}$.

References

[1] G.W. Hammett, Ph.D.Thesis,Princeton University,(1986).
[2] JET, Annual report(1988).
[3] G.D. Kerbel and M.G. McCoy, Physics Fluids **28**, 3629(1985).
[4] T.H. Stix, Nuclear Fusion **15**, 737(1975).
[5] C.S. Chang and P. Colestock, Physics Fluids **2**, 310(1990).

PARASITIC COUPLING OF THE FRINGING FIELDS OF AN ION-BERNSTEIN WAVE ANTENNA*

S.C. Chiu, V.S. Chan, F.W. Perkins,† and S. Puri‡

General Atomics
San Diego, California 92186-9784, U.S.A.

Ion-Bernstein wave (IBW) heating is an important method of heating a tokamak plasma. In past experiments, the loading of an IBW antenna is known to be considerably higher than that predicted by linear theory. It was attributed to background loading due to unknown mechanisms. Here, we propose that a possible mechanism is the coupling of the fringing fields of the Faraday screen to a short wavelength electrostatic mode. This mode is highly dissipative and can be propagative or evanescent, depending on the edge parameters. The problem is formulated as a mixed boundary value problem and solved by singular integral technique. Numerical results indicate that this can be a significant parasitic coupling mechanism whose magnitude at typical edge parameters can be significantly larger than the coupling to the desired IBW. It is insensitive to variation in magnetic field, which is in sharp contrast to theoretical predictions for IBW coupling. The dependence of the coupling to plasma and antenna parameters will be presented. Relevance to experiments will be discussed.

Ion-Bernstein wave (IBW) heating is considered to be a promising method of heating a tokamak plasma.[1,2] Ion-Bernstein wave experiments have been or are being carried out in several tokamaks.[3–6] It was known[6,7] that the loading of an IBW antenna was considerably larger than that predicted by linear theory of coupling.[8,9] A significant qualitative difference between theory and experiment is that while theory predicts a sharp peak in loading near the cyclotron harmonics, experiments do not indicate such a sharp dependence on B_0. Here, we propose that a possible mechanism is the parasitic coupling of the fringing fields due to diffraction by the Faraday screen to short wavelength torsional mode. The mode is insensitive to B_0 once the frequency is well above the fundamental harmonic. Fringing diffractions by periodic screens in vacuum has been studied.[10] Here we study the coupling of such fields to plasma.

We consider a simple model. Assume y (poloidal) independence. The Faraday strips are (Fig. 1) periodic in z (toroidal), each of width W and separated by gaps of width g. A uniform plasma is at $x \geqslant 0$ in a static magnetic field, $B_0\hat{z}$. The antenna current strip, at $x < 0$, excites a long wavelength oscillating field, whose z-component at $x = 0$ is $(E_0\, e^{i\omega t} + \text{c.c.})$. The boundary conditions for the fringing fields, $\widetilde{E}$, are, assuming no charge accumulation at the gaps,

*This is a report of work sponsored by the U.S. Department of Energy under Contract No. DE-AC03-89ER53277.

†Princeton Plasma Physics Laboratory, Princeton, New Jersey 08544, U.S.A.

‡Max-Planck-Institut für Plasmaphysik, Garching bei München, F.R.G.

$$\left.\begin{aligned} \tilde{E}_z &= -E_0 \qquad \text{at the strips} \quad , \\ \tilde{E}_x &= 0 \qquad\quad \text{at the gaps} \quad . \end{aligned}\right\} \tag{1}$$

The plasma wave excited by the fringing fields satisfies the electrostatic dispersion relation $K_{xx}\, n_x^2 + K_{zz}\, n_z^2 = 0$, where n_x, n_z are refractive indices in x and z directions; K_{xx}, K_{zz} are plasma dielectrics which include electron Landau damping. The electric potential of the fringing field can be written as

$$\varphi = \sum_{n\neq 0} f_n \exp i(nk_0 z)\, e^{-|n|\lambda_n x} \quad , \tag{2}$$

where $k_0 = 2\pi/\ell_0$, $\ell_0 = W + g$, and $\lambda_n = k_0\sqrt{K_{zz}/K_{xx}}$, describing a decaying or outgoing wave. At $x = 0$, Eq. (1) implies that for $z_m = z - m\ell_0$,

$$\sum_{n\neq 0} n f_n\, e^{ink_0 z} = \Phi_0 \quad , \qquad \text{for } |z_m| < W/2 \quad , \tag{3}$$

$$\sum_{n\neq 0} |n|\, \lambda_n f_n\, e^{ink_0 z} = 0 \quad , \qquad \text{for } W/2 < |z_m| < \ell_0/2 \quad , \tag{4}$$

where $\Phi_0 = -i(E_0/k_0)$. The problem is then to solve for f_n satisfying Eqs. (3) and (4).

The antenna is recessed in a box of poloidal height h_A, toroidal length, L_A, and radial depth W_B. The current strip has width, d, and is at distance, Δ, from the Faraday screen. Taking only the lowest Fourier mode of the fields and currents in the cavity, and defining the loading resistance to be $R = 2P/I^2$, we have

$$R = \frac{k_0^2 h_A L_A \omega}{8\pi}\, Im\left[\sum_{n\neq 0} \frac{K_{zz}}{|n|\lambda_n}\, |g_n|^2\right] \cdot \frac{\omega^2}{c^4}\left(\frac{16}{\nu d}\right)^2 \sin^2\left(\frac{\pi d}{h_A}\right) \frac{e^{-2\nu\Delta}}{[1+\coth\nu(W_B-\Delta)]^2} \quad , \tag{5}$$

where $Im(x)$ denotes the imaginary part of x, $g_n = nf_n/E_0$, and $\nu = \sqrt{(\pi/k_A)^2 - (\omega/c)^2}$. Let $W/\ell_0 = 0.5$, and assume $\phi(z)$ at $x = 0$ has the sawtooth waveforms of Fig. 1 with zero at the gaps, one can estimate R in two regimes: (a) At low densities, $K_{xx} > 0$, the dependence in plasma parameters is $R \propto \sqrt{n_e}/T_e$. (b) At high densities, $K_{xx} < 0$, the mode is propagating, and $R \propto n_e/\sqrt{T_e}$. The characteristic impedance is

$$R_0 = \frac{\omega^2 h_A L_A \ell_0 \omega_{pe}\sqrt{|K_{xx}|}}{c^4\nu^2 d^2} \cdot 9 \times 10^{11}\ \text{(ohms)} \quad . \tag{6}$$

The resistance is typically several ohms, and thus can possibly dominate the loading.

In a special case of constant K_{zz} and K_{xx} which are independent of n_z, an approximate analytic solution can be obtained by the Green's function method. Normalizing lengths in z in units of $W/2$ and x in units of $(W/2)\sqrt{K_{zz}/K_{xx}}$, one obtains

$$E_z(0,z) = \frac{E_0}{\pi(1+B)} \cdot \sum_{n=-\infty}^{\infty}\left[-\pi + \frac{2\, z_n}{\sqrt{z_n^2-1}}\,\mathrm{sgn}\,(z_n - 1)\right] \quad , \qquad \text{for } |z_n| > 1 \quad , \tag{7}$$

where $z_n = z - n\ell_0$, and $B \simeq 0.24/(1+g/W)^2$. On the strips, $E_z(0,z) = E_0$, while at the edge of the gap, near $|z_n| \sim 1-\epsilon$, there is a singularity of order $1/\sqrt{\epsilon}$.

Equations (3) and (4) can be cast into the well-known Riemann-Hilbert boundary value problem which is solvable by the singular integral technique.[11] The resulting equations can be solved for g_n. From Eq. (5), the loading resistance can be calculated. We describe the numerical results. In the case of cold, low density plasma, $\delta_m \to 0$, and the solution has been checked with the analytic solution in Eq. (7). We find that, to obtain good agreement for $E_z(0,z)$, a large number of modes have to be used. Nevertheless, we find that only a few modes are necessary in order to calculate the loading resistance accurately. The variation of the parasitic loading resistance with various plasma and shield parameters is shown in Figs. 2 through 4. In these figures, the antenna parameters are $L_A = 82$ cm, $d = 16$ cm, $h_A = 40$ cm, $\Delta = 2.5$ cm, $W_B = 14$ cm, and frequency $f = 38$ MHz. The variation with density temperature has been verified to be in accordance with analytic predictions Figure 2 shows the insensitivity of R to B_0, which is in sharp contrast to coupling to IBWs. The inverse variation of R with atomic weight is apparent from Eq. (5). Here, the second harmonic of hydrogen is at $B_0 = 1.25$ T. Of importance is the variation of R with the shield parameters, gap width, g, and period, ℓ_0. As shown in Figs. 3 and 4, R decreases with increasing g and decreasing ℓ_0. Thus, to minimize parasitic coupling, one should have open mini-blind type of shield rather than closed mini-blind type. From the above, the loading resistance is seen to be typically several ohms, *i.e.*, considerably larger than loading to IBW. Thus, the loading measurements may be completely dominated by parasitic loading.

In summary, we investigated the parasitic coupling of the fringing fields of the Faraday screen of an IBW antenna to a short wavelength electrostatic mode. It is found that the parasitic loading can be a significant coupling mechanism for an IBW antenna. It is also found that parasitic loading can be minimized by increasing gap width between the shield strips. The loading is insensitive to change in magnetic field B_0, which is reminiscent of what is found in DIII-D IBW experiment.[6] The order of magnitude of loading is several ohms, which is similar to predictions from the present theory.

The authors would like to acknowledge useful discussions with R. Pinsker, M.J. Mayberry, and M. Porkolab.

References

[1]S. Puri, Phys. Fluids **22**, 1716 (1979).
[2]M. Ono, T.H. Stix, *et al.*, in *Plasma Physics and Controlled Nuclear Fusion Research, Brussels*, 1980 (International Atomic Energy Agency, Vienna, Austria, 1981), Vol. II, p. 501.
[3]M. Ono, P. Beiersdorfer, *et al.*, Phys. Rev. Lett. **60**, 294 (1988).
[4]J. Moody, M. Porkolab, *et al.*, Phys. Rev. Lett. **60**, 298 (1988).
[5]M. Ono, T. Watari, *et al.*, Phys. Rev. Lett. **54**, 2339 (1985).
[6]R.I. Pinsker, M.J. Mayberry, *et al.*, in *Proceedings of the 8th Topical Conference on Radio-Frequency Power in Plasmas* (R. McWilliams, Ed.), Irvine, California, 1988 (AIP), p. 314.
[7]M. Porkolab, private communications.
[8]M. Brambilla, Nucl. Fusion **28**, 549 (1988).
[9]S.C. Chiu, M.J. Mayberry, and W. Bard, General Atomics Report GA-A19600, submitted to Nuclear Fusion.
[10]F.W. Perkins, in *Heating in Toroidal Plasmas* (Proc. 4th Int. Symp. Rome, 1984), Vol. 2, International School of Plasma Physics, Varenna (1984) p. 1148.
[11]F.D. Gakhov, *Boundary Value Problems* (translated by I.N. Sneddon), (International Series of Monographs in Pure and Applied Mathematics, Pergamon Press, Oxford, London, 1966).

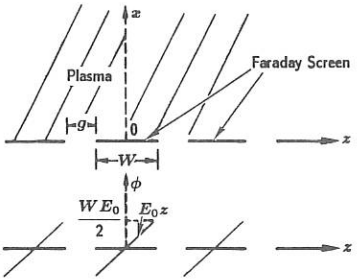

FIG. 1. Schematics of the geometry of the problem and potential ϕ at the Faraday screens.

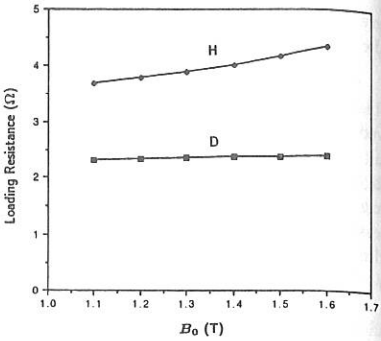

FIG. 2. Loading resistance versus B_0 for H and D–plasmas; $n_e = 6 \times 10^{11}$ cm^{-3}, $T_e = 2.5$ eV, $\ell_0 = 2$ cm, $g = 1.0$ cm.

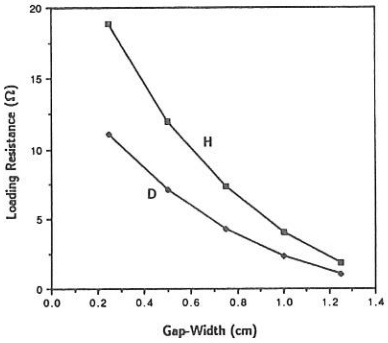

FIG. 3. Loading resistance versus g for H and D–plasmas; $B_0 = 1.4$ T; other parameters same as Fig. 2.

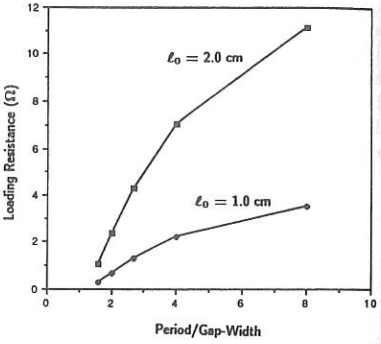

FIG. 4. Loading resistance versus ℓ_0/g for two periods, $\ell_0 = 2$ cm and 1 cm. Plasma is deuterium; other parameters same as Fig. 3.

MODE COUPLING BETWEEN I.C.R.F. WAVES PROPAGATING OUTSIDE THE B-∇B PLANE

B. M. Harvey and R. A. Cairns

Department of Mathematical and Computational Sciences,
St Andrews University, St Andrews, Fife, Scotland

The wave differential operator is obtained directly from the perturbed Vlasov equation. Expressions for the conductivity tensor elements are obtained consistently to first order in the equilibrium magnetic field gradient. Conditions on the parallel wavenumber and the magnetic field gradient for which such a method is valid are given. The expressions are then used to model the case of minority and second harmonic ion cyclotron heating.

The forms of the electromagnetic and kinetic power flows and the cyclotron damping are obtained simply.

The differential equations are solved numerically as a linear combination of boundary value problems for the perturbing electric fields using standard NAG library routines, and the transmission, reflection and mode conversion are calculated for a range of k_y and k_z values.

On setting k_y to zero, excellent agreement is found between the results obtained from our code and published results from codes by other authors.

THE VLASOV EQUATION

The starting point for our method is the Vlasov equation. As in the case of a hot homogeneous plasma, the field quantities f,$\underline{B}$ and $\underline{E}$ are linearised and then the perturbed equation is Fourier transformed in z and t but not in x (the dependence of the inhomogeneity). For clarity and to facilitate comparison with other methods, the plasma equilibrium distribution f_o is taken to be Maxwellian with no applied electric field and therefore spatially homogeneous.

$$i(k_y v_y + k_z v_z - \omega) f_1 + v_x \frac{df_1}{dx} + \omega_c \left(v_y \frac{df_1}{dv_x} - v_x \frac{df_1}{dv_y}\right) = -\frac{q}{m} \underline{E} \cdot \frac{df_o}{d\underline{v}} \qquad (1)$$

Again as in the case of a constant background magnetic field, the number of dependent variables can be further reduced by a change of velocity coordinate system to cylindrical coordinates.

$$\omega_c \frac{df_1}{d\phi} + i(w - k_z v_z) f_1 - \frac{v_\perp}{2}(e^{i\phi} + e^{-i\phi}) \frac{df_1}{dx} - \frac{v_\perp}{2}(e^{i\phi} - e^{-i\phi}) k_y f_1 = \frac{-q f_o}{m v_\perp^2} (v_\perp (E_- e^{i\phi} + E_+ e^{-i\phi}) + 2E_z v_z) \qquad (2)$$

$$v_x = v_\perp \cos\phi \qquad v_y = v_\perp \sin\phi \qquad E_- = E_x - iE_y \qquad E_+ = E_x + iE_y$$

Using the fact that f_1 is a single valued function of ϕ to write f_1 as a Fourier series in ϕ:

$$f_1(\phi+2\pi) = f_1(\phi) \qquad f_1(\phi) = \sum_{n=-\infty}^{n=\infty} f_{1,n}\, e^{in\phi}$$

$$f_{1,n} = A_n\left(\frac{d}{dx} - k_y\right) f_{1,n+1} + A_n\left(\frac{d}{dx} + k_y\right) f_{1,n-1} + A_n D_n \qquad (3)$$

$$A_n = \frac{v_\perp}{2ik_z v_t(\xi_n - \bar{v}_z)} \qquad \xi_n = \frac{\omega + n\omega_c}{k_z v_t} \qquad \bar{v}_z = \frac{v_z}{v_t}$$

$$D_{-1} = -\frac{2qf_o}{mv_t^2} E_+ \qquad D_o = -\frac{4qf_o}{mv_t^2} E_z \qquad D_{+1} = -\frac{2qf_o}{mv_t^2} E_- \qquad D_n = 0 \quad |n| > 1$$

If, after integration over v_z ,the coefficients A_n are slowly varying, it is reasonable to consider terms up to first order in the magnetic field gradient when evaluating $\underline{\underline{\perp}}$.

For non-resonant terms this simply implies that $\underline{B}_o$ must be slowly varying. More importantly, the resonant coefficients must also be slowly varying. Thus if the wave enters a region where the effects of the (n)th harmonic resonance become significant, then in order to truncate the parameter gradient terms, it is required that

$$\frac{v_t}{\omega_c}\frac{d\xi_n}{dx} \quad « \quad 1$$

If the magnetic scale length is L, the restriction is n^2 « $(k\,L)^2$.

CONDUCTIVITY TENSOR

Equation 3 has already been tackled for the case $k_y = 0$ (Harvey and Laing, 1990) to any order in the 'perpendicular wavenumber'. For $k_y \neq 0$ the conductivity tensor terms can still be obtained to any order (Harvey and Cairns, 1990) although the expressions are significantly messier.

If we are interested only in slowly varying electric fields we can truncate the electric field gradient terms, just as, in the homogeneous case, the same condition is used to truncate the series expansions in k_x. For the case of minority fundamental and majority harmonic cyclotron resonances we can truncate the electric field gradient terms at second order for the majority species and zeroth order for the minority species. Discarding the highest order non-resonant terms for each species leaves a conductivity tensor of particularly simple form.

$$i\omega\mu_o\sigma_{1,1} = \left(\frac{d}{dx} + k_y\right) G_2 \left(\frac{d}{dx} - k_y\right) + G_1 = i\omega\mu_o\sigma_{2,2} \qquad i\omega\mu_o\sigma_{2,1} = -i\omega\mu_o\sigma_{1,2} = \omega\mu_o\sigma_{1,1} + iG_o$$

$$G_o = \frac{4\omega_{Pi}^2}{3c^2} \qquad G_1 = \frac{\omega\eta\omega_{Pi}^2}{k_z v_t c^2} Z(\xi_{-1}) - G_o \qquad G_2 = \frac{\omega_{Pi}^2}{\omega k_z v_t}\frac{v_t^2}{c^2} Z(\xi_{-2})$$

ξ_{-1} = minority fundamental resonance $\qquad$ ξ_{-2} = majority harmonic resonance

ω_{p_i} = majority ion plasma frequency η = minority ratio

Combining Maxwell's equations with the conductivity tensor in the usual manner gives a system of coupled ordinary differential equations which govern the spatial evolution of the perturbing electric field.

$$\nabla x \nabla x \underline{E} - i\omega\mu_o \sigma . \underline{E} - \frac{\omega^2}{c^2} \underline{E} = \underline{0}$$

This system of equations can be solved numerically using a NAG library routine based on PASVA3 (Pereyra, 1979).

POWER FLOW

Clearly the electromagnetic energy density, $T = (\varepsilon_o \underline{E}^* . \underline{E} + \mu_o \underline{H}^* . \underline{H})/2$, is independent of time. Differentiating term by term and employing Maxwells equations gives.

$$\text{real} (\underline{E}^* . \nabla x \underline{H} - \underline{H}^* . \nabla x \underline{E} - \underline{E}^* . \underline{J}) = 0$$

$$\text{real} (\nabla . (\underline{E}^* x \underline{H}) - \underline{E}^* . \underline{\sigma} . \underline{E}) = 0$$

Where the first term is the divergence of the poynting vector. Using Maxwell's equations again and our expression for the conductivity tensor the power flow equation is obtained.

$$\text{real}\left(\frac{d}{dx}(E_y^* H_z) - (E_+^*(G_1 + (\frac{d}{dx} + k_y) G_2 (\frac{d}{dx} - k_y))E_+ + E_x^* i G_o E_y - E_y^* i G_o E_x)\frac{1}{i\omega\mu_o}\right) = 0$$

$$\Rightarrow \frac{d}{dx}(\text{Im}(E_y^* (\frac{dE_y}{dx} - ik_y E_+) - E_+^* G_2 (\frac{dE_+}{dx} - k_y E_+))) = -|E_+|^2 \text{Im}(G_1) - |\frac{dE_+}{dx} - k_y E_+|^2 \text{Im}(G_2)$$

The second term on the left hand side is the divergence of the particle energy flux, the first on the right hand side is the cyclotron damping due to the minority species and the last is the harmonic damping term.

For the case $k_y = 0$ the power flow equation reduces to the form obtained by Cairns & Fuchs (1989).

RESULTS

The results in this paper were obtained for a 5% hydrogen minority in a deuterium plasma with a temperature of 2keV and an electron density $3 \times 10^{19} m^{-3}$ in a magnetic field of the form

$$B = 3(1 - \frac{x}{L}) \text{ Tesla} \qquad L = 1.32m$$

Results from our code with $k_y = 0$

k_z	6	7	8	9	10
T	25.1	29.2	34.2	39.8	46.4
R	33.1	26.5	20.5	15.3	11.1
C	16.6	16.7	15.7	13.6	10.4
T	24.7	28.8	33.8	39.4	46.2
C	71.1	64.8	56.6	46.8	35.6

Results from the code of Imre and Weitzner quoted by Fuchs and Bers

6	7	8	9	10
25.4	29.5	34.4	40.0	46.4
32.9	26.4	20.4	15.3	11.1
16.7	16.8	15.7	13.5	10.4
25.2	29.3	34.2	39.9	46.2
70.6	64.3	56.3	46.6	35.6

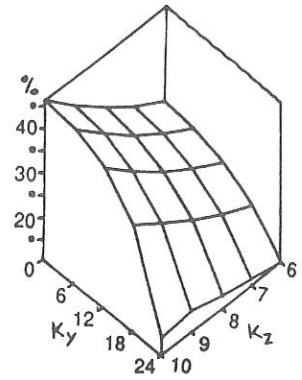

Transmission

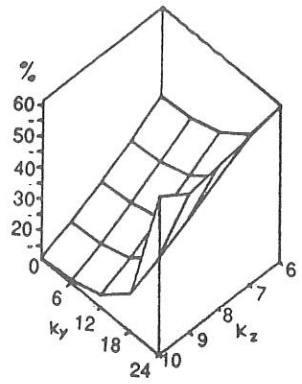

Reflection

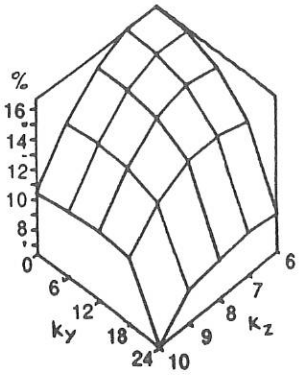

Mode Conversion (fast wave incident from low field side)

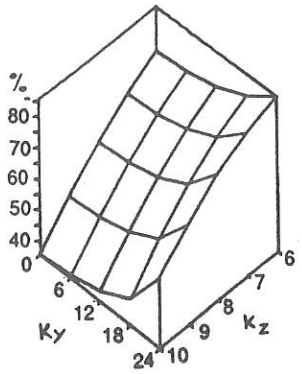

Mode Conversion (fast wave incident from high field side)

ACKNOWLEDGEMENTS

This research was supported by grants from the United Kingdom Atomic Energy Authority and the Science and Engineering Research Council.

REFERENCES

Cairns R. A. and Fuchs V., 1989 Physics of Fluids B, 1, 350.
Fuchs V. and Bers A., 1988 Physics of Fluids, 31, 3702
Harvey B. M. and Cairns R. A., submitted to Plasma Physics and Controlled Fusion.
Harvey B. M. and Laing E. W., 1990 Journal of Plasma Physics
Pereyra V., 1979 Lecture Notes in Computer Science, 76, 67

AN ANALYSIS OF RIDGED WAVEGUIDE FOR PLASMA HEATING BY USING INTEGRAL EQUATION METHOD

T. HONMA, A. YONETA, M. TSUCHIMOTO and H. IGARASHI

ABSTRACT

Ridged waveguides are used for ion cyclotron radio frequencies (ICRF) plasma heating, so that the analysis of ridged waveguides has been getting important to produce high temperature plasmas in the nuclear fusion machines. Since the governing equation of the problem is expressed by the Helmholtz equation, so many authors have analyzed the ridged waveguides by using domain type numerical methods. However, the boundary integral equation method (B-IEM), which is one of boundary type numerical methods, has not been applied to analyze the ridged waveguides. In this paper, in order to obtain the cut-off wavenumber of the waveguides from the determinant search of the system matrix, we use the fundamental solution of the Helmholtz equation, which is expressed by the Hankel function with the wavenumber as its argument. Furthermore, we consider the Helmholtz equation as the Laplace equation with an inhomogeneous term, so that we have a possibility to apply the boundary-domain integral equation method (BD-IEM) to this problem. In this method, we only use the fundamental solution of the Laplace equation and then the problem is reduced to the eigen value problem solved by the standard numerical technique. We compare BD-IEM solutions with theoretical values and B-IEM solutions and show that BD-IEM is useful to analyze the ridged waveguides. Numerical results in this paper are summarized as follows :

(1) The integral equation method is applied to the analysis of the ridged waveguides, so that cut-off wavenumbers and electromagnetic field distributions are obtained.

(2) Relative errors for higher modes are worse than those for lower modes and relative errors for TM modes are smaller than those for TE modes in the integral equation analysis.

(3) For ridged waveguides, solutions with good accuracies are obtained from the integral equation method.

STUDY OF THE NEUTRON YIELD BEHAVIOUR IN COMBINED ICRH AND NBI HEATED DISCHARGES ON TEXTOR

G.Van Wassenhove, Th.Delvigne, F.Hoenen[1], A.M.Messiaen, J.Ongena, R.R.Weynants, J.W.Yang[2+]

Laboratoire de Physique des Plasmas - Laboratorium voor Plasmafysica
Association "Euratom-Etat belge"- Associatie "Euratom-Belgische Staat"
Ecole Royale Militaire - B 1040 Brussels - Koninklijke Militaire School

[1]Institut für Plasmaphysik,Forschungszentrum Jülich GmbH ,
Association EURATOM-KFA, P.O.B. 1913, D 5170 Jülich, FRG

[2]Southwestern Institute of Physics,Leshan, P.R.China

1. INTRODUCTION

Applying ICRH on a NB heated plasma (deuterium beam in deuterium plasma) on TEXTOR leads to significant increases of the neutron yield, which may reach 80% when the auxiliary heating powers P_{RF} and P_{NI} are equal. The increase in the neutron emission comes partly from the increase in the electron and ion temperature and from the change in density of the target plasma but a residual contribution remains unexplained. Direct acceleration of ions of the beam by RF fields could be responsible for this augmentation.
The experimental set-up is presented in section 2. The third section presents an original calibration procedure which is based on the neutron estimation at the switch on of the neutral injection . This calibration has the advantage to be mainly dependent on well known plasma parameters. The fourth section deals with the neutron yield measured during combined co injection of deuterium and ICRH. In the last section the increase in neutron production due to direct acceleration of the ions of the beam by the RF field is estimated using a simple model.

2. EXPERIMENTAL SET UP

The neutron yield in TEXTOR is measured, for this experiment, with a large dynamic range counting system constituted of two BF3 detectors surrounded by polyethylene and two liquid scintillators surrounded by lead [1]. One of the BF3 detectors and the two liquid scintillators are located near the tokamak. The second BF3 tube is located outside the concrete shielding of TEXTOR and is never saturated.

3. CALIBRATION PROCEDURE

An absolute calibration of the neutron yield is obtained by comparing the measured neutron yield at the start-up of the injection of a deuterium beam in a deuterium target plasma with the predictions of the following theoretical model. The neutron production is dominated by beam-plasma interaction. We take t=0 at the switch on of the neutral beam injection. At a time t much shorter than the slowing down time (τ_{sc}) of the beam ions in the plasma, the total number of emitted neutrons is approximately given by:

$$N(t) = 2\,\pi\,R \int_0^a N(t,r)\; 2\,\pi\,r\,dr \qquad (1)$$

+ EEC grantee of the Association "Euratom-Belgium State"

where a is the plasma small radius and:

$$N(t,r) = n_D(r)\ t\ [\dot{n}_{b1}\ \sigma_{DD}(v_b,T_i)\ v_b + \dot{n}_{b2}\ \sigma_{DD}(v_b/\sqrt{2},T_i)\ v_b/\sqrt{2}] \qquad (2)$$

In these relations: N (t,r) is the total number of neutrons produced at radius r and at the time t after the start-up of the beam; σ_{DD} is the cross section of the neutron production taking into account correction for non-zero ion temperature [2,3]; v_b is the velocity of the fast component of the beam and $\dot{n}_{b1}(r)$, $\dot{n}_{b2}(r)$ are the number of atoms of the beam of energy E_b and $E_b/2$ ionized at radius r per time unit, the contribution of the component at energy $E_b/3$ has been neglected.

An estimation of the radial profile of $\dot{n}_{b1}(r)$, $\dot{n}_{b2}(r)$ is obtained using the TRANSP code [4]:

$$\dot{n}_{bi}(r) \approx \frac{I_i}{\pi s^2}\ \exp(-r^2/s^2) \qquad i=1,2 \qquad (3)$$

where I_1, I_2 are the number of atoms injected by the beam respectively at full and half energy. For line integrated densities between 1.4 and 3.1 10^{13} cm^{-3}, s varies between 16 and 23 cm.

The calibration has been made for discharges with low effective charge Z_{eff} in the ohmic phase and $n_D(r) \approx n_e(r)$. The slope of the total neutron yield at the start-up can thus be approximated by:

$$\frac{dN}{dt} = n_e(0)\ [I_1\ \sigma_{DD}(v_b,T_i(0))\ v_b f_1 + I_2\ \sigma_{DD}(v_b/\sqrt{2},T_i(0))\ v_b/\sqrt{2}\ f_2] \qquad (4)$$

where $n_e(0)$ and $T_i(0)$ are respectively the central density and the ion temperature. The factors f_1 and f_2 take into account the effects of beam and density profiles; their values vary between 0.75 and 0.9 for the analyzed discharges. We compare in figure 1 the evolution of the neutron yield divided by $n_e(0)$ measured for two discharges of different densities. At the start-up of the NI pulse, their time evolution is similar as expected from Eq. 4.
The main advantage of this new calibration is that the neutron yield only depends on well known quantities: $\sigma_{DD}(v_b,T_i(0))$, $n_e(0)$, v_b; the major uncertainty comes from the ion temperature. Nevertheless, an error of 500 eV on the ion temperature only leads to an error of 10% on the calibration factor.

4. NEUTRON YIELD DURING COMBINED CO INJECTION OF DEUTERIUM AND ICRH.

The evolution of the neutron yield during a discharge with combined NBI and ICRH heating is given in fig 2. The NBI (1.5 MW) starts at t= 0.7 s and the ICRH (1.5 MW) at t=1.7 s. Also shown is the prediction of a theoretical model which has been cross-checked by means of the TRANSP code and has the following elements:

$$N(t) = \sum_{i=1}^{2} \int_0^a I_i(r)\ n_D(r)\ \frac{\tau_{sc,i}(r)}{3} \left(\int_0^{\ln(1+x_{b,i}^3(r))} \sigma(v)\ v(\zeta)\ d\zeta \right) dr \qquad (5)$$

with

$$\zeta = \frac{3t}{\tau_{se}}$$

$$v(\zeta) = v_b \left[(1+x_b^{-3})\ e^{-\zeta} - x_b^{-3} \right]^{1/3} \qquad (6)$$

$$x_b = \frac{v_b}{v_c}$$

v_c is the critical velocity and τ_{se} is the slowing down time on the electrons.

The density decrease of the target plasma induced by the ions of the beam is taken into account and is given by:

$$n_D(r) = n_e(r) - \sum_i \dot{n}_{bi}(r)\ \tau_{sc,i}(r) \qquad (7)$$

During the ICRH phase relation (5) is applied taking into account the actual achieved n_D, T_e and T_i values.It is noted that the prediction agrees well during the pure beam phase but that the experimental yield exceeds the prediction during the combined phase. The ratio R of the measured neutron yield during NBI+ICRH to the neutron yield predicted by (5) is plotted versus the ICRH power in fig. 3 for a set of discharges. This ratio, which measures the unexplained fraction of emitted neutrons , is roughly proportional to the RF power.

5. THEORETICAL ESTIMATION OF THE INCREASE OF NEUTRON EMISSION DUE TO DIRECT ACCELERATION OF IONS OF THE BEAM BY RF FIELDS

During combined NI+ICRH heating, an acceleration of the beam ions by the RF fields could explain the high neutron production. In Ref. 5 a model has been proposed where the energy of all the beam ions increases at the same rate δE. This model will be later improved to better describe the present harmonic interaction and is used as a first approximation.
Calling $P_{RF,1}$ the RF power absorbed by the ions of the beam, then:

$$\delta E = \frac{P_{RF,1}}{\dot{n}_b\,\tau} = \frac{P_{RF,1}\,E_B}{P_{NI}\,\tau} \qquad (8)$$

The total acceleration then takes the form:

$$\frac{dv}{dt} = -\frac{1}{\tau_{se}}\,\frac{v^3 + v_c^3}{v^2} + \frac{\delta E}{mv} \qquad (9)$$

If $\delta E/mv \ll 1$, it is possible to calculate analytically the new slowing down time of the ions:

$$\tau = \tau_{sc}\left[1 + \frac{\tau_{se}\,\delta E}{m\,v_c^2}\,G(x_b)\right] \qquad (10)$$

where the function G is given in [5].

As the neutron yield is approximately proportional to τ, as can be deduced from Eq. (5), the increase in the neutron emission due to the direct acceleration of the beam ion is easily computed using relation (10); the ratio of neutron yield during NBI + ICRH to the neutron yield during NBI is presented in figure 4 as a function of $P_{RF,1}/P_{NI}$ for different values of v_b/v_c. Note that the results are rather insensitive to the latter ratio. An additional RF power equal to 40 % of NI power absorbed by the ions of the beam can explain the R=1.3 value observed experimentally.

5.CONCLUSIONS

The neutron yield increase measured during the ICRH phase of a NBI heated discharge can only partly be explained by changes in T_e, T_i and n_D unless the error bars on these quantities are much larger than believed.A possible explanation of the remaining part is due to direct acceleration of ions of the beam by the RF power.
A new calibration method for the total neutron yield has also been proposed.

REFERENCES

[1] Th. Delvigne et al,(to be published).
[2] K. Hübner et al., 12th Eur. Conf. on Contr. Fusion and Plasma Phys. , Budapest 1985, part I, 231
[3] D.R Mikkelson, Princeton Plasma Physics Laboratory PPPL-2566, 1988
[4] R.J. Hawryluk in Physics of plasmas close to Thermonuclear Conditions, edited by B.Coppi et al., Vol 1, p19, ECE Brussels, 1980.
[5] K. Okano, N. Inoue, T. Uchida, Nucl. Fusion **23** (1983) 235

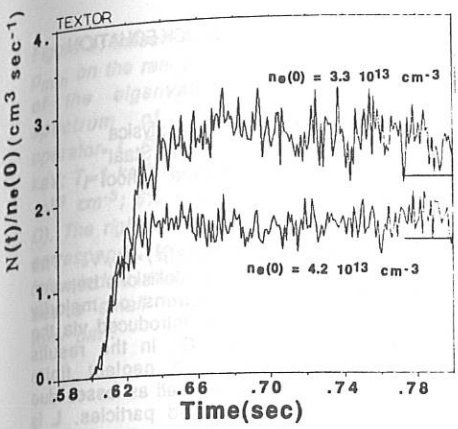

Fig.1 Time evolution of neutron yield divided by the central density at the start-up of the beam. The theoretical predictions of the model of Eq. (5) for the steady state neutron yield are also given.

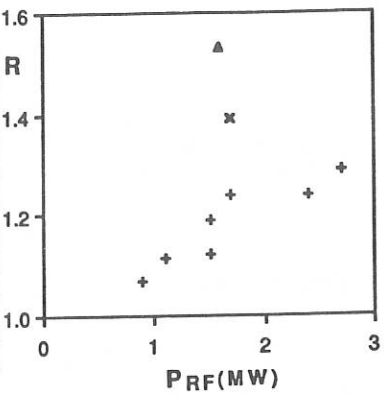

Fig.3 Ratio of measured neutron yield during NBI + ICRH to the neutron yield predicted by Eq. (5).

(I_p=340 kA, B_t=2.25 T, $\frac{n_H}{n_D}$ = 0.1, #41701,41730)
+ 2.3 $10^{13}cm^{-3} \leq n_e(0) \leq 2.810^{13}$
× $n_e(0) \approx 2.\ 10^{13}cm^{-3}$
Δ $n_e(0) \approx 1.5\ 10^{13}cm^{-3}$

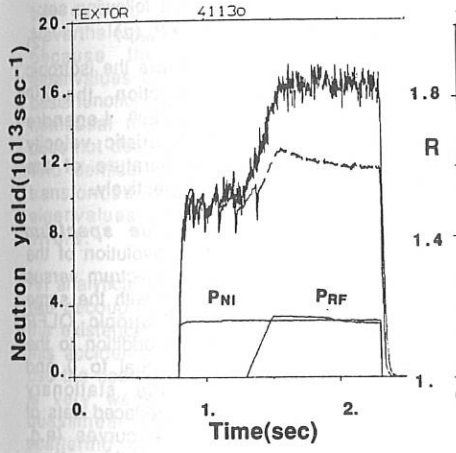

Fig.2 Time evolution of neutron yield, beam power and RF power for discharges with combined NBI and ICRH.The interrupted line is the prediction of Eq. (5).

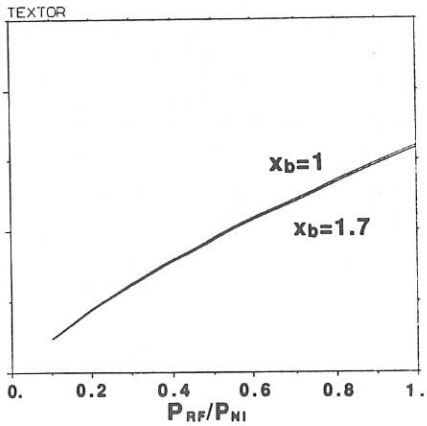

Fig 4 Evolution of the ratio of neutron yield during NBI + ICRH to the neutron yield during NBI as a function of $P_{RF,1}/P_{NI}$ for different values of v_b/v_c.

EIGENFUNCTIONS OF THE ANISOTROPIC QUASILINEAR FOKKER-PLANCK EQUATION

D. Lebeau, Ph. De Toffol, R. Koch

Laboratoire de Physique des Plasmas - Laboratorium voor Plasmafysica
Association "Euratom-Etat belge" - Associatie "Euratom-Belgische Staat"
Ecole Royale Militaire - B 1040 Brussels - Koninklijke Militaire School

Abstract

We study numerically the eigenfunctions of the anisotropic quasilinear Fokker-Planck equation in presence of ICRH and hence the non-stationary distribution function of the minority ions. The behaviour of the eigenvalues for various heating levels is investigated. By comparing with the isotropic model [1], we observe new features in the eigenvalues. The characteristic times involved in the power transfer to the background species and in the evolution of parallel and perpendicular energies are examined as well as the effect on the anisotropic distribution function of ICRH amplitude modulation for different frequencies.

Introduction

In this paper we solve the non-stationary anisotropic quasilinear Fokker-Planck (QLFP) equation with an eigenfunction expansion. Such a numerical analysis is well-suited to interpret modulated RF discharges since the main ICRH absorption mechanism in TEXTOR is fundamental cyclotron heating of the minority particles. The extension of our previous isotropic model [1] to an anisotropic one gives a refined idea of slowing down mechanisms and allows to interpret measurements like, for instance, the diamagnetic energy.

The Fokker-Planck equation

The anisotropic QLFP equation for the minority distribution f is written [2]:

$$\partial f/\partial t = L(f) \text{ with } L = C + Q \qquad (1)$$

This equation can be expressed in the ($v_{//}$, $v_{\perp}$) or (v, μ) coordinates, with $v_{//}$ ($v_{\perp}$) being the velocity of minority particles parallel (perpendicular) to the magnetic field; $v=\sqrt{v_{//}^2+v_{\perp}^2}$, $\cos(\mu)=v_{//}/v$. The operator **C** describes the collisions between minority ions and electrons or majority ions. The RF heating is introduced via the quasilinear operator **Q**. In the results presented hereafter, we neglect finite Larmor radius effects as well as losses due to confinement or trapped particles. **L** is non-Hermitian and negative definite.

Diagonalization

To compute the eigenfunctions and the eigenvalues, we project the operator **L** on a set of orthogonal basis functions in order to obtain an array [L] which is then diagonalized (see details in [1]). The main difficulty is to find a set of basis functions close enough to the eigenfunctions. Good results are obtained with the following set:

$$f_{b_{l,m}} = f_{iso}(v)\, H_{2l}(v/v^*)\, P_m(\mu) \qquad (2)$$

where f_{iso}, H_{2l}, P_m and v^* are the isotropic stationary distribution function, the n^{th} Hermite polynomial, the $2l^{th}$ Legendre polynomial and a characteristic velocity associated with the temperature of the isotropic minority tail respectively.

Eigenvalue spectrum

In figure 1 we present the evolution of the real part of the eigenvalue spectrum versus the heating power. (A figure with the same parameters but for the isotropic QLFP operator is given in [1]). In addition to the first eigenvalue which is equal to 0 and which corresponds to the stationary solution, we observe two interlaced sets of eigenvalue evolution. Some curves (e.g. curve A, B, D,...) rise steeper than others (e.g. curve C, E,...), eventually leading to crossing.

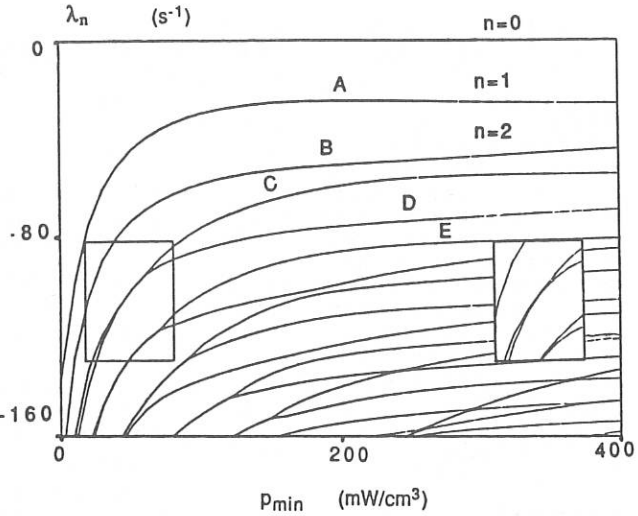

Figure 1: Influence of P_{min} on the real part of the eigenvalue spectrum of the operator L (T_e=1.4 keV; T_i=1 keV; n_{eo}=3 10^{13} cm^{-3}; 6% H in D). The right window corresponds to the left window when L has a small imaginary part.

Around this crossing (see the left window in figure 1), the two eigenvalues are complex conjugate. This suggests the existence of an intrinsic oscillation mechanism which can be excited by the RF modulation. Nevertheless, we dismiss this hypothesis because the imaginary part of the eigenvalues changes when the number of basis functions is increased and because the numerical method for the diagonalization does not deal with Jordan canonical arrays. Two identical real eigenvalues are therefore transformed into two complex conjugate eigenvalues because of the numerical errors.

An analytical separation of the operator into two decoupled equations explains not only the existence of interlaced curves but also this accidental degeneracy. To do this, we use the coordinates (v, μ) when the heating is very weak and assume an isotropic quasilinear operator and a pitch-angle scattering coefficient independent of v. When the heating is very strong, on an other hand, we use the coordinates ($v_{//}$, $v_\perp$) and neglect this last coefficient [3]. The eigenvalue spectra become respectively:

$$\lambda_{l,m} = \lambda_l^{\nu} + \lambda_m^{\mu} \quad \text{or} \quad \lambda_{l,m} = \lambda_l^{\nu_{//}} + \lambda_m^{\nu_\perp} \qquad (3\text{-}4)$$

Therefore, for the same specific parameters, different values of l and m can lead to the same eigenvalue. To show clearly the separation of the real part of the eigenvalues around the degeneracy point, we add a small imaginary part into the pitch-angle scattering operator and separate in the complex plane the two interlaced eigenvalue spectra (see the right window in figure 1).

Figure 2 shows the contour plots of the first six eigenfunctions for high (500 mW/cm^3) heating power. The stationary function exhibits the characteristic egg-like shape with the presence of a strong anisotropic tail. For the other eigenfunctions, modes expressed in the coordinates ($v_{//}$, $v_\perp$) are identifiable.

Stationary solution

A first application of the method is the study of the stationary distribution function. Figure 3 presents cross-sections of that function for a RF power density of 300 mW/cm^3 in the two cases $v_{//}$=0 (D) and $v_\perp$=0 (B). Curves A,C,E represent respectively the isotropic function without

heating, with 300 mW/cm^3 and with 450 mW/cm^3 of RF power. As expected, intuitively curves B and D are in between curves A,C and C,D. The slopes of curves D and E are asymptotically equal. Figure 4 presents the evolution of $p_{min,e}$, $p_{min,i}$, $T_{//}$ and $T_{\perp}$ as a function of the RF power: $p_{min,e(i)}$ is the power given by minority ions to electrons (majority ions) and $T_{//}$ ($T_{\perp}$) is the temperature associated with the parallel (perpendicular) energy content of the stationary solution. We point out that, in our case, the physical mechanisms neglected in this study (trapped particles, detailed losses or finite Larmor radius) tend to reduce the strong anisotropy exhibited.

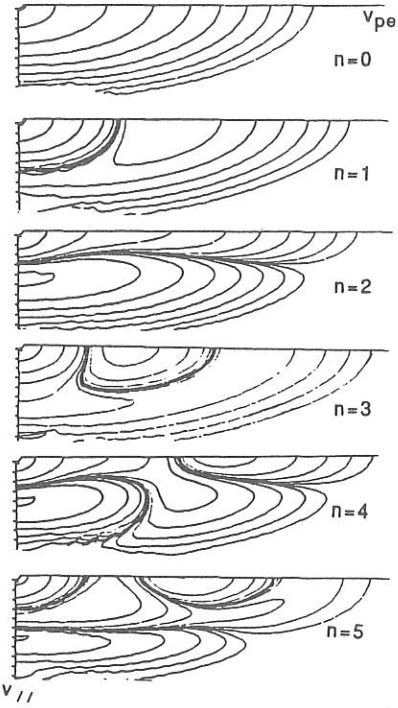

Figure 2: Contour plots of the first six eigenfunctions of L (T_e=1.4 keV; T_i = 1 keV; n_{eo}=3 10^{13} cm^{-3}; 6% H in D; p_{min}=500 mW/cm^3).

RF modulation

As a second application, we introduce a perturbed quasilinear operator Q_1 to take into account the effect of RF modulation at pulsation Ω:

$$\partial f/\partial t = L(f) + Q_1(f)\cos(\Omega t) \qquad (5)$$

Using the eigenfunction expansion $f = \sum_{i=1} a_i f_i$, this equation is transformed into a set of first order differential equations:

$$\partial a_i/\partial t = \lambda_i a_i + \sum_{k=1}^{n} q_{i,k} a_k \cos(\Omega t) \qquad (6)$$

where $[q] = [Z]^{-1}[Q_1][Z]$ and $[Z]$ is the matrix of the eigenvectors of $[L]$. For small perturbation, the $a_{i\,(i>1)}$ are small with respect to a_1 which stays constant. Calling $A_i(\Omega)$ the Fourier component of $a_i(t)$, solutions of equation 6 are:

$$A_i(\Omega) = q_{i,1}\, a_1 / (j\Omega - \lambda_i) \qquad (7)$$

Therefore, we can write the transfer function of a moment M:

$$M(\Omega) = \sum_{i=2} A_i(\Omega)\, M_i \qquad (8)$$

M_i being the moment M computed for the eigenfunction i. On figure 5, we show the amplitude and phase evolution of $p_{min,e}$,

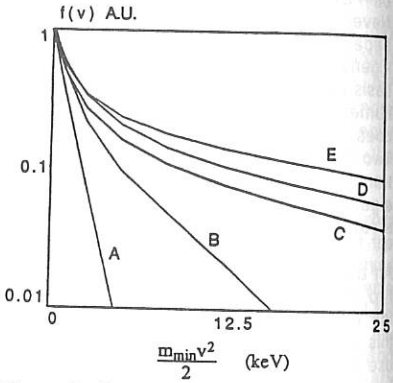

Figure 3: Stationary distribution function
A: f_{iso} (p_{min}= 0 mW/cm^3)
B: $f_{o|v_{per}=0}$ (p_{min}= 300 mW/cm^3)
C: f_{iso} (p_{min}= 300 mW/cm^3)
D: $f_{o|v_{//}=0}$ (p_{min}= 300 mW/cm^3)
E: f_{iso} (p_{min}= 450 mW/cm^3).

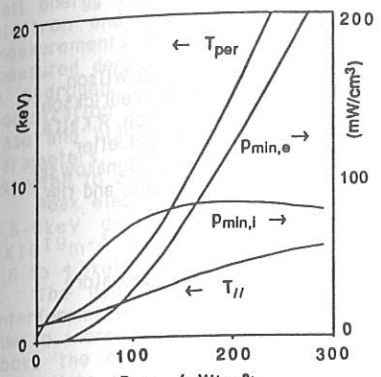

Figure 4: Evolution of $T_{//}$, T_{per}, $p_{min,i}$ and $p_{min,e}$ versus p_{min} (T_e=1.4 keV; T_i = 1 keV; n_{e0}=3 10^{13} cm^{-3}; 6% H in D).

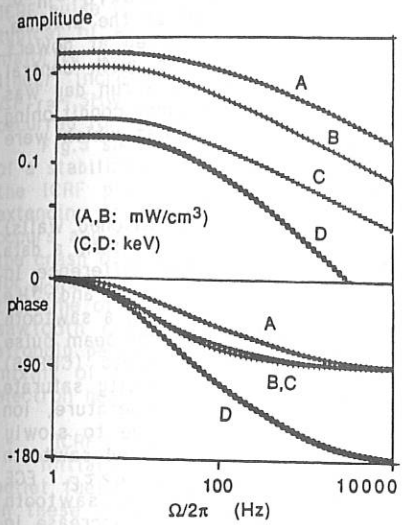

Figure 5: Transfer functions between $p_{min,i}$ (A), $p_{min,e}$ (B), T_{per} (C), $T_{//}$ (D) and the RF heating versus frequency (p_{min}=50 mW/cm³; $|\tilde{p}_{min}|$=50 mW/cm³; T_e=1.4 keV; T_i=1 keV; n_{e0}=3 10^{13} cm^{-3}; 6% H in D).

$p_{min,i}$, $T_{//}$ and $T_{\perp}$ as a function of the frequency. On one hand, the amplitude of $p_{min,e}$, $p_{min,i}$, and $T_{\perp}$ decreases as $1/\Omega$ and the phase reaches -90° at high frequency, which means that the interactions between these quantities and the RF are governed by only one characteristic time. For strong RF heating, this time reaches about $t_{se}/2$ (t_{se} being the electron slowing-down time [2]) for $T_{\perp}$ and $p_{min,e}$, but is much smaller for $p_{min,i}$. On the other hand, there are two characteristic times in the transfer function between the parallel energy and the RF.

Time evolution

A third application of the code is the study of the evolution of different moments for an arbitrary time-dependent RF scenario. This is done by resolving directly the set of equations (6) in which a time-dependent function is substituted for $\cos(\Omega t)$. This allows, for instance, to simulate the evolution of the different moments at the switch-on/switch-off of the RF.

Conclusion

We have presented the preliminary results of a code which calculates the eigenfunctions of the anisotropic QLFP operator. This non-hermitian operator does not seem to present intrinsic oscillation mechanisms but simply degeneracy for some values of the parameters. Eigenmodes are identifiable in (v, μ) and in $(v_{//}, v_{\perp})$ respectively at low and large heating. To analyse RF modulation experiments, the transfer function between different moments has been determined. In this respect, results from the isotropic model are qualitatively conserved for the power transfered to the background species.

References

[1] D. Lebeau, R Koch et al. (1990) Plasma Phys. Contr. Fusion, **32** 249

[2] T.H. Stix (1975) Nucl. Fusion **25** 435

[3] M.P. Evrard (1989) Proc. 14th European Conf. on Controlled Fusion and Plasma Physics, Venice. European Conf. Abstracts Vol. 12B part I. p.7

ICRF HEATING UP TO THE 4.5 MW LEVEL ON TFTR

J.Stevens, P.Colestock, *D.Hoffman, J.Hosea, C.K.Phillips, J.R.Wilson, M.Beer, M.Bell, M.Bitter, R.Boivin, N.Bretz, *C.Bush, A.Cavallo, E.Fredrickson, G.Greene, G.Hammett, K.Hill, A.Janos, D.Jassby, F.Jobes, D.Johnson, R.Kaita, S.J.Kilpatrick, B.LeBlanc, K.McGuire, S.Medley, Y.Nagayama, D.Mueller, D.Mansfield, K.Owens, H.Park, A.Ramsey, J.Schivell, G.Schmidt, E.Synakowski, J.Strachan, B.Stratton, G.Taylor, S.vonGoeler, K.L.Wong, S.Zweben, and the TFTR group,

Princeton Plasma Physics Laboratory; *Oak Ridge National Laboratory

INTRODUCTION

ICRF plasma heating experiments with powers up to 4.5 MW have been carried out on TFTR. Each of the two antennas has a pair of toroidally separated polodial current straps, with one antenna having end fed resonant loops while the other antenna is centrally fed with top and bottom tuning capacitors. We have operated primarily in the H-minority regime with f=47 MHz, antenna pairs driven out-of-phase, B_o=3.24T, $\bar{n}_e \approx 1.5\text{-}4.5 \times 10^{19} m^{-3}$, I_p=1.0-1.8MA, and power densities of up to 0.8 kW/cm^2 at the antenna. Stabilized sawteeth[1-2] lasting for times $t > \tau_E$ were observed at powers above ≈2.6 MW in deuterium and above ≈4 MW in helium with central deposition. Operationally, conditioning only at the start of a run day was needed for helium majority discharges. Between shot vacuum conditioning greatly improved ICRF operation in deuterium majority plasmas which were run after the vessel walls were boron coated.

CONFINEMENT IN HIGH RECYCLING DISCHARGES

ICRF experiments in high recycling discharges (i.e.unconditioned walls) were carried out with both D and ^{4}He majority gases in order to form a data base for comparison with other experiments. No apparent difference in global energy confinement time was observed between the D and ^{4}He majority gases. The effect of 3MW of ICRF H-minority heating on a sawtooth stabilized discharge is shown in Fig.1. The 50ms, 2MW neutral beam pulse (Fig.1f) was for charge exchange recombination spectroscopic (CHERS) measurements of $T_i(r)$. Stored energy and line integrated density saturate after several energy confinement times while electron temperature, ion temperature, density peaking factor, and D-D neutrons continue to slowly increase throughout the 0.9sec ICRF pulse. Thus, this stabilized sawtooth discharge continues to evolve on a resistive time scale $\tau_{L/R} > \tau_E$. ECE measurements of the inversion radius before and after a sawtooth stabilization period of ≈0.8sec indicate an approximately 50% increase in the q=1 radius.

Results from a density and current scan in D with $P_{rf} \approx 3$MW in which all shots had stabilized sawteeth are shown in Fig.2. The global energy confinement time, τ_E, shows a weak density dependence (Fig.2a) and an approximately linear current dependence except for a possible saturation at the I_p=1.8MA level ($q_{cy} \approx 3.15$). Energy confinement times range from 1.2-1.5 x L-mode scaling (Fig.2b).

Total stored energy measured from the diamagnetic and equilibrium

magnetic signals is plotted in Fig.2(c) for the 1.8MA shots. An estimated tail energy fraction of 15-30% is derived from the total energy minus the electron and ion thermal energy content from ECE and CHERS. These measurements are compared with the Stix calculation for tail energy using measured density and temperature profiles and agree well at higher density. A hydrogen concentration above 20% occurred during the week after boronization which significantly weakened the damping in the H-minority case and placed the H resonance near the antenna for the ^{3}He-minority parameters. The use of deuterated diborane in the recent boronization is expected to avoid this problem.

Peak electron temperatures increase from ohmic levels of 1.5-2.5keV to 3.5-6keV during 3MW of ICRF heating as $\overline{n}_e$ decreases from 4.5 to $2X10^{19}m^{-3}$ (Fig.2d). Peak ion temperatures measured by CHERS range from 1.8 to 4.3keV during the ICRF for those conditions.

The density peaking factor measured with a multichannel infrared interferometer, $n_e(0)/\langle n_e\rangle$, initially decreases during the ICRF heating pulse due to increased edge fueling (Fig.1e). However, the $n_e(0)/\langle n_e\rangle$ curve lies above the ohmic curve for sawtooth stabilized periods >0.5sec (Fig.2e). Other data for sawtoothing discharges in ^{4}He show that $n_e(0)/\langle n_e\rangle$ versus density late in the ICRF pulse lies on the ohmic curve. Thus, the final density profile is not affected by the ICRF power except for the extra peaking due to sawtooth stabilization.

The radiated power fraction is 30-40% for the shots in the P_{rf}=3MW scan. Z_{eff} measured by visible bremsstrahlung increased by ≈0.2 during the ICRF pulse (Fig.2f) and showed a decrease as a function of density which is typical of all TFTR discharges. X-ray PHA measurements of Z_{eff} in ^{4}He majority plasmas with out-of-phase drive of the antennas show a small linear increase with power, with $\Delta Z_{eff}\approx 0.3$ and $\Delta Z_{metals}\approx 0.1$ for $\Delta P_{rf}\approx$4.5MW. However, a sudden jump in metal impurities ($\Delta Z_{metals}\approx 0.1$) occurred for in-phase operation at the 1 MW power level.

Fig.3 shows radial profiles of $T_e(r)$ and $n_e(r)$ before and after the crash of a stabilized sawtooth for a shot where the crash occurred midway through the ICRF pulse. Such crashes resulted in a flattened pressure profile extending to $r/a\approx 0.7$. A rapid loss of a fraction of the total energy also occurs and reheating is typically slow ($>\tau_E$). The fraction of energy lost in the crash of stabilized sawteeth ranges from 10% for $q_{cy}\approx 3.15$ down to <2% for $q_{cy}\approx 5.6$. Minority tail proton losses (0.5-1 MeV) showed a spike around the time of a giant crash but showed an unexplained decrease during normal sawtooth crashes. Modeling indicates that the RF power deposition is strongly peaked ($\Delta r\approx$0.2m) in stabilized sawtooth discharges while sawtooth mixing of the fast ions in the core is required to explain the central electron heating rates in sawtoothing discharges.[3]

ICRF COMBINED WITH PELLET FUELING AND ICRF COMBINED WITH BEAMS

Initial experiments were carried out combining ICRF central heating and pellet fueled plasmas.[4] ICRF coupling at the 2.5MW level has been achieved in these discharges. Highly peaked ($n_e(0)\approx 1.4x10^{20}m^{-3}$) pellet fueled discharges showed a period of enhanced electron and ion confinement during the ICRF pulse. An order of magnitude increase in neutron rate to $>10^{14}$n/s occurred during a 2.5MW ICRF+pellet shot compared to ICRF or pellets alone.

Combined ICRF plus beams in low recycling discharges has shown that ≈2MW of ICRF power contributes the same incremental stored energy as beams but heats electrons. However, neutron production is lower in the ICRF plus beam case because of fewer beam-beam reactions.

Modification of one antenna during the February 1990 vacuum opening is

expected to raise the available power to the 6 MW level.

ACKNOWLEDGEMENTS

We thank the TFTR and ICRF technical staffs for their fine efforts and Drs. H.Furth, R.Hawryluk, D.Meade, and P.Rutherford for their support of the ICRF project. This work supported by U.S.D.O.E. contract #DE-AC02-76-CHO-3073.

REFERENCES

[1]D.Campbell, et.al., PRL60(1988)2148.
[2]R.B.White, et.al., PRL60(1988)2038.
[3]C.K.Phillips, et.al., Proc. 8th Top. Conf. RF Power in Plasmas, Irvine, 1989.
[4]G.L.Schmidt, et.al., (IAEA-CN-50/A-IV-1) Proc.12th Int. Conf., Nice, 1988.

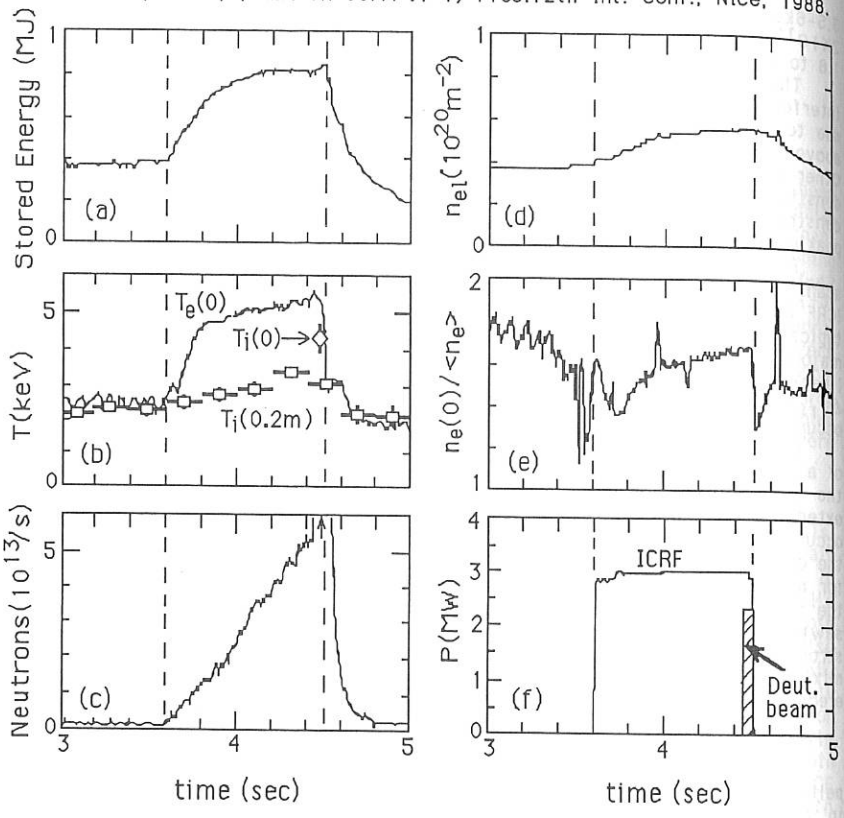

Fig.1 Time behavior of plasma parameters with 3MW of ICRF H-minority heating of a D-majority plasma with R_o=2.61m, B_o=3.24T, and Ip=1.8MA. Te(0) from ECE and Ti(0) from CHERS are measured on the magnetic axis (R≈2.70m) in Fig.1(b) while T_i(0.2m) from the X-ray crystal is measured ≈0.2m off the magnetic axis.

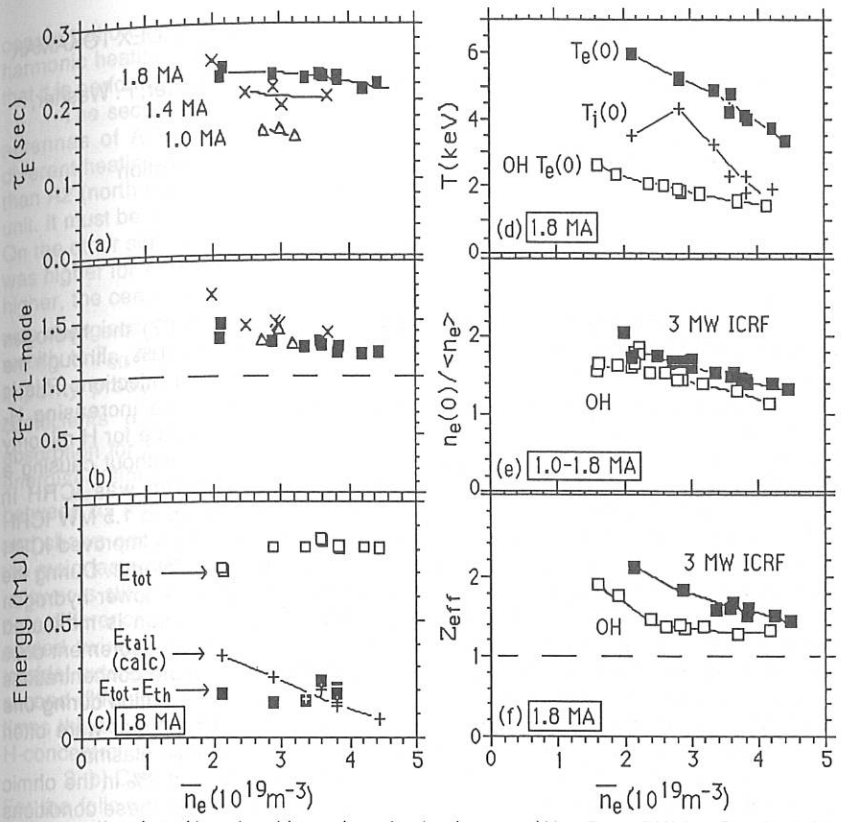

Fig.2 H-minority heating in deuterium with $P_{rf} \approx 3$MW, $B_o = 3.24$T, $R_o = 2.61$m, a=0.96m, and high recycling wall conditions.

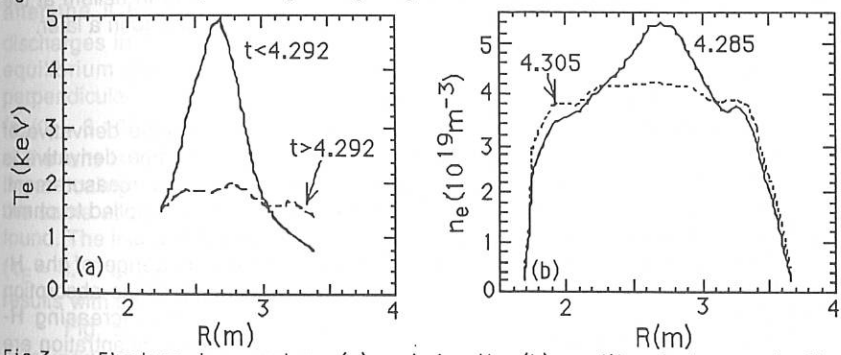

Fig.3 Electron temperature (a) and density (b) profiles before and after the crash of a stabilized sawtooth at t=4.292sec.

ICRF HYDROGEN MINORITY HEATING IN THE BORONIZED ASDEX TOKAMAK

F. Ryter, F. Braun, F. Hofmeister, J-M. Noterdaeme, K.- H. Steuer, F. Wesner,
ICRH-Group, ASDEX-Group

Max-Planck-Institut für Plasmaphysik, Euratom-Association
D-8046 Garching

1. Introduction:

Since the divertor of ASDEX has been modified (1986-87) the hydrogen concentration in deuterium plasmas could not be reduced below 10%, although the machine was operated for long periods of time with deuterium injection. This is probably due to desorption in the divertor as indicated by the increasing H-concentration during a deuterium injection pulse. As a consequence for H-minority heating in deuterium, the maximum power into ohmic plasmas without causing a disruption was limited to few hundred kW. A partial solution was ICRH in combination with deuterium injection which allowed us to apply up to 1.5 MW ICRH to the plasma. The beneficial role of the injection is attributed to an improved ICRH absorption and to the higher energy flux and temperature in the divertor. During the last ICRH campaign we operated mainly in helium plasmas for a lower hydrogen concentration and the vessel was boronised. The H-concentration is measured routinely by a mass spectrometer in the divertor chamber. This measurement does not give a fast response to eventual changes and also no absolute concentrations in the main plasma, but it gives a reliable estimate of the time evolution during one discharge or from shot to shot. The data from the mass spectrometer were often cross-checked with charge exchange measurements from the main plasma.

In helium discharges the hydrogen concentration is around 2% in the ohmic phase but it increases up to 8% as ICRH is applied (Fig. 1). Under these conditions the maximum available power (2.7 MW) could be applied to the plasma without causing a disruption. This is partly due to the low H-concentration in helium at the beginning of the ICRH pulse but also to the boronisation, as discussed in a later.

2. Confinement:

2. a) Absorption

The global absorption of the ICRH is calculated from the time derivative of the plasma energy at the ICRH turn-on or turn-off. The energy time derivative is taken from the equilibrium beta which is fast enough (1 ms) for this measurement. The absorption measured earlier in ASDEX [1] was 60% for ICRH applied to ohmic target plasma. We measured the absorption motivated by two reasons.

The first reason was to try to take into account the influence of the H-concentration. Fig. 2 shows the results and indicates a decrease of the absorption with increasing H-concentration, as expected. Because of the increasing H-concentration during the ICRH pulse, the points obtained at low concentration are measured at the beginning of the ICRF pulse whereas the ones at high

concentration are measured at the end of the pulse. We checked for second harmonic heating that the measurement of the absorption does depend on the fact that it is performed at the ICRH turn-on or turn-off.

The second reason for which we measured the absorption was that the two antennas of ASDEX, which are essentially identical, for the first time showed different heating efficiencies: antenna A1 (south-east) was almost 20% less efficient than A2 (north-west), as measured on the plasma energy increase per ICRH power unit. It must be noted that the antenna resistance for A1 was 10% larger than for A2. On the other side, the total power radiated by the plasma for a given plasma energy was higher for A1. In agreement with these observations, the loop voltage was 20% higher, the central electron temperature lower and Z_{eff} only slightly higher when A1 was energised. This implies for A1 more metallic impurities which contribute only weakly to Z_{eff} but strongly to the radiated power. It is well documented that the ICRH impurity production is mainly iron [2]. The measurements of the absorption coefficients α_1 and α_2 for A1 and A2 are reported in Fig. 3 and show that the absorption for A1 is lower than that of A2 (as in Fig. 2). When both antennas are energised simultaneously with the same power, the absorption is the average between α_1 and α_2. This consistent with the higher impurity level observed for A1 and shows once more that, in ASDEX, the non-absorbed ICRH-power is possibly the main factor of the impurity production [2]. The reason why the absorption for A1 is lower is still not understood. Both antennas have one loop and are identical. The only difference is the surrounding: antenna A1 has on each side metallic carbon coated "wings" which have the same poloidal extension as the antenna and a toroidal extension of 30 cm. This could affect the density in front of the antenna. A second difference of the surroundings is the boronisation layer which was 5 to 10 times thinner around A1 than around A2. We did not measure any difference of the H-concentration when one or the other antenna was energised.

2. b) Confinement scaling:

For the following results we take the averaged value of the absorption which was measured: $\alpha_1 = 0.50$, $\alpha_2 = 0.65$. Fig. 4 shows the plasma energy (measured 100 ms after the ICRF turn-on) versus total deposited power ($P_{OH} + \Sigma\alpha_i P_i^{ICRH}$) for discharges in helium. The plasma energy from the diamagnetic loop and from the equilibrium give identical results within the error bars, indicating no strong perpendicular anisotropy due to the ion tail. We attribute this to the high density ($n_e(0) \approx 8\ 10^{19}\ m^{-3}$) for which the 90° pitch angle scattering and the thermalisation of the ions is fast (≈10 ms for 20 keV). We recognise clearly the well known offset linear scaling law for three different values of the plasma current. If we had taken the same absorption for both antennas, two different confinement times would be found. The incremental confinement time increases proportionally to plasma current ($\tau_E \approx 0.09$ Ip [ms, kA]) as expected for the L-mode and in agreement with earlier results with second harmonic heating [1].

Fig. 5 give results obtained for deuterium plasmas with ICRH alone and combined with deuterium injection for a density of $3.2\ 10^{19}\ m^{-3}$. The offset linear scaling is clear and the points NI+ICRH are aligned with injection alone with an

incremental confinement time of 30 ms corresponding to earlier measurements [3]. However, the incremental confinement time is lower than the one found in helium (Fig. 3) for the same value of the current. We attribute this difference to an effect of the density which is lower for these deuterium discharges. Due to the fact that the ICRH points are well aligned with the injection ones, as extensively documented earlier for ASDEX, we suppose that the absorption for the deuterium case is correct.

3. Boronisation.

With boronisation, Z_{eff} is close to unity during the ohmic phase and the density limit is 20% higher. For the particular case of ICRH, the production of metallic impurities during the RF pulse is strongly reduced. This is illustrated in Fig. 6 where the results for an old boronisation layer and a fresh one are compared. With boronisation, the maximum power which can be applied to ohmic target plasma is higher than with carbonisation or without any coating [4]. We suppose that 2.7 MW could be successfully applied to an ohmic plasma thanks to the boronisation. For ICRH, an important phase is the ICRH turn-on. It induces a rapid density increase at the plasma edge and consequently in the divertor which is strongly cooled. This cooling is faster than the heating due to the increase of the plasma energy by the ICRH. If this cooling is too strong, a MARFE develops and a disruption occurs. Under boronised conditions the density is better controlled and this deleterious effect is reduced compared with other cases, allowing higher ICRH power. The boronisation allows us also to operate at high line averaged density ($6.5\,10^{19}$ m^{-3}) due to the higher density limit and the reduced cooling of the divertor. At high density the radiation power is lower for a given plasma energy.

Conclusion.

The difficulties of controlling the H-concentration for minority heating in ASDEX were not totally solved by operating in helium plasmas but it gave us the possibility to work at high power without the help of the injection. The boronised walls also contribute to the high power and high density operation. Under these conditions the off-set linear scaling is clearly obtained as well as its proportionality with plasma current.

Acknowledgment

We wish to thank the operation teams of the ICRH, ASDEX, and NI groups. We are particular grateful to our colleagues who performed the boronisation.

References:

[1] K. Steinmetz et al., Nucl. Fus. 29 (1989) 277-293

[2] J.- M. Noterdaeme et al., Fusion Eng. Des. 12 (1990) 127

[3] J.- M. Noterdaeme et al. 12th IAEA Conf. Nice Vol. 1 (1988) 583

[4] F. Ryter et al. Fusion Eng. Des. 12 (1990) 267

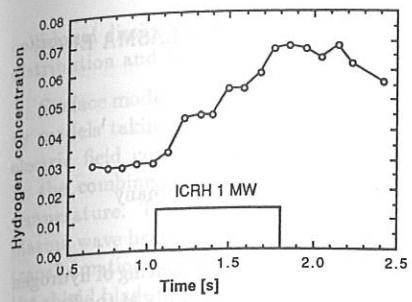

Fig. 1 Time evolution of hydrogen concentration in an Helium plasma with ICRH.

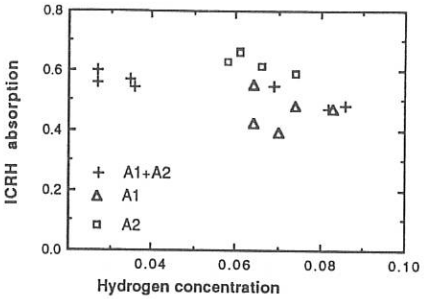

Fig. 2 ICRH absorption in helium plasmas versus hydrogen concentration

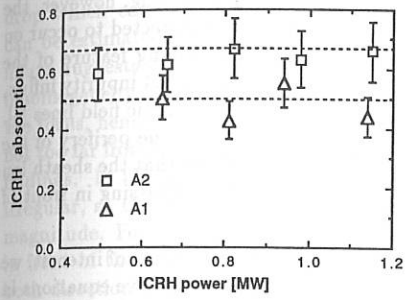

Fig. 3 ICRH absorption in helium plasmas versus ICRH power.

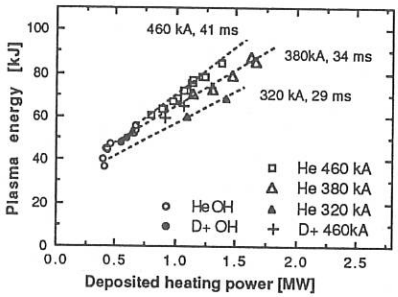

Fig. 4 Plasma energy versus total heating power in helium for different plasma currents.

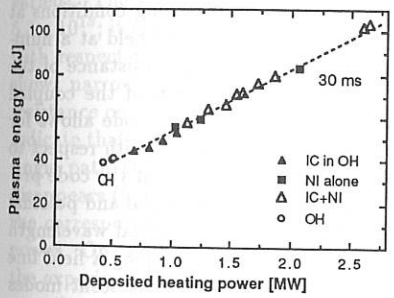

Fig. 5 Plasma energy versus heating power in deuterium plasma with and without injection.

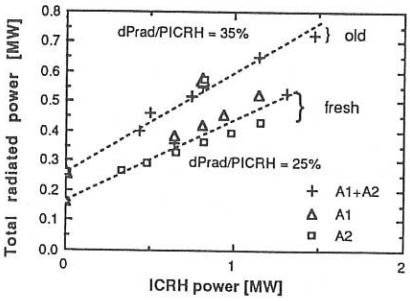

Fig. 6 Volume integrated plasma radiation versus ICRH power in helium plasmas for an old and a fresh boronisation

INDUCTION OF PARALLEL ELECTRIC FIELDS AT THE PLASMA EDGE DURING ICRF HEATING

M. Brambilla, J.-M. Noterdaeme

Max-Planck Institut für Plasmaphysik
Euratom Association - D 8046 Garching - Fed. Rep. Germany

Spectroscopic monitoring of metal lines during second harmonic heating of hydrogen in ASDEX [1] has shown that impurity production was not localised only at the Faraday shield and the protection limiters of the antenna. A strong influx of metal ions was also observed from a region of the bottom divertor entrance plates, peaked toroidally at the antenna position and one to two meters wide. One of the most plausible mechanism for impurity production is ion acceleration in the the h.f. sheath [2-3] which forms when magnetic field lines hit a metallic surface. For efficient sputtering, however, the h.f. should induce a potential drop of several hundred eV; this is expected to occur on field lines which link flux directly from the antenna. The astonishing feature of the ASDEX result is that the section of the plates responsible for the largest inpurity influx, while physically close to the antenna, is not connected to it by magnetic field lines [4]. We present here results which suggest that the h.f. can excite near the perifery of the plasma non localised parallel electric fields of sufficient strength, so that the sheath ion acceleration mechanism does not have to be confined to field lines passing in front of the antenna.

To investigate the behaviour of the h.f. electric field in the situations of interest, we have used the code FELICE, which solves the Finite Larmor radius wave equations in a plane stratified model of the tokamak for each partial wave with specified wavevectors k_y and k_z in the ignorable directions (poloidal and toroidal respectively). The integration is made over the whole plasma cross-section, so that global eigenmodes can be put in evidence, although their exact location and quality factor are expected to be somewhat altered by toroidicity [5]. After imposing the matching conditions at the antenna and the wall, Fourier synthesis allows to reconstruct the field at a number of positions in the plasma and its surface; knowing the loading resistance of the antenna, it is also possible to evaluate their intensity as a function of the coupled power. Particularly useful in these investigations is the fact that the code allows for an arbitrary orientation of the antenna and the Faraday shield blades with respect to the static magnetic field. For the parameters of the ASDEX experiment the code predicts resonant excitation of torsional-like surface modes with low toroidal and poloidal wave-numbers (typically $n_\varphi = \pm 4$, $m_\vartheta = \pm 1$, corresponding to a toroidal wavelength of about 4 m) and large parallel field. The maximum voltage drop along a field line can be almost 1 kV for a coupled power of 1 MW. These radially evanescent modes have a penetration depth of a few centimeters, are associated with a non-negligible

collisional dissipation in the scrape-off plasma, but do not otherwise influence the field distribution and the power deposition profiles in the plasma core.

Surface modes resonantly guided along the plasma surface have been predicted [6-7] by models taking into account only the cold compressional wave (so that no parallel electric field could be anticipated). Usually however they are strongly suppressed by the combined effects of smooth density profile, finite electron inertia, and finite temperature. The modes observed in the code seem rather to belong to the electron plasma wave branch of the dispersion relation, in a situation in which subsequent mode transformation to a Bernstein wave [8] is not possible. In particular, for their excitation the shield blades must make a finite angle to $\vec{B}_o$. Note also that in all runs the density at the Faraday screen was well above the Lower Hybrid Resonance density.

Fig. 1 shows the parallel field E_z at the plasma surface along four magnetic field lines at different poloidal positions (0, 25, 50 and 75 cm from the equatorial plane; the antenna half-length is 49.5 cm), in a case with a strong surface mode. The potential drop which could be sustained through a sheath if such a line were to cut a wall can be estimated as $V_m \simeq E_z\lambda/4 \simeq 0.8$ kV. Because of the simplified geometry, the figure suggests that this potential drop could exist on *any* field line; the poloidal inhomogeneity however is likely to restrict the region of strong E_z to the outer half of the torus, hence to field lines which, even if not transiting in front of the antenna, are not too far from it in the toroidal direction. This is consistentent with the experimental findings. In the absence of the surface mode, E_z is 5 to 10 times weaker and quite irregular, so that the maximum potential drop is reduced by more than one order of magnitude. For comparison, $E_\perp$ has typically a peak of 0.2 kV/m (always at 1 MW) in front of the antenna, decreases to ~ 0.05 kV/m already at 20 cm away from it in both directions, and is completely insensitive to the presence of the surface mode.

Fig. 2 shows the maximum potential drop V_m along field lines ($E_z\lambda/4$ at 1 MW) and the antenna resistance R_a predicted by the code as functions of the central density (the profile corresponds to the one measured at 5.1×10^{13} peak density, and was not varied). The surface mode manifests itself as a broad peak in V_m at densities below 5.5×10^{13}; it disappears at higher densities. In fig. 2 the angle of Faraday shield blades with respect to $\vec{B}_o$ is the experimental one of 3.9 degs. Angular exploration (fig. 3) shows narrow peaks of R_a at particular angles: surface modes appear as a parasitic resistance on the loading, contributed by a single partial wave. The n_φ power spectra indicate that global eigenmodes are also present, in agreement with the relatively weak single path absorption, but are stronger at higher densities where the surface mode disappears (figs. 2 and 3b). Volume resonances are easily distinguished by the fact that the corresponding increase of R_a *lowers* the electric field needed to transmit a given power. On the whole, the predicted values of R_a are two to three times larger than the experimental ones; the discrepancy can be somewhat reduced by disregarding the contributions of low n_φ modes, which is overestimated in slab geometry [5].

In conclusion, we have shown that the excitation of torsional surface eigenmodes can give rise to strong parallel electric fields near the plasma surface, which can cause ion acceleration by h.f. sheaths and trigger impurity production from regions of the wall not connected to the antenna by magnetic field lines.

References.

[1] J.V. Hoffmann et al., Fusion Eng. Des. **12** (1990) 185.

[2] F.W. Perkins, Nucl. Fus. **29** (1989) 583.

[3] R. Chodura, J. Neuhauser, 16th Europ. Conf. on Plasma Physics and Controlled Fusion, Venice 1989, Vol. 2 p. 1089.

[4] J.-M. Noterdaeme et al., Fusion Eng. Des.**12** (1990) 127.

[5] M. Brambilla, T. Kruecken, Nucl. Fus. **28** (1988) 1813.

[6] Messiaen et al., Heating in toroidal plasmas, Rome 1984, Vol. 1 p. 315.

[7] R.C. Cross, A.B. Murphy, Plasma Phys. Contr. Fusion **28** (1986) 597.

[8] M. Ono, K.L. Wong, G.A. Wurden, Phys. Fluids **26** (1983) 298.

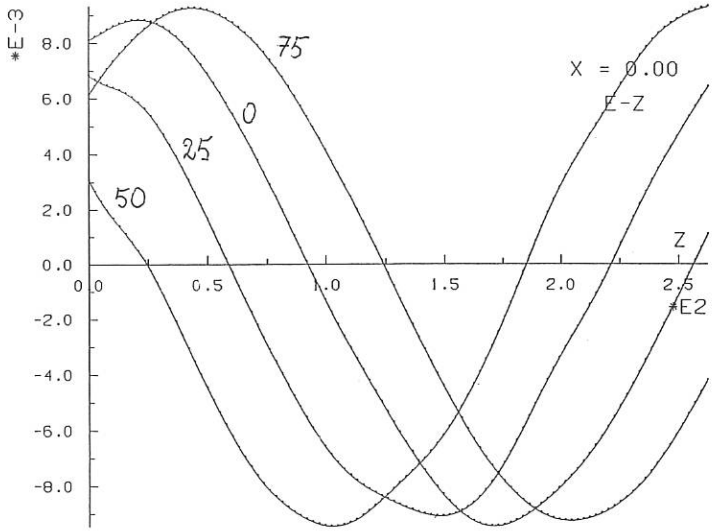

Fig.1 - Parallel electric field (kV/cm at 1 MW) along magnetic field lines at the plasma surface.

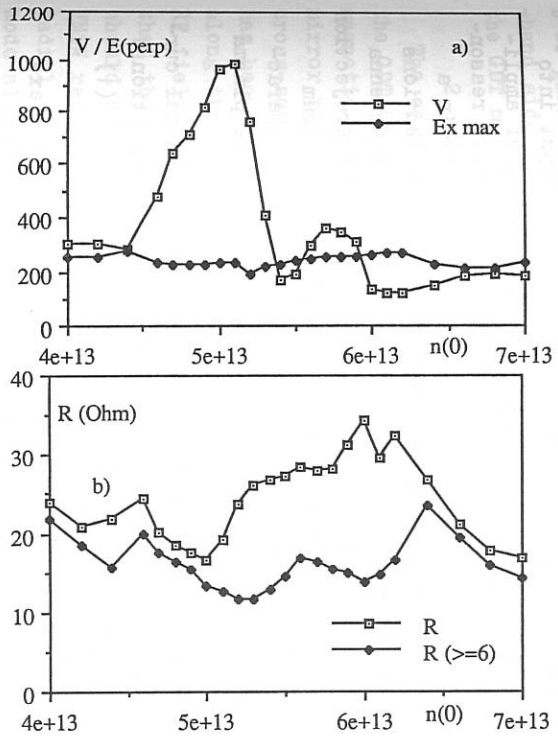

Fig. 2 - a) Voltage drop and perpendicular field at 1 MW
b) resistance (with and without low n-phi modes) vs central density.

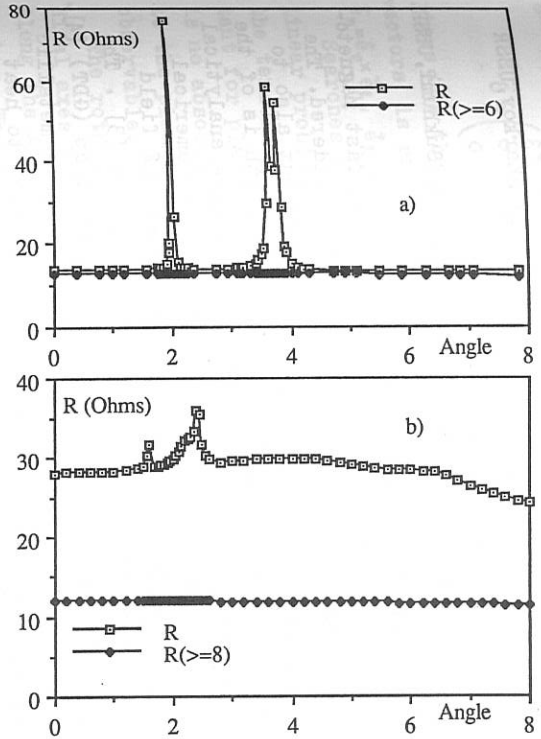

Fig. 3 - Resistance vs Faraday screen angle:
a) Central density 5.1E13; b) central density 6.2E13.

ION-CYCLOTRON ABSORPTION OF FAST MAGNETOSONIC WAVES BY COLD MINORITY IONS IN AN OPEN TRAP

V.E.Moyseenko, V.V.Pilipenko, V.I.Zamkov
Kharkov Institute of Physics and Technology; Kharkov, USSR

G.G.Zukakishvili, A.M.Borozenets
I.N.Vekua Institute of Physics and Technology; Sukhumi, USSR.

1. THE PROBLEM DEFINITION

The realizability of minority ion heating using fast magnetosonic waves (FMSW) in an open trap [1,2] is considered. The method may be used not only for plasma heating but also to produce "sloshing" ions. Since the FMSW wavelength is of the order of the open trap size it is hard to utilize analytical methods. In order to solve the problem posed, a numerical code PLFEM is developed which allows to compute RF field structures in the traps filled with a cold plasma [3] . The computations are carried out for a gas-dynamic trap (GDT) [4].

For FMSW, the GDT plasma column surrounded by a metallic chamber represents a cavity. It is more justified to heat the plasma under the conditions of the FMSW global (volume) resonance since in this case the antenna power input into the plasma increases as a result of resonant rise of amplitudes in the RF fields. Due to this fact, it is more reasonable to make search for global FMSW eigen-resonance in a plasma column, to find electromagnetic field distributions under the resonance conditions, then to select the antenna system so that the FMSW resonance electrical field projection onto the antenna current direction should be of maximum value, and in the end, to calculate electrodynamic characteristics for those antennas in conjuction with the plasma load.

The RF field generation in the plasma using external currents (antenna currents) is described in Maxwell equations:

$$\mathrm{rot}\,\mathrm{rot}\,\vec{E} - \frac{\omega^2}{c^2}\hat{\varepsilon}\vec{E} = \frac{4\pi i\omega}{c^2}\vec{j}_e \qquad (1)$$

where ω and $\vec{j}_e$ are the RF heating frequency and the external current density, respectively. The dielectric

permeability tensor $\hat{\varepsilon}$ is equal to unit for the GDT vacuum region, while for the plasma region

$$\hat{\varepsilon} = \begin{pmatrix} \varepsilon^{+} & 0 & 0 \\ 0 & \varepsilon^{-} & 0 \\ 0 & 0 & \infty \end{pmatrix}, \quad \varepsilon^{\pm} = 1 + \sum_{\alpha} \frac{\omega_{p\alpha}^2}{\omega_{c\alpha}(\omega_{c\alpha} \mp \omega)}$$

where α is the ion species number. The system of $(\vec{e}_{+}, \vec{e}_{-}, \vec{e}_{n})$ vectors is related with the magnetic field lines $\vec{e}_{\pm} = \frac{1}{\sqrt{2}}(\vec{e}_{n} \mp i\vec{e}_{\varphi})$, $\vec{e}_{n} = \vec{e}_{\varphi} \times \vec{e}_{h}$, $\vec{e}_{h}$ - unit vector in the magnetic field direction.

Searches for global resonances for FMSW take shape of a linear problem for eigenvalues $\mathrm{rot}\,\mathrm{rot}\,\vec{E} - \frac{\omega^2}{c^2}\vec{E} = \lambda\hat{\eta}\vec{E}$. Here the tensor $\hat{\eta} = (\hat{\varepsilon}(n_0) - \hat{I}) / n_0 \cdot \frac{\omega^2}{c^2}$, n_0 is the norming constant for plasma densities, and $\hat{I}$ is the unit tensor. If there is no absorption in the plasma, the eigenvalue of λ corresponds to the plasma density value for which the global resonance is observable.

The rotation symmetry in the trap relative to the longitudinal axes allows us to fulfill Fourrier series expansion along the azimuth φ ($d/d\varphi = im$), where m is the azimuthal mode number. The reflectory symmetry in the trap relative to the $z = 0$ plane allows to select even and odd parts in the right-hand side of the equation when solving it; thus, one half of the GDT may be considered separately.

2. NUMERICAL RESULTS

The calculations have been performed for the parameters of the GDT CP-2M device under the construction (Fig.1) [5] . The magnetic field value, B, at the trap centre is 2.7 kG, the mirror ratio is 50, and the plasma column radius at the central cross-section is 10cm. The radial plasma density distribution has been assumed to be parabolical one. The plasma density along the magnetic field was considered to be constant. The RF field frequency, $\omega = 2.75 \cdot 10^7\ s^{-1}$ has been chosen such that the cyclotron resonance region for the minority ions should be near the central cross-section of the GDT. Global FMSW resonances of TE_{102} type have been studied: the first radial eigenmode, the azimuthal wavenumber m=0, the first odd mode along the longitudinal coordinate. Hydrogen minority concentrations varied within the range of 0-5%. Fig.2a shows

distributions of electrical field amplitudes in a purely deuterium plasma. In a plasma without hydrogen additives, the FMSW absorption does not take place, the eigenvalue for λ is real, and the global resonance has a zero width. With hydrogen additives introduced, collisionless (residual) FMSW damping takes place at the cyclotron resonance location, $\omega = \omega_{cH}$. When the hydrogen concentration, C_H, is less than 0.5% and greater than 3%, the absorption is small. For C_H=1.5%, the absorption has its maximum value and the resonance width $Im\lambda/Re\lambda$ is 0.119 (see Fig.2b). A considerable amount of absorption for this case is due to both direct cyclotron FMSW absorption and local Alfven resonance generation near the $\omega = \omega_{cH}$ zone.

Fig.3 shows distributions of the fields generated by the antenna system (four half-turns situated in symmetry relative to the z=0 plane and phased so that to ensure a predominant generation of the TE_{102} mode; see Fig.1) in a D_2 plasma with the 1.5% concentration of hydrogen additions. The similarity in the RF field distributions shown in Figs.2b and 3 is an evidence of the FMSW resonance generation. The resistance provided by the plasma per a half-turn is 0.153 Ohm.

3. CONCLUSIONS

The plasma heating method is offered in an open trap geometry, based on cyclotron interactions between minority ions and global FMSW eigen-resonances in the plasma. Severe collisionless cyclotron absorption of the FMSW energy by the minority ions is found out within the cold plasma approximation, the absorption taking place for hydrogen additive concentrations from 0.5 to 3%. For the most favourable concentration of the additives, C_H=1.5%, the relative resonance width, reaches the value of 0.1.

REFERENCES

1.Stix T.H. Nucl.Fus.,1975, v.15, N5, p.737-754.
2.Longinov A.V.,Stepanov K.N. RF Plasma Heating, ed.by Litvak A.G.,Gorky, 1983,pp.105-210.
3.Mirnov V.V.,Ryutov D.D.Itogi Nauki i Tekhniki.Fizika Plazmy, Moscow, 1988, v.8, p.77,
4.A.M.Borozenets et al. Proc.of the 4-th Conf.on Eng.Probl., Leningrad, 1988, p.46.
5.Moyseenko V.E. et al.Preprint N89-62, Kharkov Inst.of Phys. and Tech., Kharkov, 1989.

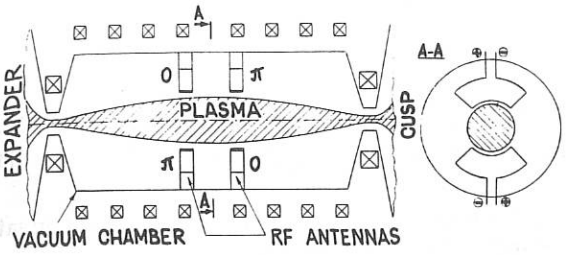

Fig.1. GDT CP-2M device layout

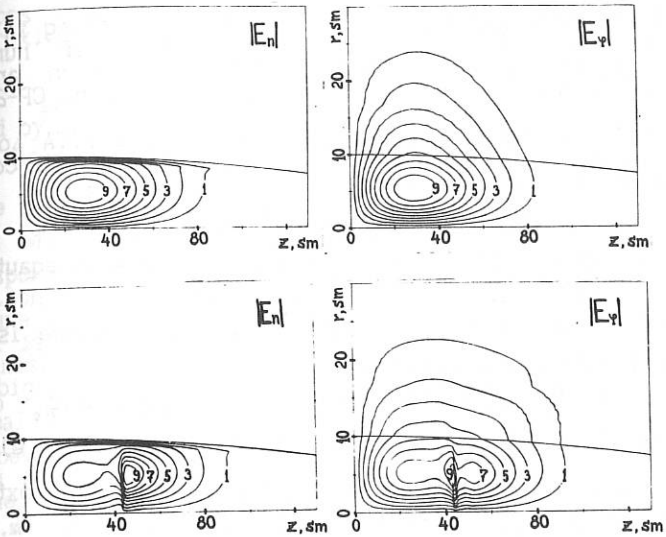

Fig.2. E_η and E_φ field level lines for global FMSW resonance (the TE_{102} mode): (a) in a pure deuterium plasma, the eigenvalue is $\lambda=3.926\cdot10^{13}$ cm^{-3}; (b) in a deuterium plasma with hydrogen minority 1.5%, the eigenvalue is $\lambda=4.397\cdot10^{13} - i\cdot5.232\cdot10^{12}$ cm^{-3}

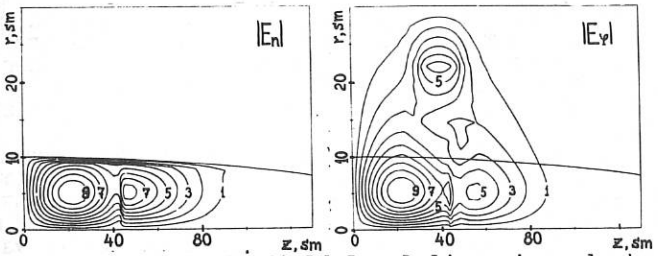

Fig.3. E and E field level lines in a deuterium plasma with 1.5% concentration of hydrogen; the fields being generated by the antenna system

RF PLASMA HEATING IN THE GAS-DYNAMICS MIRROR TRAP

*) Garina S., Ivanov A.A., Potapenko I.F., **) Elfimov A.G.

*) M.V.Keldysh Institute of Applied Mathematics Acad. Sci. USSR
**) I.N.Vekua Institute of Physics and Technology, Sukhumy, USSR

There exist some suggestions on plasma heating in mirror machines [1]. In this work the results of numerical investigations of RF fields, power absorbtion and ion velocity distribution function for the trap CP-2M are presented.

We have developed two-dimensional code FITA to treat these aspects of heating in the tandem mirror. We consider axisymmetric ion-electron plasma oscillations as

$$E(t,r,\varphi,z)=E(r,z)\exp(-i\omega t+m\varphi).$$

The HF fields are found by solving the wave eqaution:

$$(\mathrm{rot\ rot}\ E) - \omega^2 E/c^2 - \omega^2 4\pi i(J+J_{ext})/c^2 = 0$$

and Ohm's law for induce currents: $J = \hat{\sigma} E$, where is cold plasma conductivity tensor [2]:

$$4\pi i\sigma_{\perp}/\omega = \sum_s \Omega_{Ps}^2/(\Omega_{Bs}^2 - \omega^2);\quad 4\pi i\sigma_{\times}/\omega = \sum_s \Omega_{Bs}\Omega_{Ps}^2/(\omega(\Omega_{Bs}^2 - \omega^2));$$

$$4\pi i\sigma_{\parallel}/\omega = \sum_s \Omega_{Ps}^2/\omega^2;\quad \Omega_{Bs} = Ze_s|B|/(M_s c);\quad \Omega_{Ps}^2 = 4\pi N_s (Z_s e)^2/M_s;$$

ν is damping factor one simulating absorption; external currents are: $J_{\varphi} \approx J_o \sin(\pi nz/l)$, $J_{\varphi} \approx J_o \cos(\pi nz/l)$; m,n are poloidal and axial wave numbers.

The fields are solved on a curviliner grid being connected with the magnetic field, using metod of support operators [3]. Equilibrium quantites are assumed to be specified on 2-D grid so that axial and radial variations are allowed.

Surface wave [4] research yields that antenna currents haveaxial wave numbers n=3,4,5 generate in the plasma natural eigen wave, which has in the plasma axial wave number N=4and absorbes with different effectiveness (Fig.1). Cavity resonance and IC resonance influence to population of absorption.

Fast magnetosonic wave for the greater density was researched (Fig.2). The power curve is more wide than in the case of surface wave, and total power absorbed is less in two orders. Cavity resonance influences to population of absorption, IC resonance doesn't. HF field radial variation is smooth.

Influence of damping factor value ν is considered. When

damping factor was small (ν=0) there are slow modes generated in the mirrors, its wavelength is close to an ion gyroradius. This mode is absorbed by electrons and doesn't attain zone of IC resonance (Fig.3).

We analysed in detail in the velocity space the ion distribution $f_i(v,\mu,t)$ of RF-heated plasma, consisting of electrons and ions, occuring during the decay of plasma density ; $v=|v|$-velocity; $0\le\mu\le\cos\vartheta\le\mu_c$, μ_c-the boundary of usual loss cone. For this function the two-dimensional nonlinear kinetic Fokker-Planck equation is solved

$$\partial f_i/\partial t = \hat{I}f + \hat{D}f,$$

$\hat{I}f$ - is Landau collisional integral. ICR heating is simulated by including the quasi-linear diffusion operator [5]

$$\hat{D}f \approx 1/v_\perp \partial/\partial v_\perp (v_\perp D_o \partial f/\partial v_\perp),\ v_\perp = v(1-\mu^2)^{1/2}.$$

The action operator $\hat{D}f$ is restricted by the section $v_\parallel^1 \le v_\parallel \le v_\parallel^2$, where the diffusion coefficient D_o is constant, it corresponds to the antenna and the ICR zone. The electron distribution is of Maxvellian type with the time-dependent temperature and density. On the every time step the ambipolar potential is calculated. The action of the RF-heating leds to the anistropic growth of the ion distrbution especially for the big velocities $v > v_{Ti}$ (Fig.4). The mean ion's energy and normal part $T_\perp$ raise (Fig.5). The density losses icrease because of RF plasma heating and the direct ion's "carrying out" from the loss hyperboloid under the quasy-linear operator effect.

CONCLUSIONS

The investigation of ICRF heating by surface and FMS waves shoed that the heating regime on FMS wave is less preferable proceeding from the absolute value of the power absored. Regime of ICR heating not far from the trap mirrors is disadvantageous. It is found that the normal temperature of subthermal ions increases rather strong as the total plasma energy and density decrease.

LITERATURE.

1. V. V. Mirnov, D. D. Ruytov/Pisma ZTF.
2. M. W. Phillips, A. M. M. Todd/Computer Physics Communications, 40,65-72,1986.
3. A. A. Samarskii, A. P. Favorskii, V. F. Tishkin, M. U. Shashkov/ Differenzialnye uravnenia,7,1317-1327,1981.
4. V. D. Shafranov/ZTF,40,241,1970.
5. T. H. Stix ,Nucl. Fus.,15,737,1975.

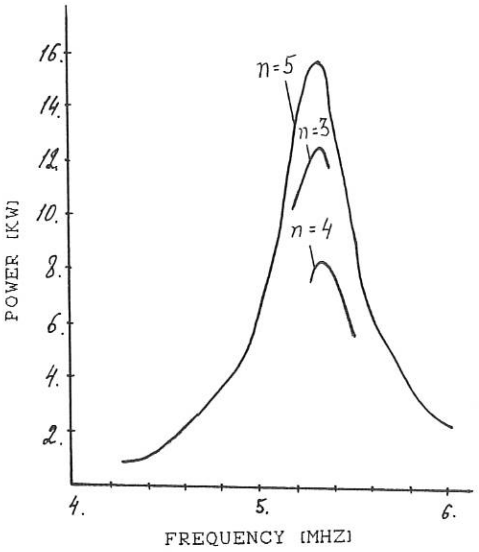

Fig.1. Power absorbed. Maximums are conformed to surface wave generating in the plasma, $m=1, n=3,4,5, n_o=10^{13}cm^{-3}$, $\nu=0,1\omega$.

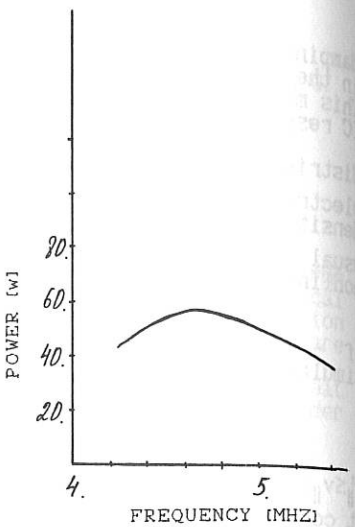

Fig.2. Power absorbed. Maximum is conformed to FMS wave generating in the plasma. $m=1$, $n=3,4,5, n_o=10^{13}cm^{-3}$, $\nu=0,1\omega$.

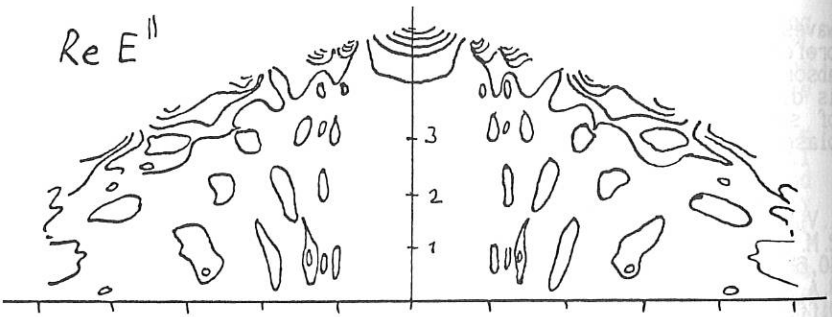

Fig.3. Contours of $E^{||}$, $m=1, n=3, n_o=10^{13}cm^{-3}, \nu=0$.

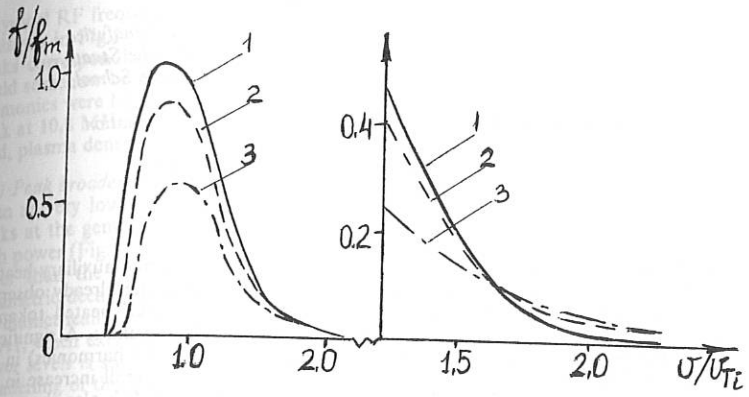

FIG. 4
Ion distribution function, $f_i(v,\mu,t)$, normalized on its maximum value in the $t = 0.2\,\tau_{ii}$ for $D_o = 0.5$; 1 - μ =0.2, 2 - μ = 0.4, 3 - μ = 0.6.

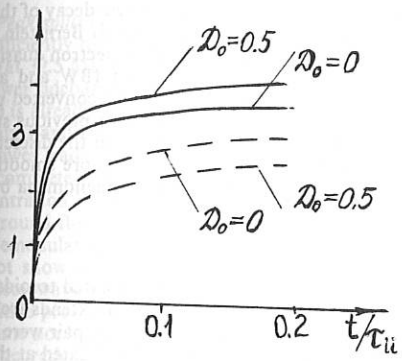

FIG. 5
The curves correspond to various values of D_o for $T_\perp / T_\parallel$ (solid lines), $e\phi / T_e$ (dashed lines).

EXPERIMENTAL STUDY OF STRONG NONLINEAR WAVE PHENOMENA DURING ICRH ON TEXTOR

R. Van Nieuwenhove, G. Van Oost, D. Bora [1] □

Laboratoire de Physique des Plasmas - Laboratorium voor Plasmafysica
Association Euratom-Etat Belge - Associatie Euratom-Belgische Staat
Ecole Royale Militaire, B-1040 Brussels - Koninklijke Militaire School, Belgium
[1] *Institut Für Plasmaphysik, Forschungszentrum Jülich, Association EURATOM-KFA, FRG*
□ *permanent address : Institute for Plasma Research*
Gandhi nagar - 382424, India

Abstract

Electrostatic fluctuation measurements in the range 0.1 - 100 MHz during auxiliary heating on TEXTOR have been performed using capacitive probes. Besides the already observed parametric decay processes in the scrape-off layer (SOL) on an ICRF heated tokamak [1,2,3], the present study revealed several additional nonlinear phenomena : A significant broadening of the frequency peaks (at the generator frequency and its harmonics) in the spectrum of the RF probe signal was observed, accompanied by an overall increase in the relatively smooth background (range 0.1 - 100 MHz) fluctuation level. It is also shown, for the first time, that the ion Bernstein waves (at the generator frequency and its harmonics), which are parasitically excited by the fast wave ICRF antenna, also decay parametrically.

Introduction

Since the first observations of parametric decay on an ICRF heated tokamak a lot of effort has been made experimentally as well as theoretically to further explore these phenomena. Recently, a correlation between parametric decay and RF energy deposition into the edge has been seen on JT60 [3]. Up till now, four different types of parametric decay of the fast wave (FW) in the plasma edge have been observed : 1) decay into an ion Bernstein wave (IBW) and an ion quasi mode (IQM) [1,2], 2) decay into an IBW and an electron quasimode (EQM) [1,2], 3) decay into two slow waves [2,5], 4) decay into an IBW and a cold electrostatic ion cyclotron wave [3]. A serious attempt to calculate the converted power has however only been performed for the first decay process [4]. Whereas previous studies of the frequency spectra of probe signals were concentrating exclusively on the discrete frequency peaks, the present study also includes phenomena which lead to more smooth features in the probe frequency spectrum. This study revealed several new phenomena but for most of them, no theoretical explanation is yet at hand.

Experimental set-up

The RF power on TEXTOR is provided by two pairs of RF antennas, located toroidally at diametrically opposite positions. In the poloidal direction, each antenna extends from the outer midplane to 7.5 ^{0} from the top of the machine. The antennas in each pair were fed in π phasing. On each antenna pair (A1 and A2), a capacitive probe [8] is located at the top of an RF antenna, thus poloidally at the top of the machine, at the same radial position as the antenna protection limiters, i.e. at r = 48.0 cm. The top part of A2 (2/13 of the original Faraday screen surface) was electrically completely closed so as to make A2 more a low field side launcher (the radiating surface does no longer cross the ion cyclotron layer near its extremity). For A1, the bottom part of the Faraday screen (5/13 of the original surface) was covered by graphite tiles as a protection against excessive heat loads caused by neutral beam shine-through.

Measurements

a) Frequency spectrum

A typical RF frequency spectrum of the capacitive probe (on A2) signal, when exciting A2, is shown in Fig.1. In contrast to previous results [8] half harmonics or other frequency peaks corresponding to parametric decay processes were observed only occasionaly. This could somehow be related to the coverage of the top part of the Faraday screen of A2. Half harmonics were however still seen when exciting A1. The frequency of the very pronounced peak at 10.8 MHz (see Fig.1) was independent of the generator frequency, toroidal magnetic field, plasma density and current. Its origin is not known.

a.1) Peak broadening

Even at very low RF power one observes already a smooth broadening of the frequency peaks at the generator frequency and its harmonics (see Fig.2). This broadening increases with power (Fig.2) and reaches (close to the ω peak) saturated values which are only 30 dB lower than the ω peak, thus orders of magnitude higher than the previously observed parametric decay processes [1,2]. The peak broadening was found to be much smaller at the diametrically opposite side of the exciting antenna as measured by the capacitive probe on A1, when exciting A2. The evolution of the frequency spectrum for three different RF power levels is shown in Fig.2. Increasing the RF power first leads to a strong asymmetric broadening of the 2 ω peak, followed by a broadening of the ω peak and an increase of the 10.2 MHz peak. At an RF power level of about 800 kW a saturation of these effects is observed. At this power level the broadening of the ω and the 2 ω peak has increased to such an extent that the fluctuation level everywhere between 0. MHz and 2 ω has increased considerably, thus leading to an overall increase of the background level. The broadening of the ω and 2 ω peaks when exciting A1 was found to be considerably lower than the corresponding broadening when exciting A2. This might be a consequence of the differences in the Faraday screen causing differences in the fringing field patterns. During auxiliary heating by neutral injection the magnitude of these effects is strongly reduced.

a.2) Peak splitting

At sufficiently high RF power levels ($\geq$ 800 kW) two sidebands are observed close to the ω peak (at 32.5 MHz), one at around 30 MHz, the other at around 35 MHz (Fig.3). Whereas the lower sideband (LSB) only becomes clearly visible at this power level, the upper sideband (USB) is already observed at 100 kW of RF power. The frequency difference between these sidebands and the ω peak increases with increasing density (Fig.3). A further increase in RF power leads to a drastic increase of these two sidebands whereby the ω peak can disappear completely (Fig.4). This complete splitting was only observed when the H- minority concentration was rather high ($\geq$ 15 %). From Fig.4 one also sees that the increase in the background fluctuation level extends up to the sixth harmonic of the generator frequency. The demodulated signal (over the range 25 - 35 MHz), which was measured simultaneously did not show a sudden decrease in this case, so that one must conclude that nearly the complete wave energy at the ω peak is converted into these two sidebands. Since the capacitive probe detects only Bernstein waves [8], this observation therefore shows, for the first time nonlinear decay of the parasitically excited Bernstein waves [7,8,9,10]. The available theoretical [6,12] and experimental [13] studies of parametric decay during IBW launch are rather limited and it was not possible to identify with certainty the type of parametric decay. The most likely candidate seems to be the decay into another IBW and an electron quasi mode (EQM). The appearance of the two side bands is usually accompanied by a superposition of a whole series of regularly spaced small frequency peaks on the overall spectrum (see Fig.3) which could be due to a cascading effect [11].

Summary

With the observation of these strong additional nonlinear processes, with special emphasis on the parametric decay of the parasitically excited Bernstein waves, a contribution to the further understanding of the direct energy deposition in the SOL during ICRF heating was made.

References

1. R. Van Nieuwenhove, et al., Nucl. Fus. 28 (9) (1988) 1603
2. R. Van Nieuwenhove, et al., Europ. Conf. Abstr. 12 B (1988) 778.
3. T. Fuji, et al., IAEA Techn. Committee Meeting on ICRH/Edge Physics, Garching bei München, October 1989, Fusion Engineering and Design, in press
4. J.A. Heikkinen, K. Avinash, Nuclear fusion, 29 (8), (1989), 1307
5. S.C. Chiu, Phys. Fluids 31 (11), (1988), 3295
6. M. Porkolab, IAEA Technical Committee Meeting on ICRH/Edge Physics, Garching bei München, October 1989, Fusion Engineering and Design, in press
7. F. Skiff, et al., Phys. Fluids 28 (8), (1985), 2453
8. R. Van Nieuwenhove, et al., IAEA Technical Committee Meeting on ICRH/Edge Physics, Garching bei München, October 1989, Fusion Engineering and Design, in press
9. R. Van Nieuwenhove , *Influence of Ion Cyclotron Resonance Heating on the edge plasma of tokamaks* , Doctoral Thesis, U.I.A., University of Antwerp, B-2610 Antwerp, April 1989.
10. J.A. Heikkinen, JET-P (89) 74
11. A. Hasegawa and L. Chen, Phys. Fluids, 18, (10), (1975),1321
12. M. Porkolab, ICRF/Edge Physics Workshop, Boulder, Colorado, April 30 - May 1, 1988
13. R.I. Pinsker, et al., General Atomics GA-A19662, May 1989, and AIP Conference Proceedings 190, 8 th Topical Conference, Irvine CA 1989, 314

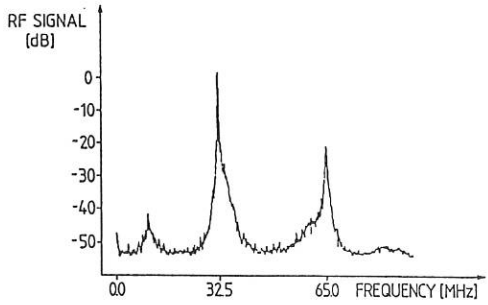

Fig.1 : Frequency spectrum of the capacitive probe (on A2) signal, when exciting A2. The transmitted RF power on A2 is P_{RF} = 1500 kW (32.5 MHz). The plasma parameters are : B_T = 2.25 T, I_p = 340 kA, $\bar{n}_{e0}$ = 3.5 10^{13} cm^{-3}, H/D ratio = 0.15, limiters at r = 46 cm, antenna protection limiter at r = 49.0 cm, boronised walls, # 40950.

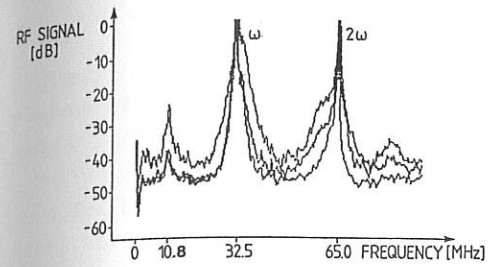

Fig.2 : Frequency spectrum showing peak broadening (at ω and 2 ω) and increased fluctuation level for three different levels of RF power (on A2) : 1) P_{RF} = 200 kW (# 40168), 2) P_{RF} = 580 kW (# 40170), 3) P_{RF} = 950 kW (# 40171). The amplitudes of the ω and 2 ω peaks are saturated in this figure. The plasma parameters are : B_T = 2.25 T, I_P = 340 kA, $\bar{n}_{e0}$ = 1.5 10^{13} cm^{-3}, H/D ratio $\leq$ 0.1, limiters at r = 46 cm, antenna protection limiter at r = 47.0 cm, boronised walls.

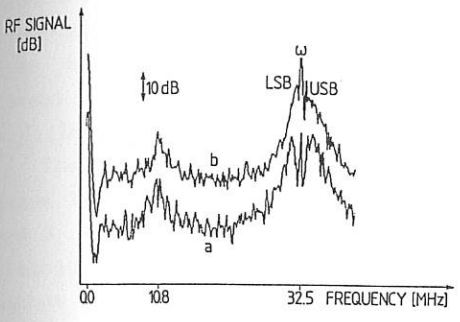

Fig.3 :Frequency spectrum of the capacitive probe (on A2) signal, when exciting A2 (P_{RF} = 800 kW) showing i) two sidebands (LSB,USB), ii) a periodic structure on the overall spectrum. The amplitude of the ω peak is saturated in this figure. The lower curve (a) corresponds to $\bar{n}_{e0}$ = 2.1 10^{13} cm^{-3} (# 40364), the upper curve (b) corresponds to $\bar{n}_{e0}$ = 0.85 10^{13} cm^{-3} (# 40362). H/D ratio $\simeq$ 0.15, other parameters are the same as in Fig.2.

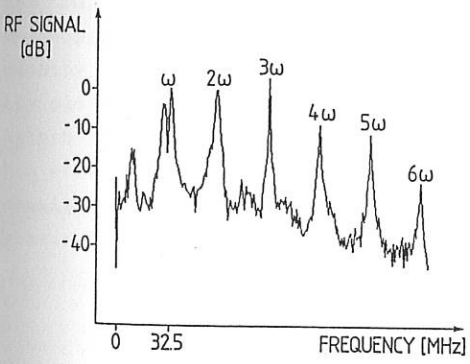

Fig.4 :Frequency spectrum of the capacitive probe (on A2) signal, when exciting A2 (P_{RF} = 1200 kW) showing splitting of the ω peak (# 40426). H/D ratio $\geq$ 0.15, $\bar{n}_{e0}$ = 2.2 10^{13} cm^{-3}, other parameters are the same as in Fig.2.

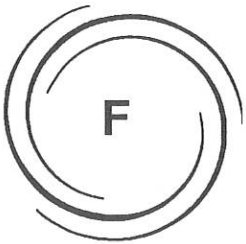

RF HEATING

F2 ELECTRON CYCLOTRON RESONANCE HEATING

SOME FEATURES OF ECRH IN INHOMOGENEOUS MAGNETIC FIELDS.

Zhil'tsov V.A., Skovoroda A.A., Scherbakov A.G.

I.V. Kurchatov Institute of Atomic Energy,

Moscow, USSR.

Abstract: Experimental results obtained under ECRH in the plasmas of open traps OGRA-4 (single superconducting baseball) and OGRA-4K (single supercoducting cusp) are discussed.

Two gyrotrons with the total power up to 150 kW were used for heating in OGRA-4 [1]. The power of the first gyrotron (wavelength 8 mm, the fundamental harmonic) was launched into plasma along the magnetic axis. The power of the second gyrotron (wavelength 5 mm) was launched at the angle of 60° respective the axis at the first and at the second (as a rule) harmonics. In OGRA-4K cusp device [2] 8 mm gyrotron launched mainly along the cusp axis was used. Experimental results given below have no adequate theoretical description at present.

1. **Dense plasma size limitation by a resonance surface.**

The experiments on both devices show that the dense plasma is mainly concentrated within the surface $B(x,y,z)=B_r$, were B_r is resonance magnetic field for ECR at the fundamental harmonic. While changing B the plasma geometry is changed without essential change in density [4]. In Fig. 1 one can see the distribution of electron density, n_e (solid line - H_α measurements, circles - interferometer), gas density, n (dash line), and the super hot electron density, n_h (crosses), along the trap axis in OGRA-4. The arrow is the ECR point for λ=8 mm. Super hot electrons have the energy up to 1 MeV and the density lower by the order of magnitude, and they determine the plasma pressure. They are almost uniformly distributed within the whole confinement region. Such behavior of super hot electrons can not be explained without attracting the mechanisms of transversal transport, e.g. neoclassical one because, of field axial asymmetry.

2. Parameters of the hot electron plasma.

At some changes in the magnetic field, gas flow and by switching off any of gyrotrons, no essential change in the maximal electron density, 5 10^{-12} cm^{-3}, occurs. Moreover, maximal density is practically the same in both facilities. An analysis of literature has shown that at ECR method of plasma creation this limit was not exceeded in other experiments with a strongly-ionized plasma, when $n/n_e < 10^{-3}$.

A rise in the diamagnetic signal in our experiments is mainly related with increase in the density of super hot electrons which is proved by a good coincidence of form of diamagnetic signal and cyclotron emission. Fig.2 shows consequent curves resulted by the experiment with 1 gyrotron on OGRA-4. Solid curve - integrated signal of diamagnetic coil, circles - cyclotron emission at wave length λ=1.95 mm in the direction normal to the magnetic field (arrow - gyrotron switch off). Note that cyclotron radiation at the high order harmonics of ECR is more sensitive to change in the energy of superhot electrons When two gyrotrons are in operation the density of super hot electrons is continuously increased (up to 75 ms).

What is the super hot electron energy determined with? We have not found an adequate answer to this question.

3. Current along the axes.

The ion flux density distribution (dots) and the electron distribution (circles) along the transversal coordinate at the plasma center (Z=0) to the West (a), to the East (b) on OGRA-4 are shown in Fig.3. In this case the gyration (8 mm) radiation is launched from one side (west). The fluxes where measured at the ends of the facility (Z=110 cm) where a strong reduction in the magnetic field takes place. One can see that, though the flux magnitudes are close to each other, a current along the axis is observed . The current equals 3 A at 30 kW of the deposited power, which does not ecceed the plasma ionization fluxes.

4. Absorption at high density and power .

In special experiments on OGRA-4 with the rarefied plasma produced by NBI, the absorption coefficient, η, at the first ECR-harmonic under longitudinal propagation (microwave generator 10 mW) was measured [5]. It has been shown that the theory adequately represents the process of ECR-absorption in an inhomogeneous magnetic field and, at the density above $n_e = 2 \cdot 10^{10}\ cm^{-3}$, η is practically equal to one. The present experiments show that a considerable power absorption ($\eta = 0.3 \div 1$) takes place at much higher density and power level.

In order to measure the penetration coefficient T at presence of gyrotron beam for various frequencies of inspection wave two horns at the angle 45° to the axis were used. The frequency dependencies of T under gyrotron operation (dots) and in 20 msec after its switching off (circles) are shown in Fig.4. Similar measurements were taken on the cusp too. Note that under gyrotron opertion the quantity T is changed in time chaotic. A relative level of these fluctuations, $\Delta T/T$, (crosses), is given in Fig.4 (an arrow - second harmonic ECR frequency). The presence of fluctuations proves the development of instability related with an anisotropy in the electron distribution function. This instability is manifested in the H_α intensity, in the fluxes beyond the mirrors, in plasma pressure etc. At present there is no non-linear model describing self regulation of electron distribution function, that provides absorption of SHF power when instability is present.

5. Wave amplitude change in the ECR-zone.

In the experiment with a cusp, the whole plasma flux outgoing along the slit was received to the insulated plate. Varying the potential of the plate one could direct the stream of cool electrons to the slit or along the axis. The results of these measurements are given in Fig.5 (1 - current to the plate, 2 - electron flux to the slit, 3 - electron flux along the axis, 4 - potential at the axis). The redistribution of

fluxes is well explained by change in the height of potential barriers for electrons along the field lines, assuming the absence of transversal transports. However, let us remember that there are two ECR-zones along the field line at the fundamental harmonic. These zones should absorb cool electrons, converting them into hot ones. The lack of this absorption, in our opinion, is connected with the fact that because of doppler effect the wave is practically completely absorbed by the hot electrons in the area of resonance point, and its amplitude at the very point of resonance is small enough not to influence the behavior of warm component. How does the energy exchange among cool, thermal, super hot electron take place? There is still no answer to this question.

1. Belavin M.I, Zhil´tsov V.A. et al.// Voprosi Atomnoj Nauki i Tekhniki, seria Termojadernij sintez 1988, v.1, p.51.
2. Belavin M.I., Golovin I.N et al // 12 ICPP and CNFR, Nice, France, Nucl. Fusion Supplement, 1989, v. 2, p.691.
3. Zhil´tsov V.A., Skovoroda A.A., Scherbakov A.G.// Preprint IAE - 4855/7, CNIIAtominform. M., 1989.
4. Zil´tsov V.A., Skovoroda A.A.,// Journal Physique C7 ,1979, v.4Ø, p.C7-663.

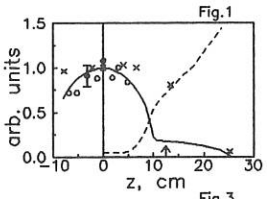

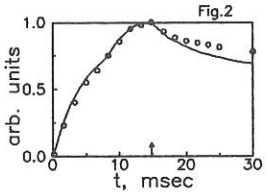

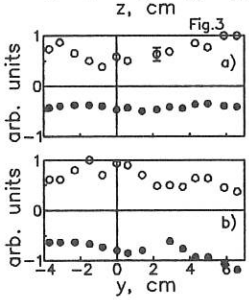

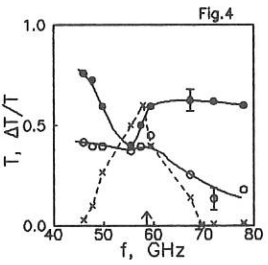

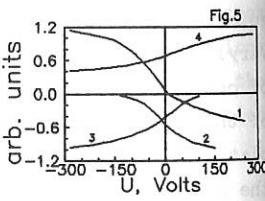

Mo 56

OBSERVATION OF "H"-LIKE PHENOMENA AT THE BEGINNING PHASE OF ECR-HEATING ON T-10.

Alikaev V.V., Bagdasarov A.A., Vasin N.L., Vershkov V.A., Grashin S.A., Rudakov D.L., Sushkov A.V., Chankin A.V., Chistyakov V.V.

I.V.Kurchatov Institute of Atomic Energy, P.O.Box 3402, Moscow, USSR.

Auxiliary heating is known to result in a significant increase of the neutral flux and H_α/D_α intensity, which is typical for "L"-mode. It's not before the certain rise in temperature and exceeding some threshold power, that transition to "H"-mode becomes possible. After that, the particle fluxes and H_α/D_α intensity fall to practically ohmic values. A high recycling value in the main plasma, causing high value of the neutral fluxes, is usually considered as one of the factors, which make difficult transition to "H"-mode.

In this case, as it may seem, the formation of "H"-mode is possible at the beginning of the central ECR-heating, before the wave of perturbation due to heating reaches the wall and causes neutral flux increase. It have been shown in the present paper, that in this case "H"-like phenomena did take place in first 10-13ms of ECRH, namely, increases of n_e and T_e gradients at the plasma periphery under the condition of ohmic values of the neutral fluxes.

The experiments were carried out at T-10 tokamak (R= 150cm, a=32cm) with plasma current I_p= 200kA as well as 400kA, average plasma density $\bar{n}_e = 3\times10^{13}cm^{-3}$, toroidal magnetic field H= 30kOe. ECR-heating was performed at the first harmonic, at the wavelength λ= 3.7mm, with full power up to 1.5MW. The n_e and T_e profiles were obtained with the use of the 8-channel interferometer and the intensity of radiation at the double electron cyclotron frequency - $2w_{he}$. Particle fluxes at the periphery were measured by the system of Langmuir probes and by the intensity of H_α/D_α from the limiter. Fig.1 shows the scheme of the experiment.

ECRH at T-10 was always accompanied by an increase of particle fluxes at the periphery up to about 10 times. It could be either due to the direct interaction between EC waves and periphery plasma, or due to the perturbation caused by heating which came to the periphery from the center of plasma column.

An analysis of time evolution of particle fluxes have shown, that the increase always appeared in two stages. First, just after beginning of the heating the fluxes increase by about 30%-50%, which gives the evidence of some direct interaction between EC waves and the periphery. However, this interaction is rather weak. Then, after the delay of about 3-13ms, the main increase up to several times begins. Fig.1 shows a set of experimental signals for the case of maximum delay. One can see, that after the first immediate increase of signals from the periphery diagnostics by about 50%, all of them stay constant for 13ms, and then the steep rise of all of the signals is observed, which is apparently caused by the arrival of perturbation from the center. Evidently, such an evolution of particle fluxes is incompatible with the usual diffusion model and is similar to the propagation of the shock wave. One can also see from fig.2, that the increase of temperature at the half radius as well as density evolution stop simultaneously with the beginning of the increase of fluxes. Fig.3 shows time evolution of the radial profiles of T_e and n_e. It's evident, that considerable widening of profiles occurs before the beginning of the fluxes rise. Since there are no noticeable changes at the radius of limiter by this time, one can suppose an increase of gradients of T_e and n_e at the periphery. However, this increase don't result in enlargement of particle fluxes, i.e. the increase in gradients decreases transport coefficients for heat and particles. Fig.3 gives the evidence that the growth of fluxes destroys previously formed steep gradient of n_e and thus automatically supports high values of fluxes at the periphery.

The investigations have shown, that the maximum value of the delay corresponded to the case in which plasma current was 200kA and ECRH was preceded by the phase with the strong flux from the valve, which resulted in a narrowing of profiles of T_e and plasma current (fig.4a). One can see from fig.4b, that in the case of plasma current 200kA and weak flux from the valve before the heating, the delay was 3 times less than one in the case of the strong flux. A similar decrease of the delay was observed with plasma current 400kA (fig.4c). Thus, the value of the delay is defined by the degree of the narrowing of T_e profile before the heating, which generally correlates with high loop voltage before the heating in that case.

The phenomenon of the "shock wave" formation didn't depend on the heating power and had been evidently observed at T-10 earlier, in the experiments on "B" and "S" regimes after switching off the valve ([1],[2]). A set of signals of that experiment is presented at fig.5. One can see, that the evolution of the probe signals and H_α/D_α intensity are quite similar to those in the case described above, but the value of the delay is increased up to 140ms. Similar phenomena

were observed at ASDEX during the transition from SOC to IOC regimes. Thus the phenomenon of locking up the fluxes at the periphery and formation of the steep gradients may be regarded as the general feature of tokamak plasma transport.

CONCLUSIONS

1. ECR-heating is a unique technique because it doesn't result in considerable interaction with plasma periphery and has a small switching time.
2. The formation of steep gradients of T_e and n_e at the periphery and, accordingly, locking up the fluxes of heat and particles is inherent to tokamak and is always observed in the process of the plasma column expansion after previous periphery cooling.
3. The arrival of the wave of temperature and density to the limiter accompanied by the sharp rise of the fluxes destroys steep gradient of n_e and automatically supports high values of the fluxes to periphery at the expence of enlarged transport coefficients.

REFERENCES.

1. Alikaev V.V. et.al., Plasma Phys. and Contr. Fus., Vol.30, No.4, pp.381-387, 1988.
2. Vasin N.L. et.al., Proc. on 15-th Europ. Conf. on Contr. Fus. and Plasma Heating, Dubrovnik, 1988, Vol.12, part 1, pp.59-62.
3. Giannone L. et.al., Max-Plank-Institute preprint No.IPP III/138, June 1989.

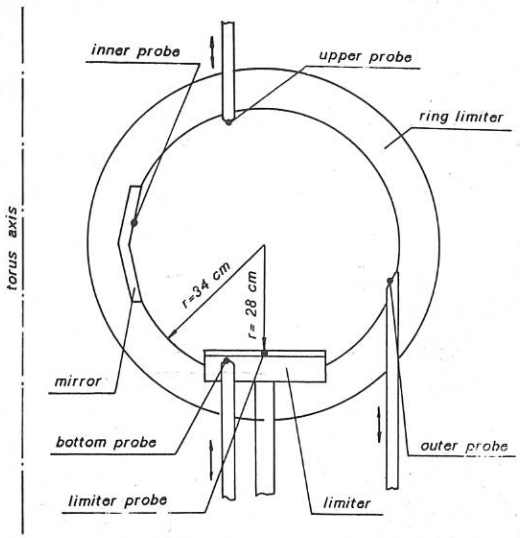

Fig.1. Scheme of limiters and probes positions in T-10.

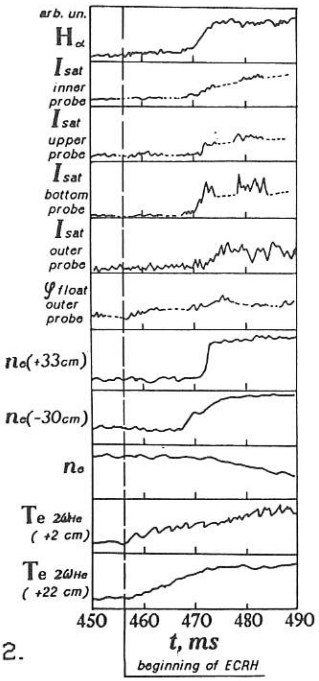

Fig. 2.

Experimental signals for the case of maximum delay

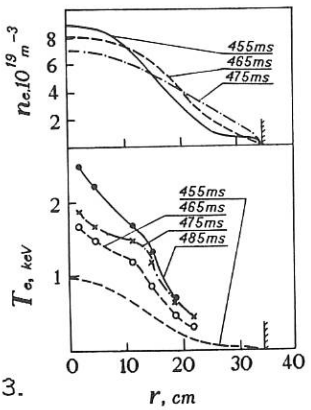

Fig. 3.

Time evolution of T_e and n_e profiles during the first 20 ms of ECRH.

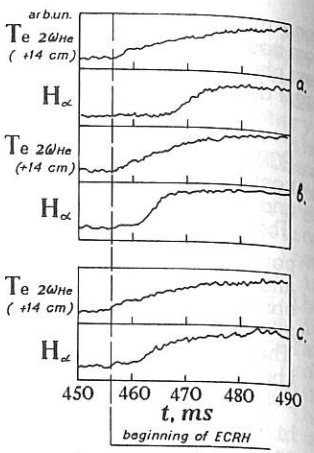

Fig. 4.

Comparison of time delays for
a.: I=200kA, strong gas puffing
b.: I=200kA, weak gas puffing
c.: I=400kA.

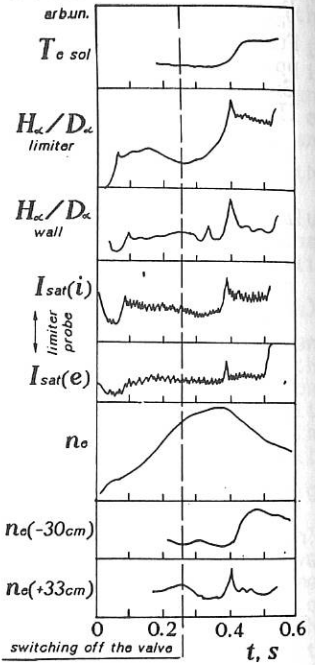

Fig. 5.

Experimental signals for the case of "S" to "B" transition.

Mo 57

REASONS FOR $\bar{n}_e$-LIMITATION -- EXPERIMENTAL STUDY IN T-10 AND SIMULATION.

Alikaev V.V., Bagdasarov A.A., Borschegovskii A.A., Vasin N.L., Vershkov V.A., Volkov V.P., Gurov A.A., Evdokimov D.B., Elizavetin D.Yu., Esipchuk Yu.V., Ivanov N.V., Kakurin A.M., Kislov A.Ya., Kislov D.A., Maximov Yu.S., Medvedev A.A., Mirenskii V.Yu., Notkin G.E., Pavlov Yu.D., Pimenov A.B., Razumova K.A., Roy I.N., Savrukhin P.V., Stepanenko M.M., Strelkov V.S., Sushkov A.V., Titishov K.B., Chankin A.V., Chistyakov V.V., Yaramyshev G.S., Yushmanov P.N.

Kurchatov Institute of Atomic Energy, P.O.Box 3402, Moscow, USSR.

1. Regimes were investigated in T-10 with achieving density limit by the additional gas puffing in the steady stage. HF power ($P_{HF} < 1.6$ MW, f = 81 GGz) was injected simultaneously with puffing. The main goal of the experiments was to search reasons for the $\bar{n}_e$ limitation. Dependence of $\bar{n}_e^{lim}$ on HF power, the puffing intensity, and the ECR position were under investigation with $B_t \sim 3$ T, $I_p = 0.2$ MA, and $q_L = 3.9$ ($a_L = 0.28$ m).

2. The specific features of plasmas of limiting density (both with and without ECH) are: i) m=2 mode bursts (Fig.1), when $\bar{n}_e$ is raised to $\bar{n}_e^{lim}$ ($t=t_k$). After that, the discharge becomes usually unstable. MHD activity with m = 2 to 6 does not vary during $\bar{n}_e$ rise up to $\bar{n}_e^{lim}$; ii) before the m=2 burst, situation arises at some $\bar{n}_e$, when the electron energy loss exceeds the input power. The electrons cool mainly at the edge ($r > r_{q=2}$).

The T_e-profile variation is illustrated in Fig.2 ($T_e^*(r,t) = T_e(r,t) / T_e(r,t_0)$, with t_0 being the instant just before the puffing). To characterize the T_e profile variation, one can use $\xi_T(t) = T_e^*(r_{q=2},t) / T_e^*(0,t)$. When $\bar{n}_e^{lim}$ is reached ($t=t_k$), $\xi_T(t_k)$ is about the same at fixed P_{HF} and it slightly decreases with P_{HF} rise. Periphery cooling results in current decrease beyond the q=2 surface within skin-time. Independence of $\xi_T(t_k)$ on the puffing intensity G_p seems to be an explanation for the gradual increase, not a decrease, of $\bar{n}_e^{lim}$ with G_p (Fig.3): $\bar{n}_e$ can be raised within the skin-time to a higher level at higher G_p.

3. As the $\bar{n}_e$ limitation is the result of periphery cooling, one would expect enhancement of the $\bar{n}_e^{lim}$ with the P_{HF} increase. Results displayed on Figs.1 and 4 confirm this expectation. But

the HF-wave refraction occurs in plasmas with $\bar{n}_e > 3.10^{19}\ m^{-3}$, which restricts the absorbed power P_{ab} and, hence, the $\bar{n}_e^{lim}$ increase with P_{HF}. The $\langle n_e \rangle_{lim}$ dependence on total heating power P_{tot} can be described (Fig.4) by $\langle n_e \rangle_{lim}, 10^{19} m^{-3} \cong 6.4\ P_{tot}, MW$.

4. In OH plasmas, poloidal asymmetry is not pronounced, as a rule, in n_e and P_{rad} profiles up to $\bar{n}_e^{lim}$. With ECRH, MARFE appears which is more pronounced at hihger P_{HF} and $\bar{n}_e \cong \bar{n}_e^{lim}$. Thus, MARFE forms beyond some threshold in input power.

5. P_{rad} increases stronger than linearly with $\bar{n}_e$ (Fig.1). At $\bar{n}_e \cong \bar{n}_e^{lim}$ and $P_{HF} = 1.6$ MW, P_{rad} is about 0.8 (P_{tot}-dW/dt), while it is not higher than 0.5 (P_{OH}-dW/dt) in OH (W is the energy content) (Fig.5). Being so high, P_{rad} dominates in the electron energy balance at $P_{HF} > 1$ MW. The P_{rad} rise at $\bar{n}_e \cong \bar{n}_e^{lim}$ is mainly due to the n_e increase in MARFE.

6.Transport enhancement at $\bar{n}_e \cong \bar{n}_e^{lim}$, $P_{tr}(t_k)/P_{tr}(t_o)$,does not exceed 1.6 in OH and 2.5 in ECH with $P_{HF} = 1.6$ MW ($P_{tr} = P_{tot}$-dW/dt-P_{rad}). Also, degradation of particle confinement τ_p is not strong: $\tau_p(t_o)/\tau_p(t_k)$ is not more than 2.5 at $P_{HF} = 1.6$ MW. In addition, n_e decrease was not rapid after H_2-pellet injection, although $\bar{n}_e$ was raised by the pellet above $\bar{n}_e^{lim}$ (Fig.6).

7. Strong poloidal asymmetry in particle transport appeared with MARFE. Namely, drastical enhancement of the D_α-line intensity was detected just on the inner side of the torus (Fig.1). Asymmetry was stronger with higher P_{HF} and, hence, with higher density in MARFE. Asymmetry in P_{rad} and transport leads to the conclusion that distortion of the energy balance and periphery cooling at P_{HF} high enough is initiated in MARFE.

8. MARFE plays apparently a noticeable role in off-axis ECH. In this case, heating just of the edge was expected to result in enhancement of $\bar{n}_e^{lim}$ at the same P_{HF} as in on-axis ECH. In reality (Fig.7a), $\bar{n}_e^{lim}$ was even slightly lower compared with on-axis ECH. In off-axis ECH, poloidal asymmetry manifested itself earlier and was more pronounced (Fig.7b). As a result, P_{rad} and $I(D_\alpha)$ increased more rapidly (Fig.7a), but in both cases of ECH, $\bar{n}_e^{lim}$ occured at the same values of P_{rad}, $I(D_\alpha)$, and density in MARFE.

9. The main features of plasma behaviour mentioned above can be described by the T-10 model of electron transport [1]:

$$\chi_e (\sim D_e) = Q^* \left(10.7 \frac{T_e^{0.5}}{n_e} \frac{r}{R} q + 0.7\, T_e^{1.5} \frac{q^2}{B_t^2} \frac{\nabla n_e}{n_e} \frac{r}{R} + 0.3 \frac{n_e}{T_e^{0.5}} \frac{q^2}{B_t^2} \right) \quad (1)$$

$$Q^*(r) = \frac{P_{tot}(r)/P_{tot}}{P_{OH}(r)/P_{OH}}; \quad \chi_e[m^2/s],\ T_e[keV],\ n_{19}[m^{-3}],\ B_t[T].$$

Simulation founded on the model indicates preferable cooling of the plasma edge (due to the 3^d term in (1)) with approach of $\bar{n}_e$ to $\bar{n}_e^{lim}$. Enhancement of transport flux on the inner side of the torus is the result of n_e rise, T_e decrease (the 3^d term in (1)), and, also, of ∇n_e increase in MARFE.

As the experiment gave no evidence of any additional mechanism of the electron transport when $\bar{n}_e$ was raised to $\bar{n}_e^{lim}$, one would expect that the electron transport obeys the same scaling over the whole range of n_e variation.

/1/ Yu.Esipchuk et al. ITER Meet.,March 1989.ITER-IL-PH-4-9-S-1

Figure Captures

Fig.1. Traces of mean density,$\bar{n}_e$, m=2 mode intensity,MHD, radiative loss,P_{rad}, D_α-line intensity,$I(D_\alpha)$, and loop voltage,U_O, without ECH (1) and with it at P_{HF}=1 MW (2) and 1.6 MW (3).$\bar{n}_e$ and $\bar{n}_{eL}$ ($\cong$ 1.4 $\bar{n}_e$) are density values averaged over the radii of chamber and limiter, respectively

Fig.2a.Relative temperature profile variation with $\bar{n}$ rise for instants marked by arrows in Fig.1a.

Fig.2b.Profile parameter ξ_T variation with $\bar{n}_e$.

Fig.3. The $\bar{n}_e$ traces for different intensities of gas puffing. P_{HF} = 0.33 MW. Start of m=2 activity is marked by "t_k".

Fig.4. Dependence of $\langle n_e \rangle_{lim}$ on total power, P_{tot}; $\langle n_e \rangle$ is the density averaged over cross-section within the limiter.

Fig.5. P_{rad} variation with P_{tot} for instants of achieving $\bar{n}_e^{lim}$.

Fig.6. $\bar{n}_e$ behaviour with the pellet injection (1) and the gas puffing (2). With pellet, $\bar{n}_e^{lim}$ was exceeded.P_{HF}=0.33 MW.

Fig.7a.Traces of $\bar{n}_e$, P_{rad}, and $I(D_\alpha)$ at different locations of heating: 1 - $\Delta R \cong 0$, 2 - ΔR=+16.5 cm, $P_{HF} \cong$ 1 MW.

Fig.7b.Temporal variation of additional phase shift δF under conditions mentioned in Fig.7a. $\delta F(t) = F(t) - F(t_o)$.

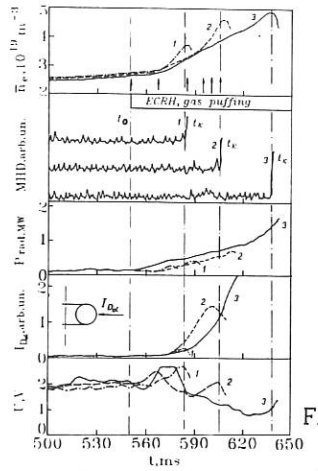

Fig.1.

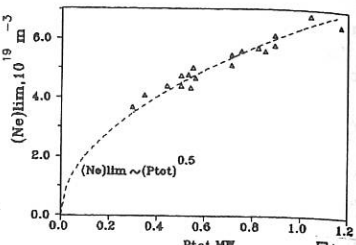

Fig.4.

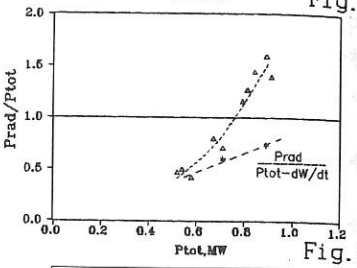

Fig.5.

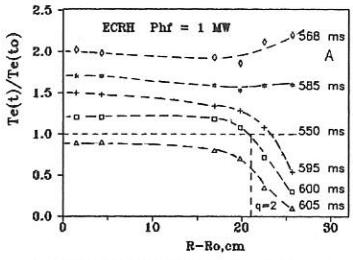

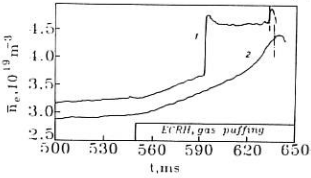

Fig.6.

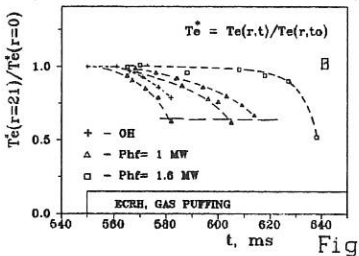

Fig.2.

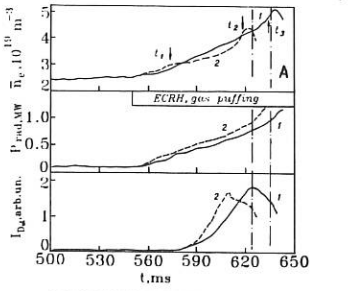

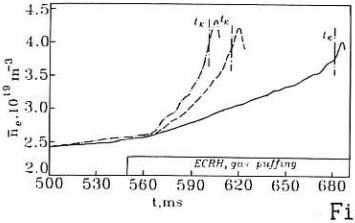

Fig.3.

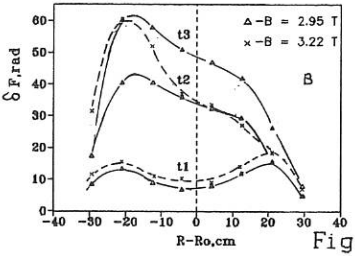

Fig.7.

OPTIMIZATION OF BREAK-DOWN AND OF INITIAL STAGE OF DISCHARGE WITH ECH IN T-10.

Alikaev V.V., Bagdasarov A.A., Borschegovskii A.A., Vasin N.L., Evdokimov D.B., Elizavetin D.Yu, Esipchuk Yu.V., Kislov A.Ya., Mirenskii V.Yu.,Notkin G.E.,Pimenov A.B.,Razumova K.A.,Roy I.N.

Kurchatov Institute of Atomic Energy, P.O.Box 3402,Moscow,USSR.

1. The EC low-voltage disharge startup and current rampup have been studied on T-10 (a_L = 0.28 m, R = 1.5 m, B_t = 2.6 to 3 T). O-mode EC power up to 2 MW was launched from the low-field side and then it was transformed to X-mode by the mirror on the backside of chamber. Two gyrotron systems, 3 units in each of them, were in operation simultaneously or consequently to prolongate the EC pulse up to 300 ms.

2. Before start of toroidal electric field E_t, which produced a plasma current I_p, EC plasma and a toroidal current I_{HF}/1/ were produced in D_2 (3 to 8.10^{-5} Torr, Fig.1a). Maximum I_{HF} occured at the optimal value of the vertical magnetic field $B_v^0 \cong 0.2\ I_{HF}/a_L$ (Fig. 1c). After transient process, $\bar{n}_e$ = 0.1 to 1.10^{19} m^{-3} was controlled by gas puffing. Maximum phase shift $F(h) \sim \int n_e dl$ was observed near the ECR location (Fig.1b). X-rays of energy up to 20 keV (Fig.1a) were emitted from bottom of the chamber, toward which the electrons drifted. On the other hand, effective T_e did not exceed 150 ev as given by the profiles of CIII and CV - line intensities. Single-pass absorption was low under such conditions, as estimation shown.

3. The E_t-pulse was switched on 35 ms after ECH start.The E_t value was controlled via the feed-back system, which provided the predetermined value of dI_p / dt. But on the front of the E_t pulse the real dI_p/dt value exceeded the predermined one and was usually about 2 MA/s as high. Therefore, I_p was steeply raised at the beginning up to 10 or 15 kA. During the I_p rise, intensity of X-ray emission, caused by the electron - wall interaction, dropped together with the decrease of the current to the limiter by factor 3 or 4. In the initial stage, the maximum on the chord profile F(h) became less pronounced. Thus, one could imagine that the rotational transform was produced in 5 to 10 ms. The surface voltage U_s set to this instant was a

function of the EC-discharge parameters as well as of B_v, $\bar{n}_e$, and EC power (Figs.1 d,e). Note, that minimum U_s was realized at $B_v = B_v^0$ with fixed P_{HF} and $\bar{n}_e$. At $B_v < B_v^0$, U_s slightly exceeded U_s^{min} (30% higher at $B_v = 0$) and it drastically increased at $B_v > B_v^0$ (8 to 10 V at B_v = 2 to 2.5 B_v^0). With P_{HF} increase, U_s decreased (and maximum I_{HF} was reached at higher B_v^0, Fig.1d). Thus, with EC heating powerful enough the low-voltage startup does not demand the careful choose of B_v. The dependence of U_s on $\bar{n}_e$ (Fig.1e) points that low $\bar{n}_e$ is favorable to minimize U_s. However, too low $\bar{n}_e$ (< $1.5 \times 10^{18} m^{-3}$) promoted the runaway electron production by E_t. Such discharges were not studied.

4. The startup stage ended by the rotational transform formation and was followed by the rampup stage. In this stage, dI_p/dt value of 0.1 to 1.7 MA/s was provided, which resulted in the I_p value of 30 to 220 kA (Fig.2a). The n_e profile was formed in 30 to 40 ms after the E_t start and did not change later, while $\bar{n}_e$ rose gradually up to 0.8 to 1.7×10^{19} m^{-3} on the flat top of the I_p pulse. After formation of the rotational transform, T_e was about 0.3 keV and then was raised in about 50 ms up to the maximum value T_e^{max}= 1.6 to 3.2 keV, which was a function of P_{HF} (Figs.2b,c). At such T_e values, the period of the I_p rise up to the flat top magnitude was of order of the skin-time.

5. Main characteristics of the rampup stage-- the loop voltage on the plasma surface U_s and the total parameter of Ejima-Wesley /2/ $C_j^t = \Delta\Psi_s^t / 0.4 \pi I_p R$, are displayed on Figs.2 d,e, with $\Delta\Psi_s^t$ being the consumption of voltseconds to the instant of start of the current flat top. Its resistive component, Ψ_s^r, was calculated using the dependence of the resistive voltage on the plasma current. The dependence, obtained for the flat top of the current pulse by the I_p-amplitude variation, was believed to be valid at any instant of the current ramp. So estimated, $C_j^r \propto \Delta\Psi_s^r$ appeared to be about 0.3 at $\dot{I}_p \geq 0.6$ MA/s and P_{HF} = 1 MW; $C_j^t \cong 0.7$ to 0.75 for the same range of parameters (Fig.2e) and maximum U_s= 1 to 2.2 V. Thus, before the beginning of the current flat top, $E_t \leq 0.1$ to 0.22 V/m. However, current profile was probably not stationary yet. To reach it, one need-

ed additional voltsecond consumption. It was amount to about 10% of Ψ_s^t at $\dot{I}_p$ = 1.2 MA/s, as estimated in the regime with the sawtooth activity. The sawteeth were believed to be a sign of formation of the stationary current profile. During this period $dI_p/dt \cong 0$ and E_t is lower than 0.1 V/m in the EC plasmas.

[1] Alikaev V.V. et al. In Plasma Phys. and Contr. Nucl. Fus. Res., IAEA, Vienna (1987) v.1, p.533.

[2] Ejima S. et al. Nucl. Fus. 22, 1313 (1982).

FIGURE CAPTIONS.

Fig.1a. Traces of surface voltage, U_s, plasma current, and mean density, $\bar{n}_e$, during EC startup.

Fig.1b. Chord profile of the phase shift F(h). ECR location is marked by arrow.

Fig.1c. Toroidal startup current vs vertical magnetic field. The optimal value $B_v^o = 0.2 I_{HF}/a_L$ is marked by arrow.

Fig.1d. Optimal B_v vs EC power; also shown are U_s's (Fig.1a).

Fig.1e. U_s vs $\bar{n}_e$ at P_{HF} = 1 MW.

Fig.2a. Traces of U_s, I_p, and $\bar{n}_e$ during the current rampup.

Fig.2b. The n_e and T_e profiles at P_{HF} = 1 MW.

Fig.2c. Central electron temperature, $T_e(0)$, vs HF power.

Fig.2d. U_s vs the current ramp rate.

Fig.2e. The total Ejima-Wesley parameter vs current ramp rate.

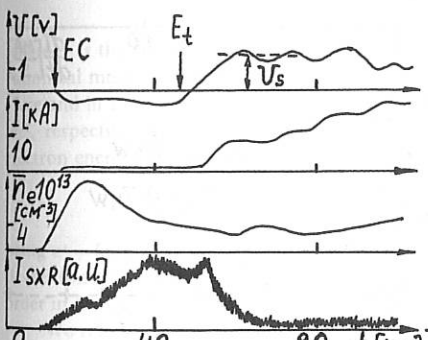

Fig. 1a

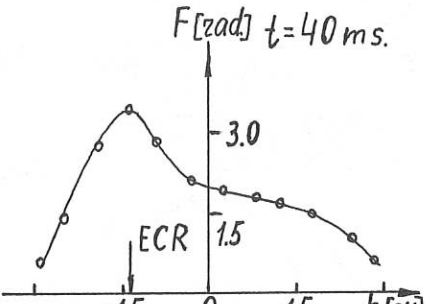

Fig. 1b

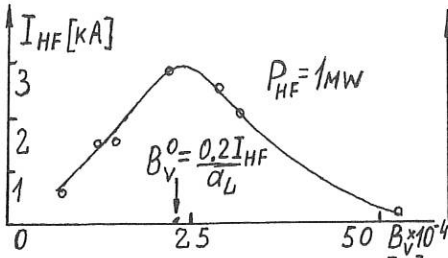

Fig.1c

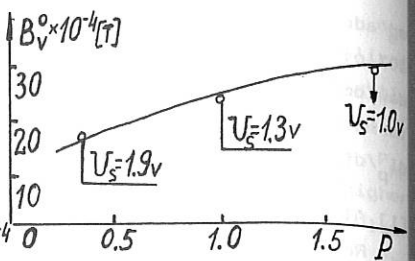

Fig.1d

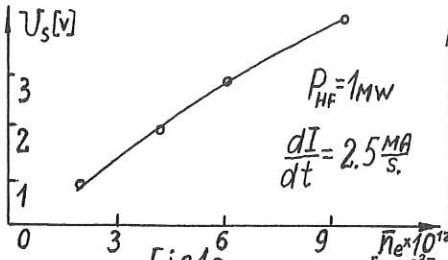

Fig.1e

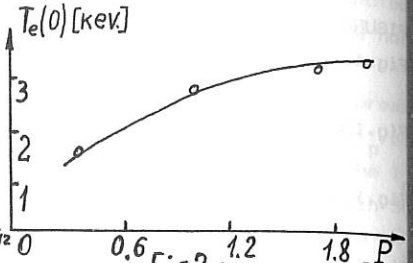

Fig 2c

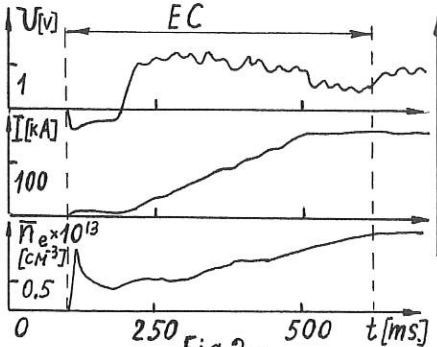

Fig. 2a.

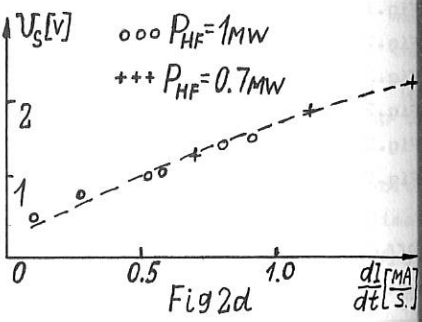

Fig 2d

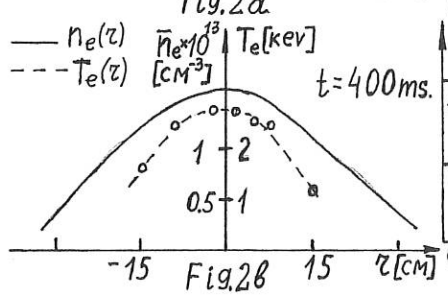

Fig.2b

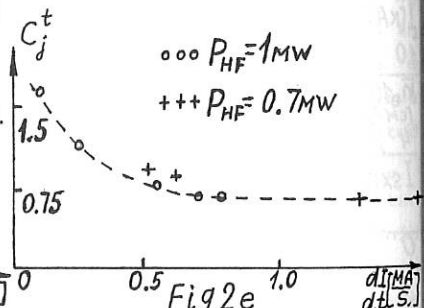

Fig 2e

NONLINEAR HEATING BY A SPATIALLY LOCALIZED ELECTRON CYCLOTRON WAVE

D. Farina, R. Pozzoli*

Istituto di Fisica del Plasma, Consiglio Nazionale delle Ricerche, EURATOM-ENEA-CNR Association, Milano, Italy

**Dipartimento di Fisica, Università di Milano, Milano, Italy.*

The problem of nonlinear interaction of a plasma with an electromagnetic wave, in the electron cyclotron (EC) frequency range, characterized by a spatial dependent amplitude, has recently received a large consideration, mainly due to the use of high power radio frequency sources in fusion plasma experiments /1-4/. Here, we present a theoretical analysis which points out the mechanism underlying the nonlinear interaction process, and provides the analytical computation of the absorbed power, at any cyclotron harmonics.

The interaction of a single electron with the electromagnetic field of a spatially localized radiation beam can be conveniently investigated using the relativistic Hamiltonian formalism. The motion of an electron interacting with an EC wave propagating perpendicularly to the magnetic field $\mathbf{B}_0$, parallel to the z axis, with a frequency $\omega \approx n\Omega$, being $\Omega = eB_0/mc$ the classical cyclotron frequency, and with a z –dependent amplitude, can be characterized by a time independent Hamiltonian

$$H(z, P_z, \theta, I) = \gamma - v_n I = H_0(P_z, I) + H_1(z, P_z, \theta, I), \tag{1}$$

with

$$H_0 = \Gamma - v_n I, \quad H_1 = -\varepsilon(z)\frac{\Theta_n(I, P_z)}{\Gamma}\cos n\theta, \tag{2}$$

where γ is the relativistic factor, $\varepsilon(z) = (E(z)/B_0)\,\Omega/\omega$, $v_n = \omega/n\Omega$, $\Gamma = \sqrt{1 + P_z^2 + 2I}$, P_z the canonical momentum conjugate to the variable z, and I and θ are action-angle variables. Here and in the following t, z, I, P_z, and H are normalized over Ω^{-1}, $c\Omega^{-1}$, mc^2/Ω, mc, and mc^2, respectively. In the absence of the perturbation ($\varepsilon(z) = 0$), I is the perpendicular electron energy $p_\perp^2/2$, and $P_z = p_z$. In Eq. (2), the polarization term Θ_n reads

$$\Theta_n = \sqrt{2I}\left[e^- J_{n-1}(b) + e^+ J_{n+1}(b)\right] + P_z e_z J_n(b),$$

being $e^\pm = (e_x \pm e_y)/2$ the right and left polarization components of the electric field, J_n the Bessel function of argument $b = N\omega/\Omega\sqrt{2I}$, and $N = kc/\omega$ the refractive index. At lowest order in Larmor radius $\Theta_n \simeq (kc/\Omega)^{n-1}(2I)^{n/2}(2e^- + N v_n e_z P_z)/(2^n(n-1)!)$.

We refer to physical situations where the electron time of flight in the radiation beam exceeds the trapping time in the wave potential, so that nonlinear effects play a major role. Moreover, during the motion the variation of the field amplitude felt by the electron is as-

sumed sufficiently slow, so that the action integral $J = 1/(2\pi) \int I \, dn\theta$ can be considered an adiabatic invariant, experiencing abrupt variations only as the separatrix between trapped and untrapped orbits in the (θ, I) plane is crossed. The breaking of J provides the connection between two unperturbed states (before and after the crossing of the beam), characterized by the same value of the Hamiltonian and, in general, by different values of the energy. A net electron energy variation is made possible by the existence of an interval of values of the unperturbed Hamiltonian H_0, where any value of H_0 pertains to two different electron states, with the same P_z and different energies. In fact, when $v_n < 1/\Gamma_z$, with $\Gamma_z = \sqrt{1 + P_z^2}$, the value $\bar{I}(P_z)$, satisfying the resonance condition $\Gamma(\bar{I}, P_z) = 1/v_n$, corresponds to a maximum $\overline{H}$ of H_0, with respect to I at fixed P_z, and in the range $H_0(I = 0, P_z) \leq H_0 \leq \overline{H}$, two different values of I correspond to the same value of H_0. In the unperturbed state, these I values characterize the two branches of the level curve $H = const.$ in the phase plane.

The trajectory of an electron with initial I_0 and P_{z0} belonging to a given branch of H crosses the separatrix at a given value of ε, say ε_s, while ε is increasing. The particle will change its energy only if its trajectory ends on the other branch of the Hamiltonian after the latter crossing of the separatrix. Since the motion is adiabatic in each different stage of the motion, excluding the separatrix crossing, the variation in the action, $\Delta I \equiv I_f - I_0$, will be equal to the jump of the adiabatic integral at the separatrix $\overline{\Delta I}(\varepsilon_s, P_{zs})$. By the constancy of H, the corresponding energy variation is $\overline{\Delta\gamma} = v_n \overline{\Delta I}$.

To determine $\overline{\Delta I}$, the values of ε_s and of P_{zs} are required. They can be computed in terms of the initial I_0, P_{z0} by means of the constancy of the adiabatic invariant J and of the Hamiltonian during the first stage of the motion

$$\begin{aligned} I_0 &= |J(\varepsilon_s, P_{zs})| \\ H_0(I_0, P_{z0}) &= H_s(\varepsilon_s, P_{zs}) \end{aligned} \tag{3}$$

being H_s the Hamiltonian on the separatrix. The condition for the occurence of the energy variation is $\varepsilon_s < \varepsilon_M$, where ε_M is the maximum value of ε. Eqs. 3 then determine the nonlinear interaction region, i.e. the region in the space of initial momenta characterizing the electrons experiencing the energy transition.

An approximate estimate of $\overline{\Delta\gamma}$ can also be given from the constancy of H, neglecting the variation ΔP_z^2: $\overline{\Delta\gamma} = 2(1/v_n - \gamma)$. Note that $\overline{\Delta\gamma}$ is independent of the field amplitude, provided that the energy transition takes place.

To compute the power absorbed by the electron population, the probability that a particle vary its energy after the crossing of the radiation beam, has to be evaluated. The transition probability is strictly related to the structure of the phase space and to the variation of the adiabatic invariant. In our case, it can be shown /1,3/ that for an uniform electron distribution in the θ variable, the probability that a particle end on a given branch of the Hamiltonian is equal to 1/2. The absorbed power per unit length in the propagation (x) direction and in the y direction, normalized over nmc^3, where n is the electron density, reads then

$$W = \int d\mathbf{P} \, \frac{P_z}{\Gamma} \, \overline{\Delta\gamma} \, f(I, P_z), \tag{4}$$

where $d\mathbf{P} = 2\pi\, dI\, dP_z$, f is the unperturbed distribution function, and the integration has to be performed on the nonlinear interaction region for positive P_z.

The computation of W requires the analysis of the conditions under which the separatrix crossing takes place, and the evaluation of the adiabatic integral on the separatrix, in order to determine $\overline{\Delta\gamma}$ and the nonlinear region. This investigation can be easily performed in two different limits: the weakly nonlinear limit, and the weakly relativistic limit.

In the weakly nonlinear limit, the Hamiltonian function can be developed around the unperturbed resonance condition $\gamma = 1/v_n$, obtaining the pendulum Hamiltonian. In this case, the analytical computation of the nonlinear interaction region is easily provided, and we obtain for the absorbed power density

$$W = -\frac{2^7}{3\pi^3 v_n}\,\varepsilon_M^{3/2}\int d\mathbf{P}\,\frac{|P_z|}{\gamma}\,[\Theta_n(I, P_z)]^{3/2}\,\frac{\partial f}{\partial I}\,\delta(\gamma - 1/v_n). \tag{5}$$

This expression exhibits the same dependence of the linear case on the derivative of the distribution function with respect to the perpendicular energy and on the resonant condition, while scales differently with ε_M and with the polarization term. In particular, it depends only on the peak ε value and not on its profile.

In the strongly nonlinear regime the interaction region can be evaluated analytically at each harmonics, in the weakly relativistic approximation, which applies to most cases of interest for plasma heating. A simple expression for the behaviour of W with respect to ε_M and v_n can not be found, since these quantities are contained in the integration limits in Eq. (4) in a non trivial way, through the adiabatic integral J.

The nonlinear interaction region for the ordinary mode at the first harmonic and for the extraordinary mode at the second harmonic is shown in Fig. 1 for different values of ε_M. For $\varepsilon_M \to 0$, it corresponds to a small region surrounding the resonance curve $\gamma = 1/v_n$. For increasing ε_M it covers an increasing area of the momentum space, which tends to saturate, occupying the whole region $I \leq 2(1 - v_n\Gamma_z)/v_n^2$, $\Gamma_z \leq 1/v_n$.

The profile of W, obtained from Eq. (4), as a function of v is shown in Fig. 2 for the case of a Maxwellian distribution, together with the linear profile and the profile resulting from a numerical code, which solves the equations of motion for a set of particles. The comparison between the integrated values of W over the propagation direction x resulting from our theory and from the simulation performed in Ref. 1 is shown in Fig. 3. The agreement is quite good in both cases. We stress the fact that in our model there are no free parameters, so that the curves are not adjusted for a better fit of the numerical results.

References

/1/ W. M. Nevins, T. D. Rognlien and B. I. Cohen, Phys. Rev. Lett. **59**, 60 (1987).

/2/ E. V. Suvorov and M. D. Tokman, Sov. J. Plasma Phys. **14**, 557 (1988).

/3/ I. A. Kotelnikov and G. V. Stupakov, Internal Report IC/88/426, International Centre for Theoretical Physics, Trieste, Italy (1988); Preprint 89-100, Institute of Nuclear Physics, Novosibirsk (1989).

/4/ D. Farina, R. Pozzoli, D. Ronzio, Internal Report FP 89/12, Istituto di Fisica del Plasma, Milano, (1989).

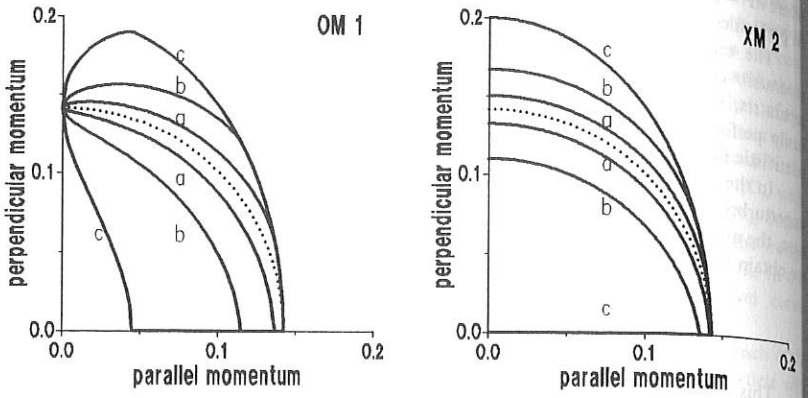

Fig. 1 - Nonlinear interaction region in momentum space for different values of α, for the ordinary mode at the first harmonic ($\alpha = 1/2\varepsilon_M kc/\Omega$), and the extraordinary mode at the second harmonic ($\alpha = \varepsilon_M e^{-}kc/\Omega$). The solid curves a, b, c refer to and $\alpha = 10^{-4}$, 10^{-3}, 10^{-2}, respectively, and $v_n = \omega/n\Omega = 0.99$. The dotted curve is the linear resonance curve $\gamma = 1/v_n$.

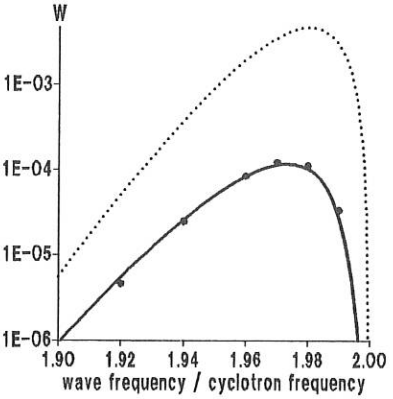

Fig. 2 - Profile of the normalized absorbed power W as a function of ω/Ω, for the extraordinary mode at the second harmonic. The parameters are $\alpha = 5 \times 10^{-3}$, and $T_e = 2\,keV$. The solid line is obtained by Eq. (4). The points represent the results obtained by means of a numerical simulation code. The linear profile is represented by the dotted line.

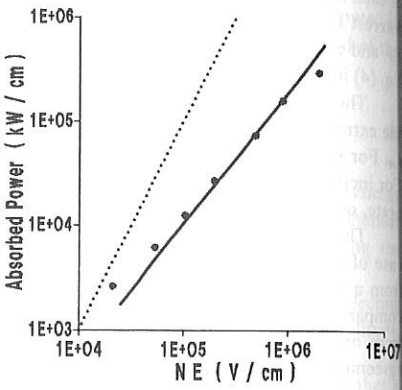

Fig. 3 - Comparison between the integrated values of W over the propagation direction x for different N_E values resulting from our model (solid line) and from the numerical simulation performed in Ref. 1 (points). The dotted line is the linear estimate. The reference parameters are $B_0 = 5\,T$, $n = 10^{14}\,cm^{-3}$, $T_e = 1\,keV$.

Mo 60

POWER ABSORPTION AND ENERGY CONFINEMENT DURING LH INJECTION IN ASDEX

R. Bartiromo

Associazione EURATOM–ENEA sulla Fusione
Centro Ricerche Energia Frascati
C.P. 65 – 00044 Frascati, Rome, Italy

F. Leuterer, F.X. Söldner, H. Murmann, L.H. Team, Asdex Team

Max–Planck -Institut für Plasmaphysik
Euratom Association
D–8046 Garching, F.R.G.

INTRODUCTION

Physical conditions which are not typical of usual tokamak operation can be realized by driving the plasma current with LH waves. The ohmic heating power can be reduced to zero together with the toroidal electric field. The temperature and current profile are not linked by the Spitzer resistivity and the shape of these profiles can be varied by changing the $n_{\parallel}$ spectrum of the LH waves [1]. It is therefore interesting to study the transport properties of the plasma in these conditions in order to gain some insight on the underlying physical mechanism.

In this paper we report about such a study in the tokamak Asdex which has already a solid data base on confinement for OH, NI and ICRH discharges. The radiofrequency system used in the experiment has been already described elsewhere [2]. Here we focus our attention on the energy confinement. Particle transport is described in a companion paper at this conference [3].

EXPERIMENTAL RESULTS

The increase of total plasma energy, as deduced from magnetic measurements, of the perpendicular energy, as measured by a diamagnetic loop and of the electron thermal energy, as measured by Thomson scattering diagnostic is shown in fig. 1 as a function of the total power input to the plasma.

These data were obtained with a power scan in a discharge with $I_p = 420kA$, $B_T = 2.8T$, $\overline{n_e} = 1.35 \times 10^{-13}$ cm^{-3} and current drive spectrum with $n_{\parallel} = 2.2$.

We observe that the increase in plasma energy is well described by an offset linear law and this is always true when the current profile is not changed by the LH driven current.

At low density, due to the high current drive efficiency, we can produce discharges with a total power input lower than the OH power in the target plasma. In these conditions we observe an increase in the total plasma energy but a cooling of the thermal bulk due to the reduced power input. This shows that the fast electrons generated by the LH waves have a confinement time which is longer

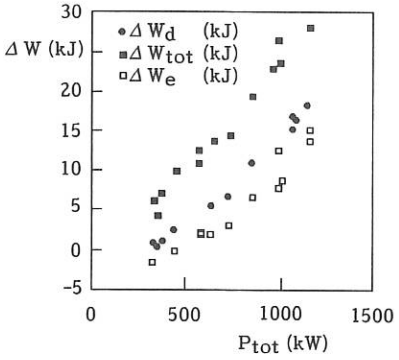

Fig. 1 – The increase of total plasma energy, diamagnetic energy and thermal electron energy is plotted as a function of the total power input (ohmic + lower-hybrid). Discharge parameters are: $Ip = 420$ kA, $B_T = 2.8T$, $\overline{n_e} = 1.35 \times 10^{13}$ cm^{-3}. Current drive operation with $n_\parallel = 2.2$.

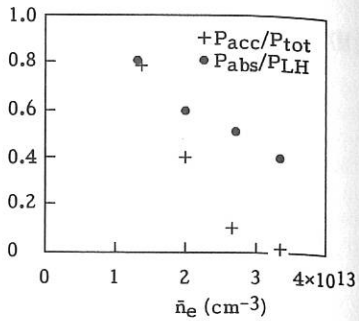

Fig. 2 – The absorption coefficient (dots) and the fraction of accessible power (crosses) is plotted as a function of the electron density for $B_T = 2.17T$, $I_p = 320$ kA and $n_\parallel = 1.8$.

than that of the bulk. The average energy of these electrons can be increased by lowering the launched $n_\parallel$ and a higher increase in the thermal electron energy is obtained for $n_\parallel = 2.2$ as compared to the case of $n_\parallel = 1.8$. This implies that the fast electrons have a confinement time shorter than the slowing down time so that they dump only part of their energy to the bulk plasma.

Different heating is observed when the direction of the launched waves is changed. The largest effect is obtained with a current drive spectrum, the lowest with an opposite current drive one. At low density ($\overline{n_e} \approx 1.3 \times 10^{13}$ cm^{-3}) we generally observe that the increase in diamagnetic energy exceeds that of the bulk electrons by an amount which cannot be accounted for by the observed ion heating. This difference is higher for the low $n_\parallel$ spectra and shows that the electron distribution function is not maxwellian in the perpendicular direction too, as a result of pitch angle scattering of resonant electrons.

When the density is increased to 2.7×10^{13} cm^{-3} the diamagnetic energy only exceeds that of bulk electrons by the observed ion heating.

POWER ABSORPTION

Before discussing the confinement time of the plasma during LH experiments, we need to evaluate the absorption coefficient for the wave power. In fact quasi-linear dumping of the launched spectrum is not sufficient to explain the observed heating and, although different mechanisms of spectral modifications and $n_\parallel$ upshift have been proposed, still the power absorption cannot be reliably calculated.

The absorption coefficient α can be measured from the rate of change in the plasma energy at the switch-on and switch-off of the heating pulse. In the case of

LH injection however, the plasma resistivity can change on a fast time scale and this leads to a fast rise of the plasma current with an associate increase in magnetic energy which has to be taken into account in the power balance. Therefore we have evaluated α from the rate of change of the total plasma energy, as given by magnetic diagnostics, and of the magnetic energy, as given by the total inductance of the plasma loop (internal + external). The method has been checked during neutral beam injection and has proven to be accurate within the experimental error of $\pm 10\%$.

For LH waves we have found that all the power in the main peak of the spectrum is absorbed by the plasma core in current drive experiments at low density, in agreement with results on current drive efficiency which are close to the maximum theoretical value. The power in the secondary peak has too high $n_\parallel$ to contribute to the driven current and is likely to be absorbed at the plasma edge. We observe higher absorption for low $n_\parallel$ spectra in agreement with the higher directivity of the grill in the corresponding phasing. In opposite current drive operation we observe a reduction in absorption of about a factor 2 with respect to normal current drive and intermediate results are obtained with symmetric spectra. This is in agreement with the observed increase in plasma energy which is maximum for current drive and minimum for opposite current drive operation.

When we increase the plasma density we find a remarkable decrease of α, in particular at lower magnetic field, as expected from accessibility considerations. In fig. 2 we show the results of a density scan with $B_T = 2.17T$ and $n_\parallel = 1.8$. The experimental data are compared with the fraction of power satisfying the accessibility condition at a plasma density equal to the line average density and a magnetic field equal to the toroidal field on axis. From this we can conclude that the decrease in α is related to the accessibility, although we also find absorption in cases where no power should reach the plasma core.

The measured absorption coefficient does not show any appreciable dependence on the launched power. We have changed $n_\parallel$ and the width of the spectrum without appreciably changing the value of α at $\overline{n}_e = 2.1 \times 10^{13}$ cm^{-3}. For the same density and $n_\parallel = 1.8$ we also changed the plasma current in order to vary the q-profile, which should influence the wave trajectory in the plasma. But this did also not affect α.

DISCUSSION

When we take into account the measured absorption, we observe the same increase in plasma energy for the same absorbed power independently of the electron density. This is shown in fig. 3 where the increase in diamagnetic energy is plotted versus the absorbed power for $n_\parallel = 1.8$ and $n_\parallel = 2.2$ with different densities and $I_p = 420kA$, $B_T = 2.8T$. Only data for $\overline{n_e} \geq 2.0 \times 10^{13}$ cm^{-3} are considered to minimize the contribution of the fast electron to the diamagnetic energy. From these plots we can deduce an incremental confinement time of 27 ms and 40 ms for $n_\parallel = 1.8$ and $n_\parallel = 2.2$ respectively. These values are lower than the ohmic confinement, therefore implying a power degradation of τ_E. Nevertheless they are comparable or even better than the corresponding values obtained with

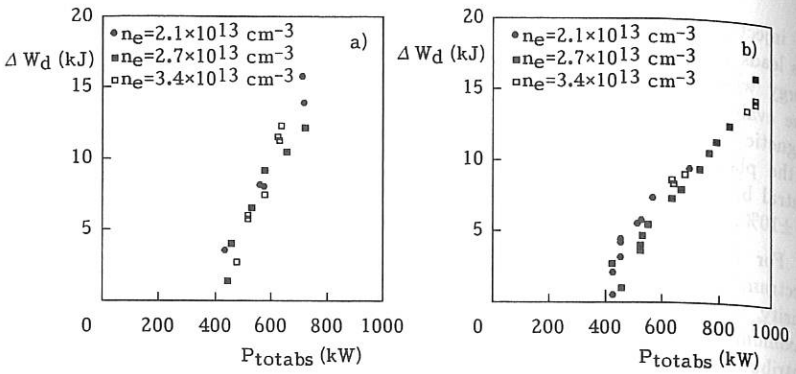

Fig. 3 – The increase in diamagnetic energy is plotted as a function of the total absorbed power (ohmic + lower hybrid) for different densities. a) $n_{\parallel} = 2.2$, b) $n_{\parallel} = 1.8$. Discharge parameters are: $I_p = 420\,\mathrm{kA}$, $B_T = 2.8T$.

neutral injection heating.

Incremental confinement times obtained during LH injection do not show an appreciable current dependence in the range 300kA ÷ 420kA. However they decreases when q is lowered below 3. Incremental confinement times obtained with neutral injection in an ohmic target plasma and in a LH current driven plasma turn out to be comparable.

The lower Hybrid experiments in ASDEX are performed in collaboration between IPP Garching, ENEA Frascati and PPPL Princeton.

REFERENCES

[1] F.X. Söldner et al., these proceedings.

[2] F. Leuterer et al., 16th Europ. Conf. on Contr., *Fusion and Plasma Physics*, Venice 1989, Vol. 4, 1287.

[3] O. Gehre et al., these proceedings.

SCATTERING AND LOCALIZABILITY OF ECH POWER IN CIT*

Gary R. Smith

Lawrence Livermore National Laboratory
University of California
Livermore, California 94550, USA

ABSTRACT

The theory of scattering by drift-wave density fluctuations is applied to electron-cyclotron heating (ECH) in the Compact Ignition Tokamak (CIT). It is found for CIT that the scattering angles are small and have a Gaussian distribution. An analytic result is given for the average number of scattering events suffered by a ray during propagation through the turbulence layer; this average number is 1.3 for the turbulence level expected in CIT. Localizability of ECH power in CIT is also studied for two choices of steering mirror. Better access to outer flux surfaces and better localization is achieved if the power is steered within a poloidal plane.

PLASMA AND MICROWAVE-BEAM PARAMETERS

We study the propagation of electron-cyclotron power in a plasma representative of the beginning of the flat portion of the current evolution. The equilibrium magnetic field B_0 is a solution[1] of the Grad-Shafranov equation. This equilibrium is characterized by a field strength of 11.2 T and a safety factor $q = 1.16$ at the magnetic axis. The $q = 2$ surface is at $\psi = 0.76$. (In this paper, flux surfaces are specified by values of the poloidal flux ψ, normalized to have values of zero at the magnetic axis and unity at the separatrix.) The electron-temperature profile is $T_e(\psi) = \hat{T}_e(1-\psi)$ with $\hat{T}_e = 20\,\mathrm{keV}$. The density profile is $n_e(\psi) = \hat{n}_e(1-\psi)^\alpha$ with $\hat{n}_e = 5\times10^{20}\,\mathrm{m}^{-3}$ and $\alpha = 0.5 + 1.5\psi^{20}$. Note that $\alpha \approx 0.5$ except very close to $\psi = 1$, where increasing α yields a smaller $n_e(\psi)$ and a bounded $dn_e/d\psi$.

The ray-tracing calculations in the next section use a ray bundle that represents a Gaussian beam with a Rayleigh length of 1.5 m and a waist of radius $w_0 = 2.2\,\mathrm{cm}$ located in the plasma core. Such a beam could be focussed and directed towards the plasma from a mirror of diameter 0.4 m located 6.7 m from the magnetic axis.

SCATTERING BY DRIFT-WAVE DENSITY FLUCTUATIONS

The scattering theory was formulated by Ott et al.[2], and a numerical method described by Hui et al.[3]. That work is directly applicable to the present situation of ordinary-mode propagation nearly perpendicular to B_0.

* Work performed for the U. S. Department of Energy by Lawrence Livermore National Laboratory under contract W-7405-ENG-48.

We assume that the density fluctuations are located on the outer flux surfaces and have a radial profile given by

$$\langle(\delta n)^2\rangle(x) = \langle(\delta n)^2\rangle(\psi_t)\left[1 - \frac{(\psi-\psi_t)^2}{(\delta\psi_t)^2}\right] \quad ,$$

with $\psi_t = 0.8$ and $\delta\psi_t = 0.2$. At each point in space, the density fluctuations are assumed to have negligible parallel wavenumbers and a perpendicular-wavenumber spectrum

$$S(k') = \left\langle(\delta n)^2\right\rangle \frac{1}{\pi\zeta_0^2}\exp\left(-k'^2/\zeta_0^2\right)$$

that is Gaussian and isotropic in the two directions $\perp B_0$.

Our estimate of the turbulence level is taken from Liewer[4]:

$$\langle(\delta n)^2\rangle^{1/2} = 10 n_e(\psi_t) r_s / L_n \quad ,$$

where $r_s \equiv c_s/\Omega_i$ is the sound speed over the ion gyrofrequency and L_n is the density-gradient scale length. Values for these parameters are calculated using the assumed density and temperature profiles and the solution B_0 of the Grad-Shafranov equation: $\psi = \psi_t$ at $R \approx 2.73\,\mathrm{m}$, where $B_0 \approx 9\,\mathrm{T}$, $T_e(\psi_t) \approx 4\,\mathrm{keV}$, $r_s \approx 1\,\mathrm{mm}$, $L_n \approx 0.23\,\mathrm{m}$, $n_e(\psi_t) \approx 2.2\times10^{20}\,\mathrm{m}^{-3}$, $\langle(\delta n)^2\rangle^{1/2}/n_e(\psi_t) \approx 5\%$, and

$$\left[\langle(\delta n)^2\rangle(\psi_t)\right]^{1/2} = 0.1\times10^{20}\,\mathrm{m}^{-3} \quad .$$

We assume that the typical perpendicular wavenumber ζ_0 of the turbulence scales as $1/r_s$. The numerical coefficient in $\zeta_0 = 0.4/r_s$ is consistent with the results of Ref. [5]. Our estimate of this wavenumber for CIT is $\zeta_0 = 0.4\,\mathrm{mm}^{-1}$.

The scattering angles are predominantly small in CIT because the dimensionless parameter $\gamma = (2\omega/c\zeta_0)^2 \approx 1\times10^3$ is large. Then the distribution of scattering angles β is essentially Gaussian, $G(\beta) = \exp(-\frac{1}{4}\gamma\beta^2)$. The largeness of γ allows us to write a simple equation for the rate of increase, during propagation of a ray through the turbulence layer, of the probability of occurrence of a scattering event:

$$\frac{dp}{ds} = \sqrt{\pi}\,\frac{(4\pi e^2/m)^2}{2c^2\omega^2\zeta_0}\,\langle(\delta n)^2\rangle(x) \quad .$$

To make further analytic progress, we relate distance s along a ray to poloidal flux ψ by $\psi(s) \approx 1 - s|\nabla\psi|$, which is a good approximation for rays propagating nearly perpendicular to outer flux surfaces and close to the equatorial plane $Z = 0$. Performing the s-integration, we find $p = \int(dp/ds)\,ds$, the average number of scattering events for a ray during passage through the entire turbulent layer. The result is

$$p \approx 3.4\times10^{-30}\mathrm{m}^4\,\frac{\delta\psi_t\,\langle(\delta n)^2\rangle(\psi_t)}{|\nabla\psi|\,\zeta_0\,f^2} \quad , \tag{1}$$

where $\langle(\delta n)^2\rangle(\psi_t)$, $|\nabla\psi|$, and ζ_0 are in MKS units, and the microwave frequency f is in GHz.

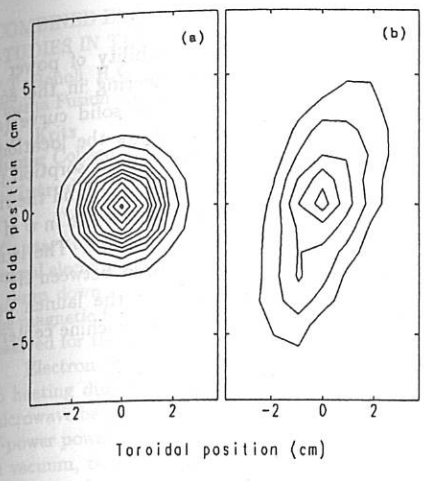

Fig. 1. Profiles of power density impinging on a surface $R = R_{res}$ near the magnetic axis for CIT plasmas (a) without turbulence and (b) with turbulence. Contour levels are multiples of 0.01 W/cm^2 for each Watt of incident power.

We evaluate Eq. (1) for CIT by using $|\nabla\psi| \approx 1.35\,\mathrm{m}^{-1}$, $f = 308$ GHz, and the parameters given previously. The result is $p \approx 1.3$, which indicates that most rays are scattered at least once. However, most of the scattering angles satisfy $\beta < c\zeta_0/\omega \approx 4°$. An angular deflection of 4° yields a 3.5 cm displacement along the 0.5 m ray path from the turbulence layer to the plasma center. For the turbulence parameters assumed here we thus find that, due to scattering, the beam broadens by only a few centimeters.

The beam broadening is illustrated in Fig. 1, in which we compare beam profiles with and without turbulence. The two cases each have an initially Gaussian beam represented by 500 rays, which are traced through the plasma to a cylindrical surface $R = R_{res}$, where the cyclotron resonance occurs. The profiles are computed from the locations of ray hits on this surface. The broadened beam in Fig. 1(b) is primarily wider in the direction perpendicular to magnetic field lines in the turbulence layer, where the field-line direction is noticeably different from the toroidal direction.

LOCALIZABILITY OF POWER DEPOSITION

For purposes of controlling sawteeth and disruptions, we wish to deposit electron-cyclotron power on a narrow range of flux surfaces near the $q = 1$ and $q = 2$ surfaces. Study of our ability to deposit power locally begins with the constraint of fixed $f = 308$ GHz, chosen to satisfy cyclotron resonance at the nominal 11 T field. We obtain underestimates of the width of the deposition layer by ignoring both scattering and the finite width and divergence of the beam. Cyclotron absorption is computed in the weakly relativistic approximation[6].

Injection of power along the tokamak equatorial plane ($Z = 0$) can result in power deposition away from the magnetic axis if a Doppler shift is produced by a mirror that steers the beam into a direction oblique to the magnetic field lines[7]. This method has limited ability to deposit power on outer surfaces (e.g., near $q = 2$) and leads to poor localization (see Fig. 2).

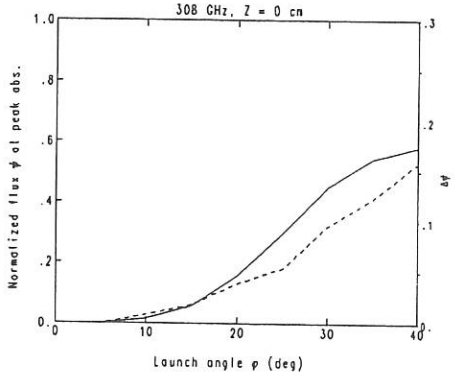

Fig. 2. Localizability of power deposition with steering in the equatorial plane. The solid curve (and the left axis) shows the location in ψ of the peak of the absorption profile. The dashed curve (and the right axis) shows the half-width in ψ of the profile at the $1/e$ point. The launch angle ϕ is measured between the ray and the line from the launch point $[(3, 0, 0)$ m] to the machine center.

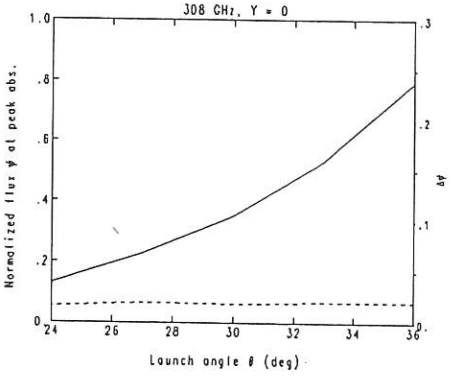

Fig. 3. Localizability of power deposition with steering in the poloidal plane. The launch angle θ is measured between the ray and a horizontal plane. Note that the range of angles θ in this figure is smaller than the range of ϕ in Fig. 2.

A more successful method involves using a mirror to steer the beam in the poloidal plane. For CIT we locate the mirror at $(X, Y, Z) = (3.5, 0, -0.3)$ m and aim the beam to intersect the resonance surface $R = R_{\rm res}$ at the desired value of ψ. As shown in Fig. 3, this method can access flux surfaces as far out as $q = 2$ and can deposit power very locally.

REFERENCES

[1] R. Pillsbury, private communication.
[2] E. Ott, B. Hui, and K. R. Chu, *Phys. Fluids* **23**, 1031 (1980).
[3] B. Hui, E. Ott, P. T. Bonoli, and P. N. Guzdar, *Nucl. Fusion* **21**, 339 (1981).
[4] P. C. Liewer, *Nucl. Fusion* **25**, 543 (1985).
[5] R. L. Watterson, R. E. Slusher, and C. M. Surko, *Phys. Fluids* **28**, 2857 (1985).
[6] I. P. Shkarofsky, *J. Plasma Phys.* **35**, 319 (1986).
[7] R. C. Myer, M. Porkolab, G. R. Smith, and A. H. Kritz, *Nucl. Fusion* **29**, 2155 (1989).

Mo 62

COMBINED ELECTRON CYCLOTRON RAY TRACING AND TRANSPORT CODE STUDIES IN THE COMPACT IGNITION TOKAMAK

P.T. Bonoli, R.C. Englade, M. Porkolab
Plasma Fusion Center, M.I.T., Cambridge, MA 02139 USA

A.H. Kritz
Hunter College, CUNY, NY USA

I. Introduction

The Compact Ignition Tokamak (CIT) operating scenario is envisaged to consist of a start-up phase in which the toroidal magnetic field (B_T), plasma current (I_p) and central electron density ($n_e(0)$) are simultaneously ramped, followed by a burn cycle and a ramp down cycle. It is important that densification and heating be carried out as the magnetic field is ramped since the available time for flat top magnetic field must be reserved for the burn phase.

Electron cyclotron radio-frequency (ECRF) power at fixed frequency is ideally suited to heating during the ramp up phase of CIT. The angle of injection of the incident microwave beam can be varied as the toroidal field is ramped, so as to maintain central rf-power power deposition [1,2]. Furthermore, since the EC wave is a propagating mode in vacuum, relatively high power densities ($\sim 100 MW/m^2$) can be easily coupled into a compact device. Finally, we note that recent advances in source technology (such as gyrotrons and FELs) make ECR heating at (280-310) GHz a viable option.

In order to realistically simulate this ramp up scenario, a combined code has been developed in which ECRF ray tracing and absorption, an MHD equilibrium calculation, and thermal and particle transport are treated self-consistently. Previous studies [1] of electron cyclotron resonance heating (ECRH) in CIT were carried out using model profiles of rf absorption based on stand-alone ray tracing and absorption calculations. In addition, these studies held the plasma current, toroidal magnetic field, and density constant in time. In the present work, a time variation in these plasma quantities is imposed and ECRF power deposition is re-calculated during rf injection so as to more realistically and self-consistently simulate ECH-assisted start-up in CIT.

The most recent CIT configuration calls for a toroidal field ramp to 11T. Thus, the present studies consider the use of an ECRF source frequency of 308 GHz, with EC waves launched in the ordinary mode (0-mode) of polarization ($\underline{E}_{rf} \parallel \underline{B}$). The critical density to which EC waves may propagate is given by $\omega_{pe}(n_{e,crit}) = \omega_{ce}$, or $n_{e,crit} \approx 1.1 \times 10^{21} m^{-3}$ (above the maximum density in CIT).

II. Toroiday Ray Tracing and Absorption

Electron cyclotron wave propagation and absorption in the CIT plasma are calculated using the toroidal ray tracing code TORCH [2], which evolved from the earlier TORAY code [3]. The ray tracing and absorption are based on the weakly relativistic formulation of Shkarofsky [4]. The ray equations are integrated in cartesian coordinates using values along a trajectory of the temperature, density, and magnetic field components, and the derivatives of these quantities that are obtained from a modification of the equilibrium package of the BALDUR 1 1/2 D simulation code [5]. This modification makes extensive use of a procedure originally developed to track a chord through the nested flux surface geometry of a toroidal device [6]. The ray tracing and absorption are recalculated during the period of ECRF injection, resulting in a self-consistent description of the rf heated plasma.

The TORCH code was constructed and is operated under the Basis system at the

National Magnetic Fusion Energy Computer Center in Livermore, CA. However, for convenience in linking this code to the BALDUR transport package, a Fortran preprocessor was used to transform TORCH statements from their Basis system form to Fortran 77 form. Numerous physical quantities associated with the wave propagation and absorption are displayed using a post-processor written for the TORAY code.

III. Transport Calculation

Spatial (ρ) profiles of electron and ion temperature, particle densities, and a representation of the poloidal magnetic field are advanced in time with a modified version of the BALDUR 1 1/2 D transport package. We assume that the electron heat flux can be written as $q_e = -M\kappa_e \nabla T_e - (M-1)\alpha_T \kappa_e T_e \nabla V/V(a)$ (conduction and inward heat pinch), with $\kappa_e = [CI(\rho)V^2(a)A(a)^{-3/2}/T_e(\rho)|\nabla V|^2][1+\gamma_o(1-P_{OH}/P_{TOT})^2 < \beta_\rho >]$. Here, ρ is a flux surface label, I_p is the current within ρ, $\rho = a$ designates the plasma boundary, and α_T describes a "canonical" profile shape $T_e \propto \exp(-\alpha_T V/V(a))$ which the transport model seeks to enforce. The constant C is chosen to fit a wide range of Ohmic experiments, and $\gamma_o \simeq 9.0$ has been found to reproduce L mode auxiliary heating results for the electron thermal energy when ion losses are suitably accounted for [7]. As a model for the anomalous ion heat flux, we take q_i to have the same form as q_e above with $\kappa_i = 2\gamma_o(1-P_{OH}/P_{TOT})^2 < \beta_p > /[1+\gamma_o(1-P_{OH}/P_{TOT})^2 < \beta_p >]\kappa_e$, so that in the limit of large auxiliary or fusion power, $\kappa_i \simeq 2\kappa_e$; neoclassical heat flux is also included. We have chosen $\alpha_T = 3.33$ and $M = 3$. The fluxes of deuterium and tritium ions, a light impurity, and thermalized fusion α particles are all described by $\Gamma_i = D\nabla n_i + \alpha_N D n_i \nabla V/(V(a)(1-V/V_a))$ where $D = \kappa_e/n_e$. Zero flux boundary conditions are arbitrarily imposed at the outer flux surface. The time evolution of the poloidal field distribution is governed by the neoclassical expression for plasma resistivity and the programming of the toroidal current. Local sources and sinks for the electron thermal energy are ohmic heating, fusion heating, ECRF absorption determined self-consistently by the ray tracing package, bremsstrahlung, syncrotron radiation, and collisional exchange with ions. The source for thermal α particles is determined by the fusion reactivity and classical slowing down, while the other ions have sources proportional to $(1-V/V_a)^{\alpha_N}$ with magnitudes chosen to yield a desired rate of density ramping.

Finally, a Kadomtsev reconnection model for sawtooth activity with an arbitrary repetition rate is employed and plasma quantities are redistributed within a mixing radius determined by conservation of helical flux.

IV. Results and Discussion

To illustrate the use of this model, we consider a CIT start-up scenario in which the central electron density is increased linearly from $6.6 \times 10^{19} m^{-3}$ to $9.0 \times 10^{20} m^{-3}$ in 7.5 sec, with a parabolic spatial profile and $Z_{eff} = 1.5$ maintained throughout; the total plasma current is ramped from 1 MA to 12 MA during the same time; and the vacuum toroidal field at the center of the vacuum vessel ($R_0 = 2.1$ m) is increased from 5 T to 11 T. The outer boundary of the plasma is held fixed with horizontal minor radius 0.645 m, elongation 1.8, and triangularity 0.4. Between 4.5 sec. and 7.5 sec., 35 MW of ECRF power (O-mode at 308 GHz) is injected into the plasma. The antenna spectrum is simply modelled by three rays launched at positions in the poloidal cross-section of (80°, 90°, 100°) with angles of injection of (100°, 95°, 85°), relative to the direction of the toroidal magnetic field. Note that the orientation of the incident microwaves in this example has not been dynamically programmed to yield central EC wave absorption throughout the field ramp.

Figures 1(a) and 1(b) show the resulting time evolution of the central densities and temperatures. Figure 1(c) gives the spatial profiles of the electron and ion temperatures in the meridian plane at t=8.1 sec., when the plasma is ignited with a total energy confinement time τ_e of 0.47 sec. Subsequently, the burn-up of deuterium and tritium, and the onset of sawteeth at t=8.7 sec., act to quench the discharge. We observe that 25 MW of injected power is not sufficient to ignite with the assumed transport and launch scenario.

The time evolution of the ECRF power deposition profile is shown in Fig. 1(d). We note the highly localized nature of the absorption and the shift toward the magnetic axis as the toroidal field is ramped. The projection of the ray paths in the poloidal plane at t=5.0 and 7.0 sec. is shown in Figs. 2(a) and 2(b) respectively. The dashed line indicates the location of the cyclotron resonance layer. Each cross mark along the ray paths indicates a 10% decrease in wave power due to cyclotron damping.

Acknowledgements

We acknowledge the contributions of Gary R. Smith to this model development and thank him for useful discussions.

Figure Captions

Fig. 1. CIT discharge evolution for $P_{RF} = 35$ MW. a) Central electron and ion density vs. time; b) Central electron and ion temperatue vs. time; c) Electron and ion temperature vs. horizontal minor radius at t = 8.1 sec.; d) ECRF power deposition in horizontal minor radius vs. time.

Fig. 2. ECRF ray trajectories with cyclotron resonance layer. Each cross represents 10% power absorption. a) t = 5.0 sec. ;b)t=7.0 sec.

References

[1] M. Porkolab, P.T. Bonoli, R. Englade, R. Myer, G.R. Smith, A.H. Kritz, 16th Eur. Conf. on Contr. Fusion and Plasma Physics (EPS, 1989), Venice, Italy, Vol. 13B, Part III, p. 1155.

[2] R.C. Myer, M. Porkolab, G.R. Smith, A.H. Kritz, Nucl. Fusion 29, (1989) 2155.

[3] A.H. Kritz, H. Hsuan, R.C. Goldfinger, D.B. Batchelor, in Heating in Toroidal Plasmas (Proc. 3rd Varenna-Grenoble Int. Symp., Grenoble, 1982), Vol. 2, CEC, Brussels (1982) 707.

[4] I.P. Shkarfosky, J. Plasma Physics. 35, (1986) 319.

[5] G. Batemann, Spring College on Plasma Physics, Trieste, Italy (1985).

[6] S. Attenburger, W. Houlberg, S. Hirshman, J. Comp. Phys. 72, (1987) 435.

[7] R.C. Englade, submitted to Nucl. Fusion; also MIT Laboratory Report PTP-89/5 (1989).

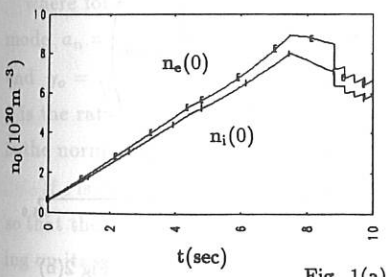

Fig. 1(a)

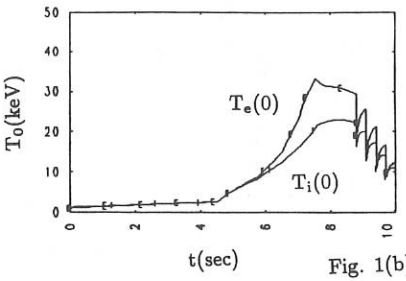

Fig. 1(b)

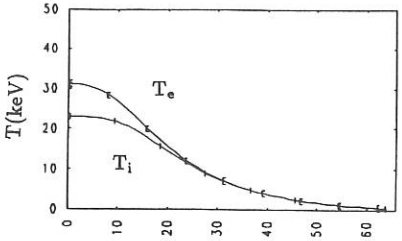

Fig. 1(c)

Fig 1(d)

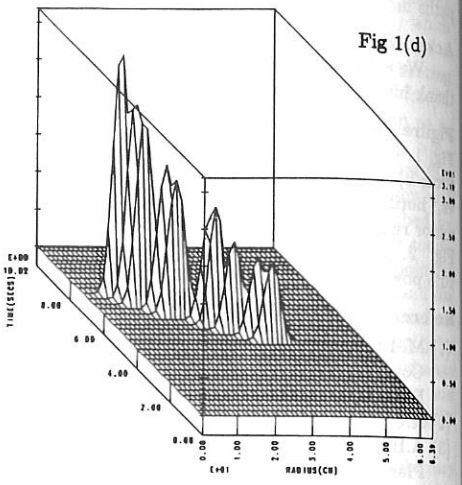

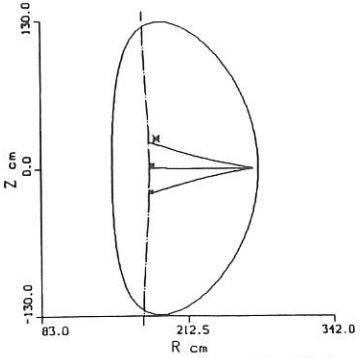

Fig. 2(a)

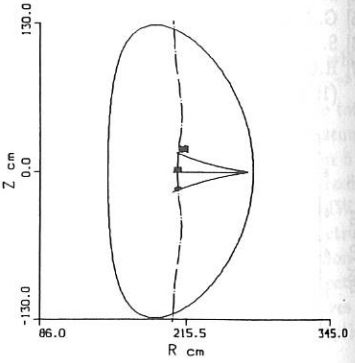

Fig 2(b)

STOCHASTIC ELECTRON ENERGY DIFFUSION IN ELECTRON CYCLOTRON HEATING

A.Mennella, R.Pozzoli, D.Ronzio

Dipartimento di Fisica – Università di Milano – MILANO – ITALY

In the last years there had been an increasing interest in the non-linear interaction between electromagnetic (e.m.) waves and charged particles. In particular it has been noticed that, under certain conditions, it is possible to accelerate these particles up to very high values of energy, due to the stochastic interaction with the wave. Existing analyses of the transition to the stochastic regime by means of e.m. waves refer to the oblique propagation[1,2,3] and cannot be simply extended to the perpendicular case. We consider here the latter physical situation.

For an electron moving in an uniform magnetic field $\vec{B}_0 = B_0\vec{e}_z$ and interacting with an e.m. wave propagating along the y axis, taking into account the two possible polarizations of the wave (*i.e.* **OM** and **XM**), the relativistic Hamiltonian can be written in canonical angle–action variables $\underline{\Theta} = (\Theta_1, \Theta_2)$, $\underline{I} = (I_1, I_2)$ as follows:

$$h = \gamma_0 - \nu I_2 + \sum_{n=-\infty}^{+\infty} a_n \cos \Psi_n \qquad (1)$$

where for the **OM** mode $a_n = -\epsilon \frac{P_\parallel}{\gamma_o} J_n(\lambda)$, $\Psi_n = \Theta_2 + n\Theta_1$ while for the **XM** mode $a_n = \epsilon \frac{\sqrt{2I_1}}{\gamma_o} b_n$, $b_n = \frac{1}{2}[(1+\rho)J_{n-1}(\lambda) - (1-\rho)J_{n+1}(\lambda)]$, $\Psi_n = \frac{\pi}{2} - \Theta_2 - n\Theta_1$ and $\gamma_o = \sqrt{1 + P_\parallel^2 + 2I_1}$, $\rho = E_{oy}/E_{ox}$, $\lambda = N\nu\sqrt{2I_1}$, N is the refractive index, ν is the ratio between the wave frequency and the electron cyclotron frequency and ϵ is the normalized amplitude of the vector potential.

If ϵ is sufficiently small, the resonance domains defined by $\dot{\Psi}_n = 0$ do not overlap, so that the particle's motion is trapped around a given resonance (say $n = \bar{n}$) depending on its initial conditions. It is therefore possible to neglect, in the series defined in

Eq. (1) , all the terms with $n \neq \bar{n}$, and reduce the number of degrees of freedom by means of a canonical transformation, obtaining:

$$\hat{h} = \gamma_0(I_{\bar{n}}) - \nu I_{\bar{n}} + a_{\bar{n}} \cos \Psi_{\bar{n}} \tag{2}$$

where $I_{\bar{n}}$ rapresents the action I_1 around the $\bar{n}$–th resonance.

To investigate the possibility of stochastic acceleration of the electrons when ϵ is increased, we study first the system around two adiacent resonances (*i.e.* setting $\bar{n} = 1, 2$ for **OM** mode and $\bar{n} = 2, 3$ for **XM** mode) by means of the level curves defined by the Hamiltonian (2) and determine the resonance locations and widths as functions of the parameter ϵ; finally we compare the two adiacent resonance layers in order to determine the occurrence of overlapping.

The level curves of $\hat{h}$ change their topology when ϵ is varied. In the **OM** case and near the first harmonic, a critical value of ϵ exists, ϵ_{OM} beyond which the separatrix is absent. When $\epsilon \leq \epsilon_{OM}$ three singular points exist, two elliptic and one hyperbolic, and we can define the width of the resonance as the width of the separatrix. When $\epsilon \geq \epsilon_{OM}$, we can consider the $\hat{h} = \gamma_{\|} \equiv \sqrt{1 + P_{\|}^2}$ curve as the separatrix. Near the second harmonic the separatrix always exist. Setting, for definiteness, $B_o \simeq 5T$ and $\omega_p/\Omega_c \simeq 0.3$, we observe that (*Fig.* 1) there is no overlapping of the two resonances if $\epsilon \leq 0.4$. This value represents the upper limit of ϵ, consistent with the first order approximation of $\hat{h}$. This implies that within this limit no significant stochastic acceleration for the electrons of the first harmonic can occur.

In the **XM** case, near the second harmonic a critical ϵ_{XM} exists, so that there is a separatrix only if $\epsilon \leq \epsilon_{XM}$, otherwise we use the $\hat{h} = \gamma_{\|}$ curve to determine the resonance width. Near the third harmonic the orbits are pendulum–like. *Fig.* 2 shows the occurrence of resonance overlapping for $\epsilon \geq \epsilon_c = 0.13$.

In order to study the dependence of ϵ_c on the external parameters (*i.e.* on $P_{\|}$ and ν) we write the overlapping condition as $I_3 - 2w_2 - 3w_3 = 0$, where I_3 represents the ordinate of the hyperbolic point relevant to the third harmonic and w_2, w_3 are the widths of the second and the third harmonic, respectively.

The dependence of the critical value ϵ_c on the parameters ν and $P_{\|}$is represented in *Fig.*3: notice that there is an absolute minimum for $P_{\|} \to 0$ and $\nu \sim 1.8$. The dependence of ϵ_c on these parameters is not very strong, and we may set the value 0.1 as the order of magnitude of the perturbation necessary for the transition to global stochasticity.

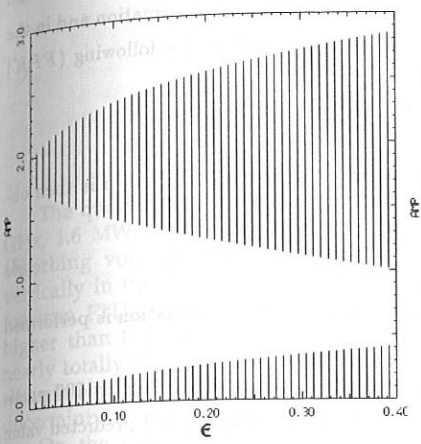

Fig. 1

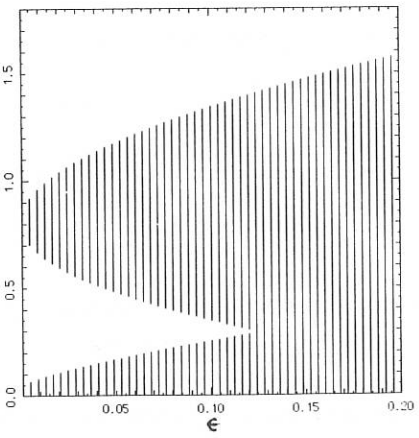

Fig. 2

Fig. 1 : Resonance width vs. amplitude field ϵ in the **OM1** case; Fig. 2 : the same for the **XM2** case; $\nu = 1.8$, $P_{\|} = 0.1$ have been used.

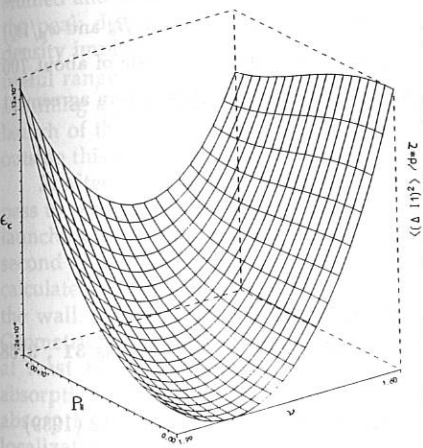

Fig. 3

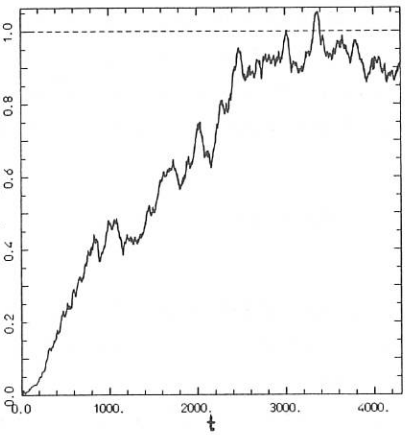

Fig. 4

Fig. 3 : Critical value ϵ_c as a function of $P_{\|}$ and ν.

Fig. 4 : Averaged diffusion coefficient $d(t)$ normalized respect to the value d_t predicted by Eq. (3); $d_t = 0.279$, $\epsilon = 0.13$, $P_{\|} = 0.1$, $\nu = 1.8$.

Finally, we investigate the stochastic diffusion in the **XM** case near the second harmonic. It is possible to show that using a random phase approximation and in the limit of very large times the distribution function f_o satisfies the following (FPK) diffusion equation[4]:

$$\frac{\partial f_o}{\partial t} = \frac{\partial}{\partial I}\left(D(I)\frac{\partial f_o}{\partial I}\right)$$

From the expansion of $D(I)$ the following averaged diffusion coefficient d is then obtained:

$$d = \frac{1}{\Delta I}\int dI\ D(I) = \frac{\pi\epsilon^2}{2\nu^2\Delta I}\sum_m m^2(m^2 - \nu\gamma_\parallel^2)b_m^2 \qquad (3)$$

where ΔI is the global variation of the action I_1 and the summation is performed only on the resonant harmonics.

In *Fig.* 4 the diffusion coefficient $d(t)$ evaluated numerically following 100 particles, is shown; we can recognize a plateau very close to the theoretical predicted value given by Eq. (3) .

The analysis of the transition to the stochastic regime for the case of an electron cyclotron wave in perpendicular propagation has been performed. We have found that the **XM** at the second harmonic is more efficient, with respect to this transition, than the **OM** at the first harmonic, and we have shown that (for the chosen B_o and ω_p/Ω_c) ϵ values around 0.1 are enough to allow the transition. At a time scale of about 700 gyroperiods the diffusion coefficient obtained by numerical simulation is in agreement with that evaluated by means of the FPK equation.

References:

1. E. VILLALON, W.J.BURKE , *Phys. Fluids* **30**, 3695 (1987)
2. C.R.MENYUK, A.T.DROBOT, K PAPADOPULOS , *Phys. Fluids* **31** , 3768 (1987)
3. K. HIZANIDIS,L. VLAHOS, C. POLYMILIS , *Phys. Fluids B* **3** , 682 (1989)
4. R.Z.SAGDEEV, D.A.USIKOV, G.M.ZASLAVSKY , *"Non linear physics from the pendulum to turbolence and chaos"* , Harwood Academic , 1988

CALCULATED POWER DEPOSITION PROFILES DURING ECRH ON THE FTU TOKAMAK

A.Airoldi, S.Cirant, S.Nowak
Istituto di Fisica del Plasma
EURATOM/ENEA/CNR Ass.- Milano - Italy

The quasi-optical antennae proposed for ECRH on FTU tokamak /1/ at 140 GHz, 1.6 MW, (Fig.1) has been designed /2/ to control the localization of the absorbing volume at fixed magnetic field by moving the microwave beams vertically in the poloidal cross section. The mean single-pass absorption in the foreseen FTU plasma, obtained with a toroidal ray-tracing code /3/, is much higher than the mean resistive loss at wall reflection. EC waves are therefore nearly totally absorbed /4/ in almost all the foreseen regimes. However, when a measurable fraction of the power is left into the beam after each single pass some uncertainty remains about the effective power deposition profile.

On the other hand, if an analysis of the temperature profile variations during ECRH is made aiming at the study of local transport coefficients (Jacchia A., this conference), it is essential to know accurately the spatial distribution of the heat source term. The demand for a very high (>95%) single pass absorption therefore limits the useful range of parameters under which transport can be studied and scaled. For central heating, the key-factor for localized absorption is the peak density. A too high density leads to severe refraction, while a low density implies low optical thickness and inadequate single pass absorption. The useful range of peak densities satisfying the requirement is $\approx 8\times10^{19}\div2\times10^{20}$ m^{-3}, assuming a parabolic temperature profile with a peak value of 1.5 keV. Outside launch of the O-mode is considered. Localized absorption could still be achieved outside this range with an efficient absorber put on the walls.

In alternative to damping the residual power left in the beam after the first pass to prevent the heating of distant magnetic surfaces, the wall opposite to the launching antennae can be treated for best reflection to take advantage of the second pass. To verify this possibility, the second pass absorption has been calculated by following each ray emerging from the plasma, after its reflection at the wall. The direction of propagation and the polarization are given by the Geometrical Optics reflection laws. Only the cases with single pass absorption of at least 80% have been considered, in order to obtain a localized overall absorption again over 95% after just two passes. A further requirement is that absorption occurs on the same magnetic surfaces, in order to maintain localization.

The lower limit of the useful range of plasma densities can be extended in this way from $\approx 8\times10^{19}$ m^{-3} down to $\approx 4\times10^{19}$ m^{-3}, still maintaining the very high overall absorption typical of the regimes at higher densities. In Fig.2 and 3 the ray tracing and the power deposition profiles at the first and second pass are shown

respectively. In Fig.4 the overall absorption vs. peak density is presented for a single and a double pass.

For off-axis heating the benefit from using second pass absorption is reduced because in general heating occurs on different magnetic surfaces (Fig.5,6). In this case the only way to get localized heating is the use of absorbing walls, at reduced overall absorption. In Fig.7 single pass absorption versus the peak density is shown for the two cases of heating the centre and a volume set at 50% of the minor radius respectively. The absorption at the different densities is calculated with different orientations of the launching antenna in order to compensate for the modified refraction.

The effective localization of the heated surfaces depends critically on the real density and temperature profiles, which have therefore to be measured accurately. Furthermore, the presence of non-thermal electrons is neglected in the calculations. It is therefore necessary to confirm with transmission measurements the correctness of the estimated power deposition profile.

To this purpose, a set of pick-up horns is put on the opposite wall to compare the predicted and the measured residual electromagnetic power density, which is determined both by absorption and by the effect of the inhomogeneous refractive index. In order to calculate the attenuation due to the lens effect, a comprehensive bundle of rays is traced up to the opposite wall assuming zero absorption. The absolute weight assigned to each ray on the basis of a gaussian distribution is then re-scaled by imposing a unitary surface integral over the phase-front outside the plasma. Attenuation due to absorption is then calculated as usual. In Fig.8 the residual power density at the wall is shown as a function of the poloidal angle for two different orientations of the antenna (close to central heating and slightly off-axis).

The predicted signal is finally obtained by taking into account, concurrently with the wave damping and refraction, also the polarization and the gain of the receiving antenna at the angle of incidence of the waves emerging from the plasma.

REFERENCES

/1/A.Airoldi et al., Proc. 14th European Conference on Contr. Fusion and Plasma Physics, Madrid 1987, v3, p976.

/2/Nowak S. et al., Proc. 7-th ECE and ECH Workshop, Hefei, China, 1989

/3/A.Airoldi et al., Lettere al Nuovo Cimento, 43, 340 (1985)

/4/A.Airoldi et al., Plasma Phys. Contr. Fusion, 30, 681 (1988)

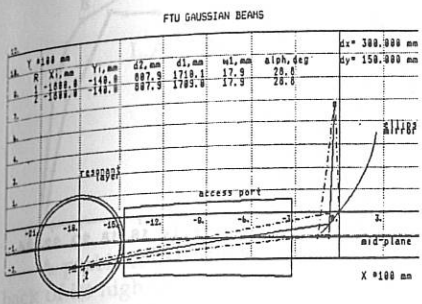

Fig.1 - Scheme of the quasi-optical system for ECRH at 140 GHz on FTU. The ellipsoidal mirrors are independently movable to scan vertically the four beams.

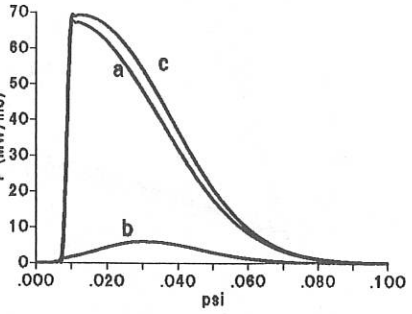

Fig.3 - Power deposition profile for the case of Fig.2.
a) first pass; b) second pass; c) total.
The total input power is 250 kW.

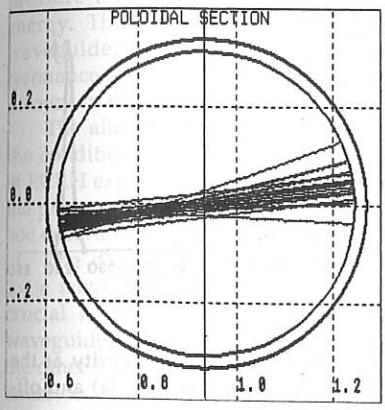

Fig.2 - Ray tracing at the first two passes for central heating.
$n_{e0}=5x10^{19}$ m^{-3}; $T_{e0}=1.5$ keV.
Single pass absorption is ≈80%.

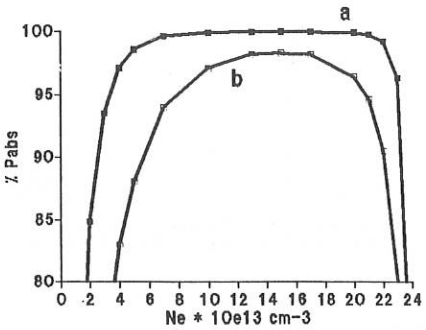

Fig.4 - Absorption as a function of the peak density for central heating.
a) double pass
b) single pass

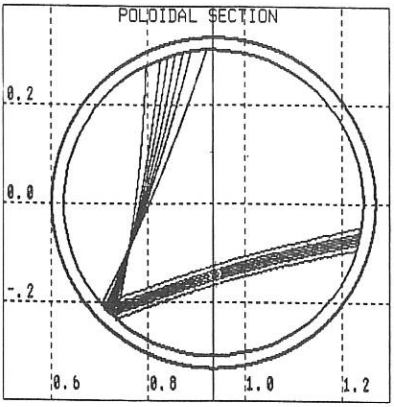

Fig.5 - Ray tracing at the first two passes for heating at 30% of the minor radius.
$n_{e0}=5x10^{19}$ m^{-3}; $T_{e0}=1.5$ keV.
Single pass absorption is ≈84%

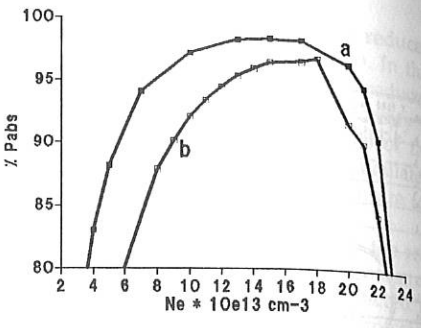

Fig.7 - Single pass absorption as a function of the peak density.
a) central heating
b) heating at 50% of the minor radius.

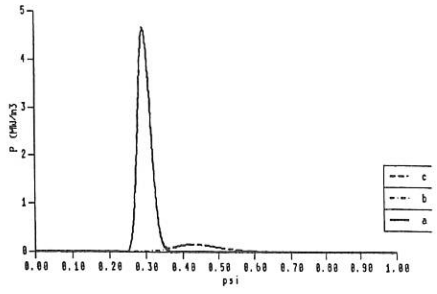

Fig.6 - Power deposition profile for the case of Fig.5.
a) first pass; b) second pass; c) total.
The total input power is 250 kW.

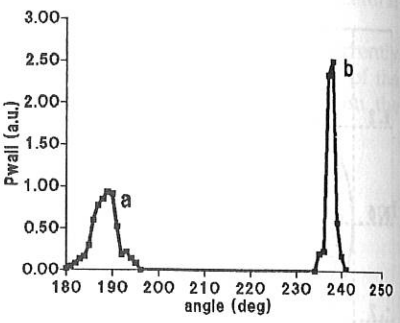

Fig.8 - Residual power density at the wall (a.u.) for near-central (a) and off-axis heating (b).

MICROWAVE BREAKDOWN OF THE NEUTRAL GAS AROUND THE EC RESONANCE IN HIGH POWER TRANSMISSION LINES FOR ECRH

L.Argenti, A.Bruschi, S.Cirant, G.Gorini, G.Granucci, F.Lucca, P.Mantica, M.Silari, A.Simonetto, G.Solari

Istituto di Fisica del Plasma
EURATOM/ENEA/CNR Ass.- Milano - Italy

A problem that may arise in high power ECRH, which represents the drawback of its high efficiency in electron heating, is the breakdown of the neutral gas filling the transmission line if the cold resonance is met outside the plasma. This typically occurs when plasma heating at down-shifted frequency or high-field-side launch ECRH is performed. Also the question can be posed if sufficiently high electric fields at the second harmonic could cause breakdown. In this case any ECRH scheme at the fundamental resonance should take into account this possibility in the design of the microwave system.

The assumptions made in existing theories /1,2/ based on diffusion processes to calculate the breakdown field are in general not satisfied in most of the cases of interest here. In fact, the mean free path for ionizing collisions at resonance is not much shorter than the waveguide size because of the low pressure ($\approx 10^{-3}$ Torr or lower) and the drop of the cross section at high electron energy. The accelerating electric field, usually an $HE_{1,1}$ mode in a circular waveguide, is strongly spatially non-uniform. Also the magnetic field at resonance can have large gradients. Relativistic effects are to be taken into account in calculating the power gain for the electrons.

The aim of this work is therefore to propose a model for the description of the conditions leading to avalanche for the specific experimental configurations of ECRH experiments. The model will be used in particular to analyse the case of the proposed experiment at 140 GHz on FTU. Its validity is being tested in an ad-hoc experiment at 28 GHz using THOR toroidal magnet /3/.

The electric breakdown can be an elusive phenomenon, in the sense that some factors difficult to predict completely can play an important role. In fact, crucial issues when microwaves are used are the wall conditioning of the waveguide system and a great care in eliminating mechanical imperfections. On the other hand, a model of the breakdown not including wall effects as secondary emission and local perturbations would still be helpful at least to point out circumstances prone to arcing. Furthermore, when Gaussian beams are to be used, as in the case of FTU, the ideal wall-free situation can be considered quite close to the real one.

Following the general assumption that breakdown is possible only if the ionization occurs before the electron loss, the approach attempted here compares the time it takes to the electron to cause charge build-up with the time it takes to

drift to the walls /4/. The avalanche time depends on the filling pressure while the loss time depends on the electric field and the geometry. As the loss time tends to decrease with increasing electromagnetic power density, then a pressure threshold for breakdown is to be expected.

The model is based on a statistical definition of local breakdown for electrons uniformly distributed over the waveguide cross-section. We start by considering N_0 identical electrons starting from rest at the same point in space. The ratio of the N_C ionizing collisions to N_0 is then a function F_i of the time given by:

$$F_i = \frac{N_c}{N_0} = 1 - \exp\left\{ - \int_0^l N_n \sigma(E) dl \right\}$$

where σ is the cross section for ionizing collisions /5/ and N_n the neutral density.The integral is taken over the electron trajectory, which is obtained by solving the exact relativistic equation of motion, as determined by the Lorentz's force. The accelerating force is the action of the electric field of the transmitted waveguide mode. The energy is then obtained for all times and points before the loss at the wall. The start from rest is assumed since the energy gained at resonance is soon much higher than any plausible initial energy for background electrons. Furthermore, excluding high energy particles statistically sporadic in the background, a non-zero initial velocity has the effect of shortening the time of permanence of the electron in the active volume, thereby reducing F_i.

We define then the value of F_i when the electron reaches the wall as the breakdown probability P_i for the i-th electron. The local breakdown condition is that the original population of N_0 electrons sitting at the point considered is at least maintained, which means that at least half of them has made an ionizing collision, or $P_i \geq 0.5$. The general breakdown condition is that local breakdown occurs at least at one point. In principle, P_i should be calculated for a comprehensive set of points for the full range of pressures and powers of interest in the chosen geometrical configuration. In practice, these extensive calculations (Fig.1) are performed only for a test electron, which is identified as the electron sitting in a position such that it first reaches $F_i=0.5$ for a few pressures. At any given power there is therefore a test electron at a specific position, which has been verified to be virtually independent on the pressure. The general breakdown condition at any power level and pressure is therefore that $P_i \geq 0.5$ for the test electron.

The calculations have been carried out for significant cases at 28 and 140 GHz, the latter being specifically aimed at foreseeing breakdown in the ECRH experiment on FTU. For all the configurations considered a minimum pressure is found below which breakdown does not occur, at any power level. For pressures above this limit a finite range of power is found for breakdown; while the lower limit is set by a too low power gain for reaching the breakdown condition, the upper one is encountered when the power gain is so high that the electron drifts away before reaching an appreciable probability for an ionizing collision, mainly because of the drop in the cross section at very high energies.

In order to test the predictions, experiments have been started at 28 GHz with a $TE_{0,1}$ mode in a circular w.g. with an inner diameter of 63.5 mm., at peak power up to ≈150 kW ($E_{peak} \approx 3.6 \times 10^5$ Vm^{-1}). The transmission line is terminated with a calorimetric matched load. In these preliminary experiments the waveguide axis has been set tangentially to the toroidal magnetic field. The waveguide is pumped through a transverse cut 1 mm wide set at resonance, compatible with conversion-free propagation of the $TE_{0,1}$ mode. For a short section between the pumping aperture and the load the continuous waveguide wall is replaced by a metallic mesh, which causes some mode conversion but negligible reflection. The hydrogen is injected inside the w.g. through this mesh by means of a piezo-electric valve, allowing the experimental measurement of the scaling of the breakdown voltage with pressure. The presence of breakdown has been detected by monitoring the light emitted through the pumping slit. Photomultipliers have been used to ensure sensitivity and fast response.

The experimental results, summarized in Fig. 4, are still affected by some uncertainty on the effective pressure because the incomplete wall conditioning can lead to gas release when the microwave power is applied. Nevertheless, breakdown is not observed when the starting pressure is below $\approx 2 \times 10^{-3}$ Torr at P_{rf} ≈100 kW. The predictions of the model for the same geometrical configuration (Fig.3) indicate a threshold an order of magnitude higher. This is partly due to a possible underestimate of the pressure and partly to the crudeness of the breakdown criterion. A more conservative condition for non breakdown should be $P_i << 0.5$. In fact the data are better reproduced both in the absolute value and in the trend of increasing the threshold as the power is decreased, if $P_i \leq 0.05$ is taken as the non breakdown condition.

The numerical analysis applied to the case of the X-mode injection by launching an HE_{11} mode at 140 GHz, 250 kW, in FTU gives a pressure threshold $\approx 10^{-3}$ Torr (Fig.2), while in the case of the O-mode launch no serious risk of breakdown is expected.

In conclusion, a model for breakdown in transmission lines to be used in high power ECRH experiments has been conceived. Its prediction of a lower pressure threshold is confirmed experimentally also quantitatively if a conservative definition of the breakdown condition is assumed. Pressures below the foreseen threshold can be achieved in real devices, ensuring therefore an arc-free operation of the system.

REFERENCES

/1/Brown S.C., Introduction to electrical discharges in gases, John Wiley & S., New York, 1966.

/2/Mc Donald A.D., Microwave breakdown in gases, John Wiley & S., New York, 1966.

/3/Argenti L. et al., Il Nuovo Cimento, **63 B**, 471 (1981)

/4/Anisimov A.I., Vinogradov N.I., Poloskin B.P., Sov. Phys. Tech. Phys, **20**, 626 (1975)

/5/Lotz W., Z. Phys., **216**, 241 (1968)

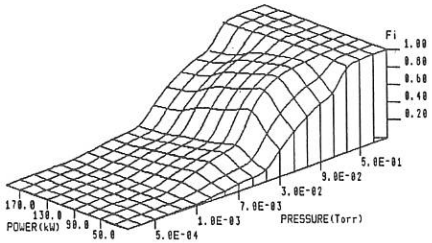

Fig.1 - Plot of the break-down probability P_i vs. P_{rf} and filling pressure.The $TE_{0,1}$ mode at 28 Ghz is propagated in a w.g with 63.5 mm i.d., with the axis tangential to the 1 Tesla toroidal magnetic field line.

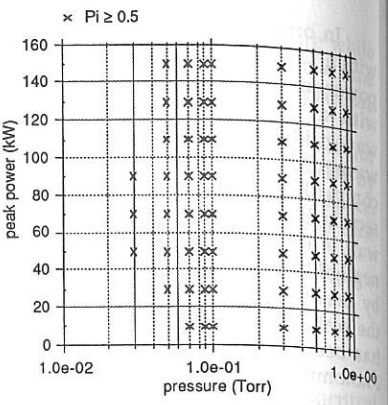

Fig.3 - The + mark indicates that the break-down condition $P_i>0.5$ is satisfied. The $TE_{0,1}$ mode at 28 Ghz is propagated in a w.g with 63.5 mm i.d., with the axis tangential to the 1 Tesla toroidal magnetic field line (R_0=43cm).

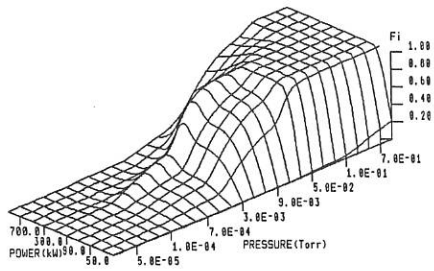

Fig.2 - Plot of the break-down probability P_i vs. P_{rf} and filling pressure.The $HE_{1,1}$ mode at 140 Ghz is propagated in a w.g with 35 mm i.d., with the axis perpendicular to magnetic field line. The field increases from 0 to 8 Tesla in 13 cm in the direction of the w.g. axis.

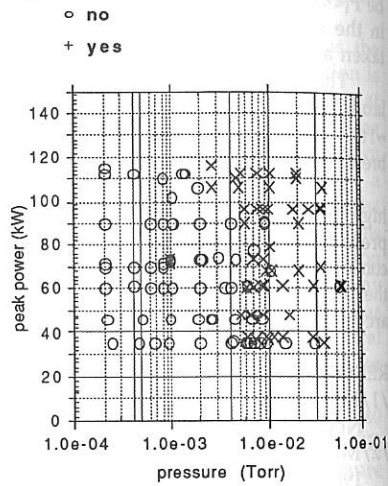

Fig.4 - Experimental occurrence (+) or absence (o) of break-down in the pressure/power domain.

Th 49

RAY TRACING STUDY OF THE SECOND ELECTRON CYCLOTRON HARMONIC WAVE ABSORPTION AND CURRENT DRIVE

S.Pešić and A.Stojić

Institute for Research in Physics,"Boris Kidrič" Institute,
P.O.B. 522, 11001 Belgrade, Yugoslavia

In the present paper the propagation and absorption of both, the extraordinary and ordinary mode near the second harmonic of the electron cyclotron frequency is investigated within the geometrical optics approximation. A fully three-dimensional ray tracing is carried out by integrating the Hamiltonian form of the geometrical optics equations in hot plasma. The ray tracing code is applied to a tokamak like plasma. The ray trajectories obtained from the hot plasma dispersion relation are compared to those calculated by solving the ray equations in the cold plasma approximation. Besides, the imaginary part of the wave vector evaluated within the weak damping limit is compared to the roots of the complete weakly-relativistic dispersion equation. The obtained power deposition profiles indicate that the central plasma region can be efficiently heated by launching waves with a moderate frequency down-shift. Furthermore, it is found that relatively large currents can be generated in preheated large-size plasmas.

HIGH POWER MODE-PURITY MEASUREMENTS ON THE 60 GHz TRANSMISSION LINE FOR ECRH ON RTP

A.G.A. Verhoeven, W.A. Bongers, R. Bosman
R.D. Damstra, O.G. Kruyt, J. Stakenborg

Association EURATOM-FOM
FOM Instituut voor Plasmafysica Rijnhuizen
3430 BE Nieuwegein, the Netherlands

1. Introduction

Mode purity measurements have been performed at both low and high power (200 kW) on several parts of the ECRH transmission line. This transmission line connects the first 60 GHz gyrotron to the RTP tokamak [1]. Measurements of the mode purity of two gyrotrons showed a high percentage of TE_{01}. This could be reconverted into TE_{02} by a phase matched TE_{01}-to-TE_{02} converter section.

The maximum rate-of-rise of the RF-power has been measured. Square wave modulations up to 100 kHz can be made and single pulses of 1 μs have been produced.

At this moment ECRH power is routinely applied to the RTP-plasma [2].

2. Transmission line setup

Two transmission lines are fed by a Varian 60 GHz (200 kW, 100 ms) gyrotron [3]. The output mode is mainly TE_{02} (fig. 1.). After the first bend the mode is converted into TE_{01} and filtered to reach a high mode purity. After the second bend the TE_{01} mode is converted into the linearly polarised TE_{11} mode and the waveguide tapered up to 63.5 mm diameter which is the diameter of the vacuum window.

The second transmission line ends in an adjustable elliptical polarized HE_{11} mode. Therefore an elliptical polarizer [4] and a TE_{11}-to-HE_{11} converter are added to the line. The last part of this line will be made of corrugated wall circular waveguide. The diameter of the vacuum window and the launcher will be 27.8 mm. An extension of the ECRH system with a 100 GHz line is under development.

3. Results of high power measurements.

The mode content of the transmission line was measured at four different places, named **A** through **D** as shown in fig. 1. Table 1 shows the results of the mode purity measurements. The mode content of the gyrotrons SN11 and SN12 contains 22.2 % and 11.6 % of TE_{01} respectively and a smaller amount of non circular modes (**A**). The mode content remains the same over a wide range of optimized gyrotron operating parameters. The first bend is designed for TE_{02}, therefore the fraction of TE_{01} that is produced by the gyrotron is reconverted before the bend into the TE_{02} mode by means of one section of the TE_{02}-to-TE_{01} converter [5]. By means of phase matching of this section, the TE_{02} fraction is minimized after the the TE_{02}-to-TE_{01} converter (**C***), and the total amount of undesired modes could be reduced from 9.8 % to 6.2 %.

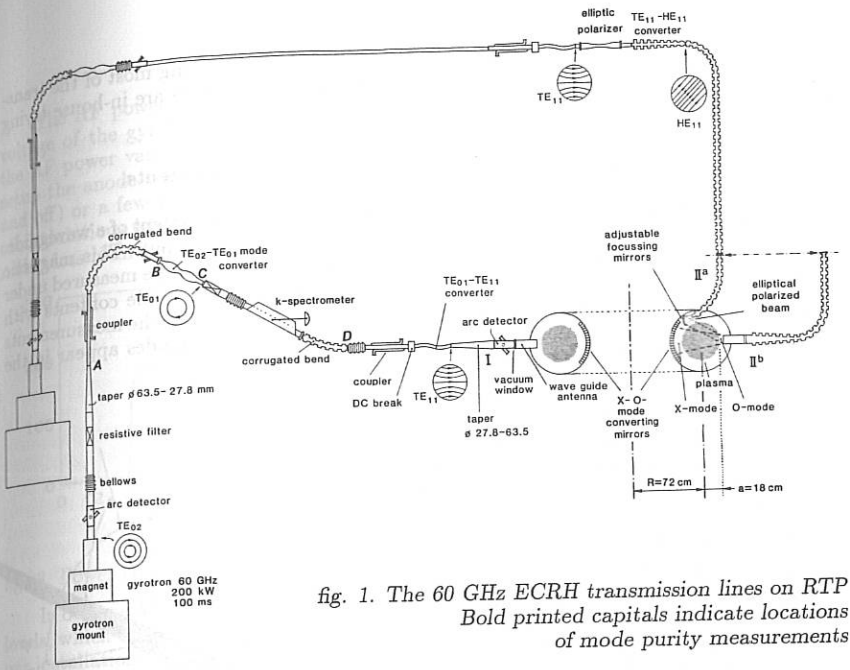

fig. 1. The 60 GHz ECRH transmission lines on RTP Bold printed capitals indicate locations of mode purity measurements

After the 30° bend (designed for TE_{01}) the mode content did not change much (**D**). The amount of non-circular modes could be depressed by adding a filter in the transmission line between the two bends (**D***).

Reflected-power measurements were performed at position **D** during pulses at the RTP vessel without plasma. The figures in Table 1 (**reflected**) are given as the percentage of the total forward power. The total level of 16.5 % of reflected power is reduced to approximately 1 % with plasma.

LOCATION	*GYROTRON*	*MODE CONTENT (%)*				
		TE_{01}	TE_{02}	TE_{12}	TE_{13}	other modes
A	*SN11*	22.2	**76.1**	0.7	0.7	0.3
B	*SN11*	7.7	**76.2**	10.0	1.6	4.5
C	*SN11*	**90.2**	3.0	3.7	1.5	1.6
C*	*SN11*	**93.8**	0.3	3.0	1.2	1.7
A	*SN12*	11.6	**80.0**	3.7	3.0	1.7
C*	*SN12*	**84.1**	0.0	6.8	2.8	6.3
D	*SN12*	**87.7**	0.0	4.5	3.7	4.1
D*	*SN12*	**93.9**	1.7	1.0	1.0	2.4
reflected	*SN12*	11.5	4.7	0.1	0.0	0.2

Table 1 Results of modepurity measurements. Desired modes are printed bold.

Gyrotron SN11 appeared to have a vacuum leakage after testing most of the transmission line. The gyrotron was replaced by gyrotron SN12 and we are in-house trying to repair the leaking gyrotron, up to now succesful.

4. Interpretation of k-spectrometer measurements.

The k-spectrometer makes it possible to determine the mode content of a waveguide. A small fraction of the magnetic field in the waveguide is coupled out. This magnetic field induces an electromagnetic wave which, due to interference, can be measured under a certain angle (ϑ) with the axis of the waveguide (fig. 2.). For mode contents with only a few modes it is easy to make an interpretation of the results of the measurements and to calculate the mode content of the waveguide [6]. If more modes appear in the spectrum the interpretation becomes more difficult.

The angle ϑ of two modes differs sometimes less than one degree which is about the resolution of the measurement. So it is very difficult to determine which mode is being measured only by looking at the angle ϑ. Furthermore sometimes two modes appear at exactly the same angle ϑ.

The magnetic field of a TE_{mn} mode at the waveguide surface has an H_z and H_φ component which vary with $\sin m\varphi$. This means that if the k-spectrometer is rotated along its axis over 360^o, $2m$ maxima and $2m$ minima will be found. By measuring at different angles φ (fig. 2.) the mode being measured can be determined by the angle ϑ and the difference in angle φ between two maxima. (This has to be done anyhow, because the peak value determines the amplitude of the mode).

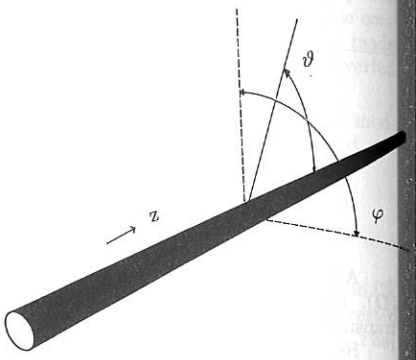

fig. 2. The k-spectrometer orientation.

In case two modes are measured at nearly the same angle ϑ it is in general very difficult to separate the contributions of the two modes, unless one of them is circular (TE_{0n}). Fortunately, circular modes dominate the largest part of the transmission line.

As already mentioned the magnetic field components H_z and H_φ of TE_{mn} vary with $\sin m\varphi$. Together with the constant magnetic field component of circular modes this results in m maxima and m minima over 360^o, because now at a certain φ the two components of the two modes are in phase, while at an angle of $\varphi + 360^o/2m$ the two components are in counter phase.

At the maximum the total magnetic field component H_{max} will be $H_{max} = H_c + H_{nc}$ where H_c is the component of the circular mode and H_{nc} the component of the non circular mode. The minimum will be: $H_{min} = H_c - H_{nc}$.

From this maximum and minimum the components of the two modes can be calculated: $H_c = \frac{1}{2}(H_{max} + H_{min})$ and $H_{nc} = \frac{1}{2}(H_{max} - H_{min})$. Expressed in powers this will be: $P_c = \frac{1}{4}(\sqrt{P_{max}} + \sqrt{P_{min}})^2$ and $P_{nc} = \frac{1}{4}(\sqrt{P_{max}} - \sqrt{P_{min}})^2$.

5. RF power modulation.

The RF power output of the gyrotron can be varied by modulation of the anode voltage of the gyrotron [7]. The RF power is a steep function of the anode voltage: the RF power varies as much as 10 kW/V due to changing the anode voltage. In our setup the anode voltage can be changed 100 % (20 kV, for switching the gyrotron on and off) or a few 100 volts (for modulation during a pulse). Fig. 3. shows the result of modulations with a frequency of 100 kHz. Fig. 4. shows the smallest pulse we could make: less than 1 μs.

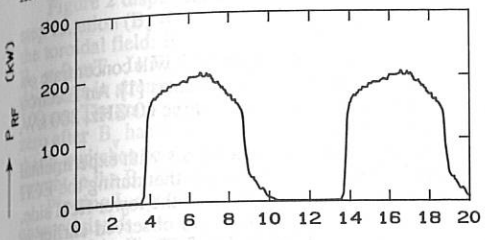

fig. 3. Power at 100 kHz modulation

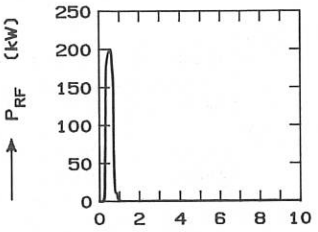

fig. 4. Small single pulse

In our anode modulator the voltage can only be switched between two preset voltage levels, which correspond to two RF-power levels. This means that it is not possible with our installation to vary the RF power continuously and therefore to ramp up slowly the RF power from the gyrotron.

However, to enable slow ramp up and down of the RF power, we have build a pulse-length modulation unit. This unit allows to switch the RF power on and off with pulses so short that the plasma responds to the time-integral of the applied RF power.

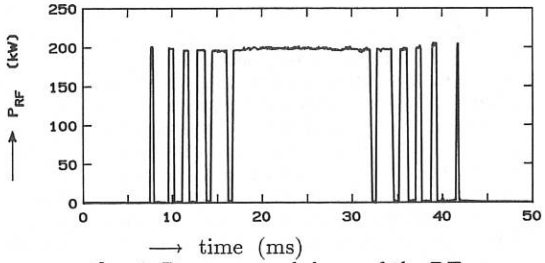

fig. 5. Ramp up and down of the RF power.

Acknowledgement: This work was performed under the Euratom-FOM association with financial support from NWO and Euratom.

References

[1] O.G. Kruyt, *et al.* Proc. 15^{th} Soft, Utrecht (1988) pp. 277-280.
[2] The RTP-team, this conference.
[3] R.W. Polman, *et al.* Proc. 16^{th} Fusion, Venice (1989) pp. 1139-1142.
[4] P. Manintveld and A.G.A. Verhoeven, Proc. 15^{th} Soft, Utrecht (1988) pp. 438-442.
[5] M Thumm, Int. J. Electronics. **61** (1988) p. 1135.
[6] W. Kasparek and G.A. Müller, Int. J. Electronics. **61** (1988) pp. 5-20.
[7] P. Manintveld and A.G.A. Verhoeven, Proc. 7^{th} APS Top. Conf. on Appl. of RF Power to Plasmas, Kissimmee (1987) pp. 25-28.

ECRH SUSTAINED BREAKDOWN PLASMAS IN RTP

R.W. Polman, R. van Andel, R. Bosman, R. Damstra, D.F. da Cruz Jr, B. de Groot, C.A.J. Hugenholtz, J.J. Koning, W. Kooijman, O.G. Kruyt, J. Lok, B.Ph. van Milligen, A.A.M. Oomens, F.C. Schüller, F.M.A. Smits, P.H.M. Smeets, J. Stakenborg, A.J.H. Tielemans, C.J. Tito, A.G.A. Verhoeven, E. Westerhof.

FOM-Instituut voor Plasmafysica Rijnhuizen, Association EURATOM-FOM, P.O. Box 1207, 3430 BE Nieuwegein, The Netherlands.

Introduction

The future research programme of the Rijnhuizen Tokamak Project RTP will concentrate on the study of transport mechanisms in strongly auxiliary heated tokamak plasmas [1]. An Electron Cyclotron Resonance Heating (ECRH) system which can comprise up to three 60 GHz, 200 kW, 100 ms gyrotrons [2] will supply the additional heating power.

ECRH is also attractive for starting-up tokamak plasmas. This paper deals with experimental results on plasmas produced and sustained by sole ECRH power. It appears that during the ECH pulse, with the RF power launched perpendicular to the magnetic field from the lower field side, a weak plasma current (I_p < 2 kA) flows in RTP. Suchlike currents were observed earlier in various devices, and for diverse experimental conditions [3,4,5,6,7]. For RTP, the dependency of the observed current on various experimental parameters will be described for 60 GHz irradiation. The ECH power ranges up to 200 kW, and the pulse lengths are up to 100 ms. The studies should yield the best scenario for low-voltage tokamak start-up.

Experimental set-up

The experiments have been carried out on the Rijnhuizen tokamak device RTP, which was put into operation in 1989. The stainless steel vacuum chamber has a major radius of 0.72 m, and a minor radius of 0.24 m. The minor radius of the plasma is 0.178 m.

The RF power is generated by one 60 GHz, 200 kW, 100 ms gyrotron and is fed to the plasma via an oversized waveguide containing various mode convertors, and a launcher mounted in the midplane at the lower field side of the torus. The power is irradiated perpendicular to the magnetic field in the nearly linearly polarized TE_{11}-mode and has been launched into the torus in O- and X-mode wave polarization. The fraction of the incident power not absorbed in single pass is reflected at the higher field side of the torus by a flat mirror under 8^0 with the toroidal direction. The toroidal magnetic field, B_T, can be varied in 9 steps and ranges up to B_T = 2.5 T. Usually $B_T(R_0)$ is 2.2 T, which corresponds to 1st harmonic 60 GHz resonance near the centre.

The experimental procedure has been simple. The torus is continuously pumped. In advance of the pulse, hydrogen gas is supplied at the proper rate to get the desired pressure, p_{fill}. After that the toroidal field B_T is applied. Then, by injecting the 60 GHz microwave power, a plasma is produced. Before or during the ECH pulse a vertical (B_v) and a radial magnetic field (B_h) can be superposed on B_T. It is possible to choose B_v and B_h stationary as well as time dependent.

No primary voltage is applied to induce the toroidal electric field which normally drives the plasma current. Nevertheless a weak plasma current, I_p, flows (I_p < 2 kA), which is initiated and sustained by the RF power. The primary transformer coil circuit is not open, but currents are either small or inhibited by a diode. The liner has no break, therefore I_p induces a current in the liner of a few hundreds of amperes in opposite direction. The observed dependence of I_p on various experimental parameters will be discussed. The results shown in the figures apply to O-mode launch. The positive directions of the fields are the directions that are used during normal tokamak pulses.

Results

1a. I_p as a function of stationary B_v and B_h:

Figure 1 shows the time dependence of the ECRH generated current I_p in case the RF pulse is on from 0 to 50 ms, and from 75 to 100 ms. The experimental conditions are $P_{ECH} \approx 200$ kW

(at the gyrotron), p_{fill} = 0.2 mtorr, B_T = 2.2 T, and B_h = 0 mT. The various curves apply to different strengths of B_v, which in this case is kept constant to avoid induction of I_p by transformer action. Note the relatively fast increase of I_p during some 15 ms, followed by a more gradual increase and saturation. When the ECRH power is switched off, I_p quickly declines to zero. After switching on the power again, I_p climbs fast to the value it would have had without interruption of the ECH pulse. At higher filling pressures the time dependence is different, as will be discussed later (Figs. 5, 6).The magnitude of I_p depends on B_v and is maximum around B_v = – 1.3 mT. The influence of B_h on I_p is usually minor, except at certain extreme values of B_v.

1b. I_p as a function of non-stationary B_v.

Figure 2 displays how I_p reacts if B_v is switched on in the course of the ECRH pulse as a step function (B_v = – 1.35 mT from t = 25 ms on). The curves apply to three different values of the toroidal field: B_T = 1.85 T, 2.07 T, and 2.25 T; the filling pressure was p_{fill} = 0.5 mtorr and B_h = 0 mT. In Fig. 3 the evolution of I_p is shown in case the vertical field increases and decreases in strength inside the ECH pulse. Here, the ECH pulse is continuously on during 100 ms. The start of the time varying field is at t = 25 ms. Curve 1 of Fig. 3 shows that I_p falls to zero after B_v has reached a value around – 2.2 mT (in keeping with the dc-results of Fig. 1), and that I_p switches on again when $|B_v|$ has decreased to a proper value. By using a three times higher current in the B_v coils, the current I_p could be pushed to reverse its direction: curve 2.

Plotting I_p against B_v yields the dynamic I_p- B_v characteristic for the considered pulse. Such characteristics are shown in Fig.4, where the two traces at negative B_v apply to the cases illustrated in Fig.3. Figure 4 is supplemented with the results for a comparable pulse with a positive swing of B_v. The static values of Fig.1, marked (Δ), indicate good agreement.

2. I_p as a function of filling pressure.

Neutral gas breakdown and plasma build-up has been obtained at filling pressures from 0.1 up to 5 mtorr. The rise rate of I_p is a clear function of the filling pressure, as illustrated in Fig. 5. Also the electron density build-up is dependent on the filling pressure. In general the reproducibility of successive shots is very good. There is some memory effect when higher filling pressures are used prior to shots with a lower p_{fill}, and there is some slight day-to-day variation, probably due to variations in wall condition.

3. The evolution of the plasma density.

The evolution of the plasma density is different from that of I_p. The value of $\int n_e dl$, measured along the central chord, does not grow from zero to a saturation level, like I_p. Instead, it increases rapidly, reaches a maximum corresponding to an ionization level of several tens per cent of the prefill gas in about 2 ms, and then decreases to some low stationary value by a quick particle loss (Fig. 6). When after 50 ms the ECH power is switched off and I_p falls to zero (see Fig. 1), $\int n_e dl$ also reduces to zero, but at a slower rate. When at 75 ms the RF power is switched on again, $\int n_e dl$ increases to approximately its previous value at a slower rate than I_p does. For the diverse experimental conditions, such as with the 60 GHz resonance location in- or outwardly displaced over about half a plasma radius (the case of Fig. 2), or with the current pushed in reverse direction (Fig. 3) the time trace of the central line density can be a shade different.

Figures 5 and 6 now explain the fast recovery of I_p at a second ECH pulse as in Fig. 1. The fast particle loss in the beginning of the first ECH pulse means that a good part of the filling gas is knocked into the wall, leaving a lower p_{fill}. At the time of the second pulse the pressure is still low (Fig. 6) since the used gas feed rate is not able to raise it substantially. Thus the second ECH pulse ionizes at a lower prefill than the first, and therefore I_p has a fast rise rate.

A typical relation between the induced current and the density is shown in Fig. 7, where I_p is plotted against $\int n_e dl$. The figure shows that I_p increases when $\int n_e dl$ decreases. The data are taken from a pulse with p_{fill} = 1 mtorr and B_T = 2.2 T. The plasma formation phase has not been omitted. At start-up the behaviour is different, and, in fact, confusing. As is shown in Figs. 1 - 7, the direction of I_p is positive for the chosen experimental parameters. However, in many cases I_p is negative during the $\int n_e dl$ spike in the first few milliseconds, while at the second ECH pulse I_p remains positive, or even shows a sharp positive spike. This is not yet understood.

4. I_p as a function of power.

The time evolution of I_p also depends on the gyrotron power. In Fig. 8 a few time traces of I_p are given for different values of P_{ECH} (B_v = – 1.1 mT, B_h = 0.3 mT, p_{fill} = 0.2 mtorr,

B_T = 2.2 T). Like in Fig. 5 the growth rate of I_p is approximately proportional to the available power per particle.

5. *I_p as a function of B_T.*

Breakdown using O-mode launch could only be obtained for toroidal fields having the 2.14 T surface (i.e. the field strength for 60 GHz fundamental resonance) located inside the vacuum vessel, as in Fig. 2.

Using fundamental X-mode launch resulted in a fast electron density build-up (100% ionization for p_{fill} = 0.2 mtorr) followed by a switch-off of the gyrotron at 1.5 ms, due to reflected power. Instead breakdown was obtained at 1.07 T, the value for 2nd harmonic resonance.

With the direction of B_T reversed, I_p proved to change sign as well. The time behaviour appeared to be different.

Conclusions

1. In general the value of B_h has little effect whilst B_v strongly influences the level of I_p. Dynamically measured $I_p(B_v)$ curves coincide well with static values.
2. The interpretation of the relation between I_p and B_v is complicated by the presence of hidden stray-field components. Further analysis is necessary.
3. The rise rate of I_p scales roughly proportional to P_{ECH} / p_{fill}.
4. Dynamically one finds I_p (:) $(\int n_e dl)^{-1}$, indicating that higher collision rates damp the anisotropy in the particle losses, thought to be responsible for the generated current.
5. Extrapolation of the results to much larger devices will be complicated by details of currents flowing in external circuitry and vessel, and of the stray-field distribution.

Acknowledgement

This work was performed under the Euratom-FOM association agreement with financial support from NWO and Euratom.

References

[1] R.W. Polman et al., Proc. 16th Eur. Conf. on Controlled Fusion and Plasma Phys., Venice (1989) Vol.III, 1139.
[2] A.G.A. Verhoeven et al., this conference.
[3] S. Kubo et al., Phys. Rev. Lett. 50, 1994 (1983).
[4] R. Wilhelm et al., Plasma Phys. and Contr. Fusion 26, 1A, 259 (1984).
R. Wilhelm et al., Plasma Phys. and Contr. Fusion 26, 12A, 1433 (1984).
[5] B. Lloyd and T. Edlington, Plasma Phys. and Contr. Fusion 28, 909 (1986).
[6] S. Park and R.J. Taylor, Appl. of Radio-Frequency Power to Plasmas: Eight Topical Conference, Irvine, CA 1989 (American Institute of Physics, New York, 1989), p. 64.
[7] V. Erckmann et al., Fusion Technol., 17, 76 (1990).

Figure Captions

Fig. 1 *Time evolution of ECRH generated currents.The curves apply to stationary B_v fields of -80 A, -100 A, -30 A, 0 A, and +90 A (from top to bottom).180 kW ECH is on from 0 to 50 ms and from 75 to 100 ms; p_{fill} = 0.2 mtorr.*

Fig. 2 *a) Time trace of ECRH generated current in case a step-function B_v field is started inside the ECRH pulse (start at 25 ms). The traces correspond to different strengths of B_T , p_{fill} = 0.5 mtorr.*

Fig. 3 *Time traces of ECRH generated current in case a time-varying B_v field is applied, p_{fill} = 0.5 mtorr.*

Fig. 4 *Dynamic I_p - B_v curve for the cases of Fig. 3.*

Fig. 5 *Time traces of I_p for various filling pressures, P_{ECH} = 200 kW, B_v = 0, B_h = 0.3mT.*

Fig. 6 *$\int n_e dl$ for the same pulse as in Fig. 2, B_T = 2.2 T.*

Fig. 7 *I_p plotted against $\int n_e dl$ for p_{fill} = 1 mtorr.*

Fig. 8 *Time traces of I_p with the gyrotron power as parameter, p_{fill} = 0.2 mTorr, B_v = 0 mT, B_h = 0.3 mT.*

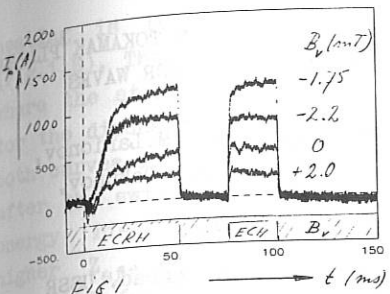

FIG 1

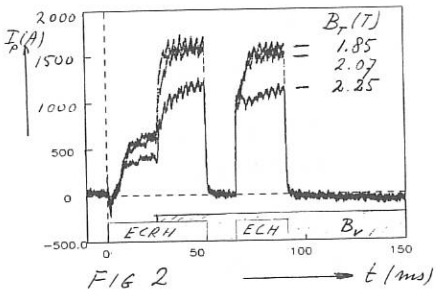

FIG 2

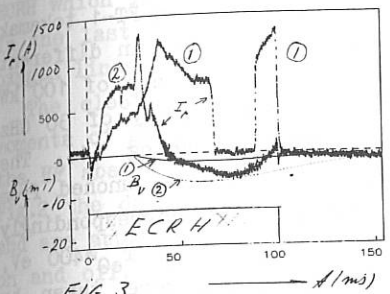

FIG 3

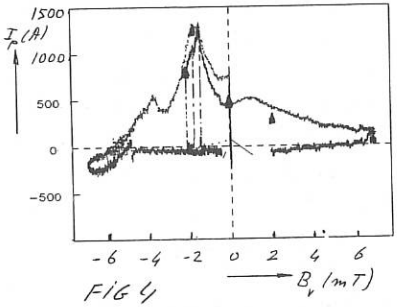

FIG 4

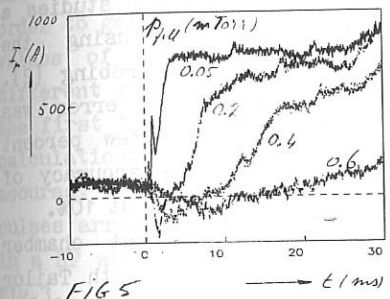

FIG 5

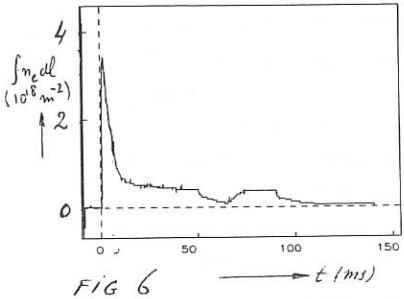

FIG 6

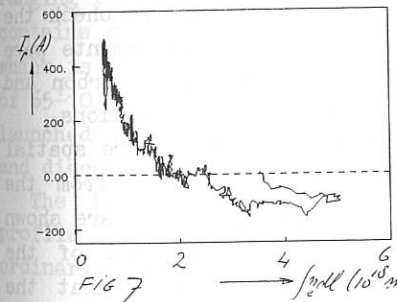

FIG 7

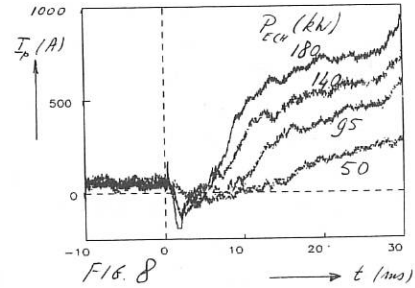

FIG 8

THE ELECTRON TEMPERATURE BEHAVIOUR STUDY IN FT-1 TOKAMAK PLASMA HEATED BY THE ORDINARY AND EXTRAORDINARY ECR WAVES

T.Yu.Akatova, D.G.Bulyginsky, M.Yu.Kantor, M.M.Larionov, S.I.Lashkul, L.S.Levin, G.T.Razdobarin, A.I.Tokunov, N.V.Shustova

A.F.Ioffe Physico-Technical Institute, Leningrad, USSR

The study of electron temperature behaviour in FT-1 tokamak (R=62 cm, a_l=15 cm) during ECRH was carried out in different discharge conditions. Two gyrotron generators each of 100 kW output with ≅0.6 ms pulse length at the frequency of 30 GHz were used in different modes of wave launching [1]. The ordinary and the extraordinary waves have been launched from the stronger and lower magnetic field sides correspondingly into the tokamak OH plasma (I_p=30 kA, B_T=1.1 T, T_{e0}≅400 eV, $n_{e0}=10^{13}$ cm^{-3}). The data on plasma heating were taken by Thomson scattering. For more detailed HF heating studies a proper diagnostic technology was developed using the multipulsed ruby laser and the multibeam plasma probing [2]. The electron temperature measurement statistical error was reduced due to novel developments to detect a few percent temperature time variations in main plasma. The accuracy of temperature measurements in plasma periphery was about 10%.

The experimental data were taken at different chamber cleaning conditions. The Z_{eff} value was about 2.5 with Tailor discharge cleaning and the chamber wall baking, whereas it was not lower than 4 with Tailor discharge being off. To check the ion plasma composition the VUV spectroscopic measurements were peformed which indicate the increase of the low-Z carbon and oxygen impurity concentrations in poor cleaning conditions.

The temporal variations of the electron temperature spatial profile during ECRH with the wave being launched from the stronger field side for different cleaning conditions are shown in Fig.1. The resonance layer position was shifted of the discharge axis by no more than 3 cm. It is seen that the

heating is less pronounced for the higher Z_{eff} discharge (Fig.1,B). This can be stated as well from the data in Fig.2 where the stored electron energy temporal dependence is shown for the discharge conditions pointed above. As it follows from both curves in Fig.2 a substantial plasma heating occures just after the switching on of the gyrotron. Afterwards the stored energy rise is slowling down which is more obvious for the higher Z_{eff} discharges (Fig.2,B). This slowing down is accounted for the deterioration of energy confinment during ECRH which is happened to be the stronger the higher is Z_{eff}. In the last case the plasma background in ionized carbon and oxygen lines is influenced by ECRH.

The electron energy content time derivative jumps at the moments of gyrotron switch on and off were taken to determine the HF absorption rate in bulk electrons. As it follows from Fig.2 the derivative jumps are apparently independent of Z_{eff} and are approximately the same while the gyrotron is switching on and off. It indicates that the HF absorption rate behaves almost unchangeable througout the auxiliary heating process. In order to get more accurate data on HF absorption rate the local values of electron energy content were determined at the different radial positions in the time before ECRH and during the first 150-200 μs period of gyrotron action. The derivative calculations with a good temporal resolution and satisfactory accuracy became possible only after the storing a lot of laser pulses arriving at the start of gyrotron action. This resulted in a HF absorption rate radial distribution which is shown in Fig.3. The main part of the absorption rate distribution ranging from the discharge axis up to one half of minor radius contains about 50 kW of the absorbed HF power. The HF power which is absorbed throughout the plasma column was found to be of 65 ± 10 kW. This value is close to the overall gyrotron power launched into plasma with account of 15% losses in waveguide and discharge chamber walls.

The temporal variations of electron temperature spatial profile and the electron energy content in a case of the ordinary wave launched from the lower field side are shown in

Figs.4 and 5. The HF absorption rate radial distribution is also presented (Fig.6). For FT-1 tokamak discharge conditions the ordinary wave absorption is ruther small,and HF power could be abserbed only after a large number of wave reflections from the chamber walls. It is just the effect which may be responsible for the observed more poor electron heating and the displacement of HF absorption zone towards the plasma periphery.

Reference:
1.D.G.Bulygynsky et al. Proceedings of the 2 Joint Grenoble-Varenna International Symposium v.1, 187, 1980
2 T.Yu.Akatova et al. This conference.

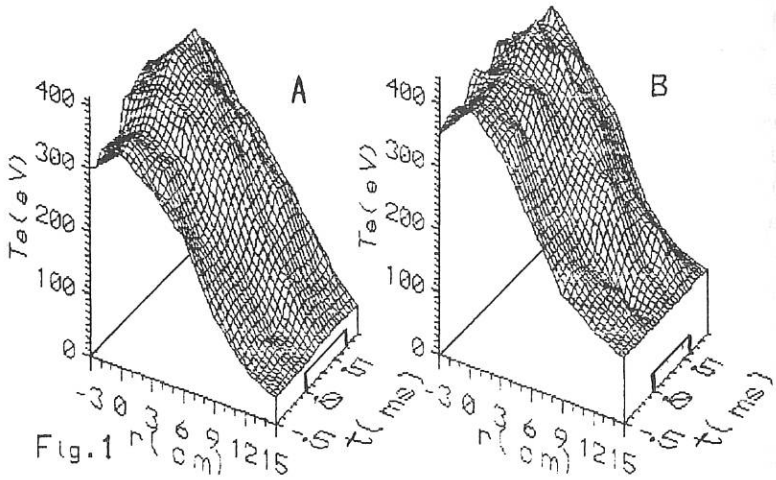

Fig.1

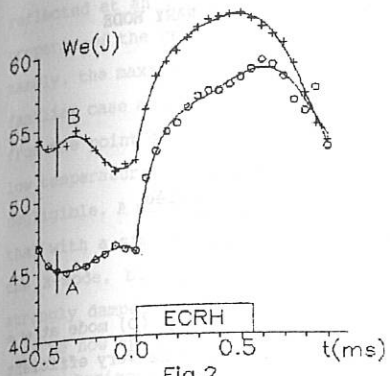

Fig.2

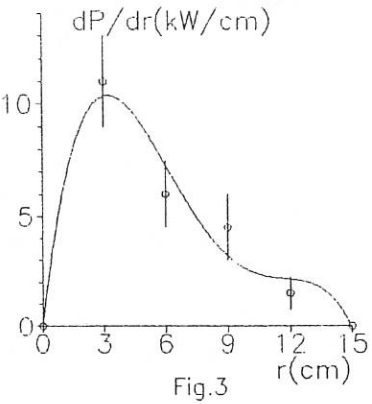

Fig.3

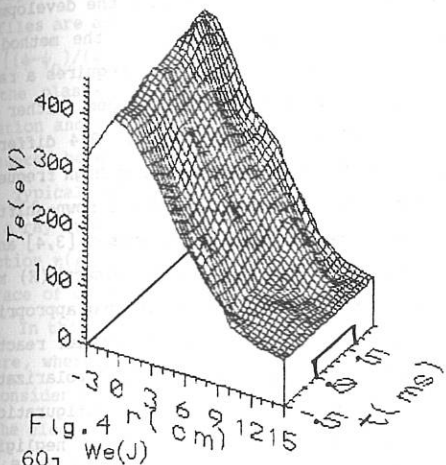

Fig.4

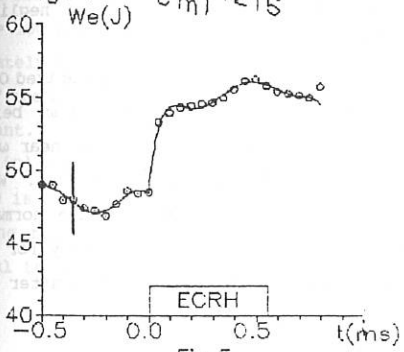

Fig.5

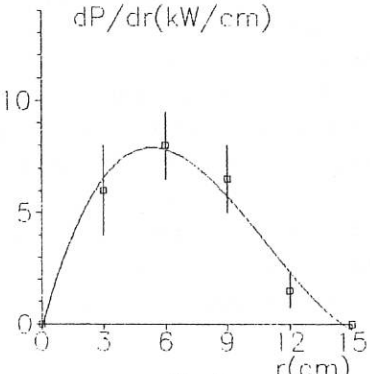

Fig.6

ELECTRON-CYCLOTRON HEATING IN NET USING THE ORDINARY MODE AT DOWN-SHIFTED FREQUENCY

I. Fidone, G. Giruzzi

ASSOCIATION EURATOM-CEA SUR LA FUSION
Département de Recherches sur la Fusion Contrôlée
Centre d'Etudes Nucléaires de Cadarache
13108 - Saint-Paul-lez-Durance (FRANCE)

Electron-cyclotron resonance absorption of the ordinary (O) mode at $\omega \simeq \omega_c$ for propagation normal to the magnetic field has proved to be very efficient for electron heating in tokamak devices [1,2], but the implementation of the method in high magnetic field tokamak reactors would require the development of high frequency wave sources. Moreover, the applicability of the method to various plasma configurations and operation regimes generally requires a range of different wave frequencies (e.g., ±10 percent), obtained either by frequency-tunable wave sources, or by a multi-frequency system (3-4 different frequencies). In order to alleviate the difficulty of developing high frequency sources, a different mode of operation based on the relativistic down-shift of the resonance frequency at oblique propagation has been proposed [3,4] and a series of applications have been discussed, using the extraordinary (X) mode launched from the tokamak top (bottom) ports [5]. This method is most appropriate for dense tokamak plasmas [6]. However, generally, in a tokamak reactor, launching the X-mode obliquely requires the appropriate elliptical polarization of the input wave and, for some peripheral magnetic field configurations, efficient tunneling through the cut-off/upper-hybrid region and negligible attenuation at $\omega = \omega_c$ at the plasma edge.

These problems are avoided for outside launch of a linearly polarized O-mode normally to the magnetic field at $\omega > \omega_p(0)$ (the plasma frequency ω_p being a cut-off frequency for the O-mode). The attenuation of the O-mode near $\omega = \omega_c$ is proportional to $n_e T_e$ and is therefore negligible at the plasma edge. We now show that the incident O-mode at an angle $\theta = 0$ with respect to the normal to the magnetic field $\vec{B}$, at down-shifted frequency (i.e., at a frequency for which $\omega = \omega_c$ is realized outside the plasma) will be totally absorbed after being

reflected at an angle $\theta \neq 0$. The success of this scenario relies on a peculiar property of the relativistic damping of the O-mode at down-shifted frequencies, namely, the maximum wave attenuation occurs for $\theta \neq 0$, in contrast with the more familiar case at $\omega \simeq \omega_c$, in which the maximum is at $\theta = 0$. The O-mode is launched from the point A in the low magnetic field side with $\theta = 0$ (see Fig. 1). In a low temperature plasma, from A to A' the attenuation of the O-mode at $\theta = 0$ is negligible. A mirror located at A' will reflect the wave at an angle $\theta \neq 0$. Note that with a simple reflecting mirror the reflected wave is also partially in the X-mode, but this is not a problem, since the X-mode at $\theta \neq 0$ is generally strongly damped too.

We now specifically refer to the NET device [7], i.e., major radius R = 6.3 m, horizontal minor radius a = 2 m, vertical elongation 2.2, B(0) = 6 T, average density and temperature $\bar{n}_e \simeq 0.8 \times 10^{14}$ cm^{-3}, $\bar{T}_e = 15$ keV. The following profiles are assumed: $n_e(\rho) = 10^{14}(1 - \rho^2)^{\frac{1}{2}}$ cm^{-3}, $T_e(\rho) = 25(1 - \rho^2)$ keV, where $\rho = [(\psi-\psi_0)/(\psi_b-\psi_0)]^{\frac{1}{2}}$, ψ is the poloidal flux function and ψ_b, ψ_0 are its values at the plasma boundary and axis, respectively. The relativistic dispersion relation and the ray equations have been discussed elsewhere [4,6] and are not presented here.

Typical results using the NET-II parameters and $f = \omega/2\pi = 100 - 125$ GHz for a ray tube of cross-section $\sigma \simeq 0.1$ m^2 are presented below. In Fig. 2, the fraction $\eta(\rho)$ of O-mode power absorbed between the launching point and the flux surface of coordinate ρ is shown, for f = 125 GHz, $\theta = 40°$ and $T_e(0) = 5$ and 6 keV. In this case, the reflected X-mode is strongly damped closer to the plasma centre, whereas the absorption of the incident O-mode at $\theta = 0$ is negligible. We consider this as the starting phase for the initiation of the plasma heating. As the electron temperature increases, the wave frequency can be decreased, down to f = 100 GHz when $T_e \simeq 20 - 25$ keV. We find that in all cases the O-mode is ultimately totally damped in the central plasma region. Note that for $T_e(0) >$ 15 keV the attenuation of the incident wave in the first transit starts to become relevant. This is illustrated in Fig. 3 for the final phase, i.e., f = 100 GHz and $T_e(0) = 25$ keV, in which the absorption of the incident wave at $\theta = 0$ (dashed curve) is 50 percent. In Fig. 4, the overall power per unit volume of the incident and the reflected O-mode deposited into the plasma is presented for different central temperatures and different values of f. For $T_e(0) = 15$ keV the value

f = 110 GHz was used. Note that, although for $T_e(0)$ = 5 keV the power deposition is broad and maximum at $\rho \simeq 0.4$, it rapidly becomes central for a slight increase of the electron temperature.

In conclusion, we have discussed an acceptable scenario for central heating in the NET device using existing wave sources (f $\simeq$ 100 - 125 GHz) and wave launching from the most accessible side of the torus. This method cumulates two main advantages, namely, low wave frequency and side launch of the O-mode. Central wave absorption occurs for the reflected O-mode at an angle $\theta \neq 0$. This is a difficulty, since a reflector is required at the inboard tokamak wall. However, this difficulty is minimized by the fact that no special polarization is required for the reflected wave, since both modes are efficiently absorbed in the plasma core.

References

[1] ALIKAEV, V., BAGDASAROV, A., BEREZOVSKII, E., et al., Plasma Phys. Contr. Fusion **29** (1987) 1285.
[2] PRATER, R., "Radio-Frequency Power in Plasmas" (Proc. 8th Top. Conf., AIP, New York, 1989), 22.
[3] FIDONE, I., GIRUZZI, G., MAZZUCATO, E., Phys. Fluids **28** (1985) 1224.
[4] FIDONE, I., GIRUZZI, G., KRIVENSKI, V., et al., Phys. Fluids **29** (1986) 803.
[5] MAZZUCATO, E., FIDONE, I., GIRUZZI, G., KRIVENSKI, V., Nucl. Fusion **26** (1986) 3.
[6] MAZZUCATO, E., FIDONE, I., GRANATA, G., Phys. Fluids **30** (1987) 3745.
[7] TOSCHI, R., "Plasma Phys. and Contr. Nucl. Fusion Research" (Proc. 12th Int. Conf., Nice, 1988), G-I-1.

Figure captions

Fig. 1 Toroidal projections of the ray paths for the incident and the reflected waves in NET-II. Dimensions are in cm.

Fig. 2 Fraction of the absorbed wave power $\eta(\rho)$ for $\theta = 40°$, f = 125 GHz and two different values of the central electron temperature.

Fig. 3 As in Fig. 2, for $T_e(0)$ = 25 keV, f = 100 GHz and for the incident wave (dashed) and the reflected O-mode (full).

Fig. 4 Total absorbed wave power density (namely, incident plus reflected O-mode) for different values of the central temperature and of the wave frequency.

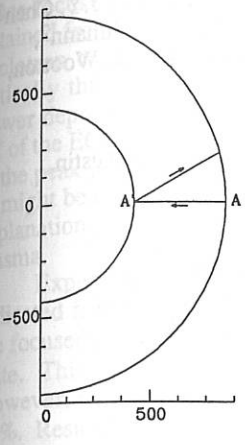

Fig.1

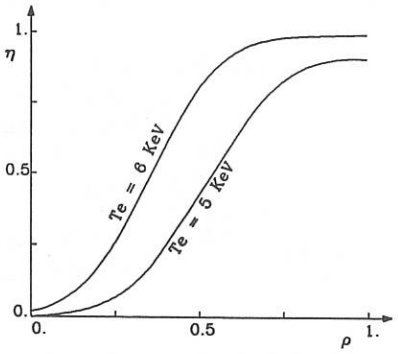

Fig.2

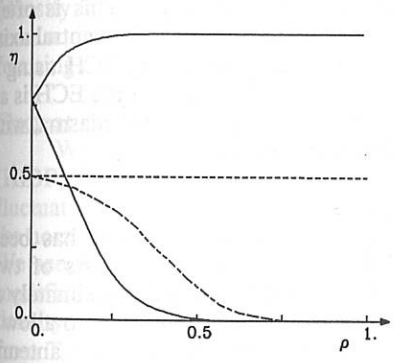

Fig.3

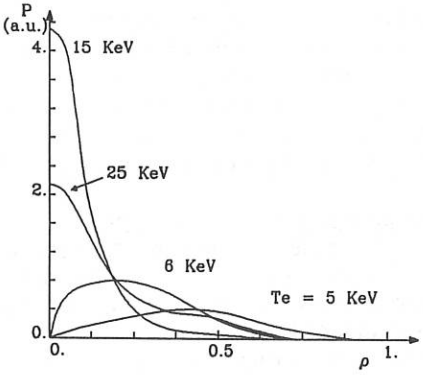

Fig.4

RECENT ELECTRON CYCLOTRON HEATING RESULTS ON TEXT*

D.C. Sing, J. Schultz, B. Richards, M.E. Austin[1], D.L. Brower[2], J.Y. Chen[3], G. Cima[4], K.W. Gentle, R.L. Hickok[5], W.L. Li[2], N.C. Luhmann[2], W.A. Peebles[2], P.E. Phillips, R. Gandy[1], P.M. Schoch[5], A.J. Wootton, X.Z. Yang[6], C.X. Yu[2]

The Fusion Research Center, The University of Texas at Austin, Austin TX 78712, USA
[1] Auburn University, Auburn AL
[2] University of California, Los Angeles CA
[3] Institute of Plasma Physics, Hefei PRC
[4] Associazione EURATOM/CNR/ENEA, Milano, Italy
[5] Rensselaer Polytechnic Institute, Troy NY
[6] Institute of Physics, Beijing PRC

Electron Cyclotron Heating experiments are being performed on the TEXT tokamak (R_0 = 1 m, a_{lim} = .26 m). We use a 200 kW, 59.7 GHz Varian gyrotron, which launches about 140 kW into the low field side of the plasma in the fundamental ordinary mode. We have found that the largest effect on the electron temperature has been obtained on high-q, non-sawtoothing discharges ($I_p \approx 120$ kA, $B_T \approx 21.6$ kG, $q_{limiter} \approx 5$ to 6, $P_{OH} \approx 200$ kW, $n_e \approx 1.6 \times 10^{19}$ m^{-3}). In these discharges (see figures 1 and 2), we have observed an increase in T_e from the OH only to the ECH case of almost 100% in a small region near the center of the discharge, as measured by Thomson scattering. This is often accompanied by a slight (order 10% or less) decrease in n_e near the central axis. Small scale fluctuations have been measured before and during ECH using a Heavy Ion Beam Probe and a FIR scattering system. The effect of the ECH is an increase the fluctuation level, $\tilde{n}/n$, by $\approx$ 25% throughout most of the plasma, with the edge fluctuation level remaining constant or decreasing.

Results with a Focusing Launcher

In order to increase the central heating effect, a launcher has been constructed with a narrower beam pattern. The launcher consists of two mirrors: a flat mirror and a concave mirror designed to focus approximately at the center of the plasma. The focusing mirror is mounted on a pivot to allow a scan in the vertical direction. In free space measurements, the new antenna system decreased the 1/e power width from ~8.5 cm to ~2.5 cm in the H-plane (vertical) direction, theoretically providing better radial localization for heating

by rf resonant at $R = R_0$. The width in the E-plane (i.e., the toroidal direction) decreased from ~7 cm to ~3 cm.

Initial results of the experiments with plasma point to a more localized power deposition profile, but not as much as would be anticipated from the free space focusing of approximately 3. Figure 3 shows a power deposition profile obtained from a measurement of second harmonic, extraordinary mode electron cyclotron emission (ECE) from the plasma. The plasma can be considered optically thick near the center for the range of parameters in the experiment. Power deposition was derived from the change in slope of the ECE at the turn off of the ECH power. We see some narrowing of the profile and a 35% increase in the peak power absorption density, although these results are not as localized as might be expected from the free space tests and ray tracing [1]. One possible explanation might be scattering of the rf by small scale density fluctuations in the plasma.

Experiments in which the deposition region was scanned vertically indicated fairly sharp profiles. For a non-sawtoothing discharge, heating with the focused mirror on-axis produced a 75 - 100% central T_e increase for steady state. This was comparable to the results obtained with the unfocused mirror. However, by moving the focus as little as 2 cm off axis, ΔT_e decreased to only 50%. Results with a sawtoothing discharge produced smaller T_e increases, and a correspondingly smaller effect of moving the resonance off-axis.

We have looked at the change in total stored plasma energy during ECH by measuring $\Lambda = (\beta_p + l_i/2)$. In contrast to the results from ECE measurements, we do see a change in the total stored energy by changing from the unfocused to the focused antenna in the non-sawtoothing, on-axis case (fig. 4), due to poorer confinement of energy deposited off-axis. We also see a decrease in the change in stored energy, ΔW, for the case of slightly off-axis heating (again, as little as 1 - 2 cm). Finally, in central heating cases where we expect good absorption (density large enough to be black but not large enough to refract the rf) we have seen a decrease in the stray power leaving the vacuum chamber when the focusing antenna is used.

Fluctuation Changes During ECH

We have also performed experiments using the heavy ion beam probe (HIBP) to determine the role of ECH and T_e as possible causes of density fluctuations which are thought to be related to plasma transport. Figure 5 shows the normalized rms fluctuation signal, $\tilde{n}/n$, near the axis before and during ECH. We see an increase in the fluctuations during ECH, which could be due to T_e modification, direct drive of the fluctuations by the ECH, or changes in the density or density gradient during ECH. To help distinguish n_e modification from T_e modification effects, we have modulated the plasma density using a gas puff. We used ECH at a reduced power and with slightly off-axis heating to greatly decrease the amount of the central T_e modulation normally present in the

gas modulation experiments. Results are shown in figure 6. Even though the modulation in the central T_e is greatly reduced, the modulation in the central $\tilde{n}/n$ signal is almost unaffected, implying that something other than central T_e is responsible for most of these fluctuations. On the other hand, in experiments where ECH was applied so as to increase the T_e modulation, an increase in $\tilde{n}/n$ during the ECH pulses was seen, implying that the ECH can play some role in determining density fluctuations.

We have performed experiments where we have looked at the fluctuation level as the resonance position was moved off axis. In these experiments, the change in central T_e upon the application of ECH was half as large for a 5-cm-off-axis heating case than the on-axis case, yet the increase in $\tilde{n}/n$ was comparable. Similarly, in going from heating at $r/a \approx .25$ to $r/a \approx .5$, central ΔT_e decreased by almost half; however, little effect was seen on the change in the fluctuation level.

Conclusions

We have constructed a focusing launcher for ECH experiments which, in the case of non-sawtoothing discharges, allows for a more precise control of the power deposition profile. Using this launcher, we have attempted to find a connection between ECH and small scale density fluctuations. The experiments reported here would indicate that changes in the fluctuation levels are not due entirely, if at all, to local changes in the electron temperature.

REFERENCES

[1] A.H. Kritz, et al., in "Heating in Toroidal Plasmas", vol.2, 707 (1982).
[2] K.W. Gentle, B. Richards, and F. Waelbroeck, Plasma Physics and Controlled Fusion **29** (9) 1077, 1987.
*Operated by The University of Texas at Austin under DOE grant No. DE-FG05-88ER53267.

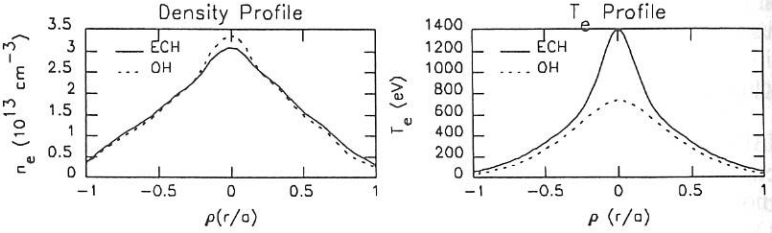

Fig. 1. $T_e(r)$ and $n_e(r)$ vs. radius with and without ECH in a high-q discharge.

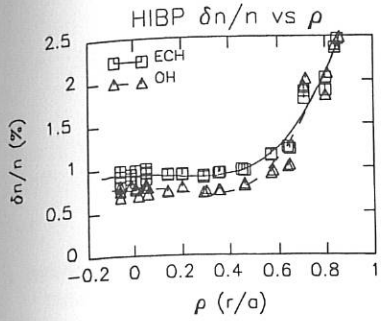

Fig. 2. ñ/n(r) vs. radius with and without ECH in a high-q discharge.

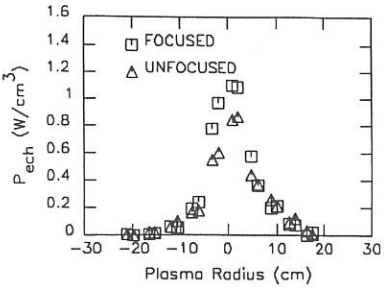

Fig. 3. ECE power deposition profiles for the focused and unfocused antennae.

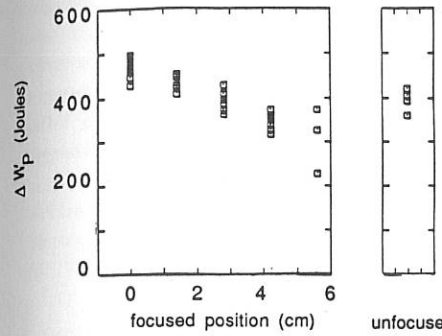

Fig. 4. Change in stored energy with ECH vs. radius for a focused mirror position scan.

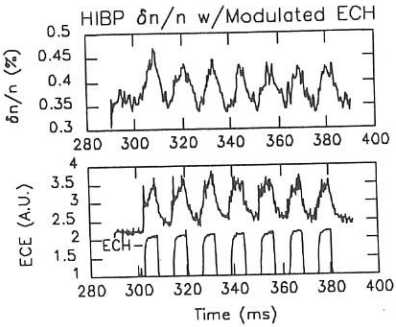

Fig. 5. ñ/n vs. time during modulated ECH

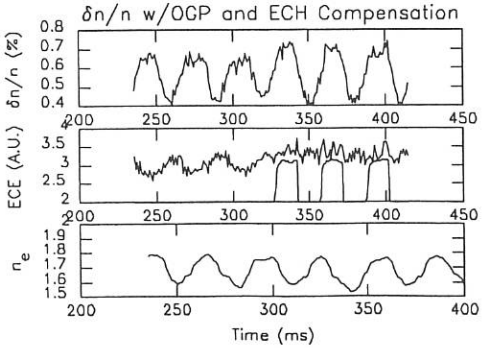

Fig. 6. $T_e(0)$ from ECE and ñ/n from HIBP vs. time for a modulated gas feed experiment with T_e compensation.

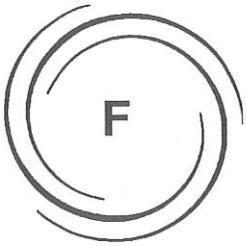

RF HEATING

F3 LOWER HYBRID HEATING

RF ALFVEN WAVE HEATING OF A HIGH-BETA PLASMA COLUMN

M. Cekic, B.A. Nelson, F.L. Ribe
University of Washington
Seattle WA 98195 - U.S.A.

1. Introduction

This paper presents results of the experimental study of the low frequency heating of a straight high β plasma column. The present experiment is the continuation of earlier High-Beta Q Machine (HBQM) efforts[1] studying azimuthally symmetric (m=0) magnetosonic waves. For this work we used a non-axisymmetric (m=±1) RF heating system (λ=0.4 m, ω=625-720 kHz) to drive waves in deuterium or protium plasmas. The variation of plasma parameters over appropriate ranges provides the means of control of the radial position of the Alfven resonant layer in the radially varying axial magnetic field.

In Sec. 2 we describe the experimental apparatus and instrumentation. Section 3 deals with the measurement results. Finally, Sec. 4 presents the comparisons between the experimental results and the theoretical predictions with the summary and conclusions.

2. Apparatus and instrumentation

The HBQM is a fast-rising, low-compression theta pinch. A single-turn aluminum segmented compression coil 260 cm long with an 11 cm inner radius is powered by a 3.6 μF, 90 kV, passively crowbarred main capacitor bank. Triggered by 9 parallel multichannel spark gaps, the main bank rises in approximately 400 nsec. The main discharge shock heats the plasma already 20%-30% preionized by a 800 G 330 kHz ringing axial magnetic field. By use of a parallel plate transformer (power crowbar) to compensate for the resistive losses, we are able to sustain an external axial magnetic field at a nearly constant 3 kG for more than 20 μsec. A uniform 230 G forward bias field is used to limit the shock action and protect the internal probes near the machine axis. Typically, the resulting quasi-equilibrium plasma column is characterized by a nearly flat density profile ($n_e \cong 7 \times 10^{21}$ m^{-3}) and a Gaussian temperature profile ($\langle T_e+T_i \rangle \cong 300$ eV, $\langle \beta \rangle \cong 0.2-0.5$).

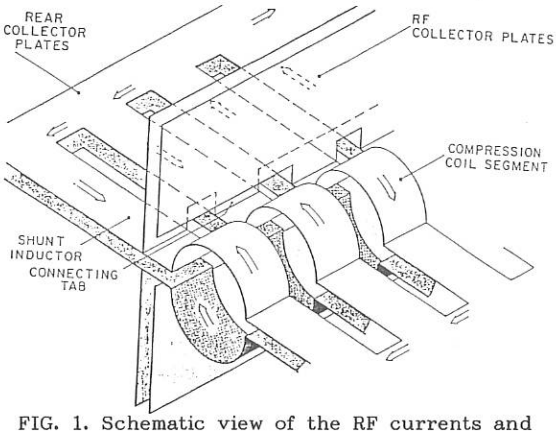

FIG. 1. Schematic view of the RF currents and the compression coil segments

The 100 MW RF heating system shown schematically in Fig. 1, uses 2 m of the segmented compression coil as the antenna. The RF capacitors (up to 40 0.25 μF-units), eight linear rail gaps and collector plates are closely coupled to the compression coil. Nevertheless, the RF current in each pair of half-coil segments and coil feed "fingers" constitutes an uncoupled surface parallel to the main B_z field and insures the independent operation of the RF system.

During the experiment we measure: RF antenna current and voltage, internal and external magnetic fields, total axial flux, and axially integrated electron number density. The antenna current is measured by differential Rogowski loops and the antenna voltage by a closely coupled flux loop. The internal magnetic field is measured by a set of four 3D (B_r, B_θ, B_z) magnetic probes. The external axial magnetic probes and flux loops, together, measure plasma diamagnetism. An axial laser interferometer is used to measure electron line density.

3. Experimental results

The experiment consists of applying the RF power to protium and deuterium plasma 4.5 μsec after the main bank discharge. At that time the shock-caused m=0 oscillations of the plasma[1] are damped to less than 10% of the initial amplitude. The presence of the plasma causes a considerable increase in the antenna loading. Figure 2 shows voltage and current signals for vacuum and 7.5 mTorr H_2 filling pressure discharges. The loading by the hydrogen plasma is measurably larger than that caused by deuterium under similar conditions.

The difference between deuterium and protium plasma response is most pronounced in comparison of time dependencies of internal B_θ. Figure 3 shows measurements from the radial array of four magnetic probes positioned at $\theta = -90^\circ$, at the axial location of the node of the axial RF field.

The protium B_θ fields are more than twice as strong as those in the deuterium plasma. Also, they show strong radial variation of the oscillation phase.

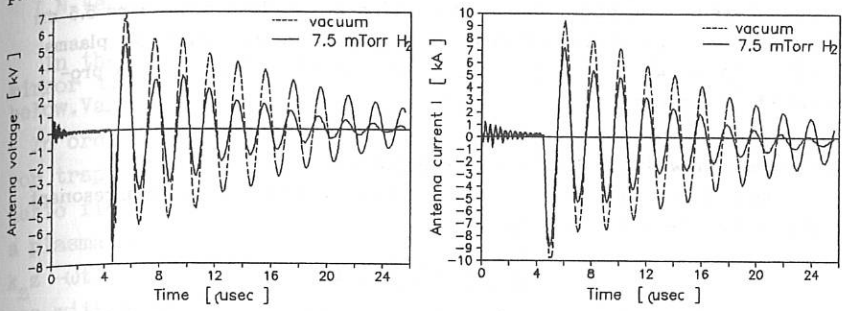

FIG. 2. Voltage and current waveforms for vacuum and protium plasma.

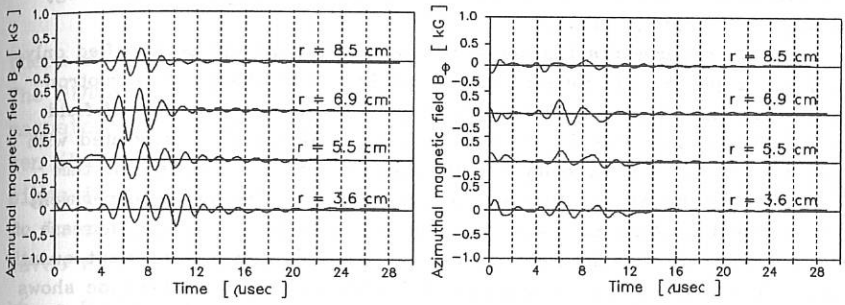

FIG. 3. Azimuthal RF fields B_θ in protium and deuterium plasma.

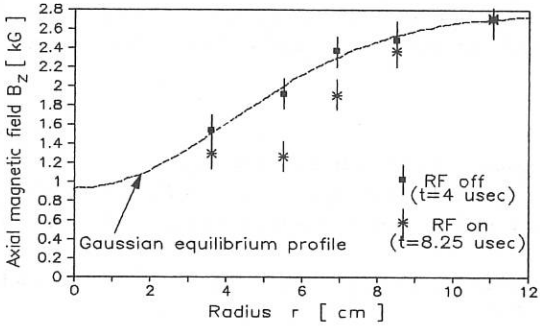

FIG. 4. B_z field profiles before and during RF discharge in protium.

The RF heating effects on the radial profiles of the equilibrium axial field B_z are shown in Fig. 4 for the protium case. Two profiles are taken at the time just before the RF bank discharge (4 μsec) and 8.75 μsec into the discharge. The distortion of the profile is localized around r= 5.5 cm and peaks in approximately 2 μsec. The effects on the deuterium plasma are 20%-30% weaker, grow more slowly and do not indicate such a pronounced localization.

4. Comparison with the theory and conclusions

The cold-plasma theory[2] predicts the existence of the Alfven resonant surfaces for the resonant condition:

$$\omega^2 = \frac{(Bk_{||})^2}{\mu_0 \rho}\left[1 - \left(\frac{\omega}{\omega_{ci}}\right)^2\right],$$

where ω is the driving frequency, B local equilibrium magnetic field, ρ plasma mass density, ω_{ci} ion cyclotron frequency , and $k_{||}$ wave number parallel to the magnetic field. At those surfaces strong resonant energy absorption is also predicted.

In our experiments the above resonant condition can be satisfied only in protium plasma. Deuterium plasma can have only simple ion-cyclotron resonance close to the machine axis (depending upon the details of field profile behavior). The theory predicts only weak damping associated with this resonance. The majority of our measurements are done at the time which places the Alfven resonance around r=6 cm. During the experiment the resonant surface can move but this motion is limited by the increase of the gradient of the axial field profile. A comparison of measurement quantities with results of the warm-plasma full-wave solving ANTENA[3] code shows only general qualitative agreement. Comparison with the finite β Vlasov-fluid model, including ion-cyclotron effects[4], will be also presented.

In conclusion, our measurements show strong antenna loading, existence of well established driven modes, and indications of strong resonant heating close to the position of the Alfven resonant surface calculated from cold plasma theory.

[1]H. Meuth and F. L. Ribe, Phys. Fluids **29**, 3050 (1986).
[2]K. Appert, J. Vaclavik, and L. Villard, Phys. Fluids **27**, 432 (1984).
[3]B. McVey, MIT Plasma Fusion Center Report, PFC/RR-84-12, Cambridge, MA 02139 1984.
[4]R. Sanchez, Phys. Fluids **24**, 40 (1981); Ph.D. Dissertation, University of Washington, Seattle, 1981.

GENERATION OF FAST MAGNETOSONIC WAVES IN A MIRROR TRAP.

Elfimov A.G., Garina S.M., Grishanov N.I.

I.N.Vekua Institute of Physics and Technology, Sukhumi, USSR.

In the present paper the wave eigenfunction are considered in mirror traps within the range of ion-cyclotron frequencies and below. Various aspects of this problem were discussed in Ref.[1].

In order to creat an idea about eigenmode behaviours in a mirror trap, we shall use a cylindrical plasma model in uniform magnetic field with a radially nonuniform density. RF fields in such a plasma may be sought as a harmonics proportional to $exp\ i(m\varphi + k_z z - \omega t)$. Within the geometric optics approximation for fast waves with characteristic small values of a longitudinal electrical field, we obtain the following dispersion relation:

$$k_z^2 = \varepsilon_1 \omega^2/c^2 - k_r^2/2 \pm \sqrt{k_r^4/4 + g^2\omega^4/c^4}\ , \qquad (1)$$

where ε_1, g -transversal permebility tensor components of plasma The *minus* sign in front of radical for $\varepsilon_1 > 0$ corresponds to fast magnetosonic (FMS) waves, while the *plus* sign refers to fast Alfven (FA) ones. For $\varepsilon_1 < 0$, FMS and FA waves correspond to opposite signs in front of the radical.

In such plasma systems, there may arise surface ($S^{\pm}$ with $m=\pm 1$) waves with dispersions at $|k_z a| \ll 1$:

$$k_z^2 = 0.5\ \omega^2 c_A^{-2}\left[1+(m/|m|)\omega/\Omega_{ci}\right];\ \text{where}\ c_A^2 = B^2(4\pi N_{oi} m_i)^{-1}. \qquad (2)$$

The corresponding dispersion curves characterizing the conplings of eigenfrequencies and eigenwavenumbers within the range of $\omega < \Omega_{cH}$ are given in Fig.1 for hydrogen plasma. Dashed lines correspond to the range of Alfven continuum. Within this region, there exists a local Alfven resonance with the waves absorbed by electrons due to Landau damping or electron-ion collisions [2].

The dispersion of waves in a mirror trap may significantly dif fer from that given in Fig.1. We use a theoretical approach here based on the geometric optics approximation for a RF field in a plasma:

$$H_z,\ div\vec{E}_{\perp} \sim J_m(k_r r)\ exp\ i\Big(\int_0^z k_z dz + m\varphi - \omega t\Big). \qquad (3)$$

We have considered here that the plasma is uniform in it's cross section, while $k_z(\zeta)$ (1) depends on the longitudinal coordinate ζ via the confining magnetic field, $B=B_o/(1-\zeta)$, where $\zeta=(R-1)|z|/RL$ R is the mirror ratio, and L is the mirror trap half-length. The plasma boundary radius is $r_o(\zeta) = a\sqrt{1-\zeta}$.

Using quantization conditions for eigenmodes: $\int_{-z_o}^{z_o} k_z dz = \pi n$, n being integers, where integration done over the wave propagation region (where $k_z^2>0$), FMS and FA wave dispersion expressions may be derived. For FA waves, the propagation region covers the whole plasma volume. For FMS waves, $z_o=RL\left[1-(\mu_{im}c_{Ao}/\omega a)^{2/3}\right]/(R-1)$ and when $\omega < \Omega_{CH}^{(o)}$, the dispersion equation will be:

$$\omega_{FMS}^2=c_{Ao}^2\left\{\mu_{im}^2/a^2 +\left[1.5\ \pi\left(2\omega^2/c_{Ao}^2 +\mu_{im}^2/a^2\right)(R-1)n/RL\right]^{2/3}\right\};\ c_{Ao}=c_A(z=0)$$

where μ_{im} is the root of Bessel function, $J_m(x)$.

Fig.2 shows the fast wave dispersions for the hydrogen plasma indicating that the FMS wave dispersion is not sensitive to the cyclotron resonance zone existence $\zeta_{CH}= 1-\Omega_{CH}^{(o)}/\omega$, where $\varepsilon_1 \to \infty$. FA waves do not reach this zone since their wavelengths become much shorter on approaching nearer to the cyclotron resonance zone, this effect being accompanied by a mighty damping of these waves. Based on Eq.(1), Fig.3 shows local values of k_z^2 versus ζ for the hydrogen plasma with deuterium impurities. It's seen that a FA wave in the neighbourhood of the cyclotron resonance of deuterium impurities $\zeta_{CD}=1- 0.5\ \Omega_{CH}^{(o)}/\omega$ undergoes tearing which indicates the possibility of the RF field transformation into cyclotron oscillations and their damping. Such circumstances may lead to the powerful heating of plasma ions and electrons.

Further, using numerical code named FITA [3], generation and absorption of RF fields are analyzed in a plasma mirror trap over the range of eigenfrequencies of FMS waves. A FMS resonance is found for the following parameters: $B_o=2.6$kG, $R=6$, $L=250$cm, $a=5$cm the RF circuit radius $b=25$cm, the casing radius $d=30$cm, the antenna multipoleness: $m=1$, $n=3$, $\omega=3.06\ 10^7$. The collisional dissipation mechanism of the waves generated is simulated with the effective collisional frequency at the level of $\nu= 0.01\ \omega$ included in the components of the dielectric constant.

Fig 4 shows the electrical field component, $E=E_r-iE_\varphi$, distributed over the radius, for the FMS resonance in different cross-sections. Figs.5,6 represent r- and z- structures of the E field and the absorbed power, respectively. The distributions obtained for RF fields and absorbed powers indicate the possibility for plasma as a result of resonant generation of FMS oscillations at the central part of a mirror trap.

REFERENCES

1. A.V.Zvonkov, A.V.Timofeev. Fizika Plazmy.1987, v.13,p.282.
2. A.G.Elfimov,A.G.Kirov,V.P.Sidorov.- In: RF Plasma Heating, Gorky,Inst.of Appl.Phys.AN USSR, 1983, p.211.
3. S.M.Garina, M.V.Dmitrieva, A.G.Elfimov, A.A.Ivanov. Preprint Keldysh Inst.of Appl. Math.,1989, N 104, 24 pages.

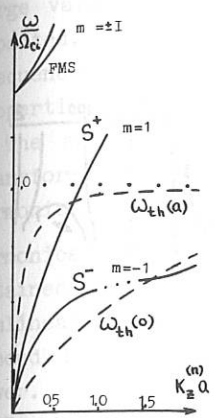

Fig.1

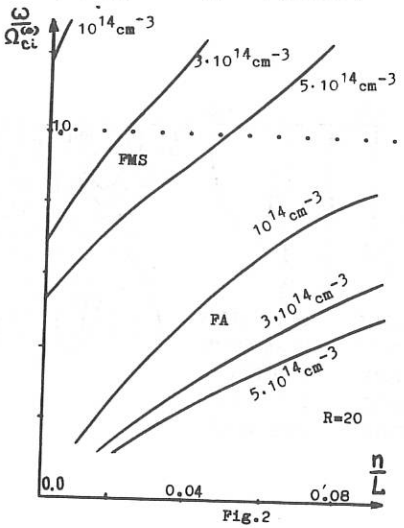

Fig.2

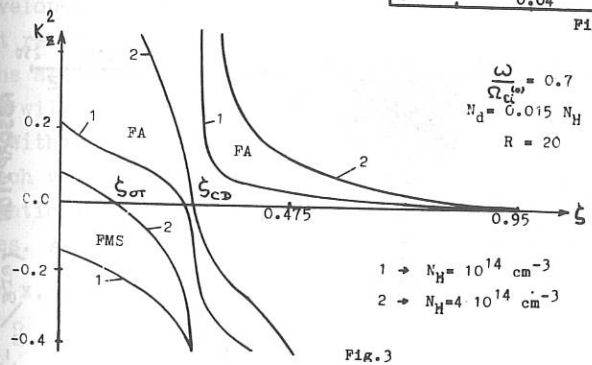

Fig.3

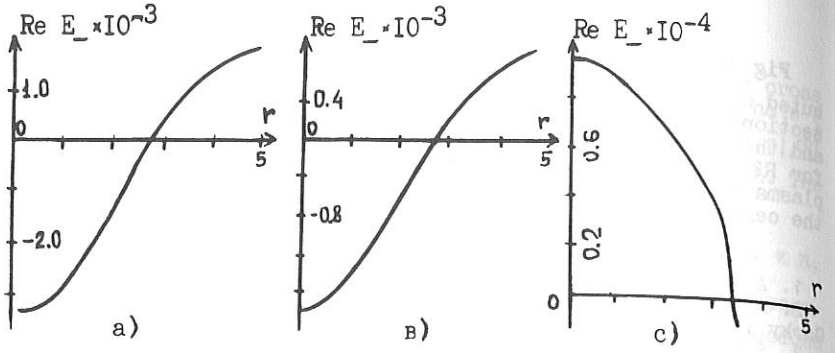

Fig.4

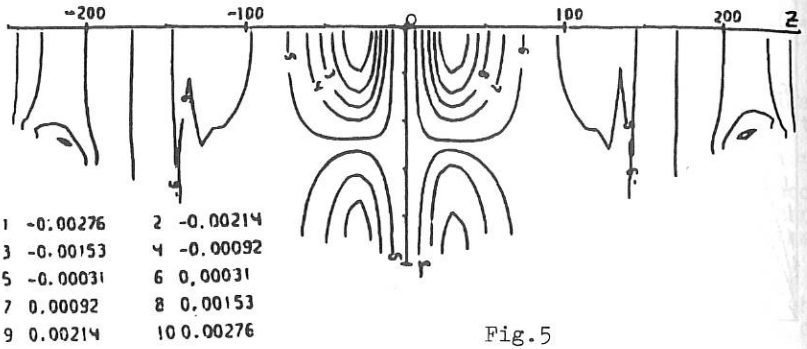

Fig.5

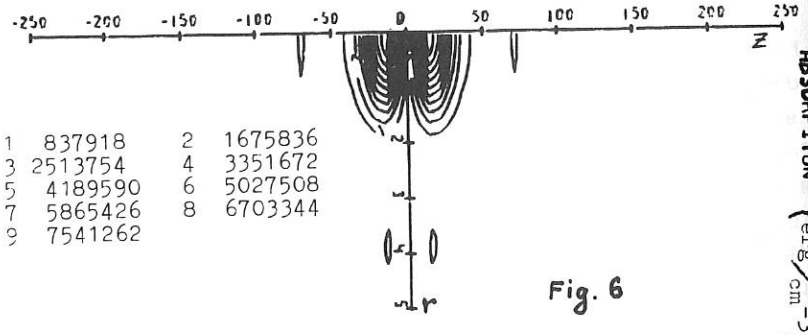

Fig. 6

NONLINEAR TRANSFORMATION OF ALFVEN WAVES IN A HOT PLASMA.

V.P.Minenko, V.P.Sidorov, V.S.Tsypin.
Sukhumi Institute of Physics and Technology,
384914, Sukhumi, USSR.

In interactions of electromagnetic fields of Alfven-range frequencies with plasmas of fusion devices or with the space plasma, RF field amplitudes near the Alfven resonance may have large values [1]. Moreover, various nonlinear effects may be expected, such as the development of harmonics with the main frequences, and RF field effects upon the plasma dispersion properties and nonlinear transformations of Alfven waves.

The authors had already considered nonlinear Alfven wave transformations in a hot plasma [2]. Resonant generations of harmonics with main frequencies had been found; however, the harmonics amplitude was $(M_i/M_e)^2 = \mu^{-2}$ times lower than its value obtained from qualitative estimations. The coefficient of a nonlinear coupling for dispersion equations of the first and second RF field harmonics was the same order of magnitude lower.

It should be expected that in a hot plasma such a degeneration would disappear with the resonance effects more notably developed. In what follows, we shall restrict ourselves with a hot rarified plasma where the finite Larmour radius effects of ions are significant. Exponentially small Landau electron damping will be neglected.

Within the geometrical optics approximation, we use an approach where the dielectric permeability tensor is taken to be kinetic while nonlinear effects are considered as hydrodynamic ones. As in Ref. [2], the equation is initial for S-harmonics (in x, y, z coordinates; $\vec{B}_o = \vec{e}_z B_o$, $\vec{N}_\perp = \vec{e}_x N_\perp$):

$$(N^2 \delta_{ik} - N_i N_k - \delta_{ik}) E_k^{(s)} = U_i^{(s)} \qquad (1),$$

In Eq. (1),

$$\vec{U}^{(\pm 1)} = \pm 4\pi i/\omega \sum_\alpha e_\alpha n_{o\alpha} \{ \vec{V}^{(n)}_{\alpha\pm 1} + \vec{V}^{(l)}_{\alpha\pm 1} / c \; [(\vec{N}\,\vec{V}_{\alpha\pm 2}) +$$

$$+ 1/c (\vec{N}\,\vec{V}_{\alpha\pm 1})^2] + \vec{V}_{\alpha\pm 2}/c (\vec{N}\,\vec{V}_{\alpha\,1}) \}; \qquad \vec{V}_{\alpha s} = \vec{V}^{(l)}_{\alpha s} + \vec{V}^{(n)}_{\alpha s};$$

$$\vec{U}^{(\pm 2)} = \pm 2\pi i/\omega \sum_\alpha e_\alpha n_{o\alpha} \{ \vec{V}^{(n)}_{\alpha\pm 2} + \vec{V}^{(l)}_{\alpha\pm 1} / c (\vec{N}\,\vec{V}^{(l)}_{\alpha\pm 1}) \} \qquad (2)$$

As distinguished from Ref. [2], we adopt:

$$\vec{V}^{(l)}_{\alpha s} = \sigma^{(s)}_{\alpha s} \vec{E} / e_\alpha n_{o\alpha}, \qquad \vec{V}^{(n)}_{\alpha s} = 4\pi \sigma^{(s)}_{\alpha s} \vec{D}^{(n)}_{\alpha s} / \omega_{B\alpha} \qquad (3)$$

where:

$$\vec{D}^{(n)}_{\alpha s} = -((\vec{V}_\alpha \nabla) \vec{V}_\alpha)_s - 1/M_\alpha (\nabla P_\alpha / n_\alpha)^{(n)}_s + e_\alpha / M_\alpha c \{ (\vec{N}(\vec{V}_\alpha \vec{E}))_s - (\vec{E}(\vec{N}\vec{V}_\alpha))_s \}$$

(the symbols are of common use).

In Eqs. (1) and (2), well-known kinetic expressions for a slightly nonhomogeneous plasma are taken as tensors of the dielectric permeability, $\hat{\varepsilon}$, and the conductivity, $\hat{\sigma}$, (see, e.g. [3]). The pressure, P_α, is derived from the adiabatic equation.

It should also noted that qualitative analyses of the finite Larmour radius effects may be done using the hydrodynamical equations including the gyroviscosity.

In the present research, the availability of the resonance found out in Ref. [2] is of great importance. The essence of this resonance is that for $\Delta_1 \cong 0$ (where Δ_1 is the definitor of the left-hand side of Eq. (1) for s=1 taken with an opposit sign), Δ_2 also turns into zero in a certain point of the space. As in Ref. [2], the resonance condition for a small Larmour ra-

dius of ions (these terms are taken into consideration as corrections) is considered in:

$$aN^6 + bN^4 + cN^2 + d = 0 \qquad (4)$$

with coefficients somewhat differing from those in Ref. [2].

$$a = \varepsilon_{zz}^{(s)} / \varepsilon_{xx}^{(s)} - \varepsilon_{zz}^{(k)} / \varepsilon_{xx}^{(k)};$$

$$b = \varepsilon_{zz}^{(s)}\varepsilon_{zz}^{(k)} / \varepsilon_{xx}^{(s)}\varepsilon_{xx}^{(k)} \left(\varepsilon_{xx}^{(s)} - \varepsilon_{xx}^{(k)}\right) - \varepsilon_{zz}^{(s)} \left(1+\varepsilon_{yy}^{(s)}/\varepsilon_{xx}^{(s)}\right) +$$

$$+\varepsilon_{zz}^{(k)} \left(1+\varepsilon_{yy}^{(k)}/\varepsilon_{xx}^{(k)}\right) + \beta_s \varepsilon_{zz}^{(k)}/\varepsilon_{xx}^{(k)} - \beta_k \varepsilon_{zz}^{(s)} / \varepsilon_{xx}^{(s)};$$

$$c = \varepsilon_{zz}^{(s)}\varepsilon_{zz}^{(k)} / \varepsilon_{xx}^{(s)}\varepsilon_{xx}^{(k)} \left(\varepsilon_{xx}^{(k)}\beta_k - \varepsilon_{xx}^{(s)}\beta_s\right) +$$

$$+ \varepsilon_{zz}^{(s)}\varepsilon_{zz}^{(k)} \left(\varepsilon_{yy}^{(s)}/\varepsilon_{xx}^{(s)} - \varepsilon_{yy}^{(k)}/\varepsilon_{xx}^{(k)}\right) + \beta_s \left[\varepsilon_{zz}^{(s)} -$$

$$- \varepsilon_{zz}^{(k)} \left(1+\varepsilon_{yy}^{(k)}/\varepsilon_{xx}^{(k)}\right)\right] - \beta_k \left[\varepsilon_{zz}^{(k)} - \varepsilon_{zz}^{(s)} \left(1+\varepsilon_{yy}^{(s)}/\varepsilon_{xx}^{(s)}\right)\right] +$$

$$+ \left(\varepsilon_{zz}^{(s)}\delta\varepsilon^{(k)} - \varepsilon_{zz}^{(k)}\delta\varepsilon^{(s)}\right);$$

$$d = \varepsilon_{zz}^{(s)}\varepsilon_{zz}^{(k)} \left(\beta_s \varepsilon_{yy}^{(k)}/\varepsilon_{xx}^{(k)} - \beta_k \varepsilon_{yy}^{(s)}/\varepsilon_{xx}^{(s)}\right) - \beta_s\beta_k \left(\varepsilon_{zz}^{(s)} - \varepsilon_{zz}^{(k)}\right) +$$

$$+ \left(\varepsilon_{zz}^{(k)}/\varepsilon_{xx}^{(k)}\delta\varepsilon^{(s)} - \varepsilon_{zz}^{(s)}/\varepsilon_{xx}^{(s)}\delta\varepsilon^{(k)}\right), \quad \beta_s = \varepsilon_{yy}^{(s)} + \varepsilon_{xy}^{(s)2}/\varepsilon_{xx}^{(s)},$$

$$\delta\varepsilon^{(s)} = N_\parallel N_\perp \left[2N_\perp^2 \varepsilon_{xz}^{(s)} + \varepsilon_{xy}^{(s)}\varepsilon_{yz}^{(s)} + \varepsilon_{xz}^{(s)} \left(N_\parallel^2 - \varepsilon_{yy}^{(s)}\right)\right].$$

The root of Eq. (4) is most interesting:

$$N^2 = - d/c - bd^2/c^3 \qquad (5)$$

Besides, $N_\perp^2 = - N_\parallel^2$. Amplitudes of second harmonics calculated from Eq. (I) (s=2), taking Eqs. (2)-(5) into account, result in

$$E_x^{(\pm 2)} = (\pm i\alpha_1 \nu/\Delta_2)(\gamma^6 N_\perp \beta_i/\mu B_o) E_x^{(\pm 1)2}$$

$$E_y^{(\pm 2)} = (\alpha_2 \nu^2/\Delta_2)(\gamma^6 N_\perp \beta_i/\mu B_o) E_x^{(\pm 1)2} \qquad (6)$$

$$E_z^{(\pm 2)} = \mu(E_x^{(\pm 2)}, E_y^{(\pm 2)}), \quad \gamma = c/c_A, \nu = \omega/\omega_{Bi}$$

The coupling coefficient of dispersion equations of the first

and second harmonics, A_2, is derived in a similar way:

$$\Delta_1 - A_1 |E_x^{(\pm 1)}|^2 = A_2 |E_x^{(\pm 1)}|^2 / \Delta_2 \qquad (7)$$

where $A_2=\alpha_3\gamma^{12}N_\perp^2\beta_i/B_o^2\mu^2$, $A_1=2\gamma^6N_\perp^2/\mu B_o^2$, $\beta_i=4\pi n_o T_i/B_o^2$, the coefficients, $\alpha_1,\alpha_2,\alpha_3$ are of the order of unity, $\nu < 1$.

Analizing Eqs. (6) for the second harmonics of the fields and a nonlinear coupling coefficient, Eq. (7), one sees that they differ from the corresponding expressions in Ref. [2] for a cold plasma by the factor $\beta_i/\mu^2 \simeq 10^2 \div 10^3$ (within the assumption of the present problem). Threfore, the resonant effects while approching the point of $\Delta_2 = 0$ in a hot plasma, are expressed much better that in a cold one, and near the Alfven resonance point, intense generation of the main frequency harmonics is to be expected. The results obtained in the present paper, make the qualitative features on nonlinear transformations much clearer. In order to enlighten the phenomenon details, the analysis based on solutions of corresponding differential equations should be done. Investigations of cases when Landau damping (both linear and nonlinear) is significant is also of great practical interest.

REFERENCES

1. T.Stix, D.Swanson. Foundation of Plasma Physics edited by R.Z.Sagdeev and M.Rosenbluth. Moscow, Energoizdat publishers, vol.1,p.p.283-333.

2. V.P.Sidorov,T.R.Soldatenkov,V.S.Tsypin. Proc. of 16th Europ. Conf. on Contr. Fus. and Plasma Physics, Venice, 1989, vol.13B, part III, p.p.1211-1214.

3. V.D.Shafranov. Voprosy teorii plazmy, Moscow, 1963, edited by M.A.Leontovich, №3, p.3.

Exeperimental Studies of Kenetic Alfven Waves on CT-6B Tokamak

Zhang Daming , Wang Long , Zheng Shaobai and Yuan Dingpu

Institute of Physics , Chinese Academy of Sciences

P.O. Box 603, 100080, Beijing , China

Abstract

We present here the studies of the shear Alfven waves on CT-6B tokamak . The low n modes of the wave were excited with a m=0 antenna and measured by a group of movable magnetic probes . The signal was analyzed by a set of phase detectors . The exciting conditions of the surface shear Alfven waves were experimentally determined . And also the radial structure of the wave field was studied .

Solving the ion Vlasov equation and electron drift kenetic equation without neglecting the electron temperature effect and the compressive term , the mode conversion condition of the shear Alfven wave to kenetic Alfven wave (KAW) in the vicinity of the resonance layer was studied in detail . The condition was found to be easier to meet than that obtained considering only the effects of ions or electrons .

As the electron beta in the vicinity of the resonance layer rose high enough , greater than (1/3)*(me/mi) , a kind of mode of new characters was observed . The radial vector of the mode was measured from time to time in the tokamak discharge which was principalely agree with the thoretical results obtained by Stix and L.Chen in the vicinity of the shear Alfven wave resonance layer . And also , the radial energy flux and the heating efficiency of the kenetic Alfven wave was analyzed experimentally .

ELECTRON ABSORPTION OF FAST MAGNETOSONIC WAVES BY TTMP IN JET

F. Rimini, D.V. Bartlett, V.P. Bhatnagar, D.J. Campbell, C.D. Challis, A.D. Cheetam, S. Corti, A.W. Edwards, L-G. Eriksson, R.D. Gill, N. Gottardi, T. Hellsten[1], J.Jacquinot, J. O'Rourke, M.J. Mayberry[2], D. Moreau[3], N.A. Salmon, P. Smeulders, D.F.H. Start, M. von Hellermann

JET Joint Undertaking, Abingdon, Oxon, OX14 3EA, U.K.
[1] Royal Institute of Technology S-10044, Stockholm, Sweden
[2] General Atomics San Diego, California, USA
[3] CEA Centre d'Etudes Nucleaires de Cadarache, France

Introduction: Direct electron damping of low frequency fast magnetosonic waves is regarded as a promising method for non-inductive current drive in future tokamak fusion reactors. Theoretical studies /1/ predict for this scheme a greater efficiency than Lower Hybrid current drive; in addition, the fast wave can propagate up to the central high-temperature high-density region of a reactor plasma while the lower hybrid propagation is greatly restricted according to the Stix-Golant accessibility criterion /2,3/. In existing experiments the presence of stronger competitive absorption mechanisms, in particular ion cyclotron damping, makes it difficult to obtain and detect significant direct absorption of the wave via Transit Time Magnetic Pumping or Electron Landau Damping. In this paper we report the first experimental observation of direct electron damping of low frequency fast magnetosonic waves in high-β JET plasmas in conditions where TTMP is estimated to be an important component in the electron-wave interaction.

Theory: Electrons interacting directly with the fast wave are accelerated in the direction parallel to the magnetic field by a combination of TTMP and ELD; the resonance condition for both mechanisms is $\omega = k_{//} v_{//}$ where ω is the wave frequency, $k_{//}$ and $v_{//}$ are the components of wave vector and electron velocity in the parallel direction. In recent theoretical works /4,5/ a key role in determining the relative strength of TTMP and ELD interaction is attributed to the parameter $\alpha = T_e \omega^2_{pi} / m_e c^2 \omega$, where T_e is the electron temperature, ω_{pi} is the ion plasma frequency and $m_e c^2$ is the electron rest energy. It is found that for $\alpha >> 1$, i.e. for low frequency waves and high-β plasmas, TTMP is the dominating component in the interaction for electrons with $E\perp$ greater than $<E\perp>$, while ELD is stronger in the opposite case of $E\perp$ less than $<E\perp>$, where $E\perp$ is the electron energy perpendicular to the magnetic field and $<E\perp>$ is the perpendicular energy averaged over the electron distribution function. In the limit $\alpha >> 1$ the current drive efficiency has the enhanced value found by Fisch and Karney; the damping is then given by

$$4k\perp_i / |k\perp| = \sqrt{\pi}\ \beta_e \xi \exp(-2\xi^2) \qquad (1)$$

where $k\perp_i$ is the imaginary part of the perpendicular component $k\perp$ of the wave vector, β_e is the electron beta and ξ is the phase velocity normalized to the electron thermal velocity v_e. The strongest absorption occurs at maximum β_e and for waves with phase velocity around $v_e/\sqrt{2}$. In the high frequency and low-β plasma case, $\alpha << 1$, the interaction is mainly via ELD for all values of $E\perp$ and the current drive efficiency is predicted to be comparable to that of the lower hybrid waves. All the fast wave experiments carried out so far /6-10/ fall in this second regime, with $\alpha \approx 0.1$ and $\omega >> \omega_{ci}$. In a reactor such a scheme would be susceptible to strong

competitive absorption by α particles. On the contrary, for the experiment in JET a low frequency and high-β scheme has been chosen because it seems more attractive for reactor plasmas, where damping by α-particles could be a strong competitive absorption mechanism. For ITER we have proposed to use frequencies below the lowest cyclotron frequency in the device to avoid all cyclotron damping and, with predicted $\alpha \approx 50$, to benefit from the improved current drive efficiency.

Experiment and results: The experiments have been carried out in hydrogen double-null X-point discharges, with plasma current of 2 MA and vacuum toroidal field of 1.34-1.44 T and combined ICRF and NBI heating. The RF power, at the frequency of 48 MHz and in dipole phasing, was square modulated at 8 Hz between 3 MW and 9 MW. The $2\omega_{CH}$ resonance was located on the high field side at about 0.4 m from the magnetic axis, such that a large portion of the plasma central region is free from mode conversion and ion cyclotron layers and wave damping can only occur via TTMP and ELD. During the combined heating phase electron and ion temperatures are strongly peaked, with central values of 3.9 keV and 2.9 keV respectively, whereas the electron density profile is broader, with on-axis value around 2.2×10^{19} m^{-3}; the volume averaged total β is 1.4 %.

The response of the electron temperature to the RF power modulation is studied using a fixed-frequency multi-channel heterodyne ECE radiometer, which views the plasma horizontally along the equatorial plane, detecting 2nd harmonic E-mode radiation /11/ : the covered region ranges from 3.07 m to 3.32 m at $B_T = 1.34$ T and from 3.30 m to 3.58 m at $B_T = 1.44$ T. In dipole antenna phasing direct electron heating due to mode conversion at the 2nd harmonic is, according to full wave calculations, only 1 % of the total power absorbed. In this situation the observed direct electron heating is predominatly associated with TTMP and ELD; in particular, since a value of $\alpha = 3$ is estimated for these discharges, TTMP is a major component in the measured damping on resonant electrons.

Direct electron absorption of the wave is evidenced by the prompt change of the slope $\dot{T}_e$ of the sawtooth ramp at the time of ICRF power switched up and down (fig.1); the discontinuity $\Delta\dot{T}_e$ in the temperature slope can be linked to the step in absorbed power density via the relation $\Delta P_e = {}^3/_2 n_e \Delta\dot{T}_e$ under the assumption that heat transport is continuous during the RF power step and that $\Delta\dot{n}_e = 0$. In our case no evident step can be detected in the density slope and the error due to neglecting this component is estimated to be at most 0.01 MW/m³. Fig. 2 shows the power deposition profile for two shots with different toroidal field. The peaked shape reflects the similar form of β_e. The power density on axis is $\approx$ 0.11MW/m³ and the total modulated power absorbed in the central region free from ion cyclotron resonance is $\approx 1.3 \pm 0.3$ MW, corresponding to 22 ± 5 % of the modulated input power.The estimate based on eqn (1), with $k_{//} = 7$ m^{-1} and $\beta_e = 1.5$ %, yields a slightly lower value of $\approx$ 17%.

The centrally peaked power deposition deduced from ECE measurements is confirmed by profiles obtained from the change in slope $\Delta\dot{\tilde{\varepsilon}}$ in the tomographically inverted soft X-ray emissivity profiles /12/. The error bars in the profile of $\Delta\dot{\tilde{\varepsilon}}$ (fig. 3) represent rms deviations and the small displacement ($\approx$ 7 cm) of the maximum from the magnetic axis is well within the uncertainties both of tomography and equilibrium calculations; the peaks outside the sawtooth inversion radius could be caused by electron heating due to mode conversion at $\omega = 2\omega_{CH}$. The total power deposited in the plasma can be estimated from the modulation in the plasma energy content which can be expressed as $\dot{\tilde{W}}_{TOT} = {}^1/_3(\dot{\tilde{W}}_{DIA} + 2\dot{\tilde{W}}_{MHD})$, where $\dot{\tilde{W}}_{DIA}$ and $\dot{\tilde{W}}_{MHD}$ are the modulated plasma energy content given by the diamagnetic loop and Shafranov shift

(fig. 1) and their different sensitivity to parallel and perpendicular energy has been taken into account. Since the global energy confinement time τ_E in the present experiment is significantly greater ($\tau_E \approx 0.18$ sec) than the modulation period τ_m, the square wave amplitude of the modulated power absorbed can be expressed as $\tilde{P}_{TOT} = 2\omega_m \tilde{W}_{TOT}/\pi$. The resulting $\tilde{P}_{TOT} = 4.4$ MW accounts for 77 $\pm$ 10% of the 5.8 MW of modulated input, which indicates that most of the power is absorbed at $2\omega_{CH}$ while the power unaccounted for is probably deposited at the plasma periphery where the poor energy confinement reduces the sensitivity of the energy diagnostics.

A comparison has been carried out (fig. 4) between the experimental deposition profile, the predictions of a ray-tracing code /13/ and a self-consistent treatment of power deposition and velocity distribution using the PION code /14/. Both codes include TTMP and ELD damping and absorption at $2\omega_{CH}$, with the PION code taking also into account the enhanced second harmonic absorption due to hydrogen tail formation. Out of the 4.4 MW of deposited modulated power the PION code calculates that 30 $\pm$ 5 % is absorbed directly by the electrons, corresponding to 1.2 $\pm$ 0.2 MW dissipated in the central region alone. This global value is in good agreement with the experimental estimate although the predicted profile is more peaked than than the profile inferred from ECE data and the central value of 0.3 MW/m^3 is higher than the measured one. According to ray-tracing calculations 38 % of the modulated input is damped by electrons, yielding an absorption of 1.2 MW in the centre, in agreement with both the experiment and the PION code. The shift of the maximum of the deposition profile of $\approx$ 0.2 m off-axis can be attributed to focussing of the rays at 0.2m inboard of the magnetic axis.

Summary: collisionless electron damping of fast magnetosonic waves has been observed in the central region, free from ion cyclotron and mode conversion layers, of JET high-β discharges in conditions where TTMP is predicted to be a significant component in the electron-wave interaction.

The experimentally determined electron heating profile is less peaked than that predicted by either ray-tracing or the PION code, although the measured total power absorbed by electrons is in good agreement with theory.

Acknowledgement: the authors are thankful to the JET Team for assistance in this work, and in particular to the tokamak operating team, the ICRF team and the diagnostic groups involved in the measurements reported here.

References

/1/ Fisch N.J. and Karney C.F., Phys. Fluids 24(1981) 27
/2/ Stix T.H., The Theory of Plasma Waves, McGraw-Hill, N.Y. 1962
/3/ Golant V.E., Sov. Phys Tech Phys 16(1972) 1980
/4/ Moreau D. et al.,Proc of the 14TH EPS, Madrid 1987,III - 1007
/5/ Chiu S.C. et al., submitted to Nucl. Fusion
/6/ Goree J. et al.,Phys Rev Lett 55(1985) 1669
/7/ Ando R. et al.,Nucl Fusion 26(1986) 1619
/8/ Ohkubo K. et al.,Phys Rev Lett 56(1986) 2040
/9/ Yamamoto T. et al.,Report JAERI-M 85-115(1986)
/10/ Pinsker R.I. et al.,Proc 7TH RF Topical Conf.,Kissimee1987 p.175
/11/ Salmon N.A. et al.,Proc. of the Joint Workshop on ECE and ECRH,Oxford 1987
/12/ Edwards A.W. et al.,Rev. Sci. Instr. 57(1986) 2142
/13/ Bhatnagar V.P. et al.,Nucl. Fusion 24(1984) 955
/14/ Eriksson L.G. and Hellsten T.,JET Report P(89)65

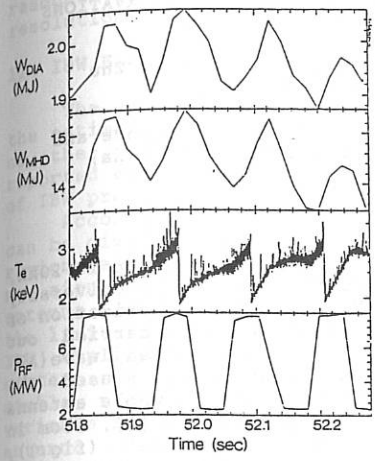

fig. 1

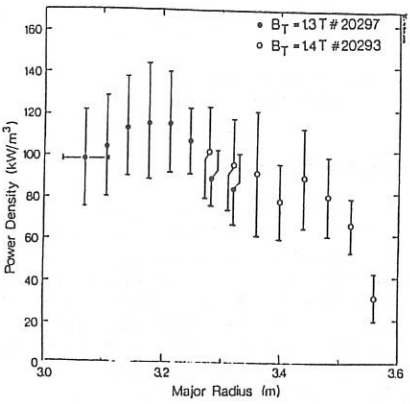

fig. 2

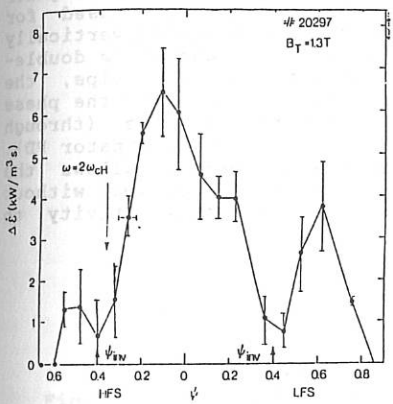

fig. 3

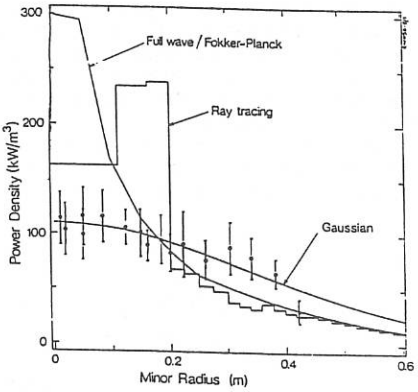

fig. 4

Figure captions

fig. 1 Response of, from top, W_{DIA}, W_{MHD} and T_e (central ECE channel) to ICRF power modulation
fig. 2 Direct electron heating profile deduced from ECE measurements
fig. 3 Profile of the discontinuity in $\Delta\dot{\varepsilon}$ in the soft X-ray emissivity plotted versus the normalized poloidal flux
fig. 4 Comparison of the observed direct electron heating profile with predictions from ray-tracing and the PION code

ION BERNSTEIN WAVE EXPERIMENTS AND PRELIMINARY OBSERVATIONS OF ALFVEN WAVE RESONANCE IN TOKAMAK KT-5B

Wandong Liu Yizhi Wen Shensheng Han Shiyao Zhu
Shude Wan Changxun Yu Zhiling Xiang

(Department of Modern Physics, University of Science and Technology of China, Hefei, Anhui 230026, P.R.China)

I. INTRODUCTION

KT-5B tokamak is a small device (R=30cm, a=10cm, Ip=10-20kA, Bt=0.3-0.6T, Teo=70-100ev, n=0.5-1.0×10^{13} cm^{-3}) at the University of Science and Technology of China (USTC). The investigation of externally launched ion Bernstein wave(IBW) has been carried out in this device since 1986, and the preliminary Alfven wave(AW) resonance was observed recently. Both the experiments used the same antenna and detection system. The radially movable antenna is a Faraday shield toroidal loop (of Nagoya type III[1], 35cm in length) installed on the weak field side of the vessel (fig.1), and is shadowed by two limiters(L1,L2), that produces the plasma parameters to be R=28.5cm, a=6.5cm, Ip=3-9kA. The RF power from transmitter(T) are at 10-20W(6-10MHz) for linear IBW launching and at 50-100W(1-2MHz) for AW excitation. Two sets of RF Langmuir probes(P1,P2) and CO_2 laser scattering system were used for detecting waves. Both probes were radically movable(P1 vertically and P2 horizontally) in which P1 is single-pin, and P2 is double-pin with a radial distance of 5mm between the two tips, the perpendicular wave number can be derived directly from the phase difference between the signals taking from the two pins (through band-filters BF and amplifiers AF to a phase discriminator PD). the plasma of low temperature in small tokamak allows the insertion of the probes to the interior of plasma without interfering seriously in discharges. The probe sensitivity to

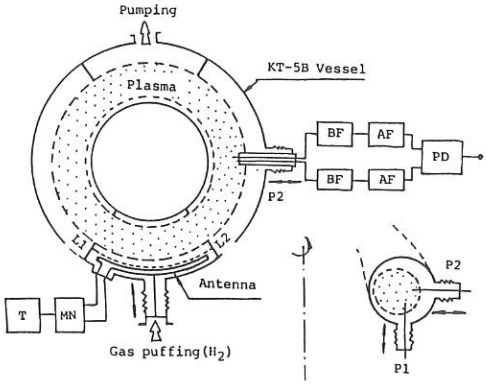

Fig.1. Diagram of experimental arrangement

plasma density fluctuation is below 5×10^{8} cm^{-3} and the position readout is better than 0.1mm, so that quite good spatial resolution can be reached on the bases of shots average.

II. IBW EXPERIMENTS

The experimental conditions for optimally exciting IBW and the estimation of the ion temperature profile in the outer region of the plasma from experimental IBW dispersion relation were reported elsewhere [2,3]. Here we are to report the experiments of IBW propagation.

According to the variation of IBW amplitude, tokamak plasma can be divided into three region: shadow region (r>a=6.5cm); edge region (a<r<5.5cm) and normal region (r<5.5cm). In shadow region, no signals related to IBW were detected, which means that IBW antenna disturbance was efficiently limited in antenna region by the limiters located at both the ends of antenna. In edge region, IBW amplitude varied quickly as it propagated towards plasma center and after one or two peaks its amplitude tended to a stable value. This phenomenon existed for all cases but the variable region get smaller when the frequency ratio ω/ω_{ci} at the antenna changed from 1.97 to 1.72 as shown in fig.2. In normal region, the IBW amplitude remained a relative stable value unless it reached the minority ions cyclotron resonance layer (ω/ω_{ci} = 1.5) (fig.1(c)).

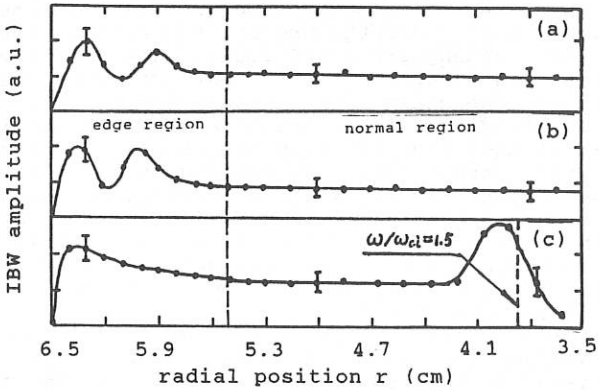

Fig.2. Variation of IBW amplitude as it propagates toward plasma center for the frequency ratio at antenna $\omega/\omega_{ci}|_{r=r_A}$= (a) 1.95; (b) 1.85 and (c) 1.72

It is noted that the edge region is a small region. The phenomena appeared in this region could not be explained as the result of interaction between IBW and plasma but probably the affection of the limiters on IBW propagation. Near the edge of plasma column, some component of IBW were shielded by the limiters and could not reach the probe position and coherent superposition of remained wave components may lead a variation picture of IBW amplitude.

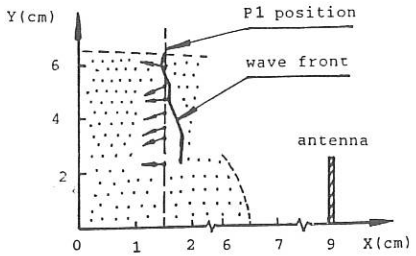

Fig.3. Typical wave front at the vertical chord of R=30cm. The small arrows represent the opposite direction of local wave vector of IBW.

By means of the vertically moved probe, the vertical wave number of IBW was measured and the typical wave front was figured in fig.3. It can see from fig.3 that the wave front near the plasma center goes somewhat backward comparing to that near the plasma edge, which was consistent with the minor section geometry.

III. Preliminary Observation of Alfven Wave Resonance

Recently, Alfven wave resonance was excited successfully by means of the longitudinal loop antenna in KT-5B tokamak, and quite interested experimental results were observed. The antenna loading deduced from the input RF power and the antenna current showed quite rich structure in the loading trace. These results are qualitatively consistent with the theory predications. Calculations made by employing the method similar to references [4,5] show that there are two non-trivial continuum modes (n,m)=(0,1) and (-1,1) under the present KT-5B tokamak experiment conditions. The loading are found to be quite sensitive to the plasma current and impurity level, but not sensitive to the magnetic field. As the plasma current increase to 6kA, there is a large (0,1) mode loading, while the plasma current decreases to 1.5kA, the (-1,1) mode appears. Keeping the plasma current at the intermediate value about 3kA, two modes coexist in the loading evolution, as shown in fig.4. The strong dependence of the loading on current is consistent with TCA results; the different effects of the current on the different modes are attributed to the sign in the formula m(m-1q)[6]. The dependence of the loading on the impurity level is attributed to the relative low β_e in KT-5B, which is also found elsewhere [7,8].

The loading peaks we observed can be interpreted as follows. According to kinetic theory, the singular resonance layer is replaced by mode conversion. In the region of $\beta_e > m_e/M$, the mode conversion process excites the kinetic Alfven wave (KAW) which propagates towards the interior of the plasma and is subsequently damped, heating the particles. Otherwise, the converted wave is reflected from the resonant layer, propagates towards the low density side, creating a surface electrostatic wave (SEW)[6,9]. Numerical result [9] revealed that in a small tokamak similar to KT-5B, when the electron temperature in the resonance area is around 50ev, the loading has strong dependence on the temperature, and large SEW loading peak appears. the DAW could also produce peaks in the loading spectrum [5], however, in our case, the loading peaks do not appear beneath the continuum threshold. For these reasons, we prefer to consider that the SEW

provide the dominant loading.

We have just begun the Alfven wave resonance experiments, resulting the primary, however, interested observations. Further investigation on the Alfven wave resonance and high power AWH experiment will be performed on the new tokamak KT-5C (upgraded KT-5B) in the near future.

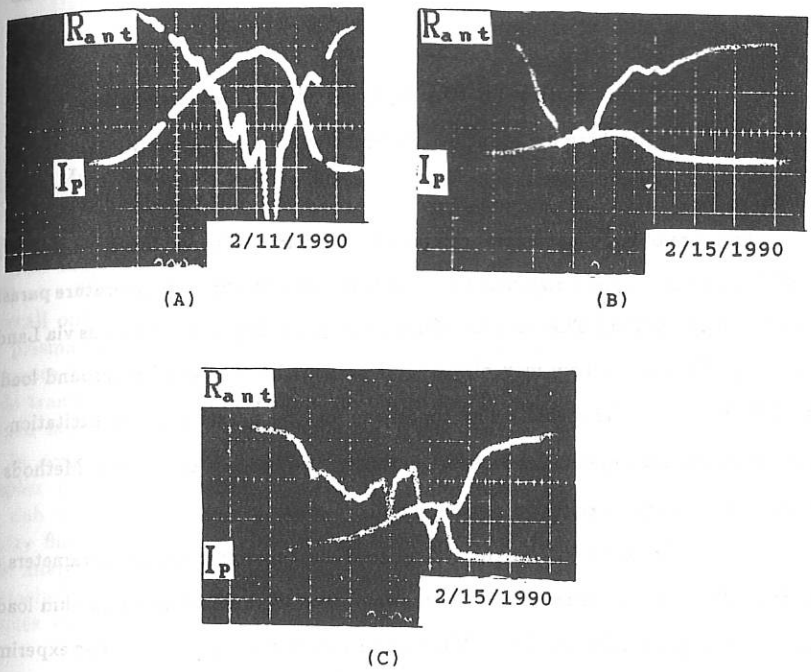

Fig.4. AWH antenna loading (10mΩ/div) at different plasma current(2kA/div), Ip= (a) 6kA; (b) 1.5kA; (c) 3kA (100μs/div)

REFERENCES

[1] M.Ono, T.Watari et al, Phys. Rev. Lett. 54,2239(1985)
[2] Liu Wandong, Wen Yizhi et al, Chinese Phys. Lett. 6,201(1989)
[3] Liu Wandong, Wen Yizhi et al, Acta Phys. Sinica, 39,212(1990)
[4] D.W.Ross et al, Nucl. Fusion, 26,139(1986)
[5] G.A.Collins et al, Phys. Fluids, 29,2260(1986)
[6] D.W.Ross et al, Phys. Fluids, 25,652(1982)
[7] M.Tanaka, T.sato and A.Hasegawa, Phys. Fluids B, 1,325(1989)
[8] T.Obiki et al, Phys. Rev. Lett. 39,815(1977)
[9] I.J.Donnelly et al, J. Plasma Phys. 36,75(1986)

EDGE-PLASMA HEATING VIA PARASITIC-TORSIONAL-MODE EXCITATION BY FARADAY-SHIELDED ION-BERNSTEIN-WAVE ANTENNAS

Satish Puri

Max-Planck Institut für Plasmaphysik, EURATOM Association,

Garching bei München, Federal Republic of Germany

Presence of large-k_z spectral component in Faraday-shielded Ion-Bernstein-Wave (IBW) antennas couples a significant amount of power to the finite-temperature parasitic torsional mode (PTM). The wave transfers its energy to the plasma electrons via Landau damping. This mechanism may play a vital part in the observed background loading in IBW heating experiments. The conditions for the parasitic mode excitation are examined and the antenna loading for some idealized cases is computed. Methods for minimizing parasitic excitation are discussed.

The antenna loading for the typical IBW heating experimental parameters due to the PTM is of the order of a few ohms compared to the fraction of an ohm loading contributed by the IBW itself. The PTM loading increases with frequency as experimentally observed. PTM loading also increases with density and Z_{eff} but monotonically drops at higher electron temperatures and for finer spacing of the Faraday shield conductors. However unlike the experiments, we do not find a strong dependence of the PTM loading upon the antenna phasing.

PROPAGATION ABSORPTION AND PARTICLE DYNAMICS OF ION-BERNSTEIN WAVE IN TOKAMAKS

A. Cardinali, R. Cesario, F. De Marco

Associazione EURATOM-ENEA sulla Fusione,
Centro Ricerche Energia Frascati
C.P. 65 - 00044 Frascati, Rome, Italy

INTRODUCTION

Direct launch of ion Bernstein waves has been considered in these last years as an alternative method for heating directly the ions in the central region of the plasma. Many experiments have been successfully performed in particular that of PLT [1] and Alcator [2,3] where a large amount of power has been coupled with a loop antenna to the plasma.

The coupling characteristics of the waveguide antenna that we want to use on FTU at a frequency of 433 MHz have been discussed elsewhere [4], here we want to recall only that they are very similar to that of the lower hybrid wave coupling. For plasma density typical of FTU and for the above mentioned frequency the LH resonance layer is located inside but in the very edge of the plasma. Hence the mode transformation from electron plasma to ion Bernstein wave [5] is expected to happen near the plasma edge and for very low density and temperatures.

In order to study the wave propagation and absorption of the IB mode the complex dispersion equation is solved in the complex domain of wavenumber in the slab geometry; so it is possible to calculate the electric field and the particle density fluctuations induced by the wave, by mean of the conductivity tensor. The same analysis is also presented when the effects of the three-dimensional geometry are included. The ray equations are thus solved in toroidal geometry using the complex dispersion function as Hamiltonian.

THE DISPERSION EQUATION

The electrostatic approximation which seems to be justified here because of the very high value of $k_\perp$ everywhere inside the plasma has led to the following dispersion relation:

$$\mathcal{E} = 1 + \sum_\alpha \frac{2\omega^2 p\alpha}{k^2 V_{th\alpha}^2}\left[1 + x_{0_\alpha}\sum_{-\infty}^{+\infty} I_n(\lambda_\alpha)e^{-\lambda_\alpha} Z(x_{n\alpha})\right] = 0 \qquad (1)$$

where

$$\lambda_\alpha = \frac{k_\perp^2 V_{th\alpha}^2}{2\Omega_{c\alpha}^2} \qquad x_{n\alpha} = \frac{\omega - n\Omega c\alpha}{k_\parallel V_{th\alpha}} \qquad (2)$$

and $Z(x_{n\alpha})$ and $I_n(\lambda_\alpha)$ are the plasma dispersion and the modified Bessel functions respectively. In the slab geometry eqn. (1) is solved in the complex plane of the wavenumber $k_\perp$ at each radial position (x) in the plasma.

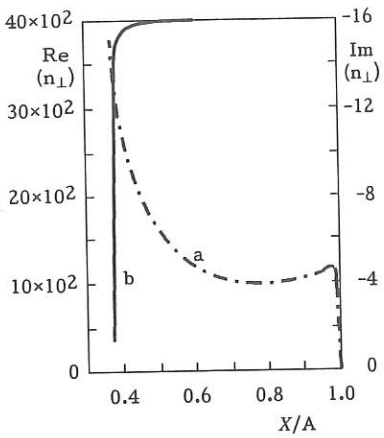

Fig. 1 – Real (a) and imaginary (b) parts of the perpendicular wavevector component plotted vs. the radial (x) coordinate normalized to the plasma radius $a = 35\,\mathrm{cm}$. $B_{oz} = 7.92T$, $\hat{n}_{e_o} = 3.5 \cdot 10^{14}\ \mathrm{cm}^{-3}$, $\hat{T}_{e_0} = \hat{T}_{i_0} = 1.5k$ eV, $f_0 = 433\,\mathrm{MHz}, k_{\parallel}\frac{c}{\omega_0} = 5$, $P_{RF} = 100\,\mathrm{KW}$. Area of the waveguide antenna $L_y \cdot L_z = 40 \cdot 8\ \mathrm{cm}^2$. Hydrogen harmonic locations:
$\frac{x}{a}|_{4\omega_{CH}} = 0.3$ $\frac{x}{a}|_{5\omega_{CH}} = 1.05$

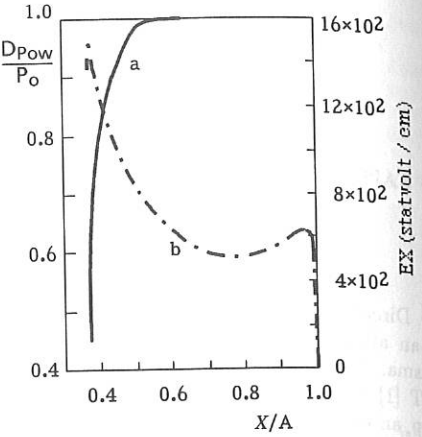

Fig. 2 – Normalized rf power (a) and electric field intensity (b) plotted vs $\frac{x}{a}$ for the same parameters of fig. 1.

The numerical method for finding the complex roots of eq. (1) is based on the Newton formula in the complex domain of variables and needs an initial guess to start.

In fig. 1a, b we show the evolution of $k_{\perp}^{\mathrm{real}}$ and $k_{\perp}^{\mathrm{imag}}$ vs. x for two different values of $k_{\parallel}$ $(k_{\parallel} = 2,5)$.

In fig. 1a can be recognized the mode transformation layer located near $x = 0,95$; there the electron plasma linearly transforms in the Bernstein wave which propagates freely toward the $\omega = 4\Omega_{ci}$ resonance where it will be totally absorbed by the ions. This can be seen in fig. 2 where the curve a represents the normalized power plotted vs x.

The curve b of fig. 2 shows the trend of the radial (x) component of the electric field. The electric field at the waveguide antenna mouth (on the plasma side) is calculated from the net rf power P_{rf} by requiring the conservation of the power flux across the waveguide–plasma interface:

$$\xi_{ac} P_{rf} = W_T(x_{w_G}) v_{gx}(x_{w_G}) L_y L_z$$

where ξ_{ac} is the fraction of accessible power (in the IBW experiment $\xi_{ac} \simeq 1$ is expected), $W_T = (E^2/16\pi)\frac{\partial \omega \varepsilon}{\partial \omega}$ is the total wave energy density and $L_y L_z$ is

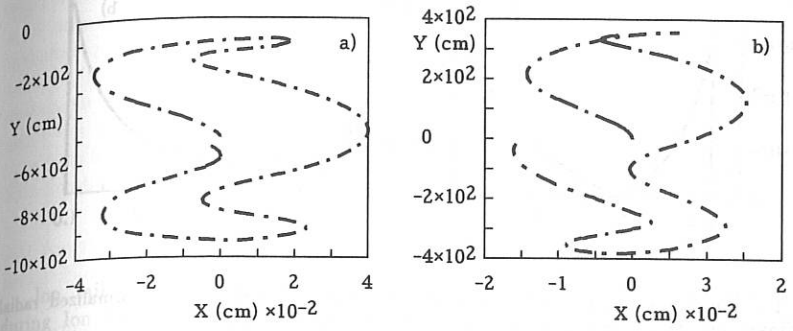

Fig. 3 – Ion trajectories in the plane perpendicular to the static magnetic field in different radial position:

$$\text{(a)}, \quad \frac{x}{a} = 0,4 \; ; \quad \text{(b)} \; , \quad \frac{x}{a} = 0,6 \; .$$

the total area of the waveguide array. The radial (x) electric field component is calculated in taking into account the conservation of the component parallel (z) to the static magnetic field in the slab geometry. The plasma density and temperature are assumed to vary along the x direction by: $n_e = n_e(0)\left[1 - \left(\frac{x}{a}\right)^2\right]$ and $T_e = T_e(0)\left[1 - \left(\frac{x}{a}\right)^2\right]^2$, where a is the limiter radius.

In order to have an idea of the ion motion induced by the IB wave we have integrated the velocity equation for a single particle. In fig. 3a, b, is shown the ion trajectories in the plane perpendicular to the static magnetic field in two different radial (x) positions. The shape of the curves depends on the distance from the ion-cyclotron harmonic resonances and the local value of the electric field.

Fig. 4a, b show the fluctuating particle density plotted vs. the radial (x) coordinate. As a particular feature of the ion response, we observe that the fluctuating ion density goes to zero at $\frac{x}{a} = 0.98$ and $\frac{x}{a} = 0.60$. This fact is due to the opposite contributions of the terms $k_x \sigma_{ixx}$ and $k_x \sigma_{izx}$.

This unidimensional picture is not satisfactory because does not account for the three dimensional effects due to the toroidal geometry. In fact when we consider the toroidal geometry $k_\parallel$ remains no longer constant and its variation along the trajectory could lead to a different behaviour of the absorption of the wave.

RAY–TRACING EQUATIONS

For having a more realistic picture of the wave propagation and absorption, we have solved the ray–equations in toroidal geometry having considered that the dispersion relation which plaies the role of Hamiltonian is a complex quantity.

The numerical solution of the ray equations has led to follow a ray of the IBW in a toroidal geometry. The ray, after a very short path in radial direction,

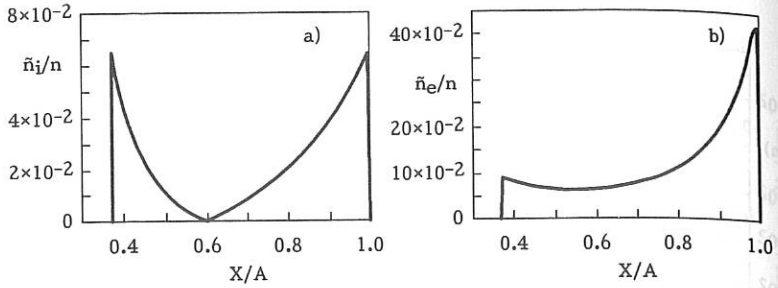

Fig. 4 – Ion (a) and electron (b) fluctuating density plotted vs. the normalized radial coordinate for the same parameters of fig. 1, and $P_{RF} = 1\,KW$.

is totally absorbed very near the plasma edge, this owing to a strong variation of $k_{\|}$ along the ray–path.

CONCLUSIONS

The IBW heating seems to be particularly indicated for tokamak–like reactor devices because the power can be coupled to the plasma by a waveguide antenna. Calculations on the propagation and absorption have been presented for FTU in the slab and toroidal geometry (ray–tracing technique) and it seems that IBW heating is very well indicated for FTU. Particular care is requested in the definition of the $k_{\|}$–spectrum at the antenna because a strong variation of the wavenumber due to the toroidal effects can lead to an anomalous peripheral deposition of the wave energy.

REFERENCES

[1] M. Ono et al. Phys. Rev. Lett. **60**, 294 (1988).
[2] J.D. Moody, T. Porkolab et al., Phys. Rev. Lett. **60**, 298 (1988).
[3] J.D. Moody, M. Porkolab, Phys. Fluids B1 (8), 1675 (1989).
[4] M. Brambilla, private communication.
[5] M. Ono, Phys. Fluids **25**, 990 (1982).

MODELLING OF THE INTERACTION OF ENERGETIC IONS WITH LOWER HYBRID WAVES ON JET

E. Barbato

Associazione EURATOM–ENEA sulla Fusione,
Centro Ricerche Energia Frascati
C.P. 65, 00044 Frascati, Rome, Italy

INTRODUCTION

Ion tail up to several MeV are generated and confined in the Jet plasma during Ion Cyclotron Heating (ICRH) experiments. When injecting Lower Hybrid Radiofrequency (LHRF) power at 3.7 GHz, such ions interact with LH waves limiting the current drive efficiency of the LH system. To study this problem a 1-D model (in the velocity space) for the wave–ions interaction has been developed which includes, besides the collisional diffusion and drag, the quasilinear LH and ICRF diffusion terms. To calculate the competition in the absorption between electrons and ions this model has been coupled to a deposition code for LH waves [1]. In sec. 1 the 1–D model and the deposition code are presented. Sec. 2 is devoted to the discussion of the numerical results. Then conclusions follow.

THE MODEL

In order to find the ion Distribution Function (DF), the steady state Fokker–Planck (FP) equation is considered, as in refs [2,3], supplemented with the IC and LH quasi–linear (QL) diffusion terms. The 1–D model of this equation is found adopting the usual Stix procedure [3] for IC waves. The following equation for the isotropic part, f_0, of the DF is obtained:

$$\frac{\partial f_0}{\partial t} = \frac{1}{\tau_s v^2}\frac{\partial}{\partial v}\left[\frac{T_i}{m_i v}\left(v_c^3 + \frac{T_e}{T_i}v^3\right)\frac{\partial f_0}{\partial v} + (v^3 + v_c^3)f_0 + v^2\tau_s(H_{IC} + H_{LH})\frac{\partial f_0}{\partial v}\right] \quad (1)$$

where τ_s and v_c are the slowing down time and the critical velocity of the minority.

The third term in eq. (1) is the QL contribution due to the IC waves which, for minority heating at the fundamental harmonic, reads: $H_{IC} = W(3n_s m_s)^{-1}K(r)$. W is the absorbed power density, n_s and m_s the minority density and mass and $K(r)$ the ICRH deposition profile. The last term in eq. (1) is the QL contribution of LH waves [2],

$$H_{LH} = \frac{\pi}{4}\frac{Z_s^2 e^2}{m_s^2\omega}\frac{c^3}{v^3}\int dn_\parallel \frac{|E(n_\parallel)|^2}{n_\perp^3(n_\parallel)}U\left(1 - \frac{c^2}{n_\perp^2 v^2}\right) \quad (2)$$

where $n_\parallel(n_\perp)$ is the wave refractive index component parallel (perpendicular) to the magnetic field. $n_\perp$ is related to $n_\parallel$ through the warm electromagnetic LH dispersion relation. $|E(n_\parallel)|^2$ is the wave energy spectrum and U is the step function indicating that only ions with $v > c/n_\perp = v_{RES}$ are able to interact with the LH waves [4]. The solution, for $v > v_c$ reads $f_0(v) = f_0(v_1)\exp[-\int_{v_1}^{v} dv\ v(\tau_s(H_{IC} + H_{LH}))^{-1}]$ where v_1 is a reference velocity. For $v < v_{RES}$ where $H_{LH} = 0$ or $v \gg v_{RES}$ where

$H_{LH} \to 0$, $f_0(v)$ reduces to the Stix solution, a maxwellian with a temperature $T_{IC} = \tau_s W/(3n_s)$. For $v \cong v_{RES}$ the contribution due to H_{LH} gives rise to a larger temperature $T = T_{IC} + T_{LH}$ with $T_{LH} = \tau_s m_s H_{LH}$. For the parameters considered in this paper T_{LH} is, for example, of the same order of T_{IC} when $P_{LH} \sim 3P_{IC}/(4/k_\parallel dr)$, where dr is the radial extension of the ICRF deposition profile. The LH wave effect on the ion DF is to flatten f_0 in the region $v \sim v_{RES}$ (for a narrow spectrum) or in the whole resonance region $c/n_{\perp MAX} < v < c/n_{\perp MIN}$ (for a wide spectrum). Note that for $v > c/n_{\perp MIN}$ the behaviour of f_0 is dominated by H_{IC}.

To analyze the competition in the absorption between ions and electrons this model (eq. 1) has been coupled to a deposition code for LH waves [1,2] which solves selfconsistently the LH wave transport equation and the QLFP equation for the electron DF. In the wave propagation model only first pass absorption solutions of the wave transport equation are considered and a cylindrical geometry is assumed. Then $n_\parallel$ is taken constant during propagation.

NUMERICAL RESULTS

All the results reported hereafter refer to the following hot ion mode Jet plasma target: minor radius $a = 1.4m$, major radius $R = 3.15m$, toroidal field $B = 3.2T$, effective ion charge $Z_{EFF} = 3$, peak electron temperature $\hat{T} = 9k$eV, peak ion temperature $\hat{T} = 18k$eV, peak electron density ranging between 2. and 5 10^{13} cm^{-3}. Parabolic density profiles and squared parabolic temperature profiles are taken. The LHRF power is assumed to be launched into the plasma according to a gaussian $n_\parallel$ spectrum $P(n_\parallel) = P_0 \exp((n_\parallel - \overline{n}_\parallel)^2/dn_\parallel^2)$ with $\overline{n}_\parallel = 2.3, 2.5, 2.7$, and $dn_\parallel = 0.2$. 10MW of ICRF power have been assumed to be coupled to the plasma according to a deposition profile of gaussian type, centered at $r = 0$ to simulate ICRH on axis, or at r=60cm to simulate ICRH off axis. To take into account the trapped banana orbit excursion afar from the magnetic surface, those profiles are taken broader (~ 40 cm) than those resulting from the standard ICRH deposition profile calculations [6]. A minority concentration of 5% has been considered for both H^+ and $^3He^{++}$ minority heating at the fundamental harmonic.

Fig. 1 shows, as an example, the LH power deposition profile on electrons and on $^3He^{++}$ ions at $\hat{n}_e = 3.2\ 10^{13}$ cm^{-3}, $P_{LH} = 6MW$ and $n_\parallel = 2.7$ for the ICRH off axis deposition case. Fig. 2 shows the $^3He^{++}$ DF at r=60cm. A flattening appears at $E = 2M$eV, corresponding to the $^3He^{++}$ resonant energy at that radial position.

Since the tail produced by ICRF are so extended toward high energy, LH wave–ion interaction occurs every time the LH power reaches the region where the ion tail lives, i.e. the region where $K(r)$ differs from zero. The ICRH deposition profile on the ions is rather well known [6], while the LH deposition is still matter of theoretical discussion and experimental investigation. So, what we can think to do, actually, is to change the LH deposition and study the absorption by fast ions when the LH deposition changes. The maximum absorption capability by fast ions will occur when the ICRH and LH deposition overlap. In the present propagation model the LH power penetration depends on $\overline{n}_\parallel$, P_{LH} and n_e, since the deposition

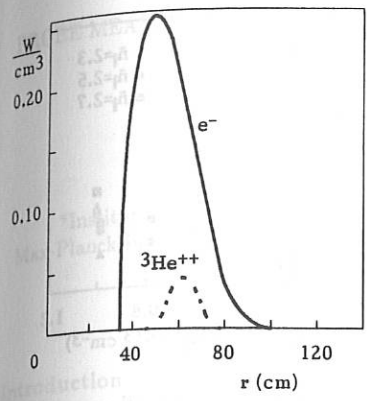

Fig. 1 – LH power density absorbed by electrons and by $^3He^{++}$.

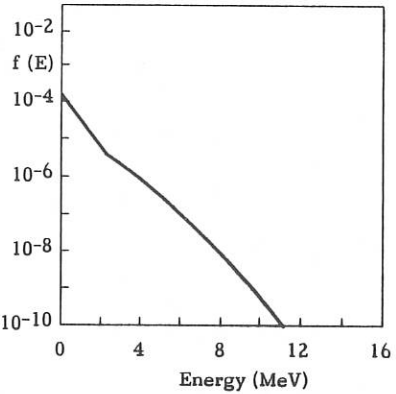

Fig. 2 – $^3He^{++}$ DF at r=60cm as it results from the solution of eq. (1).

on the electrons depends on these parameters. Penetration improves the lower are $\overline{n}_\parallel$ and n_e and the larger is P_{LH}. So different $n_\parallel$ (2.3,2.5,2.7), P_{LH} (2,4,6,8, 10MW) and $\hat{n}_e$ values (2,3.2, 4, 510^{13} cm^{-3}) have been considered. All the results of these deposition calculations are collected in Fig. 3 where the percentage of the LH power absorbed by H^+ (H^+ minority heating) is shown as a function of $P_{LH}/\hat{n}_e^2$ for the different launched $\overline{n}_\parallel$ values. The ICRH deposition profile for this case is the central one. As shown in the figure the maximum absorption capability ($\sim 22\%$) occurs for $\overline{n}_\parallel = 2.3$ and at high $P_{LH}/\hat{n}_e^2$ values when LH power achieves the center. This could be a quite irrealistic situation since toroidal effects (not considered in the present LH propagation model) generally prevent such a central LH deposition. Nevertheless central interaction between LH waves and high energy ions has been experimentally observed on Asdex [7] during combined 1.3 GHz and neutral beam injection experiment.

Increasing the ICRF power up to 20MW enhances the LH absorption by H^+, especially at low $P_{LH}/\hat{n}_e^2$ and brings the maximum absorption capability to 25%. For the off axis ICRF deposition case the absorbed power by H^+ ranges between 15% (at low $P_{LH}/\hat{n}_e^2$ and $\overline{n}_\parallel = 2.7$) and 30% (at high P_{LH}/n_e^2 and $\overline{n}_\parallel = 2.3$).

Similar calculations have been performed for the $^3He^{++}$ minority heating case. First, we note that for the same W/n_s value, T_{IC} for $^3He^{++}$ is 3/4 smaller that T_{IC} for H^+. Second, the $^3He^{++}$ resonant energy is 3 times larger. As a consequence the $^3He^{++}$ population able to interact with LH waves is smaller than the H^+ population for the same plasma condition. Then we expect a lower absorption of LHRF power by $^3He^{++}$. Fig. 4 shows the percentage of LH power going to $^3He^{++}$ accelerated by 10MW of ICRF power according to an off axis deposition. In this case absorption is larger for larger $\overline{n}_\parallel$–values. Indeed increasing $\overline{n}_\parallel$ makes the deposition more peripherical but makes also the ion resonance energy

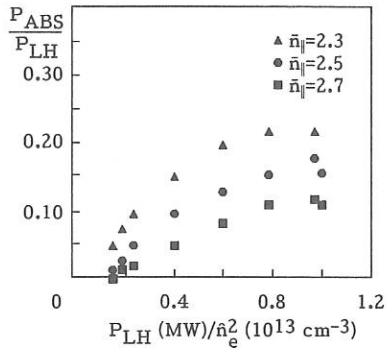

Fig. 3 – Fraction of the LH power absorbed by H^+ vs $P_{LH}/\hat{n}_e^2$ for 3 $\overline{n}_{\|}$ values, during on axis ICRH.

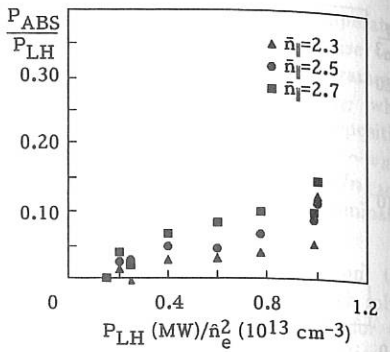

Fig. 4 – Fraction of the LH power absorbed by $^3He^{++}$ vs $P_{LH}/\hat{n}_e^2$ for 3 $\overline{n}_{\|}$ values, during off axis ICRH.

smaller. The two effects compete and, in this case, the second one dominates. The maximum absorption capability is actually 15%.

CONCLUSIONS

The effect of LH waves on the ion DF (which remains mainly distorted by the ICRF waves) is to flatten the DF close to the resonant region. The temperature outside such region is dominated by the ICRF term. For given plasma and RF conditions, the percentage of the LH power absorbed by the fast ions depends on the overlapping degree of the LH and ICRH deposition profiles. The percentage of LH power absorbed by fast H^+ has been found to range between few percents up to 30%in the worst cases. While the $^3He^{++}$ absorption capability results lower and ranges between few percents up to 15%.

This work was supported by the art. 14 JET contract n. JJ9/9001.

REFERENCES

[1] E. Barbato, *Theory of Fusion Plasmas*, Lausanne (1988), 577.

[2] E. Barbato, F. Santini sub. for publication.

[3] T.H.S. Stix., in *Application of RF waves to tokamak plasmas*, (course and workshop, Varemia) **1** (1985) 251.

[4] C.F.F. Karney, Phys. Fluids **22** (1978) 2188.

[5] N.J. Fisch, Rev. Mod. Phys. **59** (1987) 175.

[6] F. Tibone et al., 15th Europ. Conf., Dubrovnik (1988) Vol. 2, 709.

[7] F. Ryter et al., 13th Europ. Conf., Schliersee (1986) Vol. 1, 101.

PROBE MEASUREMENTS OF LOWER-HYBRID WAVENUMBER SPECTRA IN THE ASDEX EDGE PLASMA

M.Krämer*, A.Carlson, and the ASDEX-Team,

*Institut für Experimentalphysik II, Ruhr-Universität, D-4630 Bochum,
Max-Planck-Institut für Plasmaphysik, EURATOM Association, D-8046 Garching,
Fed. Rep. Germany

Introduction

Knowledge of the lower-hybrid (LH) wavenumber spectra is of basic importance to understand lower-hybrid heating (LHH) and lower-hybrid current drive (LHCD) in tokamak plasmas. A useful method to obtain information on the wavenumber spectra is the two-point correlation analysis with probes. In the present investigation, this diagnostics - often used to study low-frequency turbulence - is applied to investigate both the low-frequency flucuations and the high frequency waves launched into the plasma by means of the LH grill antenna. Thus, the influence of the low-frequency turbulence on the high-frequency LH waves (scattering) as well as the effect of the RF fields on the LF fluctuations can be studied. One important question of these investigations is wether the measured RF spectra are similar to the expected (theoretical) antenna spectra.

Experiment

Due to the strong heat load of the probes, the measurements can be performed only in the edge plasma outside the separatrix (minimum radial position $3-4cm$ with respect to the grill mouth). Hence, we are limited to the region outside the LH resonance cone and, thus, only indirect information on the LH spectra can be obtained. Here, the densities are one order of magnitude lower than in the plasma center and the LH wave dispersion changes into the dispersion of plasma waves, i. e. $k_\perp/k_\parallel = \omega_{pe}/\omega$.

LF and RF Correlation Analysis[1]*:* A square array of four RF probes (coaxial leads to the tips, probe tips from Molybdenum, $r_p = 0.3mm$, $L_p = 1mm$, probe distance $3mm$, one probe $2mm$ radially extended) is used to detect the signals in the edge plasma of ASDEX $83\,cm$ distant from the LH grill antenna. The RF signals ($f_0 = 2.45GHz$) are converted into the LF range by heterodyning ($f_{LO} = f_0 + 250kHz$) before they are transmitted to a transient digitizer (sample rate $1MHz$). Simultaneously, the LF fluctuation signals are taken whereby the probe tips are biased into the ion saturation regime. From each pair of the four Fourier-analysed signals (RF and LF signals, respectively), we obtain one phase difference as a function of frequency. Altogether, we have three phase differences which can be related to the three wavenumber components. Using the statistical method as described by Beall et al.[2], an estimate of the spectral density $S(\mathbf{k},\omega)$ can be computed. Two different sets of measurements were taken: measurements with fast (F) probe

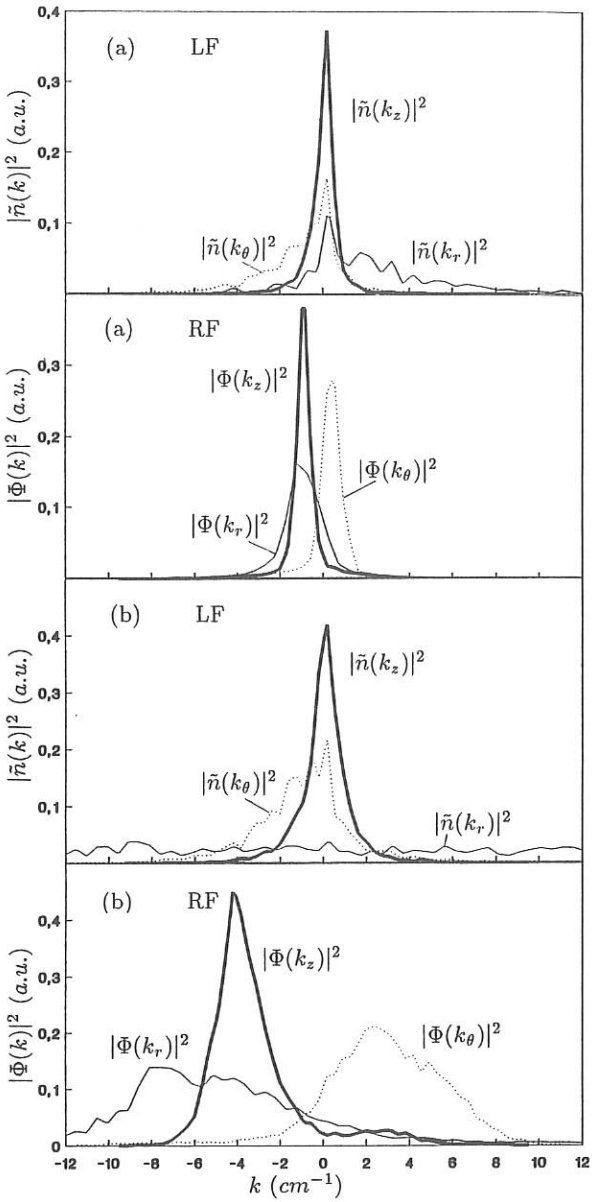

Fig.1 LF and RF wavenumber spectra (frequency-integrated spectral density) for LHH ($0\pi0\pi$ grill phasing) at $r = 209cm$ ($r_{grill} = 212.5cm$).- (a) $P_{RF} = 30kW$, (b) $P_{RF} = 780kW$.- $B_0 = 2.8T$, $I_p = 460kA$.

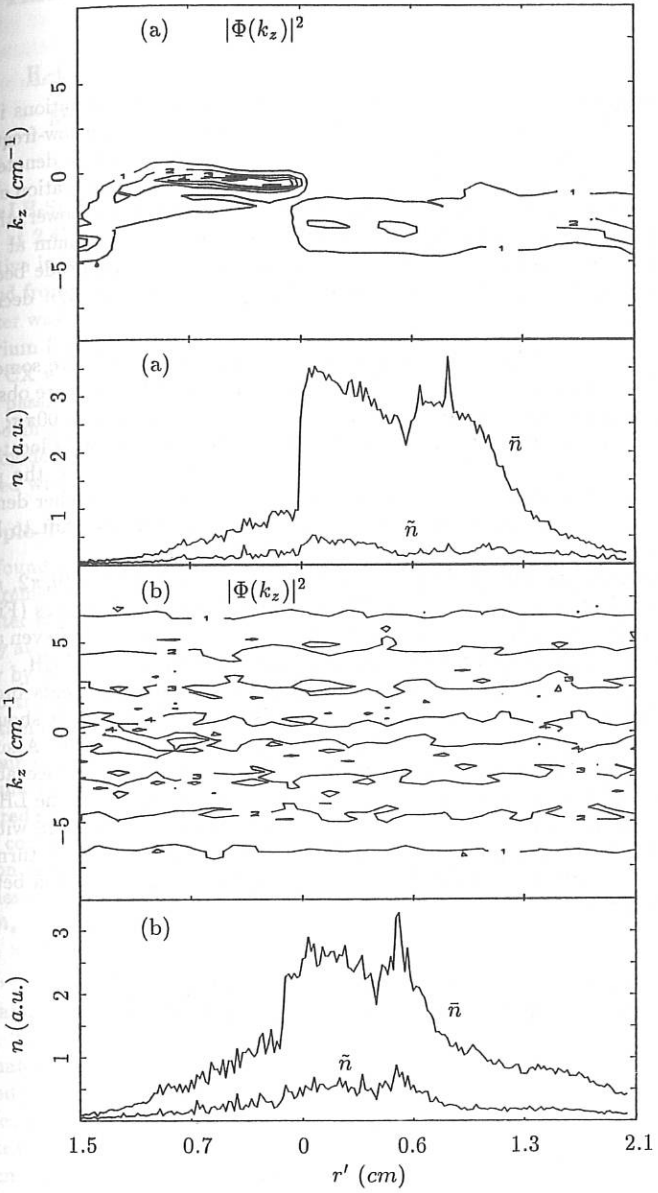

Fig.2 Radial profiles of the RF parallel wavenumber spectra and the mean and the fluctuating density for (a) LHH, $P_{RF} = 90/780kW$ and (b) LHCD, $P_{RF} = 60/510kW$.- Jump of the RF power slightly before the maximum probe position ($r' = 0$ or $r = 209cm$).

motion ($\tau \approx 50msec$, one spectrum per shot) and measurements with slow (S) probe motion ($\tau \approx 1sec$) enabling one to take radial profiles of the spectra.

Results

Low Frequency Spectra: The main features of the low-frequency fluctuations in the presence of the RF fields are as without additional heating: (1) The low-frequency turbulence is mainly two-dimensional, i. e. $k_z \approx 0$ (Fig. 1. Here, z denotes the direction parallel to the magnetic field). (2) The main portion of the fluctuation energy travels in ion diamagnetic (negative θ) direction.- With increasing RF power, the LF fluctuation spectra broaden in wavenumber and frequency (power maximum at a few kHz). In addition, the mean density and the density fluctuation amplitude becomes appreciably larger at higher RF powers whereas the fluctuation level $\tilde{n}/n$ decreases (Fig. 2).

High Frequency Spectra: The results of the RF spectral measurements are somewhat different for the two sets of shots. For the F-measurements, the RF waves are observed to propagate in negative toroidal direction for all antenna phasings ($0\pi0\pi$; $00\pi\pi$; $0, \pi2, \pi, ...$). This is in agreement with the expectation since the probe array is located on the left-hand side of the grill. For lower densities ($n_e \approx 2 \times 10^{19} m^{-3}$), the power maxima are observed roughly at the antenna wavenumber whereas, at higher densities ($n_e \approx 4 \times 10^{19} m^{-3}$), spectral broadening is seen and the RF spectra shift to larger parallel wavenumbers.

The S-measurements were performed with LHH ($0\pi0\pi$)- and LHCD ($0, \pi2, \pi, ...$)-phasing of the grill at a density $n_e \approx 4 \times 10^{19} m^{-3}$ and different RF powers (Figs. 1 and 2). In the latter case (Fig. 2b), the k_z-spectra become extremely broad even at the lowest RF powers although the LF turbulence is similar as in the case of LHH.

For LHH (Figs. 1 and 2a), the spectra of all wavenumber components broaden and shift to larger wavenumbers when the RF power is raised. Moreover, it should be noted that the radial component of the phase velocity is directed inward. Assuming the dispersion of plasma waves which are known to be backward waves (see above), one can conclude with some care that one portion of the RF power leaves the LH cone and reaches the plasma edge. Finally, comparing the RF wavenumber spectra with the corresponding LF spectra, in particular the poloidal wavenumber spectra, it turns out that the spectra are strongly correlated thus indicating the strong interaction between the RF waves and the LF turbulence.

[1] M.Krämer, N. Sollich, and J. Dietrich, J. Plasma Phys. **39**, 447 (1988).
[2] J.M.Beall, Y.C.Kim, and E.J.Powers, J.Appl.Phys. **53**, 3933(1982).

TRANSITION FROM ELECTRON- TO ION- INTERACTION OF LH-WAVES IN ASDEX

H.-U. Fahrbach, W. Herrmann, F. Söldner, LH-Team, ASDEX-Team

Max-Planck-Institut für Plasmaphysik, EURATOM Association
D-8046 Garching, Fed. Rep. Germany

The LH-System of ASDEX is described in [1]. In our experiments up to 1 MW LH-power at 2.45 Ghz was launched into deuterium plasmas for 1s. Wave spectra with a refractive index $\bar{N}_{\|}$ up to 4.4 were applied. The line-averaged electron density $\bar{n}_e$ was scanned from 1.3 to $5.4 \times 10^{19} m^{-3}$ at a plasma current of 420 kA. A neutral particle analyzer was used to measure the perpendicular charge-exchange neutral hydrogen and deuterium flux up to 10 and 20 keV, respectively. In addition to the passive method active CX was applied with a diagnostic neutral hydrogen beam. The main advantage of the passive analysis is its continuous applicability during the discharge. The active method in principle allows space-resolved measurements, but normally in the pulsed beam mode only. Comparing the results of both methods can help to localize phenomena detected with the passive method.

Ripple-Trapped Particles

As found already in earlier investigations, the neutral flux in passive line integrated measurements increases strongly during LH-heating, if the analyzer is viewing through the outer region of the plasma in the drift direction of ripple-trapped ions. This flux is usually attributed to ripple trapped ions which have gained sufficient high perpendicular energy by interaction with the LH-waves. They drift out of the plasma before they are able to transfer their energy to the bulk plasma. The flux disappears within the time resolution of the analyzer (ca. 1ms), when the LH-power is switched off [2, 3].

In our experiments this fast neutral flux was measured with the analyzer viewing a plasma radius of 30 to 35 cm. The spectra of deuterium and hydrogen flux were measured up to 10 and 20 keV, respectively. The slope of the spectrum at higher energies would correspond to temperatures of about 1 to 4 keV, if a maxwellian distribution function is assumed. The passive flux at two energies is shown for different plasma densities and LH-spectra in Fig.1. With $\bar{N}_{\|}= 2.2$ it rises roughly linearly with density up to $\bar{n}_e = 4 \times 10^{19} m^{-3}$. Between 4 and $5.4 \times 10^{19} m^{-3}$ the rise is many times steeper. At $5.4 \times 10^{19} m^{-3}$ the H^o-flux is considerably higher than the D^o-flux at the same energy, although in the ohmic phase of these discharges it is 5 to 10 times smaller.

We attempted to locate the fast particles by measurements with the active doping beam. The active signal is locally defined to the plasma volume common to the approximately vertical diagnostic beam and the analyzer sightline, which enters from the outer edge. To the passive signal all parts of the sightline can contribute so far as the particles are not lost on their path through the plasma. No fast deuterium particles up to 10 keV could be found in the plasma region along the beam inside the plasma radius of 35 cm. For hydrogen, which could be analyzed up to 20 keV, the situation is not that clear. Here a flux of fast particles can be seen. This, however, is independent on

density and LH-power and is present even in ohmic discharges and can be attributed to double charge-exchange of diagnostic beam particles. It therefore seems to be justified to conclude, that the fast particles are generated and present only at the plasma edge.

At lower plasma densities the LH-waves interact predominantly with the electrons and ions are heated consecutively by collisions with the electrons. With increasing density electron heating drops and the LH-waves start to interact directly with the ions [4]. The observed strong flux rise of fast particles between 4 and $5.4 \times 10^{19} m^{-3}$ indicates the transition region from electron- to ion-interaction of LH-waves.

Measurements with LH-waves with higher refractive index $\bar{N}_{\|}= 4.4$ were performed at a density of $\bar{n}_e = 2.8 \times 10^{19} m^{-3}$. The detected neutral fluxes are much higher than for $\bar{N}_{\|}= 2.2$ at the same density. Also here the H^o-flux is stronger than the D^o-flux at the same energy. This is indicates an improvement of LH-ion-interaction with both: increased $\bar{N}_{\|}$ and reduced particle mass, i.e. smaller difference between wave and particle energy.

Ion Temperature Determination

From the actively and passively measured spectra ion temperatures were derived. Radial profiles were gained by variation of the vertical inclination of the analyzer sightline on a shot to shot basis. Only the side opposite to the ion drift direction was used for temperature evaluation. In Fig. 2a the central ion temperature difference to the ohmic phase before LH-heating is plotted against density. Fig 2b shows the central electron temperature difference obtained with the YAG-laser system. The large scatter of the points are due to the uncertainties of the measurements and the fact that different experimental situations are summarized in the data. Fig. 2b also shows the range of the central ion temperature one would expect for pure wave-electron interaction and subsequent ion heating through equipartition with the electrons. Ion temperatures were calculated from measured electron temperatures and densities under the assumption that the confinement in the inner region of the plasma does not change from OH- to LH-phase. As can be seen in the diagram the ion temperature would increase with density and above $\bar{n}_e = 3 \times 10^{19} m^{-3}$ it would fall again.

Comparing Figs. 2a and b one can see that up to $\bar{n}_e = 3 \times 10^{19} m^{-3}$ the measured ion temperatures are consistent with pure direct electron heating. Towards higher densities they exceed more and more the values from the calculation described above. This, however, cannot be regarded as an indication for direct ion heating near the plasma center, because it is questionable, whether the temperatures obtained by the passive method are actual central temperatures in this situation, as will be discussed below. Regarding the data in detail one can find one point only, which is - within the uncertainties of the methods - definitely in contradiction to pure direct electron heating. This point is a passive measurement and therefore lacking space resolution. Active measurements were not possible at this density. The points at $\bar{n}_e = 4 \times 10^{19} m^{-3}$ are rather close to the range defined by the calculation.

Temperature Decay Time

The argument against the central temperature interpretation of these passive results is the short decay time of this temperature after switching off the LH-power. This decay

time decreases with density, whereas the LH temperature increases. At the highest density the decay time is shorter than 10 ms and after 20 ms the passive temperature has reached the ohmic value again. This decay is too fast to possibly refer to the central bulk plasma and it is clearly slower than that of the ripple trapped particles. One has to consider the possibility that the passive thermal spectrum is flattened by the superposition of other unidentified contributions. Their intensity cannot be much higher than that of the bulk plasma but just sufficient to produce a slight curvature of the spectrum. No high energy tail can be identified in the spectra from the central region. In the passive spectra which are recorded when the analyzer is inclined towards the plasma edge opposite to drift direction one can find two regions which may be attributed to different origin. The low energy part is similar to the ohmic case spectra at this radius, and from about 3 to 7 keV the spectrum has a rather constant slope which is typical for a temperature around 1 keV. These observations are consistent with the assumption that during LH there may "warmer" particles be created not far from the plasma edge, which are quickly lost, possibly by charge-exchange with the high neutral density there. Active data would then reflect the central temperatures, but the passive ones might be considerably overestimated. This is indicated by the arrow in Fig.2a.

Summary

CX-measurements show an increase of suprathermal neutral flux with density during LH-heating. For deuterium and $\bar{N}_{\|}$=2.2 the effect is week below $\bar{n}_e = 4 \times 10^{19} m^{-3}$, between 4 and $5.4 \times 10^{19} m^{-3}$ the dependence is much stronger, indicating that the transition from electron- to ion- interaction of LH-waves takes place in this range. For hydrogen and for LH-waves with $\bar{N}_{\|}$= 4.4 a comparable strong effect is observed already at the low density of $3 \times 10^{19} m^{-3}$ Direct wave-ion-interaction, however, is confirmed only for the plasma edge. The ion temperature increase during LH-heating found at high densities decays with a time constant of 5 to 15 ms after LH-power being switched off and can therefore not be regarded as bulk plasma heating. There are indications that the passive charge-exchange spectrum from the centre is deviated by contributions of moderately heated ions near the plasma edge.

Acknowledgement

We would like to thank our collegues from Ioffe Institute, Leningrad, for providing the CX analyzer, and their assistance in putting it into operation. We also wish to acknowledge gratefully the operation of the diagnostic beam by Dr. H.M.Mayer.

The Lower-Hybrid experiments are performed in collaboration between IPP Garching and ENEA Frascati and PPPL Princeton.

References

[1] F.Leuterer et. al., 16th EPS-Conf., Venice 1989, part 4, p.1287;
[2] F.Leuterer et. al., Plasma Physics and Contr.Fusion, Vol. 27, p.1399 (1985);
[3] F.Leuterer et. al., 10th IAEA-Conf. London 1984, Vol. 1, p.597, Vienna (1985);
[4] F. Söldner et al., Workshop on Applications of RF-Waves to Tokamak Plasmas, Varenna (1985), Vol. 2, p.740

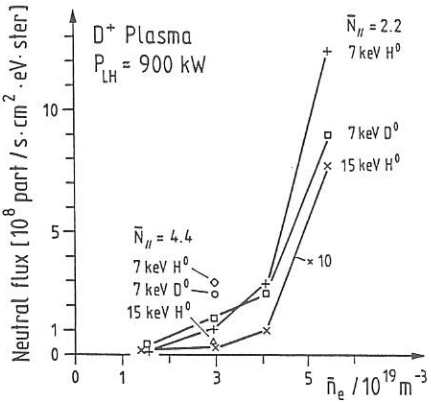

Fig. 1: Passive neutral flux for analyzer sight line tangential at plasma radius of 32 cm in the ion drift direction.

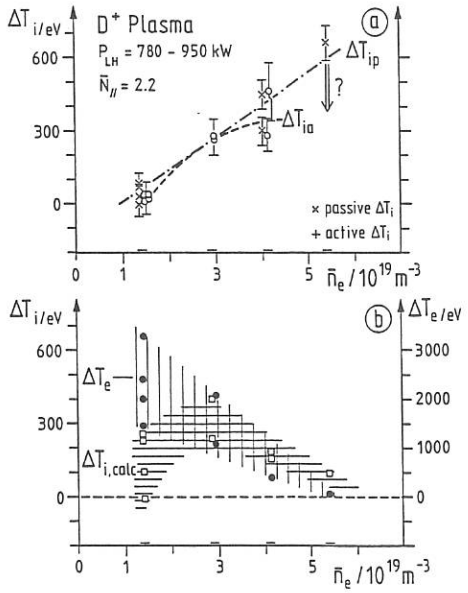

Fig.2a: Ion temperature increase during LH deduced from passive (ΔT_{ip}) and active (ΔT_{ia}) measurements viewed through the plasma centre. The arrow indicates that the passive values are probably overestimated.

Fig.2b: Temperature increase of electrons (measured) and ions (calculated for pure wave-electron interaction).

ALFVEN WAVE HEATING IN ASDEX

G.Besson, G.G.Borg, J.B.Lister, Ph.Marmillod.

Centre de Recherches en Physique des Plasmas
Association Euratom-Confédération Suisse
EPFL, 1015 Lausanne, Switzerland.

F.Braun, A.B.Murphy, J.-M. Noterdaeme, F. Ryter, and F.Wesner.

Max Planck Institut fur Plasmaphysik
Boltzmannstrasse 2, Garching bei Muenchen
Bundesrepublik Deutschland

An experiment has been completed on ASDEX to study the response of the plasma to Alfvén wave heating (AWH). Antenna excitation was provided by the old TCA rf generator with an output power capability of 500 kW. Two poloidal loop antennas were installed at the east and west ends of the tokamak allowing either N = 1 or N = 2 phasings. Since the largest antenna coupling to the Alfvén resonance is provided by the m = 1 surface wave, [1], the antennas consisted only of a single element on the low field side, whereas in TCA the antennas are located on the top and the bottom of the torus. The antenna elements consisted of 2 parallel bars of inductance 730 nH and, as in TCA, were left unshielded [2]. A typical antenna circulating current of 2 kA peak at 1.80 MHz was provided for the experiments.

The excited wave spectrum consisted of discrete Alfvén wave (DAW) peaks separated by a featureless wave continuum (see the wavefield trace in Fig. 3); characteristic of the spectrum already observed in TCA [1]. A dispersion plot of density versus toroidal field is shown in Fig. 1 for the (n,m)=(2,1) DAW. The curve on the left shows the characteristic dependence on Alfvén speed and the curve on the right shows the location of the (2,1) DAW with respect to the (2,0) and (2,1) continuum thresholds. In addition to the Alfvén spectrum at the fundamental frequency, a spectrum of harmonic waves is also excited in the plasma edge as in TCA [2].

A typical plasma response to AWH is shown in Fig. 2 for 1 kA peak (approx) in the antenna and 50 kW delivered to the plasma. The Alfvén pulse occurs at 2.1 s and lasts 400 ms. During this pulse the most important plasma effect is an

uncontrolled density rise. Profile measurements of Z_{eff} revealed that the density rise is not due to impurities. Even though the loop voltage is observed to increase at the beginning of the rf, it tends to decrease later in the pulse. No observable change in the charge exchange flux of low energy neutrals and a general decrease in H_α (Fig. 3) at the time of the rf pulse suggests that a change in recycling is not responsible. These conclusions have already been suspected from previous AWH experiments in TCA and are now known to be independent of whether or not the antennas are electrostatically shielded [2]. The density rise is accompanied by increases in $\beta + l_i/2$, β_{dia}, P_{rad}, T_e, T_i and plasma energy. The maximum power that could be delivered to the plasma (450 kW approx.) was limited by plasma disruption.

An interesting effect of AWH is the so called spectral discontinuity observed on certain plasma parameters. An example is shown in Fig. 3 (I_p = 400 kA) where the density rises and breaks just after a DAW at 1.3 s. The effect on the plasma appears to be a sudden decrease in energy and particle confinement.

The heating analysis has always been complicated by the effects of the increasing plasma density. Strong electron heating has been observed using Thomson scattering [3], however the effect of AWH is to increase the saw tooth amplitude and not the base temperature compared with the ohmic temperature at the same density. From the plasma energy calculated from the diamagnetic loop, one can compare the heating during rf with that of gas puffs which give rise to a similar density increase in the same shot. An example is shown in Fig. 2 where a gas puff density rise occurs between 0.9 and 1.2 s. A set of plasma energy loci versus density are shown in Fig. 4. Although it was a general result of the experiments that the effect of rf on the plasma was largest at lowest density, there is no significant qualitative difference between gas puffing and AWH. However a more detailed set of observations than these is required to observe separate heating.

Finally, a series of experiments with AWH applied during a long 1 MW NBI pulse failed to produce any observable effect in addition to that of NBI. The density rise observed with AWH into ohmic discharges was absent, although the coupling may be reduced by changes in the edge profiles during NBI.

REFERENCES

[1] Collins G.A., Hofmann F., Joye B. et. al. Phys. Fluids, **29**, 2260 (1986).
[2] Borg G.G. and Joye B. *'An experimental study of Alfvén wave heating using electrostatically screened antennas in TCA'*. Paper presented at this conference.
[3] Joye B., Lietti A., Lister J.B. et. al. Phys. Rev. Letters, **56**, 2481 (1986).

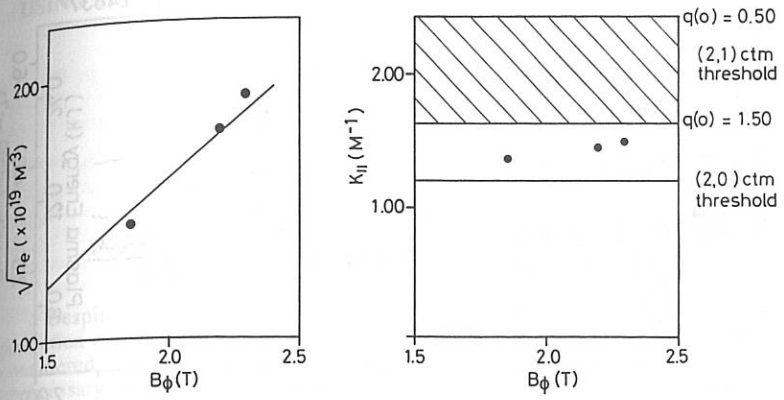

Fig. 1. Plot of the dispersion relation in the density-toroidal field plane for the (2,1) DAW.

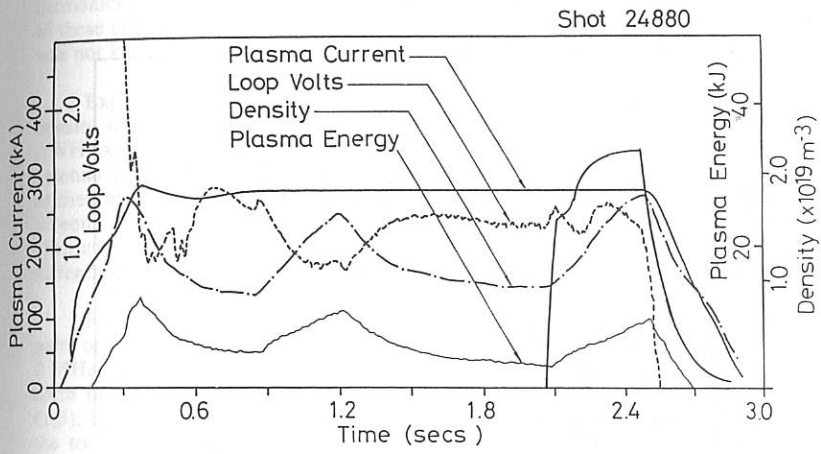

Fig. 2. A typical discharge in ASDEX with a gas puff at 0.9 s and an AWH pulse at 2.1 s.

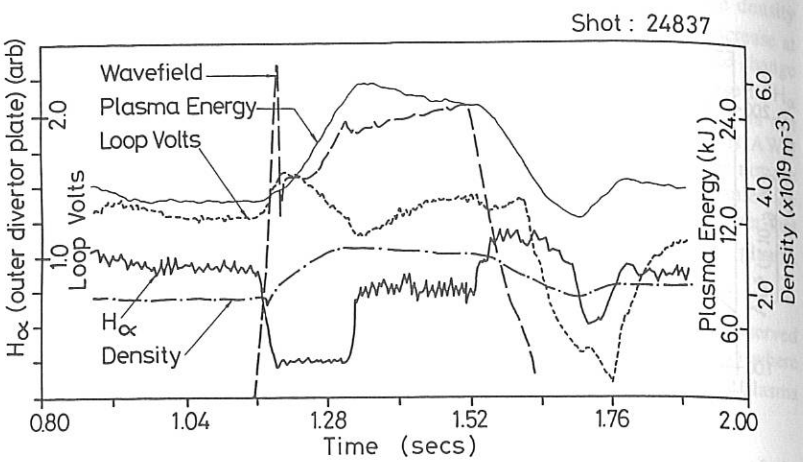

Fig. 3. Shot showing the effect on plasma energy, density ,loop volts and H_α emission during a spectral discontinuity.

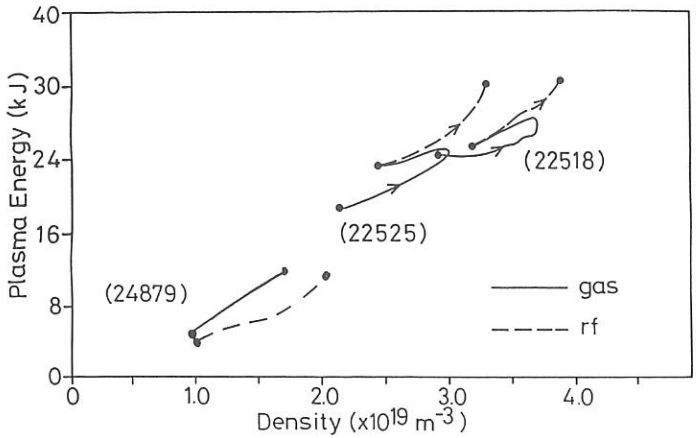

Fig. 4. Comparison of plasma energy versus density for gas puffs and AWH pulses for various plasma conditions

AN EXPERIMENTAL STUDY OF ALFVEN WAVE HEATING USING ELECTROSTATICALLY SHIELDED ANTENNAS IN TCA

G.G. Borg and B. Joye

Centre de recherches en Physique des Plasmas
Association Euratom-Confédération Suisse
EPFL, 1015 Lausanne, Switzerland

Despite the wide acceptance of electrostatic screens in ICRH for the protection of the plasma from the near fields of rf antennas, it has always been considered that low voltages at low frequency have made such screens unnecessary in Alfvén wave heating (AWH) [1]. Despite this, AWH performs rather poorly as a heating method; the results being confused by a density rise up to 300% of the target density. It is now known that the density increase arises neither from impurity injection nor from a change in recycling. In addition, an extensive range of phenomena have been observed in the plasma scrape-off layer (SOL). During AWH, the SOL density is observed to decrease, the SOL floating potential is perturbed in a way that reflects the Alfvén wave spectrum, the antennas charge negatively and draw a large current from the plasma and harmonics have been observed on the edge wave fields. The cause and correlation of these effects with each other and their impression on the bulk plasma response was not known.

Experimental results from the TORTUS tokamak [2] have indicated that the density increase might be eliminated by electrostatic screens. In their case, two AWH experiments were performed. In the first, an unshielded OFHC copper loop antenna was excited at a given power and, in the second, the same antenna was excited at the same power after installation of an aluminium, TiN coated, slotted screen. The density increase in the first case was shown to be completely eliminated in the second, although spectroscopic measurements revealed a difference in the plasma O(II) and Cu(I) content for each case.

Recently, electrostatic screens have been installed in TCA. TCA has four pairs of top and bottom antennas in each quadrant of the torus which are excited at 2 MHz. Each antenna consists of 6 parallel poloidal bars fed in push-pull. Screens were only installed on two pairs of antennas. On antenna top and bottom pair (1,5), the screens consist of a capacitive divider of 11 earthed blades parallel to the toroidal field and a fully grounded side limiter at the front and back of each antenna. The screens were made of the same material as the antenna, stainless steel, to avoid a possible confusion in the interpretation of experimental results due to impurities. On antenna pair (2,6) the screens are identical except that the blades are not earthed. This permits a comparison to be made between electrostatic and floating screens for identical conditions of plasma coupling. The

screens do not significantly alter the antenna near magnetic field. Antenna pairs (3,7) and (4,8) were left unshielded. The experimental arrangement is shown in Fig. 1.

Some physical quantities measured in the SOL are shown in Fig. 2 for excitation of antenna pair (3,7) (Fig. 2a) and antenna pair (1,5) (Fig. 2b) with a similar antenna current. The natural polarisation V_{pol}, probe floating potential V_{flot}, measured on unexcited antenna 4, and ion saturation current I_{sat}, measured by applying negative polarisation to antenna 4, have all been significantly reduced by the screens. In addition, the current drawn from the plasma by the antennas was completely eliminated. The poloidal wave field component detected by a pick up coil in the SOL is shown plotted in the complex plane during the passage of a discrete Alfvén wave [1]. There is evidently no clear effect of screens on the relative amplitude of the first harmonic (4 MHz) and the fundamental (2 MHz) component; thus eliminating a possible explanation of the harmonics in terms of a Langmuir interaction between the antenna and the SOL plasma. From these results one can simply conclude that the basic technical requirement of the screens has been met. We also mention that there is no differernce observed in the results for antenna pairs (1,5) and (2,6).

Results for the average plasma parameters are shown in Fig. 3, including an ohmic discharge (Fig. 3d) for reference. Comparison of the case for excitation without screens (antenna pair (3,7) in Fig. 3a) and with screens (antenna pair (1,5) in Fig. 3b and pair (2,6) in Fig. 3c) reveals very little difference in the response of any of the plasma parameters that cannot be attributed to the difference in antenna power for each case. In particular, the density increase, which is known to scale with rf power and be almost entirely responsible in itself for the observed changes in $\beta + l_i/2$ and the soft X-ray flux, has not been significantly reduced by screens.

In conclusion, we note that the main benefit of screens in AWH is to 'clean up' most parasitic phenomena from the plasma SOL which are, without doubt, linked to the direct contact between the plasma and the unshielded antenna. This benefit, however, does not, in any way, for better or for worse, alter the plasma bulk response to AWH. The separate challenges to reveal the origin and importance of the harmonics and to comprehend the response of a tokamak plasma to high power Alfvén waves still remain.

References

[1] Collins G. A., Hofmann F., Joye B. et. al. Phys. Fluids, **29**, 2260 (1986).
[2] Ballico M.J., Brennan M.H., Cross R.C. et. al. Plas. Phys. and Contr. Fus. **30**, 1331 (1988).

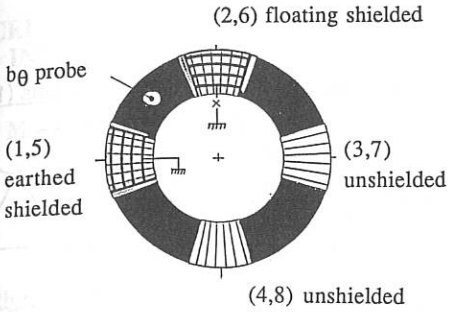

Fig. 1. Top view of TCA showing the antennas and the wave probe.

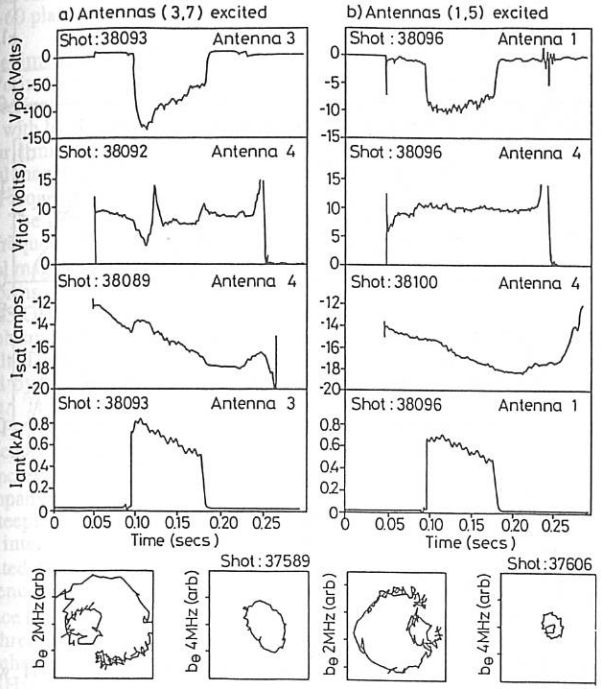

Fig.2. Effects of rf on the SOL, during AWH with a) unshielded antenna pair (3,7) and b) shielded antenna pair (1,5).

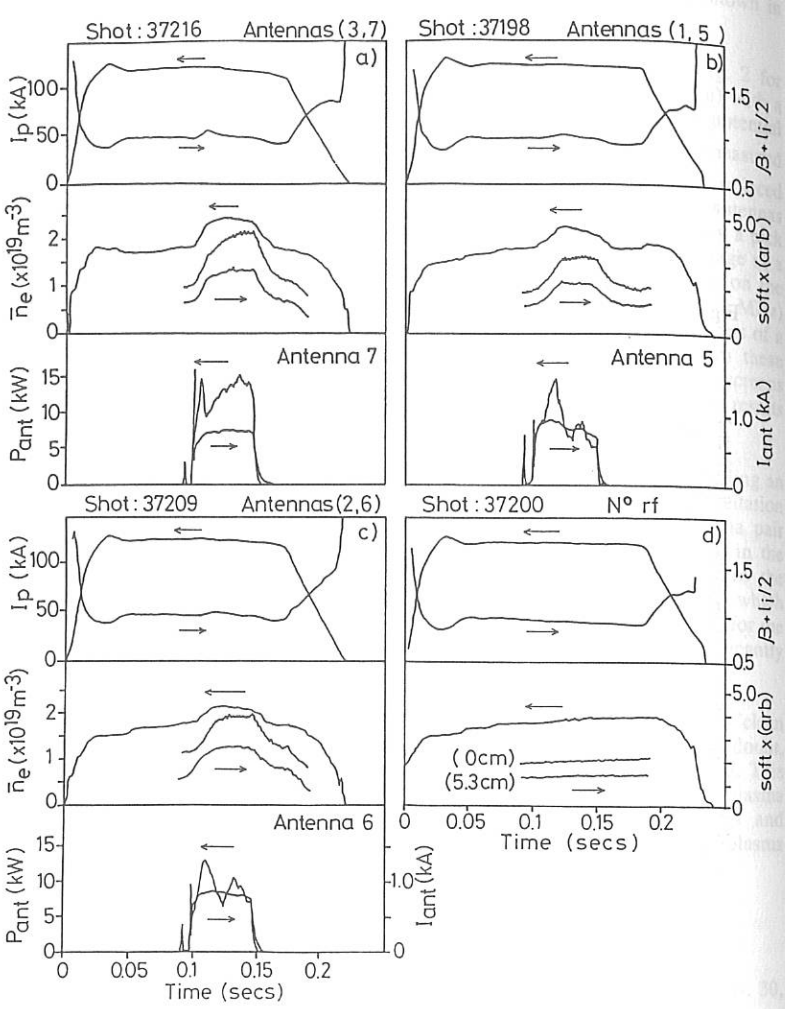

Fig. 3. Effect of rf on the average plasma parameters during AWH with a) unshielded antenna pair (3,7), b) earthed, shielded antenna pair (1,5), c) floating, shielded antenna pair (2,6) and without AWH, d).

ACCELERATION OF BEAM IONS IN SIMULTANEOUS INJECTION OF NB AND LH WAVE ON JT-60

M. Nemoto, O. Naito, K. Ushigusa, T. Imai, Y. Ikeda,
Y. Kusama, K. Tobita, H. Takeuchi and JT-60 Team

Naka Fusion Research Establishment,
Japan Atomic Energy Research Institute,
Naka-machi, Naka-gun, Ibaraki-ken 311-01 JAPAN

1.Introduction

For future tokamaks like ITER or FER, combined current drive with high energy neutral beams(NB) and lower hybrid waves(LH) will be carried out aiming at establishment of current profile control, where NB and LH drive current in the center and outer region, respectively /1/. It is very important to predict the absorption of LH power by high energy α-particles leading to decrease in current drive efficiency. Coupling characteristics of LH wave for beam ion of NB have been investigated by simultaneous injection of NB and LH wave into the JT-60 plasmas /2,3/.

2.Experimental results and discussion

We investigated frequency and beam energy dependences of beam ion-wave coupling characterized by a critical density of the beam acceleration resulted from interaction of LH waves with hydrogen beam ions. Experiments were carried out in hydrogen plasmas with near-circular limiter configurations and following parameters; plasma current Ip=1.5 MA, the toroidal magnetic field B_T=4.5 T, major radius R=3.04 m and minor radius ap=0.89 m.

1) Frequency dependence

The LH system on JT-60 uses a multi-junction type launcher /4/ and is able to vary the wave frequency from 1.74 GHz to 2.23 GHz with the sharp refractive index N// parallel to the toroidal magnetic field. Here, we injected the waves with fixed peak N// of 2.2. Figure 1 shows waveforms of simultaneous injection of LH and NB when frequencies of LH were 1.74, 2.0 and 2.23 GHz, and beam energy was 65 keV. High power NB injection around 20 MW would raise plasma density and make the accurate measurement of the acceleration phenomena difficult. Therefore, we injected lower NB power around 2 MW from a beam-line which was viewed by a CX analyzer /5/ in order to obtain a good signal to noise ratio of CX energy spectra. The top column shows time evolutions of line-integrated electron density and NB power P_{NBI}. The electron density was raised with a constant rate by a feedback control system. The second column shows the evolution of CX flux intensities $\ln F_i$ of 150 keV for three LH frequencies. The flux intensities show clear differences in critical densities of the acceleration. Accompanying with the increase in accelerated ions by LH, the power absorbed by electrons were steeply decreasing, as shown in the third column. Vertical axis in the column is a product of the intensity of non-thermal electron cyclotron emission (ECE) at $1.5\omega_{ce}$ and the line-integrated density. Here, data for 2.23 GHz case was absent because of the ECE system error. Differences in injected LH powers shown in the bottom column for three cases did not influence the essential characteristics. Typical ion energy distributions at $\overline{n_e} = 1.8 \times 10^{19}$ m^{-3} for those three cases are shown in Fig.2. In the case of 1.74 GHz, shown with closed circles, the most enhanced beam acceleration up to 200 keV occurred. On the other hand, the tail slope of 2.23 GHz case shown with closed triangles was similar to the case of NB only. The ion acceleration was due to the absorption of LH wave because electrostatic probes did not detect parametric decay waves in these discharges.

In an electro-static cold plasma approximation, LH wave satisfies the following dispersion relation

$$\left(\frac{k_{//}}{k_{\perp}}\right)^2 = \left(\frac{N_{//}}{N_{\perp}}\right)^2 = \left(\frac{f}{f_{pe}}\right)^2 + \left(\frac{f}{f_{ce}}\right)^2 - \left(\frac{f_{pi}}{f_{pe}}\right)^2, \qquad (1)$$

where $k_{//}$ and $k_{\perp}$ are wave numbers parallel and perpendicular to the magnetic field, and f, f_{pe}, f_{ce} and f_{pi} are pump-frequency, electron plasma-, electron gyro- and ion plasma-frequency, respectively. Here, we define two parameters, which indicate absorption rates of LH power by electrons δ_e and ions δ_i /6,7/ as

$$\delta_e \equiv \left(F_\delta \frac{v_e}{v_{//}}\right)^2$$

$$\delta_i \equiv \left(\frac{v_B}{v_{\perp}}\right)^2,$$

where v_e and v_B are electron and beam ion velocities, and $v_{//}$ and $v_{\perp}$ are LH phase velocities parallel and perpendicular to the magnetic field. These parameters mean that if they are close to unity, each species is easy to absorb LH wave power. Also, we define a ratio $\delta = \delta_i/\delta_e$ which gives a critical density between electron and ion heating when $\delta=1$. Using beam energy E_B and the electron temperature T_e, we can re-write Eq.(1) as

$$\left(\frac{f}{f_{pe}}\right)^2 = \frac{m_e E_B}{F_\delta^2 m_p T_e \delta} - \left(\frac{f}{f_{ce}}\right)^2 + \left(\frac{f_{pi}}{f_{pe}}\right)^2, \qquad (2)$$

where m_e and m_p are masses of electron and proton as beam species. The critical electron density n_e^c in units of 10^{19} m^{-3} when $\delta=1$ are given as follows

$$n_e^c = \frac{2.28 f_G^2}{\frac{E_B}{F_\delta^2 A_B T_e} + \gamma - 2.34\left(\frac{f_G}{B_T}\right)^2}, \qquad (3)$$

where f_G is LH wave frequency in GHz, E_B and T_e are in eV, B_T is in Tesla, A_B is atomic mass of injected beam species and γ is defined as

$$\gamma \equiv \frac{1}{\overline{n_e}} \sum_i \frac{Z_i^2 \overline{n_i}}{A_i}$$

$\overline{n_e}$ and $\overline{n_i}$ are densities of electron and ion, the summation in γ is performed over ion species "i" with charge state Z_i and atomic mass A_i.

We calculated a dependence of the critical electron density on LH frequency with typical JT-60 experimental parameters of injected beam energy E_{B0}=65 keV, T_e=3.0 keV, B_T=4.5 T and γ=0.8 for Z_{eff}=3 assuming carbon as a dominant impurity. As collisions between bulk plasma and beam ions produced high energy ions up to injected NB energy, we took account of a spread of beam energy ΔE of 10 keV from a CX energy spectrum obtained from only NB heated plasma. Using $E_B = E_{B0} + \Delta E$, a satisfactory result was obtained at F_δ=2.75. Figure 3 shows that the calculation result with a solid line is in good agreement with the experimental data with closed circles. Here, we converted the critical density into an averaged one $\overline{n_e}^c$ with a coefficient which was based on a parabolic density profile.

2) NB energy dependence

Next, in order to investigate the dependence on beam energy, we carried out an experiment with NB of E_{B0}=40 keV, LH wave of f=2.0 GHz and peak $N_{//}$=2.2, the same B_T and configuration as previous experiment. The electron density when accelerated ions of 120 keV were detected was 2.35×10^{19} m^{-3} as shown in Fig.3 with open circle. The correlation between the generation of high energy ions and the product of the nonthermal ECE intensity and the electron density was similar to that in the case of 65 keV injection. The dependence of the critical density on beam energy was calculated from Eq.(3) using the previous parameters and also taking account of ΔE of 10 keV. The result is shown in Fig.3 with a broken line. The dependence is also consistent with the experimental data shown with open circles.

3.Summary

The beam acceleration by LH wave was studied with the limiter plasmas on JT-60. It was evidenced that critical density to couple beam ions was in good agreement with the prediction from the simple LH wave dispersion relation. The critical density is approximately proportional to the square of the LH frequency and to the reciprocal of the injected beam energy. The results can clearly predict the interaction of the α-particles with LH wave in the future tokamak.

Acknowledgements

The authors would like to express their gratitude to Drs. M. Yoshikawa, T. Iijima, S. Tamura and A. Funahashi for their continuing encouragement and support.

References

/1/ ITER conceptual design : Interim report, IAEA,VIENNA,p.91(1990).
/2/ K.Ushigusa, et al., Nucl. Fusion, 29(1989)265.
/3/ T.Imai, et al., Nucl. Fusion, 30(1990)161.
/4/ Y.Ikeda, et al.,Nucl. Fusion, 29(1989)1815.
/5/ Y.Kusama, et al.,15th European Conference on Controlled Fusion and Plasma Heating, Dubrovnik, vol.12B part1, p.167(1988).
/6/ J.G.Wegowe and G. Tonon, Proc. of IAEA Technical Meeting on Non-Inductive Current Drive in Tokamaks, Culham, CLM-CD, vol.2, p.343(1983).
/7/ F.Alladio, et al., Nucl. Fusion, 24(1984)725.

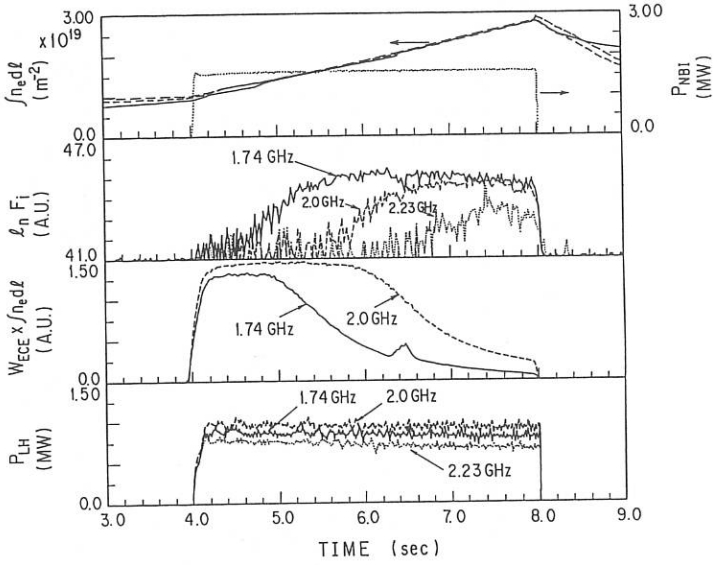

Fig.1 Time evolutions of line density, injected neutral beam power, CX flux intensity, product of $1.5\omega_{ce}$ wave and line density and injected LH wave power.

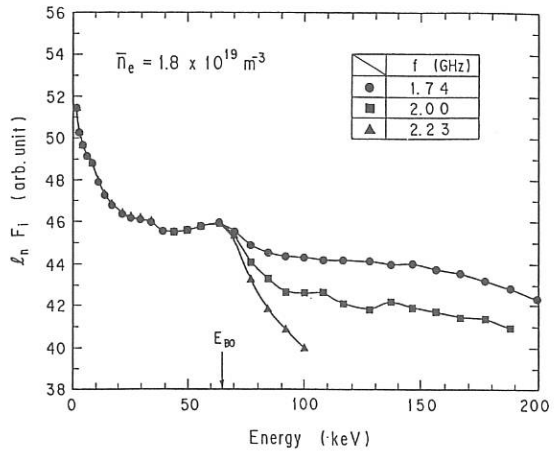

Fig.2 Typical ion energy distributions measured from CX analyzer

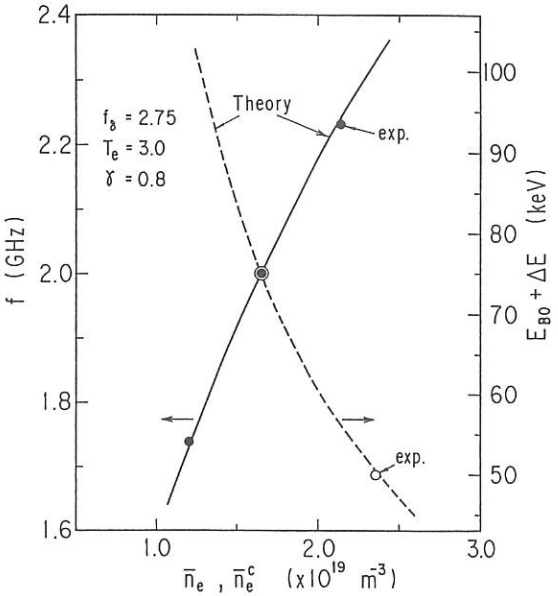

Fig.3 Comparison with experimental data and calculation with respect to the critical density of the beam acceleration.

STOCHASTIC HEATING OF CHARGED PARTICLES BY TWO MODES OF PLASMA OSCILLATIONS

V.S.Krivitaky & S.V.Vladimirov

General Physics Institute, Moscow, U.S.S.R.

As it is well known, temporal dependence of the particles distribution due to their interaction with some (longitudinal) waves in turbulent plasma is described in the first approximation by the quasilinear equation (see, e.g., Ref. [1])

$$\frac{\partial \Phi_{\vec{p}}}{\partial t} = \pi e^2 \int d\omega d\vec{q}\ \frac{|E_{\omega\vec{q}}|^2}{q^2} \left(\vec{q}\cdot\frac{\partial}{\partial \vec{p}}\right)\delta(\omega - \vec{q}\cdot\vec{v})\left(\vec{q}\cdot\frac{\partial}{\partial \vec{p}}\right)\Phi_{\vec{p}} \equiv \qquad (1)$$

$$\equiv Q^{QL} \equiv J\Phi_{\vec{p}}$$

where e is an electron charge, $\Phi_{\vec{p}} = \langle f_{\vec{p}} \rangle$ is the electron distribution function averaged upon the statistical ensemble, and $|E_{\omega\vec{q}}|^2$ is a correlation function of Fourier components of the electric field in a (resonant) wave.

Taking into account a nonlinear wave interaction (in so called turbulent resonance broadening theories when the waves obey Cherenkov condetion $\omega - \vec{q}\cdot\vec{v} = 0$ and/or in the case of nonlinear scattering of the wave $(\omega, \vec{q})$ into the wave $(\omega_1, \vec{q}_1)$ when the scattering condition $\omega - \omega_1 (\vec{k} - \vec{k}_1)\cdot\vec{v} = 0$ is fulfilled) results only in some modification of the quasilinear diffusion coefficient. Thus it does not change the principal form of the equation (1) describing the diffusion of the particles in the momentum space (i.e. differential operator acting upon the dictribution function in the corresponding expression for the collision integral remains the second order in $\partial/\partial p$ (see Ref. [1])).

But besides these corrections to the deffusion coefficient connected with the scattering and/or the resonance broadening there is also a new nonlinear effect which changes the general form of the collision integral. This effect appears in the third order in field approximation and corresponds to a nonlinear interaction of plasma particles simultaneously with two types of oscillations: the resonant ones $|E_{\omega\vec{q}}|^2$ for wh ch the Cherenkov

resonance conditions (with some particles)

$$\omega - \vec{q}\cdot\vec{v} = 0 \qquad (2)$$

is fulfilled, and the nonresonant ones $|E_{\Omega k}|^2$ which do not satisfy both the condition of Cherenkov resonance:

$$\Omega - \vec{k}\cdot\vec{v} \neq 0 , \qquad (3)$$

and the condition of scattering resonance

$$\Omega - \omega - (\vec{k} - \vec{q})\cdot\vec{v} \neq 0 . \qquad (4)$$

Nonlinear collision integral corresponding to the process described above is [2]

$$\frac{\partial \Phi_{\vec{p}}}{\partial t} = Q^{QL} + Q^{NL} \equiv J\Phi_{\vec{p}} + [I, J]\Phi_{\vec{p}} , \qquad (5)$$

where $[I, J] = IJ - JI$ is a commutator of operators I and J. The operator I is given by the following expression:

$$I = \frac{e^2}{2}\int d\Omega\, d\vec{k}\, |E_{\Omega k}|^2 g_{ij} \frac{\partial}{\partial p_i} \frac{1}{(\Omega - \vec{k}\cdot\vec{v})^2} \frac{\partial}{\partial p_j} , \qquad (6)$$

where $g_{ij} = \langle e_i e_j^* \rangle$ is the polarisation tensor which is equal to $1/2\,(\delta_{ij} - k_i k_j / k^2)$ for transversal waves.

Nonlinear collision integral Q^{NL} is quite different from the quasilinear integral Q^{QL} (1). Namely, Q^{NL} has more high (the third) order in $\partial/\partial p$ than Q^{QL} has. That is why the second term in Eq. (5) may in some cases have the same order of magnitude as the quasilinear contribution Q^{QL}, although Q^{NL} has an additional small factor $W/(n_e T_e) \ll 1$ with respect to Q^{QL} (W is an energy density of the nonresonant waves, n_e and T_e are the electron concentration and temperature respectively).

Let us consider (in one-dimensional case) a group of the heated (accelerated) particles which distribution is described by the function Φ_p. It is convenient to introduce an energy distribution Φ_ε. From Eq. 5 for the function Φ_ε one can get

$$\frac{\partial \Phi_\varepsilon}{\partial t} = -\frac{\partial}{\partial \varepsilon}\left(\Phi_\varepsilon F(\varepsilon)\right) + \frac{1}{2}\frac{\partial^2}{\partial \varepsilon^2}\left(\Phi_\varepsilon G(\varepsilon)\right) - \frac{1}{3}\frac{\partial^3}{\partial \varepsilon^3}\left(\Phi_\varepsilon H(\varepsilon)\right) . \qquad (7)$$

The function $F(\varepsilon)$ describes a systematic acceleration of particles, and the functions $G(\varepsilon)$ and $H(\varepsilon)$ describe a fluctuating acceleration (heating) of particles:

$$\left\langle \frac{\partial}{\partial t}\varepsilon \right\rangle = \langle F(\varepsilon)\rangle ,$$

$$\left\langle \frac{\partial}{\partial t}(\Delta\varepsilon)^2 \right\rangle = \left\langle 2\Delta\varepsilon \frac{\partial \varepsilon}{\partial t} \right\rangle + \langle G(\varepsilon)\rangle , \qquad (8)$$

$$\left\langle \frac{\partial}{\partial t}(\Delta\varepsilon)^3 \right\rangle = \left\langle 3\left((\Delta\varepsilon)^2 - \langle(\Delta\varepsilon)^2\rangle\right)\frac{\partial \varepsilon}{\partial t} \right\rangle + \langle 3\Delta\varepsilon G(\varepsilon)\rangle + \langle H(\varepsilon)\rangle ,$$

where $\Delta\varepsilon = \varepsilon - \langle\varepsilon\rangle$ and the angular brackets mean averaging over the distribution Φ_ε. We can see that besides the "usual" heating $\left\langle \frac{\partial}{\partial t}(\Delta\varepsilon)^2 \right\rangle$ there appeares the "cubic" heating $\left\langle \frac{\partial}{\partial t}(\Delta\varepsilon)^3 \right\rangle$ determined by the nonlinear interaction.

The nonlinear interaction modifies also the heating process. One can obtaine [3] that for sufficienty narrow initial distributions of resonant particles and waves a heating efficiency may increase in

$$\frac{W}{n_e T_e}\left(\frac{v_{Te}}{v}\right)^4 \frac{1}{\delta^2} \qquad (9)$$

times in comparison with the quasilinear heating, where W is an energy density of the resonant waves, n_e and T_e are electron density and temperature, $v_{Te}^2 = T_e/m_e$, $\delta^2 = (\Delta v)^2/v^2 + (\Delta q)^2/q^2$ where v and q are connected by the resonance condition (2).

REFERENCES

1. Tsytovich V.N. Theory of Turbulent Plasma. N.Y., Consultants Bureau (1977).
2. Vladimirov S.V., Krivitsky V.S. Fizika Plasmy, vol. 16, p.452, (1990)[Sov. J. Plasma Phys., vol. 16, N 4 (1990)].
3. Vladimirov S.V., Krivitsky V.S. Kratkie Soobschenia po Fizike N 1, p.37, (1990)[Sov. Phys., Lebedev Inst. Reports N 1 (1990)].

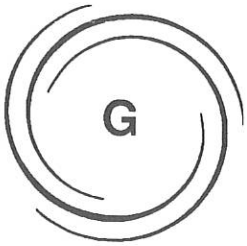

CURRENT DRIVE AND PROFILE CONTROL

G1

G1 ELECTRON CYCLOTRON CURRENT DRIVE

ON THE FILLING OF THE "SPECTRAL GAP" BY PARTICLES IN THE PROCESS OF A DRIVEN CURRENT GENERATION

S.I.Popel, V.N.Tsytovich

P.N.Lebedev Physical Institute of the Academy of Sciences of the USSR. Theoretical Department. USSR, 117924, Moscow B-333, Leninsky prospect, 53

Abstract

To describe currents driven by the lower-hybrid (LH-)waves and in particular to eliminate the discrepancy between the calculated on the base of the standart theoretical treatment of current drive [1] and observed magnitudes of a driven current an approach is proposed in which the radiative-resonant interactions (RRI) [2] between electrons and the LH-waves are taken into account. The RRI are shown to lead to the increase of the resonant region. The gap between the lowest phase velocity of the LH-waves and the thermal velocity of electrons (the spectral gap) diminishes and is filled by particles. The RRI corresponding to the nonlinear resonance namely the radiative-resonant scattering interactions are shown to provide sufficiently effective generation of the fast particles carrying a driven current. It is considered the influence of the nonlinear effects such as the induced scattering. The magnitudes of the growth-time and the efficiency of a driven current generation are obtained. The proposed theoretical scheme permits to obtain the magnitude of a driven current, its growth-time and the efficiency of its generation in accordance with observations.

1. Fisch N.J. Rev. Mod. Phys., 59, 175 (1987).

2. Tsytovich V.N. Phys. Reports, 178, 261 (1989).

THE EFFECT OF THE INDUCED RF CURRENT DENSITY PROFILE DURING LOWER-HYBRID CURRENT DRIVE ON THE EVOLUTION OF THE q PROFILE AND SAWTEETH STABILIZATION

M. Shoucri, I.P. Shkarofsky, S. Jardin[1], A. Kritz[2]

Centre canadien de fusion magnétique(CCFM), Varennes, Québec,Canada J3X1S1

We apply the Princeton Tokamak Simulation Code (TSC) [1] to study the effect of the RF current density profile on the evolution of the q profile and other parameters during lower-hybrid current drive. The MHD equations are evolved in time consistently with the RF current density profile and the plasma transport. Experimental studies [2] show that sawteeth oscillations are suppressed by lower-hybrid current drive in high density Alcator C plasmas (n_e=1.1x10^{14}cm^{-3}, P_{rf}=600kW at 4.6 GHz). However, when the power is raised well above the threshold required for stabilization (P_{rf}>900kW), the sawteeth return after 40-50 msec of stabilized operation. More recently, results obtained in the ASDEX experiments [3] show that with lower-hybrid RF at high power, sawteeth are stabilized through the whole duration of the pulse. An m=2 mode, which leads to a plasma disruption, is also excited.

To understand these different results, several simulations are presented here applying the TSC code, where a current of 200 kA is driven by 0.8MW of RF power at 3.7 GHz, using parameters relevant to the Tokamak de Varennes. The power is deposited according to the profile

$$P_{rf} \propto \frac{d^2}{(r-a)^2+d^2}\; r^{a_1}(1-r)^{a_2} \tag{1}$$

where r is the position along the radius normalized to the plasma radius. The coefficients a, d, a_1 and a_2 are inputs, which may be constant or may be allowed to evolve in time. The model developed in TSC assumes an RF current density profile based on Luckhardt's [4] and Fisch's [5,6] theories. Fisch's formula is modified for the case of a wide RF spectrum (see Appendix A), namely

$$J = J_{\max} F \tag{2}$$

$$J_{\max} = \frac{16\pi m \varepsilon_o^2 c^2}{e^3 n_o}\; \frac{1}{(5+Z)\ln\Lambda}\; \left[\frac{v_t^2}{c^2}\; \frac{v_2^2 - v_1^2}{2\ln v_2/v_1}\right]\; P \tag{3}$$

MKS units are used. P is the power density in watts/m^3, n_0 is the peak electron density (2.75 x 10^{19} m^{-3} in the present calculation), $v_t = (T_e/m)^{1/2}$ with T_e being the electron temperature, v_1 is the lower limit (in velocity space normalized to v_t), of the RF spectrum (usually 2-3 v_t), v_2 is the upper limit, calculated from the accessibility condition (limited to 10 v_t, since higher velocity particles will generally run away and be lost), and F is a loss factor, less than unity, multiplying Fisch's formula, calculated by Luckhardt [4].

---

1 PPPL, Princeton University, Princeton, N.J., U.S.A.

2 Princeton University and Hunter College/CUNY, New York, N.Y., U.S.A.

The Spitzer conductivity σ_S in the TSC Code is modified to include a contribution σ_H coming from the hot population and derived here from Refs.[5-8],namely

$$\frac{\sigma_H}{\sigma_S} = \frac{8P_N}{7.52(Z+3)\Lambda_E(Z)} \frac{v_2^4 - v_1^4}{4\ln v_2/v_1} \quad (4)$$

with

$$\Lambda_E(Z) = \frac{3.4(1.13+Z)}{Z(2.67+Z)} \quad (5)$$

The first simulation is effected with a fixed profile peaking off-axis at a=0.4 with d=0.3, a_1=0 and a_2=0.28 in Eq.(1). Figure 1 shows that at equilibrium after a time (t) of 377 msec, the plasma current profile (T curve) and the impressed RF current profile (L curve) have approached each other. Figure 2 illustrates the time evolution of the q profile from t=150.3 (lower curve) to 302.1 msec (upper curve), the latter at equilibrium. At the start (t=0), the q profile is the same as the lowest curve in Fig.3, varying from q<1 in the center to q>3 near the edge. A study of the stability of the equilibrium at t=302.1 msec, with the PEST2 code, confirms the presence of an m=2 oscillation. A second simulation is effected with the same parameters as the first one, but with the parameter a varying from 0.4 to 0.15 in the first 50 msec. This simulates an inward diffusion of the power density profile. Figure 3 shows the time evolution of the q profile. Initially, the profile rises above 1 in the center, which stabilizes the sawteeth oscillations. Thereafter, the profile evolves again to below 1 in the center and the sawteeth oscillations would appear, a result consistent with Ref.[2].

As a general conclusion, current drive with a profile peaking off-axis results in a q profile above 1 in the center and possibly the excitation of an m=2 mode if q exceeds 2. On the other hand, a profile peaking close to the axis, favors a q profile with a value less than 1 in the center and the excitation of sawteeth oscillations.

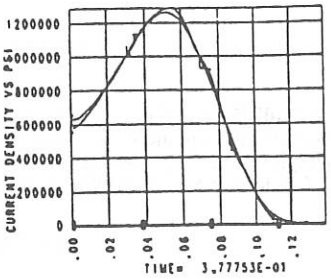

Figure 1

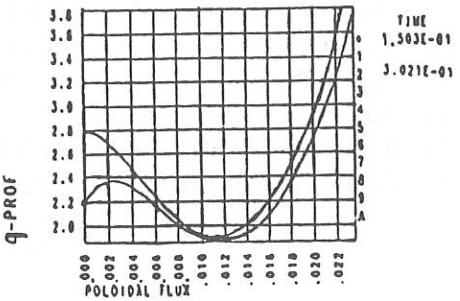

Figure 2

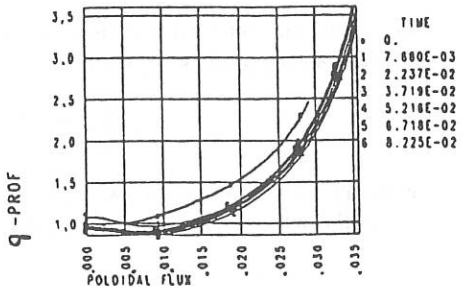

Figure 3

ACKNOWLEDGEMENTS

The Centre canadien de fusion magnétique is a joint venture of Hydro-Québec, Atomic Energy of Canada Limited and the Institut National de la Recherche Scientifique, in which MPB Technologies Inc., Canatom Inc. and the Université de Montréal also participate. It is principally funded by AECL, Hydro-Québec and INRS.

REFERENCES

[1] S.C. Jardin, N. Pomphrey, J.L. De Lucia, J. Comp., Phys. 66, 481 (1986).

[2] M. Porkolab et al, in Plasma Physics and Controlled Fusion (Proc. 13th Int. Conf. Schliersee, 1986), see also Knowlton S. et al, "Sawteeth Stabilization Experiments on Alcator C", APS Fall Meeting (1986); Bull. Am. Phys. Soc. Vol. 31.

[3] F. Leuterer et al., AIP Conference Proceedings 190, editor R. McWilliams, "Radio-Frequency Power in Plasmas", p.95, N.Y., (1989).

[4] S.C. Luckhardt, Nuc. Fusion 27, 1914 (1987).

[5] N. Fisch Rev. Modern Phys. 59 175 (1987).

[6] N.J. Fisch, Phys. Fluids 28, 245 (1985).

[7] K. Yoshioka et al, Phys. Fluids 31, 1224 (1988)

[8] S.P. Hirshman, R.J. Hawryluk, B. Birge, Nuc. Fusion 17, 611 (1977).

APPENDIX A : Relations for a Wide RF Spectrum

Fisch's expression (Ref. [5], p. 196) for J/P_d assumes the following form for a wide one-dimensional lower-hybrid spectrum parallel to B with $v \approx v_{||}$

$$\frac{J}{P_d} = \frac{ne v_t J_N}{P_d} = nm\nu v_t^2 \frac{\int dv \;\; S_W \;\; \partial\chi/\partial v}{\int dv \;\; S_W \;\; \partial(mv^2/2)/\partial v}$$

where J is the current density, J_N is J normalized to nev_t , P is the power input density, P_d is P normalized to $\nu nm v_t^2$, with

$$\nu = \frac{\omega_p^4 \ln\Lambda}{4\pi n v_t^3}, \quad v_t^2 = \frac{T_e}{m}, \quad \omega_p^2 = \frac{ne^2}{\varepsilon_0 m}$$

S_W is the spectrum of waves in velocity (v) space along B. In the presence of an electric field E in one-dimensional space parallel to B, ($|\mu| = 0$), Fisch gives $\chi = \chi_0 + \chi_1 E$, where

$$\chi_0 = \frac{e \;\; v^4}{\nu v_t^3 (5+Z)}, \quad \chi_1 = \frac{1}{3m}\left(\frac{e}{\nu v_t^3}\right)^2 \frac{v^6}{(3+Z)}$$

For a wide RF spectrum, one has to integrate S_W over the velocity extent of the spectrum. Suppose it extends from v_1 to v_2. The values of the integrals depend on the form of S_W, but Yoshioka et al [7] have demonstrated that a good approximation is to replace S_W for LH spectra by the form $S_W \propto v^{-2}$. Then

$$\frac{J}{P_d} = nmvv_t^2 \frac{\int_{v_1}^{v_2} dv v^{-2} \partial\chi/\partial v}{\int_{v_1}^{v_2} dv v^{-2} \partial(mv^2/2)/\partial v}$$

yielding for the above $\chi = \chi_0 + E\chi_1$

$$\frac{J}{P_d} = \frac{4nev_t}{(5+Z)}\left[\frac{v_2^2 - v_1^2}{2v_t^2 \ln(v_2/v_1)}\right] + \frac{2ne^2E}{mv(3+Z)}\left[\frac{v_2^4 - v_1^4}{4v_t^4 \ln(v_2/v_1)}\right]$$

The second part gives an hot RF induced conductivity

$$\sigma_H = \frac{2ne^2P_d}{mv(3+Z)}\left[\frac{v_2^4 - v_1^4}{4v_t^4 \ln(v_2/v_1)}\right]$$

The Spitzer conductivity can be approximated [8] as a function of the effective ion charge number Z, thus

$$\sigma_S = 3\left(\frac{\pi}{2}\right)^{1/2} \frac{ne^2 \Lambda_E(Z)}{mv}$$

with

$$\Lambda_E(Z) = \frac{32}{3\pi Z}\left(\frac{Z+1.13}{Z+2.67}\right) = \frac{3.4}{Z}\left(\frac{Z+1.13}{Z+2.67}\right)$$

Consequently

$$\frac{\sigma_H}{\sigma_S} = \frac{2}{3}\left(\frac{2}{\pi}\right)^{1/2} \frac{P_d}{(3+Z)\Lambda_E(Z)}\left[\frac{v_2^4 - v_1^4}{4v_t^4 \ln(v_2/v_1)}\right]$$

Fisch [6] uses P_N, the normalization of P to $v_0 nmv_t^2$ rather than $vnmv_t^2$, where $v_0 = 2v$, giving $P_d = 2P_N$. This changes the numerical constant in front to $(4/3)(2/\pi)^{1/2} = 8/7.53 = 1.06$, and this is the factor given in the text in Eq.(4).

The first part of J/P_d assumes the following form upon replacing P_d by the actual power density, $P = nmvv_t^2 P_d$.

$$J = \frac{16\pi m\varepsilon_0^2 c^2}{ne^3(5+Z)\ln\Lambda}\left(\frac{v_t}{c}\right)^2\left[\frac{v_2^2 - v_1^2}{2v_t^2 \ln(v_2/v_1)}\right]P$$

This is the relation given in the text in Eq. (3).

THE 3.7 GHZ LOWER HYBRID CURRENT DRIVE SYSTEM FOR THE TOKAMAK DE VARENNES

A. Hubbard[a], J. Bagdoo[b], G.-A. Chaudron[b], R. Décoste[a], Y. Demers[b], V. Fuchs[a], V. Glaude[c], I. P. Shkarofsky[b]

Centre canadien de fusion magnétique, Varennes (Québec), CANADA

[a]IREQ, Institut de recherche d'Hydro-Québec, Varennes (Québec) CANADA
[b]MPB Technologies Inc., Dorval (Québec) CANADA
[c]Université de Montréal, Montréal (Québec) CANADA

1. INTRODUCTION

A lower hybrid heating and current drive system is presently being constructed for the Tokamak de Varennes (TdeV). This medium sized fusion experiment has parameters $R = 0.86$ m, $a \leq 0.27$ m, $B_T = 1.5$ T and $I_p \leq 300$ kA. It has recently been fitted with a double-null, closed divertor. A major part of the scientific program of the tokamak is the study of impurity control and plasma-surface interactions under near steady-state conditions. To this end, the magnetic coils are capable of producing 30 second pulses. Non-inductive current drive is necessary to extend the plasma discharge duration from its 1-2 second length in the present ohmic regime.

The lower hybrid current drive system will operate at a frequency of 3.7 GHz to avoid possible density limitations. Up to 1.1 MW will be injected into the plasma, giving a high power density of 1 MW/m^3. Due to the low magnetic field, the waves must be launched at a high $N_{//}$ to remain accesssible to the center at moderate densities ($N_{//acc} = 3.0$ for $n_o = 4 \times 10^{19} m^{-3}$).

The preliminary technical design of the RF system has been presented elsewhere[1]. Its main features, including some recent modifications, are summarized below. In section 3 the predicted performance of the system, based both on empirical scalings and theoretical simulations, is discussed. Section 4 outlines some of the planned lower hybrid experiments.

2. TECHNICAL DESIGN OVERVIEW

The RF system, shown schematically in Fig. 1, will use two Thomson-CSF klystrons, each with an output power of 500 kW for 30 s or up to 650 kW for 10 s. Each klystron will feed one row of a multijunction antenna, consisting of 8 4-way modules (Fig. 2). Within a module, the phasing is fixed at 90°, while the relative phasing of the modules can be adjusted in real time (< 200 ms) using high power phase shifters. This highly flexible arrangement permits us to vary the spectral peak $N_{//o}$ in the range 2.2 to 3.6 for different operating scenarios and, if desired, to launch spectra with different $N_{//}$ components from each row of the grill. Figure 3 shows results of a multijunction coupling code[2], which predicts a narrow spectrum ($N_{//} \approx 0.4$ FWHM) with low reflectivity and near constant directivity over a wide range of phasings.

The antenna consists of 16 identical modules. The preferred construction material is GlidCop[3], a copper-aluminum oxide dispersion combining low RF losses with good mechanical strength at high temperatures. The grill mouth will be of stainless steel. Tests of fabrication techniques are in progress. The exit dimensions of the secondary waveguides are 76 x 5.5 mm, giving a maximum power density at the grill mouth of 4.2 kW/cm^2 (70 kW per module). The grill will be operated at a temperature of 200°C to control outgassing and cooled between shots. The entire assembly, including a power splitting network which is placed just outside the vacuum windows, is movable by ± 7 cm between shots to optimize the edge coupling density at about $1.8 \times 10^{18} m^{-3}$. Smaller corrections during a discharge will be made using the fast (≈1 ms) radial position control system of the TdeV.

An important part of the LHCD system is RF measurement and control. Heterodyne power and phase measurements are to be made at the entrance to each of the antenna modules and at several points in the transmission line. A fast digital feedback and protection system[4] based on real time processors regulates the klystron output and performs a power balance and other system checks, in a 40 μs cycle. Slower tasks such as event sequencing, system monitoring and high power phase control are handled by programmable logic controllers. Reference waveforms for the power and phase can be preprogrammed and/or calculated in real time from plasma parameters (I_p, n_e, V_L, etc.).

3. PREDICTED PERFORMANCE

The major factor affecting our current drive performance is expected to be the unusually high value of $N_{//o}$ (2.9 at 0° phasing). Relatively little data on current drive efficiency exists in this regime. A recent experimental scaling carried out on ASDEX[5], at constant I_p and $\bar{n}_e$ and with $N_{//}$ varied in the range 1.5 - 2.8, shows very good agreement with the theoretical prediction

$$\eta \equiv \frac{\bar{n}_e(10^{19}m^{-3})\ I_p(kA)\ R(m)}{P_{HF}(kW)} \propto \frac{4}{5+Z_{eff}} \frac{1}{\langle N_{//}^2 \rangle}$$

if the average value $\langle N_{//}^2 \rangle$ is taken to be simply $N_{//o}^2$. Scaling these results to the TdeV, for $N_{//}$= 2.9 and 60% directivity (defined here as the fraction of the total launched power contained in the main peak of the spectrum), gives a predicted efficiency of 0.41. With P_{tot}= 1 MW, we then expect to be able to drive a current of 200 kA at densities up to $\bar{n}_e = 2.4 \times 10^{19} m^{-3}$.

Both RF current drive and transformer recharge have been simulated using a modified Bonoli-Englade code[6]. Changes made to the code include the possibility of feedback on the plasma current or V_L and inclusion of the radial diffusion of current carried by the fast electrons. Simulations of pure RF current drive show that even for relatively high density and $N_{//}$ ($n_o = 4.0 \times 10^{19}$ m^{-3}, $N_{//}$= 3.3) the efficiency is quite good, with η = 0.33 (directivity of 60% is assumed). At $N_{//}$= 2.9, we should then get η = 0.42, in good agreement with the above experimentally based predictions.

Given the high level of RF power, significant increases in electron temperature ($\Delta T_e \approx 1$ keV) and moderate increases in T_i are also predicted. During divertor operation, it is hoped to be able to enter the H-mode regime.

For transformer recharge, the simulation code predicts that, with the density reduced to $n_o = 2.7 \times 10^{19} m^{-3}$ and with about 900 kW of power in the peak at $N_{//}=3.3$, V_L can be maintained at -0.5 V, giving a recharge time of ≈ 5 s. This corresponds to a recharge efficiency $\eta_{rech} \equiv -V_L I_p / P_{RF}$ of 0.11, comparable to that achieved on Alcator C[7]. Full recharge was not possible on Alcator or in other experiments, due to limited RF pulse duration.

In an experimental situation we would typically lower both the density and $N_{//}$ during recharge, presumably improving the above efficiency. It therefore appears feasible, by varying $N_{//}$, to alternate periods of OH-asssisted current drive at relatively high density with periods of transformer recharge. We are currently extending simulations to model more accurately the effect of the negative electric field and runaway electrons. This will enable us to determine the optimum density for recharge.

4. PLANNED EXPERIMENTAL PROGRAM

The flexibility and high power density of the LH system for the TdeV will permit us, in addition to extending the pulse length of the tokamak to a near steady-state regime, to carry out new current drive and heating experiments, some of which are relevant to the ITER design. The planned program includes:

- Current drive at high $N_{//}$ and low wave energy (30-60 keV). The effect of non-accessibility to the center can be assessed by operating at high density ($\bar{n}_e \geq 4 \times 10^{19} m^{-3}$). We will also be able to check whether current drive saturation occurs at very high RF power density.
- Comparison of limiter and divertor operation, including effects of high suprathermal flux on divertors.
- Full transformer recharge.
- LH-assisted current ramp-up, with $N_{//}$ ramped according to changes in n_e.
- Tailoring the current profile by launching a two-component $N_{//}$ spectrum.
- Significant plasma heating ($P_{RF}/P_{OH} \approx 3$), with possible H-mode.

We also plan to study questions of a more fundamental nature, such as the effect of different wave spectra on the suprathermal electron distribution and current profile, and the role of edge density fluctuations on coupling. To this end, a number of diagnostics dedicated to RF experiments will be added to the set already on the tokamak, which has good viewing access. Current profile diagnostics include an SMM polarimeter and a planned neutral beam injector. Vertical electron cyclotron emission and/or absorption measurements will be used to determine f(v). Hard X-ray and pulse height analysers are to be upgraded. A set of fast measurements will enable correlation of grill reflections, density fluctuations and parametric instabilities.

5. CONCLUSION

A long pulse lower hybrid current drive and heating system is being prepared for the TdeV. It will operate at f=3.7 GHz and with a power of 1.0-1.3 MW, giving a high power density of 1 MW/m^3. Experimental scalings and theoretical simulations predict a current drive efficiency of 0.4 at its central $N_{//}$ of 2.9. Operating scenarios include full RF current drive for 30 s, at $I_p = 200$ kA and $\bar{n}_e = 2.0 \times 10^{19} m^{-3}$, and alternating periods of OH-assisted current drive and transformer recharge. The system should be well placed to study physics issues relevant to ITER. Operation is expected in 1992.

ACKNOWLEDGEMENTS

We would like to thank Drs. S. Bernabei, C. Gormezano and G. Tonon for helpful discussions and suggestions on the design of the RF system. The Centre canadien de fusion magnétique is a joint venture of Hydro-Québec, Atomic Energy of Canada Limited and the Institut national de la recherche scientifique, in which MPB Technologies Inc., Canatom Inc. and the Université de Montréal also participate. It is principally funded by AECL, Hydro-Québec and INRS.

REFERENCES

1. R. Décoste et al, 8th Top. Conf. on RF Power in Plasmas (Irvine, USA, 1989), AIP Conf. Proc. 190, 130.
2. X. Litaudon and D. Moreau, JET Report JET-R(89)01 (1988).
3. Registered Trade Mark, SCM Metal Products, Inc..
4. J. Bagdoo et al, Int. Conf. on Accelerator and Large Exp. Physics Control Systems (Vancouver, Canada, Nov. 1989) (to be published).
5. F. Leuterer, Lower Hybrid Workshop, Princeton, USA (1989) (unpublished).
6. V. Fuchs, I.P. Shkarofsky, R.A. Cairns, P. Bonoli, Nucl. Fus. 29(9) (1989).
7. Y. Takase, S. Knowlton and M. Porkolab, Phys. Fluids 30(4) 1169 (1987).

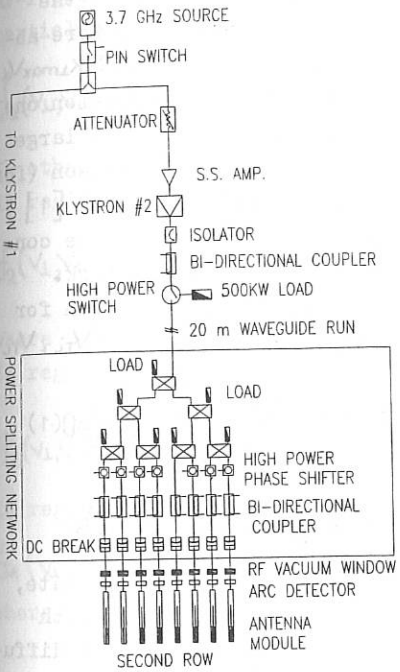

Fig. 1 Schematic of the RF system.

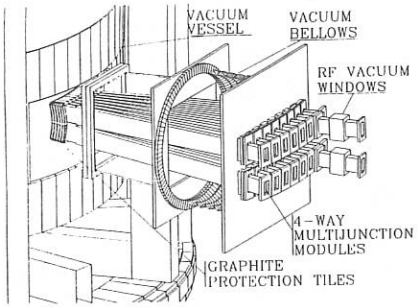

Fig. 2 View of multijunction antenna.

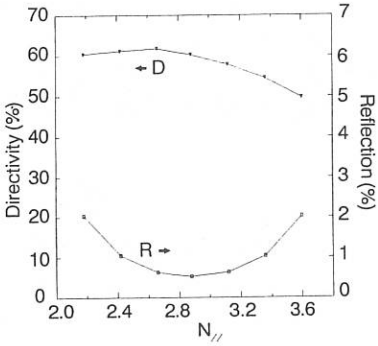

Fig. 3 Directivity of spectrum and total reflection. Module phasing is -90° to 90°.

EFFECT OF QUASI-LINEAR DISTORTIONS ON THE LH-WAVE CURRENT DRIVE IN A REACTOR-TOKAMAK

V.S.Belikov, Ya.I.Kolesnichenko, O.A.Silivra

Institute for Nuclear Research, Ukrainian SSR
Academy of Sciences, Kiev, USSR

The α-particle distribution function is found with taking into consideration the quasi-linear distortion caused by LH waves which results in both the acceleration of alphas above 3.5 MeV and the anisotropization of their distribution in the velocity space. The influence of quasi-linear distortion of alpha distribution on the efficiency of current drive and the absorbed RF power is studied. The comparison of the obtained results with the earlier known one is carried out.

Fast α-particles interact with LH waves through the resonance $\omega = k_\perp v_\perp$ (the notations are usual). Therefore absorption of RF energy by alphas is absent provided $\omega > k_{\perp max} v_\alpha$ where $v_\alpha = 1.3 \times 10^9 cm \cdot s^{-1}$. But to satisfy this condition one should use a generator of RF field with the relatively large frequency which is not desirable for the technical reason (for instance, it is necessary to have $\omega > 6.5 GHz$ for ITER [1]. That is why the case of $\omega < k_{\perp max} v_\alpha$ is of interest. The consideration of this case is a subject of the present work.

We proceed from the following quasi-linear equation for the high energy α-particles ($v \gg v_c$, $v_c \sim (m_i/m_e)^{1/6} v_{Ti}$, v_{Ti} the ion thermal velocity):

$$\frac{1}{\tau_s}\left(\frac{\partial}{\partial v_\parallel} v_\parallel + \frac{\partial}{v_\perp^2 \partial v_\perp} v_\perp^2\right)\left(1+\frac{v_c^3}{v^3}\right) f_\alpha + \frac{\partial}{v_\perp \partial v_\perp} v_\perp D(v_\perp) \frac{\partial f_\alpha}{\partial v_\perp} + \frac{S_\alpha}{4\pi v_\perp^2} \delta(v - v_\alpha) = 0 \quad (1)$$

where [2]

$$D(v_\perp) = \frac{e_\alpha^2 c^3}{2m_\alpha^2 \omega v_\perp^2} \int \frac{dn_\parallel}{n_\perp^3} \frac{|E(n_\parallel)|^2}{\sqrt{v_\perp^2 - c^2/n_\perp^2}} \eta\left(v_\perp^2 - c^2/n_\perp^2\right),$$

$n_{\parallel,\perp} = c k_{\parallel,\perp}/\omega$, $S_\alpha = n^2 \langle \sigma v \rangle / 4$ the fusion reaction rate, τ_s the alpha slowing down time caused by collisions with electrons. It follows from Eq.(1) that the quasi-linear diffusion occurs along lines $v_\parallel = const$. The smallest transverse velocity of alphas interacting with the waves ($v_{\perp r} = c/n_{\parallel max}$) is determined by the condition for existance of resonance, the lar-

gest one is determined by competition of the alpha acceleration due to quasi-linear process and alpha slowing down due to Coulomb collisional slowing down. Therefore we may conclude that the velocity distribution of α-particles is anisotropic and contains the particles with the transverse energies $\mathcal{E}_\perp > \mathcal{E}_\alpha$, $\mathcal{E}_\alpha = 3.52$ MeV.

To find a solution of Eq.(1) it is convenient to divide the space $(V_\perp, V_\parallel)$ in four regions according to Fig.1. In the first region ($|\chi| > \chi_c$, $\chi = V_\parallel / V$, $\chi_c \equiv \sqrt{1 - V_{\perp r}^2 / V_\alpha^2}$) the presence of RF-field does not affect α-particles and hence

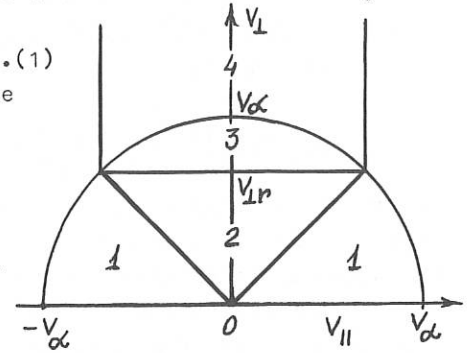

Fig.1

$$f_1(V_\perp, V_\parallel) = \frac{S_\alpha \tau_s}{4\pi (V_c^3 + V^3)} \eta(V_\alpha - V) \quad (2)$$

In other regions the solution has the following form:
In region 2 ($V_\perp \leq V_{\perp r}$, $|\chi| \leq \chi_c$)

$$f_2(V_\perp, V_\parallel) = \frac{S_\alpha \tau_s V_r^3}{4\pi V_\alpha V_{\perp r}^2} \cdot \frac{V_c^3 + V^3 V_{\perp r}^3 / V_\perp^3}{(V_c^3 + V^3)(V_c^3 + V_r^3)} \quad (3)$$

where $V_r = \sqrt{V_{\perp r}^2 + V_\parallel^2}$
In region 3 ($V_{\perp r} \leq V_\perp \leq V_{\perp\alpha} = \sqrt{V_\alpha^2 - V_\parallel^2}$, $|V_\parallel| \leq \chi_c V_\alpha$)

$$f_3(V_\perp, V_\parallel) = \frac{S_\alpha \tau_s}{4\pi V_\alpha \Psi(V_\perp, V_\parallel)} \left\{ \int_{V_{\perp r}}^{V_\perp} \frac{\Psi(V_\perp', V_\parallel) dV_\perp'}{\tau_s D(V_\perp') V_\perp'} + \frac{V_r^3}{V_{\perp r}^2 (V_c^3 + V_r^3)} \right\} \quad (4)$$

In region 4 ($V_\perp \geq V_\alpha$, $V_\parallel \leq \chi_c V_\alpha$)

$$f_4(V_\perp, V_\parallel) = f_3(V_{\perp\alpha}, V_\parallel) \Psi(V_{\perp\alpha}, V_\parallel) / \Psi(V_\perp, V_\parallel) \quad (5)$$

where

$$\Psi(V_\perp, V_\parallel) = \exp \left\{ \int_{V_{\perp r}}^{V_\perp} (1 + V_c^3 / V'^3) V_\perp' / \tau_s D(V_\perp') dV_\perp' \right\}$$

When obtaining Eqs(4),(5) the alpha slowing down along the parallel velocities is neglected that is justified when $\chi_c \ll 1$ or when the quasi-linear process is much stronger than the slowing down one .

Let us assume that the wave spectrum is narrow. Then for the case of $\xi \gg 1, \xi = (\pi/4)\tau_s \mathcal{E}_d^2 V_{ir}^3 E^2 / (m_d \omega V_d^5)$ we find the fast α-particle density in the following form:

$$n_\alpha \cong \frac{S_\alpha \tau_s}{3}\left\{\ln\left(1+\frac{V_\alpha^3}{V_c^3}\right)+\frac{\xi^{2/5}}{1-\chi_c^2}\right\} \qquad (6)$$

Here the first term describes the α-particle density in the absence of RF field, the second one is connected with the tail formation due to RF field. It is seen that the second term is dominant provided the sufficiently large wave amplitude. Note that the value of n_α determined by Eq.(6) is less than the value obtained in Ref.[2] by a factor of 2÷3. (In Ref.[2] the isotropic solution for $f(V)$ is found).

It is of interest to know the α-particle density in the tail of distribution. Considering particles with $V_\perp > \hat{V}_\perp$ where $\hat{V}_\perp$ is the arbitrary fixed value of $V_\perp$ we obtain

$$n_\alpha^{tail}(x) \cong \frac{2\xi}{\pi}\frac{\chi_c}{1-\chi_c^2}\frac{S_\alpha \tau_s}{x^3}\exp\left\{-\frac{\pi x^5}{10\xi}\left(x^2+\frac{5}{3}\frac{V_{ir}^2}{V_\alpha^2}\right)\right\} \qquad (7)$$

where $x = \sqrt{\hat{V}_\perp^2 - V_{\perp r}^2}/V_\alpha$. It is assumed that $x^5 \gg \xi$.

It follows from Eq.(7) that the most of alphas has the transverse velocities which do not exceed $\mathcal{E}_{\perp max}$ given by

$$\mathcal{E}_{\perp max} \simeq \left(\frac{10\xi}{\pi}\right)^{2/5}\mathcal{E}_\alpha + m_\alpha V_{ir}^2/2 \qquad (8)$$

In particular, $\mathcal{E}_{\perp max} = 2\mathcal{E}_\alpha$ for $\xi = 1$, $\mathcal{E}_{\perp max} = 4.4\,\mathcal{E}_\alpha$ for $\xi = 10$.

For the absorbed power the following expressions may be found using Eq.(1):

$$P = 2\pi m_\alpha \int_{-\chi_c V_\alpha}^{\chi_c V_\alpha} dV_\parallel \int_{V_{\perp r}}^{\infty} dV_\perp V_\perp^2 D(V_\perp) \frac{df_\alpha}{dV_\perp} \qquad (9)$$

For $\xi \gg 1$ Eq.(9) may be transformed into

$$P \cong 3 m_\alpha S_\alpha V_\alpha^2 \xi^{4/5} \frac{\chi_c}{1-\chi_c^2} \qquad (10)$$

Comparing Eq.(10) with the corresponding expression in the absence of quasi-linear evolutions (P_o) we conclude that

$$\frac{P}{P_o} \cong 0{,}6 \frac{V_{\perp r}}{V_\alpha} \chi_c \xi^{-1/5} \qquad (11)$$

where $P_o = m_\alpha V_\alpha^5 S_\alpha \xi / (V_c^3 + V_{\perp r}^3)$. We see that the ratio P/P_o decreases with ξ . In particular, $P/P_o = 0.3$ for $\xi = 1$ and $P/P_o = 0.2$ for $\xi = 10$. These values are smaller by a factor of 3÷5 in comparison with those of Ref. [2]. Therefore taking into account the calculations of Ref. [2] for the power absorbed by electrons we may conclude that the use of the frequency $\omega < k_{\parallel \max} V_\alpha$ in ITER like tokamak does not lead to essential decrease of the current drive efficiency. But it is clear that to find the lower boundary of the acceptable frequencies the special calculations are required.

References

1. Barbato E., Santini F. Report at TC IAEA meeting on alpha particles, Kiev, 1989. Fusion Technology, to be published.
2. Karney C.F.F. Phys. Fluids, 22 (1979), 2188.

PARAMETRIC DECAY INSTABILITIES STUDIES IN ASDEX

A. Cardinali, R. Cesario, F. Paoletti*, V. Pericoli Ridolfini

Associazione EURATOM-ENEA sulla Fusione
Centro Ricerche Energia Frascati
C.P. 65 - 00044 Frascati, Rome, Italy

Search for possible effects of parametric decay instabilities (PDI) on LH current drive and heating was conducted on Asdex through the analysis of the signal collected by a RF probe located in the scrape off layer plasma. The frequency spectrum, whose shape is unaffected by the position of the probe [1], was characterized by two parameters: the width of 2.45 GHz pump line at $-10db$ from the maximum Δf_p, and the intensity of the first satellite, downshifted in frequency from the pump by one ion cyclotron frequency evaluated at the torus outer edge.

The plasma parameters for this study lie in the following ranges: line averaged density $1.3 * 10^{13} \leq \overline{n}_e \leq 5 * 10^{13}$ cm^{-3} plasma current $300 \leq I_p \leq 420kA$, toroidal field $2.17 \leq B_T \leq 2.8T$, coupled LH power $0.3 \leq P_{LH} \leq 1.6MW$, peak value of the launched $N_\parallel$ spectrum $1.5 \leq \hat{N}_\parallel \leq 4.4$. The main results are:

SATELLITE INTENSITY

A well defined threshold both of P_{LH} and $\overline{n}_e$ exists for the onset of the first satellite. Its intensity firstly grows exponentially with P_{LH} then saturates, see circles in fig. 2. Before saturation it decreases considerably if either I_p or B_T are raised. The threshold power drops rapidly with $\overline{n}_e$, see circles in fig. 3. The growth of these instabilities is determined by the conditions of the edge plasma, density and temperature, the coupled power and by the convective losses, determined in turn by the grill dimensions [2]. A code previously developed for FT experiment, can satisfactorily reproduce the behaviour of the threshold power P_{th} [3], full circles in fig. 3. Values for the Asdex edge density and temperature are taken from [4].

With this same code the different development of PDI, when either one or both rows of the grill are excited, are also well explained [3].

The growth of one or more ion cyclotron satellites does not seem to affect greatly the current drive properties of the LH wave, at least until they are $15db$ below the pump, as is most often the case, except for $\overline{n}_e \geq 4.7 * 10^{13}$ cm^{-3}.

PUMP SPECTRAL BROADENING

Triangles in fig. 2 and 3 describe the behaviour of Δf_p versus P_{LH} and $\overline{n}_e$ respectively. An approximately linear increase is observed in either case. The influence of B_T and I_p is similar to the ion cyclotron PDI case, namely Δf_p decreases increasing either B_T or I_p. The status of the walls is also important, indeed Δf_p became smaller after boronizing the Asdex vacuum vessel.

Differently from the ion cyclotron sidebands the magnitude of Δf_p appears to affect remarkably the current drive properties of the LH waves. This has been

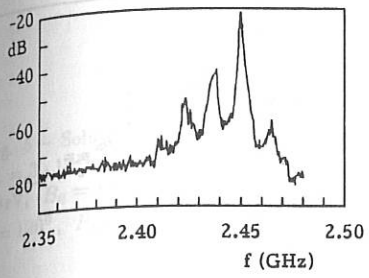

Fig. 1 – Typical parametric decay spectrum for well developed instabilities.

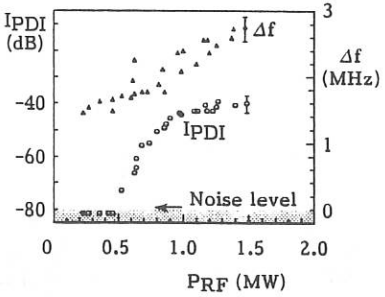

Fig. 2 – Pump spectral broadening (Δ) and first satellite intensity ($\circ$) versus P_{LH} $\hat{N}_{\|}=1.8$, $\overline{n}_e=2.7*10^{13}$ cm^{-3}, $I_p=320kA$, $B_T=2.17T$.

established from the analysis of CD efficiency values, η_{CD}, on a large data base selected in such a way to avoid the problem of the waves accessibility to the plasma core. The effect of the other quantities which can modify appreciably η_{CD} [5], as $\hat{N}_{\|}$ and the impurity content Z_{eff}, has been taken into account normalizing η_{CD} to the case $\hat{N}_{\|}=1.8$ and $Z_{\text{eff}}=1$. This normalized efficiency η^*_{CD} should be constant for the selected data set independently of plasma parameters like $\overline{n}_e$, I_p and B_T, but variations as large as 50% are instead observed. Looking for an explanation of this effect a remarkable correlation of η^*_{CD} with Δf_p has been found, as shown in fig. 4.

This can be tentatively explained as follows. The spectral broadening can be due to either PDI, involving ion sound frequencies, or scattering by density fluctuations. Both processes can modify the launched $N_{\|}$ spectrum [6]. If we assume that the frequency shift of a sideband is a measure of its change in $N_{\|}$, we can consider useful for CD only that fraction of the power within a small fixed interval Δf_0 around the pump frequency. This fraction can be easily evaluated from the experimental spectra as a function of Δf_p, and the decrease of η^*_{CD} with Δf_p can be calculated. Δf_0 is taken as a free parameter. A best fit procedure on the experimental values of η^*_{CD} has given the dashed curve in fig. 4, with $\Delta f_0=0.8$ MHz.

In conclusion ion cyclotron PDI do not affect greatly CD efficiency and their behaviour can be satisfactorily predicted by the theory, on the contrary pump spectral broadening degradates remarkably CD efficiency probably because of a related change in the launched $N_{\|}$ spectrum.

PARAMETRIC DISPERSION RELATION AND DECAY INSTABILITIES

We consider the propagation, in a plasma magnetized by a static magnetic field B_0, of a lower hybrid pump wave (ω_0, k_0) with finite extent which decays into a low frequency mode (ω_1, k_1) and two high frequency sidebands $(\omega_1 \pm \omega_0, k_1 \pm k_0)$. The plasma is assumed locally homogeneous, i.e., $k_\perp \gg |\nabla n/n|$, $|\nabla T/T|$, where

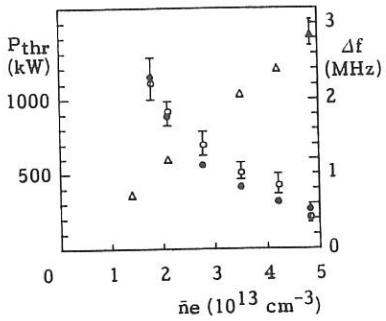

Fig. 3 – Experimental (o) and calculated (•) P_{th} and Δf_p (Δ) versus $\overline{n}_e$. $P_{LH}=1$ MW, $I_p=420kA$, $B_T=2.8T$, $\hat{N}_{\parallel}=1.8$.

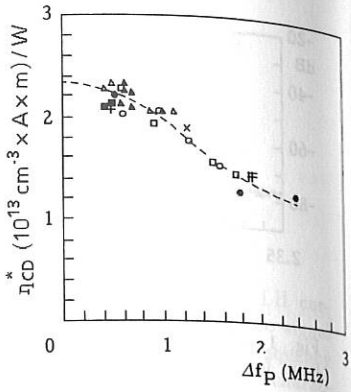

Fig. 4 – Experimental and calculated (dashed curve) η^*_{CD} values vs. Δf_p

$k_\perp$ is the perpendicular (to B_0) wave vector of the waves involved and n and T are the plasma density and temperature. The parametric dispersion relation is [7]

$$\varepsilon(\omega_1,k_1)=\frac{\mu^+}{\varepsilon(\omega_1+\omega_0,k_1+k_0)}+\frac{\mu^-}{\varepsilon(\omega_1-\omega_0,k_1-k_0)} \tag{1}$$

where $\varepsilon(\omega,k)=1+\chi_i(\omega,k)+\chi_e(\omega,k)$ is the dielectric function and $\chi_i\chi_e$ are the linear susceptibilities. For $\omega_{1R}<k_{1\|}\,v_{\rm the}$, i.e., when the response of the electron in the parallel (to B_0) direction is adiabatic, we can assume

$$\mu^{\pm}=\frac{\chi_e(\omega_1,k_1)-\varepsilon(\omega_1,k_1)\omega_{\rm pi}^4}{4\omega_0^2k_1^2c_s^2\varepsilon(\omega_1,k_1)}\left[1+\frac{\omega_1}{k_{1|}v_{\rm the}}Z\left(\frac{\omega_1}{k_{1|}v_{\rm the}}\right)\right]^2\sin^2\delta^{\pm}\frac{U^2}{c_s^2} \tag{2}$$

In this formula, Z is the Fried–Comte plasma dispersion function, ω_{pi} the ion plasma frequency, c_s the ion sound velocity, $U=E_0c/B_0$ the ExB drift velocity of electrons, and $\delta^{\pm}=\Delta k_{2,3\perp}$, $k_{0\perp}$ the angle between $k_{2,3\perp}$ and $k_{0\perp}$, as $k_{2,3}=k_1\pm k_0$.

The solutions of Eq. (1) in the ion-cyclotron frequency range $\omega_{1R}\approx n\omega_{ci}$, $n=1,2,\ldots$, for the Asdex plasma parameters were examined in a previous work [8]. The R.F. power thresholds of the parametric instabilities expected by these solutions are found in a good agreement with the thresholds observed during the lower hybrid experiment in Asdex [3].

Here we present the results of the study of the parametric dispersion relation in

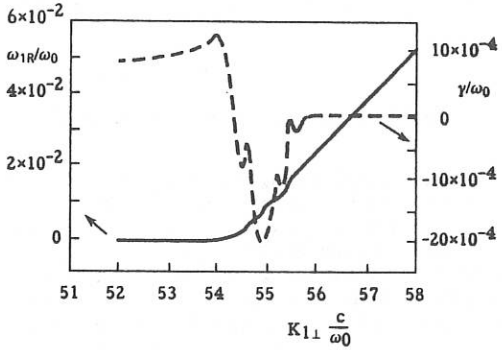

Fig. 5 – Solutions of Eq. (1) for $n_e = 3 \cdot 10^{12}$ cm^{-3}, $T_e = T_i = 20$eV, $B_0 = 1.8T$, $k_{1\parallel}\frac{c}{\omega_0} = 12$, $\delta = 120^0$, $P_{RF} = 100$kW.

the ion–sound frequency range, $\omega_{1R} \approx |k_{1\parallel}| v_{thi}$, which are relevant to the observed pump wave broadening phenomenon. For a given numerical calculation we have assumed $k_{1\perp}$ as an independent variable, keeping fixed the other plasma and R.F. parameters. In order to find the solutions of eq. (1) with higher growth rate, we have examinated many cases with different values of the radial (x) coordinate and $k_{0\parallel}$, $k_{2,3\parallel}$, $k_{2,3\perp}$, $k_{1\parallel}$, $k_{\perp\parallel}$, $\delta^{\pm}$.

In fig. 5 is shown a branch of solutions of eq. (1) with $\frac{k_{1\parallel} c}{\omega_0} = 12$, $\delta^- = 120^0$. We observe that the maximum growth rate value $\frac{\gamma}{\omega_0} \simeq 1.3 \cdot 10^{-3}$ is expected for a sideband whose frequency shift by the pump wave is $\frac{\Delta\omega}{\omega_0} \simeq 0.9 \cdot 10^{-3}$. Differently from the branch of solutions of eq. (1) which is shown in ref. [9], we find, as a feature of the solutions shown in fig. 5 only stable solutions with $\gamma < 0$ in the ion-cyclotron frequency range. The R.F. power threshold estimated in taking into account the connective effects due to the finite extent of the pump wave, is of about 100kW. It is possible to conclude that such an ion–sound quasimode driven parametric instability can be responsible of the broadening of the frequency and the $k_{\parallel}$ spectrum of the launched wave.

FOOTNOTE AND REFERENCES

(*) JET Joint Undertaking, Abingdon, (U.K.)

[1] R. Cesario, V. Pericoli Ridolfini, Nucl. Fus. **27**, (1987), 435.

[2] C.S. Liu et al., Phys Fluids, **27**, (1984), 1709.

[3] V. Pericoli Ridolfini et al. "*Study of the parametric decay instabilities in the 2.45 GHz experiment on Asdex*" Proc. 8th Topical Conf. on Radio Freq. Power in Plasmas, Irvine, CA (U.S.A.), May 1989.

[4] K. McCormic et al., Proc. 16th Europ. Conf. on Controlled Fusion and Plasma Physics, Venezia 1989, p. 895.

[5] N.J. Fisch, Rev. Mod. Physics **59**, (1987), 175.

[6] V. Pericoli Ridolfini et al., RT/FUS 90.3.

[7] V.K. Tripathi, C.S. Liu, Phys. Reports 130, 143 (1986).

[8] A. Cardinali, R. Cesario, F. Paoletti, 16th Eur. Conf. on Controlled Fusion and Plasma Physics, Venezia 1989, III, 1178.

QUASILINEAR THEORY FOR SPATIALLY DELIMITED WAVE PATTERNS

E. Canobbio* and R. Croci

IPP–Euratom Association, Garching, F.R.G.; (*) CEC, Brussels, Belgium

The usual quasilinear (QL) theory implies waves whose amplitude is constant in space, a restriction which is particularly inconvenient in the case of the LH waves. Indeed, it is precisely in this case that an adequate treatment of both the QL effects and the resonance cone features is instrumental to the understanding of current drive (inter alia). In this paper the QL theory is extended to cover such situations. For simplicity we consider particles moving in a temporally constant and spatially uniform magnetic field $\vec{B}$ perturbed by an electrostatic field. In a cartesian reference system with z along the magnetic field let the electric field be given by $E_j \equiv \alpha_j \exp\left[i(\omega t - k_\parallel s)\right] + \text{c.c.}$, where $s \equiv z - k_\perp x/k_\parallel$, $\alpha_1 \equiv (\alpha/\sqrt{l})\exp\left[-s^2/l^2\right]$, $\alpha_3 \equiv (k_\perp/k_\parallel)\alpha_1$, $\alpha_2 = 0$ (the general theory is developed in ref. [1] as well as in a forthcoming publication). The discussion is conducted mainly in the reference system defined by the unperturbed particle trajectories in phase space described as functions of z. We denote the old variables by (x_j, v_j), with $x_1 \equiv z$, and the new variables by (ς_j, w_j), with $\varsigma_1 = z$ and $w_1 = v_z$. In the latter reference system the Boltzmann equation takes the form

$$\frac{\partial f}{\partial t} + w_1 \frac{\partial f}{\partial \varsigma_1} + \left[\left(A_j e^{i\omega t} + \text{c.c.}\right)\frac{\partial f}{\partial v_j}\right] = [C(f)]\,, \tag{1}$$

where $A_j \equiv (q/m)E_j$, $\Omega \equiv qB/mc$ and q, m are the charge and the mass of the particles; repeated indices have to be summed and the brackets indicate that the quantities they embrace have to be taken in the new reference system. The explicit form of the collision term is given later. We formally develop f in the following way:

$$f(x_j, v_j, t) = f_o(x_j, v_j, t) + \sum_{n\neq 0} f_n(x_j, v_j, t) e^{in\omega t}\,, \tag{2}$$

where the time scales of f_o and f_n are large in comparison with $1/\omega$. By neglecting f_n with n larger than 2 and by noting that $f_{-1} \equiv f_1^*$ from eq. (1) one gets

$$\frac{\partial f_o}{\partial t} + w_1 \frac{\partial f_o}{\partial \varsigma_1} + \left[A_j \frac{\partial f_{-1}}{\partial v_j}\right] + \left[A_j^* \frac{\partial f_1}{\partial v_j}\right] = [C(f_o)]\,,$$

$$(i\omega + \nu) f_1 + \frac{\partial f_1}{\partial t} + w_1 \frac{\partial f_1}{\partial \varsigma_1} + \left[A_j \frac{\partial f_o}{\partial v_j}\right] = 0\,, \tag{3}$$

where $C \approx -\nu f_1$ has been substituted in the equation for f_1 because $\nu \ll \omega$. The time derivative will be neglected with respect to ωf_1; thus f_1 has the following form for $v_1 > 0$:

$$f_1 = -e^{-i(\omega - i\epsilon)\varsigma_1/w_1} \int_{-\infty}^{\varsigma_1} e^{i(\omega - i\epsilon)\sigma/w_1} \left[\frac{A_j}{v_1}\frac{\partial}{\partial v_j} f_o\right] d\sigma \equiv \frac{1}{w_1} \mathcal{S}\left\{\left[A_j \frac{\partial}{\partial v_j} f_o\right]\right\}. \tag{4}$$

The solution for $v_1 < 0$ is obtained by putting the lower limit of the integral equal to ∞. By taking into account the definition of the new reference system one gets

$$f_1 = \mathcal{S}\left\{\frac{[A_1]}{w_1}\left(\frac{\partial f_o}{\partial w_1} - \frac{\sigma\Omega}{w_1^2}\frac{\partial f_o}{\partial w_2}\right) - \frac{[A_3]}{w_1}\left(\frac{\cos\psi(\sigma, w_2)}{w_3}\frac{\partial f_o}{\partial w_2} + \sin\psi(\sigma, w_2)\frac{\partial f_o}{\partial w_3}\right)\right\}, \tag{5}$$

where $\psi(\varsigma_1, w_2) \equiv (\varsigma_1\Omega/w_1) + w_2$. The process described by f_o when f_1, given by eq. (5), is inserted in the first of eqs. (3) is diffusion in velocity space if the effect of the integral operator $\mathcal{S}$ on $\partial f_o/\partial v_j$ is to multiply $\partial f_o/\partial v_j$ by some function; in other words, the interaction of the particles with the electric field in the interval $(-\infty, \varsigma_1)$ (for $w_1 > 0$) should not appreciably depend on the previous interaction in the interval $(-\infty, \varsigma_1)$. Let us integrate by parts in the operators $\mathcal{S}\{\}$ of eq. (5):

$$w_1 f_1 = \mathcal{S}\{[A_1]\}\frac{\partial f_o}{\partial w_1} + \frac{\Omega}{w_1^2}\mathcal{S}\{\sigma[A_1]\}\frac{\partial f_o}{\partial w_2} - \frac{1}{w_3}\mathcal{S}\{[A_3]\cos\psi\}\frac{\partial f_o}{\partial w_2} - \mathcal{S}\{[A_3]\sin\psi\}\frac{\partial f_o}{\partial w_3}$$

$$+ \textit{terms containing the derivative of } f_o \textit{ and of } \frac{\partial f_o}{\partial w_1} \textit{ with respect to } \sigma\,. \qquad (6)$$

When collisions dominate, and Larmor radius effects can be neglected, $\partial f_o/\partial v_j$ can be taken out of the operator $\mathcal{S}$, because the logaritmic derivative of $\partial f_o/\partial v_j$ with respect to ς_1 is sufficiently small, f_o being approximately a Maxwellian. In this case from the first of eqs. (3) and eq. (6) one easily derives the diffusion coefficients. When Larmor radius effects are not negligible the scale of variation of f_o in ς_1 (being of the order of the Larmor radius) is much smaller than the scale of variation of $[A_i]$. We then take the average over w_2, which cancels small–scale effects and allows introduction of diffusion coefficients. The mean of f_o, which will be denoted by g_o, can be sustituted for f_o in $\langle [A_i^*] f_1 \rangle$ if the mean value of the deviation of f_o from g_o is negligible, as we assume. Equation (6) then simplifies to

$$w_1 f_1 \equiv \mathcal{S}\{[A_1]\}\frac{\partial g_o}{\partial w_1} - \mathcal{S}\{[A_3]\sin\psi\}\frac{\partial g_o}{\partial w_3}\,. \qquad (7)$$

The appropriate approximation of the collision term in the electron equation (the only one we consider here), in the regime of LH electron current drive is the linearized, high velocity limit, whose averaged form is, when g_o is Maxwelian in w_3,

$$\langle [C] \rangle = \frac{\partial}{\partial w_1}\left[D_{FP}\frac{\partial g_o}{\partial w_1} + D_{FP}\frac{2w_1}{v_t^2} g_o \right], \qquad (8)$$

where $D_{FP} \equiv \nu v_t^5/w_1^3$. The coefficient of the diffusion parallel to the magnetic field is given by

$$-w_1 D_{QL} \equiv \langle ([A_1^*]\,\mathcal{S}\{[A_1]\} + c.c.)\rangle \equiv 2\alpha_1 \sum_n J_n^2\left(\frac{k_\perp w_3}{\Omega}\right)\int_{-\infty}^{\varsigma_1} \alpha_1 \cos(\Delta_n(\sigma - \varsigma_1))\, d\sigma\,, \qquad (9)$$

where $\Delta_n \equiv (\omega - n\Omega)/w_1 - k_\parallel$. The integral can be expressed by means of the 'plasma dispersion function'

$$w_1 D_{QL} = \alpha^2 \exp\left[-2s^2/l^2\right] \sum J_n^2 Im\left\{Z\left((l\Delta_n/2) - is/l\right)\right\}. \qquad (10)$$

This expression is valid only when $|D_{QL}| \ll D_{FP}$, as we shall see later. Therefore, as D_{QL} is proportional to $1/w_1$ when $|w_1|$ goes to infinity, for large velocity it is no longer correct. When l is infinite, α_1 is constant and from eq. (9) follows the known

result $D_{QL} = 2\pi\alpha^2 \sum J_n^2 \delta(w_1 \Delta_n)$. When α_1 is not constant, the diffusion coefficient is usually defined as the linear superposition of the diffusion coefficients corresponding to the different k–components of the electric field. We denote it by D_u and get

$$w_1 D_u = 2\pi\alpha^2 \sum_n J_n^2 e^{-(l\Delta_n/2)^2} . \tag{11}$$

A simple relation between D_{QL} and D_u exists only when $s \ll l$: from the known properties of the Z function we then obtain $D_{QL} = D_u/2\sqrt{\pi}$. The gradient of the electric field amplitude modifies D_{QL} through $l\Delta_n$ at the exponent; an increase of the gradient moves the velocity v_m at which $D_{QL} \lesssim D_{FP}$ towards smaller velocity, thereby increasing the number of particles which interact with the electric field. The value of v_m for $n = 0$, the case of interest for the electrons, and $s \ll l$ is given by $l\Delta \approx 1$, i.e. $v_m \approx (l\omega)/(1+lk_\parallel)$. Moreover, l also modifies the quotient D_{QL}/D_{FP}. When $lk_\parallel$ is smaller than 2 (large gradient) the diffusion coefficient is larger than D_{FP} at all $w_1 > v_m$. When $lk_\parallel$ increases D_{QL} is larger than D_{FP} in a region whose relative amplitude $(v_M - v_m)/v_m$ is proportional to $1/lk_\parallel$; it then becomes smaller than D_{FP}, and finally larger than D_{FP} when w_1^2 is larger than approximately $(\nu v_t^5/\alpha^2)\exp\left[l^2 k_\parallel{}^2/4\right]$. When $s \leq l$, D_{QL} can be much larger than D_u, and thus v_m evaluated for D_{QL} can be smaller than the value of v_m evaluated for D_u. Leaving the resonance ($\Delta = 0$) has a much less drastic effect on D_{QL} than on D_u. The equation for g_o is

$$w_1 \frac{\partial g_o}{\partial \varsigma_1} - \frac{\partial}{\partial w_1}\left[(D_{QL} + D_{FP})\frac{\partial g_o}{\partial w_1} + \frac{2w_1}{v_t^2} D_{FP} g_o\right] = 0 . \tag{12}$$

If the ς_1–derivative can be neglected, one gets the usual solution

$$\ln g_o \approx -\frac{w_3^2}{v_t^2} - \frac{2}{v_t^2}\int_0^{w_1} \frac{w_1 D_{FP}}{D_{QL} + D_{FP}}\, dw_1 , \tag{13}$$

which exhibits a 'plateau' for w_1 larger than v_m. However, the condition that the ς_1–derivative of g_o be negligible (a necessary condition in order that the terms not explicitly written in eq. (6) be negligible, i.e. in order that diffusion coefficients can be defined) is

$$\left| w_1 \frac{\partial g_o}{\partial \varsigma_1} \right| \ll \left| \frac{\partial}{\partial w_1}\left(2 w_1 g_o D_{FP}/v_t^2\right) \right| \approx \frac{4 D_{FP}}{v_t^2} . \tag{14}$$

Since from eq. (13) the value of the ς_1–derivative increases with velocity, the restriction imposed by eq. (14) is such that eq. (13) describes, strictly speaking, only the beginning of the 'plateau'. A consequence of eq. (13) is that where $D_{QL} \gg D_{FP}$ the quantity which varies slowly with respect to $|A_1|$, and hence can be taken out of the operator S, is $(D_{QL} + D_{FP})(\partial g_o/\partial w_1)$ and not $(\partial g_o/\partial w_1)$. With this in mind, we obtain the following definition of D_{QL}, valid for every value of D_{QL}/D_{FP} :

$$w_1 D_{QL}(\varsigma_1) = 2(D_{QL}(\varsigma_1) + D_{FP})\alpha_1(\varsigma_1) \sum_n J_n^2 \int_{-\infty}^{\varsigma_1} \frac{\alpha_1(\sigma)\cos(\Delta_n(\sigma - \varsigma_1))}{D_{QL}(\sigma) + D_{FP}}\, d\sigma . \tag{15}$$

It can be shown that the total diffusion coefficient $(D_{QL} + D_{FP})$ which follows from this equation is positive definite. An approximation to g_o better than that given by eq. (13) is obtained from the equation for β, the logarithm of g_o, which follows from eq. (12) and which is approximated by

$$(D_{QL} + D_{FP})\frac{\partial \beta}{\partial w_1} + \frac{v_t^2}{2}\frac{D_{QL} + D_{FP}}{D_{FP}}\frac{\partial \beta}{\partial \varsigma_1} = -2\frac{w_1}{v_t^2}D_{FP}\,. \tag{16}$$

The characteristics of eq. (16), which are given by $(\partial \varsigma_1/\partial w_1) = v_t^2/2D_{FP}$, allows the solution of eq. (16) to be written in the form

$$\ln g_o = -2\int_0^{v_z/v_t} \frac{u\,du}{1+\gamma(u, v_z/v_t, s/l)}\,, \tag{17}$$

where $\gamma \equiv \frac{1}{D_{FP}(u)} D_{QL}\left(u, \left((s/l) + (v_t^3/2l)\int_{v_z/v_t}^{u} (1/D_{FP}(\tau))\,d\tau\right)\right)$.

Equation (17) describes the logarithm of a Maxwellian up to the value of v_z where $D_{QL} \approx D_{FP}$. Then it describes a (more or less flat) 'plateau', whose width can be deduced by the following argument. In eq. (17) the velocity also appears in the ς_1–dependence, so that uD_{QL} decreases exponentially when $(v_t^3/2)\int_{v_m/v_t}^{u} (1/D_{FP})\,d\tau$ is larger than l. In other words, γ becomes smaller than unity, and therefore β is approximately equal to $-(v_z^2/v_t^2)$, for two reasons: the first is a change of the order $\Delta v \approx \omega/lk_\parallel{}^2$ of the u variable of D_{QL}; it is comparable with the quantity $(v_M - v_m)$ introduced previously. The second reason is a change of the order l of the ς_1–dependence, which is induced, owing to the characteristics, by a change in velocity given by $\delta v \approx 2lD_{FP}/v_t^2$, a quantity which, in the one–dimensional case, has the more appealing form $(\delta v/v_t) \approx (l/\lambda(v_m))$, where λ is the free path of a particle with $v_z = v_m$. The smaller of the two quantities $(\delta v, \Delta v)$ determines the width of the 'plateau'; for $l^2k_\parallel{}^2 > (\omega^4/k_\parallel{}^3\nu v_t^3)$, which is a quantity much larger than unity, one has $\delta v < \Delta v$. In this situation (gradient of α_1 small with respect to wavelength and mean free path, in particular $\alpha_1 = const.$) the 'plateau' extends over the whole region (v_m, v_M). When $l^2k_\parallel{}^2 < (\omega^4/k_\parallel{}^3\nu v_t^3)$ the width of the 'plateau' is smaller than the preceding one and is proportional to the collision frequency. On the other hand, whereas in the first case there is a 'plateau' only for values of s smaller than l, in the second case the limit value for s is $(v_M^4 - v_m^4)/8\nu l v_t^3$. The total area of the 'plateau' region in the $((s/l), v_z^4)$ plane is in both cases the same. In conclusion, at variance with the usually assumed QL theory for constant amplitude waves the phase–space region where g_o has a 'plateau' is not defined by the condition $D_{QL}\big((v_z/v_t), (s/l)\big) > D_{FP}$.

[1] Quasilinear space–dependent diffusion in the lower hybrid waves regime; E. Canobbio and R. Croci, IPP 6/284 (November 1989).

PARAMETRIC STUDY ON LOWER HYBRID CURRENT DRIVE EFFICIENCY FOR NEXT STEP DEVICES

H. Takase, K. Okano and A. Hatayama*

Toshiba Research and Development Center,Toshiba Corp.,Kawasaki,JAPAN

*Fusion Technology Development Office,Nuclear Fusion Division, Toshiba Corp.,Tokyo,JAPAN

1. INTRODUCTION

Lower hybrid current drive (LHCD) is the most reliable way among various r.f. current drive methods. However, some difficulties still remain in its application to reactor grade plasmas, for example, improvement in the current drive efficiency. In this study, assuming a steady state current drive, we scan various parameters, especially temperature, and discuss its potential as a current driver in next step devices by using a newly developed analysis code. The result of simulations partially shows electron temperature dependence of lower hybrid current drive efficiency as found in experimental results of JT–60[1]. This dependence takes place by large shift of the parallel refractive index $n_{\parallel}$ due to the toroidal effect. Finally, we discuss the maximization of current drive efficiency by the optimization of electron temperature.

2. LHCD CODE FOR NON–CIRCULAR TOKAMAK PLASMAS

The analysis code consists of three modules. These modules are 1)free boundary MHD equilibrium code, 2)ray tracing code for non–circular tokamak plasmas and 3)relativistic Fokker–Planck code with two–dimensional effects based on quasi–linear theory. The equilibrium code gives profiles of density $n_{e,i}$ and temperature $T_{e,i}$ (subscripts e and i mean electron and ion, respectively) for tokamak plasma with an arbitrary cross section by solving Grad–Shafranov equation. Density and temperature profiles are taken to vary as ψ^{α}, where ψ is poloidal flux function, with α=0.5 and 1.0 for density and temperature, respectively. The ray tracing code calculates the wave propagation and absorption with a very high accuracy on basis of geometrical optics approximation. This code adopts the Adams–Moulton method of the 8–th order for the numerical method, and the B–spline method of the 4–th order for interpolating of the numerically computed ψ. The accuracy of the ray tracing code is estimated from its deviation from the dispersion relation along a ray trajectory, and the maximum deviation is less than 10^{-8}. The Fokker–Planck code with two–dimensional effects computes the electron velocity distribution functions on individual magnetic surfaces, using the formulation in Bonoli and Englade[2]. The accuracy of this Fokker–Planck code is checked by the analytical solution of a one–dimensional Fokker–Planck equation and the

computed wave absorption energy from the electron distribution function compared with the computed wave damping energy from ray tracing code. The calculation flow is carried out as follows; after reference equilibria are obtained by the equilibrium code, the ray tracing and the Fokker–Planck calculation are iterated by about 7 to 15 times until the current density profile J_{rf} becomes a steady state (within about 1% error).

3. $\langle T_e \rangle$ DEPENDENCE OF CURRENT DRIVE EFFICIENCY

We have carried out calculations of current drive efficiency in steady state operation with the ITER plasma (major radius R_P =5.5m, minor radius a=1.8m, elongation κ=2.0, plasma current I_P =18MA and toroidal magnetic field B_T =5.3T). The current drive efficiency is defined by $\eta_{CD} = \langle n_e \rangle I_{rf} R_P / P_{abs}$, where $\langle n_e \rangle$, I_{rf} and P_{abs} are the volume averaged density, r.f. current and absorbed wave power, respectively. The η_{CD} dependence on the spectrum width $\Delta n_{\parallel}$, the parallel refractive index $n_{\parallel}$ and the electron temperature T_e were investigated for many parameters. The results of calculations in this study are summarized at Figs. 1 ~ 3. Figure 1 shows a typical ray trajectory. The parameters used were $n_{\parallel}$=2.0, wave frequency f=4.6GHz, $\langle n_e \rangle = 0.9 \times 10^{20} m^{-3}$, volume averaged temperature $\langle T_e \rangle = \langle T_i \rangle$ =4.4 keV, and effective charge Z_{eff} =2.0. In Fig. 1, the solid line is the magnetic surface and the dotted line is the ray trajectory. After the lower hybrid waves are launched from outer periphery and are reflected at the plasma surface, the wave power is almost absorbed in the plasma.

Figure 2 shows various quantities along the ray trajectory for the same parameters, where ϕ is toroidal angle, r is half width of flux surface labeled by ψ and P_W is the normalized wave power. In Fig. 2(b), we should note that the toroidal effects due to the high elongation induce large shift from the initial $n_{\parallel}$ as it propagates through the plasma. Parameters scans were done with various central $n_{\parallel}$ and spectrum widths $\Delta n_{\parallel}$. For simplification, we assumed that the power spectrum has a rectangular distribution and other parameters were equivalent to the case of Fig. 1. It was found that the case of central $n_{\parallel}$=2.0 and $\Delta n_{\parallel}$=0.2 maximized η_{CD} .

Figure 3 shows the dependence on the volume averaged electron temperature $\langle T_e \rangle$ of the current drive efficiency η_{CD} and the normalized current density profiles generated by the lower hybrid wave. The $\langle T_e \rangle$ value was scanned from 4.4keV to 25keV and the lower hybrid wave power was fixed at 30MW. In the lower temperature region ($\langle T_e \rangle \leqq$ 10keV), the current drive efficiency increases in proportion to the temperature. This dependence agrees with experimental results on JT–60[1]. The current drive efficiency becomes maximum near 17keV and its value is larger than $0.40 \times 10^{20} m^{-2}$ A/W. Furthermore, in a higher temperature region ($\langle T_e \rangle \geqq$ 20keV), the current drive efficiency is independent of temperature. Lower hybrid waves relatively penetrate into the plasma core in the lower temperature region (see Case 1 in Fig. 3), while the current density profiles are hollow in the higher temperature region (see Case 3 in Fig. 3).

4. DISCUSSIONS

In this section, we discuss about the temperature dependence of

the current drive efficiency as shown in Fig. 3. In the previous section, the large shift of the initial $n_{\parallel}$ was noted. Here, we assume that the ray trajectories are hardly affected by temperature. We found this assumption is usually acceptable in the parameter range considered here. In the lower temperature region, the lower hybrid wave is absorbed at a high $n_{\parallel}$ as it propagates through the plasma (see the Case 1 region in Fig. 4). According to the quasi-linear theory, a high $n_{\parallel}$ results in a small current drive efficiency. On the other hand, in the case of $\langle T_e \rangle \simeq 17$keV, the lower hybrid wave is absorbed at a low $n_{\parallel}$ (see the Case 2 region in Fig. 4). This, in turn, results in a large current drive efficiency. In the higher temperature region, the lower hybrid wave cannot penetrate into the plasma core and is absorbed at the plasma surface before large shift of the initial $n_{\parallel}$ (see the Case 3 region in Fig. 4). Therefore, the current drive efficiency is constant with respect to temperature.

In conclusion, the volume averaged electron temperature of the current drive efficiency can be explained by large shift of the parallel refractive index in the framework of the ray tracing and the quasi-linear Fokker-Planck codes. If it is possible to optimize the effective $n_{\parallel}$ at wave power damping, we can obtain higher current drive efficiency. Since the condition is sensitive to the temperature profile, the initial $n_{\parallel}$ and $\Delta n_{\parallel}$, we should carefully select these parameters. Although it is possible to maximize the current drive efficiency, it cannot be avoided the hollow profile of the current density. Therefore, we should jointly use another current drive method for plasma core (for example, neutral beam)[3].

REFERENCES

[1] K.Usigusa, et al., in Plasma Physics and Controlled Nucl. Fusion Research 1988 (Proc. 12th Int. Conf., Nice, 1988), IAEA-CN-50/E-3-1.

[2] P. T. Bonoli and R. C. Englade, Phys. Fluids 29 (1986) 2937.

[3] R. S. Devoto, et al., in Controlled Fusion and Plasma Physics (Proc. 16th Eur. Conf., Venice, 1989), Vol.13B, Part IV, EPS(1989)1295.

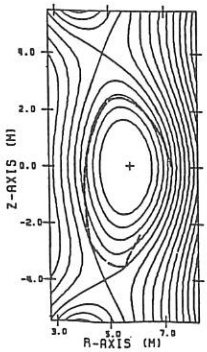

Fig. 1 Ray trajectory (dotted line) and magnetic surface (solid line) in poloidal plane.

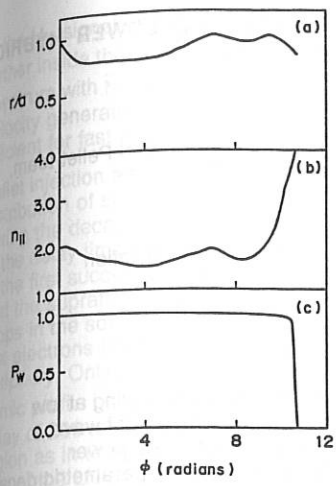

Fig. 2 $n_{\parallel}$ shift and power absorption along the ray trajectory (a) Variation in r/a versus toroidal angle ϕ (b) Variation in parallel refractive index $n_{\parallel}$ versus toroidal angle ϕ (c) Variation in normalized lower hybrid wave power P_w versus toroidal angle ϕ

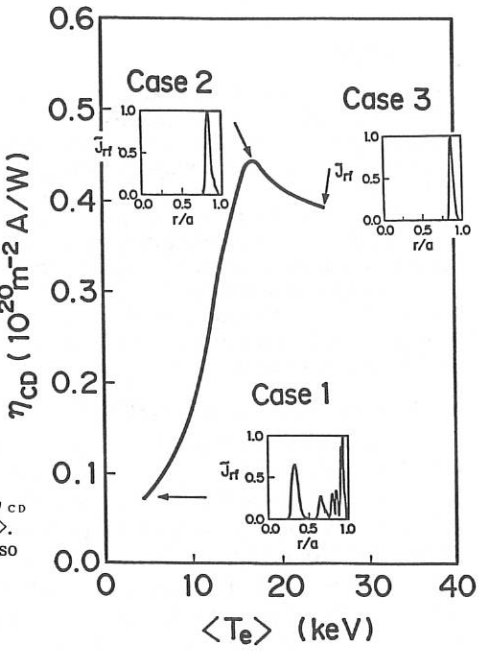

Fig. 3 Current drive efficiency η_{CD} versus volume average temperature <Te>. The LH-driven current profiles are also shown for <Te> = 4.4.17 and 25 keV.

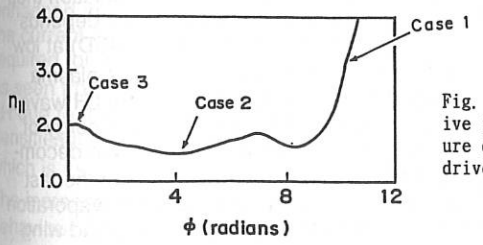

Fig. 4 Variation in parallel refractive index $n_{\parallel}$ for interpreting temperature dependence of lower hybrid current drive efficiency

COMBINED OPERATION OF PELLET INJECTION AND LOWER HYBRID CURRENT DRIVE ON ASDEX

F.X.Söldner, R.Lang, R.Loch, V.Mertens, H.S.Bosch, F.Leuterer, and Pellet-team, LH-team, ASDEX-team

Max-Planck-Institut für Plasmaphysik, EURATOM Association
D-8046 Garching, Fed. Rep. of Germany

Introduction

Lower Hybrid waves are successfully used for current drive and heating at low density. Their application at high density is impaired by the problem of wave accessibility to the central plasma region and it may be impeded by power depletion near the plasma edge through nonlinear processes like parametric decay instabilities. Efficient heating at high density could be achieved by launching LH waves into plasmas with peaked density profiles /1/. Peaking of the density profile is routinely obtained with particle fuelling by pellet injection /2/. This also provides superior energy confinement /3/. The combination of pellet injection and LH waves might therefore allow for current drive and heating in the central region of high density plasmas with good overall confinement properties. The first successful experiments with simultaneous operation of Lower Hybrid-current drive and pellet injection are reported in this paper.

Pellet Ablation with Lower Hybrid

Multiple pellet injection is performed on ASDEX with a centrifuge delivering up to 80 pellets during a single discharge with velocities up to 600 m/s /4/. In the combined experiments with Lower Hybrid, deuterium pellets of small size ($N \approx 4 \times 10^{19}$ particles) were injected with a repetition rate of 17-25 Hz at a velocity of v = 200 m/s. For investigations of the pellet ablation process we monitored the emitted H_α radiation with fast light detectors. Additionally we took photographs to get information about the spatial distribution of the ablation.In ohmic target plasmas the pellets penetrate to about half the plasma radius. The ablation profile is plotted in Fig. 1a. In combined experiments with Lower Hybrid, pellet injection is started at low initial density where the LH current drive efficiency is high /5/. The ablation then is dominated by suprathermal electrons, and the mass deposition profile depends strongly on the LH wave spectrum. With Lower Hybrid Current Drive (LHCD) at low $N_{||}$ ($\bar{N}_{||}$=1.8, $\Delta\varphi = 75^o$), the pellets are ablated in a narrow zone near the plasma periphery, as seen from the sharp peak close to the separatrix in Fig. 1b. LH waves with high phase velocities produce suprathermal electrons with a mean energy of $E_S \approx 70$ keV under these conditions. Such high energy electrons can cause decomposition and ablation of the pellets in a short time due to the absorption of the fast electrons in the interior of the pellets /6/. The gas cloud arising from the evaporation of the solid pellet expands along the torus and results in an additional broad wing

of the H_α signal in Fig. 1b. With LH waves of higher $N_{||}$ the pellets are ablated further inside the separatrix as shown in Fig. 1c. In this case a symmetric LH spectrum with $\bar{N}_{||}=4.4$ ($\Delta\varphi=180^o$) was launched. The LH waves of lower phase velocity generate fast electrons with lower mean energy which are then less efficient for fast pellet evaporation.

Pellet injection after the end of the LH pulse can probe the level and the radial distribution of suprathermal electrons. The location of the mass deposition of pellets during the decay phase of the suprathermal electrons is plotted in Fig. 2 in function of the delay time between turn-off of the LH and start of pellet injection. Penetration of the first successive pellets after the LH pulse remains shallow in spite of the fact that the suprathermal electron population is depleted by each pellet as indicated by drops in the soft X-ray emission. This can be explained by slow outward diffusion of fast electrons from the central region refilling the fast electron population near the periphery. Only about 100 ms after the LH pulse the ablation profile resembles the ohmic profile but the penetration depth at this time is still short with $\Delta/a\approx0.25$. With a delay of 200 ms to the end of the LH pulse, pellets penetrate again to the same region as in the preceding ohmic phase. This clearly shows the long confinement time of the LH-generated suprathermal electrons. A quantitative analysis of the transport coefficients of the fast electrons is under way.

Global Plasma Parameters and Energy Confinement

In discharges with pellet injection during LH the central electron density rises after injection of each pellet though ablation takes place near the plasma periphery. The density profile starts peaking already with the first pellet in contrast to the pellet injection into ohmic target plasmas where $n_e(r)$ begins to peak typically after 2-3 pellets. The evolution of various global plasma parameters for pellet injection during LHCD is shown in Fig.3. The line averaged density continues to rise after the initial jump with the first 3 pellets, indicating the inward flow of particles. For later pellets, $\bar{n}_e$ remains on successive flat top levels and it decays only slowly after the end of pellet injection. The density profile first flattened during the gas puff fuelled LHCD phase, peaks gradually during pellet injection, with the profile factor $Q_n = n_{eo} / < n_e >$ rising from ~1.4 to ~1.8. The β_p values, as obtained from magnetic measurements and from Thomson scattering for the thermal electron energy content, respectively, increase with pellet injection. The difference between the increments in β_p^{dia} and β_p^{equ} disappears with rising density due to weaker anisotropy of the electron distribution at higher density. There the electron heating is slightly reduced as seen from a saturation of $\beta_p{}^{el}$. But during this period ion heating is enhanced and leads to a strong rise of the neutron production. With rising density the current drive efficiency is diminished and the residual ohmic power input required for maintaining the total plasma current at its flat top value is slowly rising as seen from Fig. 3. The energy confinement time τ_E first reduced after start of the LH due to the increase in total power /7/, rises again with pellet injection. At higher densities it saturates due to a degradation of the LH power absorption coefficient which is assumed as constant $\alpha=0.75$ for the curve of τ_E plotted in Fig. 3.

The increase of β_p with density for pellet injection during LHCD is similar to the behaviour with pellet injection into ohmic target plasmas as shown in Fig.4.

Particle Transport

A well known common feature of pellet fuelled discharges is the strong peaking of their electron density profiles. Pellet injection into LHCD discharges exhibits a somewhat lower but noticeable enhancement of the central profile peaking of ~ 35 % (see Fig. 5) compared to ~ 50 % of the corresponding ohmic heated case. This is especially remarkable since during LH injection the deposition zone of the pellet particles is shifted outward close to the plasma boundary where also the conventional gas-puff refuelling takes place.

The flattening of the steady state profile in the central region during LH alone, as seen in Fig. 5, is correlated to the low toroidal electric dc field when most of the plasma current is driven by LH waves /8/. At higher densities $\bar{n}_e = 3.5 \times 10^{13}$ cm^{-3} when the loop voltage rises again the central peaking develops.

Approximately the same net inward flux of particles is found during the density build up with peripheral pellet ablation during LH as with the deeper penetration into ohmic target plasmas. Assuming a radially constant diffusion coefficient D and an inward velocity V linearly increasing with minor radius r, the central profile evolution can be satisfactorily reproduced by the following coefficients:

$D_{bulk}(m^2/s) = 0.05$ **(OH)** $/ 0.056$ **(LH)** $\quad V(r/a=0.5)(m/s) = -0.38$ **(OH)** $/ -0.25$ **(LH)**.

The accuracy of the deduced coefficients is estimated to +/- 25 %. The data indicate a slight reduction of the inward pinch in the central region correlated to the lowered toroidal electric dc field during LH current drive.

In the experiments with combined operation of LH-current drive and pellet injection peaking of the density profile and enhanced central heating could be obtained also with peripheral pellet ablation.

The Lower Hybrid experiments are performed in collaboration between IPP Garching, ENEA Frascati and PPPL Princeton.

References

/1/ Yoshino,R., et al., IAEA Workshop on Pellet Inj. and Tor. Conf., Ising 1988, 27.
/2/ Kaufmann, M., et al, Nuclear Fusion **28,** 827 (1988).
/3/ Mertens, V. , this conference.
/4/ Mertens, V. , et al., 15th Europ. Conf. on Contr. Fusion and Plasma Physics, Dubrovnik 1988, Vol. 1, 39.
/5/ Leuterer, F., et al. , this conference.
/6/ Pégourié, B., Y. Peysson, this conference.
/7/ Bartiromo, R., et al., this conference.
/8/ Gehre, O., et al., this conference.

Figure Captions

Fig.1: Ablation profiles for pellet injection into an ohmic target plasma (**a**) and in combination with Lower Hybrid: low-$N_{||}$ current drive (**b**), and high-$N_{||}$ symmetric wave spectrum (**c**). $B_t = 2.3$ T, $I_p = 300$ kA for all discharges. The dashed line indicates the position of the separatrix.

Fig.2: Variation of the pellet penetration depth with the delay between switch-off of the LH and injection of the pellet. $B_t = 2.3$ T, $I_p = 300$ kA, $\bar{n}_e = 2 \times 10^{13}$ cm^{-3}.

Fig.3: Temporal evolution of various plasma parameters for a discharge with pellet injection during LHCD ($P_{LH} \approx 620$ kW, $\bar{N}_{||} = 1.8$, $\Delta\varphi = 75^o$).

Fig.4: Temporal evolution of β_p and $\bar{n}_e$ during pellet injection into an ohmic plasma.

Fig.5: Normalized density profiles during LHCD with pellet fuelling (solid line) and with gas-puff fuelling (dashed), and during a standard ohmic discharge (dotted curve). The arrow at r = 0.35 m indicates the pellet penetration depth.

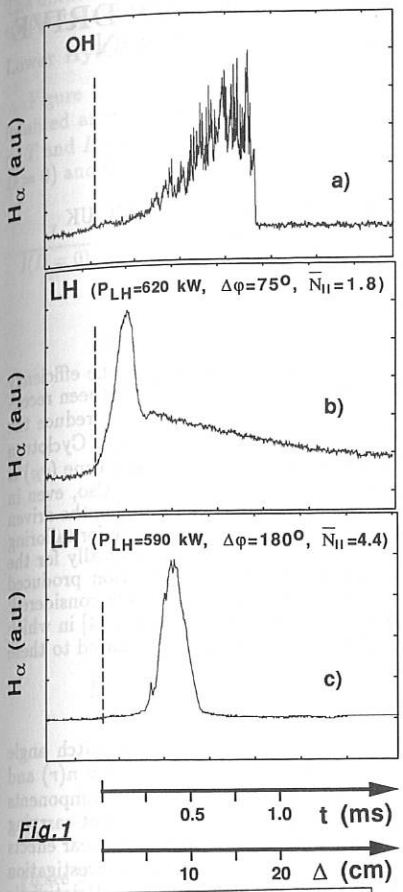

Fig.1

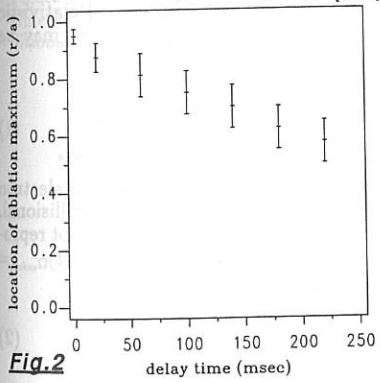

Fig.2

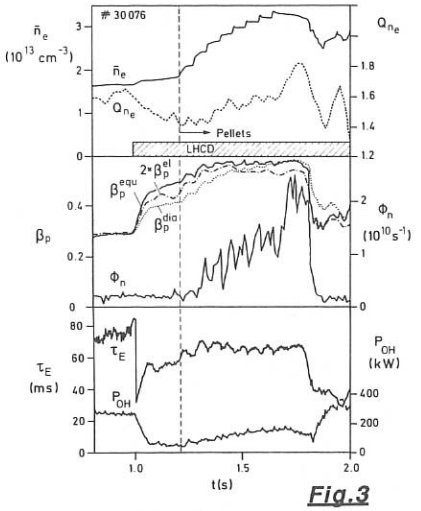

Fig.3

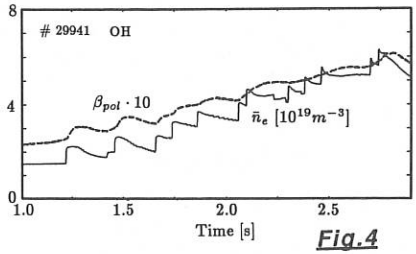

Fig.4

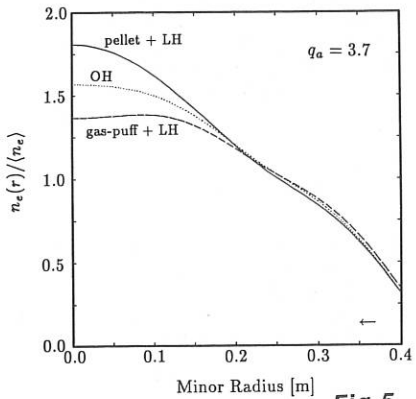

Fig.5

TRANSPORT EFFECTS ON CURRENT DRIVE EFFICIENCY AND LOCALISATION

M Cox, J S McKenzie and M R O'Brien,

AEA Technology, Culham Laboratory, Abingdon, Oxon OX14 3DB, UK
(Euratom/UKAEA Fusion Association)

INTRODUCTION

In this paper we discuss the effects of radial transport of electrons on the efficiency and profiles of radiofrequency and Ohmic current drive in tokamaks. It has been recognised theoretically [1, 2, 3] and experimentally [4] that such processes can reduce the potential current drive efficiency of both Lower Hybrid (LH) and Electron Cyclotron Resonance Heating (ECRH) in tokamaks in which the energy confinement time (τ_E) is comparable with or less than the collision time of the heated electrons. Also, even in tokamaks in which this condition is not satisfied, radial transport can broaden the driven current profile, and perhaps limit the effectiveness of the use of current drive for tailoring the current profile to control localised MHD modes. Here we solve numerically for the perturbed current-carrying component of the electron distribution function produced by balancing collisional, heating and transport processes. Three cases are considered: current drive by LH waves; the ECRH current drive experiments on CLEO [4] in which the discrepancy between observed and predicted driven current was attributed to these effects; and the effect on Ohmic current drive.

Electron Fokker-Planck Equation

The electron distribution function $f(v,\theta,r)$ (with v the speed, θ the pitch angle and r the flux surface radius) is assumed close to a Maxwellian f_0 of density $n(r)$ and temperature $T(r)$: $f(v,\theta,r) \simeq f_0(v,r) + f_1(v,r)\cos\theta$. We neglect Legendre components of the distribution of higher order as we are only interested in the current-carrying component $f_1(v,r)$. This linearisation and truncation of f means that non-linear effects (e.g. quasilinear flattening) and trapping corrections are not included: their investigation awaits a three dimensional code, preparation of which is well advanced. Relativistic effects are also ignored in this study. The steady-state equation for $f_1(v,r)$ may be written

$$\frac{\partial f_1}{\partial t} = 0 = \left(\frac{\partial f_1}{\partial t}\right)_{coll} + \left(\frac{\partial f_1}{\partial t}\right)_{ECRH} + \left(\frac{\partial f_1}{\partial t}\right)_{LH} + \left(\frac{\partial f_1}{\partial t}\right)_{\Omega_{mic}} + \left(\frac{\partial f_1}{\partial t}\right)_{trans} \quad (1)$$

The collision term includes the linearised intego-differential form for electron-electron collisions, and pitch angle scattering with ions of effective charge Z. The collisional, ECRH and LH terms are those used by Cordey, Edlington and Start [5] and are not reproduced here. The remaining terms in equation (1) represent Ohmic heating $(\partial f_1/\partial t)_{\Omega_{mic}} = (-eE/m_e)\,\partial f_1/\partial v_\parallel$ with E the electric field, and radial transport

$$\left(\frac{\partial f_1}{\partial t}\right)_{trans} = \frac{1}{r}\frac{\partial}{\partial r}\left\{r\left(D\,\frac{\partial f_1}{\partial r} + V f_1\right)\right\} \quad (2)$$

The diffusivity D and pinch velocity V are assumed independent of v in this paper for simplicity, although this is not necessarily a requirement of the code.

Lower Hybrid Current Drive

Figure 1 shows the effect of radial transport on LH current drive with absorption localised around $r' = a/2$. Heating was for $v_{\|} = 3\ (2T_e/m_e)^{1/2}$, $V = 0$, $Z = 1$, and n, T and D were assumed independent of r. The total current I (normalised to that for $D = 0$) and the width of the current profile W ($W^2 = 2\int_0^a r\,(r-r')^2\,j(r)dr / \int_o^a r\,j(r)dr$)

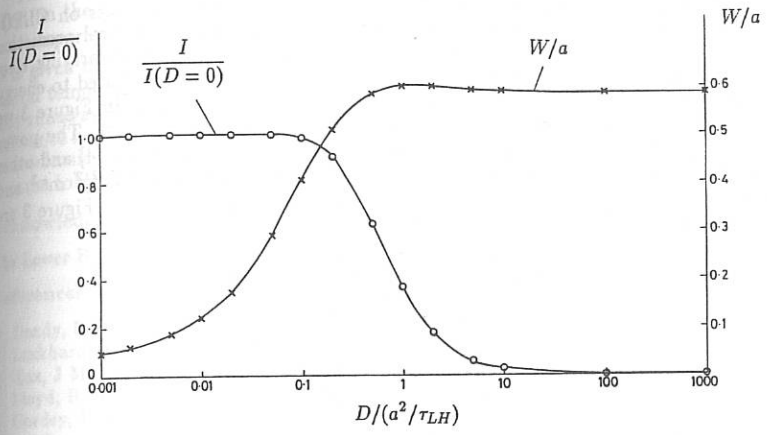

Figure 1: The effect of transport on the current I and current profile width W of LH current drive.

Figure 2: Different current profiles for the conditions of Figure 1.

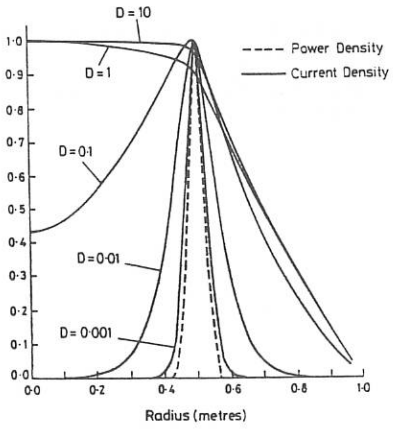

are plotted as functions of D normalised to a^2/τ_{LH} with a the minor radius and τ_{LH} the collision time of the heated electrons $\tau_{LH} = (4\pi\varepsilon_0^2 m_e^2 v_\parallel^3)/(n_e e^4 ln\Lambda) \simeq 0.05 K^{3/2}/n_{19}$ msecs with K the kinetic energy in keV and n_{19} the density in $10^{19} m^{-3}$. Figure 2 shows the resulting current profiles for various values of D. The diffusive nature of the transport broadens the current profile even for small values of D, and this may have consequences for the proposed use of rf current drive to modify the current profile on devices such as JET.

CLEO ECCD Experiments

In 60GHz second harmonic X mode ECRH current drive experiments on CLEO, the observed driven current was approximately one third of the theoretical prediction neglecting transport effects [4]. Since the collision time of the current-carrying electrons was approximately equal to τ_E ($\sim$ 1msec) this shortfall was attributed to energy loss processes interfering with the establishment of the rf current [1]. In Figure 3 we show predicted current profiles for the CLEO experimental conditions [4]. The power deposition profile was chosen to match that from ray tracing calculations [4] and other parameters were $R/a = 0.9/0.13$m, $Z = 2$, $n(r) = 6 \times 10^{18}\ (1 - r^2/a^2)^2$ m^{-3} and $T(r) = 1.3\ (1 - r^2/a^2)^3$ keV. The total currents for the five cases shown in Figure 3 are tabulated below:

$nD\ (10^{19} m^{-1} s^{-1})$	$V(ms^{-1})$	$I(kA)$
0	0	14.3
2	0	10.2
4	0	6.4
6	0	4.4
6	$4rD/a^2$	5.9

The diffusivity was taken to vary inversely with the plasma density to model the increase in the thermal conductivity χ near the edge of the plasma observed in many tokamaks. The values of nD used are similar to those of $n\chi$ observed in tokamaks which

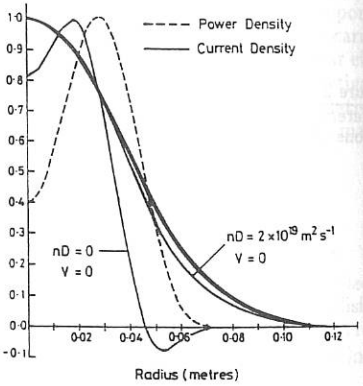

Figure 3:
Current profiles for varying amounts of transport for the CLEO ECCD experiments. Only two curves are labelled as the others are almost indistinguishable.

is reasonable as the heated electrons are at or close to thermal energies ($v_{\|} \simeq (2T_e/m_e)^{1/2}$). As Figure 3 shows, even small amounts of transport radically alter the current profile and for higher values of D, even if a pinch term is present, the profile tends to the same canonical form. In the CLEO ECCD experiments the driven current was $\sim$ 4-5kA corresponding to a reasonable value of nD.

Ohmic Current Drive

The effects discussed above also apply to Ohmic current drive and Figure 4 shows the effect on the Ohmic current of including radial diffusion of electrons ($V = 0$). Density and temperature profiles are of the form $X(r) = X_0(0.1 + 0.9(1 - r^2/a^2))$, $Z = 1$ and D is given normalised to a^2/τ_c with $\tau_c \simeq 0.05T_0^{3/2}/n_0$ msecs where T_0 and n_0 are the central temperature (keV) and density ($10^{19}\mathrm{m}^{-3}$). The electric field is assumed small so that runaway electrons do not contribute significantly to the current. The increase in resistance in tokamaks with $\tau_E \lesssim$ few τ_c can be comparable with or greater than that due to neoclassical effects and might contribute to the anomalously high resistance observed in some tokamaks at low density [6] and reverse field pinches [7].

Acknowledgement

The Lower Hybrid work in this paper was performed as part of a Task Agreement for JET.

References

[1] Dendy, R O, and O'Brien, M R, Nucl. Fus. 29 (1989) 480.
[2] Luckhardt, S C, Nucl. Fus. 27 (1987) 1914.
[3] Rax, J M, and Moreau, D, Nucl. Fus. 29 (1989) 1751.
[4] Lloyd, B, et al, Nucl. Fus. 28 (1988) 1013.
[5] Cordey, J G, Edlington, T, and Start, D F H, Plas. Phys. & Contr. Fus. 24 (1982) 73.
[6] Artsimovich, L, et al, Proc. of 3rd Int. Conf. on Plas. Phys. & Contr. Nucl. Fus. Res., Novosibirsk, (1968). Translated in Special Supplement to Nucl. Fus., (1969) 17.
[7] Bodin, H A B, Proc. of Phys. of Mirrors, Reverse Field Pinches and Compact Tori, Varenna, (1987), Vol. I , 307.

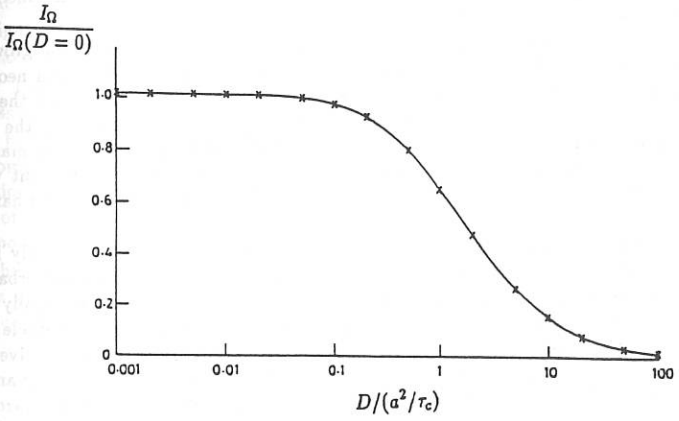

Figure 4: The effect of transport on the Ohmic current I_Ω.

M=2 MODE LIMIT ON LOWER HYBRID CURRENT DRIVE IN ASDEX

H. Zohm, H. Bruhns, F. Leuterer, O. Klüber, F. X. Söldner

Max-Planck-Institut für Plasmaphysik,
EURATOM-IPP Association D-8046 Garching, FRG

1. Introduction

In a steady-state tokamak, the plasma current drive cannot be purely inductive as the transformer has to be recharged. Therefore noninductive current drive by radiofrequency waves is an important topic in fusion research.

In ASDEX, a 2.45 GHz Lower Hybrid system provides up to 3 MW power in the generator. With two multiwaveguide grill antennae the form of the spectrum can be varied in a wide range. Directional spectra are used for Lower Hybrid current drive (LHCD). During LHCD, the current profile $j(r)$ is changed due to the localized power deposition [1] of the waves. This effect can give rise to changes in the MHD behaviour of LHCD discharges. One well known effect is the suppression of sawteeth instability [2]; the unfavourable effect of destabilizing a (2,1) tearing mode is subject of this paper.

2. MHD mode behaviour

Figure 1 shows an example of a LHCD discharge where drastic changes in the MHD mode behaviour occur: At t = 1.65 s, a (2,1) tearing mode is destabilized. This is in agreement with the fact that in this case LHCD tends to steepen the gradient of $j(r)$ around the q=2 surface [1]. A tearing mode stability analysis shows that this leads to higher values of the instability parameter Δ'; nevertheless quantitative predictions cannot be given within the uncertainties of the measurement of the current profile.

In a first phase, the growth of the mode is purely exponential. The exponential growth time τ is 23 ms, which is well above the growth time of about 1.7 ms expected from neoclassical Spitzer conductivity. This effect might be explained by the observation, that the current in LHCD discharges is mainly carried by suprathermal electrons which enlarges the resistive timescale; if we apply the tearing mode scaling ($\tau \propto \tau_{res}{}^{3/5}$) we find that the plasma behaves like the electron temperature was enhanced by a factor of 18. This is consistent with the high tail temperature of the suprathermal electron population as determined from hard-X-ray measurements.

The mode then reaches a quasi-saturated phase, in which the growth is nearly linear in amplitude of the perturbed magnetic field B_r. The strength of the magnetic perturbation can reach several percent of the equilibrium poloidal field. During this phase, the initially rotating mode structure slows down and comes to rest. This phenomenon, known as mode locking, can be explained by a model of the interaction of the rotating mode with the resistive vacuum vessel as well as the interaction with static error field due to nonexact positioning and shape of the vacuum field coils [3]. In this phase, also a flattening of the density profile around the q=2 surface is observed [4]. The locked mode leads to a disruption, terminating the discharge at t = 1.77 s.

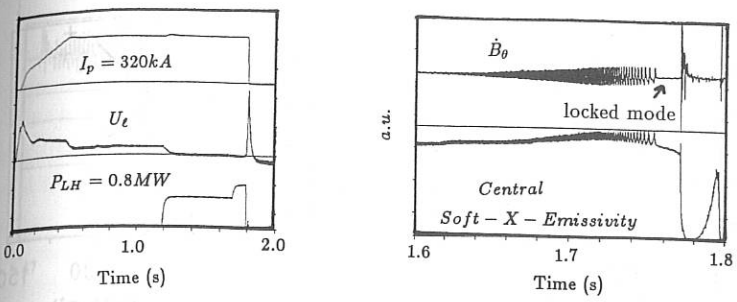

Figure 1: MHD activity during LHCD: Temporal evolution of plasma current, Lower Hybrid power and loop voltage (a) and m=2 mode activity indicated by a $\dot{B}_\theta$ trace and soft-x-ray emissivity viewing through the centre (b). The locked mode itself cannot be seen on $\dot{B}_\theta$.

From Soft-X-Ray tomography, for some shots a (1,1) mode can be detected. This mode initially rotates at a frequency different from that of the (2,1) mode. During the growth of the (2,1) the frequency of the (1,1) changes to that of the (2,1), indicating toroidal mode coupling.

3. LH-power limit due to m=2 induced disruptions

The above described scenario leading to a disruption is often observed in ASDEX LHCD discharges where the transformer loop voltage U_ℓ is substantially reduced or even inverted as the current is driven by the RF. For the two current drive spectra routinely used on ASDEX ($\Delta\Phi = 90°$, $N_{||} = 2.2$ and $\Delta\Phi = 75°$, $N_{||} = 1.8$) a database of m=2 induced disruptions has been set up. It is found that the amount of RF-power transferred to the plasma at which disruptions occur is rising with the product of line averaged density $\bar{n}_e$ and plasma current I_p, i.e. with the amount of LH-driven current. Figure 2 shows this dependence for the two different spectra.

In Figure 2, also the power needed to drive the whole current (i.e. to reach $U_\ell = 0$) is shown assuming a constant current drive efficiency $\eta = \frac{\bar{n}_e I_p R_0}{P_{LH}}$, R_0 being the plasma major radius. The value of $\eta = 1.2 \times 10^{19} \frac{A}{m^2 W}$ corresponds to standard conditions with boronized walls assuming $Z_{eff} = 3.5$ in the range of low densities [5].

This behaviour is not a strict limit to the power transferable to a discharge. There have been some experiments where a higher amount of LH-Power could be transferred without a disruption. Nevertheless Figure 2 shows that there is a limit to the region of safe LHCD operation in ASDEX. The limit is of course dependent on the parameters determining the radial power deposition of the LH-waves, i.e. mainly $\bar{n}_e$, B and the spectrum of the wave.

All this shows that, apart from the effect of sawteeth and m=1 stabilization, the profile changes by LHCD can lead to unfavourable conditions so that the parameters for LHCD performance have to be carefully adjusted.

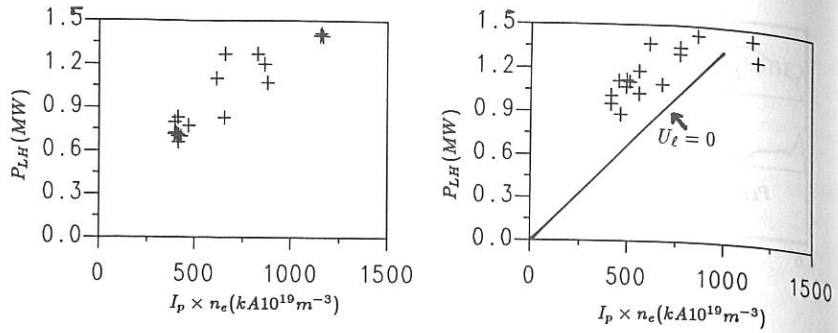

Figure 2: Statistics of m=2 disruptions: The LH-power transferred to the plasma before a disruption rises with the product of plasma current I_p and line averaged electron density $\bar{n}_e$; the two diagrams refer to different current drive spectra, a) $\Delta\Phi = 75°$, b) $\Delta\Phi = 90°$; for the latter case, the power needed to reach $U_\ell = 0$ is shown in the experimental range of full current drive. Here, a constant current drive efficiency was taken.

4. Possibilities of disruption control

The m=2 induced disruption during LHCD is characterized by a preceding long period with slow growth of the mode amplitude and the locking of the mode. The question therefore arises if feedback control of the mode can be achieved during the growth period in order to avoid the final disruption.

A possibility to avoid a disruption after mode locking is the so called unlocking of the mode, i.e. forced plasma rotation by unidirectional neutral beam injection. An example is shown in Figure 3 where a locked mode occured during LHCD and was then unlocked by the NBI. The typical time interval between locking and the disruption is about 20 ms in LHCD shots which is enough to unlock the mode. It has to be mentioned that the m=2 mode does not vanish after unlocking; this means that unlocking may avoid a disruption but does not change the unfavourable current profile. The toroidal force balance for the unlocking of a locked mode has been explained by a model of the locked mode including viscous coupling of the m=2 island to the entire plasma in Ref. [3]. For a density of $\bar{n}_e = 1.5 \times 10^{19} m^{-3}$ a NBI Power of 1.5 MW is required to unlock the mode.

Attempts have been made to trigger of a NBI pulse at the occurrence of the locked mode. We use a suited n=1 combination of saddle loops, integrated on a slow timescale, to detect the moment when the magnetic perturbation comes to rest; on this timescale, the rotating mode is not seen. We also checked the possibility of using the m=2 amplitude of rotating modes for the trigger; in this case modes which grow on a fast timescale (e.g. 1 ms) or even grow in a locked state might not be detected whereas the triggering by the saddle loops also works in other scenarios. An example for the saddle loop trigger signal is shown in Figure 3.

5. Conclusions

It has been shown that the changes in the current profile induced by LHCD may lead to the destabilization of an m=2 mode leading to mode locking and disruptions. As the MHD stability of current profiles is sensitive to small changes, the profile control by LHCD might be

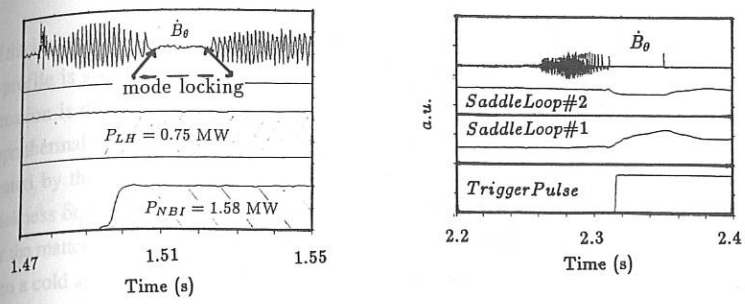

Figure 3: Unlocking of a locked mode: A situation where a locked mode produced by LHCD was unlocked using NBI is shown in a); Figure b) shows the on-line trigger signal for a locked mode during another shot: The vanishing of the Mirnov signal ($\dot{B}_\theta$) at t = 2.3 s indicates the occurrence of a locked mode which can be seen on the integrated n=1 saddle loop combination; the resulting trigger signal inferred from their difference can be used for feedback control.

a sophisticated problem. Discharges with high RF-Power input where all the current is driven by the RF are especially sensitive to these disruptions, the maximum tolerable power input rising with the product of I_p and $\bar{n}_e$, if not special care is taken of the power deposition profile.

For the study of disruption control by unlocking of locked modes the LHCD discharges are well suited because of the enlarged resistive timescale due to the suprathermal electrons produced by the RF; this allows for a longer time interval to be used for detecting and unlocking locked modes. It should be mentioned, though, that the NBI Power needed for unlocking rises with the magnetic fields involved (i.e. the plasma current and the error fields) and the density (inertia) of the plasma. This means that in big machines the possibility of such feedback control has to be checked by simulations of the toroidal force balance and might require high NBI powers.

References

[1] F. X. Söldner, this conference .

[2] F. X. Söldner et al., Phys. Rev. Lett. **57** (1986).

[3] H. Zohm, A. Kallenbach, H. Bruhns, G. Fussmann, and O. Klüber, IPP Report I/251 (1989).

[4] M. E. Manso et al., this conference .

[5] F. Leuterer, this conference .

EVAPORATION RATE OF AN HYDROGEN PELLET IN PRESENCE OF FAST ELECTRONS

B.Pégourié, Y.Peysson

Association EURATOM-CEA sur la Fusion Contrôlée
Centre d'Etudes Nucléaires de Cadarache B.P.n°1
13108 Saint-Paul-lez-Durance, France

INTRODUCTION

Pellets injected during ECRH or LHCD experiments show a shallow penetration when compared with the ohmic case [1-3]. This shortening is recognized to be due to the low density population of higher energy electrons generated by these methods and question their compatibility, at high power levels, with pellet refuelling. In order to investigate this latter point, we present a simple model taking into account the main physical effects. We show that, once the pellet is vaporized, a dense and cold cloud survives sufficiently to contribute to the total penetration of the matter in the discharge. We discuss the behaviour of the total pellet lifetime with the proportion of suprathermal electrons, their energy, the pellet radius and its velocity.

MODEL DESCRIPTION

The NGS model [4] is assumed to be valid for a Maxwellian distribution after proper averaging [5]. Due to the energy dependence of the electrons penetration depth in the ice, a more thorough description of the ablation is required as soon as an energy distribution is considered. Since the ice thermal diffusivity is sufficiently low for the heat transport to be neglected (the temperature uniformization time in a 0.1cm radius pellet is of order 0.1s), the temperature distribution inside the pellet is given by the integral over the time of the power profile deposited by the electrons. At the pellet surface, the boundary condition is $\varepsilon = \mu_s \approx$ 0.01eV, where ε is the mean energy per molecule. For all the molecules located in a layer of thickness δr_p, ε reaches μ_s in a time δt, which yields the pellet radius regression speed $\dot{r}_p = \delta r_p/\delta t$. In other words, the energy flux falling on the neutral cloud is able, in a time interval δt, to increase by $\dot{\varepsilon}\delta t = \mu_s - \varepsilon(t)$ the energy of the molecules located at $r_p(t) - \dot{r}_p\delta t$ and to heat a quantity of matter equal to $4\pi r_p^2 \dot{r}_p \delta t$ until it is fully ionized and deposited in the discharge. Such a situation is displayed on Figure 1 (dashed line) for a temperature $T_e = 2$ keV and for a pellet radius $r_p = 0.05$ cm.

The presence of a suprathermal tail does not modify significantly the neutral cloud hydrodynamics (because the stopping power of gaseous H_2 decreases rapidly with the energy

of the incident electrons): the values of $\dot{\varepsilon}\delta t$ and $\dot{r}_p\delta t$ remain therefore unchanged. However, the ε-profile is significantly disturbed, which yields an heating in volume of the pellet. Such a situation is displayed on Figure 1 (full line) for a distribution including 1% of T_s = 25keV suprathermal electrons. It can be seen that $\delta r_p^* > \dot{r}_p\delta t$. The layer of thickness $\dot{r}_p\delta t$ is principally heated by the bulk electrons and deposited in the discharge as previously, but the layer of thickness $\delta r_p^* - \dot{r}_p\delta t$ is only heated by the suprathermal tail. This heating is by far insufficient for the matter to be fully ionized and deposited in the plasma in the time interval δt. It constitutes then a cold and dense cloud of gas which expands at a velocity close to the instantaneous sonic speed: $c_s = [(\gamma-1)(\varepsilon-\mu_s)/2m_{H2}(\gamma+1)]^{1/2}$. This increase in volume results in an increase of the ablation rate (in mass) proportionnally to $(1+c_s\delta t/r_p)^{4/3}$. For electronic distributions relevant of LHCD experiments, the energy of the fast tail can be as high as 500keV. The ε-profile is then extremely flat (its characteristic thickness increases as $T_s^{1.72}$). One can then consider that, once ε reaches μ_s, the whole remaining part of the pellet transits into a gaseous phase and begins to expand.

RESULTS

Two simulations for TORE SUPRA are presented on Figure 2. The pellet has an initial radius r_{p0} = 0.15 cm and is injected with a velocity $V_p = 10^3$ m/s. The plasma has a minor radius a = 0.7 m; the profiles are of the form $A(r) = A_0(1- r^2/a^2)^\beta$. We compare a purely ohmic case (Maxwellian distribution: $n_{e0} = 5\ 10^{13}$ cm^{-3}, β = 1; T_{e0} = 2 keV, β = 2) and a typical LHCD experiment (identical bulk plasma, plus a suprathermal tail whose characteristics are: n_{s0}/n_{e0} = 0.1%, β = 3; $T_{s//}$ = 750 keV forward, $T_{s\perp}$ = 150 keV = $T_{s//}$ backward; energy cut-off at 600keV, β = 0). The penetration depth is lowered by a factor as large as 2.5 in presence of fast electrons. The radius of the pellet (or of the cold cloud which follows its vaporization) is also shown (dashed lines): in the LHCD case, ε reaches μ_s in the whole pellet for a penetration depth $L_p \approx 7$ cm. From this point, the remaining part of the pellet survives under the form of a dense expanding cloud which is itself ablated by the bulk electrons. This second phase of ablation has approximately the same duration that the first one.

The reduction of the pellet lifetime due to the suprathermal tail can be well characterized by the ratio L_p^*/L_p of the penetration depths with and without fast electrons. The value of L_p^* depends on the balance between the two phases of ablation described above, which depends itself on the temperature and density profiles. To focus on the influence of the pellet and fast tail parameters on L_p^*, all the results presented in this section are computed with plasma parameters identical to those used for the two simulations of fig.2. The influence of the mean energy of the fast tail is displayed on Figure 3 for three pellet radii. The computations are performed with an isotropic suprathermal component of the distribution and with n_s/n_e = 0.1%. At low energies, the pellet acts as a thick target and a small decrease of L_p^*/L_p (slightly depending on r_p) is

observed with increasing T_s. This behaviour ends as soon as the pellet can be considered as a thin target: L_p^*/L_p tends towards an asymptotic value independent on r_p and T_s, but which strongly depends on n_s/n_e, by far the most important parameter for the pellet lifetime evaluation (see Figure 4). The relative penetration depth varies from 0.5 and 0.2 when n_s/n_e increases from 10^{-3}% to 1%. The influence of the pellet velocity is only marginal: a large increase in V_p (up to a factor 3) improves L_p^*/L_p by only 15%. More generally, the weak dependence of L_p^*/L_p with r_p and V_p means that the global scaling of the NGS model with respect to the pellet characteristics remains unchanged: $L_p^* \propto (r_p^{5/3} V_p)^{1/3}$.

CONCLUSION

Two phases can be distinguished in the interaction of a pellet with fast electrons: the pellet is first heated in volume until it is vaporized, then the resulting cold and dense neutral cloud is heated and expanded until the whole matter is deposited in the discharge. For the set of plasma parameters we have considered, these two phases have approximatively the same duration and thus contribute equally to the matter penetration (which is reduced by a factor 2 to 5 when compared with the ohmic case). The results display a high sensitivity to the proportion of fast electrons but are nearly independent on their energy.

References:

[1] Schissel D.P., Baur J., Bramson G. *et al.*, Nucl. Fus. **27** (1987) 1063.

[2] Büchl K., Vlases G.C., Sandmann W. *et al.*, Nucl. Fus. **27** (1987) 1939.

[3] Drawin H.W., Géraud A., Nucl. Fus. **29** (1989) 1681.

[4] Parks P.B., Turnbull R.J., Phys. Fluids **21** (1978) 1735.

[5] Pégourié B., Dubois M.A., Nucl. Fus. **29** (1989) 745.

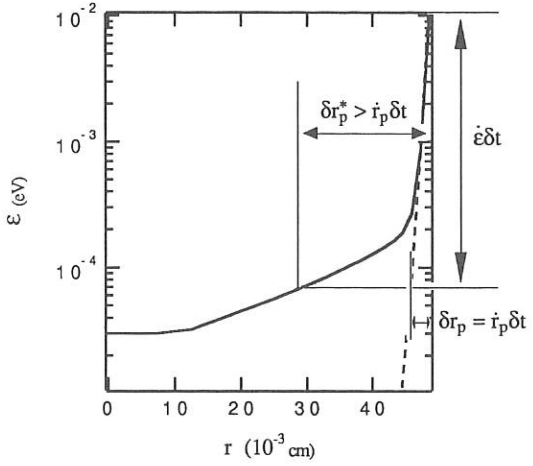

Figure 1:
Temperature distribution inside the pellet with (full line) and without (dashed line) fast electrons.

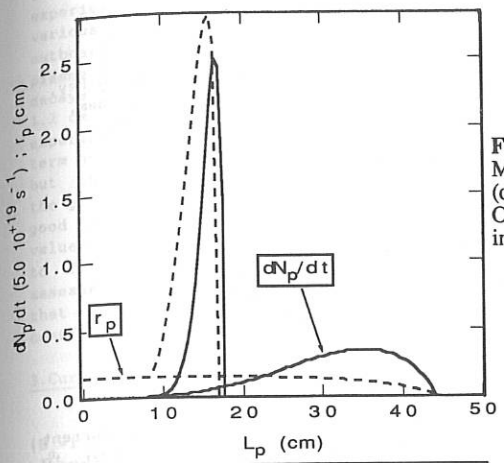

Figure 2:
Matter deposition profile and pellet (or cold dense cloud) radius for typical Ohmic and LHCD experiments in TORE-SUPRA.

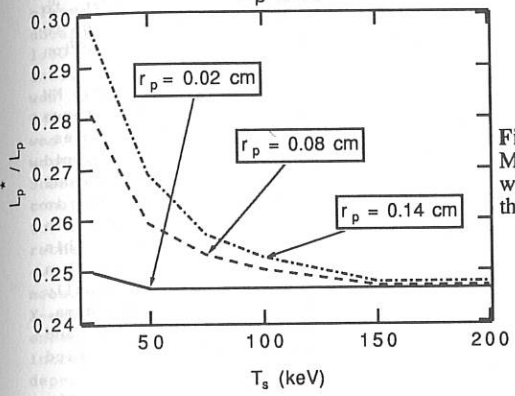

Figure 3:
Modification of the pellet penetration with the energy of the fast tail for three different pellet radii.

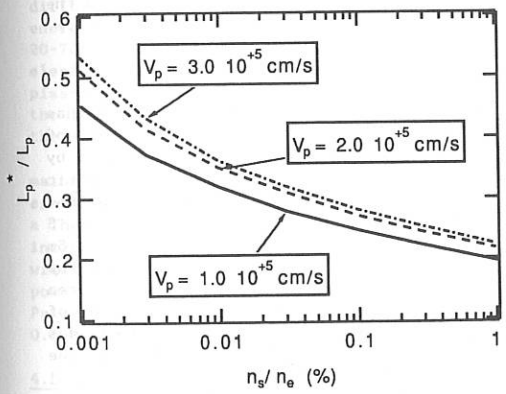

Figure 4:
Modification of the pellet penetration with the proportion of fast electrons for three different pellet velocities.

LOWER HYBRID WAVE EXPERIMENTS IN TORE SUPRA

M.Goniche,D.Moreau,G.Tonon,G.Berger-By,P.Bibet,J.P.Bizarro,
J.J.Capitain,G.T.Hoang,X.Litaudon,R.Magne,Y.Peysson,J.M.Rax,G.Rey,
J.L.Bruneau,B.De gentile, C.DeMichelis,T.Fall,C.Gill,D.Guilhem,
W.Hess,T.Hutter,J.Lasalle,P.Lecoustey,G.Martin,M.Mattioli,
B.Moulin,P.Monier,F.Parlange, A.L.Pecquet,P.Platz,
L.Rodriguez,M.Talvard,J.C.Vallet,D.Van Houtte

Association EURATOM-CEA
Département de recherche sur la fusion controlée
Centre d'Etudes Nucléaires de Cadarache
F 13108 Saint Paul-lez-Durance

1. Introduction

One of the main goals of Tore Supra is the study of Current drive and profile control by means of lower hybrid waves. In order to investigate the current drive efficiency at high densities,up to 10^{20} m^{-3} ,a RF system has been designed at 3.7 GHz to avoid interaction with the ions.

The system is composed of 16 CW klystrons,delivering 0.5 MW each,which feed 2 antennae connected to 2 adjacent ports of the torus /1,2/. One antenna is made from the assembly of 16 evacuated modules. Each module has 3 stages of internal power dividers: an hybrid junction,with a short circuit on the balance port, in the poloidal direction and two E-plane bijunctions in the toroidal direction in such a way that 8 reduced-section (8.5x72 mm^2)waveguides are terminating the module. It has been experimented that this "multijunction" concept allows a good coupling of the wave with a lower reflection coefficient /3/ than a conventionnal launcher.Finally an array of four poloidal rows of 32 waveguides are facing the plasma. This allows to excite a narrow N// spectrum centered at $\langle N//\rangle=1.9$ and of total width $\Delta N//=0.5$. By phasing the modules, $\langle N//\rangle$ can be varied from 1.5 to 2.3 with a decrease of directivity of less than 10%.

The two launchers have been installed on Tore Supra and the whole 16-klystron generator has been operated from the control system.

2.LH waves coupling

A study of the coupling of LH waves to the edge plasma has been carried out from the HF measurements available at the input of each module. For each coupler, these RF measurements are performed by 16 bidirectional couplers and the incident and reflected electric fields are determined in phase and amplitude . These 32 incident and reflected fields are related to each other by a scattering matrix S which has been calculated from the intrinsic matrix of the modules Sm and the plasma admittance matrix Sp. Sm ,which takes into account the geometry of the modules (power dividers ,phase shifters...), has been experimentally determined at low HF power for the different type of modules /4/.Sp, which expresses the intercoupling of the 32 waveguides by the plasma and which depends on the edge plasma density Ne and the density gradient ∇Ne, has been computed from the SWAN code /5/.

The experimental Sij terms were determined as follows:during a single plasma shot (Ip=0.60 MA,Ne=6.10^{18} m^{-3}),each module i of a row was sequentially fed by a 100-ms pulse. With 32 pulses achieved in a

5-s sequence, each Sij terms were measured 4 times.As an example, the experimental amplitude of the S_{66} term has been drawn on figure 1 for various positions of the grill, at a radius Rg, with respect to the outboard limiter, at a radius Rl. With no measurement of the edge plasma density, it was assumed for the computation that the density decays from the limiter ($n_0 = 2.10^{18} m^{-3}$) with an e-folding length λn = 1.2 cm.The general shape of the curve is correctly simulated, although experimental values are slightly higher than expected . For the S_{66} term no large difference is found between the top and bottom modules but this is not the case for most of the modules: with a density at the grill mouth twice the cut-off density (for Rg-Rl=2cm), there is a good agreement for the lower row of modules with the theoretical values of Sii whereas the upper modules would require a lower density to fit the data (figure 2).As predicted by the theory, it was assessed,with a higher plasma density,when all the modules are fed that good coupling can be achieved and the power reflection coefficient lies between 1 and 2 %.

3.Current drive experiments

Current drive experiments were achieved at low toroidal field (B_0=1.85 T) in helium , hydrogen and deuterium plasmas at constant plasma current.The best results, with large loop voltage drop, were obtained in hydrogen, at low volume averaged density (Ne=0.5 to $1.10^{18} m^{-3}$), with up to 1.0 MW of power injected into the torus.In these experiments, the ideal launched N// spectrum,centered at 1.9, was distorted for different reasons:the coupling was poor (R~6%),only 6/7 over 8 klystons were delivering power,the phasing of the modules was inacurate.However up to 75% of the current was driven by the LH waves (Phf=730 kW) in a 430 kA discharge with an increase of the Shafranov parameter $\Lambda=(\beta p+li/2)$ of 0.2 (figure 3).The short time constant of variation of Λ suggests that this increase is mainly due to the kinetic pressure of the fast electrons created by the LHW (βp) rather than to a modification of the current profile (li). Some other evidences of the fast electron tail have been found from the measurements of the electron cyclotron emission (ECE) and the hard X-ray (HXR) spectrometry. From 7 Fabry-Pérot lines ,a strong enhancement of the total ECE (50-500GHz) was observed. The relative increase, normalized to the thermal level, $\Delta ECE/ECEth$ has a linear dependence with the injected power for each set of data obtained with different plasma densities and coupling conditions (figure 4).The energy of HXR Bremsstrahlung emission was analyzed in the range of 20-700 keV and shows the existence of a wide spectrum of fast electrons up to 200 keV when 0.8 MW is injected into a deuterium plasma (figure 5).For different HF powers, the relative increase of the integrated HXR signal is proportional to the relative increase of the ECE.

During these experiments, an increase of the brightness of the main impurities (C,O,and Ni) was measured with the grazing incidence spectrometer. With preliminary electron temperature measurements from a Thomson scattering system, it was inferred that the Ni influx increases by 13 % with an injected power of 0.7 MW, in good agreement with numerical simulations. Nevertheless the ratio of total radiated power, measured with bolometers, to the total injected power Prad/(Poh+Phf) does not vary significantly when the HF power (between 0.3 and 1.0 MW) is switched on: this ratio is kept between 25 and 35%.

4.Discussion and conclusions

A relevant parameter for current drive experiments is the

efficiency that we shall define here as:

η = ⟨Ne⟩.R.Ihf/Phf where ⟨Ne⟩ is the volume averaged density (10^{19} m^{-3}), R the major radius (m), Ihf the current driven by the LH waves (A) and Phf the injected power (W). In this paper, for non-zero loop voltage discharges, the temperature variation is assumed negligible and Ihf can be expressed as:

$Ihf = Ip.(V_1 - V_2)/V_1$ where V_1 and V_2 are the loop voltage before and during the HF.

Theoretically, η can be written /6/ as follows:

$$\frac{\langle Ne\rangle.R.Ihf}{Phf} = \frac{78.\alpha}{\langle N//\rangle^2.(Z+5)} + \frac{761.\alpha.V_2}{\langle N//\rangle^4.\langle Ne\rangle.R.(Z+3)}$$

where α = Pabs/Phf is the absorption coefficient

For 2 hydrogen plasma densities, the efficiency has been plotted as a function of $V_2/(\langle Ne\rangle.R)$ on figure 6. The experimental data suggest that around 50% of the injected power could have been absorbed between N//=1.4 (accessibility) and 7.5 (strong Landau damping). A rough power balance, where the energy content is supposed to be kept constant, gives a similar value for α.

It is well established that wave accessibility can play a key role in the CD efficiency /7/. However for these experiments at low toroidal field (B_0=1.8 T), the same current drive efficiency (η=0.5 - 1.0), as measured on the PETULA-B 3.7GHz experiment, was obtained, the lower field (1.8 vs. 2.7 T) being compensated by a narrower spectrum (0.5 vs. 2.0).

Experiments at 3.9 T are being prepared and it is expected, with better coupling and accessibility conditions, that the CD efficiency will be enhanced by a factor 2 to 3 at low density.

References

/1/ G.Rey et al. 15th Symp. on Fus.Techno. Utrecht,514 (1989)
/2/ R.Magne et al. 15th Symp. on Fus.Techno. Utrecht,524 (1989)
/3/ M.Goniche et al. 13th Eur.Conf.on Control.Fus.,Vol.2,369 (1986)
/4/ P.Bibet al. Rep. EUR-CEA-FC-1388 (1990)
/5/ D.Moreau and T.K.Nguyen Rep. EUR-CEA-FC-1199 (1983)
/6/ J.M..Rax, Phys.Fluids 31,1111 (1988)
/7/ F.Parlange et al. 11th Int. Conf. on Plasma Physics,525 (1987)

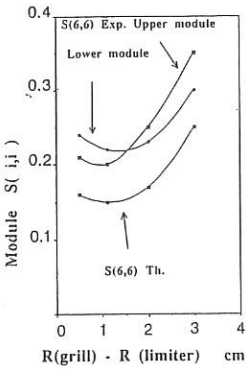

Fig.1 Theoretical and experimental S_{66} amplitude

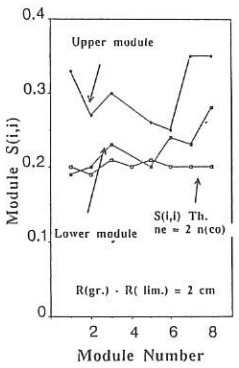

Fig.2 Theoretical and experimental Sii amplitudes

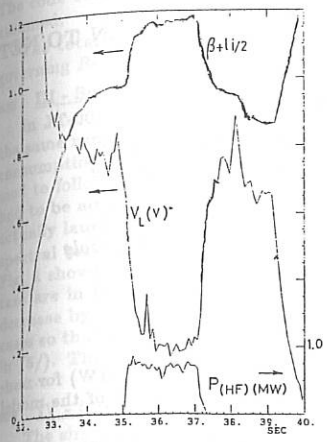

Fig.3 Loop voltage and βp+li/2 signals (Phf=730 kW)

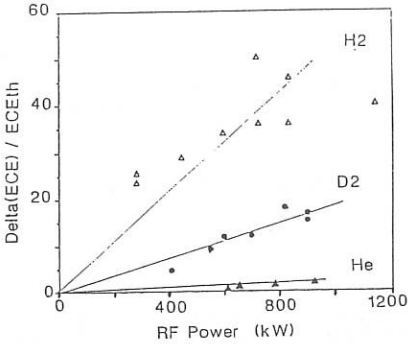

Fig.4 Relative increase of ECE vs injected RF power

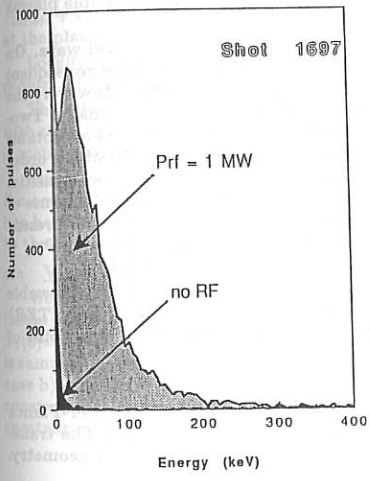

Fig.5 Hard X-ray emission spectra (Prf=0 and 1 MW)

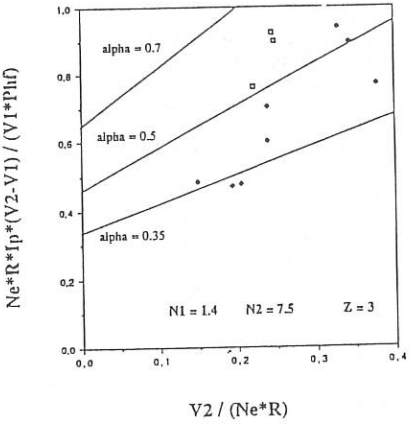

Fig.6 CD efficiency vs V2/(Ne.R)

MODELLING OF PLASMA CURRENT RAMP-UP BY LOWER HYBRID WAVES: COMPARISON WITH EXPERIMENTS AND APPLICATION TO NET

J.-G. Wégrowe

The NET Team, c/o Max-Planck-Institut für Plasmaphysik, D-8046 Garching bei München, Federal Republic of Germany

G. Zambotti

Dipartimento di Fisica Nucleare e Teorica , Universitá, Pavia, Italy

ABSTRACT

In this paper, we investigate the potential of Lower Hybrid Waves (LHW) for non-inductive current ramp-up assist in NET/ITER after testing the validity of the model used on experimental results.

A comparison of code simulations with experimental results in ASDEX was presented in /1/. In the present work, JT-60 Lower Hybrid Wave current ramp-up experiments are modelled and the agreement with experiments is found to be satisfactory.

Preliminary results obtained with the code applied to ITER parameters show that 20 to 30Vs can be saved, operating at an average plasma density of 1.5 10^{19} m^{-3} , using a launched LHW power around 20MW.

I - Introduction.

Injection of LHW power is considered in NET and ITER to provide current profile control through partial current drive during long burn operation. Further, non-inductive current ramp-up assist, by saving transformer flux, can provide an extension of the inductive burn duration, and/or allow to run the machine at the largest possible plasma current.

Non-inductive current ramp-up assist in a reactor is constrained in several ways. On the one hand, to minimize the amount of additional power required - and the consequent plasma heating - one has to operate at sufficiently low plasma density. However, the total power acceptable in the power exhaust system decreases rapidly with density. Two-dimensional modelling of the scrape-off layer and divertor plasma[3] shows that acceptable divertor operation can be achieved at powers into the scrape-off layer (SOL) of the order of 100MW at average density $\bar{n}_e \geq 10^{20}$ m^{-3} . Detailed modelling at lower densities and powers remains to be carried out. Similarly, the constraints imposed by the use of a limiter in the early phases of the ramp-up have also to be assessed. For the present study, we have chosen to examine the domain $\bar{n}_e \geq 1.5\ 10^{19}$ m^{-3} injected power $P_{LH} \leq$ 25MW (of which a fraction of the order of 1/2 will be conveyed to the SOL).

On the other hand, the tolerable stresses in the transformer also limit the allowable flux swing saving obtained by non-inductive means. Present estimates[4] (for ITER) permit to consider a flux saving of the order of 50Vs as reasonable from this point of view.

II - Description of the model:

The Lower hybrid package LOCH is based on a 1-D , non-relativistic Fokker-Planck equation including the toroidal electric field and is briefly described in /1/. The transport code MINIBANG[2] coupled to it, solves the transport equations in circular geometry.

In the present simulations, the electron heat conduction is the sum of the neoclassical and an anomalous term; the ion conductivity and diffusivity are taken to be neoclassical. The code computes a corona equilibrium; a recycling coefficient at the wall of unity is assumed.

The total plasma current $I_p(t)$ is imposed as a boundary condition in the equation governing B_θ.

III - Simulation of JT-60 results.

In JT-60[5] current ramp-up assisted by 1.6MW of LHW power and performed at the same ramp-up rate as pure ohmic ramp-up during 2s, permitted to reduce the flux consumption by 2Vs, as shown in Fig. 1. In the simulation, energy confinement is assumed to follow the Kaye-Goldston scaling. The launched wave power spectrum however had to be adjusted (main lobe extending from $N_{//} = 1.5$ to $N_{//} = 6$) with respect to the actually launched spectrum (main lobe extending from $N_{//} = 1.5$ to 2.5) to simulate the spectral broadening as generated, for instance, by diffraction on the magnetic ripple[6]. Fig. 1 shows the results obtained. The surface voltages in the ohmic and LHW assisted case are in fair agreement with the observations. The internal inductance is found to decrease by almost the same amount during the ramp-up in both the ohmic and LHW cases so that about 90% of the Vs saving pertain to the resistive part (as also concluded in /5/). The experimental value of the electron temperature was not available for this shot.

IV - Conditions selected for simulations of the next step device

The simulations presented are based on the following device parameters $R = 6m$, $a = 2.1m$, $B_0 = 4.85T$, $\kappa = 2.2$ (ITER parameters[7]).

The shape of the plasma cross-section evolves with time during the ramp-up phase. In the present exploratory simulations, this evolution has not yet been taken into account; rather the plasma is assumed to fill the chamber all along the ramp-up phase. We use an equivalent radius $a_{eq} = a\sqrt{(1+\kappa^2)/2}$ where a is the plasma radius in the equatorial plane, and κ the elongation.

The global energy confinement is described by the 'ITER confinement scaling'[8]:

$$\tau_E^{(s)} = 0.048\ \bar{n}_{e20}^{0.1}\ \kappa^{0.5}\ R_m^{1.2}\ a_m^{0.3}\ B^{0.2}\ P_{ext,MW}^{-0.5}\ I_{p,MA}^{0.85}\ A_i^{0.5}$$

where $\bar{n}_{e20}$ is the volume averaged density in terms of 10^{20} m^{-3} ; A_i is the average ion mass number; and P_{ext} is the externally applied power, for which we chose $P_{ext} = P_{LH,abs} + V_{surf} I_p$ - $P_{LH,abs}$ being the to LHW absorbed power and V_{surf} the loop voltage at the plasma surface.

Locally, the electron heat conduction is taken to be $\chi_e \propto a_{eq}^2/\tau_E$ i.e. constant over the radius. The confinement is given by the Bohm's value inside the q=1 surface.

The width of the $N_{//}$ spectrum is taken constant, the upper $N_{//}$ boundary evolving with time in accordance with a 'feed-back formula', to ensure that the peak of deposition is maintained around some fixed radius (here a/2).

The present study was focused on a range of parameters expected to comply with the constraints imposed by power exhaust system and poloidal field system, further it has been restricted to a 'fast' ramp-up scenario where the ramp-up time is comparable to the ohmic one. An appreciably larger Vs saving is expected in a 'slow' scenario[9].

V - A Reference case

We compare purely ohmic (a) and LHW assisted ramp-up (b). In both cases, the initial plasma resulting from an ohmic equilibrium is characterized by $\bar{n}_e \simeq 1.5 \cdot 10^{19} m^{-3}$, $T_e(0) = 2keV$, $Z_{eff} \simeq 1.6$ (impurity is oxygen), and a plasma current of 5MA. The current is ramped-up linearly at a rate of 0.5MA/s up to 22MA and then maintained constant. In case b), the LHW input power is ramped-up from zero to 20MW in 10s, then maintained constant till the end of the current ramp-up and subsequently switched-off. The LHW spectrum width is $\Delta N_{//} = 2$ (full width of main lobe).

The global confinement time calculated from the energy content (electrons and ions) and the total power input to the particles ($\int (p_{LH} + E.j) d^3x$) was in these run $\tau_{global} \simeq 0.6\ \tau_{E,\ ITER}$.

Fig. 2 shows the density of the driven current, Fig. 3 the toroidal electric field and Fig. 4 the safety factor. The latter remains quasi-monotonic during the whole ramp-up phase. Various output quantities from the code are shown in Fig. 5. The flux consumption at the end of the current ramp-up is reduced by 23Vs in case (b) with respect to (a). The final value of the internal inductance is only slightly larger in (b) so that practically only the resistive flux consumption is reduced.

■ VI -Variation of the injected LHW power.

Fig. 5 also shows the effect of varying the injected LHW power. The flux saving $\Delta\Phi$ just at the end of the ramp-up period is found to be roughly proportional to the injected power (as is the case in the JT -60 experiments). The flux saving scales as $\Delta\Phi \simeq 1$Vs/MW.

For LHW power levels larger than 30MW, the q profile becomes non-monotonic, a situation which could be undesirable from the point of view of MHD stability.

In the absence of further heating which freezes the current profile, a part of the Vs saving is lost again after ramp-up, due on the one hand to the cooling itself accompanied by an overshoot in the resistive surface voltage, and on the other hand to the relaxation of the low-l_i profile. These effects are seen in runs in which the LHW power is maintained without current drive after the ramp-up (e.g. using a symmetrical spectrum).

■ VI -Variation of the spectrum width.

Varying the spectral width from $\Delta N_{//} = 0.2$ to 3 leads to the following observations. Though the current drive efficiency is much less in the case of narrow spectrum $\Delta N_{//} = 0.2$ (all spectral components being at relatively low phase velocities), the amount of flux saving at the end of ramp-up is larger (by 10Vs) than for $\Delta N_{//} = 3$. This can be understood when noting that the temperature profiles are very different in both cases. The LHW deposition zone - which was adjusted to be around mid-radius in these runs - is much narrower for $\Delta N_{//} = 0.2$: this results in a strong heating of the plasma core while the edge is not heated up; hence, the electric field drop at the onset of the LHW power diffuses rapidly outwards. This series indicate the potential advantage of narrow spectra, (such as delivered by the LHW system designed for burn conditions).

■ Concluding remarks.

In conclusion, these preliminary results confirm the viability, for NET/ITER, of LHW assisted ramp-up though the modelling results have been obtained using various assumptions and simplifications, the impact of which has still to be assessed.

A transformer flux saving of about 20 to 30Vs (providing a reserve in burn duration of 130-180s) appears achievable using a moderate LHW power level of 20-30MW at an average plasma density of about 1.5 10^{19} m^{-3} in a fast ramp-up scenario. These values are expected to be compatible with plasma MHD stability, power exhaust and poloidal field system constraints. Larger flux savings are expected for slow ramp-up and/or larger input power.

The technical requirements for application of the LHW both during the burn phase and for assisting current ramp-up appear after preliminary review to be achievable using a single LHW system currently being designed.

/1/ J.-G. Wégrowe, G. Zambotti, P.J. Lalousis , "Modelling of Lower Hybrid Current Drive Experiments ", Proc. 16th Eur. CCPP, Venice It., 1989
/2/ O. de Barbieri and A. Nocentini, 14th Conf. CFPP, Madrid, 1987, vol III, p.836
/3/ M. Harrison et al. , this conference
/4/ Internal Rpt. ITER IL-PF-1-9-27
/5/ JT-60 Team, presented by N. Nagami, 16th. Eur. Conf. CFPP, Venice, 1989, Plasma Phys. and Contr. Fusion, Vol 31, No 10, p. 1597, Aug. 1989; O. Naito, "Volt-second saving by LHCD", Nuclear Fusion, to be published;K. Ushigusa, invi ted paper, this conference

/6/ J.-G. Wégrowe, "Broadening of LHW Spectra by Magnetic Ripple, Simulation of experimental results and Applications to NET" , Top. Conf on RF power in plasmas, Irvine, 1989
/7/ ITER Documentation Series, No. 14, "ITER conceptual design: Interim Report", IAEA, Vienna, 1990
/8/ ITER Documentation Series, No. 10, "ITER physics design guidelines" Report", IAEA, Vienna, 1989
/9/ G. Pereverzev, ITER internal note IL-PH-6-0-S-5, Feb 1990

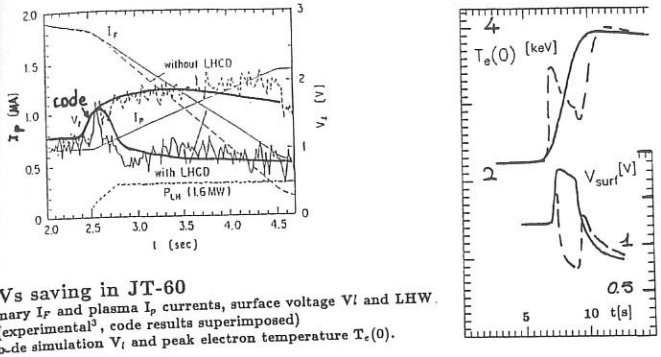

Fig. 1: Vs saving in JT-60
above: Primary I_F and plasma I_p currents, surface voltage Vl and LHW power P_{LH} (experimental[3], code results superimposed)
at right: Co-de simulation V_l and peak electron temperature $T_e(0)$.

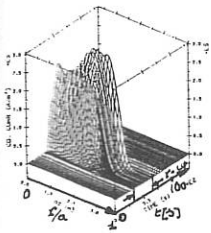

Fig. 2: ITER LHW assisted ramp-up
Density of the driven current, $P_{injected}$ = 20MW

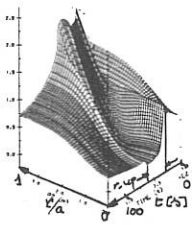

Fig. 3: ITER LHW assisted ramp-up
Toroidal electric field, $P_{injected}$ = 20MW

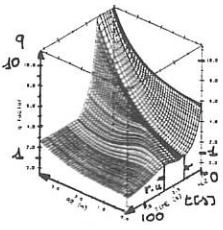

Fig. 4: ITER LHW assisted ramp-up
Safety factor, $P_{injected}$ = 20MW

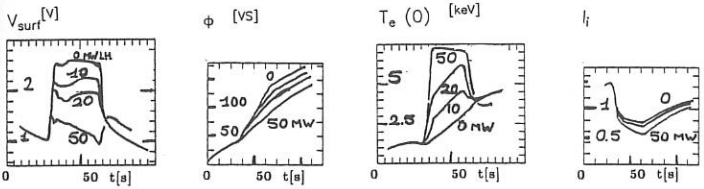

Fig. 5: Ohmic and LHW assisted current ramp-up in ITER:
surface voltage V_s, integral flux consumption Φ, (LHW injected power: 0-10-20-50MW), peak electron temperature T_e, internal inductance l_i (0-20-50MW) for Ohmic ramp-up and various levels of injected LHW power.

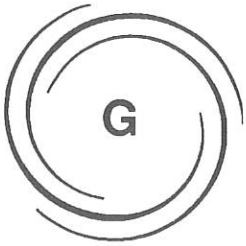

CURRENT DRIVE AND PROFILE CONTROL

G2

G2 LOWER HYBRID CURRENT DRIVE

NUMERICAL STUDIES OF AN ELECTRON CYCLOTRON CURRENT DRIVE EFFICIENCY AND THE ROLE OF TRAPPED PARTICLES

Yu.N.Dnestrovskij*, D.P.Kostomarov, A.G.Shishkin, A.P.Smirnov

*I.V.Kurchatov Institute of Atomic Energy, Moscow, USSR
Moscow State University, Moscow, USSR

Abstract. The two-dimensional bounce-averaged kinetic model is developed to simulate a multispecies magnetized plasma for the investigation of electron cyclotron current drive efficiency in tokamak plasma. The wave-particle interaction is assumed to be described in the framework of quasi-linear theory. The poloidal localization of launched RF power on a given magnetic surface is taken into consideration.

Model. The basic equation governing the process of current drive by electron cyclotron waves in tokamak geometry on a given magnetic surface is the kinetic equation for the time evolution of the electron distribution function f_e in velocity space:

$$\frac{\partial f_e}{\partial t} = L_{st}[f_e] + L_{ec}[f_e], \qquad (1)$$

where L_{st} is the linearized Fokker-Planck operator of Coulomb collisions of superthermal electrons with Maxwellian electrons and ions. L_{ec} is the quasi-linear diffusion operator for electron cyclotron waves; t is the time. In Eq.(1) we have chosen the velocity v, the magnetic moment $s=\frac{v_\perp^2 B_0}{v^2 B}$ as independent variables in velocity space. Here B is the tokamak magnetic field, B_0 - the value of B on the magnetic axis, $(v_\parallel, v_\perp)$ - the cylindrical coordinates in velocity space, $v_\parallel=(\vec{B}\cdot\vec{v})/|\vec{B}|$, $v_\parallel=\sigma\sqrt{v^2-v_\perp^2}$, $\sigma=\pm1$. For simplicity we assume the magnetic surfaces to be circular with the radius ρ. In (v,s) coordinates the basic equation (1) disintegrates into three equations: for the distribution function of trapped particles f_e^0 in the region $1-\varepsilon < s < 1+\varepsilon$ ($\varepsilon=\frac{\rho}{R}$, R - the

major radius) and for the distribution functions of passing particles moving along the magnetic field f_e^+ ($\sigma=+1$) and in opposite direction f_e^- ($\sigma=-1$) in the region $0< s <1-\varepsilon$.

To average the Fokker-Planck operator L_{st} we multiply it by element of volume in phase space d^3v in coordinates (v,s) and then integrate over poloidal angle θ. As a result we obtain bounce-averaged operator $\hat{L}_{st}$:

$$\hat{L}_{st}[f_e]= \sum_\beta \frac{v_e^3}{\tau_e}\frac{Z_\beta^2}{v^2}\frac{n_\beta}{n_e}\cdot\Big[J_1\frac{\partial}{\partial v}\cdot\Big(\frac{T_\beta a_\beta}{m_\beta v}\cdot\frac{\partial f_e}{\partial v} + \frac{m_e}{m_\beta}\cdot a_\beta f_e\Big) + 4\,\frac{c_\beta}{v}\cdot\frac{\partial}{\partial s}\cdot\Big(sJ_2\cdot\frac{\partial f_e}{\partial s}\Big)\Big] . \qquad (2)$$

Here $a_\beta(v,\rho)= \frac{4}{\sqrt{\pi}}\int_0^u \exp(-x^2)x^2dx$,

$$c_\beta(v,\rho)= \frac{u}{\sqrt{\pi}}\Big[\exp(-u^2) + (2/u - 1/u^3)\int_0^u \exp(-x^2)x^2dx\Big], \qquad (3)$$

$$J_1(\rho,s)= \frac{1}{2\pi}\int_{-\theta^*}^{\theta^*}\frac{d\theta}{\sqrt{1+\varepsilon\cdot\cos\theta-s}}, \quad J_2(\rho,s)= \frac{1}{2\pi}\int_{-\theta^*}^{\theta^*}\sqrt{1+\varepsilon\cdot\cos\theta-s}\;d\theta, \qquad (4)$$

where $\theta^*=\pi$ for passing particles and $\theta^*=\arccos(\frac{s-1}{\varepsilon})$ for trapped particles [1], $u=v/v_\beta$. Other notations are standard.

The bounce-averaged diffusion operator is:

$$\hat{L}_{ec}[f_e] = \frac{1}{v^2}\frac{\partial}{\partial v}\cdot\Big[v^2 s\cdot\hat{\overset{Q}{\underset{-}{J}}}_1\cdot\frac{\partial f_e}{\partial v} + 2vs\cdot\hat{\overset{Q}{\underset{-}{J}}}_2\cdot\frac{\partial f_e}{\partial s}\Big] +$$

$$\frac{1}{v^2}\frac{\partial}{\partial s}\cdot\Big[4s\cdot\hat{\overset{Q}{\underset{-}{J}}}_3\cdot\frac{\partial f_e}{\partial s} + 2vs\hat{\overset{Q}{\underset{-}{J}}}_2\cdot\frac{\partial f_e}{\partial v}\Big] , \qquad (5)$$

$$\hat{\overset{Q}{\underset{-}{J}}}_1(\rho,v,s)= \frac{1}{2\pi}\int\frac{\hat{\overset{Q}{\underset{-}{D}}}\cdot d\theta}{\sqrt{1+\varepsilon\cdot\cos\theta-s}}, \quad \hat{\overset{Q}{\underset{-}{J}}}_2(\rho,v,s)= \frac{1}{2\pi}\int\hat{\overset{Q}{\underset{-}{D}}}\cdot\sqrt{1+\varepsilon\cdot\cos\theta-s}\;d\theta$$

$$\hat{J}_3^{\mp}(\rho,v,s) = \frac{1}{2\pi}\int \hat{D}^{\mp}\cdot(1+\varepsilon\cdot\cos\theta-s)^{3/2}\,d\theta\,, \qquad \hat{D}^{\mp}=\hat{D}^{\mp}(\rho,v,s,\theta)\,. \tag{6}$$

At the boundary between passing and trapped particles we require distribution functions and fluxes in s direction to be continuous:

$$f_e^0\Big|_{s=1-\varepsilon+0} = f_e^+\Big|_{s=1-\varepsilon-0} = f_e^-\Big|_{s=1-\varepsilon-0}\,, \tag{7}$$

$$2\left(I_{st}^0+I_{ec}^0\right)\Big|_{1-\varepsilon+0} = \left(I_{st}^++I_{ec}^++I_{st}^-+I_{ec}^-\right)\Big|_{1-\varepsilon-0}\,. \tag{8}$$

We use the following expression for $\hat{D}$:

$$\hat{D}=\tilde{D}_0(\rho)\cdot\left[H(v_\parallel-v_1)-H(v_\parallel-v_2)\right]\cdot(\varphi_2-\varphi_1)/2\pi\,, \tag{9}$$

where φ_1 and φ_2 are the toroidal boundaries of launched RF power, $H(v)$ - the Heaviside function, v_1 and v_2 are the boundaries of resonance region in velocity space.

Numerical results. Equation (1) has been solved numerically. In Fig.1 the dependence of electron cyclotron current drive efficiency η on the values of ε for the absorption on the external side (curve I),the internal side (II) and also on the top of magnetic surface (III) is depicted. Since the level of input RF power is quite low ($D_0=0.01$, $D_0=\tilde{D}_0\cdot\tau_e/v_e^2$), the deviation of the electron distribution function from the Maxwellian one is small. Comparing these three curves,we find that the efficiency η is highest for internal absorption and lowest for external one. This is due to increase in number of trapped particles on the top and the low field side of tokamak as compared to the high field side. The curve IV are the results obtained for the case when power absorption is not localized. The dashed curve shows the values of η obtained by the solution of the integro-differential equation [2] with neoclassical corrections.The method of its solution is given in Ref.3.The dot-dashed line depicts the dependence of $\Delta(\varepsilon)$ which is the ratio of internal absorption efficiency to external one. The dependence of current drive efficiency η on the low boundary of resonance region v_1 is shown in Fig.2. It can be seen that increase in v_1 leads to the increment of efficiency and to the reduction of Δ.The marked reduction is due to the fact that wave-induced push of an initially passing electron into the trapped-particle part of phase space requires a greater level of incoming

RF power with a rise of v_1. It follows from Fig.2 that the results obtained are in a good agreement with those of Ref.4 (Fig.4) for ε=0.07.

In Fig.3 the efficiency η is depicted as a function of D_0 for v_1=2.9; v_2=3.5; ε=0.08. It can be seen that the increase in D_0 does not lead to significant rise of efficiency in contrast to the results for homogeneous plasma from Ref.4.

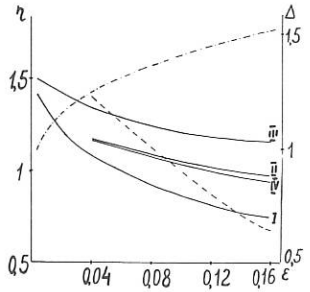

Fig. 1

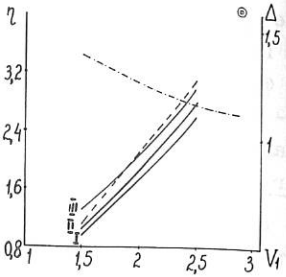

Fig. 2

Fig.1 η and Δ vs ε; v_1=1.5 I-(θ_1,θ_2)=(-10°,10°), II-(80°,100°), III-(170°,190°), IV-(0°,360°). θ_1, θ_2- boundaries of poloidal localization of absorbed RF power.

Fig.2 η and Δ vs v_1; ε=0.08, D_0=0.01. I,II,III, dashed, dot-dashed lines have the same meaning as in Fig.1. © corresponds to the results of Ref.4.

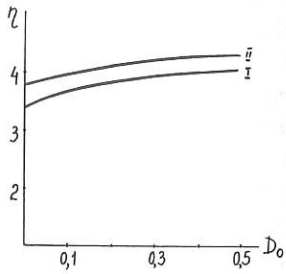

Fig. 3

Fig.3 η vs D_0.

References

1. A.V.Gurevich, Ya.S.Dimant, Reviews of Plasma Physics, ed.Kadomtsev B.B.,Moscow, Energoatomisdat,1987.
2. M.N.Rosenbluth *et al.*, Phys.Fluids **15**, 116, (1972).
3. A.P.Smirnov, A.G.Shishkin,ITER-IL-PH-6-9-S-24,Garching,(1989).
4. Yu.N.Dnestrovskij *et al.*, Nucl.Fusion **28**, 267, (1988).

IMPACT OF SOURCE POWER SPECTRUM ON ECRH CURRENT DRIVE EFFICIENCY

A.G.Shishkin, A.P.Smirnov, V.V.Parail*

Moscow State University, Moscow, USSR
*I.V.Kurchatov Institute of Atomic Energy, Moscow, USSR

The electron cyclotron current drive efficiency in plasma with external electric field is investigated. Recently the analytic asymptotic formulas for current density, dissipated power density and current drive efficiency for the case of lower hybrid waves were obtained in Ref.1. In this paper the interaction of electron cyclotron waves with plasma is studied for variable RF power profile by the same method as in Ref.1.

The electron distribution function f_e in the presence of electron cyclotron waves within the framework of quasi-linear theory is given by:

$$\frac{\partial f_e}{\partial t} = L_{st}[f_e] + L_{ec}[f_e] + \frac{eE}{m_e}\cdot\frac{\partial f_e}{\partial v_\parallel} \quad . \tag{1}$$

L_{st} is the linearized Fokker-Planck collision operator, L_{ec} is the quasi-linear diffusion operator for electron cyclotron waves where the diffusion coefficient D_{ec} is a function of parallel velocity $v_\parallel$: $D_{ec}=D_0(u-u_1)^\alpha H(u-u_1)$, $u=v_\parallel/v_e$, $u_1=v_1/v_e \gg 1$, $D_0=const \ll 1$, $\alpha=const$, $H(u)$ - Heaviside function, v_e-electron thermal velocity, v_1 - the lower boundary of resonance region determined by the source power spectrum. By the method of Ref.2,3 analytic formulas for current density j, dissipated power P and their ratio S=J/P usually called current drive efficiency were obtained. The formu las for current density for $\alpha=0;1;2$ are expressed as:

$$j_{ec}^{(\alpha)}=(j_{ec}^{0})_\alpha\cdot(1+\theta_{ec}^{(\alpha)}\gamma) \quad , \qquad \theta_{ec}^{(\alpha)}= A^{(\alpha)}+\beta, \tag{2}$$

$$(j^0_{ec})_\alpha=\frac{3n_e e v_e D_0}{(Z+5)\sqrt{\pi}}\cdot\exp(-u_1^2)\cdot u_1^{1-\alpha}\cdot I^{(\alpha)}_{ec}\left(1+\frac{b^{(\alpha)}}{u_1^2}\right), \tag{3}$$

$$I^{(0)}_{ec}=1, \qquad I^{(1)}_{ec}=I^{(2)}_{ec}=1/2,$$

$$b^{(0)}=-\frac{3}{2}(1+1/(Z+3)), \qquad b^{(1)}=b^{(0)},$$

$$b^{(2)}=7-\frac{27}{(Z+3)}+\frac{6}{(Z+3)(Z+1)},$$

$$A^{(\alpha)}=\frac{4}{Z+5}(u_1^4+a^{(\alpha)}u_1^2), \qquad \beta=\frac{4}{3}u_1^2(1+1/(Z+3)),$$

$$a^{(0)}=-\frac{1}{2}(4+9/(Z+3)), \quad a^{(1)}=a^{(0)}+2, \quad a^{(2)}=a^{(0)}+4,$$

where $\gamma=E/E_{cr}$, $E_{cr}=4\pi n_e e^3 \ln\lambda/T_e$, $\ln\lambda$-Coulomb logarithm, $(j^0_{ec})_\alpha$ - current excited by waves for $\gamma=0$.

For dissipated power and efficiency we find:

$$P^{(\alpha)}_{ec}=(P^0_{ec})_\alpha\cdot(1+B^{(\alpha)}_{ec}\gamma) \tag{4}$$

$$(P^0_{ec})_\alpha=\frac{m_e n_e}{\sqrt{\pi}}\cdot\left(\frac{D_0 v_e^2}{\tau_e}\right)\cdot\exp(-u_1^2)u_1^{-1-\alpha}\cdot K^{(\alpha)}_{ec} \tag{5}$$

$$K^{(0)}_{ec}=1, \quad K^{(1)}_{ec}=1/2, \quad K^{(2)}_{ec}=1/4$$

$$B^{(0)}=A^{(0)}, \quad B^{(1)}=A^{(1)},$$

$$B^{(2)}=\frac{4}{Z+5}\left(u_1^4+\frac{u_1^2}{2}\left(7+\frac{9}{(Z+3)}\right)\right),$$

$$S^{(\alpha)}_{ec}=(S^0_{ec})_\alpha\cdot(1+C^{(\alpha)}\gamma), \tag{6}$$

$$(S^0_{ec})_\alpha=\frac{e v_e \tau_e}{T_e}\cdot\frac{u_1^2}{(Z+5)}M^{(\alpha)}_{ec}\left(1+\frac{d^{(\alpha)}}{u_1^2}\right), \tag{7}$$

$$M^{(0)}_{ec}=6, \qquad M^{(1)}_{ec}=M^{(2)}_{ec}=3/2,$$

$$d^{(0)}=b^{(0)}+1/2, \qquad d^{(1)}=b^{(0)}, \qquad d^{(2)}=b^{(2)}/2 ,$$

$$c^{(0)}=\beta, \quad c^{(1)}=\beta, \qquad c^{(2)}=\frac{10u_1^2}{(Z+5)}+\beta .$$

The principal terms of the current $(j^1_{ec})=(j^0_{ec})_\alpha\,\theta^{(\alpha)}_{ec}\gamma$ and the power $(P^1_{ec})=(P^0_{ec})_\alpha\,B^{(\alpha)}_{ec}\gamma$ for $u_1^2\gg1$ are proportional to u_1^4 with the same coefficients. As a result, the efficiency depend on the electric field to a much lesser extent then the current and power

A conservative difference method, conserving the number of particles, is used for the numerical approximation of Eq.(1) [3]. From numerical solution of Eq.(1) by 2D code it was found that the behaviour of the function $j^{(\alpha)}_{ec}(\gamma)$ is really close to the exponential one:

$$j^{(\alpha)}_{ec}=j^{(\alpha)}_{ec}(D_0,\gamma)\approx(j^0_{ec})_\alpha\cdot\exp(\hat\theta^{(\alpha)}_{ec}\gamma)$$

and the coefficients $\hat\theta^{(\alpha)}_{ec}$ for given α depend on two parameters only $\hat\theta^{(\alpha)}_{ec}=\hat\theta^{(\alpha)}_{ec}(u_1,Z)$ and do not depend on D_0. In formula (2) the main linear term in γ for $D_0\ll1$ is derived for the current $j^{(\alpha)}_{ec}$. In this case, $\hat\theta^{(\alpha)}_{ec}=\theta^{(\alpha)}_{ec}$. The weak dependence of $\hat\theta^{(\alpha)}_{ec}$ on D_0 allows us to make a conclusion on the proximity of $\hat\theta^{(\alpha)}_{ec}$ and $\theta^{(\alpha)}_{ec}$ for $D_0\geqslant1$, too. Indeed, from the numerical results we can see that $\hat\theta^{(\alpha)}_{ec}$ and $\theta^{(\alpha)}_{ec}$ agree well.Hence, we obtain an approximate formula for the current:

$$j^{(\alpha)}_{ec}(\gamma,D_0)\approx(j^0_{ec})_\alpha\cdot\exp(\theta^{(\alpha)}_{ec}\gamma)$$

where $\theta^{(\alpha)}_{ec}$ is determined by formula (2).

A comparison between the analytical formulas (2) and (6) shows that with a rise in the electric field the efficiency rises much more slowly than the current. The calculations done for high D_0 confirm this conclusion and bear witness that the dependence $S^{(\alpha)}_{ec}$ on γ is of the exponential type:

$$S^{(\alpha)}_{ec}(\gamma,D_0)=(S^0_{ec})_\alpha\cdot\exp(\hat c^{(\alpha)}\gamma)$$

The dependence $\hat{C}^{(\alpha)}$ on D_0, as that for the current, is very weak and $\hat{C}^{(\alpha)}$ is close to $C^{(\alpha)}$. The proximity of $C^{(\alpha)}$ and $\hat{C}^{(\alpha)}$ allows us to conclude that an approximate formula:

$$S_{ec}^{(\alpha)}(\gamma, D_0) \approx (S_{ec}^{0})_{\alpha} \cdot \exp(C^{(\alpha)}\gamma)$$

can be used to find the current drive efficiency in the presence of an electric field for a wide range of launched power.

Thus the electron current density and power dissipated density are found to be proportional to $u_1^{1-\alpha}$ and $u_1^{-1-\alpha}$ for $(j_{ec}^{0})_{\alpha}$ and $(P_{ec}^{0})_{\alpha}$ correspondingly and the efficiency in its principal term does not depend on α. Hence, the current and the power are much more sensitive to D_{ec} profile than the efficiency.

References.

1. A.P.Smirnov, A.G.Shishkin. Fiz.Plazmy **16**, 110, (1990).
2. N.J.Fisch. Phys Fluids **28**, 245, (1985).
3. Yu.N.Dnestrovskij, D.P.Kostomarov *et al.*, Nucl.Fusion **28**, 267, (1988).

ELECTRON CYCLOTRON CURRENT DRIVE AND TEARING MODE STABILIZATION IN ITER

*L.K.Kuznetsova**, *V.V.Parail**,
A.G.Shishkin, *A.P.Smirnov*, *F.S.Zaitsev*

*I.V.Kurchatov Institute of Atomic Energy, Moscow, USSR
Moscow State University, Moscow, USSR

ABSTRACT

The possibility of using EC-ordinary waves both for the support of stationary current and for tearing mode m=2, n=1 stabilization in ITER is numerically investigated. The calculations of the propagation of EC waves, the local current drive efficiency, the absorption coefficient, current profiles and total current in plasma were used for determination of current drive efficiency. Relativistic effects are included in the electron cyclotron resonance condition.The electron trapping is found to substantially reduce the current drive efficiency.

The propagation of EC waves was calculated by using a ray tracing technique [1]. The dispersion relation for cold plasma was chosen. To calculate the current profile and the efficiency of current drive it is necessary to find the values of local current drive efficiency .To determine the local current drive efficiency η the method of Ref.2 is used. The treatment applies to large aspect ratio ϵ^{-1} Tokamaks. The perturbation to the Maxwellian distribution is expressed as the sum of the perturbed distribution function for untrapped electrons and the neoclassical correction in Legendre polynomial representation. The integro-differential equations obtained were solved numerically by the iterational method. We used the full expressions for all coefficients instead of the asymptotic formulas that were used in Ref.2. This reduces the order of discontinuity at v=0 and facilitates the numerical solution. The iteration parameter was proportional to v^3 which led to convergence acceleration.

In Fig.1 the solid curve shows the values of η plotted against $u_0=(\omega-\Omega)/k_\parallel v_e$ for the nonrelativistic case (S=0, where $S = \Omega \cdot v_e/(2k_\parallel c^2)$) and for S=0.08 for ϵ=0; 0.05 and 0.1. The dashed curves are results obtained by asymptotic formulas from Ref.3.The excellent agreement between curves can be

seen. The dot-dashed line shows the efficiency obtained without integral term. The dependence of current drive efficiency η on the relativistic resonance condition parameter S is shown in Fig.2 for $\epsilon=0$; 0.05 and 0.1. It can be seen that the effect of trapping substantially reduces efficiency. At the same time we can conclude from Fig.2 that the increase in S softens the effect of trapped particles.The relativistic resonance condition is shown to have important effect on the efficiency of current drive by ECRH. For some values of u_0 and ϵ the ratio of efficiency for S=0.08 to efficiency for S=0.16 is nearly 2.

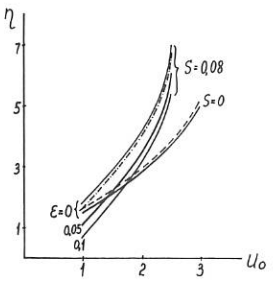

Fig. 1

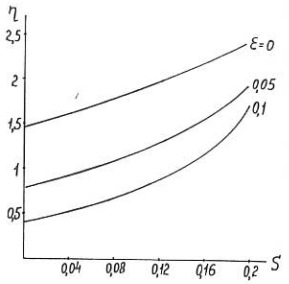

Fig. 2

To calculate the current profile and the efficiency of current generation $\eta_{cd}=\bar{n}_e I_0 R_0/P_0$(A/W 10^{20}m^{-3}) it is necessary to find the values of absorption coefficient. It was calculated on the basis of [4] in a following way. A cold plasma approximation was used for description of dispersion and polarization effects. The relativistic resonance condition and relativistic maxwellian distribution function were taken into account. Both first and second harmonics were taken into account. The absorbed power was distributed uniformly over magnetic surface.

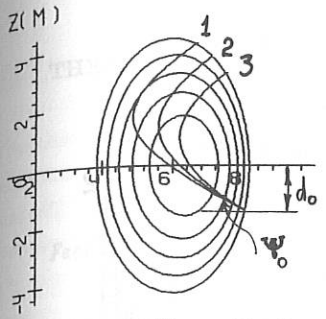

Fig.3

Fig.3 The projection of O-wave trajectories on (ROz) plane: 1)$\xi_0=37^o$; 2)$\xi_0=42^o$; 3)$\xi_0=47^o$. $d_0=-1.5m$; $\psi_0=25^o$; f=190GHz.

Fig.4 (a) The damping rate for three waves along their trajectories. $|R-R_0|$ is the distance from magnetic axis. (b) Current density profiles. (Parameters are the same as in Fig.3).

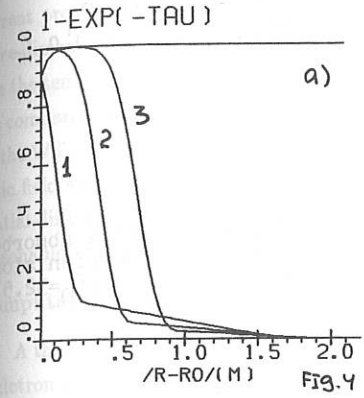

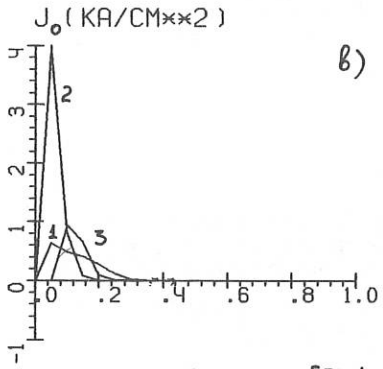

Fig.4

Calculations were performed for $R_0=6m$; $a_0=2.15m$; $B_0=5.3T$; $n_{e0}=1*10^{20}m^{-3}$; $T_{e0}=30keV$; $Z_{eff}=2.16$; elongation - $\lambda=1.7+0.3s^2$ and Shafranov shift of magnetic axis 0.4m . The calculations were done for temperature and density distributions: $T_e=T_{e0}(1-s^2/a_0^2)$; $n_e=n_{e0}(1-s^2/a_0^2)^{1/2}$. We changed the the range of ECW frequency f=180-210GHz;,the vertical displacement of point of launch $d_0=-0.75m$, $-1.5m$; the angle between the wave vector and the perpendicular to magnetic field ξ_0; the angle between wave vector and its projection on the horizontal plane ψ_0. The optimal parameters obtained from simulations are: $\eta_{cd}{}_{max}\approx 0.26$. ($I_0\approx 6.2MA$, $P_0=100MW$). $d_0=-0.75m$, f=200GHz, $\xi_0=39^o$, $\psi_0=12^o$; If $d_0=-1.5m$, f=190GHz, $\xi_0=42^o$, $\psi_0=25^o$, than $\eta_{cd}{}_{max}\approx 0.22$ ($I_0\approx 5.6MA$).

For example the damping rate and the current profiles, corresponding to trajectories in Fig.3 are shown in Fig.4(a,b).

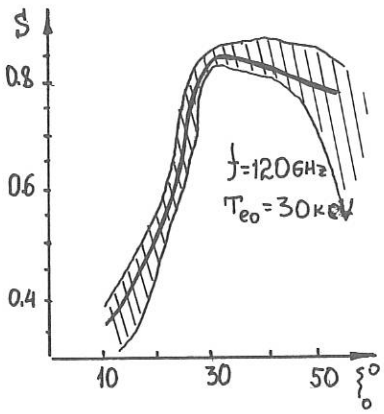

Fig.5. The area of energy absorption on along magnetic flux coordinate s in depend on ξ_0. R_0=6m; a_0=2m; B_0=5T; n_{e0}=1*10^{20} m^{-3}.

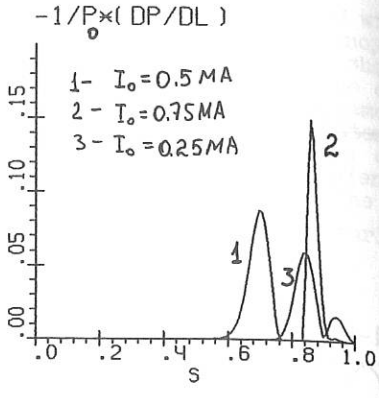

Fig.6. Relative absorbed power distribution along s. 1)$\xi_0=25^o$; 2)$\xi_0=32.5^o$; 3)$\xi_0=42.5^o$.

The conditions for tearing mode stabilization near the surface q=2 by EC-waves were studied. In accordance with the requirement on the amplitude and localization of the driven current [4], the typical parameters of EC-system needed for stabilization of tearing mode were determined. The calculation shown,that m=2 tearing mode in ITER can be stabilized by input of about 20MW ECW with frequency f≈120GHz. The optimal range for angles is:$\xi_0=30^o-34^o$ for T_{e0}=20-30keV.In this case ECW power is absorbed in s≈0.85. For example, Fig.5 show the situation of maximum (solid line) and a halfwidth (shade area)of ECW power absorbed along the magnetic flux coordinate s depending on the injection angle ξ_0. The profile of power absorption is shown in Fig.6 for $\xi_0=25^o$; 32.5^o; 42.5^o and T_{e0}=30keV.

1. N.Stix, The theory of plasma waves. M., 1965.
2. A.Ferreira et al.,Plasma Phys. V.26, (1984), p.1565.
3. Yu.N.Dnestrovskij et al., Nucl. Fusion. V.28, (1988), p.267.
4. M.Bornatici et.al., Nuclear Fusion, V.23, (1983), p.1153.
5. E.Westerhof, Nuclear Fusion, V.27, (1987), p.1929.

THREE-DIMENSIONAL FOKKER-PLANCK ANALYSIS ON RF CURRENT DRIVE IN TOKAMAKS

A. Fukuyama and T. Ueeda

Faculty of Engineering, Okayama University, Okayama 700, JAPAN

Spatial diffusion of fast electrons across the magnetic field line broadens the induced current profile and reduces the current drive efficiency[1,2]. We numerically solve the three-dimensional Fokker-Planck equation including a radial diffusion term and calculate the temporal and spatial evolution of the electron velocity distribution. The results are compared with the experiment of second-harmonic electron cyclotron current drive on the WT-3 tokamak[3,4,5]. The dependence of the current-drive efficiency on the magnetic field strength agrees with the experimental result. The calculation with a simple spatial-diffusion model shows considerable reduction of the current drive efficiency for reasonable values of the diffusion coefficient.

Computational Model

A three-dimensional Fokker-Planck code is newly developed to describe the electron cyclotron current drive. This code incorporates the trapped-particle effect, the relativistic effect and the spatial diffusion. We assume cylindrical magnetic surfaces and write the bounce-averaged Fokker-Planck equation for an electron distribution $f(p,\theta,r,t)$ as

$$\frac{\partial f}{\partial t} = C(f) + Q(f) + L(f) + S, \tag{1}$$

where (p,θ) are the momentum space coordinates specified on the low-field-side midplane and r is the radial coordinate on the poloidal plane. The Coulomb collision term $C(f)$ is linearized for the Maxwellian field-particle distribution. The resonant diffusion term $Q(f)$ is calculated for a Gaussian microwave beam on a midplane. The incident power determines the intensity of the electric field uniform along the beam axis. The spatial diffusion term is given by

$$L(f) = \frac{1}{r}\frac{\partial}{\partial r} r D_{rr} \frac{\partial f}{\partial r}. \tag{2}$$

We assume spatial uniformity of the diffusion coefficient $D_{\rm rr}$ and velocity dependence of the form, $D_{rr} = D_{rr0}(1-p^2/p_{\rm th}^2)^{\alpha}$, where $p_{\rm th}$ is the momentum of the thermal particle.

The source term S locally supplies particles with the initial temperature and maintains the radial profile of the electron density.

Plasma parameters are chosen according to the current-drive experiment on the WT-3 tokamak using the second-harmonic electron cyclotron wave: $R = 0.65\,\mathrm{m}$, $a = 0.2\,\mathrm{m}$, $f = 56\,\mathrm{GHz}$, $B(0) = 0.8 \sim 1.2\,\mathrm{T}$, $n_e(0) = 4 \times 10^{18}\,\mathrm{m}^{-3}$, $N_{\parallel} = 0.5$. The initial temperature used in the calculation, 4 keV, is much higher than that observed in the experiments, 200 eV. The X-mode wave is horizontally launched from the outside of the torus. The width of the microwave beam is 4 cm. The initial density and temperature profiles are assumed to be parabolic.

Result Without Spatial Diffusion

When incident power of 110 kW is injected, the single-path absorbed power is about 31.1 kW. In the absence of the spatial diffusion, the maximum of the driven current, 36.5 kA, is obtained when the second harmonic cyclotron resonance is located at the slightly high-field side of the plasma center, $B(0) = 0.97\,\mathrm{T}$. Figure 1a shows the radial profiles of the current density. The current density monotonically increases with the formation of the fast electron tail and almost saturate 50 ms after the RF power is switched on. The global current drive efficiency η, defined by the ratio of the total current I_{RF} and the total absorbed power P_{RF}, increases with the increase of the incident power.

Effect of Spatial Diffusion

In the presence of spatial diffusion, the fast electron produced near the plasma center diffuses to the peripheral region. Figure 2 shows the momentum distribution at different radial points at $t = 50\,\mathrm{ms}$. The momentum is normalized by p_{th}. In the case without spatial diffusion (Fig. 2a), fast ions produced along the relativistic cyclotron resonance curve diffuses in momentum space by pitch angle diffusion. When $D_{rr0} = 0.25\,\mathrm{m}^2/\mathrm{s}$ and $\alpha = 0$ (Fig. 2b), the fast electron diffuses radially and some of them are forced to be trapped particles. This effect also reduces the driven current in addition to the loss of fast electrons. The current diffuses radially and the current density is strongly reduced as shown in Fig. 1b. In this case, the total absorbed power is 40 kW and the driven current 18.7 kA. The efficiency η is reduced to 40 % of the value without spatial diffusion. The D_{rr0} dependence of η is shown in Fig. 3. The particle confinement time τ_{p} is 20 ms for $D_{rr0} = 0.25\,\mathrm{m}^2/\mathrm{s}$ and inversely proportional to D_{rr0}. In the WT-3 experiment, the energy confinement time of the fast electrons is estimated as 6 ms. The efficiency η for $\tau_{\mathrm{p}} = 6\,\mathrm{ms}$ is 0.15 A/W[5], which is less than the experimentally observed efficiency.

Dependence on Magnetic Field Strength

Since the parallel velocity of the resonant electrons changes sign on the high-field and low-field sides of the cyclotron resonance, global current-drive efficiency η depends on the location of the resonance. Figure 4 shows the dependence of η on the magnetic field strength $B(0)$. We find that η is not anti-symmetric owing to the relativistic effect. This behavior is qualitatively agrees with the experimental observation.

Discussion

In the present calculation, we have assumed that the initial momentum distribution is isotropic. In the experiments, the anisotropic electron tail is produced in advance by an ohmic electric field and the internal electric field is generated according to the change of the current profile. The self-consistent analysis including the induced DC electric field and the effect of multiple path absorption of the wave will be reported in a near future.

Reference

[1] S. C. Luckhardt, Nucl. Fusion **27** (1987) 1914.

[2] R. O. Dendy, M. R. O'brien, Nucl. Fusion **29** (1989) 480.

[3] H. Tanaka *et al.*, Phys. Rev. Lett. **60** (1988) 1033.

[4] H. Tanaka *et al.*, Proc of 15th Europ. Conf. on Controlled Fusion and Plasma Heating, Dubrovnik, (1988).

[5] H. Tanaka, Proc. of US-Japan Workshop on Advanced Current Drive Concept, Livermore, (1990).

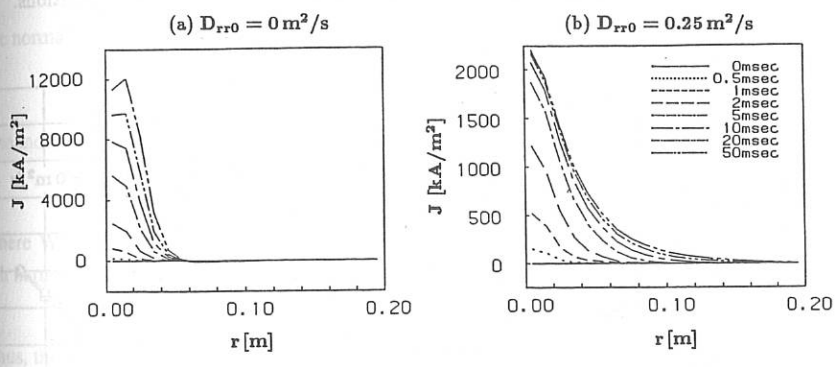

Fig. 1 Radial profile of current density.

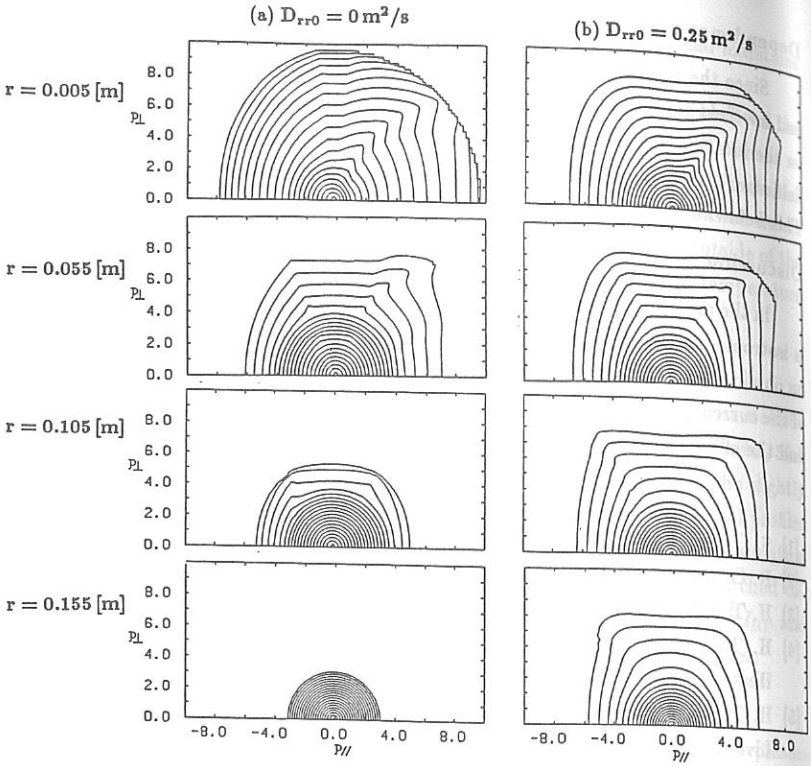

Fig. 2 Momentum distribution at different radial positions.

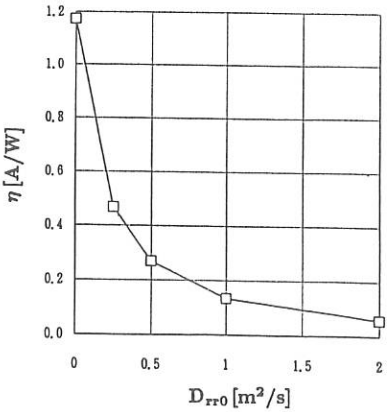

Fig. 3 D_{rr0} Dependence of η

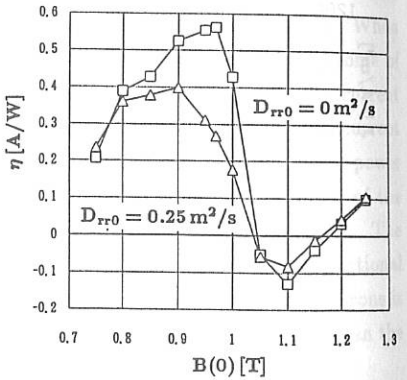

Fig. 4 B(0) Dependence of η

Mo 86

LINEAR EVALUATION OF CURRENT DRIVE IN TJ-II

F. Castejón and C. Alejaldre

Asociación EURATOM/CIEMAT para Fusión.
28040, Madrid. Spain.

INTRODUCTION

The current generated in the Flexible Heliac TJ-II by low power density EC waves is computed. Since stellarators are net current free devices, even low current densities can be important for the confinement properties and can modify the iota profile. Specifically, the current profile control one obtains using EC waves can be very useful to compensate deleterious currents, like the bootstrap one, and also to modify the iota profile.

THE FISCH AND BOOZER FUNCTION AND THE RESONANT VELOCITY

The induced current parallel to the magnetic field at a given position in the momentum space and for a given absorbed power density, can be obtained using the response function of Fisch and Bozer [1]. For the particular case of oblique EC waves, in the relativistic case, for Z=1, the response function can be written as [2], [3]

$$\Im(\vec{v}) = \frac{\delta J(\vec{v})}{\delta P(\vec{v})} = \frac{A}{2}\left[N_{\parallel} G(v) - \frac{v_{\parallel}}{v^2}(\gamma+2)G(v) + \frac{2 v v_{\parallel}}{\gamma^2} \right],$$

where we have introduced the constant $A=mc^2/(4\pi\Lambda e^3 n_0)$ and the function

$$G(v) = 2\left(\frac{\gamma+1}{\gamma-1}\right)\frac{v^2 - 2\gamma\ln\gamma}{\gamma v},$$

the normalized electron momentum and the Lorentz factor:

$$\vec{v} = \frac{\vec{p}}{mc} \quad ; \quad \gamma = \left(1+v^2\right)^{1/2}.$$

The induced current density will then be given by

$$J(\vec{r}) = \int d\vec{v}\ \ \Im(\vec{v}) \sum_n W_n(\vec{v}),$$

where W_n is the power density absorbed in the interval (v, v+dv) for frequencies near the nth harmonic of the cyclotron frequency and satisfies

$$W_n(\vec{v}) \propto \delta(\gamma - Y_n - N_{\parallel} v_{\parallel}).$$

Thus, the induced current can be written in the following way:

$$J(\vec{r}) = \sum_n \int_{v_-}^{v_+} dv_{\parallel}\ \Im(v_{\parallel})\ W_n(v_{\parallel})$$

where all the quantities are evaluated at the resonant momenta and

$$v_{\pm} = \frac{1}{1-N_{\parallel}^2}\left(N_{\parallel}Y_n \pm \sqrt{N_{\parallel}^2 - 1 + Y_n^2}\right).$$

Following reference [4], the main contribution to the current at every harmonic will come from the electrons in the momentum space which more strongly interact with the wave packet, as far as the modification of the distribution function can be considered as a perturbation. This electron momentum is the so called Collective Resonance Momentum and is obtained from the equation

$$\frac{dW_n(v_{\parallel})}{dv_{\parallel}} = 0 \quad \Rightarrow \quad v_{\parallel} \approx v_{R\pm} \equiv \frac{N_{\parallel}Y_n}{1-N_{\parallel}^2} + \frac{n}{\mu N_{\parallel}} \pm \sqrt{\frac{N_{\parallel}^2 - 1 + Y_n^2}{\left(1-N_{\parallel}^2\right)^2} + \left(\frac{n}{\mu N_{\parallel}}\right)^2}$$

There are two possibilities, depending on the sign of $N_{\parallel}$:

$$N_{\parallel} < 0 \quad \Rightarrow \quad v_{R-} < v_- < v_{R+} < v_+ \quad \Rightarrow \quad v_R = v_{R+}$$
$$N_{\parallel} > 0 \quad \Rightarrow \quad v_- < v_{R-} < v_+ < v_{R+} \quad \Rightarrow \quad v_R = v_{R-}$$

The corresponding resonant perpendicular momentum is computed from the resonance condition. This being an odd function of ($v_{\parallel}$ $N_{\parallel}$) the perpendicular component is given for both cases by

$$v_{R\perp} = \frac{2n}{\mu N_{\parallel}}\left(\sqrt{N_{\parallel}^2 - 1 + Y_n^2 + \left(\frac{n\left(1-N_{\parallel}^2\right)}{\mu N_{\parallel}}\right)^2} - \frac{n\left(1-N_{\parallel}^2\right)}{\mu N_{\parallel}}\right)$$

Finally we can approximate the current density, parallel to the magnetic field, for oblique wave propagation, by:

$$J(\vec{r}) = \sum_n \Im(\vec{v}_R)\, P_n(\vec{r}),$$

where P_n is the power density absorbed near the nth harmonic and the response function is evaluated at the collective resonant momentum for that harmonic:

$$\vec{v}_R = \left(v_R, v_{R\perp}\right).$$

THE INDUCED CURRENT IN TJ-II

The absorbed power is computed as in reference [5] using a weakly relativistic model for the dielectric tensor, which has been adapted to the ray tracing code RAYS. As a numerical example we choose a case with strong absorption, in which X mode waves at second harmonic (f=53.2 GHz) are launched. The electron density and temperature at the magnetic axis are n_0=1.4 x 10^{19} m^{-3} and T_0=0.8 keV. The ray tracing code gives the ray path, which

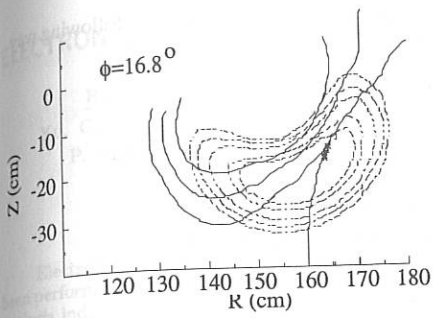

FIGURE 1

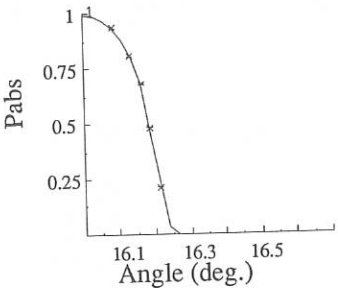

FIGURE 2

is presented in figure 1, and the imaginary part of the wave vector, $k''_{\perp}$, along the path. The absorbed power density is computed following the eikonal theory (see figure 2). It can be also seen that the absorption takes place for $N_{||}>0$ and at upshifted frequencies (see figures 3 and 4).

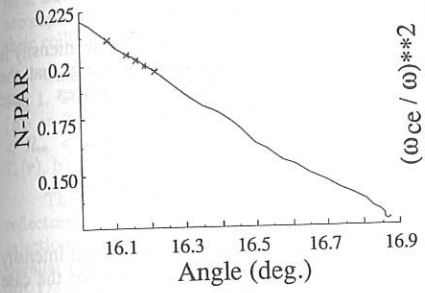

FIGURE 3

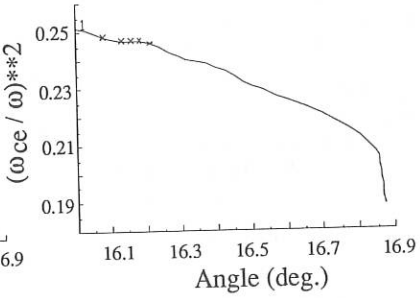

FIGURE 4

We consider the current density uniform on every magnetic surface. The averaged absorbed power density is given by [3]:

$$P(r) = \frac{2k''_{\perp} P_0 \exp\left(-2\int_0^{s(\vec{r})} k''_{\perp} \frac{\vec{v}_g}{v_g} d\vec{r}\right)}{4\pi^2 R_0 \rho(r)|\cos\varphi|} \qquad \rho(r) = \begin{cases} r & ; \ r \geq s^{1/2} \\ s^{1/2} & ; \ r < s^{1/2} \end{cases},$$

where r is the distance from the magnetic axis, s is the section of the microwave beam (s=25 cm^2 in the TJ-II), φ is the angle defined by the group velocity and the normal to the magnetic surface, in a plane of constant toroidal angle φ, R_0 is the major radius (R_0=1.5 m in the TJ-II) and P_0 is the total power delivered by the antenna (P_0=200 kW in the TJ-II).

The induced current is in the helical direction and it can be computed in the following way

$$J(r) = \Im(\vec{v}_R)\, P(r)\, \frac{\vec{h}\cdot\vec{B}}{hB} \quad ,$$

where **B** is the magnetic field and **h** is a vector parallel to the helical direction:

$$h_x = -\left[R_0 + r\cos(-4\phi)\right]\sin\phi + 4r\sin(-4\phi)\cos\phi$$
$$h_y = \left[R_0 + r\cos(-4\phi)\right]\cos\phi - 4r\sin(-4\phi)\cos\phi$$
$$h_z = -4r\cos(-4\phi)$$

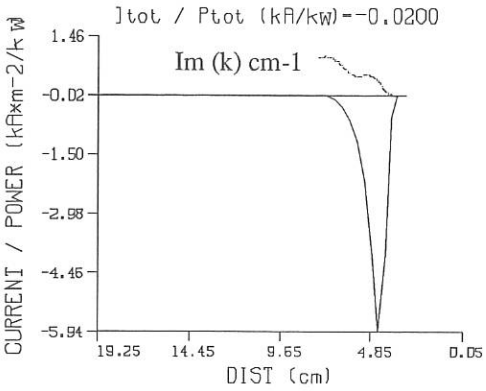

FIGURE 5

The current density profile versus the distance from the magnetic axis is presented in figure 5. The imaginary part of the wave vector, $k''_{\perp}$, is also shown (in cm^{-1}). The minus sign means that the current is in the clockwise direction.

The net current intensity is computed assuming that the magnetic surfaces are toroidal, as follows

$$I = 2\pi \int_0^a dr\, r\, J(r)$$

We obtain a total intensity of about I=-4 kA for the case considered. This result should be corrected by the effect of the trapped particles and by quasi-linear modification of the power absorption, which could be important in this case, since the averaged power density is about 5 W/cm^3.

REFERENCES

[1] N. J. Fisch and A. H. Boozer. Physical Review Letters **45**, 720 (1980)

[2] N. J. Fisch. Physical Review A **24**, 3245 (1981)

[3] V. Krivenski, I. Fidone, G. Giruzzi, G. Granata, R. L. Meyer and E. Mazzucato. Nuclear Fusion **25**, 127 (1985)

[4] I. Fidone, G. Granata and J.Johner. Physics of Fluids **31**, 2300 (1988)

[5] C. Alejaldre, F. Castejón and M. J. Taboada. Proceedings of the 17th European Conference on Controlled Fusion and Plasma Physics. EPS, part III, 1115. Venice (1989)

Mo 87

ELECTRON CYCLOTRON CURRENT DRIVE EXPERIMENTS ON DIII–D*

R.A. James,† G. Giruzzi,‡ A. Fyaretdinov,¶ B. de Gentile,‡
Yu. Gorelov,¶ R. Harvey, S. Janz,§ J. Lohr, T.C. Luce, K. Matsuda,
P. Politzer, R. Prater, L. Rodriguez,‡ R. Snider, V. Trukhin¶

General Atomics, San Diego, California, USA

Electron Cyclotron Current Drive (ECCD) experiments on the DIII–D tokamak have been performed using 60 GHz waves launched from the high field side of the torus. Preliminary analysis indicates rf driven currents between 50 and 100 kA in discharges with total plasma currents between 200 and 500 kA. These are the first ECCD experiments with strong first pass absorption, localized deposition of the rf power, and τ_E much longer than the slowing-down time of the rf generated current carriers. The experimentally measured profiles for T_e, n_e and $Z_{\rm eff}$ are used as input for a 1D transport code and a multiple-ray, 3D ray tracing code. Comparisions with theory and assessment of the influence of the residual electric field, using a Fokker-Planck code, are in progress. The ECH power levels were between 1 and 1.5 MW with pulse lengths of about 500 msec.

ECCD experiments[1] worldwide are motivated by issues relating to the physics and technical advantages of the use of high frequency rf waves to drive localized currents.[2] ECCD is accomplished by preferentially heating electrons moving in one toroidal direction, reducing their collisionality and thereby producing a non-inductively driven toroidal current.[3]

The poloidal cross section for a typical discharge used in these experiments is shown in Fig. 1. These discharges are limited on the inside wall, with the ECH fundamental resonance (B_T = 2.14 T) located at $R_{\rm res}$ = 1.6 m and the magnetic center located between 1.55 m < R_m < 1.60 m. Diagnostics consist of: a) radial electron cyclotron emission (ECE) for $T_e(r)$, b) CO_2 interferometry for $n_e(r)$ and c) visible bremsstrahlung for $Z_{\rm eff}(r)$.

The launching hardware, located on the inside wall at z = +13 cm, consists of 8 sub-reflectors aimed at +15° and one aimed at +30°. These angles are relative to perpendicular injection along the major radius and "+" indicates a direction such as to drive an rf current parallel to I_P. The experimental antenna pattern is approximately a Gaussian beam with a 10° 1/e half-width.

METHODS OF ANALYSIS

For all discharges, the total toroidal current was held constant by using the constant I_P feedback circuit. As a result of the ECH, the loop voltage is reduced below its Ohmic value during rf injection by two concurrent processes. The first is a reduction of the global resistance of the plasma, which results as the thermal electron temperature increases, and the second is the presence of rf current drive.

Since a small inductive voltage remains during the rf phase, a two step process is applied in order to calculate $I_{\rm rf}$. First the global change in the resistance of the plasma during the rf phase is quantified by measuring changes in T_e and $Z_{\rm eff}$. With I_P fixed, this procedure is equivalent to determining the inductive voltage necessary to drive *all* the toroidal current

* This is a report of work sponsored by the U.S. Department of Energy under Contract No. DE-AC03-89ER51114.

† Lawrence Livermore National Laboratory.

‡ Association Euratom-CEA, TORE SUPRA, Cadarache, France.

¶ Kurchatov Institute, Moscow, USSR.

§ University of Maryland.

during the rf phase. Differences between this calculation and the measured loop voltage are then attributed to the presence of an rf driven current.

Combining the steady-state circuit equation during the rf phase, $I_P = [V_l(exp)/R(rf)] + I_{rf}$, with that of the Ohmic phase, $I_P = V_l(oh)/R(oh)$, we get:

$$I_{rf} = I_P \left[1 - \frac{V_l(exp)}{V_l(oh)} \frac{R(oh)}{R(rf)}\right] \qquad (1)$$

where $V_l(exp)$ is the experimental loop voltage and R is the plasma resistance. By setting $I_{rf} = 0$ in Eq. (1), we can determine the inductive voltage that would be necessary during the rf phase to drive *all* the toroidal current: $V_l^* = V_l(oh)\,[R(rf)/R(oh)]$. Combining this with Eq. (1) gives the desired equation for I_{rf}:

$$I_{rf} = I_P \left[\frac{V_l^* - V_l(exp)}{V_l^*}\right] \qquad (2)$$

EXPERIMENTAL RESULTS

Figure 2 shows the time history for discharge #65218: plasma current (I_P), ECH power, loop voltage, central electron temperature, line averaged electron density, magnetic center (R_m), and the first time derivative of the sum of currents flowing in the Ohmic and equilibrium field coils. The loop voltage is proportional to the last signal. The discharge has obtained a "stationary state" since all quantities have stopped evolving by $t = 2200$ ms.

As defined, V_l^* is the inductive voltage necessary to drive *all* the plasma current during the rf phase. This is calculated by a 1D transport code[4] using as inputs the experimental measurements of I_P and the radial profiles for $T_e(r)$, $n_e(r)$ and $Z_{\text{eff}}(r)$. The profile data is used to calculate the plasma's global resistance. Bootstrap current, less than 10% of the total current, is included in the code calculations. The transport code calculates $V_l^* = 0.7$ V in the Ohmic phase, within 5% of the experimental value, and $V_l^* = 0.4$ V during rf injection. During the rf phase, $V_l(exp) = 0.33$, thus Eq. (2) gives $I_{\text{rf}} = 70$ kA.

A 3D, ray tracing code[5] is used to study the ray trajectories and determine the first pass absorbed power. The launched radiation pattern is represent by 30 rays, and the resulting trajectories in the poloidal plane are shown in Fig. 3. Over 99% of the incident power is absorbed and deposited on the inboard side of the resonance. Of the rays that are not fully absorbed, their first pass attenuation averages about 98%.

Using the same experimental profiles and an electric field of 0.03 V/m, a bounce-averaged Fokker-Planck (F.P.) code[6] calculates $I_{\text{rf}}(\text{F.P.}) = 95$ kA. The influence of the electric field and a comparision with theory are presently being evaluated. The code indicates that damping takes place near $2v_{th}$. The slowing down time, or thermalization time for these energetic electrons ($\tau_s \simeq 1$ msec) is such that they should completely thermalize before being lost, $\tau_e \simeq 35$ msec. The F.P. ECH power deposition profile, Fig. 4b, compares well with that calculated by the ray tracing code, Fig. 3b.

The Fokker-Planck code's prediction of the horizontal ECE spectrum is compared to the experimental measurement in Fig. 4. Distortion of the electron distribution is confined to the central 1/3rd of the profile, and is characterized by an average perpendicular temperature of about 15 keV. The strong non-thermal ECE emission at large radii is the result of relativistically downshifted 2nd harmonic emission from the centrally localized energetic electrons. The absence of agreement in the range of $0.6 \leq r/a \leq 0.8$ is consistent with downshifted 3rd harmonic emission from energetic electrons near the edge of the profile. This suggests that radial transport of these electrons from the core is an important aspect of these discharges, a physics issue not accounted for by the F.P. calculations.

REFERENCES

1. Lloyd, B., *et al.*, Nucl. Fusion **28**, 1013 (1988) and H. Tanaka, *et al.*, Phys. Rev. Lett. **60**, 1033 (1988).
2. Prater, R., Eighth Topical Conference on Radio-Frequency Power in Plasmas, AIP Conference Proceedings No. 190 (AIP, New York, 1989), p. 22.
3. Fisch, N.J., Rev. Mod. Phys. **59**, 175 (1987).
4. Pfeiffer, W.W., *et al.*, General Atomics report GA-A16178 (1980).
5. Matsuda, K., IEEE Transactions on Plasma Science **17**, 6 (1989).
6. Giruzzi, G., Phys. Fluids **31**, 3305 (1988).

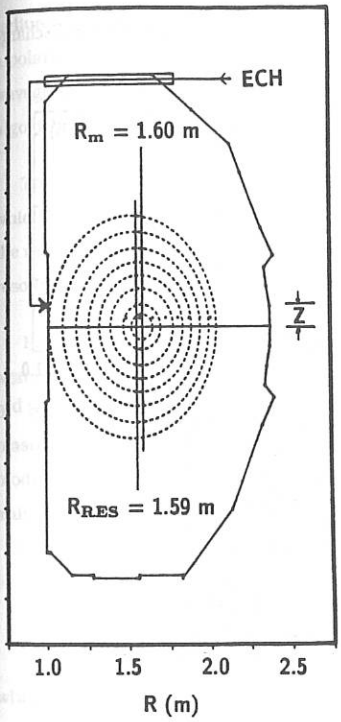

Fig. 1. Poloidal cross section for discharge #65218 at 2370 msec.

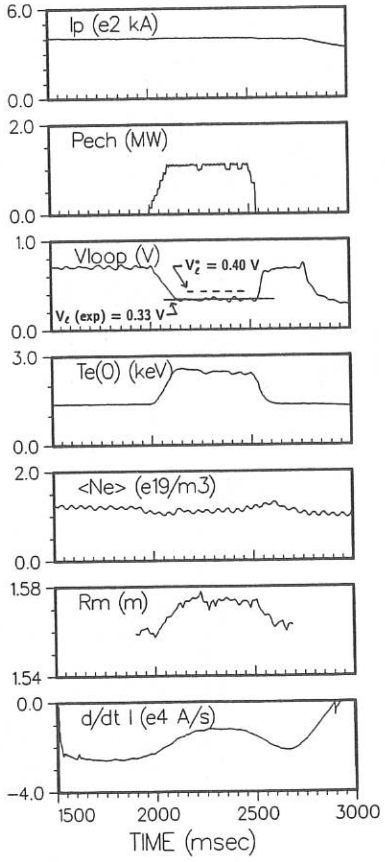

Fig. 2. Time evolution for discharge #65218.

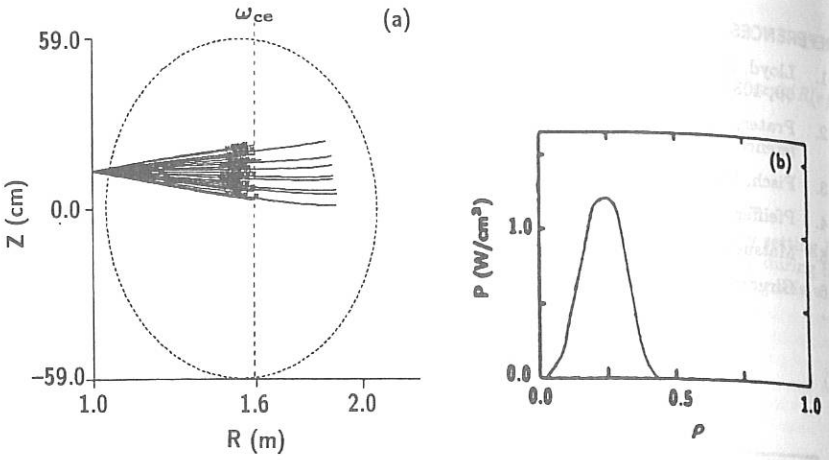

Fig. 3. (a) Ray trajectories, and (b) ECH deposition profile from ray tracing code for discharge #65218 at 2370 msec.

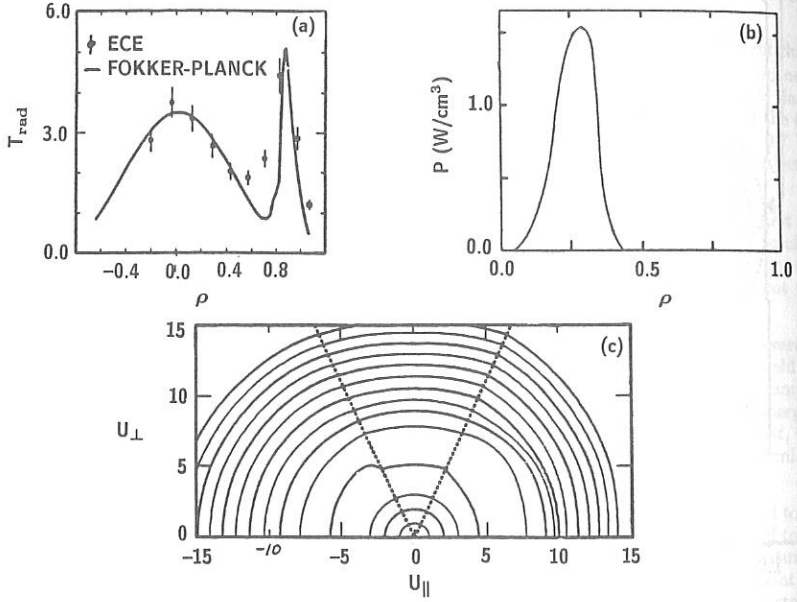

Fig. 4. (a) $T_{rad}(\rho)$ from ECE and Fokker-Planck code, (b) ECH deposition profile from Fokker-Planck code, and (c) computed distribution function at $\rho = 0.32$, momenta normalized to $(m_e T_e)^{1/2}$.

Investigation of Electron Cyclotron Emission in the ASDEX Tokamak during Lower Hybrid Current Drive and Heating.

K. Wira, A. Eberhagen, V. Merterns and ASDEX-Team

Max Planck Institüt für Plasma Physik

8046, Garching bei München, FRG

It is known that the electron cyclotron emission (ECE) spectrum is sensitively affected by the presence of the suprathermal electron population in the plasma. During ASDEX lower hybrid (LH) current drive and heating experiment, suprathermal electrons are generated by 2.4 GHz of LH and a maximum of 3 MW launched power.

The ECE spectrum is measured by a conventional vibrating Michelson interferometer with ~ 25 msec of time resolution. The interferometer views the plasma along a major radius of the equatorial plane through a wedged fused quartz window, a focussing TPX lens, a polarizing grid for selecting the extraordinary mode and ~ 8 meters of 1" transmitting waveguide. The ECE spectrum is recovered through a standard Fast Fourier Transform algorithm.

The system was absolutely calibrated with a large surface hot source, T > 500°C, 175 cm^2, which is comparable to a black body radiator. A 2-mm klystron was also used to re-check the response of the system. The system sweeps from ~100 GHz to ~300 GHz with an ~11 GHz resolution and measures up to the 4^{th} harmonic in normal experimental conditions.

For obtaining the suprathermal plasma state, the measured ECE spectrum is compared against a simulated spectrum of a slab, two-temperature plasma model from downshifted 3^{rd} harmonic to ~ 300 GHz. The choice of a simple model is used so that the suprathermal plasma state can be evaluated relatively quickly and processed at local work stations. The model has a bulk plasma temperature with an isotropic Maxwellian distribution and an anisotropic tail,

$$f_{st}(p_{||}, p_{\perp}) = C \begin{cases} \exp[-p_{||}^2/2T_{||} - p_{\perp}^2/2T_{\perp}] & 0 < p_{||} < p_{||\max} \\ \exp[-p^2/2T_{\perp}] & 0 > p_{||} \\ 0 & p_{||} > p_{||\max} \end{cases}$$

where p is the momentum of the electron.

The model neglects diamagnetic effects so that the toroidal field follows a simple $1/R_{maj}$ behaviour, where R_{maj} is the major radius. The cyclotron resonance condition is ω

$= n\omega_0/\gamma = n\omega_0/\sqrt{1+p_n^2}$ where ω_0 is the rest mass cyclotron resonance frequency. The thermal emission and absorption are calculated from the second to a maximum of seven harmonics and the suprathermal emission and absorption are calculated from the second to a maximum of fourteen harmonics for energies up to 500 KeV.

In the model, the thermal emission and absorption are assumed to obey Kirchhoff's law;

$$I_n^{(x,o)}(\tau) = \frac{\omega_{n0}^2(r)\, T_{rad}^{(x,o)}(r)}{8\pi^3 c^2} \quad \text{and} \quad T_{rad}^{(x,o)} = T_e(r)\left(1 - \exp[-\tau_n^{(x,o)}(r)\right),$$

where T_e is the local electron temperature and τ_n is the local thermal optical depth of the n^{th} harmonic given by Bornatici.[1] The calculation is carried out both for X- and O-modes.

The model has the option of choosing either the assumed bulk plasma temperature and density profile or the experimentally measured temperature (YAG Thomson scattering or ECE second harmonic) and density (YAG/HCN) profiles. The suprathermal electron profile is assumed to be either the hollow (double Gausian), Gausian with adjustable peak position, square or constant fraction of the background plasma profiles.

The emission from the suprathermal electrons is obtained from integrating the single particle emissivity over the velocity distribution.[2] We assume that the distribution is the same at all points in the plasma; the integration is then reduced to a one dimensional integral for each polarization;[3]

$$j_n^{(x)} = \frac{q^2\omega}{c} p_n^3 \int dy\, (1-y^2)\, J_n'^2(z)\, f(p_n, y)$$

$$j_n^{(o)} = \frac{q^2\omega}{c} p_n^3 \int dy\, y^2\, J_n^2(z)\, f(p_n, y), \text{ and } z = \frac{n}{\gamma} p_n \sqrt{1-y^2}.$$

Suprathermal absorption is also included.

A one-pass radiative transfer calculation is carried out using the normal radiative transfer formula;

$$I(\tau) = I_0\, e^{-\tau_0} + \int_0^{\tau_0} d\tau \frac{j}{\alpha} e^{-\tau},$$

which is then followed by multiple wall reflection with constant (with respect to both time and frequency) reflectivity and a polarization scrambling factor. The reflectivity of the wall is chosen to be 0.8, with 0.3 for the polarization scrambling factor. These numbers were obtained from the previous experiments and from a recent third harmonic intensity

estimation during a standard discharge. The emission and absorption are calculated at integer values of frequency between 90 and 400 GHz.

Typical experimental parameter are B=2.8 T, $n=1.4\times10^{13}$ cm^{-3} and I_p = 420 KA. Figure 1 shows the typical ECE spectrum before and after the LH is applied. The ECE spectrum changes very quickly after the LH is launched and then remains relatively unchanged until the next wave. This indicates that the suprathermal population and distribution do not vary too much during LH injection phase. The suprathermal state persists ~ .4 sec after the wave is turned off.

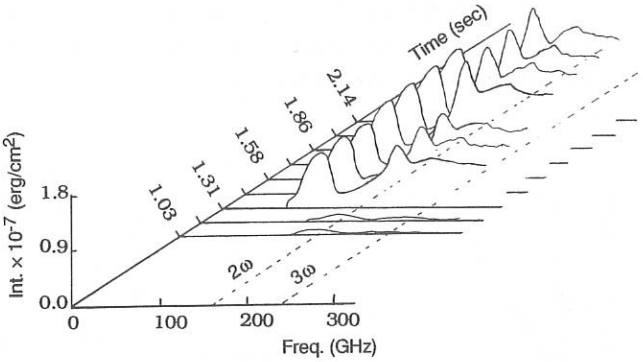

Fig. 1 ECE spectrum during LH current drive.

In the power scan series, the LH wave was launched at two power levels. For ϕ = 90°, with an asymmetric launched wave spectrum, the suprathermal electrons have a hollow profile with its peak located at ~ 6 - 11 cm off the plasma axis. At the initial power level, the profile is relatively narrow, and later it broadens out at the 2nd power level, Fig. 2. The obtained broadened profiles agree quite well with the tangential hard X-ray derived profiles.

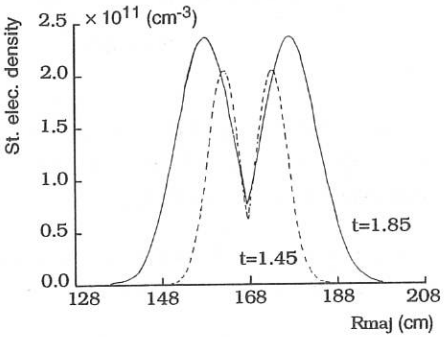

Fig. 2 Suprathermal electron profile at 2 different time.

Figures 3 and 4 show the suprathermal electron population and $T_\perp$ versus launched power at two different bulk plasma densities, $n=1.4\times10^{13}$ cm^{-3} and 2.8×10^{13} cm^{-3} respectively. In both cases, the suprathermal distribution remains relatively unchanged, $T_\perp \approx 85$ ~100 KeV and $T_{||}$=400 KeV. In general, different $T_{||}$ values, 100 - 450 KeV, only

slightly affect the simulated ECE spectrum, as expected. The choice of 400 KeV results from the hard X-ray measurement.

The suprathermal population increases with the launched power, but it levels out after ~0.5 MW. In a low density discharge, the suprathermal electron population saturates at approximately .8 % of the line integrated bulk plasma electron population, Fig. 3. In high density discharges, the suprathermal electrons have a similar distribution, but with much lower population. In the low power regime, the population is an order of magnitude lower than for the low density case, but it increases very rapidly with launched power, Fig. 4.

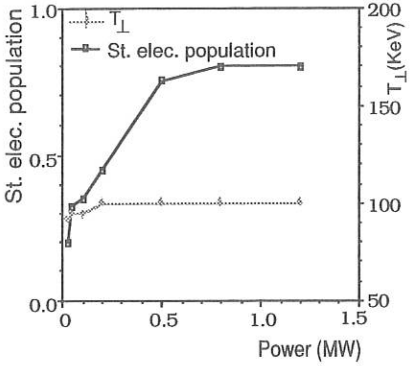

Fig. 3 Suprathermal electron population (% of bulk plasma population) and $T_\perp$ versus LH launched power at $n=1.4\times10^{13}$ cm^{-3}.

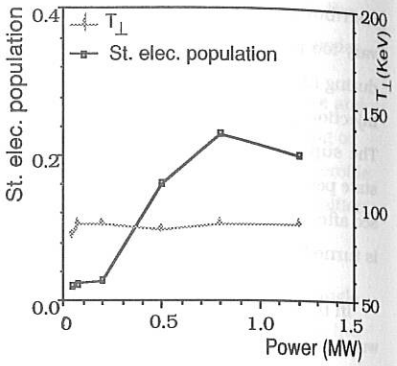

Fig. 4 Suprathermal electron population (% of bulk plasma population) and $T_\perp$ versus LH launched power at $n=2.8\times10^{13}$ cm^{-3}.

In the near future, the ECE spectrum with a symmetric launched wave will be analyzed and compared with the asymmetric case. The result will be discussed in the poster.

The authors would like to thank T. Luce for his effort in developing the computer program.

References

1. M. Bornatici, R. Cano, O. de Barbieri and F. Engelmann, Nucl. Fusion **23**, 1153 (1983)

2. G. Bekefi, Radiation Process in Plasmas, Wiley, 1966

3. T. Luce, Superthermal Electron Distribution Measurements with Electron Cyclotron Emission, Ph. D. dissertation, Princeton Univ., 1987.

ELECTRON CYCLOTRON CURRENT DRIVE FOR $\omega < \omega_c$

S Arshad, M Cox, N Deliyanakis, A N Dellis, T Edlington, S J Fielding, J Hugill, P C Johnson, B Lloyd, S Manhood, M O'Brien, B J Parham, A C Riviere and D C Robinson

AEA Technology, Culham Laboratory, Abingdon, OX14 3DB, UK.
UKAEA/Euratom Fusion Association

Introduction

The absorption of electron cyclotron waves with one sign of $k_{\|}$ is expected to drive current in a tokamak through the creation of 'asymmetric resistivity' in the electron population (ECCD). The High Field Side (HFS) launch facility on DITE tokamak has been used to study ECCD at the fundamental resonance using the X-mode. The EC wave then couples strongly to the plasma, interacting with tail electrons first. Here we report the results of ECCD experiments for a range of antenna angles and resonance positions at a wave frequency of 60GHz and with power levels up to 285kW. The observed changes in loop voltage are consistent with an ECCD current which is about one half of that predicted.

The DITE Experimental Arrangement

The rf power was launched from the HFS from three antennae [1]. The mirrors used to direct the rf power towards the magnetic axis could be rotated so that the angle between the wave vector and toroidal field could be varied between nominally parallel and antiparallel values. The graphite limiters were positioned so that $R = 1.19m$ and $a = 0.23m$. Helium discharges were used to provide good density control at $\bar{n}_e \lesssim 10^{19}m^{-3}$. Other parameters were $I_p \lesssim 40kA$, $2.2 < B_\phi < 2.4T$ and $0.26 < | n_{\|} | < 0.57$ at the antennae. Feedback stabilisation provided close control of the plasma position and current.

The information available for all discharges included V_ℓ, $\beta_p + \ell_i/2$, β_{dia}, I_p and B_ϕ from standard diagnostics, line average density $\bar{n}_e$ at 1.17m, microwave power (P_{RF}) from each of the three antennae, and soft X-ray profiles from vertical and horizontal diode arrays.

The electron temperature was measured by a 14 channel ECE receiver detecting the O-mode at the fundamental resonance. The ECE data, converted to T_e profiles, showed non-thermal emission on the low field side due to the presence of a small hot electron group, but the emission on the high field side behaved thermally. During heating some 60GHz signal was detected in the 59 and 60.5GHz channels but at the higher magnetic field strengths where these channels lay on the low field side, values for $T_e(0)$ and the profile shape could be obtained for the high field side of the profile. The receiver and complete waveguide system was calibrated against thermal sources at 77° and 900°K. The value of T_e during ohmic heating was obtained from the SXR spectrum using a SiLi detector.

Calculation of I_{RF} from the data

The tokamak operates at constant I_p so that the magnitude of I_{RF} is obtained from analysis of the changes in V_ℓ for co (CO) and counter (CTR) launch directions of the EC waves (corresponding to $\underline{k}.\underline{I}_p > 0$ and $\underline{k}.\underline{I}_p < 0$ respectively). The current drive efficiency is small so that with $\lesssim 285kW$ available V_ℓ is not reduced to zero. Strong electron heating occurs however so that V_ℓ is reduced from the ohmic heating (OH) value by the consequent change in plasma resistance (R_p) as well as by any ECCD which may be present. Further, the heating efficiency can differ for the two directions of launch so calculation of I_{RF} requires some knowledge of the changes in R_p (that is, T_σ and Z_{eff}). With rf current drive present, the total plasma current in equilibrium is $I_p = I_{RF} + V_\ell/R_p$. The bootstrap current is ignored here but is included later. Both I_p and V_ℓ are known. If it is assumed that I_{RF} does not change between CO and CTR launch directions, the equation for I_p and its form for counter current drive (with the sign of I_{RF} changed) can be combined to yield

$$I_{RF} = I_p(1-\propto)/(1+\propto) \quad \text{with} \quad \propto = \frac{V_{CO}}{V_{CTR}}.\frac{R_{pCTR}}{R_{pCO}} \tag{1}$$

In the initial analysis the relative changes in R_p are taken to be proportional to $(\beta_{dia}/\bar{n})^{3/2}$. Note that this estimate for $T_\sigma^{3/2}$ is insensitive to profile shapes for constant $(\beta_{dia}/\bar{n})$. Thus the values of I_{RF} are based on

$$\propto = \frac{V_{CO}}{V_{CTR}}.\left(\frac{\beta_{dia\ CO}}{\beta_{dia\ CTR}}.\frac{\bar{n}_{CTR}}{\bar{n}_{CO}}\right)^{3/2} \tag{2}$$

The effect of changes in Z_{eff} is discussed below.

Experimental Results

The values of I_{RF} obtained using (1) and (2) are shown in Figures 1(a), 1(b) and 1(c) for different values of resonance position, antenna angle and total ECH power. Two antennae were used with 140kW (or 70kW) launched on the median plane and 145kW at the poloidal azimuth of 135° [1] with combinations of these values for the power scan.

The value of $\Delta(\beta_p + l_i/2)$ was decreased (increased) by CTR (CO) current drive indicating changes in the current profile which were supported by the absence (presence) of sawteeth in the CTR (CO) cases. The behaviour of V_ℓ at the end of the power pulse differed in the two cases as expected from such inductance changes as shown in Figure 2 where the time behaviour predicted by the diffusion code HERMES is shown for comparison. The ECE data indicated a broader temperature profile for CTR injection compared with CO but both were more peaked than the OH target discharge which also lacked sawteeth.

The SXR emission from the plasma core, normalised to $\bar{n}_e^2$, showed a larger increase during heating than expected for constant Z_{eff}, with more of an increase occuring for CTR injection. The SXR emission intensity analysis assumed a mixture of He, C and O and was used to predict the relative change in Z_{eff}. The central temperature (ECE) for CO injection exceeded that for CTR injection. Using the values shown in Figure 1 for I_{RF}, the values for the current drive efficiency $\eta_{ECCD}\left(= \frac{\bar{n}_{20}\, I_{RF} R}{P_{RF}}\right.$, where $\bar{n}_{20}$ is in units of $\left.10^{20} m^{-3}\right)$ lie between 0.6×10^{-3} and $4.7 \times 10^{-3} Am^{-2}W^{-1}$.

More Detailed Analysis

To obtain a comparison with the values of I_{RF} expected from present theoretical models the HERMES code was used to define plasma conditions consistent with all the available data for the discharges corresponding to the point (A) in Figure 1. The effects of neoclassical resistivity and bootstrap current were included since it was difficult to match the plasma parameters without these. The experimental data and code values are shown in Table 1 including values of I_{RF} consistent with the data. A better match to the plasma parameters would probably be obtained if a more complex expression for the temperature profile shape was used. Using this description of the plasma, the predicted I_{RF} with $V_\ell = 0$ from ray tracing and Fokker-Planck codes [2] was 14kA (11kA) for CO (CTR) injection respectively. Note that the HERMES code does not contain synergistic effects due to the combination of loop voltage and ECCD whereas the Fokker-Planck code clearly shows strong synergistic effects but does not allow for the bootstrap current contribution. With these reservations we conclude that the observed changes in loop voltage are consistent with an ECCD current which is about one half of that predicted in this way. However particle diffusion across flux surfaces has been shown to reduce ECCD efficiency [3]. The observed ECCD efficiency in CLEO [4] was 3× less than that predicted without transport effects, but the inclusion of transport is able to explain some of this discrepancy [3]. In DITE the effect of transport will be smaller due to the higher electron density and larger minor radius for example but evaluation of this will be the subject of further study.

Table 1: Results from diffusion code HERMES

	CO (♯36969)		CTR (♯36970)	
	OH	ECCD	OH	ECCD
V_{loop}	1.86	0.51	1.91	1.06
	(1.8)	(0.5)	(1.93)	(1.05)
β_{dia}	0.3	088	0.41	0.84
$\Delta\beta_{dia}$	0.58		0.43	
	(0.64)		(0.47)	
l_i	1.64	2.03	1.61	1.50
$\Delta(\beta_p + l_i/2)$	0.78		0.38	
	(0.63)		(0.28)	
Z_{eff}	2.3	3.2	2.5	3.4
		(3.2-3.4)		(3.7-4.1)
$T_e(0)ev$	(500)	(1330)	(500)	(1000)
$\bar{n}_e(10^{18}m^{-3})$	(4.4)	(7.0)	(6.2)	(7.3)
α_T	3	4.7	3	3.5
	(3)	(4.9-6.8)	(3)	(3.8-5.4)
α_n	1.5	1.5	1.5	1.5
$I_{BS}(kA)$	2.7	8.1	3.8	7.9
$I_{RF}(kA)$		8.0		-5.6
$\left(\propto \frac{T_e}{n(Z+5)}\right)$				

Bracketed numbers are experimentally determined.
T_e, n_e profiles are defined by $x = x(0)(1-\rho^2)^\alpha$.
$B_\phi = 2.34T$, $I_p = 37kA$.

Acknowledgements

The authors gratefully acknowledge the excellent support provided for this experiment by the DITE and ECRH operations teams.

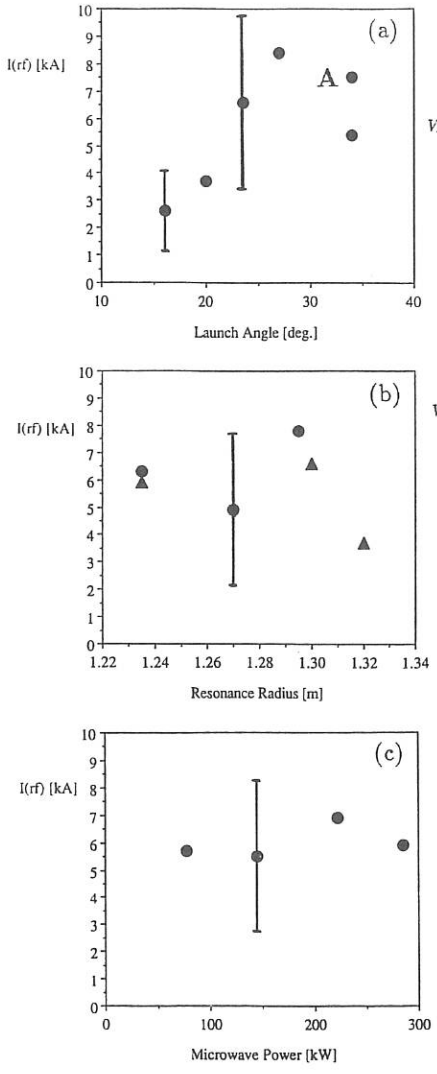

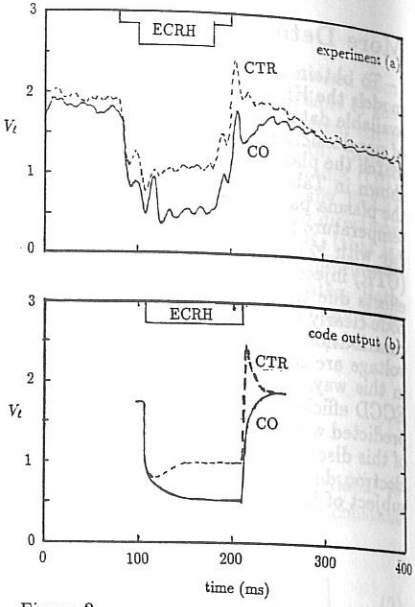

Figure 2
Variation of loop voltage with time for CO and CTR injection.
(a) Experimental traces, and
(b) Calculated behaviour for CO and CTR injection using the HERMES diffusion code.

Figure 1
Experimental values of deduced ECCD current (I_{RF}) using equations (1) and (2).
(a) I_{RF} as a function of the angle between $\underline{k}$ and $\underline{R}$ at the antennae
($I_p = 35{-}38kA$, $B_\phi = 2.34T$, $P_{rf} = 285kW$).
(b) I_{RF} as a function of the resonance position
($\triangle$ $I_p = 34 - 37kA$, angle = 23.5°, $P_{rf} = 285kW$;
• $I_p = 38 - 39kA$, angle = 34°, $P_{rf} = 268kW$).
(c) I_{RF} as a function of 60GHz power at the antennae ($I_p = 36 - 38kA$, angle = 23.5°, $B_\phi = 2.28T$).

References

[1] Dellis, A N et al and Moeller C P, et al, Proc. of 6th Joint Workshop on Electron Cyclotron Emission and Electron Cyclotron Heating, Oxford, 1987, Culham Report CLM-ECR (1987) pp 347 and 355.
[2] M R O'Brien, M Cox and D F H Start, Nucl. Fus. 26 (1986) 1625.
[3] See paper by M Cox, J S McKenzie and M R O'Brien, this Conference.
[4] B Lloyd, T Edlington et al, Nucl. Fus. 28 (1988) 1013.

CURRENT DRIVE EXPERIMENTS AT THE ELECTRON CYCLOTRON FREQUENCY

V. Erckmann, U. Gasparino, H. Maaßberg, H. Renner, M. Tutter
W VII-AS Team
Max-Planck-Institut für Plasmaphysik,
EURATOM Association, D-8046 Garching, FRG

W. Kasparek, G.A. Müller, P.G. Schüller, M. Thumm
Institut für Plasmaforschung, Universität Stuttgart, FRG

1. Introduction

The experimental investigation of non-inductive current drive by electromagnetic waves in the electron cyclotron range of frequencies and the comparison with theoretical predictions attracts increasing interest in both, tokamak as well as stellarator research. In spite of the low current drive efficiency (compared to Lower Hybrid Current Drive) Electron Cyclotron Current Drive (ECCD) is a candidate for MHD-mode control and current profil shaping in tokamaks and stellarators due to the high localization of the driven currents and the capability to drive currents in the plasma centre in large machines. ECCD is an appropriate tool for the control of the pressure effects on the profile of the rotational transform, particularly the bootstrap current in stellarators. This is a crucial condition to maintain good confinement properties in low shear configurations such as W VII-AS /1/. Basic experimental investigations were performed at the W VII-AS stellarator, where the small EC-driven currents are not masked by large inductively driven currents as in tokamaks. The theoretical treatment of ECCD in stellarators would require a Fokker Planck solution in full phase space taking into account the complex magnetic field configuration (trapped particles, loss cone effects) which is untractable. In a first approach, we have compared our experimental data to a simple analytical current drive model (linearized in slab geometry) which is incorporated in a ray-tracing code /2/. In a second step, we have analysed the sensitivity of the model with respect to simplified assumptions on trapped particles and quasi-linear effects./3/.

2. ECCD Experimental Results. Comparison with Theory

The ECCD experiments were performed at the W VII-AS stellarator with up to 0.8 MW rf-power at 70 GHz. Up to four linearly polarized rf-beams were launched at the 2nd harmonic extraordinary wave polarization from the low field side. The resonant magnetic field and the cutoff density are 1.25 T and $n_{e,crit} = 3.1 \cdot 10^{19}$ m^{-3}, respectively. The rf-beams were directed towards the plasma at arbitrary toroidal launch angles by a set of independently movable focussing mirrors mounted inside the vacuum chamber /4/. An important input quantity for ECCD evaluations is the single pass absorption of the rf-waves, which was directly measured for perpendicular incidence by a 35 pick-up waveguide array mounted at the inner vessel wall opposite to the launching mirrors. In all cases discussed here, total absorption of the waves in a single transit through the plasma was found within the experimental errors.

The EC-driven current was experimentally determined by two different methods, where the pulse duration was chosen long enough to obtain stationary global plasma behaviour:

In a first experiment, the toroidal launch angle of the rf-beams was varied while the total net plasma current was kept close to zero ($I < 0.2$ kA) by feedback control with the OH-transformer. The change of the required loop voltage ΔU with respect to perpendicular launch

(no ECCD) was measured as a function of the launch angle. With the known plasma resistivity, which was measured independently, the EC-driven current was evaluated straightforward. This method is based on the assumption that the bootstrap current contribution remains constant, in other words, that the profiles of n_e and T_e do not change very much during the launch angle scan, which holds for small launch angles. Although the stored plasma energy changes from + 20 to - 40 % depending on counter- or co-current drive with respect to the bootstrap current, the energy change is < 10 % for launch angles < 10°. In Fig. 1 the loop voltage increment ΔU is plotted versus the toroidal launch angle at the resonance layer

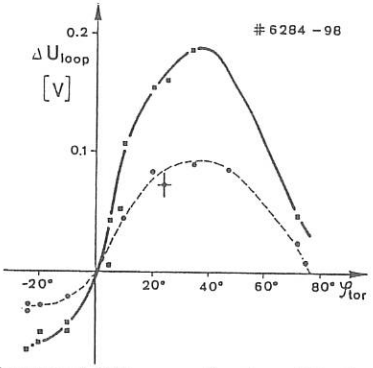

Fig. 1: Loop voltage increment ΔU_{loop} as a function of the launch angle φ_{tor} for discharges, where the net plasma current is controlled by inductive current drive (I_p < 0.2 kA). An rf-power of 0.35 MW (solid curve) and 0.17 MW (dashed curve) was applied for current drive.

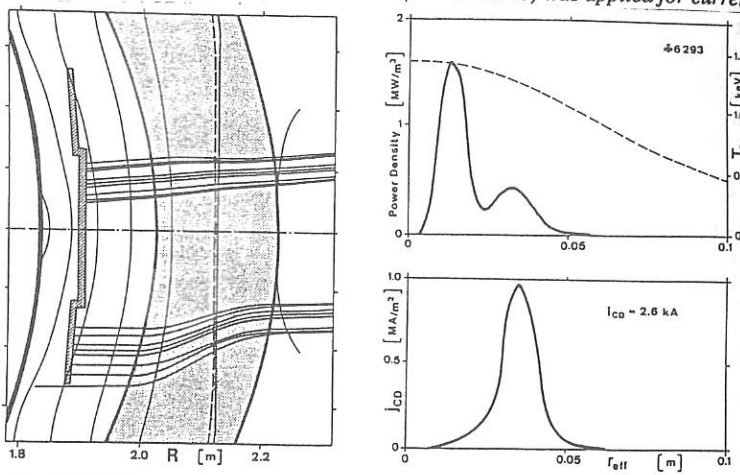

Fig. 2: LEFT: Ray-tracing.geometry (horizontal cut in the z = 0 plane). The shady region indicates the plasma column. Two rf-beams are launched from the right (low field side), the upper one in perpendicular direction, the lower one with an oblique angle of 27°.
RIGHT TOP: EC-power deposition profile (solid curve), and electron temperature from Thomson scattering diagnostics (dashed curve).
RIGHT BOTTOM: Current density distribution as a function of the average minor radius.

including refractive effects for a total rf-power of 0.35 MW. The central plasma density and electron temperature measured by Thomson scattering was $n_{eo} = 2.2 \cdot 10^{19}$ m^{-3} and $T_{eo} = 1.6$ keV, respectively. The maximum driven current was 2.5 kA. Equivalent scans at lower densities show an increased contribution of suprathermal electrons, which is beyond the simplified Fokker-Planck model used here. The dashed curve is obtained for a scenario, where one rf-beam (0.17 MW) was launched perpendicularly and the launch angle of the second beam was scanned, the solid curve is obtained if the launch angle of both rf-beams is scanned together.

The result of a 3-D ray tracing simulation of the experiment based on the measured profiles of n_e and T_e is given in Fig. 2. In this example, one rf-beam is launched perpendicularly from the right (low field) side and a second beam is launched at 10° with respect to perpendicular, which finally results in 27° launch angle at the resonance layer due to beam deflection. The power deposition profiles as well as the driven current density distribution is also given as a function of the average minor radius. The perpendicular beam does not contribute to current drive. The EC-wave driven current is evaluated by an analytical model /2/ incorporated in the ray tracing code which gives an upper limit for ECCD because trapped particle effects are neglected. $Z_{eff} = 4$ was assumed. As seen from Fig. 3 (left), where the calculated total driven current is plotted versus the launch angle for one (0.17 MW, dotted line) and two rf-beams (0.35 MW, solid line), respectively, the experimental results are qualitatively well described. In particular, the launch angle for maximum current drive and the linear increase of ECCD with rf-power agree well. The absorption layer is shifted radially outward with increasing launch angle which is responsible for the decrease of the driven current at large launch angles, where T_e decreases, the fraction of trapped particles increases and the mismatch of the linear polarized wave increases.

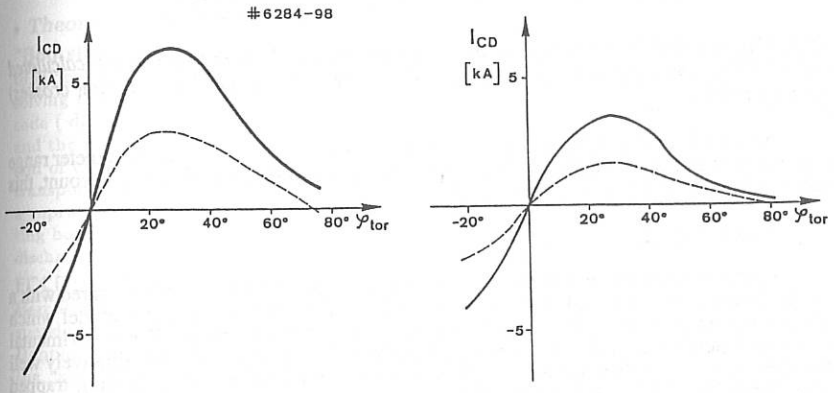

Fig. 3: Calculated EC-driven current for an rf-power of 0.17 MW (dashed curve) and 0.35 MW (solid curve) as a function of the rf-wave launch angle, where trapped particles are neglected (LEFT) and included (RIGHT) Both simulations are based on the measured profiles of n_e and T_e which are the same as in Fig. 1.

This simple ECCD model, however, overestimates the ECCD efficiency by typically a factor of 3 compared to the experimental findings, indicating that trapped particle effects can not be neglected. An improved version of the model /3, 5/ includes the interaction with a trapped particle population in the long mean free path regime of ~ 20 % on axis and ~ 40 % in the outer plasma region which is evaluated for the magnetic field topology in W VII-AS. As a result, the driven current is reduced to 60 % (Fig. 3 right).

In a second experiment, the launch angle of up to 4 rf-beams was adjusted to balance the bootstrap current without making use of the OH-transformer (counter current drive). Scanning the rf-power from 0.17 - 0.75 MW, the electron temperature from $0.8 < T_e < 1.9$ keV and the electron density from $1.1 < n_{eo} < 2.8 \cdot 10^{19}\ m^{-3}$, the bootstrap current varies from $0.8 < I_{Boot} < 4.3$ kA.

The total EC-wave driven current I_{CD} was again simulated as described previously. For the measured radial profiles of n_e and T_e, I_{CD} normalized to the bootstrap current I_{boot} is plotted versus the absorbed rf-power in Fig. 4. The dominant electron component of the bootstrap current ($T_e >> T_i$) was calculated by the DKES code which tends to underestimate the measurements /3/.

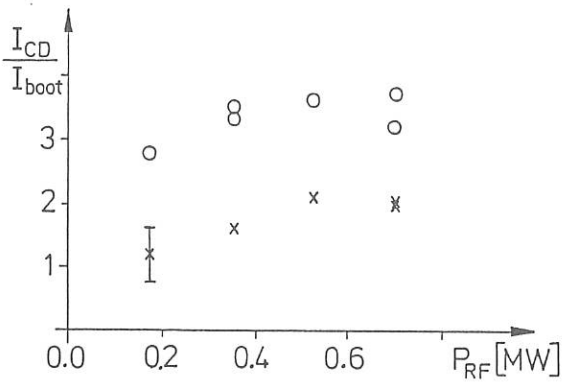

Fig. 4: Calculated EC-wave driven current I_{CD} normalized to the bootstrap current (calculated by the DKES code) plotted versus the absorbed rf-power without (circles) and with(crosses) trapped particles.

As seen from Fig. 4, the data points scatter around 3 - 4 over the wide parameter range given above if trapped particles are neglected. If trapped particles are taken into account, this ratio is reduced to typically a factor of 1 - 2.

3. Conclusions

Electron cyclotron current drive was investigated experimentally and compared with a simple theoretical model neglecting trapped particle effects and an improved model which includes the interaction of EC heated electrons with trapped particles. The experimental parameter dependende on the EC wave launch angle and rf-input power are qualitatively well described by both models. Quantitatively, however, the simple model neglecting trapped particles results in ECCD efficiencies which are typically a factor of 3 to 4 higher than the experimental data. This discrepancy is reduced to values around 2 if a realistic population of trapped particles is included in the model. The remaining discrepancy for both experimental scenarios is within the experimental uncertainties and the simplified assumption of the theory.

References

/1/ H. Renner et al., Plasma Physics and Contr. Fusion, 31, (1989), 1579-1596
/2/ U. Gasparino et al., Proc. 16th Europ. Conf. on Plasma Physics and Contr. Fusion, Venice, Italy, Vol. II, 631
/3/ U. Gasparino et al., this conference
/4/ V. Erckmann et al., Fusion Technology, Vol. 17, (1990), 76
/5/ M. Taguchi, Plasma Physics and Contr. Fusion 31 (1989), 241

NON-INDUCTIVE CURRENTS IN W VII-AS:
experimental results and theoretical modelling

U. Gasparino, V. Erckmann, H. Maaßberg, W VII-AS Team

Max-Planck Institut für Plasmaphysik
Association EURATOM-IPP, D-8046 Garching, FRG

ECRH Group

Institut für Plasmaforschung der Universität Stuttgart
D-7000 Stuttgart, FRG

• *Introduction* •

Stellarator-devices offer the possibility of studying non-inductive currents without the presence of a strong "obscuring" ohmic component. The net toroidal current (of the order of a few kA) observed during ECRH-discharges in W VII-AS (major radius R= 2 m, average minor radius $< a > = 0.2$ m) is modelled as the superposition of a neoclassical ("bootstrap") component and a component directly driven by the heating mechanism (ECCD: Electron Cyclotron Current Drive).
The boostrap current determined experimentally is (up to a factor of two) larger than the neoclassical predictions (for the electron contribution alone) based on the DKES code. The experimental dependence of ECCD on the toroidal injection angle of the waves is as expected theoretically and the experimental efficiency agrees fairly well with the results of simplified models. Possible effects on ECCD due to trapped particles (present also on plasma axis for the WVII-AS configuration) and the high deposited ECRH-power densities reached experimentally (up to several W/cm^3) are theoretically discussed.

• *Theoretical Models* •

"Bootstrap Current": WVII-AS is characterized by a rather complex magnetic field topology /1/. The neoclassical transport coefficients have been evaluated numerically by solving the linearized drift kinetic equation in magnetic flux coordinates using the DKES code (developed by S.P. Hirshman and W.I. van Rij /2/). On the basis of DKES-results and the measured temperature and density profiles, the profiles of the bootstrap current and of the neoclassical parallel conductivity are estimated. The effects of ECRH on the transport coefficients themselves (through induced electron trapping and generation of a suprathermal component) are outside of this model. This can become critical, affecting both the plasma conductivity and the bootstrap current, in low density, high power discharges.

ECCD: The ECRH deposited power and driven current are estimated by means of a 3-D Hamiltonian ray tracing code in the WVII-AS magnetic field topology, using the cold dispersion relation and an absorption coefficient for general angle of propagation (relativistic Doppler shifted resonance condition) based on a Maxwellian distribution function. Using the "adjoint property" of the linearized collisional operator, in the case of homogeneous plasma (no trapped particle effects) the evaluation of the driven current reduces to a convolution with the classical Spitzer function for the electric conductivity. This function can be evaluated very rapidly (in dependence of the effective charge Z_{eff}) using a sufficiently accurate energy polynomial expansion, the coefficients being determined through a variational principle /3/. This approach can be extented to include trapped particle effects in long mean free path regime (in this case a convolution with the neoclassical solution of the conductivity problem would appear). Introducing an approximate collision operator, the problem has been recently reduced to the solution of an ordinary differential equation in dependence of two parameters (Z_{eff} and f_t, the "fraction of trapped particles") /4/. While in /4/ the differential equation was solved through an expansion in Sonine polynomials (and evaluating the expansion coefficients from an infinite system of coupled

equations), we have used a generalization of the variational principle already used for the homogeneous case. In this way the driven current can be directly estimated by the ray-tracing with a minimum amount of computing time for both the case with and without trapped particle effects.
With the aim of investigating quasi-linear effects on the ECRH absorption and current drive, the non-linear Fokker-Planck equation solver /5/ has been implemented. The analyzed equation is of the type:

$$(\frac{\partial f_e}{\partial t})_{coll} + (\frac{\partial f_e}{\partial t})_{ECRH} + (\frac{\partial f_e}{\partial t})_{trap} + (\frac{\partial f_e}{\partial t})_{loss} = 0$$

where $(\partial f_e/\partial t)_{coll}$ is the collision operator, $(\partial f_e/\partial t)_{ECRH}$ the quasi-linear operator, the quasi-linear tensor component $D_{\perp\perp}(v_{\parallel}, v_{\perp})$ being obtained by the ray-tracing, for a specific magnetic surface:

$$(\frac{\partial f_e}{\partial t})_{ECRH} = \frac{1}{v_{\perp}} \frac{\partial}{\partial v_{\perp}} [\, v_{\perp} D_{\perp\perp}(v_{\parallel}, v_{\perp}) \frac{\partial f_e}{\partial v_{\perp}} \,]$$

$(\partial f_e/\partial t)_{trap}$ an increment of pitch angle scattering in the loss-cone region of velocity space to force the fast isotropization of the bouncing trapped particles /6/:

$$(\frac{\partial f_e}{\partial t})_{trap} = \frac{1}{sin(\theta)} \frac{\partial}{\partial \theta} [\, \nu_{trap}(v, \theta) sin(\theta) \frac{\partial f_e}{\partial \theta} \,] \qquad (\ \theta \text{ being the pitch angle })$$

and $(\partial f_e/\partial t)_{loss}$ a model operator describing the energy loss (related to radial transport) in velocity space (necessary to reach a steady state in high power density conditions). Different models for the loss term have been analyzed: an isotropic convective term of the form $(\partial f_e/\partial t)_{loss} \propto (\ v^2 - < v^2 >) \cdot f_e$ (in case of an anisotropic distribution function also parallel momentum can be lost), the extension conserving parallel momentum and a loss term limited in the loss-cone region of velocity space (to simulate loss of electrons trapped in local magnetic mirrors).

• *Experimental Conditions* •

"Bootstrap Current": In ECRH-experiment a plasma is built up and heated, starting from a neutral gas target. Associated to finite plasma energy a net current is experimentally observed. This current reverses its sign by a reversal of the direction of the magnetic field and is interpreted as bootstrap current. Due to the strong correlation between the global energy confinement properties and the edge value of the rotational transform found in low-shear devices /7/, operation in the narrow ι regimes with optimum confinement during the whole duration of the discharge required external current control, in most cases by a small loop voltage.

ECCD: Two main ECCD-scenarios have been analyzed experimentally /8/. In the first case the ECCD was used to counterbalance the bootstrap current, the ECCD-efficiency being obtained in unit of bootstrap current. In the second scenario, the ECRH-beams with perpendicular launching were replaced by other ECRH-beams with oblique launching and equivalent power, the toroidal launch angle ($k_{\parallel}$-spectrum) was changed shot by shot. Due to the strong relation between confinement properties and boundary value of the rotational transform, the total plasma current was controlled by the Ohmic-transformer. Nevertheless, changes in the current profiles affected the global confinement properties and macroscopic consequences could be observed in the plasma energy content ($\Delta W_p/W_p$ up to $-40 \div +20\%$ for ECCD co- and counter-bootstrap, respectively).

• *Theory vs. Experiment* •

"Bootstrap Current": Fig. 1 shows the result of the analysis of the current behaviour for series where temperature and density profiles have been measured by Thomson scattering ($0.9 \cdot 10^{13} < n_{e,0} < 4.5 \cdot 10^{13}$ cm^{-3} ; $0.4 < T_{e,0} < 2.5$ keV). The EC-waves were injected perpendicularly (with respect to the magnetic field direction) so that the contribution of ECCD should be minimized. In the figure, I_{pl} and V_{loop} correspond to the measured

net current and loop voltage respectively, while $I_{boot,DKES}$ and R_{DKES} are the predicted bootstrap current and plasma resistance. The sign of the current reverses, reversing the magnetic field, only the absolute value is reported in the figure. The observed deviation from the expected one to one proportionality can be compensated only partially by the ion bootstrap component (not included in the present theoretical analysis due to the experimental uncertainty in the ion temperature profiles, but estimated to be less than 30% of the electron contribution), whereas at low density the ECRH-induced suprathermal component (experimentally observed), decreases the plasma resistance and increases the discrepancy. Uncertainty in Z_{eff} plays a minor role (I_{boot} and V_{loop}/R show a quite similar Z_{eff} dependence).

ECCD: In (X)-mode, 2^{nd}-harmonic, resonance on axis ECCD-experiments the r.f. power is expected to be absorbed by thermal electrons and the central plasma region is in long mean free path regime. In WVII-AS a non-negligible amount of trapped electrons is present also on plasma axis. The "fraction of trapped particles" f_t on axis is $\approx 20\%$, around $\iota = 1/3$ and $\approx 25\%$ for $\iota \approx 1/2$. At the plasma edge f_t reaches values of $\approx 40 \div 50\%$. The presence of these trapped electrons would tend to decrease the ECCD-efficiency: power directly absorbed by them doesn't contribute to ECCD; trapping (ECRH increases the perpendicular energy) of passing particles causes a contribution opposite to the Fisch-Boozer one; the parallel momentum collisionally transferred from passing to trapped particles is lost. While the first two mechanisms strongly depends on the position of the resonance and can be minimized moving the resonance close to the maximum of the magnetic field, the third one would always be present. In the WVII-AS experimental conditions these effects reduce the ECCD-efficiency typically $30 \div 40\%$. Up to an angle of $\approx 30°$ from perpendicular this reducing factor is nearly independent of the launching angle itself. For bigger injection angles the current evaluated with trapped particles shows a steepler decay and it can even slightly reverse its sign (trapping effect overcompensating the Fisch-Boozer mechanism). The very good qualitative agreement found between the experimental and the theoretical dependence of ECCD on launching angle /9/ is valid for both approaches. At the large injection angles, where the efficiency with trapped particles decays more steeply, the ECCD-efficiency is low and the uncertainty (profile effects, deposition profile, percentage of the power coupled as X-mode) is too large to permit a discrimination /8/.

By means of the model Fokker-Planck equation the dependence of the ECCD-efficiency on input power was analyzed. The results related to a discharge where the EC-driven current was counterbalancing the bootstrap component are shown in Fig. 2 for the effective radius where the maximum deposition occurs ($r_{eff} = 1.5$ cm). At power densities greater than 5 W/cm^3 the efficiency starts to degrade. The case with and without trapped particles shows a very similar qualitative behaviour. The dependence on the energy loss model is analyzed for the case corresponding to 10 W/cm^3. The full points above the curves correspond to the ripple loss model, the ones below to the isotropic convective loss model while the two curves were obtained using the parallel momentum conserving convective loss model. For low power density the dependence on the loss model vanishes.

The quantitative analysis of the ECCD-efficiency has brought to quite similar results for all the cases analyzed up to now. As a representative example, we report on the results relative to the series of Fig. 2. Here the EC-driven current (four gyrotrons) counterbalances (within few hundreds A) the bootstrap component. No loop voltage being applied (so that in the analysis the uncertainty in the plasma conductivity could be avoided). For $Z_{eff} = 4$ the bootstrap current evaluated by DKES is $I_{boot,DKES} = 2.7$ kA, the ECCD-driven current evaluated by the ray-tracing is $I_{ECCD,hom} = 8.5$ kA neglecting trapped particles, while with trapped particles it is reduced to $I_{ECCD,t.p.} = 5.2$ kA. Recalling that $I_{boot,DKES}$ represents probably an underestimation (recall Fig. 1), the efficiency with trapped particles is within the rather large "error bars" of the analysis. This conclusion is only slightly dependent on the assumed value for Z_{eff}. Although deposited power densities up to 50 W/cm^3 are evaluated by the linear ray-tracing in case of high input power and peaked on-axis deposition, there is no experimental evidence for a degradation of the ECCD-efficiency, X-mode, 2^{nd} harmonic launching, so far.

• *Conclusions* •

A simplified theoretical approach describing the plasma current as the superposition of a bootstrap and a ECCD-component, independently evaluated, agrees fairly well with the experimental findings. Considering the complexity of the problem, where transport, quasi-linear and trapped particle effects are strongly linked together in the magnetic topology of WVII-AS stellarator this result is fairly satisfactory. More definite conclusions on the role played by trapped particles and high power densities on the ECCD-efficiency will be obtained by more appropriate experimental investigations (e.g. ECCD in local minima of the magnetic field and highly localized input power).

• *References* •

/1/ J. Kisslinger et al., Fusion Tech. (Proc. 12^th Symp. 1982), Pergamon (1983), 1051
/2/ S.P. Hirshman et al., Phys. Fluids 29 (1986), 2951
/3/ S.P. Hirshman, Phys. Fluids 23 (1980), 1238
/4/ M. Taguchi, Plasma Phys. and Contr. Fus. 31 (1989), 241
/5/ A.A. Mirin et al., Comp. Phys Comm. 51 (1988) 373
/6/ Yu.N. Dnestrovskij et al., Nucl. Fus. 28 (1988),267
/7/ H. Renner et. al., Plasma Phys. and Contr. Fus. 31 (1989), 1579
/8/ V. Erckmann et al., this conference
/9/ U. Gasparino et al., (Proc. 16th EPS, Venice 1989), Vol. II, 631

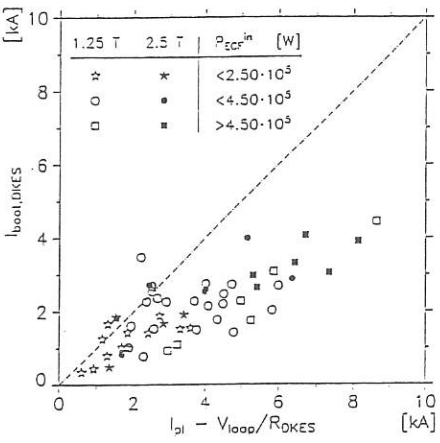

Fig. 1

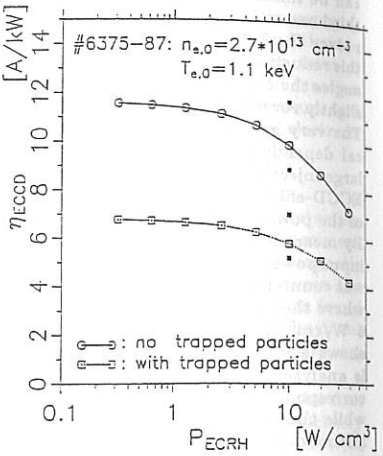

Fig. 2

• *Figure Captions* •

Fig. 1: Current components for the shots where density and temperature profiles have been measured by Thomson scattering. I_{pl} and V_{loop} corresponds to the measured net current and loop voltage, $I_{boot,DKES}$ and R_{DKES} are the predicted bootstrap current (only electron contribution) and plasma resistence. A one to one proportionality should be expected.

Fig. 2: ECCD-efficiency as a function of the absorbed power density. The full points corresponding to P_{ECRH} = 10 W/cm^3 show the dependence on the model used for the energy loss term. At low power densities this dependence becomes negligible.

CURRENT DRIVE BY ELECTRON-CYCLOTRON AND FAST WAVES IN DIII-D

G. Giruzzi and I. Fidone

Association EURATOM-CEA sur la Fusion
Département de Recherches sur la Fusion Contrôlée
Centre d'Etudes Nucléaires de Cadarache
13108 - Saint Paul-lez-Durance (FRANCE)

1. Introduction. Current drive by Landau-damped waves has proved to be successful in present-day tokamak devices, where the slow mode in the lower-hybrid frequency range was used. However, the extrapolation of the same method to the reactor regime, i.e, temperature and density 5 to 10 times higher, is questionable, since in this case the penetration of the slow mode is restricted to the plasma periphery, because of strong Landau damping [1]. The fast mode is a better candidate for current drive in high temperature plasmas. In fact, like the slow mode, it interacts with the electrons by parallel diffusion, thus the current drive efficiency is comparable, but the wave damping is much weaker and penetration to the plasma core is possible at reactor-relevant density and temperature. On the other hand, due to the low damping rate, the investigation of fast wave (FW) current drive in present-day tokamak devices is difficult, since a basic electron temperature of several keV is required for complete wave absorption. Therefore, FW current drive in present-day tokamaks can only be realized in the presence of another electron heating method, such as, for instance, electron cyclotron (EC) resonance heating. An experiment of this type is planned in the DIII-D tokamak [2] at a magnetic field $B \approx 1$ Tesla, using fast waves at 60 MHz, i.e., in the ion cyclotron frequency range, combined with second-harmonic EC heating. Generally, in low density plasmas, EC heating tends to generate superthermal electrons which, in turn, can be accelerated in the toroidal direction by the fast waves, and this will affect the FW current drive efficiency. A similar scenario, i.e., combined EC and lower-hybrid current drive, was investigated theoretically [3]. As shown in Ref. 3, for wave powers at the MW level, the currents driven by the two waves do not add linearly and the efficiency is generally enhanced by a favourable cross-effect. In the presence of two high power waves, current generation is the result of a complicate kinetic evolution, and the efficiency of the process can only be evaluated by means of a (two-dimensional in velocity space) Fokker-Planck code. Similar effects are expected also in the combined EC-FW experiment planned in DIII-D, and could actually be exploited to maximize the global current drive efficiency, by using the optimum wave launching configuration.

The kinetic aspect of the problem is here investigated by means of a 2-D Fokker-Planck code [4], including a FW parallel diffusion term [5]. A case is considered, in which both waves are absorbed in the plasma core, using typical parameters of the DIII-D experiment [2] and an EC wave beam at $\omega > 2\omega_c$, obliquely injected in the equatorial plane from the low field side and polarized in the extraordinary mode, which yields optimum current drive efficiency. The kinetic evolution of the electron distribution is evaluated for different values of the FW and EC wave power, in order to investigate the transition from the linear regime, in which the currents generated by the two waves add linearly, to the non-linear regime, in which the total efficiency is found to be higher than both separate efficiencies. The DIII-D experiment is found to be in the non-linear regime, and the current drive efficiency scales favourably with a further increase of the FW power.

2. Theoretical model. The kinetic evolution of the electron distribution function f during rf current drive is described by the Fokker-Planck equation

$$\frac{\partial f}{\partial t} = \left\langle \left(\frac{\partial f}{\partial t}\right)_{EC} \right\rangle + \left\langle \left(\frac{\partial f}{\partial t}\right)_{FW} \right\rangle + \left\langle \left(\frac{\partial f}{\partial t}\right)_{coll} \right\rangle \qquad (1)$$

where the brackets denote flux-surface averaging, and the three terms in Eq. (1) describe the effects of EC, FW and Coulomb collisions, respectively. The EC term and the collision term are discussed in Ref. 3;

they both include relativistic effects. The collision term is the high energy expansion of the Fokker-Planck collision operator, valid for values of the electron momentum $p \gg (mT_e)^{1/2}$, where m and T_e are the electron mass and the electron temperature, respectively. The FW quasilinear term is

$$\left(\frac{\partial f}{\partial t}\right)_{FW} = \frac{\partial}{\partial u_{||}} D_{FW} \frac{\partial f}{\partial u_{||}} \qquad (2)$$

where $\mathbf{u} = \mathbf{p}/(mT_e)^{1/2}$ and the expression of the FW diffusion coefficient D_{FW} is extensively discussed in Ref. 5. Here we assume a Gaussian $n_{||}$ spectrum for the FW power inside the plasma, thus

$$D_{FW} = D_s(n_{||}) \frac{u_\perp^4}{|u_{||}^3|} \left\{ \left[1 - \frac{2}{u_\perp^2} \left(1 + \frac{\omega_{ce}}{\omega} \frac{\mu D \varepsilon_{33}^R}{|\varepsilon_{33}|^2 (S - n_{||}^2)} \right) \right]^2 + \left[\frac{2}{u_\perp^2} \left(\frac{\omega_{ce}}{\omega} \frac{\mu D \varepsilon_{33}^I}{|\varepsilon_{33}|^2 (S - n_{||}^2)} \right) \right]^2 \right\} \qquad (3)$$

where $\mu = mc^2/T_e$, D, S, and ε_{33} are defined in Ref. 5, $n_{||}$ is the FW parallel refractive index, related to the electron momentum via the Cherenkov resonance condition $n_{||} = m\gamma c/p_{||}$, $m\gamma$ is the relativistic mass and

$$D_s(n_{||}) = D_0 \exp\left[- (n_{||} - \bar{n}_{||})^2 / (\Delta n_{||})^2 \right] .$$

Note that for $u_\perp \ll 1$ the expression in Eq. (1) is dominated by the terms in round brackets, which correspond to Landau damping. On the other hand, for high $u_\perp$ the Landau terms are negligible and wave damping is dominated by the transit time magnetic pumping (TTMP) effect. In this limit, the FW diffusion coefficient becomes very large, since it is proportional to $u_\perp^4$. Level curves of D_{FW} in the $u_{||}$, $u_\perp$ plane are shown in Fig. 1, for parameters typical of the DIII-D experiment [2], i.e., $\bar{n}_{||} = 5$, $\Delta n_{||} = 3$, B = 1.02 Tesla, $n_e = 1.5\ 10^{13}$ cm^{-3}, $T_e = 4$ keV. Note the different structure of the level curves in the Landau region ($u_\perp < 2$) and in the TTMP region ($u_\perp > 2$). For increasing $u_\perp$, D_{FW} gets very large and the level curves are no longer plotted. This peculiar structure of the FW diffusion coefficient has an important consequence: although for a Maxwellian plasma the wave damping is mainly due to the Landau effect, in the presence of EC waves, which tend to populate the electron distribution at high $u_\perp$, the TTMP effect is no longer negligible in the evaluation of both the wave damping and the current drive efficiency.

3. Numerical results. We now consider an EC wave beam of frequency 60 GHz, injected in the equatorial plane from the low field side at an angle of 20° with respect to the normal to the magnetic field. For typical DIII-D parameters (a = 60 cm, R = 160 cm, B(0) = 1.02 Tesla, $n_e(0) = 1.5\ 10^{13}$ cm^{-3}, $T_e(0) = 4$ keV and the profiles considered in Ref. 2), this beam is strongly damped in the plasma core. The kinetic evolution of the electron distribution function in the plasma centre is then computed for $Z_{eff} = 2$, both for a very low wave power $P_0 = 0.01$ MW and for a high power level, i.e., $P_0 = 1$ MW, where P_0 is the wave power reaching the plasma centre. The resulting absorbed wave power density, driven current and ratio W/I (in Watts/Ampères) are presented in Table I. It appears that both power absorption and current drive efficiency increase with P_0, since for high wave power the population of the energetic tail is enhanced. We then consider a FW power of 2 MW, and assume that it is absorbed within a radius $r \leq a/3$. This yields an average power density of 1.5 W/cm^3, which corresponds approximately to $D_0 = 0.05$. The kinetic evolution at r = 0 is then computed for several values of D_0, and the results are presented in Table I. It appears that also for the FW absorption and efficiency increase with the injected wave power. Finally, we consider the case of simultaneous injection of EC and FW. The steady-state distribution function in the case of $P_0 = 1$ MW and $D_0 = 0.1$ is shown in Figs. 2-4 (solid lines), together with the corresponding one for $P_0 = 0$ (dashed lines). Table I shows that for low wave power both the absorbed powers of the two waves and the driven currents add linearly. On the other hand, for high wave power, the current drive efficiency increases when the two waves are simultaneously used. This favourable cross effect can be explained by the fact that in the presence of EC waves a high $u_\perp$

population is created, in the region where the FW diffusion coefficient is very high. These electrons are then efficiently accelerated in the parallel direction. Being less collisional than low $u_\perp$ electrons, their contribution to the driven current is higher. Note, however, that also the absorbed power changes for increasing wave power levels, thus the absorption profiles are spatially redistributed. Therefore, these preliminary results need to be confirmed by a full 3-D Fokker-Planck calculation, including a self-consistent spatial evaluation of both EC and FW power absorption.

REFERENCES

[1] BONOLI, P.T., PORKOLAB, M., Nucl. Fusion **27** (1987) 1341.

[2] MAYBERRY, M.J., et al., *Radio-Frequency Power in Plasmas* (Proc. 8th Top. Conf., AIP, New York, 1989), 298.

[3] FIDONE, I., et al., Nucl. Fusion **27** (1987) 579.

[4] MEYER, R.L., et al., Comp. Phys. Comm. **40** (1986) 153.

[5] CHIU, S.C., et al., Nucl. Fusion **29** (1989) 2175.

FIGURE CAPTIONS

Fig. 1 Level curves of the FW diffusion coefficient.

Fig. 2 Level curves of the steady-state solution of the Fokker-Planck equation, for $P_0 = 1$ MW and $D_0 = 0.1$. EC+FW (solid line) and FW alone (dashed line).

Fig. 3 Parallel distribution function, for the cases shown in Fig. 2.

Fig. 4 Perpendicular temperature, for the cases shown in Fig. 2.

Table I

	P_0(MW)	D_0	P (W cm^{-3})	J (A cm^{-2})	W/I (W/A)
EC	0.01	0	0.033	4.3	7.6
EC	1	0	4.23	1057	4.0
FW	0	0.001	0.025	3.9	6.4
FW	0	0.05	1.60	275	5.8
FW	0	0.1	3.21	659	4.9
FW	0	0.2	5.97	1490	4.0
EC+FW	0.01	0.001	0.058	8.3	7.0
EC+FW	1	0.05	5.10	1450	3.5
EC+FW	1	0.1	6.37	1970	3.2
EC+FW	1	0.2	8.75	3104	2.8

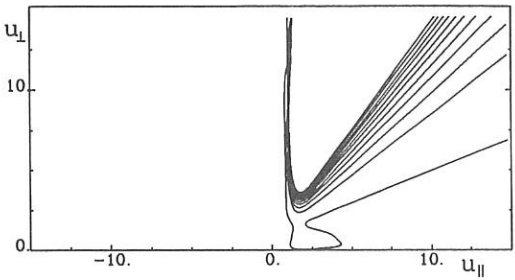

Fig.1

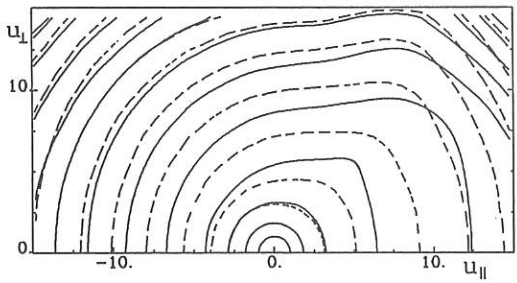

Fig.2

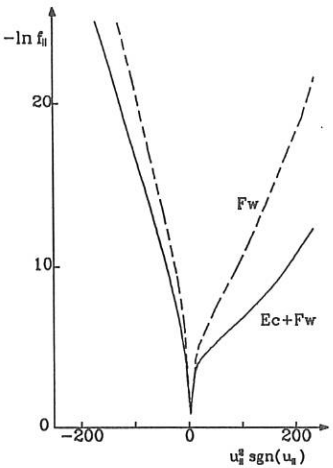

Fig.3

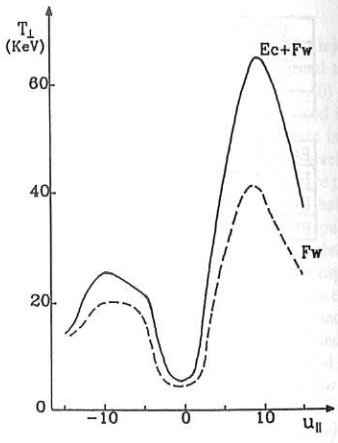

Fig.4

LOWER HYBRID CURRENT DRIVE IN DITE

BLloyd, M W Alcock, S Arshad, G Fishpool, S J Fielding, T C Hender, J Hugill, P C Johnson, S J Manhood, G F Matthews, A W Morris, R A Pitts, A C Riviere, D C Robinson, C Silvester, P R Simpson, G Vayakis and C D Warrick

Culham Laboratory, Abingdon, Oxon OX14 3DB, UK
(Euratom/UKAEA Fusion Association)

INTRODUCTION

Lower Hybrid Current Drive (LHCD) experiments have been carried out on the DITE tokamak ($R/a \sim 1.19/0.23m$) at 1.3 GHz with powers up to 250 kW at the antenna. The system utilised a four-waveguide titanium grill, previously employed on PETULA, fed via a 60m transmission line by a high power klystron used previously on ASDEX. Prior to installation on DITE, passive waveguides were installed on the grill and it was poloidally shaped to match the DITE plasma boundary. After baking of the grill and glow discharge cleaning in argon, full power operation was established within a few days of operation. For current drive studies with grill phasing $\Delta\phi = 90°$, the main spectral lobe is rather broad ($\Delta N_{\|} \sim 4$) and is centered at $N_{\|} \sim 2.75$.

CURRENT DRIVE EFFICIENCY

The scaling of current drive efficiency with magnetic field, electron density, plasma current and RF power was investigated, primarily to enable predictions of the volt-second reductions that might be achieved by LHCD in COMPASS-D to be made. Experiments were conducted in hydrogen with $B_\phi \sim 0.9 - 2.5T, \bar{n}_e \sim 0.5 - 1.5\text{x}10^{19}m^{-3}, I_p \sim 75 - 125kA$ and $P_{LH} \lesssim 250kW$. Although the loop voltage, V, could be reduced to a very low level it was not possible to reduce V to zero in the above parameter ranges. By analogy with the usual current drive figure of merit for the current drive efficiency with electric field E=0, we have evaluated the efficiency of OH flux reduction using the parameter $\eta' = (\bar{n}_e/10^{20})(\Delta V/V)I_pR/P_{LH}$. In fig 1 it is seen that $\Delta V/V$ saturates strongly (and η' is therefore reduced) as P_{LH} increases. This behaviour is reminiscent of that observed in PETULA [1]. Guided by previous work by Van Houtte et al [1] and the Fisch expressions for the conductivity of RF-heated plasma [2] we have been able to model the data at 75 kA and 105 kA in fig 1 by assuming an RF-driven current determined by the asymptotic efficiency at large $P_{LH}(E \to 0)$ together with a plasma conductivity of the form,

$$\sigma_{RF} = \sigma_{OH} + \sigma'$$

where $\sigma'/\sigma_{OH} \propto P_{LH}$ for $P_{LH} < 45kW$ and saturates at $\sigma'/\sigma_{OH} \lesssim 1$ for $P_{LH} \geq 45kW$. σ_{OH} is the conductivity of the OH target plasma. The limited data at higher plasma currents appears to indicate $\Delta V/V$ independent of P_{LH} over the range 75-200 kW.

It is seen in fig 1 that the current drive efficiency appears to increase with increasing I_p. This behaviour, which has also been observed in other devices, is also exhibited in fig 2 where the density dependence is illustrated. It is not thought that this current dependence is due to the effect of the residual E-field since it is often found that for the same RF power and $\bar{n}_e$ a lower loop voltage can be achieved at higher current. It is more consistent with a q-dependence possibly associated with variations in the T_e profile as proposed in [3]. At high magnetic fields ($B_\phi = 2.3T$) it is seen in fig 2 that $\Delta V/V \propto 1/\bar{n}_e$ (i.e. $\eta' = \text{const}$) (except at the highest densities where one may begin to encounter the current drive density limit) whereas at low B_ϕ (1.2 T), η' is not only significantly reduced but decreases with increasing density due to the influence of limited

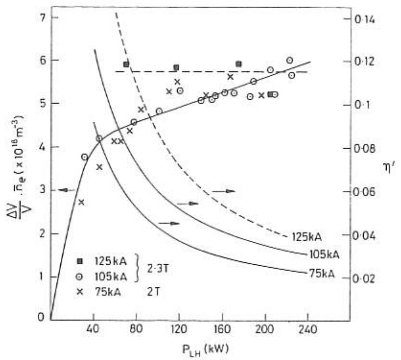

Fig 1 Dependence of loop voltage reduction and η' on net power (forward minus reflected) P_{LH} at the antenna.

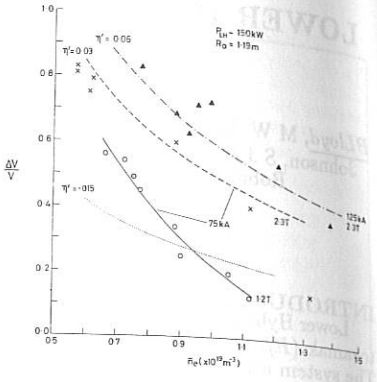

Fig 2 Dependence of loop voltage reduction on $\bar{n}_e$ for various plasma currents and magnetic fields.

wave accessibility under these conditions.

CONTROL OF INSTABILITIES

Stabilisation of sawteeth was readily demonstrated during LHCD but was usually accompanied by excitation of a large m=1,2; n=1 instability (fig 3). The m=1 oscillations, localised in the vicinity of the inversion radius are clearly visible in fig 3. The time taken to stabilise the sawteeth is plotted in fig 4 as a function of the lower hybrid power. Sawteeth can be stabilised even for powers $P_{LH} \lesssim 50kW$ but in this case the time taken becomes very long and plasma parameters are not constant. Clearly, prompt ($\lesssim 10ms$) stabilisation requires powers $\gtrsim$80-100 kW. At the higher powers there is a small increase (decrease) in period (amplitude) and stabilisation is complete within 5-10 sawteeth. There is little change in inversion radius. Magnetic measurements indicate a slight decrease in ℓ_i during the RF pulse at the highest powers. At the lowest powers, the inversion radius increases by $\lesssim$ 1 cm and the sawtooth period steadily increases by a factor x3 during the long delay between RF turn-on and stabilisation. For powers in excess of $\sim$180 $\pm$ 20 kW, (i.e. $\sim$x2 that required for prompt sawtooth stabilisation), the m=1, m=2 oscillations are either absent or appear when the sawteeth are initially stabilised then decay to zero over a few tens of ms. The location of the internal m=1 mode remains approximately constant as its amplitude is reduced. Simultaneous feedback stabilisation of the m=1 and m=2 oscillations has also been achieved during LHCD at low RF power using m=2 windings inside the DITE vacuum vessel [4]. Sawtooth stabilisation is usually accompanied by a central peaking of the soft x-ray emission profile (e.g. as seen in fig 3) suggesting an improvement in central confinement. m=1 stabilisation often (but not always) results in a further slight peaking. Sawtooth stabilisation was not observed when a symmetric lower hybrid spectrum was launched for heating studies. Furthermore, at high q(a), (i.e. $\sim$6), when sawteeth were absent from the initial OH target plasma, LHCD did not lead to destabilisation of the m=2 instability.

The switch-off of lower hybrid power often leads to the onset of the Parail-Pogutse instability which was stabilised in DITE by ECRH as in earlier experiments.

PLASMA EDGE BEHAVIOUR

The installation of both lower hybrid and electron cyclotron systems on DITE pre

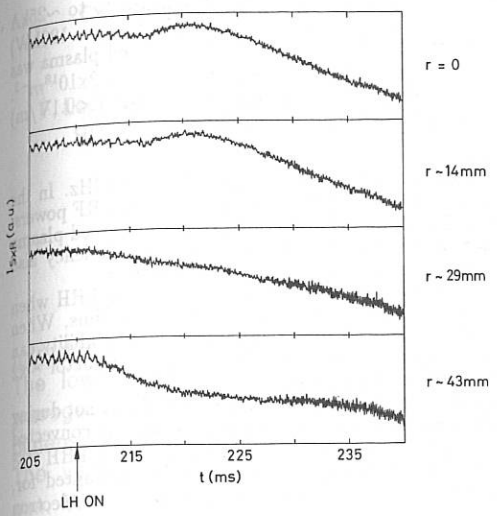

Fig 3 Sawtooth response during LHCD. The channels show line-integrated soft x-ray emission along horizontal chords near the plasma core.

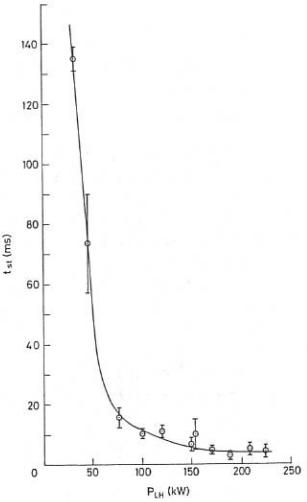

Fig 4 Time delay between RF turn-on and sawteeth stabilisation, t_{st}, as a function of lower hybrid power, P_{LH}. $I_p = 105kA, B_\phi = 2.25T, \bar{n}_e \sim 8\text{x}10^{18}m^{-3}$.

sented an excellent opportunity to compare and contrast the edge plasma response in the same device. During LHCD, $\bar{n}_e$ is usually observed to fall by 20-30% in the absence of gas puffing. The electron density in the plasma scrape-off layer (SOL) typically decreased by a factor x2-3 and the total particle flux to the pump limiter, evaluated by interpolating between probes distributed over the limiter surfaces, decreased by a factor x3-4 [5]. Coupled with an observed decrease of the fluctuation levels, $\tilde{E}_\theta$ and $\tilde{n}_e$ and in the wall H_α signal, there is strong evidence for an increase in particle confinement. There is a decrease in T_e by typically ~30% in the SOL. These observations are in complete contrast to those with ECRH where $\bar{n}_e, n_{edge}, T_{edge}, \tilde{E}_\theta, \tilde{n}_e, H_\alpha$ emission and the particle flux to the limiter all increased. During lower hybrid heating (LHH), when a symmetric spectrum was launched, no decrease in n_{edge}, T_{edge}, $\tilde{E}_\theta$ or $\tilde{n}_e$ was evident.

Global power balance has been studied by comparing the convected power to the edge (obtained from probe measurements assuming a constant power transmission factor for the sheath) with the total power input less the radiated power. Good power accounting is observed during ECRH, LHH and in ohmically heated discharges. However during LHCD virtually none of the input P_{LH} is observed in the convected flux at the boundary suggesting that a large fraction of the power deposition is very local and/or power loss occurs via a high energy component in the electron distribution which would not be registered in the Langmuir probe bias range (-100V).

LOW-VOLTAGE START-UP

Preliminary studies of combined ECH and LHCD start-up in the presence of a small but finite d.c. electric field have been carried out. The OH primary voltage was limited so that, in the absence of plasma current, a maximum voltage of 2V (i.e., $\bar{E} \lesssim 0.3$V/m) was

induced around the torus. With such OH assistance I_p could be ramped up to ~25kA in ~0.5s with P_{LH} ~55kW. The discharge was initiated with ECH (P_{ECH} ~120kW) and adequate coupling of the LH waves into the low density ECH-produced plasma was possible without the need for phase-switching. The final density was $\bar{n}_e \sim 2\text{x}10^{18} m^{-3}$. Further work is required to demonstrate that such a scenario (but with E<0.1V/m) would allow start-up in devices such as ITER with sufficiently high reliability.

SUMMARY AND CONCLUSIONS

LHCD experiments have been carried out in the DITE tokamak at 1.3 GHz. In the presence of a d.c. electric field the current drive efficiency is enhanced at low RF powers, an effect which can be explained on DITE, as on other devices, by an increased plasma electrical conductivity in the presence of RF power. The current drive efficiency also improves with increasing plasma current, possibly reflecting a q-dependence.

Sawtooth stabilisation is readily observed during LHCD but not during LHH when a symmetric spectrum is launched. There is little change in the inversion radius. When sawteeth are stabilised an m=1, 2; n=1 instability usually appears. This instability can in turn be stabilised by resonant magnetic feedback or by raising P_{LH} by a factor ~x2 over the level required for prompt sawtooth stabilisation.

An increase in the particle confinement time is observed during LHCD but not during LHH. During ECRH τ_p decreases. By measuring the radiated power and the convected power to the plasma edge, good global power accounting is observed during LHH and ECRH. However, during LHCD only a small fraction of P_{LH} can be accounted for, suggesting power loss is very local and/or via a high energy component in the electron distribution.

Finally low-voltage start-up (E<0.3V/m) has been demonstrated in DITE using ECH and LHCD-assisted ramp-up.

ACKNOWLEDGEMENTS

The loan of equipment from IPP Garching and CEA Cadarache is gratefully acknowledged. It is a pleasure to thank Steve Knowlton (MIT) and Didier Moreau (CEA) for providing access to lower hybrid coupling codes.

REFERENCES

[1] D Van Houtte et al, Proc. 4th Int. Symp. on Heating in Toroidal Plasmas, I (1984) 554.
[2] N J Fisch, Phys. Fluids, 28 (1985) 245.
[3] C Gormezano et al, Proc. 13th Euro. Conf. on Contr. Fus. and Plasma Heating, Schliersee, II (1986) 311.
[4] A W Morris et al, Phys. Rev. Lett., 64 (1990) 1254.
[5] B Lloyd et al, Proc. 8th Top. Conf. on RF Power in Plasmas, Irvine, (1989) 14.

Coupling of the 2 x 24 Waveguide Grill at 2.45 GHz in ASDEX

F. Leuterer, F. Söldner, M. Münich, F. Monaco, M. Zouhar, R. Bartiromo[1], S. Bernabei[2], C. Forrest[2], A. Tuccillo[1], ASDEX-team, Pellet-team

Max Planck Institut für Plasmaphysik
EURATOM - IPP Association, D 8046 Garching, FRG
1) ENEA - Frascati, Italy, 2) PPPL - Princeton, USA

Introduction

The lower hybrid grill used in ASDEX consists of two arrays of 24 waveguides each, arranged one on top of the other. The inner dimensions of the guides are 10 x 109 mm with 4 mm walls inbetween. The vertical separation between the centers of the two grills is 160 mm. With a phasing of $\Delta\phi = 180°$ we generate a symmetric spectrum centered around $N_{||} = 4.4$, with a width of $\Delta N_{||} = 0.8$. The phase can be set arbitrarily with a corresponding shift in $N_{||}$, /1/. The grill is toroidally and poloidally shaped according to the toroidal geometry. The whole grill structure is surrounded by protecting graphite tiles, which are directly attached to the grill walls.

Influence of protecting tiles around the grill

In a first experimental campaign these tiles protruded beyond the waveguides by 3 mm. In these conditions the average reflection coefficient <R> was much higher than expected. Nevertheless, the distribution of the reflection coefficients in the individual waveguides, R_n, did show some essential features, like symmetric patterns for symmetric spectra or the reversal of the asymmetric patterns when switching the phasing from normal to opposite current drive,/1/,. Fig.1 shows <R> measured at the upper grill array as a function of the rf-power for different phase settings. From the fact that <R> decreases with lower $N_{||}$ and from the distribution of R_n near the grill edge we conclude that we had a very low edge density in front of the grill. We also found that <R> was rather insensitive to variations of the line averaged electron density n_e (in the range 1.3 to $5 \cdot 10^{13} cm^{-3}$), or the main plasma position R_p (in the range of 1.65 to 1.68 m), or the grill position R_g (from 2.122 to 2.127 m). The

separatrix position is $R_s = R_p + 0.4$ m and the position of the fixed protection limiters in ASDEX is $R_l = 2.120$ m.

Based on these observations we assumed that a very low density layer, with an effective radial extent of 1 to 2 mm, was existing in the immediate front of the waveguides between the protruding graphite tiles, which was rather insensitive to the main edge plasma parameters. In fact, introducing a vacuum gap of up to 2 mm in the coupling code strongly enhances the calculated reflection coefficient to values as observed.

The graphite tiles have meanwhile been replaced by another set which do no longer protrude beyond the metal walls of the waveguides. The global reflection coefficient <R> is now more than a factor of two lower than before, as seen in Fig.2 as compared to Fig.1. The characteristic features like symmetric reflection patterns for symmetric spectra and reversal of the patterns for normal and opposite current drive are again clearly existing. For low $N_{||}$, like $\Delta\phi$ = 90° or ϕ = oo$\pi\pi$... , <R> is now less then 10% even up to a power of 1.8 MW, corresponding to a power density of $\approx$ 4 kW/cm^2 at the grill. There is now a distinct dependence on plasma position, showing a characteristic change in the reflection patterns of the edge waveguides on both sides of the minimum in the average <R>. The density measured by x-mode reflectometry at the grill position under good coupling conditions for current drive agrees roughly with the density for which we expect from coupling calculations a minimum for <R>,/2/. At high $N_{||}$, like $\Delta\phi$ = 180°, <R> is higher and reaches values near to 20%. Here too, we have a clear dependence on plasma or grill position, but within the possible variations we could not yet reach a minimum of <R>. From the structure of the reflection pattern we conclude that the edge density is still too low for the high $N_{||}$ waves. There is still a variation of <R> with power, although not quite as strong as in the case with protruding tiles. We think that the cause is a variation of edge plasma parameters due to the ponderomotive force and electron heating, /3/.

Control of coupling conditions

Coupling of lower hybrid waves to the plasma depends mainly on the edge density. Therefore the distance between the grill and the plasma, $d_{g-p} = R_g - R_s$ is usually the most critical parameter to be adjusted. It also depends strongly on the frequency since the cutoff density varies

with f^2. For the 2.45 GHz grill on ASDEX the best coupling in current drive experiments is obtained with $d_{g-p} \approx 4.5$ cm. With larger distance and thus decreasing edge density the overall reflection <R> increases rapidly.

In experiments where lower hybrid current drive was combined with pellet injection, /4/, we found that the coupling could be considerably improved in cases with a large distance between plasma and grill. In Fig.3 incident, reflected and net rf-power are plotted for $d_{g-p} = 7.5$ cm. During the gaspuffing phase in the first 0.25 sec the reflection coefficient <R> ≈ 60%. After begin of repetitive pellet injection it drops rapidly to <R> ≈ 7%. The pellets are ablated near the plasma periphery by suprathermal electrons generated by the lower hybrid waves, /4,5/. This leads to an increase of the density in front of the grill and thus to an improved coupling. During pellet injection the coupling remains insensitive even to large displacements of the plasma away from the grill antenna. In Fig.4 incident, reflected and net rf-power are plotted for a discharge in which the distance d_{g-p} is increased from 4.5 to 11.5 cm during the lower hybrid pulse by shifting the plasma towards the inner wall of the torus. With simultaneous pellet injections the reflection coefficient <R> does not exceed 16%, whereas in gas fuelled discharges it would rise to 100% for these large distances d_{g-p}. The single pellets are barely seen on the curves for reflected and net power for large d_{g-p}. It seems therefore that the density in front of the grill is mainly determined by the gas cloud arising from evaporation of the pellets near the plasma periphery and less by the particles deposited further inside the separatrix.

Based on these observations, we studied the sensitivity of the coupling to the position of the gas inlet in gas fuelled discharges. In fact the overall reflection coefficient could be reduced by 30% by activating a gas valve near to the grill, compared with values obtained when the gas was filled into the vessel from a valve located 180° away from the grill.

This experiment has been performed in cooperation between IPP-Garching, ENEA-Frascati and PPPL-Princeton.

References

/1/ Leuterer F. et al., 16th European Conference on Controlled Fusion and Plasma Physics, Venice 1989, Vol. IV, p.

/2/ Schubert R. et al.,this conference

/3/ Petrzilka V., Inst. of Plasma Physics, Czechoslovak Academy of Sciences, internal report 9/89
/4/ Söldner F. et al., this conference
/5/ Büchl K. et al., 26th APS-Meeting, Plasma Physics Division, Boston, Nov.1984

Figures

Fig.1: Overall reflection coefficient <R> of the upper grill array in the experimental phase with protruding graphite tiles

Fig.2: Overall reflection coefficient <R> of the both grill arrays in the experimental phase with nonprotruding graphite tiles

Fig.3: Temporal evolution of incident, reflected and net lh-power of the lower grill array with simultaneous operation of lower hybrid current drive and repetitive pellet injection with a large grill-plasma distance of d_{g-p} = 7.5 cm.

Fig.4: Temporal evolution of incident, reflected and net lh-power of the lower grill array with continuos pre-programmed increase of the grill-plasma distance d_{g-p} during repetitive pellet injection

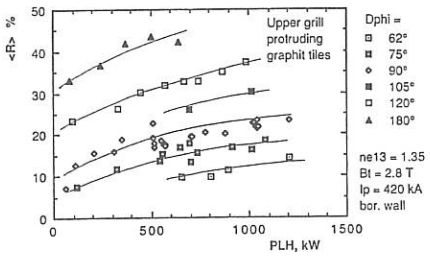

Fig. 1

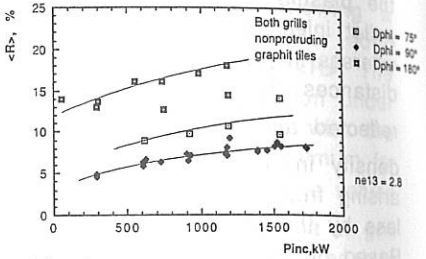

Fig. 2

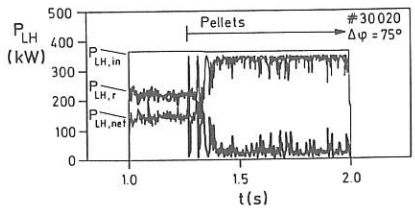

Fig. 3

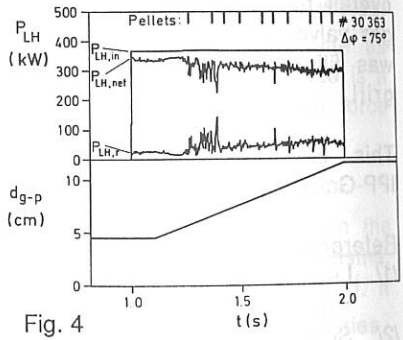

Fig. 4

Lower Hybrid Current Drive Efficiency at 2.45 GHz in ASDEX

F. Leuterer, R. Bartiromo[1], S. Bernabei[2], F. Söldner,
ASDEX-, LH- and NI-teams

Max Planck Institut für Plasmaphysik,
EURATOM-IPP Association, D-8046 Garching, FRG
1) ENEA, Frascati, Italy, 2) PPPL, Princeton, USA

The lower hybrid antenna consists of two stacked arrays of 24 waveguides each in which the phase can be set arbitrarily. Their dimensions are 10 x 109 mm with 4 mm walls,/1/. A phasing of $\Delta\phi$ = 180° yields a peak value of the $N_{||}$-spectrum of 4.4, its width is $\Delta N_{||}$ = 0.8.
The experiments are performed with a feedback controlled plasma current I_p so that the sum of rf-driven current I_{rf} and inductively driven current I_{ind} is constant. At sufficiently high rf-power all the plasma current can be driven by the lower hybrid waves and the loop voltage is then zero. From these shots we can determine the current drive efficiency η_0 at zero electric field

$$\eta_{0,exp} = n_e\, I_p\, R \,/\, P_{lh} \,, \quad (10^{13} cm^{-3} Am/W) \qquad (1)$$

where n_e is the line averaged density and R is the major radius of the plasma. Fig. 1 shows experimental results at low density as a function of the grill phasing, respectively $N_{||}$. Fig. 2 shows the density dependence and we recognize the decreasing efficiency for the 75 ° spectrum because of deminishing accessibility.
Assuming homogeneous current density and absorbed power density profiles, full absorption of the accessible power by the fast electrons, and a confinement time longer than their slowing down time, we can derive from theory,/2/, the zero electric field efficiency in the same units as

$$\eta_{0,theor} = 1240/\{\ln\Lambda(5+Z_{eff})\ \langle N_{||}^2\rangle\} \qquad (2)$$

with /3/

$$\langle N_{||}^2\rangle^{-1} = \frac{\int_{N_{||acc}}^{\infty} P(N_{||})/N_{||}^2\, dN_{||} - \int_{-\infty}^{-N_{||acc}} P(N_{||})/N_{||}^2\, dN_{||}}{\int_{-\infty}^{\infty} P(N_{||})\, dN_{||}} \qquad (3)$$

$N_{||acc}$ is determined from the plane wave accessibility condition with the line averaged density n_e and the central magnetic field. We neglect any possible broadening or upshift of the spectrum. The results of this calculation are also shown in figs.1 and 2. In fig. 1 the dashed lines indicate the range in Z_{eff} encountered in these experiments due to different wall conditions. In fig. 1 all

spectra, except the one for $\Delta\phi = 67°$, satisfy the accessibility condition and the agreement with the experiment is quite good. In fig.2 the spectrum with $\Delta\phi = 75°$ suffers from decreasing accessibility when n_e increases, however in the experiment more then we expect on the basis of our assumptions. One reason for this may be nonlinear effects,/4/.
If the power is not sufficiently high the loop voltage does not drop to zero. The efficiency for current drive in the presence of an electric field has been calculated in a number of papers,/5/. We use for our comparison with theory an analytic approximation for η normalized to the efficiency η_0 without E-field /6/

$$\eta/\eta_0 = \ln\{(1-X_2)/(1-XX_2)\}/(XX_2-X_2), \qquad (4)$$

with $X_2 = \alpha u_2^2 E_N$, $X = (N_{||2}/N_{||1})^2$, $\alpha = 12/(Z_{eff}+7)$, $u_2 = v_{ph2}/v_{th}$ and $E_N = E/E_{Dreicer}$. The index 2 relates to the upper boundary of the phase velocity spectrum. With the same assumptions as before and with the circuit equations we obtain

$$P_{lh}/P_{lh0} = (1-U_{lh}/U_{oh}\cdot T)/(\eta/\eta_0). \qquad (5)$$

U_{lh} and U_{oh} are the loop voltage during the lower hybrid and the ohmic phase, T describes the enhancement of the plasma conductivity due to bulk heating or a change in Z_{eff}, and P_{lh0} is the power needed to reach zero loop voltage in these conditions. The term X_2 can be expressed as $X_2 = U_{lh}/U_{oh} \cdot A$, with

$$A = 0.023(Z_{eff,oh}+0.72)/(Z_{eff,lh}+7)\cdot I_p/n_e(N_{||2})^2 T_{e,oh}^{3/2}.$$

I_p, n_e, T_e are in units kA, $10^{13}cm^{-3}$, kV. Except for $N_{||2}$ all these quantities can be determined experimentally.
In figs.3 and 4 we compare experimental results at two different densities with this theory. They were obtained with $B_t = 2.8$ T and $I_p = 420$ kA. The curves have been calculated with an average value A determined experimentally and with a calculated $N_{||2}$, and for various values of T. At high density, fig.3, the agreement is quite good and the variation of T can be explained by the observed electron heating with increasing power, ($T_e(0)$ rises from 1.4 kV to 3 kV). At low density we find already at low power (up to $P_{lh}/P_{lh0} \approx 0.25$) a strong drop in loop voltage which would require $T \approx 2$. This cannot be explained by bulk heating. In this range the loop voltage is not yet low enough and we observe runaway electrons which may carry part of the plasma current and which are not included in this simple theory. At high power where the electric field is near zero the high value of T can again be explained by the observed strong electron heating, ($T_e(0)$ rises from 2 kV to 7.5 kV). Comparisons at different current drive spectra and plasma currents yield the same result.
With a symmetric spectrum of waves we drive in principle currents in both toroidal directions, however according to equ. 4, with

different efficiencies. Thus a net current drive results. Assuming that both these currents can be additively described by equ. 4, we obtain for the normalized characteristics

$$P_{lh}/P_{lh0} = (1-U_{lh}/U_{oh} \cdot T)/\{\eta(+E_N)/\eta_0-\eta(-E_N)/\eta_0\} \qquad (6)$$

These characteristics never reach $\Delta U/U_{oh}= 1$, i.e. zero loop voltage. In figs.5 and 6 we compare measured and calculated results again for two densities. As in the case with asymmetric spectrum we find reasonable agreement at high density when we take heating into account. At low density, fig.6, the high values of T resulting from the comparison can again not be explained by bulk heating. The production of runaway electrons is in this case even stronger than in the proper current drive situation since the remaining electric field is higher for the same launched power.
We have also studied current drive during neutral beam injection in a L-mode plasma. Fig.7 shows the loop voltage drop as a function of rf-power during injection of 1 MW of neutral beam power. In the combined NBI and LH phase the density did rise from 2.1 to 2.4 . $10^{13}cm^{-3}$. For the comparison with LH current drive alone we therefore show in fig.7 two characteristics obtained at the densities 2.1 and 2.8 . $10^{13}cm^{-3}$. From this we conclude that the current drive efficiency is the same with and without neutral beam injection for these parameters. The point of zero loop voltage for this case is marked in fig.2 as the thick cross.

This experiment has been performed in cooperation between IPP - Garching, ENEA - Frascati and PPPL - Princeton.

/1/ F. Leuterer et al., 16. European Conference on Controlled Fusion and Plasma Physics, Venice 1989, Vol. IV, p. 1287
/2/ C.F. Karney, N. Fisch, Phys. Fluids 28,116,(1985)
/4/ V. Pericoli, this conference
/3/ J. Stevens et al., Nucl. Fusion 28,217,(1988)
/5/ N. Fisch, Review of Modern Physics 59,175,(1987)
/6/ K. Yoshioka et al., Phys. Fluids 31,1224,(1988)

Fig.1: Steadystate current drive efficiency as function of $N_{||}$
Fig.2: Steadystate current drive efficiency as function of density
Fig.3: Calculated and measured drop in loop voltage for partial current drive at $n_e = 2.8 \cdot 10^{13}cm^{-3}$, cd-spectrum $\Delta\phi = 90°$
Fig.4: Calculated and measured drop in loop voltage for partial current drive at $n_e = 1.35 \cdot 10^{13}cm^{-3}$, cd-spectrum $\Delta\phi = 90°$
Fig.5: Calculated and measured drop in loop voltage for partial current drive at $n_e = 2.8 \cdot 10^{13}cm^{-3}$, symm.spectr. $\phi = 00\pi\pi...$
Fig.6: Calculated and measured drop in loop voltage for partial current drive at $n_e = 1.35 \cdot 10^{13}cm^{-3}$, symm.spectr. $\phi = 00\pi\pi...$
Fig.7: Loop voltage drop as function of rf-power during neutral beam injection, cd-spectrum, $\Delta\phi = 90°$

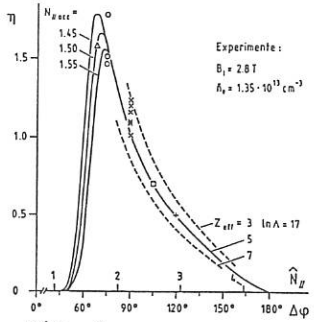

Fig. 1

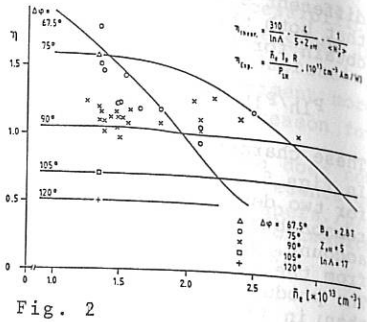

Fig. 2

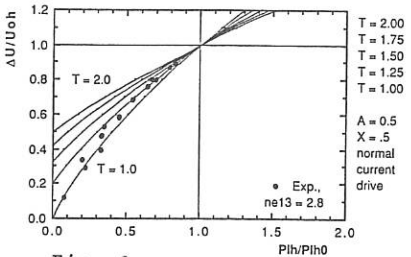

Fig. 3

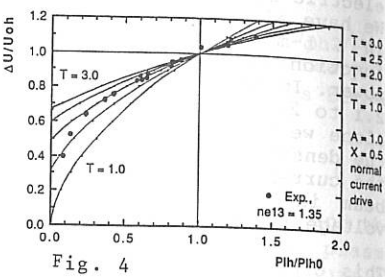

Fig. 4

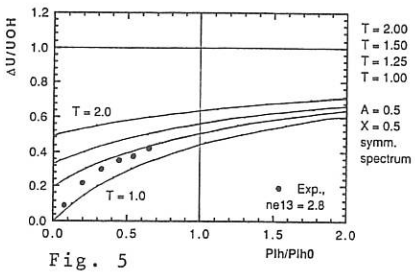

Fig. 5

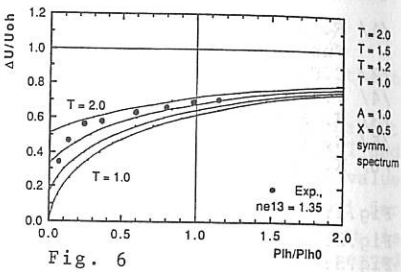

Fig. 6

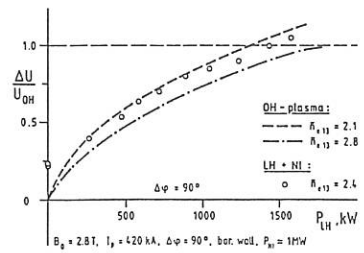

Fig. 7

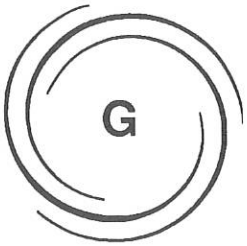

CURRENT DRIVE AND PROFILE CONTROL

G3

G3 OTHERS

SIMULATION OF FAST WAVES CURRENT DRIVE BY MULTI-LOOP ANTENNAE IN ITER

M. V. Dmitrieva

M. V. Keldysh Institute of Applied Mathematics

V. L. Vdovin, S. V. Fedorov

I. V. Kurchatov IAE, Moscow, USSR

3D-simulation of current drive by fast magnetosonic waves (FMSW) in the range of ICR frequencies and lower ones (60-4.25 MHz) for the parameters of ITER-technology phase [1] (a=1.8 m, R=5.5 m) has been done with developed ICTOR-code [2]. On the basis of reference operators, [3], the completly conservative schemes for Maxwell's equations have been derived. The multi-loop antennae located at low field side or at the top of the torus are used. The current drive (CD) efficiency, taking account of trapped electrons in C. Karney-D. Ehst model [4], for $\overline{T}$ =18 keV and Z_{eff}=2.2 is γ=0.25-0.3 (table).

Three frequency ranges are considered: 60 MHz ($\omega \gtrsim 2\omega_{cT}$), 17 MHz ($\omega < \omega_{cT}$) and 8.5-4.25 MHz. The phase velocities are of the order of thermal electron one and higher. A very peaked current profile at f=55-60 MHz (Fig. 6) is expanded at the transition to 17 MHz, and current passes within a half of the minor plasma radius at f=4.5 MHz. For the scenario with new ITER in a single null configuration (a=2.15 m, R=6 m, b/a=2) we have obtained more broadened power deposition profile with an antenna located at the top of the torus (Fig. 4). With the new consideration of trapped particles effects (RF diffusion in the curvilinear magnetic field, and only then bounce averaging)

[5], the CD efficiency is γ=0.6 for Z_{eff}=1.8.

An another interesting opportunity to drive the current by FMSW within the plasma column middle and outwards from it in low frequency range (f~10 MHz) is a simultaneous excitation of the several nearly degenerative cylindrical modes coupled in a 'toroidal resonance' (<m>~4) is shown in Fig.2. Some of these found modes are localized poloidally. Their excitation in the torus interior not only would rise about two times the CD efficiency, since trapping effects are essentially reduced due to [5], but will broaden significantly the current profile.

The ion absorption in the mode of operation with $\omega \gtrsim 2\omega_{cT}$ (~ 60 MHz) doesn't exceed 20 %, the alpha absorption is insignificant for a reactor with R/a > 3 [2].

REFERENCIES

1. ITER definition concept, v.I, IAEA,1989 (Vienna)
2. Vdovin V.L.,Fedorov S.V.,Dmitrieva M.V., ITER ICRF workshop, August 1989
3. Dmitrieva M.V.,Tishkin V.F. et al, Preprint IAM -197, 1986
4. Ehst D. et al, ITER CD/H modelling meeting, June 1989 (Garching)
5. Vdovin V.L. et al, ITER F workshop, February 1990 (Garching)

f MHz	T_e kev	DA cm	TA cm	DFI rad	N^{sp}_{max}	$N^{Q_{tot}}_{max}$	Q_{tot} Wt	γ_i^{LD}	γ_i^{TTMP}	N
55	36	25	65	.314	18	18	210	0.231	0.211	14±22
17	9	12	27	.314	7	7	148	0.102	0.125	5±13
17	16	17	75	.314	7	11	126	0.131	0.17	3±11
17	25	22	45	.314	5	7	156	0.222	0.282	2±10
17	36	25	55	.314	5	6	161	0.287	0.355	2±10
8.5	36	50	100	.628	5	5	136	0.186	0.188	1±9
4.5	36	50	100	.99	8	9	72	0.089	0.139	4±12
4.5	36	50	100	.314	2	2	90	0.239	0.235	1±8

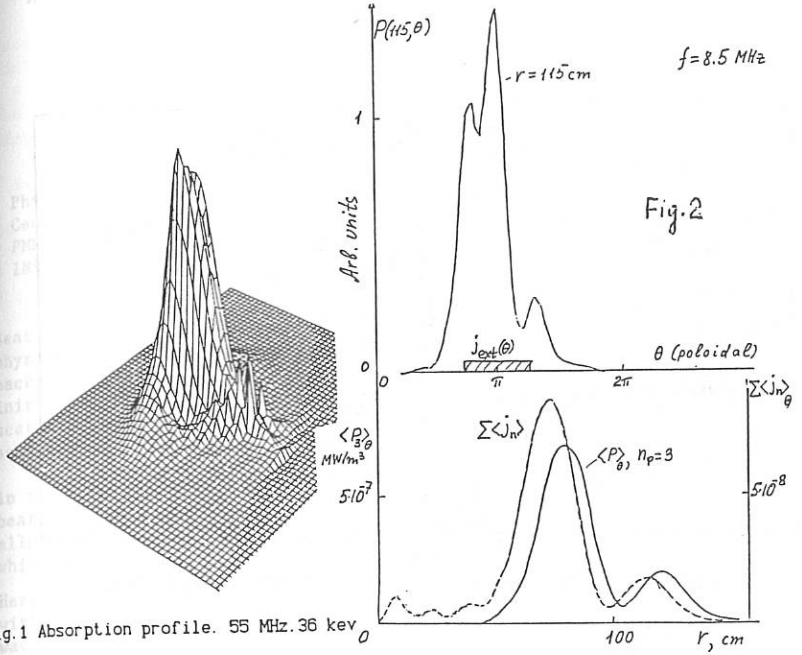

Fig.1 Absorption profile. 55 MHz. 36 kev

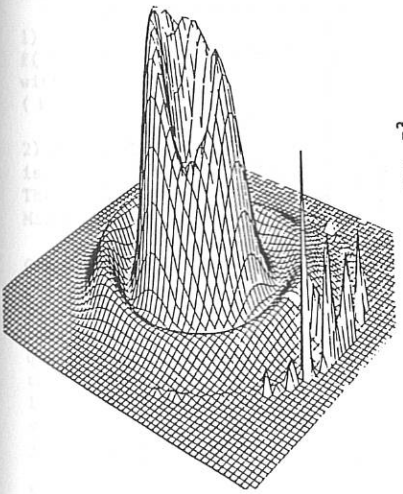

Fig.3 Absorption profile. 4.5 MHz. 36. kev

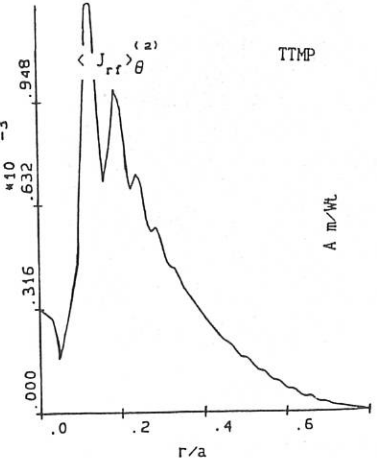

Fig. 4 Averaged current profile.
Top antenna. 17 MHz.

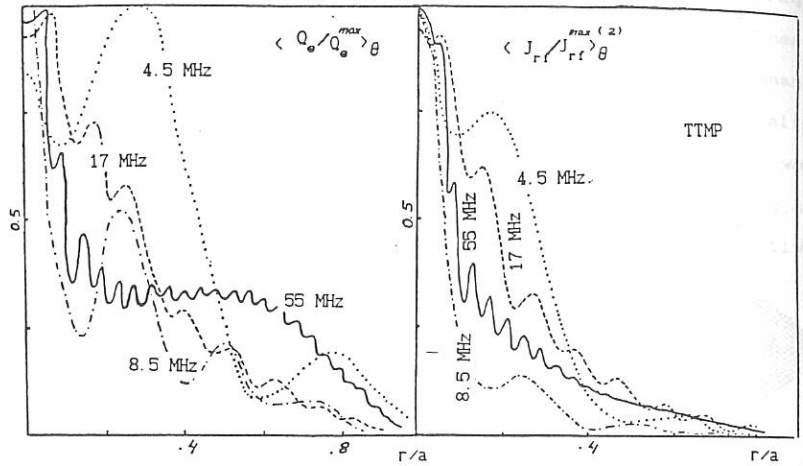

Fig.5 Averaged absorption pfrofile.

Fig.6 Averaged current profile.

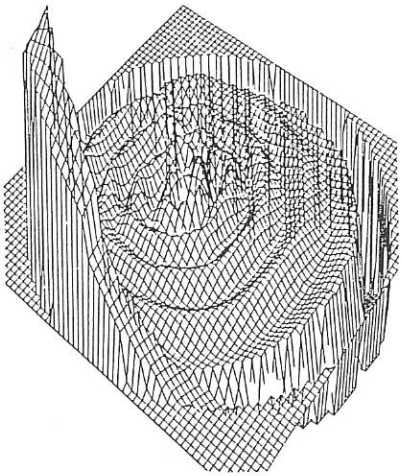

Fig.7 Field Re E_r . 17 MHz.

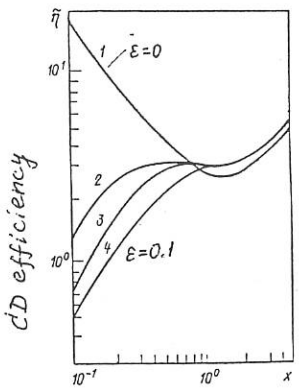

Fig. 8

A 1-2/2 D EULERIAN VLASOV CODE FOR THE NUMERICAL SIMULATION OF BEAT CURRENT DRIVE IN A MAGNETIZED PLASMA.

A. Ghizzo[1], P. Bertrand[1], M. Shoucri[2], M. Feix[3], T.W. Johnston[4], E. Fijalkow[3]

1 Physique Théorique, Université de Nancy-1, Nancy, France
2 Centre Canadien de Fusion Magnétique (CCFM), Varennes, Québec, Canada
3 PMMS-CNRS, Université d'Orléans, France
4 INRS-Energie, Université du Québec, Varennes, Québec, Canada

Beat wave current drive and heating are of increasing interest in the physics of toroidal plasma[1]. We present numerical simulations of Raman backscattering (BRS) in a strong magnetized plasma. In this process, an initial right hand polarized electromagnetic pump wave decays into a scattered wave and an electrostatic plasma wave (EPW) which traps and accelerates the electron, producing a current.

In the case of relativistic electrons produced from Raman scattering or beat wave (without magnetic field) the use of an eulerian Vlasov code allows a relatively economical calculation of the phase space structures which are simply invisible in normal particule codes [2,3].

Here we extend the previous code to the case of a magnetized plasma with an external field $\vec{B}_0 = B_0 \vec{e}_x$ in the direction of the incoming pump wave. Since particles are accelerated in the same direction, we consider two models with one spatial dimension:

1) A 1-2/2 D Vlasov model in which the electron distribution function $f(x, p_x, p_y, p_z, t)$ obeys the relastivistic Vlasov-Maxwell equations, with a longitudinal EPW field E_x and transverse electromagnetic modes (in the plane $\vec{e}_y, \vec{e}_z$) propagating in the $\vec{e}_x$ direction .

2) A simplified 1 D model in which the transverse kinetic description is represented, in a fluid approach, by the mean velocity $u_\perp(x, t)$. The more simple distribution function $f(x, p_x, t)$ obeys the 1 D Vlasov-Maxwell equations supplemented by the fluid equation for $u_\perp(x, t)$.

Comparisons are presented between the two models. For simplicity, both are periodic in space. Plasma parameters are: thermal velocity $v_{th} = 0.08\ c$ (i.e. T=3.2 keV), electron cyclotron frequency $\omega_c = \sqrt{2}\ \omega_p$, (M.T.X. like parameters), incident laser quiver velocity $v_{osc} = 0.10\ c$ and frequency $\omega_0 = 2.8\ \omega_p$. BRS is expected to produce an EPW with $\omega_e = 1.12\ \omega_p$ then the length of the periodic box is chosen to be 3 times the wave length of EPW. Notice that Forward Raman Scattering (SRS) is also possible; in the latter case the wave length of the corresponding EPW is just the length of the box.

Numerical experiments using the 1-2/2 D model have been carried out using a grid $N_x N_{px} N_{py} N_{pz} = 32 \times 128 \times 32 \times 32 = 4\,194\,304$ mesh points. Typical time step is $0.16\ \omega_p^{-1}$. Results are displayed in figs 1.The time evolution

of the pump energy is shown in fig 1a and exhibits, indeed, the decay into a scattered light (fig 1b) and the EPW (fig 1c). Thus this process leads to the generation of accelerated particles and therefore to a longitudinal current density(fig 1d); energies are normalized to mc^2 units, time is normalized to the inverse plasma frequency ω_p and velocities are normalized to the velocity of the light c . Furthermore, detailed examination of the distribution function in the $x-p_x$ phase space plane is given in figs 1e and 1f; both contour plots and 3D representation of the distribution averaged on p_y and p_z are given at time t = 300.1 (fig 1e) and time t = 350.9 (fig 1f), showing not only the expected formation of a 3 vortex structure due to BRS, but also the emergence of a one period structure at the end of the run which may be related to FRS.

A second series of simulation is conducted using the 1 D Vlasov code, with a grid $N_x N_{p_x} = 128 \times 512 = 65536$ mesh points only and a better $x-p_x$ resolution than the full kinetic 1 2/2 D code. Figs 2 exhibit the results obtained with the latter over a longer time (810 ω_p^{-1} instead of 410 ω_p^{-1}). Both model are in good agreement. Furthermore the oscillatory behaviour after BRS saturation has been identified as FRS. Phase space plots (fig 2f) reveals also the one period stucture due to FRS.

Finally the 1-D Vlasov code with fluid description for the transverse motion appears to be a very efficient tool to study particle dynamics for beat wave or Raman scattering in magnetized plasma.

Acknowledgments.

The Authors are indebted to the "Centre de Calcul Vectoriel pour la Recherche" (Ecole Ploytechnique, Palaiseau, France) for computer time alloocation on the Cray-2 computer.

References.

1. B. Cohen, Lawrence Livermore National Laboratoratory report, Technical Memorendum, January 13, 1988.

2. A. Ghizzo, P. Bertrand, M. Shoucri, T.W. Johnston, E. Fijalkow, and M.R. Feix.
Journal of Computational Physics, in press.

3. P. Bertrand, A. Ghizzo, T.W. Johnston, M. Shoucri, E. Fijalkow and M. R. Feix.
Physics of Fluids, in press.

THE 1-2/2-D MODEL

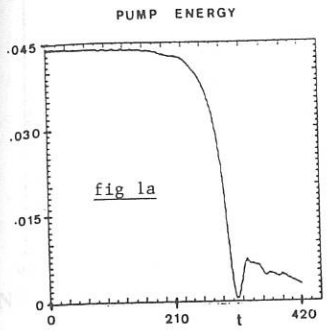

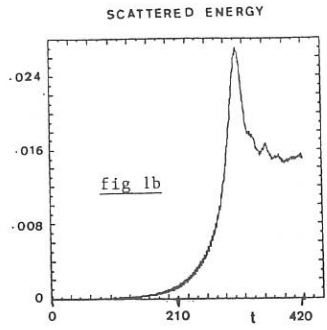

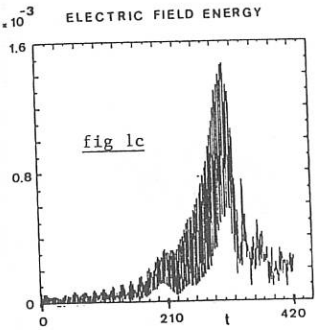

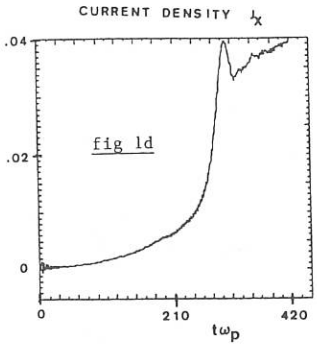

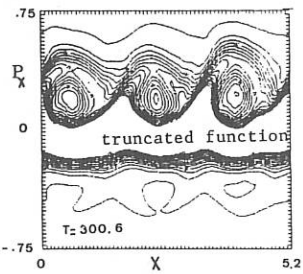

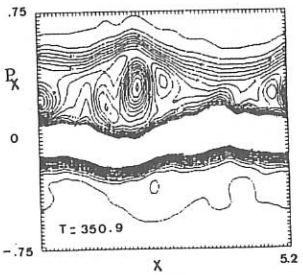

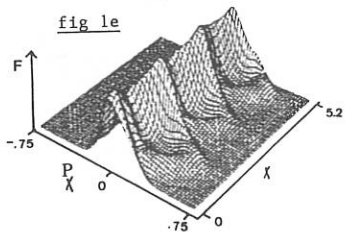

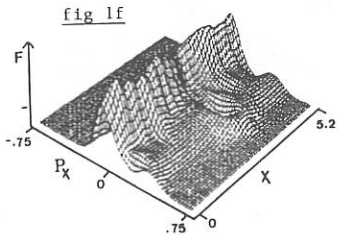

THE 1-D MODEL

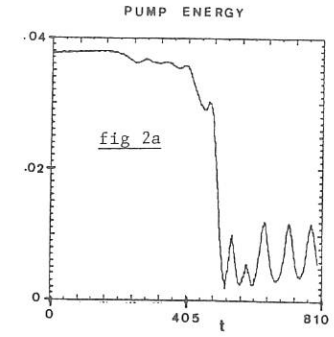

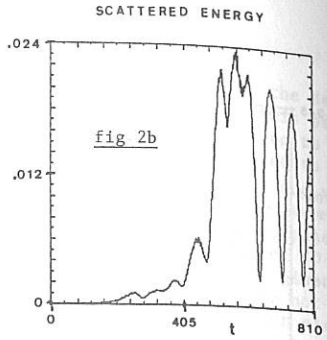

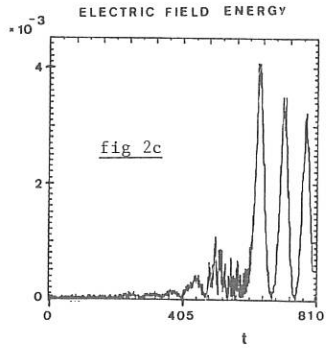

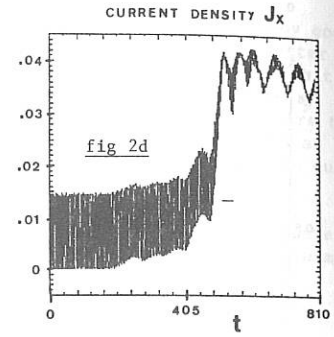

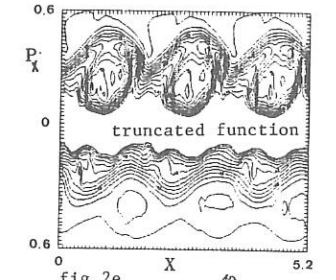

fig 2e
T= 540

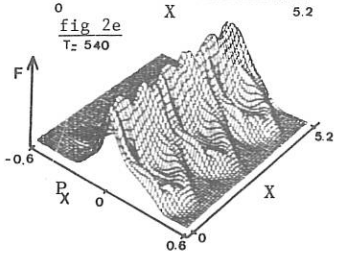

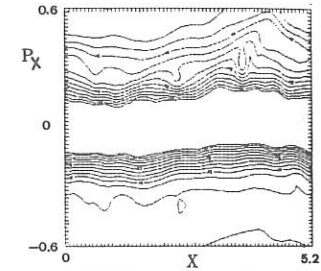

fig 2f
T = 800

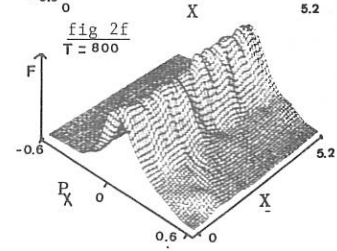

HIGH FREQUENCY CURRENT DRIVE BY NONLINEAR WAVE-WAVE INTERACTIONS

S.J. Karttunen[1], T.J.H. Pättikangas[2] and R.R.E. Salomaa[2]

[1]Technical Research Centre of Finland, Nuclear Engineering Laboratory
P.O. Box 169, SF-00181 Helsinki, Finland
[2]Helsinki University of Technology, Department of Technical Physics,
SF-02150 Espoo, Finland

1. INTRODUCTION

In the high frequency regime ($\omega \sim \Omega_e$) ideas of the current drive in tokamak plasmas are mainly based on the electron-cyclotron waves generated by hf-gyrotrons. The progress in free-electron-laser (FEL) technology opens new interesting possibilities for the current drive. This is due to the potential of FELs for GW peak powers, high efficiencies, and low cost per watt as compared with conventional gyrotrons [1]. Large peak powers apply to the excitation of nonlinear wave-wave processes which produce high phase velocity ($v_{ph} \gg v_e$) electrostatic modes. These modes accelerate the resonant electrons to large parallel velocities $v_{\|} \simeq v_{ph}$ producing a slowly decaying current.

Large amplitude electrostatic plasma waves can be excited by the beat-wave (BW) interaction or by the parametric decay of intensive FEL radiation. In the beat-wave method two counterpropagating [2] or collinear [3] pump waves can be used. In the stimulated Raman scattering (SRS) the lower frequency electromagnetic wave grows up from the noise level. The advantage of the SRS current drive over the BW-method is that only a single frequency FEL is needed. A weak, broadband seed laser can provide appropriate starting noise. In contrast to the beat-wave current drive the SRS-method is less sensitive to detuning from the exact resonance.

The operation above the high frequency cut-offs provides an easy access into the plasma centre which makes possible to control the current and q-profiles. In addition, the FEL current drive works also in reactor relevant conditions, because there are no limitations for the plasma density like in the LH current drive. These features make the SRS and BW methods particularly attractive for bootstrap current seeding, which may considerably enhance the overall current drive efficiency [3].

2. STIMULATED RAMAN PROCESS

In stimulated Raman scattering an intense electromagnetic pump wave (T) decays into a scattered wave (T') and a longitudinal plasma wave (L): $T \rightarrow T' + L$. Energy and momentum conservation relations for the waves are $\omega_0 = \omega_s + \omega$ and $\mathbf{k_0} = \mathbf{k_s} + \mathbf{k}$, where "0" and "$s$" refer to the pump wave and to the scattered wave, respectively.

We assume a simple geometry in which all waves propagate parallel to the magnetic field. This gives the best current drive efficiency according to 2D-calculations [4]. The

pump wave can be either right (RCP) or left (LCP) circularly polarized. Modifications caused by the magnetic field to the Raman process are included in our analysis. These are particularly important at low frequencies where the current drive is expected to be most efficient.

Both Raman forward (SRS-F) and backward (SRS-B) scattering can be used to current drive. SRS-B has a larger gain and the momentum transfer to the plasmon is more efficient. The phase velocity of the SRS-B plasmon, however, is fairly small in a hot well underdense plasma so that Landau damping severely limits the growth of the SRS-B instability. In SRS-F the plasmon phase velocity $v_{ph} = \omega/k$ is much higher and its linear damping is very weak. This indicates that SRS-F can dominate over SRS-B even though its gain is smaller. The high phase velocity $v_{ph}/c = 0.7 - 0.95$ means that SRS-F generates nearly collisionless electrons which leads to a slow decay of the resulting current. An apparent problem is the coupling of the high phase velocity plasmon to the electron distribution. The coupling takes place in the strong pump limit when the plasmon amplitude is large enough to trap electrons from the tail of the distribution. An interesting possibility is the simultaneous operation of SRS-B and SRS-F which may substantially enhance the fast electron production. The SRS-B generates a large number of medium fast electrons, which increases the tail damping and electron acceleration by the SRS-F plasmon.

The basic gain length for SRS-B and SRS-F is

$$L_g = \frac{2\sqrt{6}}{\alpha_B}\left(\frac{c}{v_0}\right)\left(\frac{\omega_p}{\omega}\right)\left|\frac{k_s}{k}\right|^{1/2}\lambda_D, \tag{1}$$

where $v_0 = e|E_0(0)|/m_e\omega_0$ is the electron quiver velocity in the pump field. The dependence on the magnetic field B_0 has been included in α_B [3]. The gain length gives a measure for the required interaction length. In most cases the SRS-F plasmon is weakly damped and the convective growth depletes the pump completely in the distance

$$L_{depl} \simeq \frac{L_g}{2}\ln\left(\frac{4}{\epsilon_N}\right), \tag{2}$$

where ϵ_N is the electromagnetic noise level. If the peak intensity of the FEL pulse is $\hat{I}_0[\mathrm{W/cm^2}]\lambda_0^2[\mathrm{mm^2}] \sim 10^8$, the gain length L_g of the SRS-F is about 20 cm and the depletion length is 0.5 m for $\epsilon_N = 10^{-4}$. If the linear damping limits the growth of the Raman scattering the depletion length is given by $L_{depl} \simeq (L_g^2/2L_a)\ln(1/\epsilon_N)$, where L_a is the linear absorption length.

3. CURRENT DRIVE EFFICIENCY

We assume that the plasma wave excited by SRS transfers all its momentum to the fast electrons. In the steady state the momentum transferred from the pump wave to the plasma wave equals the momentum transferred from the plasma wave to the

Table 1: *Current drive and FEL parameters for SRS-F with* $j_T = 2.5\ MA/m^2$, $r_c = 0.3$ *and* $\epsilon_N = 10^{-4}$ *for both wavelengths. The plasma parameters as in Fig. 1.*

LCP pump wave	$\lambda_0 = 1.06$ mm	$\lambda_0 = 1.8$ mm
CD efficiency $n_e RJ_T/P$ [A/Wm^2]	2×10^{20}	10^{20}
peak intensity $\hat{I}$ [Wcm^{-2}]	2.7×10^8	9.3×10^7
pulse length t_p [ns]	30	50
pulse repetition rate ν_{rep} [Hz]	94	325
gain length L_g [m]	0.1	0.05
depletion length L_{depl} [m]	0.53	0.27

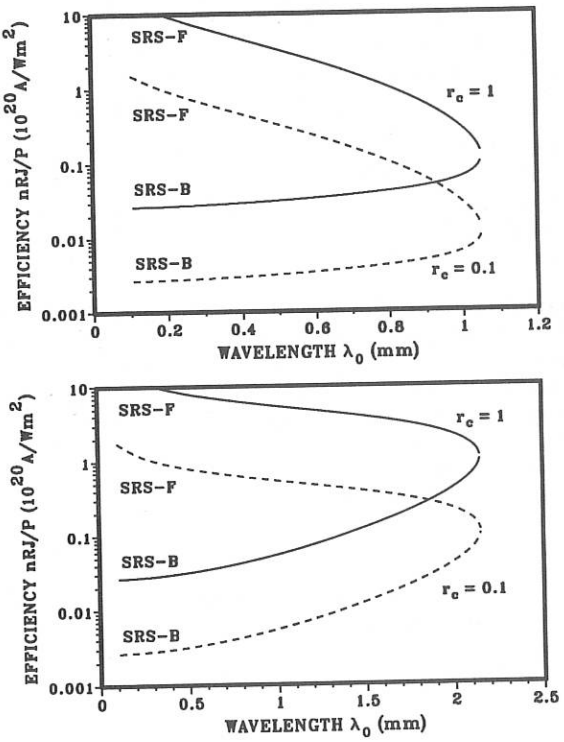

Figure 1: *CD-efficiency (3) versus pump wavelength for* $r_c = 1$ *and* 0.1, $Z = 1.3$, $n_e = 10^{20} m^{-3}$, $T_e = 10\ keV$ *and* $B_0 = 4.81\ T$. *Upper frame (RCP), lower frame (LCP).*

resonant electrons. The efficiency of the momentum transfer is described by the relative action transfer r_c from the pump wave to the plasma wave. The current drive efficiency is obtained by balancing the momentum obtained by the resonant electrons and the momentum lost by them in collisions (see ref. [2]). In units [A/Wm^2] the result is

$$\frac{n_e R J_T}{P} = 2.39 \times 10^{13} \frac{\epsilon_F^{3/2}[\mathrm{eV}]}{Z^2 \ln \Lambda} \left(\frac{\omega}{\omega_0}\right)\left(\frac{kc}{\omega}\right)\left(\frac{k_0 c}{\omega_0}\right) r_c, \tag{3}$$

where ϵ_F is the fast electron energy corresponding to the plasmon phase velocity and $\ln \Lambda$ is the Coulomb logarithm.

Figure 1 illustrates the current drive efficiencies (3) for various pump wavelengths λ_0. Notice that the plasmon wavenumber k and ϵ_F in Eq. (3) depend on the pump wavelength, too. Figure 1 predicts high current drive efficiencies for the SRS-F process, because it produces less collisional electrons than SRS-B. At short wavelengths the efficiencies are similar for the RCP and LCP cases, but at long wavelengths the LCP pump leads to more efficient current drive. In addition, the behaviour of the RCP wave may be complicated by the cyclotron damping near $\omega_{0,s} = m|\Omega_e|$.

The power P in the current drive efficiency (3) is the average FEL output power. A high peak power $\hat{P}$ (or peak intensity $\hat{I}$) is required to exceed the threshold of SRS. The relation between the peak and average quantities is $P = \nu_{rep} t_p \hat{P}$ where t_p is the pulse length and ν_{rep} is the pulse repetition rate. Table 1 shows some typical current drive and FEL parameters for the LCP pump wave.

The pump frequencies close to the cut-off frequency are expected to give the best current drive efficiency in terms of the quantum efficiency ω/ω_0. The phase velocity of the SRS-F plasmon is somewhat reduced which increases the generation of fast electrons. In this region also SRS-B is expected to operate so that strong coupling to the electron distribution is anticipated due to simultaneous SRS-B and SRS-F. Near the cut-off frequencies the FEL beam propagation becomes more complicated. Our preliminary ray tracing calculations indicate that the beam curvature does not play any significant role for $\omega_{0,s} > \omega_p$ in agreement with ref. [2].

References

1. M. J. van der Wiel, P. W. van Amersfoort, Fusion Eng. Design **11** (1989) 245.
2. B. I. Cohen et al., Nucl. Fusion **28** (1988) 1519.
3. J. A. Heikkinen, S. J. Karttunen, R. R. E. Salomaa, Nucl. Fusion **28** (1988) 1845.
4. M.R. Amin, R.A. Cairns, Nucl. Fusion **30** (1990) 327.

POSSIBILITY OF ION CURRENT DRIVEN BY RF HELICITY INJECTION

K. Hamamatsu, A. Fukuyama*, S.-I. Itoh**, K. Itoh** and M. Azumi

Japan Atomic Energy Research Institute, Naka Fusion Research Establishment, Naka-machi, Naka-gun, Ibaraki, 311-02.
*Faculty of Engineering, Okayama University, Okayama, 700.
**National Institute for Fusion Science, Chikusa, Nagoya, 464-01, Japan

1. Introduction The injection by RF-waves with helicity has been proposed to the tokamak plasma as a promising current drive scheme by Ohkawa [1]. Recently, the relation between RF-driven current and RF helicity conservation is clearly explained in Ref. 2,3. We obtain the conversion relation of RF-helicity to the OH helicity in the range of ion cyclotron frequency. It is found that the RF helicity is not exactly converted to the DC helicity associated with the plasma current under any helicity conservation laws [4]. We found, however, the helicity force originated from the $<\tilde{V}\times\tilde{B}>$- force can be expected as a current drive force. Especially, the $<\tilde{V}\times\tilde{B}>$ - force acted on fast ions is interested. We solve the wave propagation equation as a boundary value problem using the one dimensional kinetic wave code. The ion driven current is calculated from the obtained wave field. The density and temperature dependences of the current drive efficiency are obtained and discussed.

2. RF Helicity and Current Drive Introducing the vector potential A ($\nabla \times A=B$), we can generally write the conservation relation of the helicity density, $H=A\bullet B$, as follows,

$$\frac{\partial H}{\partial t} + \nabla \bullet \left(A \times \frac{\partial A}{\partial t} + 2\,\phi B\right) = -\,2\,E\bullet B \qquad (1)$$

where the relation $E = \nabla\phi - \partial A/\partial t$ is used. We divide the field quantities into the stationary component sustained by the Ohmic drive and the RF oscillating part. RF field part is calculated using the equation of motion and continuity equation. Under the constraint that the parallel current is fixed, the reduction of the OH electric field, $-\delta E_{0\parallel}$, is obtained as

$$-\left(\delta E_{0\parallel}\, B\right) = \lambda < \tilde{E} \bullet \tilde{B} > \qquad (2)$$

where <> indicates the time average over the wave period and the symbol ~ denotes RF oscillating part. The coefficient λ may be interpreted as the conversion coefficient of the RF helicity to the OH helicity. The explicit from of λ is expressed in Ref. 4. The RF helicity current drive is caused by the $<\tilde{V}\times\tilde{B}>$ - force, which is usually accounted for in revaluating the dynamo force. It is an

important result that the obtained conservation coefficient λ is not necessarily unity. This means that the coefficient λ is not constrained by the conservation of total helicity but dictated by the other mechanism of current drive.

3. Ion Driven Current The absorption of wave helicity takes place in the case where waves are absorbed through the cyclotron damping, Landau damping and TTMP. The $<\tilde{V}x\tilde{B}>$ - force appears for electrons and ions. It must be noted that the ion driven current and electron driven current flow in the opposite directions.

We estimate the ion driven current due to ion cyclotron resonance. The ion flow is driven by the $<\tilde{V}x\tilde{B}>$ - force. The Ohkawa current associated with this ion flow is evaluated by using the neoclassical formula. The net current $j_{||i}$ is given as

$$j_{||i} = h\,(v_d\ ,\ Z_{eff})\, q_i\, n_i\, v_{d||}$$

$$v_{d||} = \frac{1}{\nu_s}\,\frac{1}{m_i n_i}\,[<\tilde{E}_{||}\tilde{\rho}_i> + <\tilde{j}_i x \tilde{B}>_{||}] \qquad (3)$$

Here ν_s^{-1} is the slowing down time of ions and the coefficient $h\,(v_d, Z_{eff})$ is the analytic expression of the classical Spitzer function, which includes the effects of electron-electron collisions and is valid for all values of $v_d = v_{d||}/v_e$ and effective charge, Z_{eff} [5]. We include the LD term and $<\tilde{V}x\tilde{B}>$ term in the expression of $v_{d||}$. If the fast ions do not exist, the ion driven current becomes negligibly small. Because the electrons absorb the input RF power and/or the ion slowing down time is reduced. Therefore, we assume the existence of the high energy ions, for example, which are injected by neutral beam. In order to calculate the wave field, power deposition profile and spacial profile of driven current, we solve the wave equation in an inhomogeneous plasma as boundary value problem.

4. Numerical Results We use a typical parameter of the JT-60 plasma: R=3m, B_T=4T, a = 0.95m, T_{eo}=T_{io} = 10 keV, Z_{eff} = 2.4. In this calculation we do not specify the antenna spectrum and treat as the Frourier decomposed mode: $k_{||}$-mode. The current drive efficiency is expressed as

$$\bar{\eta}_{CD} = \frac{I\bar{n}_e R}{P_{IC}} \qquad (4)$$

where I is a total driven current, P_{IC} is a total input RF power and $\bar{n}_e$ is a line averages electron density. $\bar{\eta}_{CD}$ is a function of $k_{||}$. The notation $\bar{\eta}_{cd}$, however, is used as the maximum value of the current drive efficiency for various $k_{||}$-mode. The velocity distribution of high energy beam ions is assumed to be isotropic Maxwellian with the temperature, T_b, and density, n_b.

Figure 1 shows the beam temperature dependence of $\bar{\eta}_{CD}$ for various plasma density, where the beam pressure is fixed at the constant value: $n_b T_b / n_{eo} = 40$ keV. As the beam temperature increases, the current drive efficiency is increasing because of a reduction of the beam-ion collision. In the high temperature region: $T_b < 300$ keV, $\bar{\eta}_{CD}$ increases with increasing of the plasma density. The density dependence of induced current is weaker than 1/n.

Figure 2 shows the dependence of $\bar{\eta}_{CD}$ on the electron temperature for various beam temperature. $\bar{\eta}_{CD}$ has a maximum value at a critical electron temperature which increases with the increase of beam temperature. In the low temperature regime below the critical temperature, $\bar{\eta}_{CD}$ increases due to the reduction of the beam-electron collision. When the electron temperature exceeds the critical one, $\bar{\eta}_{CD}$ begins decreasing. In the high temperature regime, the condition of the electron Landau damping is satisfied and the electron current is driven in the opposite direction. This situation is presented in Fig. 3, where the radial profile of electric field, Ey, power deposition profile and the distribution of driven current are shown. The plasma parameters are $n_{eo} = 3 \times 10^{20}$ m^{-3}. $T_{eo} = T_{io} = 30$ keV, $T_b = 600$ keV and $k_{||} = 10$ m^{-1}.

5. Conclusion and Discussion We have studied the possibility of ion driven current based on the RF helicity injection. In order to calculate the radial profile of driven current, we use the one dimensional full-wave code. The high energy ions are indispensable for the high efficient current drive. In this report, the fast ions are assumed to be injected by neutral beam, where the beam energy must be exceeded several hundreds kilo volts. The density dependence of driven current is weaker than 1/n. The obtained drive efficiency is in a same order of the conventional methods, i.e. LH-current drive, etc. In the reactor grade tokamak, however, the α-particles have the high energy enough to be hoped. The calculation for α-particles has been left as an open problem. In the rarely collisional regime, the velocity distribution of high energy particles will be anisotropic. The problems in connection with trapped particles will have to be further investigated.

References

1. T. Ohkawa, Comments on Plasma Physics and Controlled Fusion 12, 165 (1989).
2. J.B. Taylor, Phys. Rev. Lett. 63 1384 (1989).
3. V.S. Chan, R.L. Miller and T. Ohkawa, General Atomic Report GA-A19732, submitted to Phys. Fluids B.
4. K. Hamamatsu, A. Fukuyama, S.-I. Itoh, K. Itoh and M. Azumi, "RF helicity injection and current drive" will be submitted.
5. S.P. Hirshman, Phys. Fluids 23, 1238 (1980).

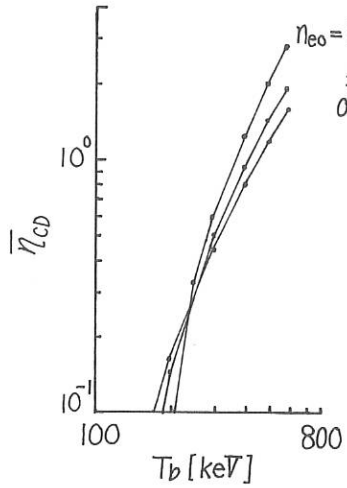

Fig.1. Beam temperature dependence of $\bar{\eta}_{CD}$

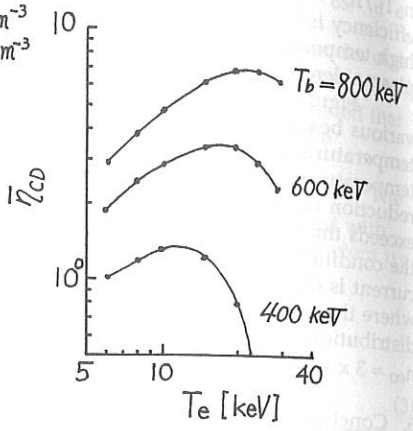

Fig.2. Electron temperature dependence of $\bar{\eta}_{CD}$

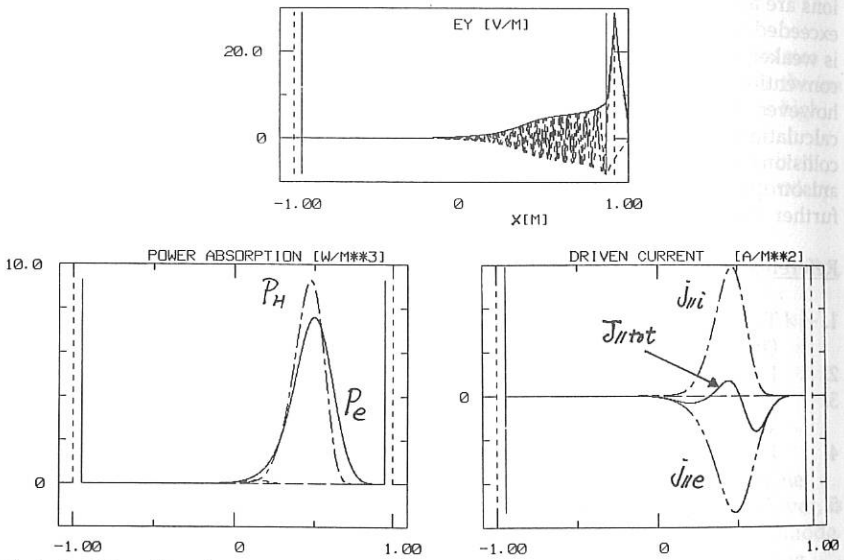

Fig.3. Radial profiles of Ey, power deposition and driven current.

DEVELOPMENT OF FAST-WAVE ICRF CURRENT DRIVE SYSTEMS AT ORNL*

R. H. Goulding, F. W. Baity, D. B. Batchelor, D. J. Hoffman, E. F. Jaeger, M. J. Mayberry,† P. M. Ryan

Oak Ridge National Laboratory, Oak Ridge, TN 37831-8071, U.S.A.

INTRODUCTION

A series of proof-of-principle fast-wave current drive (FWCD) experiments in the ion cyclotron range of frequencies (ICRF) will begin soon on the DIII-D tokamak at General Atomics [1,2]. These experiments will use a four-strap, 2-MW phased antenna array designed and built at Oak Ridge National Laboratory (ORNL) [2]. The antenna array will operate at a frequency of 60 MHz and is expected to drive currents at 0.25 to 0.5 MA in moderate-density ($\bar{n}_e \sim 1.3 \times 10^{19}$ m^{-3}) plasmas with $T_{e0} \sim 4$ keV and a toroidal field $B = 1$ T. We discuss development work undertaken at ORNL to predict the performance of the phased array and its feed circuit and to assist in the design of future FWCD systems.

RF MAGNETIC FIELD MEASUREMENTS

A full-scale mock-up of the FWCD antenna array for DIII-D was constructed to examine the wave spectrum produced by the design geometry, including the effects of three-dimensional (3-D) structures, for which adequate models have not been available in the past. These structures include slotted septa between current straps and the Faraday shield. The mock-up has also been used to determine the electrical characteristics of the array from a transmission line standpoint and to test proposed configurations of the feed circuit for the array. Figure 1 is a drawing of the actual antenna array. The current straps are 11 cm wide and 45 cm long and are grounded at one end. The straps are oriented vertically, and each strap is located in a cavity 22 cm wide bounded on each side by a septum. The outer septa (between straps 1 and 2 and between straps 3 and 4) are not shown in Fig. 1 for reasons of clarity. The inner septum between straps 2 and 3, which is formed from the inner walls of the two antenna cavities, is slotted with horizontal slots extending from the front Faraday shield surface to 1 cm behind the straps, as shown in Fig. 1.

The toroidal component of the rf magnetic field produced by the mock-up array was measured with a loop probe scanned in the toroidal direction 6 cm in front of the Faraday shield, corresponding to the approximate distance from the antenna surface to the magnetic field separatrix. Three configurations that involved altering the geometry of the outer septa have been examined.

Figure 2 shows the power spectra calculated from the rf magnetic field measurements for (a) solid outer septa, (b) horizontally slotted outer septa, with slots extending from the front Faraday shield surface to 1 cm behind the straps, and (c) no outer septa or Faraday shield. The most directional spectrum is produced with no septa, but this option is precluded by mechanical

*Research sponsored by the Office of Fusion Energy, U.S. Department of Energy, under contract DE-AC05-84OR21400 with Martin Marietta Energy Systems, Inc.

†General Atomics, San Diego, CA 92138, U.S.A.

and electrical design constraints. Case (a),with slots only in the inner septum, was investigated because it minimizes the power split required between the two pairs of antennas in the initial feed circuit configuration, as discussed below. For the spectrum generated with slotted septa, 53% of the total power is present in the peak at $k_z = 8$ m^{-1} and 38% in the peak at $k_z = -20$ m^{-1}, where k_z is the wave number in the toroidal direction, versus 43.6% and 45.5%, respectively, for the unslotted septa. The approximate attenuation between the antenna face and the k_z-dependent location of the plasma cutoff layer was determined using the diverted L-mode density profile given in ref. [3]. The spectra corresponding to Figs. 2(a) and (b) with this evanescence effect taken into account are shown in Fig. 3. The spectrum generated with slotted septa has 68% of the power in the peak at $k_z = 8$ m^{-1} and 25% in the peak at $k_z = -20$ m^{-1}, versus 61% and 33%, respectively, for the unslotted septa. Slotting the septa increases the ratio of power in the positive k_z peak to that in the negative k_z peak from 1.8 to 2.7; by this simple measure, the directionality of the spectrum is significantly increased. On the basis of this measurement, the outer septa in the actual antenna were slotted. Current drive efficiency and loading produced by the measured spectra are now being calculated with the ORION full-wave code [4].

ANTENNA MODELING

A 2-D magnetostatic code [5] has been developed to model phased antenna arrays and is being used to model the effect of slotting the outer septa on the vacuum antenna spectrum. Since the code models a 2-D cross section of the array in a horizontal plane, the slots are modeled by reducing the distance that the septa extend from the antenna backplane. The Faraday shield is not modeled in this code.

In Fig. 2, the dotted lines show the vacuum power spectra calculated by the magnetostatic code for (a) solid and (b) slotted outer septa. To obtain a good fit to the data, the "slotted" septa in the model were extended an additional 1 cm past the ends of the actual slots. The geometry for the slotted sidewall case is shown in Fig. 4. In addition, the observation plane was taken to be 4.5 cm in front of the antenna cavities instead of the actual 6 cm. If this is not done, the power fraction in the dominant positive k_z peak is higher and that in the negative k_z peak is lower than the measured values, as would occur if the calculated currents were closer to the array backplane than the observed currents. The following possible reasons for the discrepancy are being investigated. (1) The presence of the Faraday shield may cause a redistribution of currents on the strap and septa, causing them to move toward the shield (2) The poloidal structure of the slotted septa may cause return currents to be located farther forward than allowed by the 2-D analog for them. (3) The angle betwen the two antenna cavities is not reproduced in the model. Because of these discrepancies, use of this model and others based on similar geometry for predictive purposes is limited. More accurate modeling of the slot effects should be possible with a 3-D code that is under development.

ARRAY FEED CIRCUIT

The feed circuit developed for the array allows the entire array to be driven by a single transmitter with 90° phase change between the currents in neighboring straps. Straps 1 and 3 are connected by a coaxial transmission line forming a resonant loop; straps 2 and 4 are connectetd to form a second loop. The loops are fed through an unmatched tee, allowing a power split between antenna pairs. This results in equal currents on all four straps. The expected behavior of the circuit has been confirmed in extensive tests with the full-scale mock-up.

Variation in the plasma resistive and reactive loading from the values for which the tuners are set causes changes in the relative amplitudes and phasing of the currents in each tee. The methods of ref. [6] were used to develop a lossy transmission line model including distributed coupling. This model is extremely accurate in predicting the circuit behavior over a range of frequencies.

Predictions of the model for effects of changes in plasma loading on antenna currents are shown in Fig. 5. In this case the relative phases of the currents on neighboring straps are insensitive to changes in resistive plasma loading, but the amplitude ratios are not. Alternate tuner settings can be chosen at which the current amplitudes are stable to these changes but the relative phasing is not. Since changes in the current amplitude and phases produces changes in the antenna spectrum, which in turn produces changes in loading, there is a self-consistent interaction between the tuning circuit and the plasma. The ORION full-wave code is being employed to understand this interaction and to simulate the performance of tuning algorithms to be used in actual experiments.

CONCLUSIONS

Toroidal wave number spectra have been measured on a mock-up of the four-strap FWCD antenna array for DIII-D. These measurements indicate that the directionality of the generated vacuum spectrum can be significantly improved by slotting the outer septa. Slotting the inner septum improves directionality and reduces the power division required between the two antenna pairs to achieve equal currents in all straps. Effects on loading and current drive efficiency remain to be calculated. A 2-D magnetostatic model of the mock-up yields spectra that approximate the measured spectra, but the effective location of appreciable currents in the model appears to be closer to the antenna backplane than would be inferred from the measured spectra. Future models should be done in three dimensions to include the full effects of Faraday shield and septum structures. A feed circuit developed for the system allows the array to be driven from a single transmitter with 90° phasing between straps and equal currents on all straps. A model of this feed circuit indicates that changes in plasma resistive and reactive loading can cause significant changes in current amplitude ratios and phasing between straps.

REFERENCES

[1] Mayberry M. J. *et al.*, AIP Conf. Proc. **190** (1989) 298.
[2] Baity F. W. *et al.*, AIP Conf. Proc. **190** (1989) 214.
[3] Mayberry M. J. *et al.*, General Atomics report GA-A19565 (submitted to *Nucl. Fusion*).
[4] Jaeger E. F. *et al.*, *Comput. Phys. Commun.* **40** (1986) 33.
[5] Ryan P. M. *et al.*, in Proc. 15th European Conf. on Controlled Fusion and Plasma Heating,
[6] Lamalle P. U., Messiaen A. M., and Vandenplas P. E., *IEEE Trans. Plasma Sci.* **PS-15** (1987) 60.

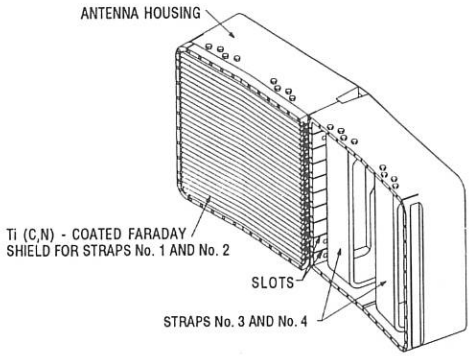

Fig. 1. The FWCD antenna for DIII-D.

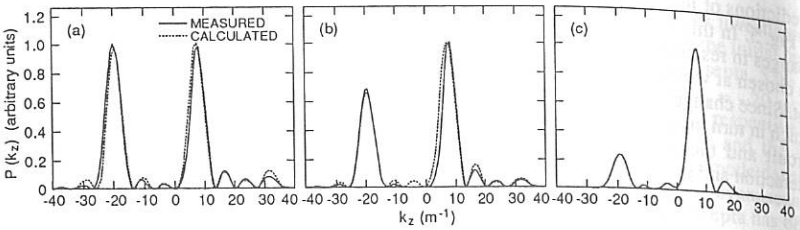

Fig. 2. Measured (solid lines) and predicted (dotted lines) vacuum k_z spectra.

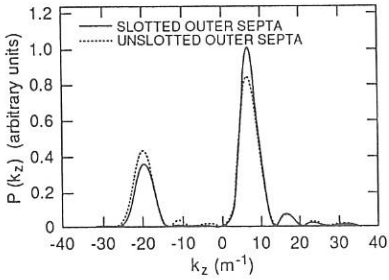

Fig. 3. Spectra with wave evanescence between the antenna and plasma cutoff layer.

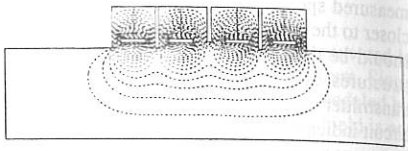

Fig. 4. Geometry and vector potential contours for 2-D magnetostatic calculation with solid outer septa and slotted inner septum.

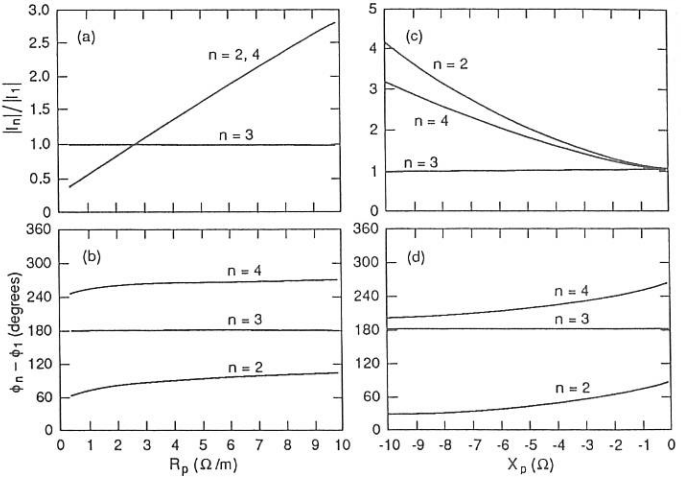

Fig. 5. Effect of changes in resistive plasma loading on (a) amplitudes and (b) phases of array element currents and of changes in reactive loading on (c) amplitude and (d) phases. "Phase stable" case: $X_{strap} = 63\ \Omega$.

CURRENT DRIVE VIA LANDAU DAMPING OF KINETIC ALFVEN WAVE IN TOROIDAL GEOMETRY

A. G. Elfimov* and S. Puri
Max-Planck Institut für Plasmaphysik, EURATOM Association,
Garching bei München, Federal Republic of Germany

It is found that Landau-damping of low-phase-velocity waves ($v_p \ll v_{te}$, the electron thermal speed) is profoundly affected by toroidicity. The proportion α_u of the wave energy imparted to the untrapped particles significantly exceeds their numerical fraction. Computed values of α_u versus v_p/v_{te} are presented. The implications of these results on low-phase-velocity-wave current drive are assessed.

REVIEW OF THE THEORY

The problem of Landau damping by trapped and passing particles in a Tokamak is analyzed in Ref.[1]. A simplified outline valid for low-frequency waves ($\omega \ll \omega_c$) starts with the linearized drift-kinetic equation

$$\frac{\partial f_0}{\partial t} + \frac{h_\theta v_\parallel}{r}\frac{\partial f_0}{\partial \theta} + \frac{inh_\phi v_\parallel}{R} f_0 - \frac{h_\theta v_\perp \sin\theta}{2R}\left(v_\perp \frac{\partial f_0}{\partial v_\parallel} - v_\parallel \frac{\partial f_0}{\partial v_\perp}\right) = -\nu f_0 + Q_0 \,, \qquad (1)$$

where $Q_0 = -\frac{e}{m} E_\parallel \frac{\partial F}{\partial v_\parallel}$, $f = F + f_0 \exp[i(n\phi - \omega t)]$, ϕ and θ are the toroidal and poloidal angles, f is the particle distribution function, F is the steady-state distribution assumed to be Maxwellian, $h_\phi = |B_\phi/B|$, $h_\theta = |B_\theta/B|$, n is the toroidal wave number, ν is the collision frequency, $E_\parallel = \sum E_m \exp(im\theta)$ is the electric field along the magnetic field direction and $v_\parallel$, $v_\perp$ are the velocity components along and perpendicular to the magnetic field direction. The plasma current is given by $j_\parallel = 2\pi e \int_{-\infty}^{\infty} v_\parallel \, dv_\parallel \int_0^{\infty} f_0 v_\perp \, dv_\perp$. The substitutions $v_\perp = u\sin\gamma$ and $v_\parallel = u\cos\gamma$, followed by the transformations $\theta' = \theta$ and $\Lambda = \sin^2\gamma\,(1 + \varepsilon\cos\theta)$ gives

$$v_\perp = u\sqrt{\frac{\Lambda}{1+\varepsilon\cos\theta}}$$

$$v_\parallel = su\sqrt{1 - \frac{\Lambda}{1+\varepsilon\cos\theta}}$$

$$\frac{\partial f_0^{(s)}}{\partial\theta} + i\left[\frac{nq}{1+\varepsilon\cos\theta} - \frac{s(\omega + i\nu)r}{h_\theta u\sqrt{1 - \frac{\Lambda}{1+\varepsilon\cos\theta}}}\right] f_0^{(s)} = \frac{\partial f_0^{(s)}}{\partial\theta} + i\chi^{(s)} f_0^{(s)} = G_0 \,, \qquad (2)$$

and

$$j_\parallel = \frac{\pi e}{1+\varepsilon\cos\theta} \int_0^{\infty} u^3 \, du \int_0^{1+\varepsilon\cos\theta} d\Lambda \sum_s s f_0^{(s)} \,, \qquad (3)$$

* Permanent Address: I. N. Vekua Institute of Physics and Technology, Sukhumi-14, 384914 USSR.

where

$$G_0 = -\frac{r}{h_\theta}\frac{e}{m}\frac{E_\parallel}{v_\parallel}\frac{\partial F}{\partial v_\parallel} = \frac{erE_\parallel}{mh_\theta v_{te}^2}F$$

$$\chi^{(s)} = \frac{nq}{1+\varepsilon\cos\theta} - \frac{s(\omega+i\nu)r}{h_\theta u\sqrt{1-\frac{\Lambda}{1+\varepsilon\cos\theta}}}$$

$q = rh_\phi/R_0h_\theta$ is the safety factor, $s = \pm 1$ for $v_\parallel \gtrless 0$ and the s summation extends over $s = \pm 1$. Equation (2) possesses the solution

$$f_0^{(s)} = \exp\left(-i\int_{-\theta_m}^{\theta}\chi^{(s)}\,d\eta\right)\left[\int_{-\theta_m}^{\theta} G_0\exp\left(i\int_{-\theta_m}^{y}\chi^{(s)}\,d\eta\right)dy + C^{(s)}\right], \tag{4}$$

where θ_m defines the maximum azimuthal extent of the particle's excursion. For passing particles $\theta_m = \pi$ while for the trapped particles $\theta_m = \cos^{-1}[(\Lambda-1)/\varepsilon]$. The integration constants $C^{(s)}$ are determined by the boundary conditions $f_0^{(1)}(\theta_m) = f_0^{(-1)}(\theta_m)$, $f_0^{(1)}(-\theta_m) = f_0^{(-1)}(-\theta_m)$ for the trapped particles and $f_0^{(s)}(\pi) = f_0^{(s)}(-\pi)$ for the untrapped particles. The current $j_\parallel$ for an electric field excitation $E_\parallel = E_m\exp(im\theta)$ becomes

$$j_\parallel = \frac{\omega_{pe}^2\epsilon_0}{i\omega}\sum_s E_m\left[\Psi_{u,m}^{(s)} + \Psi_{t,m}^{(s)}\right], \tag{5}$$

where

$$\Psi_{u,m}^{(s)} = \sqrt{\frac{2}{\pi}}\frac{isr\omega}{h_\theta v_{te}(1+\varepsilon\cos\theta)}\int_0^\infty U^3\exp(-U^2)\,dU\int_0^{1-\varepsilon}d\Lambda$$
$$\times\left[\int_{-\pi}^{\theta}\frac{\exp\left(imy - i\int_y^\theta\chi^{(s)}\,d\eta\right)}{1-\exp\left(-i\int_{-\pi}^{\pi}\chi^{(s)}\,d\eta\right)}dy\right.$$
$$\left.+\int_\theta^\pi\frac{\exp\left(imy - i\int_{-\pi}^{\theta}\chi^{(s)}\,d\eta - i\int_y^\pi\chi^{(s)}\,d\eta\right)}{1-\exp\left(-i\int_{-\pi}^{\pi}\chi^{(s)}\,d\eta\right)}dy\right], \tag{6}$$

$$\Psi_{t,m}^{(s)} = \sqrt{\frac{2}{\pi}}\frac{isr\omega}{h_\theta v_{te}(1+\varepsilon\cos\theta)}\int_0^\infty U^3\exp(-U^2)\,dU\int_{1-\varepsilon}^{1+\varepsilon\cos\theta}d\Lambda$$
$$\times\left[\int_{-\theta_m}^{\theta_m}\frac{\exp\left(imy - i\int_{-\theta_m}^{\theta}\chi^{(s)}\,d\eta - i\int_y^{\theta_m}\chi^{(-s)}\,d\eta\right)}{\exp\left(-i\int_{-\theta_m}^{\theta_m}\chi^{(s)}\,d\eta\right) - \exp\left(-i\int_{-\theta_m}^{\theta_m}\chi^{(-s)}\,d\eta\right)}dy\right.$$

$$-\int_{-\theta_m}^{\theta} \frac{\exp\left(imy - i\int_{y}^{\theta}\chi^{(s)}\,d\eta - i\int_{-\theta_m}^{\theta_m}\chi^{(-s)}\,d\eta\right)}{\exp\left(-i\int_{-\theta_m}^{\theta_m}\chi^{(s)}\,d\eta\right) - \exp\left(-i\int_{-\theta_m}^{\theta_m}\chi^{(-s)}\,d\eta\right)}\,dy$$

$$-\int_{\theta}^{\theta_m} \frac{\exp\left(imy - i\int_{-\theta_m}^{\theta}\chi^{(s)}\,d\eta - i\int_{y}^{\theta_m}\chi^{(s)}\,d\eta\right)}{\exp\left(-i\int_{-\theta_m}^{\theta_m}\chi^{(s)}\,d\eta\right) - \exp\left(-i\int_{-\theta_m}^{\theta_m}\chi^{(-s)}\,d\eta\right)}\,dy\Bigg], \tag{7}$$

ϵ_0 is the permittivity of free space and $U^2 = u^2/2v_{te}^2$. The power absorbed per unit volume is given by $P = \frac{1}{2}\Re\left[j_{\|}E_{\|}^*\right]$. Integrating over ϕ and θ, gives the fraction of the power imparted by the wave to the untrapped particles at radius r as

$$\alpha_u(r) = \frac{\Re\int_{-\pi}^{\pi}\sum_s \Psi_{u,m}^{(s)}(1+\varepsilon\cos\theta)\exp(-im\theta)\,d\theta}{\Re\int_{-\pi}^{\pi}\sum_s\left[\Psi_{u,m}^{(s)} + \Psi_{t,m}^{(s)}\right](1+\varepsilon\cos\theta)\exp(-im\theta)\,d\theta} \tag{8}$$

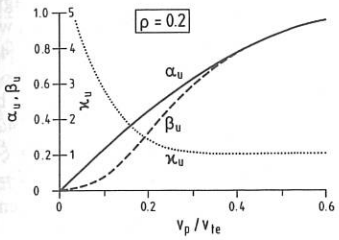

Fig. 1

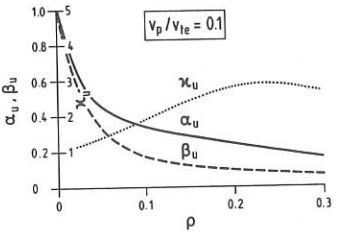

Fig. 2

COMPUTATIONAL RESULTS

The parameters used in the computations are $R_0 = 5\,m$, plasma radius $a = 1.25\,m$, $\rho = r/a$, aspect ratio $A = R_0/a = 4$, $q = (1-\rho^2+\rho^4/3)^{-1}$, $n_e = 2\times10^{20}\,m^{-3}$, $T_e = 25\,keV$, $m = 0$ and $n = 8$.

Figure 1 is a plot of α_u, the fractional energy absorbed by the untrapped electrons and β_u, their fractional abundance versus v_p/v_{te} for $\rho = 0.2$. As expected, $\kappa_u = \alpha_u/\beta_u \approx 1$ for larger phase-velocity waves ($v_p/v_{te} \gtrsim 0.4$). For the low-phase-velocity-wave ($v_p/v_{te} \lesssim 0.4$) current drive, κ_u exceeds unity because of the dominant presence of trapped electrons with an inherently diminished capacity for Landau damping. These results would lead to an upward revision of the current-drive efficiency by the *subthermal* schemes. For typical kinetic-Alfven-wave current drive [2] parameters with $v_p/v_{te} \approx 0.1$, $\alpha_u \approx 0.25$ and $\kappa_u \approx 2.8$, i.e., the power coupled into the untrapped electrons exceeds their relative abundance almost by a factor of three.

Figure 2 shows α_u, β_u and κ_u as a function of ρ assuming $v_p/v_{te} = 0.1$. A broad maximum with $\kappa_u \approx 2.9$ occurs at $\rho \approx 0.25$. The initial increase in κ_u is caused by the increase in the trapped particle population at larger ρ.

DISCUSSION AND CONCLUSIONS

We find significant enhancement in the energy absorbed by the passing particles in comparison with their numerical abundance. For the case of kinetic-Alfven-wave current drive this enhancement is of the order of three, so that almost a quarter of the wave energy is deposited in the passing particles constituting less than one-tenth of the population resonant with the wave at $v_p/v_{te} \approx 0.1$.

Furthermore, in Ref.[2] it is pointed out that the strict requirements of the conservation of the canonical angular momentum would lead to substantial recovery of the wave momentum, initially imparted to the trapped particles, for the purpose of current drive. The trapped electrons suffer inward Ware pinch [3] as they gain momentum from the wave. In *steady state*, an equal number of trapped electrons undergo inverse Ware pinch via collisions with the *bulk-plasma* population. The fraction of the momentum initially imparted to the trapped particle population is given by $\alpha_t = 1 - \alpha_u$. The inverse Ware pinch transfers the fraction

$$\alpha_{t\to u} = \frac{\tilde{\nu}_{ee}}{\tilde{\nu}_{ee} + \tilde{\nu}_{ei}} (1 - \sqrt{\varepsilon})\alpha_t \approx \frac{K(\xi)\nu_{ee}}{\nu_{ee} + \nu_{ei}} (1 - \sqrt{\varepsilon})\alpha_t \approx \frac{K(\xi)}{1 + .5Z} (1 - \sqrt{\varepsilon})(1 - \alpha_u)$$

back to the circulating *bulk-plasma* electrons, where $(1 - \sqrt{\varepsilon})$ is the fraction of the circulating electrons in the plasma bulk, ν_{ee} and ν_{ei} are Spitzer collision frequencies and $K(\xi)$ is a correction factor due to the magnetic field effects on ν_{ei}. Anomalous magnetic field effects lead to an enhancement of ν_{ei} for the trapped electrons with $r_{ce} \lesssim \lambda_D$, where r_{ce} and λ_D are the electron gyroradius and plasma Debye length, respectively [4]. If one assumes that the wave momentum given to the trapped electrons with $r_{ce}/\lambda_D \leq \xi$ is irretrievably lost, while the remainder is collisionally redistributed between the bulk-plasma electrons and ions in the ratio ν_{ee}/ν_{ei}, one obtains $K(\xi) = \exp\left(-\omega_{ce}^2\xi^2/4\omega_{pe}^2\right)$. The currently available information is insufficient to ascribe a precise value to ξ; we assume a conservative figure of $\xi = \sqrt{2}$. Further assuming $\omega_{ce}^2/\omega_{pe}^2 = 1/2$ and $Z = 1.5$ gives $K(\xi) \approx 0.78$ and $\alpha_{t\to u} \approx 0.30$, so that the net fraction of the wave momentum contributing to the kinetic-Alfven-wave current drive becomes

$$\alpha_u^T = \alpha_u + \alpha_{t\to u} \approx 0.55 \; . \tag{9}$$

This value of α_u^T is substantially the same as was found in Ref.[2] which did not include the mutually cancelling effects arising from (i) increase in the fraction of energy absorbed by the untrapped electrons and (ii) anomalous magnetic-field effects on ν_{ei}.

One concludes that a current-drive efficiency of $R_0 n_{20} I/P \approx 2$ (similar to that found in Ref.[2]) would be feasible using the subthermal kinetic-Alfven-wave current drive. This efficiency figure is at least a factor of five higher than the alternative approaches such as lower-hybrid and fast-wave current drives.

REFERENCES

[1] N. I. Grishanov and F. M. Nekrasov, Sov. Phys. Plasma Phys. **16** (1990)230.
[2] S. Puri and R. Wilhelm, in *8th Topical Conference on Radio-Frequency Power in Plasmas*, Irvine, California, (1989); published in *AIP Conference Proceedings No. 190*, AIP, New York, (1989)458.
[3] A. A. Ware, Phys. Rev. Lett. **25** (1970)15.
[4] K. Matsuda, Phys. Rev. Lett. **49** (1982)1486.

RF CURRENT DRIVE BY A STANDING ALFVEN WAVE IN THE R-O DEVICE AS A POSSIBLE EFFECT OF RF HELICITY INJECTION

A.G.Kirov, A.V.Sukachov, D.A.Voytenko, M.A.Stotland

I.N.Vekua Institute of Physics and Technology, Sukhumi, USSR

Anomalous steady-state current drive by a standing Alfven wave is observed in the R-O stellarator. The functional dependence of the current upon the plasma parameters indicates the current is related with RF helicity injection.

1. Steady-state currents in the R-O stellarator are generated both by travelling and standing Alfven waves (AW) /1,2/. The current may be generated by travelling AW via their momentum transfer to electrons, and also, by standing or travelling AW due to an average RF force acting both on electrons and ions (so-called RF helicity injection /3/). For the second case, according to the estimates, the current drive efficiency may be much greater than that of a dragging current /3/.

2. The experiments have been done in the R-O $l=3$ stellarator with a quartz discharge chamber: $R=50$ cm, $b=5$ cm, $a_{pl}=3.5$ cm, $B_T \leq 8$ kGs, $\iota_o \leq 0.8$, $\tilde{P}<400$ kW, $\bar{n}_e=(0.5\text{-}8)10^{13}$ cm^{-3}, $\bar{T}<100$ eV, H_2, $I_{OH}=0$. The helical RF antenna consists of 8 helical conductors enclosing the entire discharge chamber. It allows to excite standing or travelling helical modes with $m=\pm 2/n=\pm 2$, $m=\pm 1/n=\pm 1$, where m and n are poloidal and toroidal wave numbers, respectively ($K_\phi=m/r$, $K_z=-n/R$). Most of experiments have been carried out with the $m=2/n=2$ mode with the frequency $f=1.2$ MHz. Plasma densities were measured by a $\lambda = 2.3$ mm microwave interferometer. Plasma temperatures were obtained from diamagnetic and double Langmuir probe measurements. Poloidal and radial RF magnetic field components were

detected by means of a magnetic probes set, the electrical field ($\tilde{E}z$, $\tilde{E}r$) was measured using a double probe.

3. The experiments with the AW excited by an external helical standing RF field have shown that there arises a steady - state plasma current up to 0.6 kA (fig.1). The current had direction so it inereased the angle of stellarator rotational transform. The sign of this current changed by the changing the direction of the toroidal magnetic field ($\vec{I}_{sw}\vec{B}_T > 0$). Fig.2 shows experimental dependences of I_{sw} currents versus toroidal magnetic field, average plasma temperature and density. As it is seen, the scaling for the current is $I_{sw} \propto \tilde{P}\bar{T}^{\gamma}/B_T$, $\gamma = 1\text{-}1{,}5$. Theoretically, such dependence may be derived from the averaged RF force acting on plasma species. This force is proportional to the $[\vec{V} \times \vec{B}]$ term in the equation of motion and it been reduced to the $\tilde{\vec{E}} \cdot \tilde{\vec{B}}$ product, i.e., the helicity injection. A similar scaling is considered in ref. /3/.

4. Travelling AW generate a dragging current as a result of their momentum absorption by electrons. The direction of this current is defined by that of the wave propagation along the torus, i.e. bythe sign of $K_z = \vec{K}\cdot\vec{B}_T/B_T \gtrless 0$. In all our experiments, the current driven by a travelling wave with $K_z = -|n|/R < 0$ ($\vec{I}_{Tw}\vec{B}_T > 0$) was higher than the one driven by a wave with $K_z = +|n|/R > 0$ ($\vec{I}_{Tw}\vec{B}_T < 0$). This fact indicates that an additional unidirectional I_h current is generated. The direction of this current coincides with that of the current generated by a standing AW ($\vec{I}_h\vec{B}_T > 0$, $\vec{I}_{sw}\vec{B}_T > 0$). In some modes with travelling AW (when $K_z > 0$, $\vec{I}_{Tw}\vec{B}_T < 0$), the additional I_h current which we regard as due to RF helicity injection may exceed the dragging current ($|I_h| > |I_{Tw}|$). Hence, the plasma current changes its sign in the circumstances: $\vec{I}_{pl}\vec{B}_T > 0$ (fig. 3). These regimes ($K_z > 0$, $\vec{I}_{pl}\vec{B}_T > 0$) usually appear for relatively large toroidal magnetic fields and plasma densities and this fact may be due to different dependences of the dragging current, I_{Tw}, and the current driven via RF helicity injection, I_h, upon the plasma parameters: $I_{Tw} \propto \tilde{P}\bar{T}_e^{3/2}K_{\parallel}/\omega n_e$

and $I_h \propto \bar{P}\bar{T}_e^{3/2}/B_T$.

5. In regimes with relatively high RF power input level ($\bar{P}/V \geq 10$ W/cm^3), the steadystate current generation is accompanied with nonlinear distortions of waveforms in the plasma interior: there arises deep regular modulation of $\tilde{E}$ and $\tilde{B}$ RF field oscillations which may develop into regular oscillation packets /2/.

References

1. R.A.Demirkhanov, A.G.Kirov, L.F.Ruchko, A.V.Sukachov. JETP Lett., 33, 1, 31-34, 1981.
2. A.G.Kirov et al. 16 Europ. Conf. on Pl. Phys. and Contr. Fusion, Venice, 1989, P8B12.
3. V.S.Chan, R.L.Miller, T.Ohkawa. General Atomics Report GA-A19585, 1989.

Captions

Fig.1. Standing AW, $m=\pm2/n=\pm2$. $B_T = 3.2$ kGs, $\iota_o=0.31$.

Fig.2. Standing AW, $m=\pm2/n=\pm2$.

Fig.3. Travelling AW, $m=-2/n=-2$, $K_z > 0$, $I_{Tw} < 0$. $\iota_o=0.31$.
a) $B_T=2.5$ KGs, b) $B_T=4.2$ KGs.

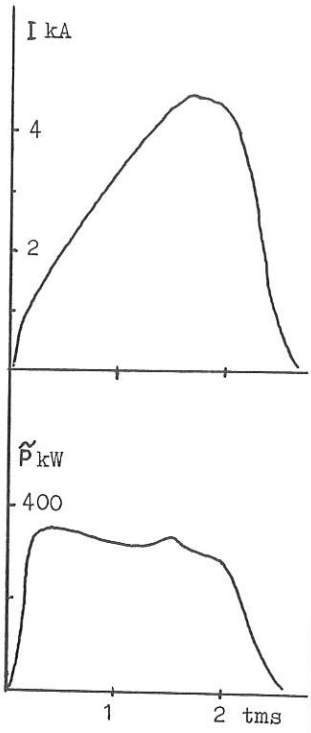

Fig. 1

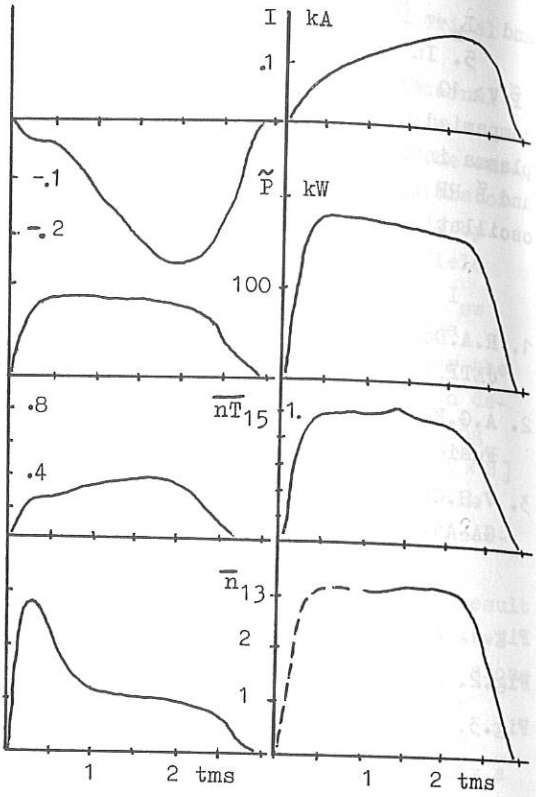

Fig.3

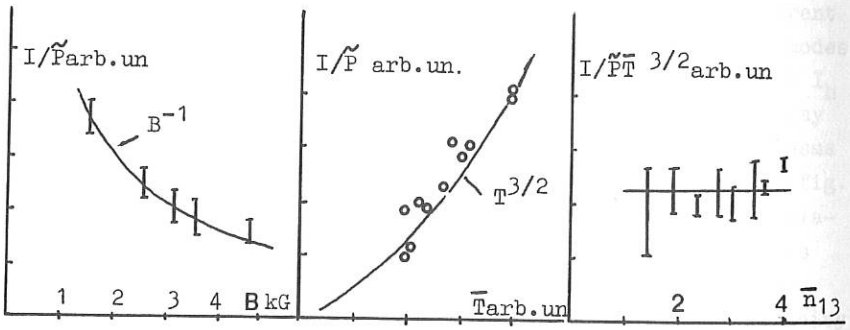

Fig.2

PROFILE CONTROL WITH LOWER HYBRID WAVES ON ASDEX

F.X.Söldner, R.Bartiromo[1], S.Bernabei[2], R.W.Harvey[3], F.Leuterer, K.McCormick, H.D.Murmann, LH-team, NI-team, ASDEX-team

Max-Planck-Institut für Plasmaphysik, EURATOM Association
D-8046 Garching, Fed. Rep. of Germany

[1]ENEA Frascati, Italy, [2]Princeton Plasma Physics Laboratory, USA,
[3]General Atomics, San Diego, USA

Introduction

Optimization of the local shape of the current density profile j(r) should improve the MHD stability and therefore the confinement behaviour of tokamaks. Sawteeth could be stabilized on ASDEX with broadening of the current profile by LH-current drive /1,2/. Also first experiments on the correlation between local current profile modifications and the form of the wave spectrum launched from the antenna had been performed with a single antenna for LH waves at 1.3 GHz /3/. The new LH system at 2.45 GHz provides high flexibility of the wave spectrum for the main goal of current profile control /4,5/.

Control of MHD activity

The impact of LH on sawteeth, m=1-modes and m=2-modes was studied for different $N_{||}$-spectra, in current drive operation and with symmetric phasing. The sawtooth repetition period τ_{st} varies strongly with the LH power, as seen from Fig. 1. The increase of τ_{st} during LH application correlates with the drop in ohmic power input. It is strongest for current drive with low $N_{||}$ ($\Delta\varphi = 75^o$, $\overline{N}_{||} = 1.8$). No change is seen with symmetric LH spectra at high $N_{||}$ ($\Delta\varphi = 180^o$, $\overline{N}_{||} = 4.4$) and opposite current drive ($\Delta\varphi = -90^o$, $\overline{N}_{||} = 2.2$). For symmetric spectra with $\overline{N}_{||} = 2.2$, the sawtooth period saturates at about twice the ohmic value $\tau_{st}^{LH} = 2\tau_{st}^{OH}$ for $P_{LH} >$ 300 kW. In this regime the reduction in P_{OH} also saturates. The variation of the sawtooth repetition period may be explained mainly by the enhanced electrical conductivity in the presence of suprathermal electrons. With LH-current drive sawteeth are suppressed. The threshold power $P_{LH} \approx 300$ kW is nearly independent of phasing. Stabilization by kinetic effects due to the suprathermal electron population can be ruled out as a larger suprathermal electron population is produced with symmetric spectra with $\overline{N}_{||} = 2.2$ than with the corresponding current drive spectrum.The reduction of the dc electric field also seems not to be decisive for sawtooth stabilization: Sawteeth persist for symmetric wave spectra with $\overline{N}_{||} =$ 2.2 up to the highest LH powers where P_{OH} and thus the electric field is reduced below the values at which sawteeth are stabilized by LH-current drive. Sawtooth suppression is achieved only with current drive spectra and seems to be related to changes in the current profile.

The LH power required for sawtooth stabilization increases with density. The same scaling is found for the old LH system on ASDEX at 1.3 GHz and the new system at 2.45 GHz as shown in Fig. 2. The resulting drop in P_{OH}, however, is larger with 2.45 GHz. A larger fraction of LH-driven current is therefore required with the higher LH frequency, and the narrower $N_{||}$-spectrum.

The m=1 mode is still present after stabilization of sawteeth as also found on PLT /6/. A q=1 surface therefore continues to exist in the sawtooth-free plasma. The amplitude of the m=1 mode grows to a much higher steady-state level after sawteeth are suppressed. With higher LH power also the m=1 mode is stabilized. In this case the internal inductance l_i slowly decreases, indicating a flattening of the current profile. Again, as for sawtooth suppression, stabilization of the m=1 mode is obtained with LH in current drive operation only. After suppression of the m=1-mode the central electron temperature rises strongly and the radial profile is peaking. The increase in the central electron temperature T_{eo}, in the peaking factor $Q_{T_e} = T_{eo} / \langle T_e \rangle$ and in the total energy content ΔW_p^{dia} with LH power is compared in Fig. 3 for current drive and symmetric spectra, both with $\overline{N}_{||} = 2.2$. Up to a power level of $P_{tot} \approx 750$ kW no difference is seen between the two spectra. For higher powers much stronger central heating, peaking of $T_e(r)$ and improved global confinement - in accordance with the larger ΔW_p - are achieved with LH current drive, compared with application of symmetric LH spectra. The bifurcation occurs at the threshold power for stabilization of the m=1 mode.This is about twice the threshold for sawtooth suppression. Stabilization of the m=1 mode was also achieved with LH current drive during NBI. Peaking of $T_e(r)$ and enhanced global confinement were also obtained in this case. While the electron temperature profile peaks strongly up to values of $Q_{T_e} \approx 5$, the current profile j(r) flattens. Current and temperature profiles can therefore be completely decoupled with LH current drive.

Local Control of the Current Profile

Optimization of plasma profiles requires control of the local LH power deposition profile. With low-$N_{||}$ current drive spectra a reduction of l_i is observed in conditions where the m=1 mode is stabilized. Local current density profile measurements with the Li-beam show only small changes of j(r) with slight flattening in the central region. The largest drop in l_i is obtained with compound $N_{||}$ spectra with low-$N_{||}$ current drive phasing applied to one grill antenna and high-$N_{||}$ phasing to the other one. This is documented in Fig. 4 for a discharge where LH waves are launched first with 700 kW in current drive phasing ($\Delta\varphi = 75^o$, $\overline{N}_{||} = 1.8$). Then in a second phase a symmetric spectrum ($\Delta\varphi = 180^o$, $\overline{N}_{||} = 4.4$) with 300 kW is added. During the first phase both β_p^{dia} and $\beta_p^{equ} + l_i/2$ increase, the latter more strongly owing to the anisotropy $\beta_p^{||} > \beta_p^{\perp}$ produced with LH. In the second phase β_p^{dia} rises still slightly, while $\beta_p^{equ} + l_i/2$ decreases strongly. The long time constant indicates a reduction of l_i and therefore appreciable flattening of j(r). Li-beam measurements demonstrate in fact a clear modification of the current distribution in the cases of such low-$N_{||}$ / high-$N_{||}$ compound spectra. During the combined injection the current density is diminished in the centre and also near the edge, while it rises between r /a=0.25 and r/a=0.5. The central region of flat current distribution grows and the gradient of j steepens in the region further outside. The safety factor q rises above 1 over the

whole plasma cross-section. This is consistent with the stabilization of the m=1 mode in these discharges.
The results on current profile broadening with different LH spectra are summarized in Fig.5. With low-$N_{||}$ spectra ($\Delta\varphi = 90^o$) a slight drop of l_i is seen only at high power. With high-$N_{||}$ spectra of symmetric phasing ($\Delta\varphi = 180^o$), l_i starts decreasing already at the lowest power applied. The latter may be explained by a broad profile of LH-generated suprathermal electrons which carry then part of the inductively driven current. With simultaneous injection of low and high-$N_{||}$ spectra the drop of l_i is larger than the sum from both spectra separately. The central electron heating from LH-current drive diminishes when the high-$N_{||}$ spectrum is added.Therefore we have to conclude that the deposition zone of the low-$N_{||}$ current drive spectrum is shifted more toward the periphery by the high-$N_{||}$ spectrum. The injection of combined $N_{||}$ spectra therefore provides a means to control the deposition profile of LH waves and the resulting current density profile.

The Lower Hybrid experiments are performed in collaboration between IPP Garching, ENEA Frascati and PPPL Princeton.

References

/1/ McCormick, K., et al., Phys.Rev.Lett. 58, 491 (1987).
/2/ Söldner, F.X., et al., Phys.Rev.Lett. 57, 1137 (1986).
/3/ Leuterer, F., et al., 13th Europ. Conf. on Contr. Fusion and Plasma Physics, Schliersee 1986, Vol. 2, 409.
Söldner, F.X., et al., 14th Europ. Conf. on Contr. Fusion and Plasma Physics, Madrid 1987, Vol. 2, 831.
/4/ Leuterer, F., et al., 16th Europ. Conf. on Contr. Fusion and Plasma Physics, Venice 1989, Vol. 4, 1287.
/5/ Leuterer, F., et al. , 8th Topical Conf. on Radio Frequency Power in Plasmas, Irvine 1989.
/6/ Bernabei, S., et al., 11th IAEA Conf., Kyoto 1986, Vol.1, 503.

Figure Captions

Fig. 1: Variation of sawtooth period and residual ohmic power input with LH power for different $N_{||}$-spectra. $B_t = 2.8$ T, $I_p = 420$ kA, $\bar{n}_e = 1.4 \cdot 10^{13}$ cm^{-3}.

Fig. 2: Variation of the threshold LH power P^*_{LH} for sawtooth stabilization and the corresponding drop in ohmic power input $\Delta P^{LH}_{OH} / P^{OH}_{OH}$ with density, for the two LH systems at 1.3 and 2.45 GHz on ASDEX.

Fig. 3: Variation of central electron temperature T_{eo}, peaking factor $Q_{T_e} = T_{eo} / \langle T_e \rangle$ and increment in energy content, ΔW^{dia}_p with total power input $P_{tot} = P_{OH} + P_{LH}$ for LH current drive (LHCD) and symmetric LH spectra (LHH).

Fig. 4: Temporal evolution of the diamagnetic beta β^{dia}_p and the sum of equilibrium beta and internal inductance, $\beta^{equ}_p + l_i/2$, during injection of a narrow current drive spectrum and a compound spectrum, as plotted in the lower part of the figure.

Fig. 5: Variation of the drop of internal inductance Δl_i with LH power for wave spectra with different phasings and for compound spectra.

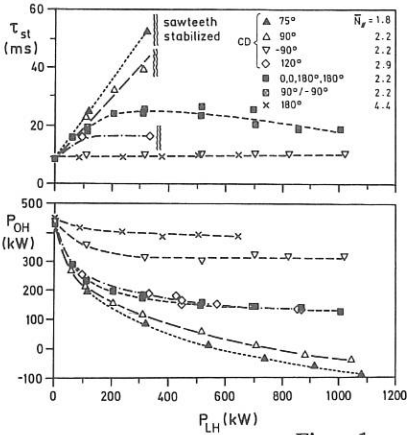

Fig. 1

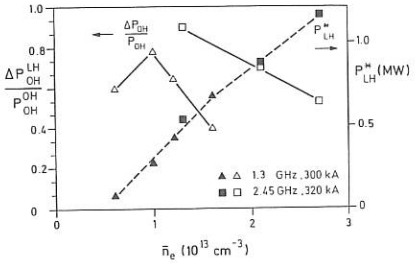

Fig. 2

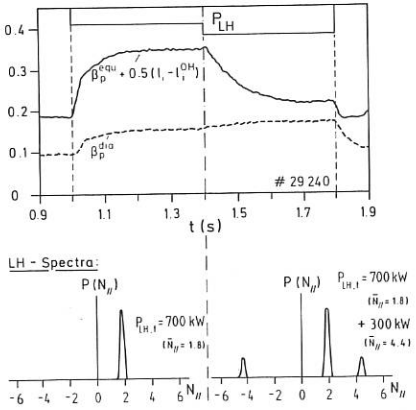

Fig. 4

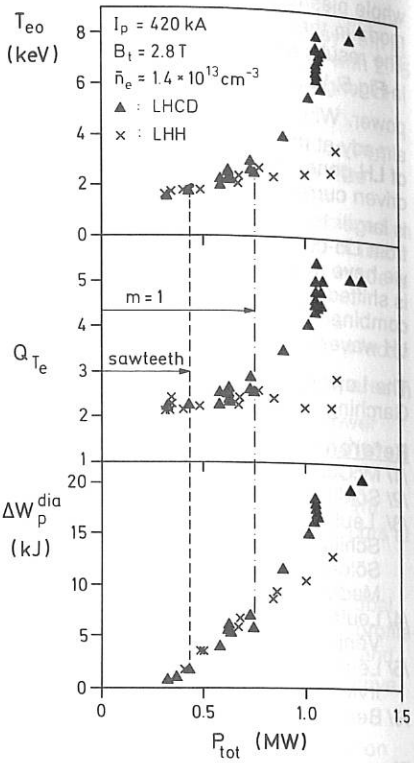

Fig. 3

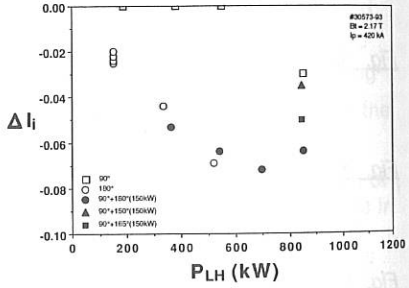

Fig. 5

TEARING MODE STABILIZATION BY LOCAL CURRENT DENSITY PROFILING IN TOKAMAK.

M.P.GRYAZNEVICH*, L.E.ZAKHAROV, A.A.SUBBOTIN, N.V.CHUDIN
I.V.KURCHATOV INSTITUTE OF ATOMIC ENERGY, MOSCOW, USSR.
* IOFFE PHYSICAL-TECHNICAL INSTITUTE, USSR ACADEMY OF SCIENCE, LENINGRAD, USSR.

The m/n=2/1 tearing is unstable in tokamaks under the condition $q_o > 1$ if there are not some peculiarities near the resonant surface $\rho_{2/1}$, $q(\rho_{2/1}) = 2$. The possibility of the tearing mode stabilization by addition of portion of a current which is localized near the resonance surface is analyzed in the paper. The calculations of a necessary stabilization criteria of the 2/1 tearing mode for the present ITER geometry are performed. The experimental test of a similar stabilization has been performed on TUMAN-3 tokamak, where the local current redistribution was produced by a small rapid increase of the total current during flat top stage at $q_a = 3.5 - 4$ when the 3/1 mode dominated. Depending on q_a value such a procedure either suppreses or destabilizes the 3/1 mode.

1. ITER tearing mode stability criteria calculations.

The following approximations has been made in the calculations:

- the plasma pressure was assumed to be zero, $\beta_j = 0$,
- the perturbations of the longitudinal magnetic field were chosen to be zero,
- a single helicity test function inside the plasma in energy principle for the tearing mode was considered, together with exact calculation of the vacuum magnetic energy.

The first constraint corresponds to the Start Of Flat Top in the ITER scenario. Two others mean that the calculated stability criteria is the necessary one. (In a circular cylinder case such a procedure gives the exact stability condition).

In Fig.1 the dependence of the tearing stability parameter $\rho_{2/1}\Delta'$ is shown as function of the internal inductance l_i (in ITER $l_1(3)$ definition) for current ITER geometry R = 6 m, a = 1.98 m, b/a = 1.98, δ = 0.2, I_{pl} = 22 MA, B_t = 4.85 T. The current distribution was specified in the form

$$j(\psi,r) = j_0\left[1 - \left(\frac{\psi - \psi_0}{\psi_b - \psi_0}\right)^{\nu_1}\right]^{\nu_2}\frac{R}{r} \qquad (1)$$

where the parameters j_0, ν_1, ν_2 has been adjusted to the prescribed I_{pl}, q_0, l_i values.

The result is that even the necessary stability criteria is violated for $q_0 > 1$ and it is marginal for $q_0 = 1$. The calculations with the triangularity δ = 0.4 show the insensitivity of the necessary stability criteria to this parameter. Note, that the tearing mode stability criteria predicts an opposite tendency from the ideal stability calculations.

The tearing mode can be suppressed by the additional current, localized on the mode resonance surface. For a pressureless plasma it is possible to obtain a general stabilization criteria for arbitrary cross-sections in the asymptotic limit $w/\rho_{m/n} \ll 1$. For a simplest additional current profile (parallel component $\Delta j_\parallel$)

$$\Delta j_\parallel(\rho) = \begin{cases} \Delta j_\parallel, & \text{at } \rho_{m/n}-\varepsilon_l < \rho < \rho_{m/n} + \varepsilon_r \\ 0, & \text{at } \rho < \rho_{m/n}-\varepsilon_l \quad \text{or} \quad \rho > \rho_{m/n}+\varepsilon_r \end{cases} \qquad (2)$$

the stabilization criteria has the form

$$\rho_{m/n}\Delta' = \frac{1}{\gamma}\frac{0.4\pi\Delta j_\parallel R}{\mu' B_t \rho_{m/n}}\left(\frac{\rho_{m/n}}{\varepsilon_r} + \frac{\rho_{m/n}}{\varepsilon_l}\right) \qquad (3)$$

where $\gamma = \left\langle \frac{g_{22}}{\sqrt{g}} \right\rangle / \left\langle \frac{\sqrt{g}}{g_{33}} \right\rangle + \frac{1}{q^2}\left\langle \frac{g_{22}}{\sqrt{g}} \right\rangle^2$ is a geometry factor, ρ is a radial coordinates in a flux coordinate system, $\mu = 1/q$.

Assuming $\varepsilon_l = \varepsilon_r$, $w = \varepsilon_l + \varepsilon_r$ the additional total current ΔI_{pl} can be written in the form: $\Delta I_{pl} = \Delta_{0.2}(w/0.2)^2$, where a normalization of w on 0.2 m is introduced for ITER. The calculations of $\Delta I_{0.2}$ for ITER on the basis of the necessary stability criteria are present in Fig.2 and gives a reasonable level of the additional current.

2. TUMAN-3 experiment with a rapid additional current ramp-up.

Attempts of a local current profile changing has been performed in the TUMAN-3 tokamak by a fast additional current ramp-up during a flat top stage in regimes with q_a = 3.5 - 4.0 (R/a = 0.55/0.24, in this experiments $B_t \cong 0.5$ T, I_{pl} = 70 - 100 kA, $T_e(0) \cong 0.4$ kev, $\bar{n}_e \cong 2 \times 10^{13} cm^{-3}$). In these regimes the m/n = 3/1 MHD activity was dominated. The penetration of the 10% additional current was simulated by the ASTRA code [2] taking into account the measurements of $T_e(\rho)$, $n_e(\rho)$, $U_s(t)$, $(\beta+l_i/2)(t)$. The results are presented on Fig.3. In a periphery plasma the semi-width of the additional current profile Δj was (0.1 - 0.2)a in the initial stage with the extension of the additional current profile at the next times. Nevertheless, the localization of the additional current gives the possibility to affect on stability of the plasma. In the experiment the increase of the total current from 76 to 85.2 kA (q_a=4 and q_a=3.6 during 0.4 ms excites the 3/1 mode MHD activity (Fig.5a), while the increase of the total current from 86.4 to 96.3 kA (q_a=3.57 and q_a=3.2) suppresses the initially unstable 3/1 mode (Fig.5b). The results of the corresponding current profile simulation together with the tearing mode stability calculations are shown in Fig.4a,b and agree qualitatively with the experimental observations.

It was predicted that even in the strongly elongated ITER plasma the m/n = 2/1 tearing mode is unstable for smooth current profiles. The generation of an additional current density which is localized near the q=2 resonance surface can stabilize this MHD mode in accordance with the obtained stabilization criteria (3). The TUMAN-3 experiment have confirmed qualitatively such a stabilization.

References:

1. L.E.Zakharov, A.A.Subbotin, N.V.Chudin. M=2 tearing mode stabilization in ITER. ITER-IL-Ph-11-o-2-S.

2. G.V.Pereverzev, P.N.Yushmanov. Prepr. of Kurchatov Institute of Atomic Energy, IAE-4545/15, 1987.

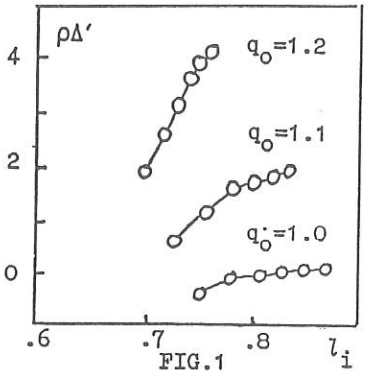

FIG.1

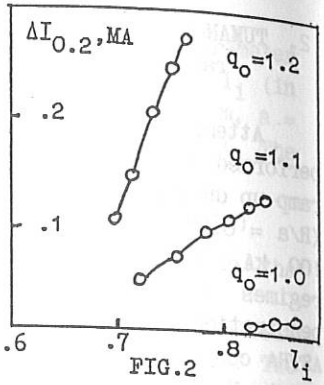

FIG.2

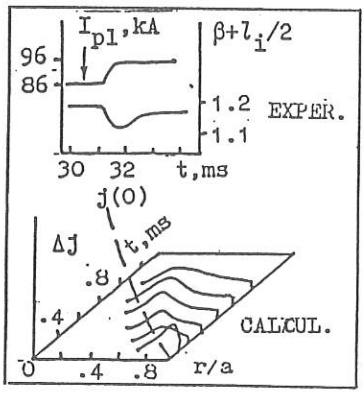

FIG.3

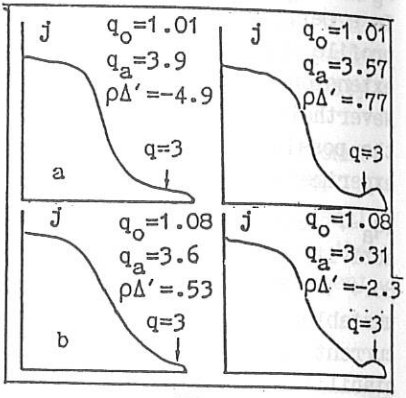

FIG.4

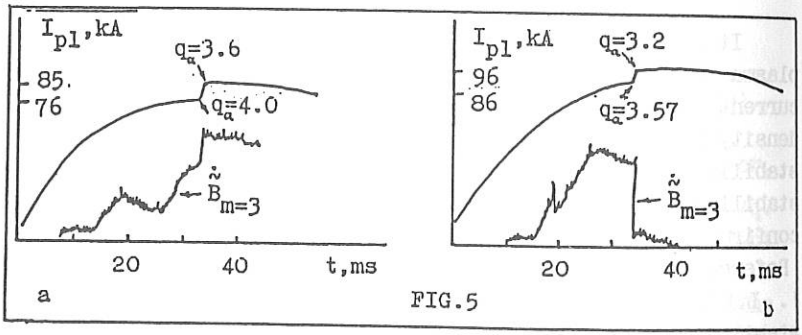

FIG.5

SURFACE WAVE ANTENNA FOR EXCITATION OF TRAVELLING FAST MAGNETOSONIC OR ION BERNSTEIN WAVES IN PLASMA

A.V.Longinov, V.A.Lukinov

Kharkov Institute of Physics and Technology, Kharkov, USSR

Introduction. The possibility of surface waves utilization for fast magnetosonic (FW) or ion Bernstein (IBW) waves excitation in plasmas in the $\omega \sim \omega_{ci}$ frequency range has been considered in /1-4/. The simplicity of slot antennas which may be used for surface waves excitation makes the application of this method under tokamak-reactor conditions /5/ rather promising. Besides, to provide CD in plasmas the antenna system must ensure the excitation of waves travelling in one direction along the magnetic field.

This report suggests and studies theoretically the possibility of surface wave antennas creation to excite in plasmas travelling IBW's or FW's using auxiliary parasitic slots in the first wall of the magnetic device. There is also considered the employment of the parasitic slot to localize the antenna radiating surface.

Description of the model. Consider the excitation of waves in plasmas with the help of a slot antenna in the presence of N parasitic slots (Fig.1a) with fixed input impedances $Z_j=U_j/j(s_j)$ where U_j is the potential difference across the j-th parasitic slot and $j(s_j)$ is the surface current density at its edge. Practically the required input impedance of the parasitic slot may be provided by switching to it a resonator, two examples of possible realizations of which being shown in Fig.1b. Limit ourselves to the case of surface wave excitation with ky=0 in the slab geometry. We perform the analysis on the basis of the theory developed in /1,2/ which uses the Fourier series expansion of the electromagnetic fields over longitudinal wave numbers $k_{\parallel}n=2\pi/L*n$ where L is the period of the excitation system along the magnetic field (along z axis).

In the presence of N parasitic slots the amplitudes of Fourier-harmonics of the exciting electric field Ezn at the antenna surface (x=-d) are presented in the form

$$E_{zn}=E_{zn}^{(0)}+1/l\sum_{j=1}^{N}U_j\exp(-ik_{\parallel}ns_j)\ , \quad (1)$$

where $E_{zn}^{(0)}$ is the amplitude of the n-th harmonic of the exciting field in the absence of parasitic slots. Using N conditions $Z_j=U_j/j(s_j)$ where $j(s_j)=\sum_n j_n\exp(ik_{\parallel}ns_j)$ and the solution of Maxwell equations in the plasma and in the vacuum gap with appropriate boundary conditions allowing to express j_n through E_{zn}, one obtains the following system of equations to determine the unknown U_j's in (1)

$$U_j/Z_j=j(s_j)=c/4/\pi H_y(s_j)=c/4/\pi\sum_n E_{zn}Y_n\exp(ik_{\parallel}ns_j),\ j=1,\ldots,N \quad (2)$$

In the general case, with the account of plasma inhomogeneity the values of the magnitude Y_n entering the expression (2) may be obtained by numerical integration of the wave equation (see e.g./3/). In this paper we limit ourselves to the excitation of IBW's in the homogeneous plasma with the sharp boundary. Then the analytical expression for Y_n

may be obtained:

$$Yn=i\omega/c/kn(1+gn+(1-gn)\exp(-2knd))/(1+gn-(1-gn)\exp(-2knd)), \quad (3)$$

where d is the vacuum gap, $kn=(k_{\parallel}^2 n-\omega^2/c^2)^{\frac{1}{2}}$ and

$$gn=icN_{i1}N_{i1}/\omega/kn/\varepsilon_3(N_{i1}-N_{i2})/(N_{i2}(N_{i2}-\varepsilon_3)-N_{i1}(N_{i1}-\varepsilon_3)) \quad (4)$$

In this expression N_{i1} and N_{i2} are the perpendicular refractive indices of IBW and the slow wave (SW), respectively, and ε_3 is the plasma dielectric tensor component. The results of numerical calculations given below are obtained at the following parameters: d-plasma, $\omega/\omega_{ci}=1.95$, B=4T, $ne=4*10^{11}$cm, Te=Ti=200 eV, d=0.5 cm, L=25 m. At these plasma parameters and vacuum gap dimensions the surface wave length $\lambda=1.72$m and its damping length $L'=7.23$ m ($L'<<L$).

The regime of IBW excitation travelling in one direction along the magnetic field. This regime may be realized using one or several parasitic slots located on one side of the driving slot. With one parasitic slot from Eqs.(1)-(2) the following expression for Ezn may be obtained:

$$Ezn=E\overset{@}{z}n(1+\exp(-ik_{\parallel}ns_1)\sum_m Ym\exp(ik_{\parallel}ms_1)/(4\pi l/c/Z_1-\sum_m Ym) \quad (5)$$

The Ezn spectrum for parameters chosen and for the distance between the driving and parasitic slots $s_1=0.43m\approx\lambda/4$ is shown in Fig.2a (solid line). For comparison here one shows with the broken line the Ezn spectrum (in the narrow driving slot approximation).

While the magnitude Yn possesses the strongly expressed maximum for $k_{\parallel}n$ close to $k_{\parallel}=ks$ of the surface wave then on fulfilling the condition $Z_1>>4\pi L/(c\sum_m Ym)$ (see (5)) one provides the strong modulation of the Ezn spectrum. Here and in what follows the results of calculations are given at $Z_1=\infty$. In Fig.2a the locations of Yn maxima corresponding to the excitation of surface waves are shown by vertical broken lines. Besides, in the presence of one parasitic slot the Ezn spectrum is asymmetric. Therefore, the intensity of the Ezn driving field for the surface wave travelling to the parasitic slot side (n>0) is much less than the Ezn intensity for the surface wave travelling in the opposite direction (n<0). There results the unidirectional excitation of the surface wave as well as of IBW in the plasma.

Fig.2b presents the RF power flux spectrum Pn of IBW's excited in the plasma in this case. The main portion of the flux in the range k <0 is seen to be transported by IBW's with k 's close to ks what provides IBW's drive in the plasma that travel in one direction ($P_-=\sum_{n<0} Pn=0.93Po$).

Fig.3 shows the /Ex/ field distribution in the vacuum gap and in the edge plasma region for the case considered. It is seen that in the plasma one may distinguish two IBW's packets of different intensities propagating in opposite directions from the driving slot along the magnetic field. The second, parasitic IBW packet is excited mainly due to the coupling with the standing surface wave on the distance between the exciting and parasitic slots.

It is necessary to note that for high unidirectionality of IBW's excitation the presence of the travelling surface wave in the region z<0 is vitally necessary what is provided when the condition L>>L' is fulfilled.

The degree of directivity of IBW radiation $1-P_+/P_0$ depends on plasma parameters and vacuum gap values but the strongest dependence is on the distance s_1 between the exciting and parasitic slots.Fig.4 gives the P_+/P_0 vs s_1 dependence.The maximum directivity is seen to be achieved when s_1 is close to the $\lambda/4$ of the surface wave.Besides,the practically active input impedance Z of the driving slot demonstrated by Q=Im Z/Re Z versus s_1 dependence shown in Fig.4 is the important advantage of the regime with $s_1=\lambda/4$.

Antenna with the localized radiating surface.The localization of the radiating surface is achieved through the utilization of not less then two parasitic slots placed on both sides of the driving slot.Fig.5 shows the /Ex/ field distribution for the symmetric location of parasitic slots $s_1=0.43$ m$=\lambda/4$ and $s_2=-s_1$, and Fig.6 corresponds to the asymmetric location with $s_1=0.43$ and $s_2=-0.86$ m$=-\lambda/2$. As is seen from Fig.5 in the symmetrical location case two IBW packets with identical intensities are excited in the plasma, the packets propagating in the opposite directions from the driving slot along the magnetic field.Then almost total radiation localization on the surface between the parasitic slots is achieved.

With asymmetric location of parasitic slots (Fig.6) the /Ex/ field distribution in the plasma also has the form of two IBW packets.However , the radiation area is localized on the one side of the driving slot between $s_2<z<0$.

In real conditions the role of parasitic slots may be played by various nonuniformities of the first wall of magnetic device,e.g. branch pipes.As follows from the said above their presence may involve considerable changes in the spectrum of the excited waves over longitudinal wave numbers. Similar role is also played by parasitic slots when using surface waves to drive FW's in the plasma/6/.

Conclusions.1.Thus employment of parasitic slots with a sufficiently high input impedance located on one side of the slot antenna allows one to provide the IBW's or FW's in the plasma travelling in one direction along the magnetic field.The radiation directivity of such an antenna may approach 100% at optimum parameters of edge plasma and vacuum gap values. The antenna considered is much simpler than the antennas used conventionally based on multiphase feeding of a large number of drivers (loops or waveguides).

2.Employment of parasitic slots located on both sides of the slot antenna gives the possibility to limit its radiating surface.There is also the possibility of asymmetric location of the radiating surface with respect to the driving slot what may be useful in practical application of such antennas in concrete devices.

REFERENCES

1.Longinov A.V.Zhurn.Tek.Fiz.(Journal of Technical Phys.) 1972,v.42,N8,p.1591.
2.Longinov A.V.,Lukinov V.A.in Contr. Fusion and Plasma Heating(Proc.15th Europ.Conf.Dubrovnik,1988),v.2,p.742.
3.Longinov A.V.,et al.in Contr. Fusion and Plasma Physics

(Proc.16th Europ.Conf.Venice,1989),v.3,p.1105.
4.Longinov A.V.,Lukinov V.A. ibid.,p.1101.
5.Longinov A.V.ITER-IL-HD-7-9-S-1.
6.Longinov A.V.,et al.Present Conference(Paper G)

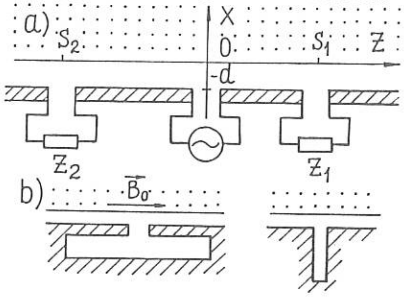

fig. 1

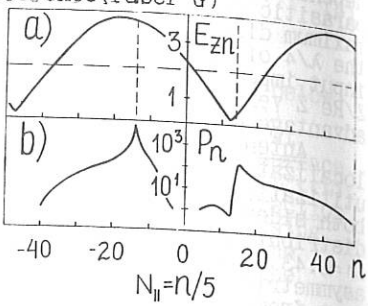

fig. 2

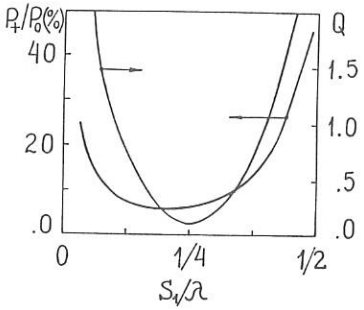

fig. 3

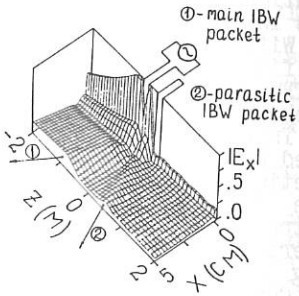

fig. 4

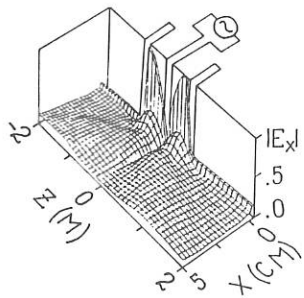

fig. 5

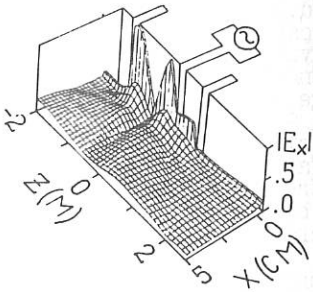

fig. 6

HARD X-RAY EMISSION DURING 2.45 GHz LH EXPERIMENTS ON ASDEX

L. Gabellieri, A.A. Tuccillo

Associazione EURATOM-ENEA sulla Fusione, Centro Ricerche Energia Frascati

C.P. 65, 00044 Frascati, Rome, Italy

Bremsstrahlung emission from suprathermal electrons in ASDEX has been measured during experiments with the new 2.45 GHz, 3 MW lower hybrid (LH) system.

A three chords radial system and a movable tangential one, with 3 inches NaI detectors, have been used to collect hard X-ray spectra ranging from 50 to 600 keV.

In order to obtain information about the interaction of the waves with fast electrons, we have investigated the dependence of the slope of the photon spectra and the photon flux intensity vs the launched LH spectrum and power, for different electron densities and plasma parameters. A broadening of the suprathermal emission is detected at increasing power and we discuss the evidence of correlations of this behaviour with sawteeth and $m = 1$ stabilization when the bulk electron temperature is strongly peaking.

The simulation with a computer code of the data collected during scans of the tangential system, together with the information from the emission measured on the radial one, allows to investigate the electron distribution function under different plasma conditions and with different launched LH waves spectra.

Moreover, in order to infer the LH deposition profile, the launched additional power was modulated at an appropriate frequency. The correlation of the bremsstrahlung emission, in different radial positions and tangential directions is analysed; the results for different plasma conditions and LH spectra are discussed.

NEUTRAL BEAM CURRENT DRIVE WITH BALANCED INJECTION

D. Eckhartt

Max-Planck-Institut für Plasmaphysik
EURATOM Association, 8046 Garching, FRG

Current drive with fast ions has proved its capability to sustain a tokamak plasma free of externally induced electric fields in a stationary state [1]. The suprathermal ion population within the toroidal plasma was created by quasi-tangential and uni-directional injection of high-energy neutral atoms, their ionisation and subsequent deceleration by collisions with the background plasma particles. In future large tokamaks of the NET/ITER-type, with reactor-relevant values of plasma density and temperature, this current drive scheme is expected to maintain the toroidal current at the plasma centre, as current drive by lower hybrid waves will be restricted to the outer plasma regions owing to strong wave damping [2]. Adequate penetration of the neutral atoms through the dense plasma requires particle energies of several hundred kilovolts per nucleon since beam absorption scales roughly with the ratio beam energy over density. The realisation of such high-energy high-power neutral beams, based on negative ion technology, is now under study.

The electric current due to the suprathermal ions is counter-acted by the bulk plasma electrons which are set in motion along the beam direction by momentum transfer from the fast ions during their slowing down. This electron screening effect is taken into account by a multiplier F_e to the fast ion current density [3]. F_e is positive for $Z_b \leq Z_{eff}$, and negative for $Z_b >> Z_{eff}$ (Z_b is the charge number of the beam ions, Z_{eff} is the effective bulk plasma charge). In the latter case the electron back-current is larger than the "primary" ion current, hence the net toroidal current flows opposite to the neutral beam direction. As an example Fig. 1 shows mod F_e for two different ion species. The radial dependence is due to neo-classical electron trapping in the toroidal magnetic field mirrors: only passing electrons can contribute to the counter current (r is normalized to the minor plasma radius r_o for an aspect ratio major over minor plasma radius of (6,65 m/1,44 m) = 4,6).

Let us now explain our concept of balanced injection with the help of Fig. 1: into a slightly contaminated DT-plasma we wish to inject two beams in quasi-tangential directions but opposite to each other with respect to the magnetic confining field lines. The co-injected "primary" beam carries D^0-atoms and serves to fuel the innermost plasma regions during thermonuclear burn. The counter-injected beam consists of carbon atoms, the resulting electric net current adds to the toroidal current driven by the D^0-beam. One can balance to zero the net momentum that is introduced by the two beams in the plasma through proper choice of their beam energy and power. This could be of advantage as it was observed in present large tokamak devices that balanced injection has a favourable effect on bulk plasma behaviour [4]. Each beam particle carries a momentum ($A_b \cdot m_p \cdot v_b$) along the direction of injection (m_p = proton mass). The number of particles injected per second and absorbed in the bulk plasma can be

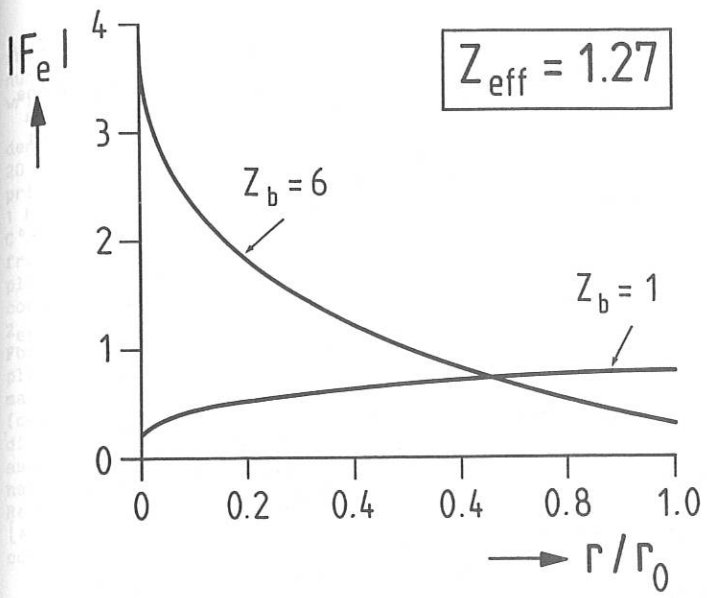

Fig. 1

expressed by an equivalent current I_b/e. Hence the total momentum introduced per second by a beam is proportional to $(I_b \cdot A_b \cdot m_p \cdot \sqrt{E_b/A_b \cdot m_p})$. Let us assume that the initial particle velocities are the same in each beam: $E_{b1}/A_{b1} = E_{b2}/A_{b2}$. Momentum balance than requires: $I_{b1} \cdot A_{b1} = I_{b2} \cdot A_{b2}$. Hence both neutral beams deposit the same amount of power in the plasma.

The presence of non-hydrogenic ions in a pure DT-plasma - be it due to either unavoidable plasma-wall interactions, to deliberate introduction of high Z-atoms, or the helium-ash production during thermonuclear burn - raises the Z_{eff}-number above unity and must be paid off by enhanced power losses. The optical radiation such as line radiation or bremsstrahlung increases, whereas the fusion power output drops as a result of DT-fuel depletion. Let us assess the changes in plasma characteristics introduced by an impurity species (Z_i) by relating the difference between contaminated ($Z_i > Z_{eff} > 1$) and clean conditions ($Z_{eff} = 1$) to the corresponding features in the clean plasma - all referring to the same electron density. We obtain for the relative changes in bremsstrahlung losses: $(Z_{eff} - 1)$; in plasma beta: $-(Z_{eff}-1)/2 \cdot Z_i$; in DT-fuel density: $-(Z_{eff}-1)/(Z_i-1)$. The electron response factor F_e grows proportional to $(Z_{eff} - 1)/Z_{eff}$, which implies that the neutral beam power required to drive a certain toroidal current through the plasma, decreases when Z_{eff} grows. Figure 2 shows how the ratio between thermonuclear fusion power output P^{th}_{fus} from the bulk plasma and the injected neutral beam power P_b changes with Z_{eff} (assumed to be uniform throughout the plasma and caused by fully ionized carbon ions).

This numerical example refers to a toroidal current of 10 MA in the NET 3A conceptual tokamak driven by injecting a beam of D^0-atoms with 1 MeV energy at an angle of 60° with respect to the magnetic field lines at the injection port [5] (neo-classical ion effects are neglected). Two plasma scenarios are considered for which deposition profiles had been computed previously assuming a rather flat density distribution [6]: curve (1) refers to $\bar{T}_e = \bar{T}_i = 20$ keV $\bar{n}_e = 1{,}25 \cdot 10^{20}$ m^{-3}, curve (2) to $\bar{T} = 10$ keV $\bar{n}_e = 0.62 \cdot 10^{20}$ m^{-3}. Both powers decrease with Z_{eff}, but at different rates. Thus their ratio has a flat maximum for $Z_{eff} = 1 \ldots 1{,}5$.

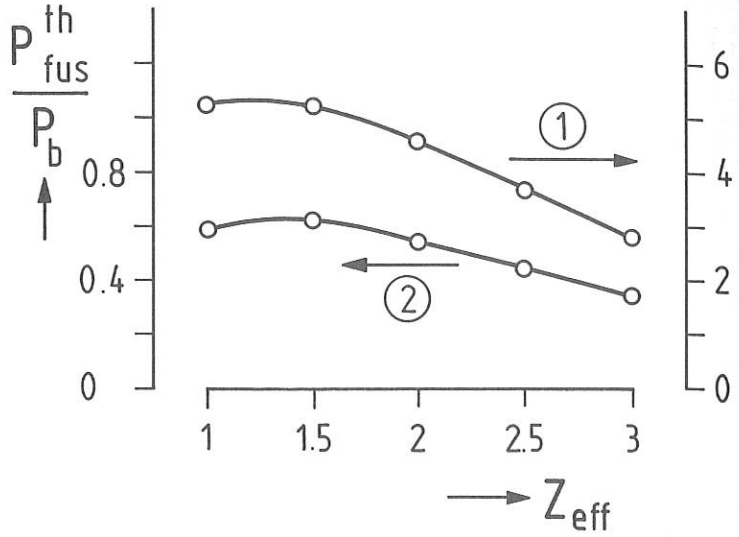

Fig. 2

Let us now become more specific about the stationary carbon ion distribution in radial direction following the unidirectional injection of a beam of high-energy C-atoms into the NET 3A bulk-plasma. To this end we have devised a very simple model: C-ions are generated according to the deposition profiles for H-atoms of the same velocity and the same injection angle, as presented in Ref. [6]; their loss is governed by radial outward diffusion of the bulk plasma with a particle diffusion coefficient which is one-fifth of the electron thermal conductivity as found by local transport analysis in JET [7]. We limit ourselves to the range $0 \leq r/r_o \leq 0{,}7$, where the radial deposition profile can be approximated by an exponentially decreasing function for $E_b = 0{,}5$ MeV/nucleon (that is 1 MeV for D^0, and 6 MeV for C^0), and where the electron thermal conductivity, and hence the particle diffusion coefficient, is nearly constant [7]. Under these conditions the diffusion equation can be solved analytically yielding a

rather flat radial distribution of carbon ions. Upon inserting relevant numbers the central density $n_C(0)$ in the high-density scenario can be written as: $n_C(0) = 1{,}023 \cdot 10^{11} \cdot I_C$, with n_C in cm^{-3} and I_C in amps.

As a numerical example we consider a burning DT-plasma in the high-density high-temperature regime of NET 3A ($n_e(0) = 1{,}5 \cdot 10^{20}\ m^{-3}$, $\bar{T}_e$ = 20 keV). We assume that a neutral beam power of 50 MW is injected by the primary beam - being delivered by 50 amps of D°-atoms with an energy of 1 MeV. Momentum balance requires the same power in the counter-injected C°-beam, that is 8,3 (equivalent) amps of 6 MeV carbon atoms. As found from the preceding equation, the resulting density of carbon ions at the plasma centre is $8{,}3 \cdot 10^{11}\ cm^{-3}$. Let us take a 5 % helium ash concentration (n_{He}/n_e) in this central region. The two impurities yield $Z_{eff} = 1{,}27$ (compared to 1,1 for He alone with the same electron density). For simplicity, we assume that this Z_{eff}-value is constant throughout the plasma cross-section. Thus a toroidal plasma current of 2,5 MA is maintained by the D°-beam [5], that by the C°-beam amounts to only 1,05 MA (owing to the shorter ion slowing down time) and it flows in the same direction. In arriving at this latter value we have again made the assumption that fast carbon and deuterium atoms of identical velocities have about the same deposition profiles in NET 3A, namely those computed in Ref. [6]. Provided that this approximation is valid we can deduce $\gamma = 0{,}30$ [A,W,m, $10^{20}\ m^{-3}$] for the current drive effiency of the combined beams (as compared to $\gamma = 0{,}42$ for the D°-beam alone).

REFERENCES:

[1] T.C. Simonen et al., Proc. 15th EPS Conf. Contr. Fusion Plasma Heating, Dubrovnik (1988), Part I, 223

[2] P.T. Bonoli, M. Porkulab, Nucl. Fusion 27 (1987) 1341

[3] D.R. Mikkelsen, C.E. Singer. Nuclear Technology/Fusion 4 (1983) 237

[4] M.C. Zarnstorff et al., Phys. Rev. Letts. 60 (1988) 1306

[5] D.Eckhartt, Final Report to NET Contract 268/87-6 (1989) (unpublished)

[6] M. Cox et al., Final Report to NET Contract 85/089/PH (1987) (unpublished)

[7] R. Bickerton, Proc. 12th IAEA Conf. Plasma Phys. Contr. Nucl. Fus. Res. Nice (1988), Vol. 1, p. 41. See in particular Fig. 18.

This work was partially done under NET-Contract 287/87 6/FU-D.

ABSORPTION CHARACTERISTICS OF 200 MHz FAST WAVE IN JFT-2M TOKAMAK

Y. Uesugi, T. Yamamoto, H. Kawashima, K. Hoshino
and JFT-2M Group

The absorption characteristics of the fast waves excited by a phased four loop antenna array has been investigated experimentally in JFT-2M tokamak. The frequency for fast wave current drive is 200 MHz which corresponds to the order of 10th higher harmonics of the ion cyclotron frequency of hydrogen. The fast wave power is absorbed by the bulk thermal electrons dominantly to heat the electron. It is shown clearly that the absorption efficiency of the excited fast waves is improved with increasing the density and temperature, and with retarding the phase velocity. Observed results are consistent with the theoretical predictions using ray-tracing calculation. The power deposition profile was deduced using synchronous detection of the modulated electron cyclotron emission by a periodic heat source. The electron thermal diffusivity and convection velocity obtained from the modulation experiment are D=(2-3) m^2/s and v=-(20-40) m/s at $\bar{n}_e=2\times10^{19} m^{-3}$ and $I_p=230$ kA, respectively. The absorption efficiency calculated from the power deposition profile is 0.3-0.4, which agrees roughly with that estimated from the initial rise of the plasma stored energy.

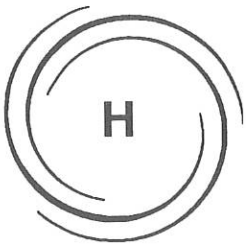

IMPURITY AND EDGE PHYSICS

SPECIAL PHENOMENA OF EDGE DENSITY FLUCTUATIONS IN HL-1 TOKAMAK

YANG Qingwei, DING Xuantong, ZHENG Yongzhen,
YANG Shikun, CAI Rengfang, DUAN Xuru

Southwestern Institute of Physics,
Leshan, Sichuan, P.R.CHINA

INTRODUCTION

The wide frequency-band ($\Delta\omega/\omega\approx1.0$) density fluctuations at the plasma edge region was studied in a lot of tokamaks [1-3], and also, in HL-1 tokamak [4]. It is well know that the turbulent fluctuation is caused by nonlinear wave-wave coupling and landou damping. A narrow-band ($\Delta\omega/\omega\approx0.1$) Quasi Coherent Fluctuation (QCF) was found at PDX tokamak which was operated at H-mode discharges with NBI heating [5]. It maybe is because of the large gradient of plasma density and temperature during H-mode discharges. In HL-1 tokamak, the QCF was observed at ohmic heating discharges. The frequency peak of QCF is in the region of $150kHz<f<200kHz$, and $\Delta\omega/\omega\approx0.1-0.4$. Perhapes, the QCF play an imporyant role in tokamak edge and associated with a special discharges.

EXPERIMENTAL

In the edge plasma experiments [6,7], the profiles of the electron density and the density fluctuations was given in Fig.1 . The large gradient of density could lead to the drift wave, and then, develop into turbulent plasma. In the usual, the fluctuations level was $\tilde{n}/n=0.3$ where n is the local electron density and $\tilde{n}$ is the amplitude of density fluctuation respectively. The spectrum of turbulent fluctuations shows the $\Delta\omega/\omega\approx1.0$ which is not as QCF's spectrum.

Many methods including langmiur probes and microwave reflectors have been used to studied the QCF in HL-1

tokamak. A movable langmiur probe array (3 probes) could change their radius from r=18.0cm to r=25.0cm (the limiter was fixed at r=20.0cm). The localed probe array (12 probes) was in the bottom of plasma and radius was 20.0cm<r<21.5cm. The 8mm and 3cm wave-length microwave was reflected at the plasma center and the plasma edge region respectively at middle density discharges of HL-1 tokamak ($Ne=2.0*10^{13}$ cm^{-3}).

The fluctuation signals was obtained during the stable discharges while no macroscope MHD instibilities. A typical electron density fluctuation signal was given in Fig.2(a). the frequency power-spectrum of fluctuation [in Fig.2(b)] was obtained by FFT from the signals of Fig.2(a). The frequency peaks have the character of $\Delta\omega/\omega\approx 0.1-0.4$ and is in the region of 150kHz<f<200kHz. The cross-correlation spectrum shows a high level correlation at this period [as it is in Fig.3(b)]. It indicates that the peak shows the character of the quasi coherent wave-wave interaction and the good propagation property. from the cross-phase spectrum [Fig.3(c)], we could estimate the wave speed is $V_\perp=6.5*10^5$ cm/s (the separation of probes is $\Delta=2.0$cm) from the $V_\perp=\omega/2\pi k$. The frequency peak indicated that it is a QCF wave and have a character of drift wave.

Either from the probes or from the 3cm microwave reflectors, the QCF phenomena could be obtained both. Sometimes the QCF spectrum was shown in the another forms as given in Fig.4 . The QCF peak does not be observed in the fluctuation spectrum of the 8mm microwave reflection signals. The large gradient of density and temperature which is in the plasma edge could lead to the drift wave and make it to propagate in the direct of poloidal. The drift wave can not propagate in the radial direct and the conditions which in the plasma center is different of it is in the edge so that no QCF peak was observed in the fluctuation spectrum of 8mm microwave reflected signals.

We want to find the relationship between QCF and the parameters of discharge (as Bt, Ip and Ne). There is weakly relation of that. Usually, the QCF peaks were found at $q_l\approx 4.0$ where the q_l is the safe factor at the limiter (when

the toroidal field Bt=2.0-2.2T and the plasma current Ip=100kA). The frequency of the QCF peaks are associated with the q_L and Ne weakly. In our experiment, the QCF peaks could be detected in all of the discharge duration. For form 1 discharges (as it is in Fig.3), the amplitude of the QCF peaks is increased by the electron density Ne as given in Fig.5 . For form 2 discharges (as it is in Fig.4), the value of $\tilde{n}_Q/\tilde{n}$ is smaller at the plasma current plateau than it is at other peroid where $\tilde{n}_Q$ and $\tilde{n}$ is the amplitude of QCF peak and the amplitude of the density fluctuations respectively.

The QCF peak does not be observed on the spectrum of the magnetic fluctuation signals. The magnetic coils were localed at r=23.0cm. It can not pick up the drift wave fluctuations expect it changes a kind of electromagnet wave. The correlation level between magnetic fluctuations and density fluctuations is lower on f>150kHz than it is on f<150kHz and it has a highest correlation level at MHD instabilities was appeared.

The authers wish to thank HUANG Keqiang, FU Bo, TANG Lixin and XU Zhengyu for useful help.

Reference:

[1] S.Zweben, P.C.Liewer, R.W.Gould, J.Nucl.Mater. 111/112(39) 1982
[2] C.P.Ritz, et al., Phys.Fluids 27(2956) 1984
[3] D.L.Brower, et al., Nucl.Fusion 27(2055) 1987
[4] YANG Qingwei, et al., Nucl.Fusion & Plasma Phys. 9(247) 1989 in chinese
[5] R.E.Slusber, et al., PPPL-2110 1984
[6] YANG Shikun, et al., in institute report
[7] YANG Qingwei, et al., in institute report

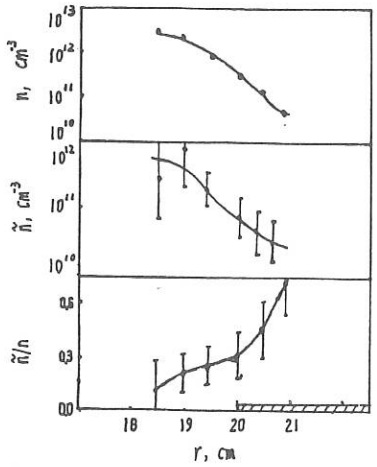

Fig.1 The profiles of the density and the density fluctuations

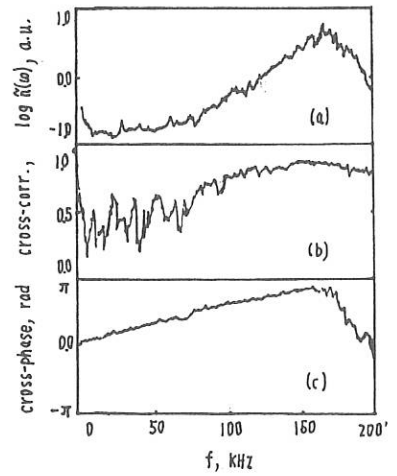

Fig.3 The spectrum of fluctuation.
(a) auto-power spectrum, (b) cross-correlation spectrum and (c) cross-phase spectrum.

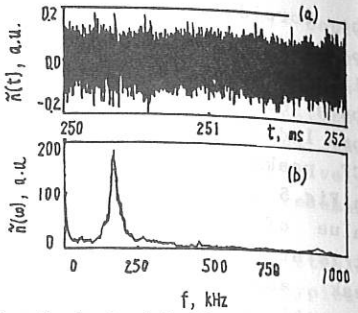

Fig.2 The signal and the QCF peak
(a) the signal of fluctuation and (b) the QCF peak.

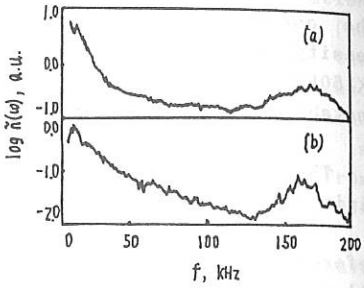

Fig.4 The auto-power spectrum of fluctuations.
(a) from the 3cm reflector and (b) from the probe.

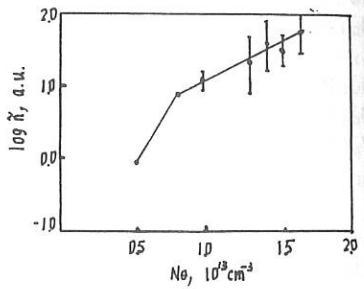

Fig.5 The relation between Ne and ñ.

INFLUENCE OF NEUTRAL INJECTION INHOMOGENEITY ON TOKAMAK EDGE PLASMA

M.Z.Tokar'

Institute for High Temperatures of the USSR Academy of Sciences, Moscow, USSR

Introduction. Puffing of cold neutral gas in tokamak edge plasma is the most simple and economical method of the increase and supporting of needed density of the charged particles. But it's possibilities are restricted by the fact that with exceeding of some critical level of the mean density $\bar{n}$ the gas coming from the puffing valve ceases to be assimilated by the plasma and the gas pressure beyond the plasma sharply grows /1/. The further rise of $\bar{n}$ needs a sharp increase of gas flux and finally it leads to the discharge disruption.

In the present paper a simple analytic model for tokamak edge plasma description taking into account strong inhomogeneity of neutral injection during gas puffing is proposed. The model permits to explain the reasons of described phenomena before disruption, to obtain the dependence of critical density of plasma $\bar{n}_c$ on the discharge parameters and to perceive possible ways of it's increase.

Model and basic equations. Let's assume an idealized geometry of a tokamak edge region permiting nevertheless to take into account the effect of inhomogeneity introduced by strong localization of the cold gas puffing - Fig.1. The gas comes through a small hole in the wall parallel to the magnetic field. The cold atoms are charge-exchanged on the plasma ions, ionized by the electrons. The appearing charged particles spread along the magnetic surfaces and diffuse across them to the wall. If recycling coefficient R is smaller then 1 the gas puffing compensates an absorption of the plasma particles by the wall.

For hydrogen isotope atoms the ionization constant k_i doesn't exceed the constant of charge-exchange k_c and with accuracy sufficient for our aims the neutrals coming from the valve can be described in diffusive approximation /2/. In this case the continuity equation has a form:

$$\vec{\nabla}\,(-D_a\vec{\nabla}\,n_a) = -k_i n_o n_a \qquad (1)$$

where $D_a=v_i\lambda_a$, $v_i=\sqrt{2T_o/m_i}$ - is the thermal velocity and n_a is the density of charge-exchanged atoms, $\lambda_a=v_i/(k_i+k_c)n_o$ is their path length; n_o, T_o are characteristic values of the plasma density and temperature in the neutral cloud ($T_i=T_1=T$ is assumed).

Boundary conditions of Eq.(1) take into account the injection of neutrals from the valve ($\vec{r}=0$), their absence far from the valve ($/r/\to\infty$) and partial absorption by the wall ($z=0$). An approximate solution of Eq.(1) we obtaine assuming that the characteristic width of the neutral cloud in z direction doesn't depend on ρ. Let's take it equals the penetration depth in the plasma of neutrals coming isotropically from the infinite wall /2/: $l_o=1/(n_o s_*)$, where $s_*=s_*(T_o)$,

$s_* = \sqrt{k_i(k_i+k_c)}/v_i$. As a result for $\bar{n}_a(\varphi) = \int_0^\infty n_a dz/l_0$ we have:

$$n_a = \frac{J_g}{(2\sqrt{\pi}\, v_i b l_0^2)}\, K_0(c\varphi/l_0), \qquad (2)$$

where $b = \sqrt{k_i/(k_i+k_c)}$, $c = \sqrt{1+1/b\ (1-R)/(1+R)}$, J_g is the total flux of atoms from the valve, K_0 is modified Bessel function.

For typical conditions of the tokamak edge region where the ionization of neutrals takes place the hydrodynamic description of the plasma is suitable since the path length of charged particles between Colomn collisions is small in comparison with characteristic dimension of the parameter change along the magnetic field and Lamor radii - in comparison with l_0. Transport equations (Ref./3/) we write with taking into account of the plasma interaction with neutrals

$$\partial \Gamma_\perp/\partial z + \partial(nv_\parallel)/\partial l = k_i n n_a \qquad (3)$$

$$\partial (m_i \Gamma_\perp v_\parallel)/\partial z + (m_i n v_\parallel^2 + 2nT)/\partial l = 0 \qquad (4)$$

$$\partial q_\perp/\partial z + \partial q_\parallel/\partial l = -k_i n n_a E_i \qquad (5)$$

Here $\Gamma_\perp = -D_\perp \partial n/\partial z$, $q_\perp$ are particle and heat flux densities in the plasma across the magnetic surfaces $V_\parallel$, $q_\parallel = -k_\parallel^e \partial T/\partial l + 5nV_\parallel T$ are the flow velocity and heat flux density along the lines of forces (co-ordinate l), $k_\parallel^e = A_k T^{5/2}$ ($A_k = 10^{20}\mathrm{cm}^{-1}\mathrm{s}^{-1}\mathrm{ev}^{-5/2}$) is the electron heat conductivity, $E_i \approx 25$ ev is energy losses on ionization and excitation of hydrogen atom. The influence of impurities on the edge plasma isn't considered here.

The dimensions of neutral cloud near the valve across and along the magnetic field are of the same order and it's necessary to take into account here only much more intensive longitudinal transport of particles and heat. After integration of Eq-s (3),(5) over l with n_a in the form of Ex.(2), one obtains the expressions for the charged particle outflux from the cloud and for heat in-flux transported into it by the electron heat conductivity and spending on the atom ionization and heating of the arising electrons and ions:

$$nv_\parallel^o = J_g/(4cl_o^2)\, \exp(-c/y//l_o), \qquad (6)$$

$$(k_\parallel^e \partial T/\partial l)^o = nv_\parallel^o (E_i + 5T_o), \qquad (7)$$

Here y is a co-ordinate on the magnetic surface perpendicular to l and the point with y=0, l=0 corresponds to the valve location.

The value $(k_\parallel^e \partial T/\partial l)^o$ can be estimated as $k_\parallel^e(T_*)\cdot(T_*-T_o)/L$, where T_* is the edge plasma temperature far from the valve and characteristic length of line of force L is determined by the cloud dimension d in y direction: $L \approx s_o/(2d)$, s_o is the magnetic surface area. According to Ex.(6) $d \approx 2l_o/c$ and from Ex.(7) it follows:

$$A_k T_*^{5/2}(T_*-T_o) \approx J_g s_o (E_i+5T_o)/(16 l_o^3) \qquad (8)$$

Now let's integrate Eq-s.(3)-(5) over the edge region excluding the neutral cloud near the valve: $/l/,/y/ \gtrsim l_o/c$. The boundary conditions are: Ex-s.(6),(7) $V_{\parallel}=q_{\parallel}=0$ at $l = L$; condition of heat flux convectivity at the wall ($z=0$): $q_{\perp} = \gamma \Gamma_{\perp} T$ ($\gamma = 5 \div 10$). The total heat flux from the discharge central part Q is also given. One obtains:

$$(1-R)s_{l_o} D_{\perp} \partial n/\partial z(z=0) = J_g w_i \qquad (9)$$

$$n_o T_o \approx \int_o n(z) T_* dz / l_o \qquad (10)$$

$$Q = J_g w_i (\gamma T_* + E_i)/(1 - R) \qquad (11)$$

where $w_i = c^{-2}$ is the ionized and assimilated by the plasma part of J_g. In Eq.(10) it's neglected by the contribution of the first term in Eq.(4) which is of order of $1-R \ll 1$. The alteration of n(z) profile due to the particle flow along the magnetic field is of the same order and it's possible to use the results obtained in Ref./4/ for situation with homogeneous recycling on the wall: $n \approx n_* \cdot z/l_*$ with $z \lesssim l_*$, $n \simeq n_*$ with $z \gtrsim l_*$, where $l_* = 2/(n_* s_*^*)$ is the characteristic width of the edge region, $s_*^* = s_*(T_*)$.

In divertor configuration the gas has a possibility to spread from the puffing location in vacuum space between the wall and separatrix. Taking into account the neutral ionization in the plasma and absorption by the wall we obtain the equation for the atom density in this space in diffusive approximation:

$$1/\varrho \; d/d\varrho \; (- v_i d_o \; dn_a/d\varrho) = - n_a v_i / d_o \cdot 2(1-AR)/(1+R)/(1+A)$$

where d_o is the space width, A is the plasma albedo for atoms.

Calculation results. The Eqs.(8)-(11) allow to calculate the edge plasma parameters with given value of Q, J_g, R. Fig.2 shows the dependences of T_*, T_o, w_i on the mean plasma density $\bar{n} = \int n(z) \cdot dz/a$, where a is the plasma minor radius, calculated for conditions of discharges in JFT-2M tokamak /1/: $s_o = 16$ m^2, Q=200 kW; $D_{\perp} = A_D/n$, $A_D = 10^{17}$ cm^{-1}s^{-1}, R=0.9 are also taken.

With increase of $\bar{n}$ upper than critical value $\bar{n}_c \approx 3 \cdot 10^{13}$ cm^{-3} T_o drops sharply because T_* is already enough low and the necessary heat flux into the cloud can be supplied with substantial difference between T_* and T_o (see Eq.(8)). With deminution of T_o down to the hydrogen ionization potential the gas assimilation efficiency sharply decreases and the gas is mainly absorbed by the wall. The following rise of $\bar{n}$ needs strong increase J_g and this is observed experimentally.

The latter leads to the strong growth of the puffed gas pressure P beyond the plasma. In JFT-2M device the neutral pressure was measured by mass spectrum analyzer (RGA). The distance between the puffing valve and the RGA flange is nearly 160 cm, d_o=13 cm /1/. Fig.3 shows the experimental (1) and calculated on the base of Eq.(12) solution (2) dependences of the pressure in RGA of deuterium puffed into discharge with walls saturated by hydrogen on the electron mean density.

Conclusion. Thus the deterioration of gas puffing efficiency with $\bar{n} > \bar{n}_c$ results from decrease of the plasma temperature near the valve lower than the hydrogen ionization potential. The further increase of $\bar{n}$ leads to, as it is easy to show, the rise of l_0 i.e. an expansion of the cold dense plasma region over the minor radius to the discharge centre. As a result it can provoke the discharge disruption. The local heating of the plasma near the gas puffing valve, for example, by the electromagnetic waves permits to prevent the plasma cooling. This way of $\bar{n}_c$ increase is worthy of further consideration.

References

1. S.Sengoku et al., J.Nucl.Mater 145-147 (1987) 556-561
2. B.Lehnert, Nucl.Fusion 8(1968) 173-181
3. S.I.Braginskii, in: Review of Plasma Physics, Ed. by M.A. Leontovich, Vol.1 (Cons. Bureau, New York, 1965) p.205.
4. A.V.Nedospasov, M.Z.Tokar', J.Nucl.Mater 93-94 (1980)248--251.

Figure captions:

Fig.1. The geometry of tokamak edge region with the gas puffing through the valve and the plasma recycling on the wall parallel the magnetic field (⟶ neutrals, - - → charged particles).

Fig.2. The calculated dependences of the edge plasma temperature near the valve (T_0) and far from it (T_*), the ionized part of the gas influx (w_i) on the plasma mean density for discharge conditions in JFT-2M tokamak (Ref./1/).

Fig.3. The experimental (1) and calculated (2) dependences of deuterium pressure in RGA on $\bar{n}$.

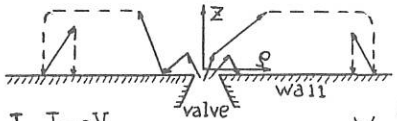

Fig. 1

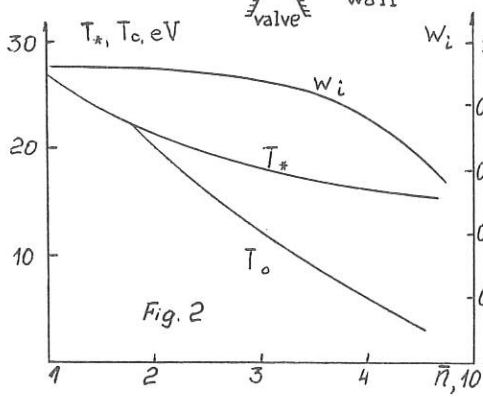

Fig. 2

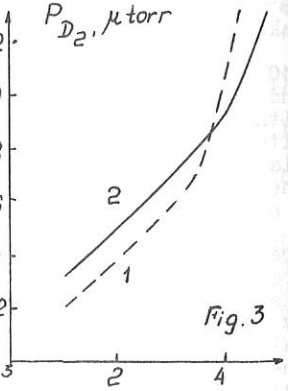

Fig. 3

INFLUENCE OF THE HELICAL RESONANT FIELDS ON THE PLASMA EDGE OF TBR–1 TOKAMAK*

C. Ribeiro, R.P. da Silva, I.L. Caldas and TBR–1 Team
Instituto de Física, Universidade de São Paulo
C.P. 20.516, 01498 São Paulo, SP, Brazil

Introduction

The control of the plasma–wall interactions deserved much attention in recent works in the field of controlled nuclear fusion research with tokamak machines. It is desirable in this machines to have, in the edge, a cold and dense plasma layer to reduce impurities liberation, to avoid the migration of non–ionized impurities to the centre of the column and to have a uniform heat deposition on the vessel/limiter. One way to attain these objectives is the enhancement of electron thermal transport by the ergodization of magnetic surfaces in the boundary layer [1]. This process can be obtained with resonant helical fields that, when superposed with the equilibrium fields, provoke the overlapping of magnetic islands and the field structure becomes chaotic. In the situation, field configuration is called helical magnetic limiter [2].

This paper describes an experimental work [3] that are in progress in TBR–1 tokamak about the influence of resonant helical fields on the plasma potential. The main parameters of the TBR–1 [4] — a small tokamak in operation at the Physics Institute of University of São Paulo — are: R (major radius) = 0.30 m; a_v (vessel radius) = 0.11 m; a (plasma radius) = 0.08 m; R/a (aspect ratio) = 3.75; B_φ (toroidal field) = 0.5 T; n_{eo} (central electron density) $\simeq 7 \times 10^{18} m^{-3}$; T_{eo} (central electron temperature) $\simeq$ 200 eV.

Experimental arrangement

In this experiment the gas used was hydrogen with a pressure of $1{,}2 \times 10^{-4}$ mbar. The vessel was conditioned with Taylor discharge cleaning and a base pressure of 1×10^{-6} mbar was obtained. No gas puffing was used.

Besides the usual diagnostics, we have used a set of magnetic probes arranged in poloidal and toroidal directions to detect Mirnov oscillations [5]. Two Langmuir probes were also used. One, coupled to a sweep generator, used for electron temperature and density measurements [6] and the other, coupled to a high impedance circuit, for floating potential measurements [3].

The helical fields (HF) were produced by electric currents circulating in a set of coils wound around the vacuum vessel [7]. In this experiment m/n = 4/1 configuration (where m and n are, respectively, the poloidal and toroidal main mode numbers) was used, since the resonant surface with q = 4 is in the plasma edge region ($r \simeq 7.2$cm). In this experiment helical currents from 0 to 450 A were used. The current source gives rectangular pulses with adjustable duration and trigger time.

All the signals from the basic diagnostic, Mirnov coils, Langmuir probes and helical coil current are coupled to a CAMAC data acquisition system based on LeCroy 2264 transient digitizer (8 bits, 8 channels, 500 kHz). The system is controlled by a IBM–PC like microcomputer.

Results

In fig. (1a) we have time profiles of four signals: plasma current (I_p), helical coil current (I_h), horizontal position (P_h) and the floating potential (V_f). The plasma current has a duration of 7 ms and maximum current of 8 kA. In this pulse there was no current in the helical coils. The floating potential is negative during the discharge, attaining a minimum value of –75 V and increasing until the end of the discharge. In the fig. (1b), where the same signals are shown, we can see the effect of HF on the floating potential. In this figure a discharge with a helical current pulse (1 ms duration and 450 A intensity) is shown. With the application of the HF there was an increase of $\simeq$ 20 V in the floating potential. A small decrease in the plasma current was also detected. In these discharges the Langmuir probe position was r = 6.6 cm.

The measurements were made with the Langmuir probe in 8 different radial positions in the region $5{,}5 \leq r\ (cm) \leq 10.8$, and 5 values for the helical current: 0, 150, 250, 350 and 450 A. In all measurements m/n = 4/1 was the dominant helical mode.

In the fig. (2a) two radial profiles of the floating potential are shown; one with the application of the HF (I_h = 450 A, continuous line) and the other without these fields (dashed line). Each point of the graphics was obtained from the average data of many tokamak pulses during the time interval of the application of the HF. If we compare these profiles we see that the effect of the HF is more intense in the regions near r = 6.6 cm ($\Delta V_f \simeq 10V$) and r = 7.7 cm ($\Delta V_f \simeq 6V$).

In fig. (2b) we also have two radial profiles of the floating potential obtained in the same conditions of the preceding figure, but with I_h = 150 A in the helical coils. The change of V_f are lower in this case than in the previous one.

Finally in fig. (3) we can see the global effect of the HF on the floating potential in the plasma edge of TBR–1 for five values of the helical coil current: 0, 150, 250, 350 and 450 A. The average potential (averaged in the region $5{,}5 \leq r(cm) \leq 10.8$) clearly increases with the helical current intensity.

Discussion and Conclusion

In summary, the reported results indicate the influence of resonant helical perturbations on the floating potential in the plasma edge of TBR–1, specially in the chaotic field regions created by resonant helical fields. Thus, for the m/n = 4/1 mode and I_h = 450A, this potential increases approximately 10V around r $\simeq$ 6.6cm. In TBR–1 the temperature is usually almost constant in time during the plasma current plateau and decays exponentially with r [6]. Thus, from the measured floating potential, it is possible to predict (supposing that the plasma temperature is not significantly modified by the HF [8]) that plasma potential increases with the helical current intensity. The observed reduction of plasma current can be explaned by an increase of the average plasma resistivity. In conclusion, we verify that helical resonant fields modifies the transport properties of the plasma in the edge of TBR–1, provoking an enhancement of electron diffusion and an increase in the plasma potential.

*Work partially supported by FAPESP, FINEP and CNPq.

REFERENCES

[1] – A.B. Rochester and M.N. Rosenbluth, Phys. Rev. Lett. 40, 38 (1978).

[2] – W. Feneberg and G.H. Wolf, Nuclear Fusion 21, 669 (1981).

[3] – C. Ribeiro, M.Sc. Dissertation, Universidade de São Paulo, Instituto de Física, São Paulo, SP, Brazil. To be presented.

[4] – I.C. Nascimento, A.N. Fagundes, R.P. da Silva, R.M.O. Galvão, E. del Bosco, J.H. Vuolo, E.K. Sanada, R.S. Dallaqua, in *Proceedings of the Spring College on Fusion Energy* (Trieste), pp. 45–50 (1981).

[5] – I.H. Tan, I.L. Caldas, I.C. Nascimento, R.P. da Silva, E.K. Sanada, R. Bruha, IEEE Trans. Plasma Science, PS–14, 279 (1986).

[6] – R.P. Da Silva, Ph.D. Thesis, Universidade de São Paulo, Instituto de Física, São Paulo, SP, Brazil (1989).

[7] – A. Vannucci, O.W. Bender, I.L. Caldas, I.H. Tan, I.C. Nascimento, E.K. Sanada, Il Nuovo Cimento, 10D, 1193 (1988).

[8] – S. Takamura, N. Ohmishi, H. Yamada and T. Okuda, Phys. Fluids 30(1), 144 (1987).

[9] – S.C. McCool et al., Nuclear Fusion 29(4), 547 (1989).

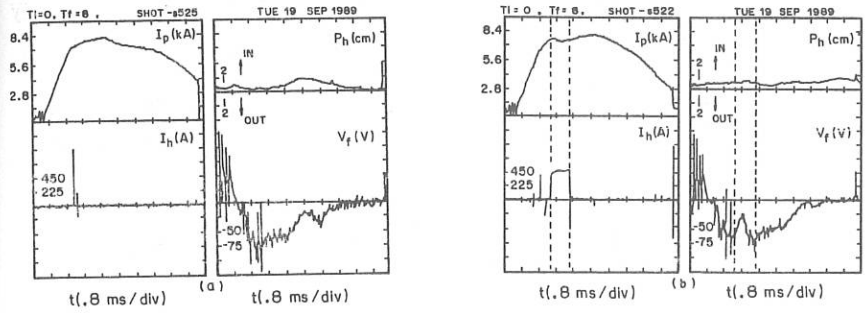

Fig. 1 – Plasma (I_P) and helical coil (I_h) currents, horizontal position (P_h) and floating potential (V_f) for discharges with $I_h = 0$ (a) and $I_h = 450$ A (b).

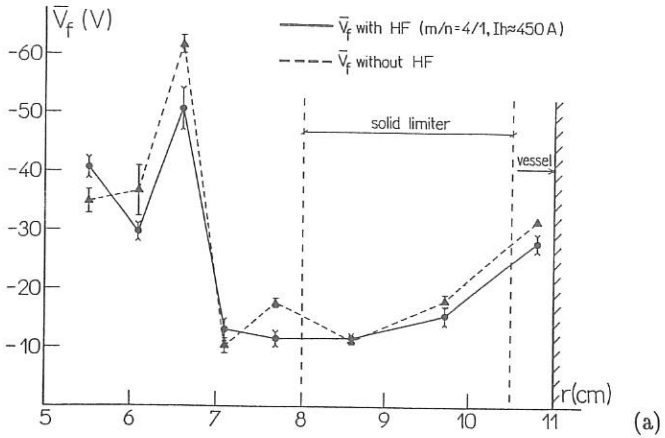

(a)

Fig. 2 – Comparisons between the unperturbed floating potential and the perturbed one by the effect of helical currents of 450 A(a) and 150 A(b).

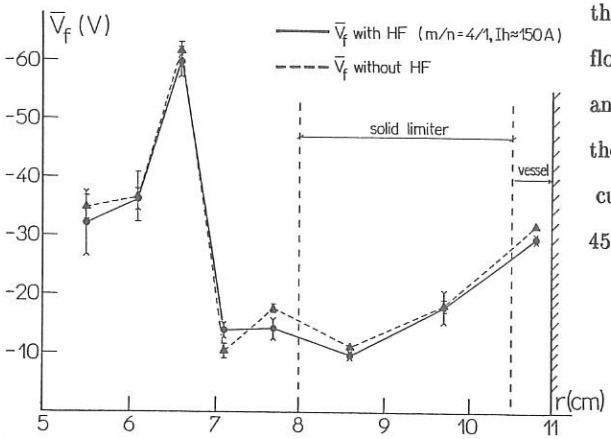

(b).

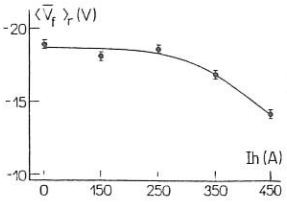

Fig. 3 – Average floating potential in the plasma edge ($5{,}5 \leq r\ (cm) \leq 10.8$) for different helical currents.

EDGE FLUCTUATION STUDIES IN ATF

C. Hidalgo
Euratom/Ciemat, Madrid, Spain

T. Uckan, J. D. Bell, J. H. Harris, B. A. Carreras, J. L. Dunlap, G. R. Dyer
Oak Ridge National Laboratory, USA

Ch. P. Ritz, A. J. Wootton, T. L. Rhodes, K. Carter
Fusion Research Center, University of Texas at Austin, USA

Introduction

Transport studies in tokamaks have shown that processes involving electrons are anomalous (i.e., transport is faster that predicted by the neoclassical theory) [1]. One of the key issues in fusion research is to understand the basic mechanisms causing the experimentally observed anomalous transport. Much effort is being done to elucidate if it can be explained by the presence of either electrostatic or magnetic fluctuations [2].

Electrostatic fluctuations have been studied in the edge region of many tokamaks. Detailed experiments carried out in TEXT tokamak [3,4] have shown that electrostatic fluctuations are large enough to explain anomalous transport in the plasma edge. It is now generally accepted that energy and particle losses in the edge plasma region of tokamaks are predominantly due to plasma turbulence.

Transport studies carried out in stellarators have shown that transport coefficients evaluated in the core region are consistent with neoclassical predictions under some conditions, whereas in the boundary the transport is anomalous [5].

Tokamak and stellarators share similar properties (nested magnetic field lines with rotational transform) but they also have important differences. In stellarators the magnetic configuration is produced by external currents; this allows to access to a wide range of magnetic configurations without requiring any driven plasma current. By comparing the structure of edge turbulence in both tokamaks and stellarators one can expect to get information about the dominant drive of the turbulence as well as about the role of the magnetic configuration on edge turbulence.

The purpose of the present investigation is to characterize edge fluctuations in ECH plasmas in the Advanced Toroidal Facility (ATF).

Experimental

ATF is a l=2, 12 field-period torsatron [6] with major radius R_0=2.10 m, average minor radius $\bar{a}$ = 0.30 m and with moderate shear (iota(a)=1.0, iota(0)=0.3). In the present investigation currentless plasmas have been achieved using a 53 GHz ECH system. Discharges with B = 1 T, $P_{ECH} \approx 200$ kW, $\bar{n}_e$=(3–6) x 10^{12} cm^{-3} and stored energy (1–2 kJ) have been studied.

Fast reciprocating Langmuir probe (an square array 2 x 2 mm of four Langmuir probes), similar to the one in TEXT, is inserted into the plasma from the top of ATF to measure density, potential and temperature using the technique describe elsewhere [7]. The probe was located one field period away from the rail limiter. Measurements have been taken in steady state of the discharge, in the vicinity of the last close flux surface (the normalized radial position, r/a, ranging from 1.2 to 0.9). Signals are digitized at 1 MHz using a 10-bit 16 kB/channel digitizer.

Local mean and fluctuation levels

Edge density and temperature are in the range $n_e \approx$ (0.5–1.5) x $10^{12}cm^{-3}$ and $T_e \approx$ (10–40) eV. The density scale length $L_n=[(1/n)(dn/dr)]^{-1}$ is about (2–4) cm, whereas the temperature gradient is smaller (L_T> 4 cm).

Density fluctuation levels systematically decrease when moving inside the plasma and they are in the range $\tilde{n}/n \approx$ (0.05–0.20). Inside the plasma the Boltzmann relationship is not fulfilled (i.e., $\tilde{n}/n \sim \tilde{\phi}_{fl}/T_e$). However, it is important to notice that the fluctuating floating potential ($\tilde{\phi}_{fl}$) is a good estimate of plasma potential fluctuations only when temperature fluctuations are much smaller than the $\tilde{\phi}_{fl}$. An upper bound for temperature fluctuations have been estimated in the proximity of the last closed flux surface (LCFS) using the triple probe technique [8,9] (Fig. 1). Whereas in the outer region of the plasma temperature fluctuations are clearly much smaller than density fluctuations, inside the plasma electron temperature fluctuations are comparable to density fluctuations.

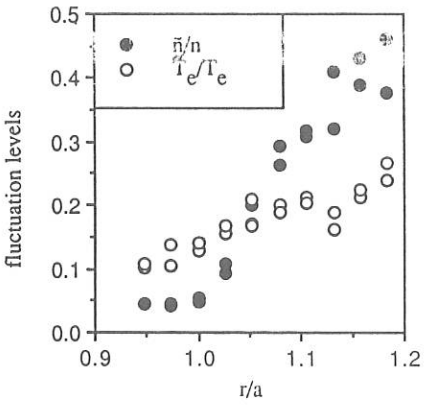

Fig. 1. Radial profiles for density and temperature fluctuations

Using the two point correlation technique we have measured the wave number-frequency power spectra S(k,ω) for potential fluctuations [10], at the frequency ω and wave number k (in the poloidal direction). The fluctuation power spectra is predominantly below 300 kHz. Trend analysis of the wave number spectra shows that inside the

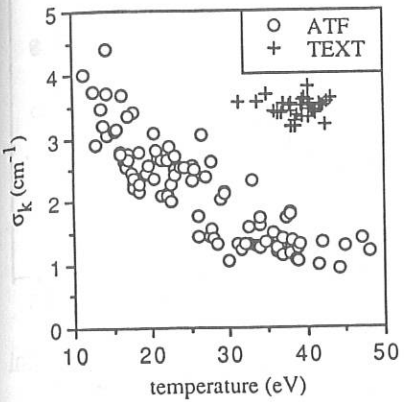

Fig. 2. Turbulent broadening as a function of the local temperature in ATF(o) and TEXT (+).

LCFS the turbulent broadening σ_k decreases with increasing local electron temperature. The poloidal correlation length thus increases with increasing temperature. As shown in figure 2, $\sigma_k \approx 1$ cm^{-1} with $\sigma_k/\bar{k} \approx 0.5$ for Te > 35 eV. It is remarkable that in the same temperature range $\sigma_k \approx 3$ cm^{-1} with $\sigma_k/\bar{k} \approx 1$ in TEXT tokamak, implying that the dominant m numbers in TEXT are 3 times larger than those in ATF. Taking into account that q(a) = 1 in ATF and q(a) ≈ 3 in TEXT, this result is consistent with theoretical expectations. The integrated spectra S(ω) and S(k) decrease for large ω and k with a dependence given by $S(\omega) \approx \omega^{-\alpha}$ and $S(k) \approx k^{-\beta}$, where $\alpha,\beta \approx 3$ and $kr_s \approx 0.1$.

Particle fluxes

From the correlation between density ($\tilde{n}$) and floating potential ($\tilde{\phi}_{fl}$) fluctuations we have estimated the particle fluxes induced by fluctuations, $\Gamma = \langle \tilde{n}\, \tilde{v}_r \rangle$, where $\tilde{v}_r$ is the fluctuating radial velocity. The frequency resolved particle flux is dominated by frequencies below 200 kHz, with an integrated particle flux $\Gamma \approx (2\text{–}5) \times 10^{15}$ cm^{-2}s^{-1}. Under the assumption of toroidal and poloidal symmetry the total particle flux induced by electrostatic fluctuations is comparable to the particle flux deduced from global particle balance.

Velocity shear layer

A change in the fluctuating phase velocity has been observed in the edge region of the plasma. Here the velocity reverses from the electron diamagnetic drift direction for r/a < 1 to the ion diamagnetic direction for r/a > 1. The existence of a velocity shear layer in the edge region of the plasma has been already reported previously [11]. At the shear layer position the plasma potential is positive and it has a maximum (i.e. the radial electric field reverses direction). The phase angle between density and potential fluctuations and between the floating probes change sign at the shear layer, resulting in an outwards particle flux. As a consequence of the decreasing of the poloidal correlation length at the shear layer, the broadening of the k-spectra peaks at $v_{ph} = 0$ (Fig. 3). Inside the last closed flux surface the temperature dependence of the phase velocity is well described by the electron diamagnetic drift velocity ($v_{ph} \approx v_{ed} \approx T_e/eBL_n$).

The influence of the magnetic configuration and rail limiter position on the shear layer has been investigated. Figure 4 shows the velocity shear layer as measured in two different magnetic configurations with the vacuum magnetic axis located respectively at 2.08 m and

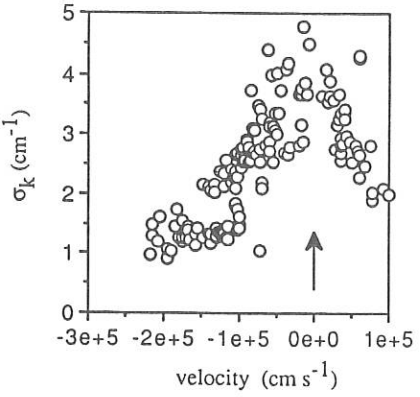

Fig. 3. Turbulent broadening as a function of the phase velocity.

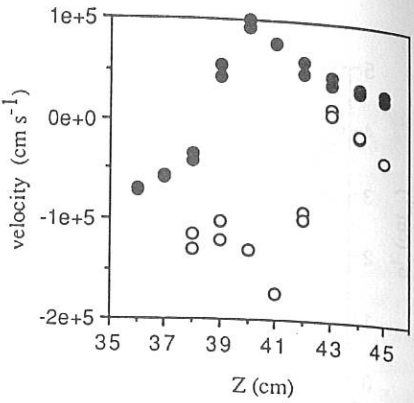

Fig. 4. Velocity shear layer at two different magnetic configurations: vacuum magnetic axis at R_0=2.08 m (o) and R_0=2.05 m (•).

2.05 m. When the vacuum magnetic axis is shifted inward (R_o=2.05 m) the shear layer position moves in the same direction, implying that the location of the shear layer is coupled with the magnetic configuration. The shear layer location does not change when the rail limiter is moved from r/a=1.0 to r/a=1.2; thus, the location of the velocity shear layer is not related with the rail limiter position.

Acknowledgements

The authors would like to thank J.N. Lebeouf. P. H. Diamond and D. R. Thayer for fruitful discussions.

References

[1] H. P. Furth, Nuclear Fusion 15, 487 (1975).
[2] P. Liewer, Nuclear Fusion 25, 543 (1985).
[3] Ch. P. Ritz, R. V. Bravenec, R. V. Schoch et al., Phys. Rev. Letters 62, 1844 (1989).
[4] A. J. Wootton et al. Plasma Physics and Controlled Fusion 30, 1974 (1988).
[5] H. Renner and W7AS Team, Plasma Physics and Controlled Fusion 31, 1579 (1989).
[6] J. F. Lyon et al., Fusion Technology 10, 179 (1986).
[7] Ch. P. Ritz, E. J. Powers, T. L. Rhodes et al., Rev Sci. Instrum. 59, 1739 (1988).
[8] S. Chen and T. Sekiguchi, J. of Applied Physics 36, 2363 (1965).
[9] Ch. P. Ritz, to be published.
[10] J. M. Bell, Y. C. Kim and E. J. Powers J. Applied Physics 53, 3933 (1982).
[11] Ch. P. Ritz, R. D. Bengton, S. J. Levinson and E. J. Powers Phys. Fluids 27, 2956 (1984).

EFFECT OF LIMITER COMPOSITION ON Z_{eff} AND RECYCLING IN JET

J P Coad, *R Behrisch, L de Kock, J Ehrenberg, F.Lama, *A P Martinelli, **J Partridge, G Saibene, R Sartori, J C B Simpson, M F Stamp, D D R Summers

JET Joint Undertaking, Abingdon, Oxon, OX14 3EA, UK
*Max-Planck Institut für Plasmaphysik, 8046 Garching bei München, FRG
**Culham Laboratory, Abingdon, Oxon, OX14 3DB, UK

Introduction

Throughout the operational history of the JET machine a variety of first-wall components have been removed from the torus and analysed to build up a picture of the state of the in-vessel surfaces and its evolution with time. The value of a comprehensive survey of in-vessel conditions has been apparent from the very first JET discharges in 1983, when molybdenum was quite unexpectedly observed in the plasma and was soon traced to contamination of the graphite limiter tiles during their final vacuum heat treatment [1]. The changes observed to the surfaces of in-vessel components are, of course, the cumulative effect of hundreds of plasma discharges under diverse operating conditions. However, this paper demonstrates that useful lessons can be learned which are just as relevant as time resolved measurements : discussion is limited here merely to analysis of belt limiters.

Analysis of Graphite limiters in use until mid-1989

JET used graphite limiters (0.4 x 0.8m) at the outer midplane as the primary contact points in 1983 - 1986 (4 being used in 1983-5 and 8 in 1986). Limiter tile analysis showed plasma ingress of nickel and other impurities originating from the inconel walls of the vessel to be primarily a two-stage process. Firstly the limiter tiles are contaminated by these elements as a result of processes like glow-discharge cleaning and disruptions as well as sputtering (especially by neutrals) during discharges, and then atoms are recycled from the limiters by sputtering directly into the plasma from near the contact point and redeposition onto the flanks [2]. In the earliest campaigns deposits of up to 10^{18} atoms cm^{-2} of nickel accrued on parts of the limiters, together with appropriate amounts of the other inconel constituents [3]. During this period there was a progressive increase in the number of carbon tiles covering the vessel walls, in order to decrease contamination of the plasmas by metals and to prevent damage to the inner wall. As more of the vessel was protected with graphite tiles the amounts of inconel found on central parts of the limiters (in contact with the plasma) decreased by about an order of magnitude, in line with the improvement in plasma purity for ohmically-heated discharges.

For the 1987-8 campaigns two continuous graphite belt limiters, one above and one below the outer midplane, were installed to cope with plasmas of much greater heating power (40 MW). The belt limiters each comprise ~850 tiles mounted side-by-side with their largest faces vertical and radial to the machine axis [4]. The plasma thus contacts one end face of each tile, and due to the shape

of the tile (bottom of Figure 1) the maximum flux occurs to either side of the tangency point. Regions of net erosion near the LCFS and deposition further from the LCFS occur on each tile and were clearly visible during the 1987-8 campaign (from the shinier appearance of eroded zones). Postmortem analysis of tiles in 1988 showed deposition near the ends of each tile, and eroded zones nearer the centre, but around the contact point revealed net deposition of somewhat variable extent (Figure 1(a)). The outer surface layers (to ~ 1μm) of several tiles were analysed, and the amounts deposited varied considerably. There were many tiles with macroscopic areas of erosion (~1mm in depth) on the edge near the tangency point, due to misalignment relative to the neighbouring tile. Material is probably lost from these areas by sublimation and hence with low emitted atomic particle velocity. The atoms would be ionised and swept along the field line with a high probability of redeposition on nearby tiles, resulting in the variable amounts of deposition observed. Extreme heating of a number of tile edges is thought to be responsible for rapid increases in Zeff for some high-power limiter discharges (carbon "blooming").

Limiters Used During JET Operations with Beryllium

As a first stage, beryllium was evaporated on several occasions over the interior of the JET vessel (including the graphite belt limiters) from four evaporator heads spaced around the outer midplane. After each evaporation the subsequent limiter discharge showed mostly beryllium as the major plasma impurity, but this was replaced by carbon within one or two pulses, and after 5-10 pulses the Be level settled down at ~7-10% of the initial concentration (which was 3-5%). However the (carbon-dominated) impurity levels in plasmas throughout the Be-evaporation phase remained at least as low as in the best-conditioned all-carbon phases. This was due to the elimination of the oxygen by gettering by the evaporated Be-layers to form beryllium oxide, as observed on various samples. It was assumed that the Be evaporated over the limiter tiles was eroded from the contact area by the plasma almost immediately, but analysis shows this is not generally the case. Examination of a tile from the lower belt reveals a layer structure right around the end face of the tile with an average analysis of 40% Be, 50%C and 10%O (excluding D), and the characteristic dips in the D profile which indicate erosion zones are absent (Figure 1(b)). A pair of tiles from the upper belt also showed both Be and D all over the tiles (Figures 1(c) and 1(d)), with some additional deposition near the tangency point. The rapid disappearance of Be in the plasma must mean erosion occurs only at isolated points, or the Be is obscured by surface roughness effects.

The graphite belt limiter tiles were then changed to beryllium tiles for the Be-phase. Maximum normal power loading was again to each side of the tangency point, as could clearly be seen with CCD cameras. However, on occasions heating occurred at the edge of a tile, often followed by melting of the Be, and emission of a droplet. After operations, close inspection of the limiters showed melting had occurred along sections of one edge of many tiles (usually the central portion), and on several tiles the melted and re-solidified zone had spread over the full width of the end face of the tile. Be and deuterium analyses have been carried out on a number of Be limiter tiles, and the results for one are shown in Figures 1(e) and (f). The decrease in the Be within the surface layer analysed towards the end of the tile nearest the midplane clearly indicates the presence of another element deposited in this region, but is in the deposition zone, and does

not contribute to Z_{eff} for limiter discharges. This is likely to be carbon, which continued to be observed using probes near the midplane even for Be-limiter discharges. Again, there is extra deuterium near the tangency point, but this appears to be associated with redeposited Be which can be seen as dark deposits on unmelted tiles in the shadow of melted regions, or within hollows on the melt surfaces. As an average over many tiles, the maximum amounts of D seen are less than for C tiles.

Analysis of In-Vessel Components for Deuterium at the Surface

A comprehensive analysis of in-vessel components has shown the deuterium inventory of the plasma-facing surfaces steadily increased during the carbon-limiter phases [5]. A progressively greater percentage of the deuterium fed into the torus to fuel the discharges was permanently retained in the vessel as the amount of carbon present in the machine increased. For the 1987-8 campaign a cross-check between the analyses and gas throughput measurements could be made. The latter suggested about 40% of the gas input is trapped in the vessel, which agrees quite well with the 25% accounted for in tile analysis, to which must be added a total of ~10 - 15% for losses due to hydrogen isotope release each time the vessel is vented [5]. The deuterium which is analysed is mostly present co-deposited with carbon on all tiles facing the plasma (the thickest deposits being on the sides of the limiters). Concentrations of up to 30% deuterium in carbon (C:D of 1:0.4) are stable at temperatures below 400°C, and the observed content of these deposits has been in the range 10 to 30%. Significant amounts of hydrogen are always observed in addition to the deuterium, and one should note that some deuterium is desorbed on venting (from less stable bonding states) before the surface analysis was performed.

The large amount of deuterium found in the walls is equivalent to the combined contents of hundreds of discharges. In the carbon phases this led to uncontrolled particle release during discharges, and density control could only be temporarily obviated by helium conditioning. There was also a hard density limit above which disruptions became inevitable. As soon as Be was added to the torus the situation changed. Much larger amounts of gas could be introduced to the torus, producing much higher densities than previously possible, and when excessive gas feed led to densities becoming unstable, marfes and softer landings generally resulted. The fraction of gas input re-emitted within 1000 secs after a discharge increased from ~20% to ~60% after Be was introduced, though the greatly increased input meant that somewhat similar amounts of deuterium were retained in the vessel per shot : despite this, no saturation effects such as uncontrolled release were observed. The results suggest two necessary effects of the Be. Firstly much larger inventories of gas can be retained at the walls during the pulse and these are released at the end of the pulse. Secondly the gas retained on a long-term basis is present in stable states. Analyses of graphite limiters, X-point and inner wall tiles after the Be phases all reveal similar surface concentrations of D to those after the carbon phases. However, the surface deposits comprise both C and Be and it appears that the properties of this composite matrix are more favourable than pure carbon with respect to deuterium retention/release.

Conclusions

The variability of belt limiter tile analysis, observed edge heating effects and shadowing, etc, prove that plasma contact at the belts is very non-uniform, and impurity release is dominated by erosion at a number of small areas of interaction on the belt edges.

Large quantities of D are present on the Be belt limiters in areas shadowed by, or within, melt zones which could be released if the topology changes.

Amounts of deuterium present at graphite tile surfaces in the vessel have not significantly changed with the introduction of Be, so the hydrogen-retention properties of C + Be must differ from pure C to explain plasma behaviour.

References

[1] J Ehrenberg et al, Proc. 12th European Conf on Controlled Fusion and Plasma Heating, Budapest 1985 p575

[2] G M McCracken et al, J Nuclear Materials 145-147 (1987) 621

[3] R Behrisch et al, ibid, p731

[4] E Deksnis, JET Report R(88)19

[5] J P Coad et al, J. Nuclear Materials 162-164 (1989) 533

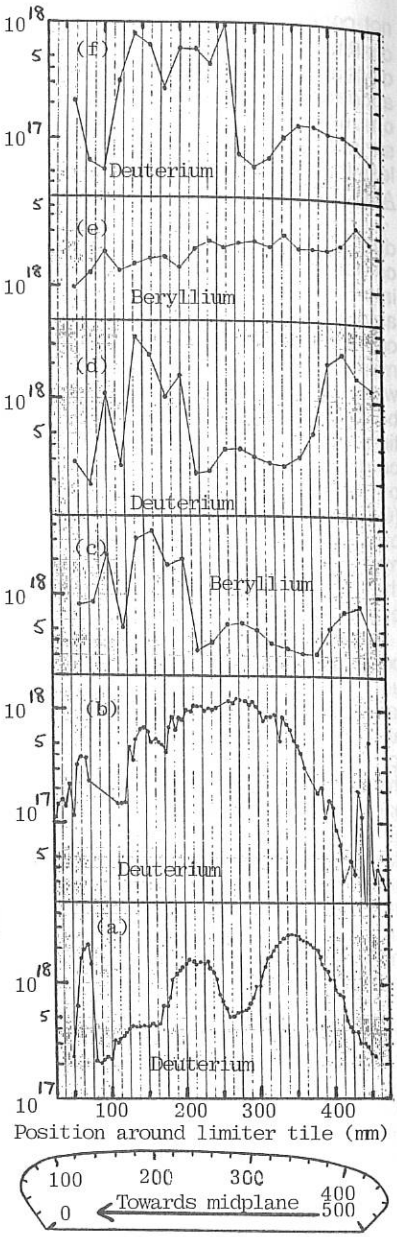

Figure 1

Deuterium and Beryllium concentration on various belt limiter tiles determined by nuclear reaction analysis (see text).

CHARGE EXCHANGE SPECTROSCOPY MEASUREMENTS OF LIGHT IMPURITY BEHAVIOUR IN THE JET BERYLLIUM PHASE

H Weisen, M von Hellermann, D Pasini, P D Morgan,
W Mandl, M F Stamp, H P Summers

JET Joint Undertaking, Abingdon, OXON OX14 3EA, UK

1) Introduction

In an effort to decrease impurity contamination, the JET 1989 programme was primarily devoted to assessing the properties of beryllium as a limiting material. In a first step beryllium was only evaporated onto the vessel walls to evaluate its gettering and pumping effects. At the end of the campaign the power handling capabilities of a pair of beryllium belt limiters were assessed. The dramatic improvements in target plasma purity and performance of additionally heated discharges can mainly be attributed to oxygen removal and improved density control resulting from the gettering action. In many conditions however the performance of high power heated discharges was limited by the appearance of hot spots on the limiting surfaces, where sublimation or melting occurred, releasing large amounts of impurities. Light impurities released into the discharge at the plasma vessel interface were diagnosed by charge exchange spectroscopy [1,2].

2) Improvements in plasma purity and performance

An overview of improvements in central deuterium dilution n_d/n_e of neutral beam heated discharges is shown in fig.1 for the different phases. (All observations during the heating pulses are represented irrespective of the discharge development). The dilution factor was obtained by adding the contributions of carbon and beryllium, which were measured simultaneously at the plasma centre. The improvement of the quality of target plasmas for heating experiments was particularly dramatic, with $Z_{eff}(0)$ decreasing from

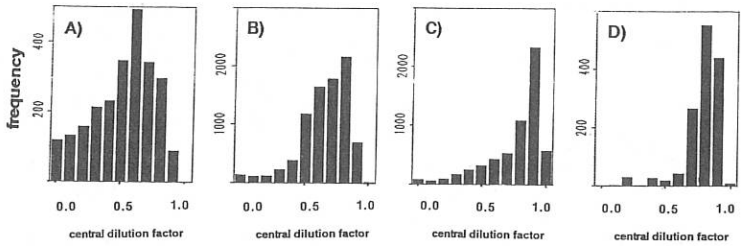

Fig. 1 Histograms of deuterium to electron density ratio A) All carbon vessel (1988), B) Be gettering, (1989), C) & D) Be belt installed, C) X–point, Be gettered, C target plates D) Be belt limiter

typically 4 without beryllium to about 1.5. The evaporation of beryllium did not lead to any appreciable Be contamination of the plasma. Be concentrations measured by CXS dropped from about 2% to below 0.5% within the first four additionally heated discharges after evaporations. The carbon concentrations of the target plasmas (≤2%) remained virtually unaffected. This behaviour is interpreted as being due to the local burning out, at the hot spots, of the about 0.2μm thick beryllium layer. This rapidly decreased the beryllium concentration in the plasma, but did not affect the gettering capabilities of the vessel surfaces, which remained unchanged for at least 50 discharges.

The improved target plasma purity, together with the better density control due to the strong pumping, lead to a substantially enhanced performance, as in fig.2a, which shows an X-point plasma with up to 17 MW of NBI which attained an ion temperature of 22 keV and and a fusion product n_d Ti τ of 9×10^{20} m^{-3}keV s in the plasma centre.

Following formation of the X-point configuration after t=8 s, the central beryllium concentration dropped steadily from an initial 3.5% to about 1%, while the central carbon concentration first increased from 0.3% to 3% at 9.5 s, before being diluted down again to 1% at 11.4 s by NB fuelling (fig.2d). Fig.2c shows that the central Z_{eff} obtained by adding the contributions of carbon and beryllium, are in good agreement with the line averaged value from visible Bremsstrahlung. Also shown in fig.2d is the carbon concentration at R=3.8m. Carbon concentration profiles remained fairly flat until 0.5 s after application of the full NBI power, when a carbon influx was first detected at the outermost CXS viewing positions, producing a hollow profile. The influx became catastrophic at 11.5 s, terminating the high fusion performance.

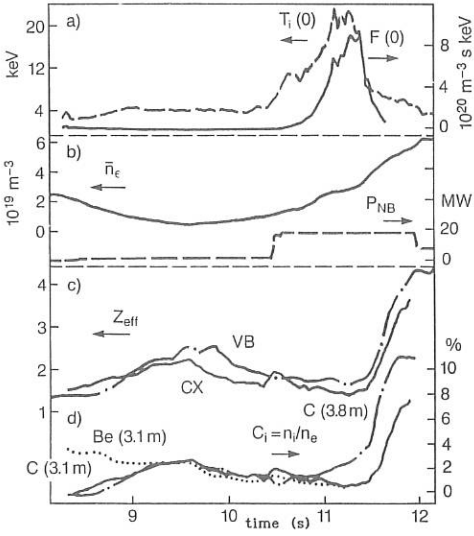

Fig.2 Impurity behaviour in a hot ion mode plasma in the double null X-point configuration. The discharge was started on the Be belt limiters. X point formation was completed at 9.5 sec. An H-mode was established between 10.8 and 11.5 sec. B_T=2.8 T, I_p=4.1 MA (pulse # 20981).
a) Central ion temperature and fusion product from charge exchange spectroscopy.
b) Line electron density and neutral beam power.
c) Line averaged Z_{eff} from visible bremsstrahlung (VB) and central Z_{eff} from charge exchange (CX).
d) Central Be (dots) and C (solid) concentrations (solid) and carbon concentration at 3.8 m (broken).

3) Impurity blooms

Sudden influxes of carbon ('blooms') have been observed when using the inner wall or the toroidal belts as limiter surfaces and for plasmas in X-point configurations. They result from hot spots on the surfaces where substantial sublimation occurs. Although limiting the performance in many cases such as in the previous example, recent experiments indicate that they can be controlled by vigourously fuelling the plasma [5,6].

The time delay for the carbon bloom, as measured from the start of the heating pulse, follows the inverse square law dependence with power predicted on the basis of a 1-D heat diffusion equation [3]. Typically carbon blooms on the inner-wall occur after 10 to 20 MJ of integrated heating power. Only 2 to 3 protruding tiles appear to be responsible for these blooms. These tiles show severe edge erosion and surface temperatures of the order of 2000° C have been inferred from IR CCD camera measurements. 10 to 20 MJ on the target plates are also sufficient to produce carbon bloom during X-point operation [4]. The energy required to produce a carbon bloom on a graphite belt limiter varied between 15 and 70 MJ according to the distance between the plasma and the RF antennae carbon protection tiles. This observation is explained by neutral beam particles which are ionised in the scrape-off layer and deposit their power directly onto the antenna tiles adjacent to the injection ports. When running the plasma well away from the RF antennae (> 3 cm) no carbon bloom was observed even after 90 MJ of integrated energy. Beryllium blooms leading to central Be concentrations exceeding 10% have also been observed with the beryllium belt limiters. Some of these blooms originated from the beryllium protection tiles of one of the RF antennae near a beam port. However even when the plasma was kept well away from the antennae, beryllium blooms still occurred, which hence must have originated from the beryllium belt limiters.

4) Impurity transport to the plasma core

The effect of an impurity influx into pure target plasmas such as obtained in the beryllium phase is to create hollow impurity density and concentration profiles. Sawteeth play an important role in transporting the impurities to the core, evident from the stepwise increase of impurity concentrations inside the inversion radius. Fig.3a shows the line electron density and electron temperature (at 3.4 m) of an H mode plasma. Also shown is the tomograghically reconstructed central soft X-ray emissivity, as transmitted through 530μm thick Be windows to reject line radiation. While most of the influx is taking place, the latter exhibits inverted or very small sawteeth, indicative of stepwise increases of core impurity densities. Since most of the X-ray emission detected was due to recombination radiation and Bremstrahlung from carbon and deuterium, we calculated Z_{eff} from the local emissivity, the electron temperature and density. The result agrees remarkably with Z_{eff} from CXS (fig.3b). In this pulse the influx appears to have been halted by a strong gas puff applied from t=11s onwards [5].

At the bottom of fig.3a we show carbon ion densities at R=3.37 and at R=3.49 m, just inside and outside the sawtooth inversion radius. Since they are so close together, relative uncertainties between the two, due to the geometry and beam attenuation calculations, are small. Between sawtooth crashes a density gradient builds up accross the inversion radius, which is

levelled at each crash. Density profiles before and after a crash are shown in fig 4a, and fig 4b shows the corresponding change in carbon density, Δn_c. Also shown is a simple model profile for Δn_c with zero volume integral to demonstrate that the small decrease in n_c outside the inversion radius accounts for the increase observed inside.

The soft X-ray and the CX measurements suggest that density profiles inside the q=1 surface remain fairly flat (within ±20%) between collapses. Since a regular increase in core densities is also observed between crashes we argue that particle transport within the inversion radius must be considerably stronger than outside where density gradients are seen to build up (fig.4). This contrasts with measurements of impurity transport using laser ablation in ohmic and RF heated limiter discharges [7], which show a strong reduction of particle transport in the central region. The present observation may be specific to H-mode plasmas. Another clue to the differences may come from the persistent n=1 MHD activity between the crashes, suggesting that the nature of this transport could be convective.

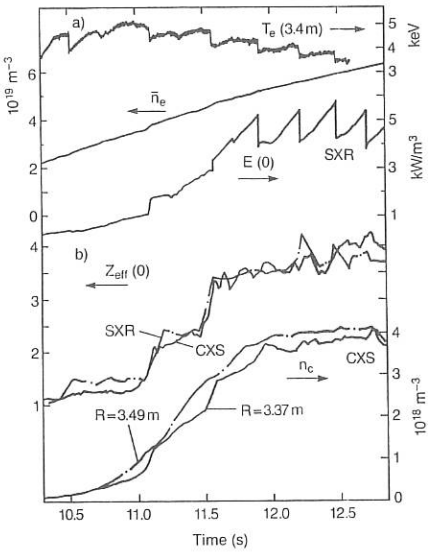

Fig.3 Role of sawteeth in transport to core in an H–mode discharge (# 20991)

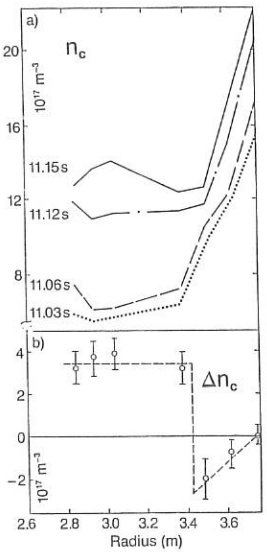

Fig.4 a) Carbon density profiles b) Change in n_c at crash

References

[1] A Boileau, M von Hellermann, M G Horton et al(1989), Nucl.Fus **29**, 1449
[2] H Weisen, M von Hellermann, A Boileau et al (1989), Nucl. Fus **29**, 2187
[3] D Pasini, D Summers, V Philipps, PSI Conf., Bournemouth, U.K., (1990)
[4] R Reichle, D Summers, M Stamp, PSI Conf., Bournemouth, U.K., (1990)
[5] D Stork et al, 31st APS, Anaheim, USA, (1989), also JET-P(89)80
[6] A Gondhalekar et al, 31st APS, Anaheim, USA, (1989), also JET-P(89)80
[7] D Pasini, M Mattioli, A W Edwards et al (1990), JET-P(90)01

RETENTION OF GASEOUS (Ar, He) IMPURITIES IN THE JET X-POINT CONFIGURATION

G. Janeschitz*, R. Giannella, H.J. Jaeckel, L. Taroni, M. Stamp, R. Barnsley, J.P. Coulon, G. Haas, P.J. Harbour, N. Hawkes

JET Joint Undertaking, Abingdon, UK
* IPP Garching, Euratom Association, FRG

Introduction:
The exhaust efficiency of divertor configurations for recycling impurities, in particular for the helium ash, is still one of the salient problems for future devices. The He exhaust capability in such machines is mainly based on two dimensional modeling of the scrape off layer. Experiments to validate such models have been carried out so far in the closed divertor configuration of ASDEX /1,2/. In these experiments Ar, Ne and He gas puffs were used to determine the divertor containment time τ_D, which characterizes the retention of recycling impurities. A pronounced dependence on the mean electron density, as well as on additional heating was observed, particularly for He.

In this paper we report on experiments undertaken to investigate the capability of an open divertor configuration for retaining gaseous recycling impurities.

Experimental findings :
Short Ar and He gas puffs are required to determine τ_D, however the JET gas injection system only allows a 300 ms pulse duration. In JET the gas is not puffed directly into the vessel, but into a pumping chamber. This chamber has a volume of 1.5 m^3 and a conductance into the JET vessel of 35000 l/sec for deuterium. The shape of the gas puff entering this pumping chamber is measured by a pressure gauge. The rise time of the pressure in this chamber is 150 ms for a combined D_2, Ar, He gas puff (50%x(5% Ar in D_2),50% He), which is used in the experiments. A good approximation of the measured gas puff is given by an exponential fit formula with a characteristic rise time τ_{puff} = 150ms.

Inside the JET vessel no such pressure measurement is available. In order to obtain the gas puff seen by the plasma the vacuum time constant of the pumping chamber has to be taken into account for He and Ar respectively. The calculation of these time constants yields 43 ms for deuterium as well as for helium, and 136 ms for Ar. In case of He the additional time constant of 43 ms is negligible compared to the rise time of the applied gas puff, whereas in the case of Ar the vacuum time constant of the pumping chamber is of the same order of magnitude. Using the above mentioned formula and assuming τ_{puff} = 150 ms for He and τ_{puff} = 300 ms for Ar the shape of the gas puff entering the vessel can be estimated

satisfactorily for both, Ar and He. The gas puff shapes so obtained are applied in the transport code calculations described below.

The combined D_2, He, Ar gas puff was injected into ohmic and moderate power neutral beam heated (8 MW from 10.0 to 14.0 sec) 3 MA double null JET X-point discharges. In contrast to the ASDEX results none of the VUV Ar line intensities (Ar VIII, Ar XV, Ar XVI) measured in the main plasma displays a pronounced peak immediately after the gas puff (Fig. 1). Only the Ar II signal obtained from a visible spectrometer shows a distinct initial overshooting when the gas puff is applied (Fig 2). The line of sight for this instrument is from the vessel mid plane to the outer divertor strike zone. This Ar II signal therefore is a measure of the injected neutral Ar flux and of the Ar flux, which recycles on several different wall components, in particular on the divertor target plate. However, this signal is not sensitive to the Ar recycling in the divertor reservoir. The divertor reservoir is partly located toroidaly between the JET target plate ribs and partly in the area enclosed by the upper belt limiter, the outer X- point plasma boundary and the upper outer scrape off of the main plasma. None of these regions is crossed by the above described line of sight. In a simplified picture, which is also used in our simulations the equilibrium value of the signal represents the Ar flux diffusing out of the scrape off plasma and hitting the chamber walls (100% recycling). For a given number of Ar particles in the whole vessel, the magnitude of this flux is solely dependent on the ratio of the global particle confinement time in the main plasma τ_p and the residence time in the divertor τ_D. The initial peak of the Ar II signal is determined by the shape of the applied gas puff and to a lesser extent by the scrape off plasma parameters, which defines the location of the ionisation source function and thus the Ar ion flux hitting the walls.

For a quantitative analysis the time dependent one dimensional impurity transport code ZEDIFF /3/, which uses measured n_e and T_e profiles is applied. The code incorporates a simple divertor model /1,3/, which acts as a reservoir loosing particles into the scrape off plasma with a time constant τ_D. With this code the time behavior of the measured Ar line intensities as well as the various neutral Ar influxes (applied and recycling Ar flux) are calculated for the ohmic X- point discharge (pulse 20993) described above. In Fig. 2 the pronounced dependence of the peak to stationary level of the calculated neutral Ar influx (applied + recycling) on τ_D is demonstrated. The comparison with the measured Ar II signal yields a τ_D of approximately 300 ms.

As mentioned already, the fraction of the neutral Ar influx, which is determined by the recycling Ar ion flux onto the wall, is to some extent dependent on the plasma parameters in the scrape off layer. These parameters are not known accurately enough to obtain τ_D solely from the Ar II signal. Therefore the τ_D value given by the Ar II signal has to be compared to the τ_D obtained from the VUV Ar intensities (Ar XV, Ar XVI, Ar VIII). In our simulation the time behavior of all VUV Ar signals turns out

to be rather independent of τ_D (Fig. 1) for τ_D < 300 ms. This behavior can be explained by the slow rise time of the applied gas puff (300 ms), which is of the order of τ_D. Values of τ_D substantially bigger than 300 ms cause a pronounced initial overshooting of the calculated VUV Ar signals, which starts to develop from τ_D = 300 ms (Fig. 1). However, even the Ar XV intensity, which displays most sensitively this overshoot in the simulation, does not reveal such a behavior in the experiment (Fig.: 1). Allowing for some inaccuracy in the simulation an upper threshold for τ_D of ~ 400 ms can thus be obtained, which supports our findings.

In the case of helium puffing the VUV He II line intensity measured during the same ohmic X- point discharge shows a small initial peaking. This peaking can be explained by the shorter rise time (150 ms) of the He gas puff in the vessel. In Fig. 3 the distinct dependence of the calculated He II intensities on τ_D is demonstrated. Again the comparison of the measured He II signal with the simulation yields τ_D ~ 300 ms.

Besides the various line intensities and fluxes the transport code also calculates the impurity particle content in the plasma and in the divertor chamber. Fig. 4 displays the number of He particles in the whole vessel (plasma + divertor chamber), as well as the He content in the plasma volume and in the divertor reservoir, respectively. A distinct dependence on τ_D can be observed. Assuming τ_D = 300 ms the calculated ratio of the He content in the divertor (accessible to pumping) to the He content in the plasma volume is approximately four (Fig.4).

The Ar puff experiments performed in neutral beam heated discharges reveal a similar upper threshold for τ_D of ~ 400 ms, which is obtained from the VUV Ar intensities using the above described procedure. However, the determination of τ_D from the behavior of the Ar II intensity can not be applied in this case, because the Ar II signal is blended by strong carbon radiation originating from the divertor target plates. In case of the He gas puff into the same NI heated discharge, there is some evidence of a deterioration of τ_D during the heating phase. However, with the experimental material available so far no conclusive statement can be given.

Discussion:

The τ_D values of ~ 300 ms obtained from ohmic X- point discharges in JET compare very well to the values found on ASDEX /1/. However, to find comparable τ_D's for ASDEX and JET does not mean that both machines have similar exhaust capabilities for recycling impurities. Important for the retention quality of a divertor in a given machine is the ratio of the residence time τ_D in the divertor and the global particle confinement time in the main plasma τ_p. This ratio determines the fraction of impurity particles stored in the divertor area, which can be possibly pumped (Fig. 4)

/1/ G. Janeschitz, G. Fussmann, P.B. Kotze et. al. Nucl. Fus. Vol.26, No.12, (1986)
/2/ G. Fussmann European Tokamak Workshop, Gut Ising (1989)
/3/ G. Janeschitz, L.B. Ran, G. Fussmann et. al. Determination of Impurity concentrations and Z_{eff} by VUV spectroscopy on ASDEX, submitted to Nucl. Fus. (Apr. 1990)

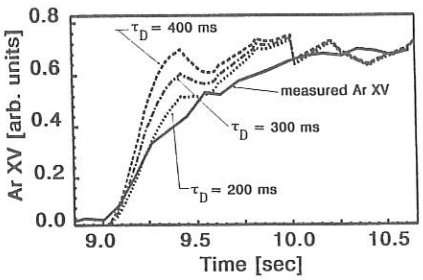

Fig. 1: Measured and simulated Ar XV intensities after an Ar puff into an ohmic X- point discharge. The slowly increasing initial overshooting of the calculated Ar XV intensity with rising τ_D is shown.

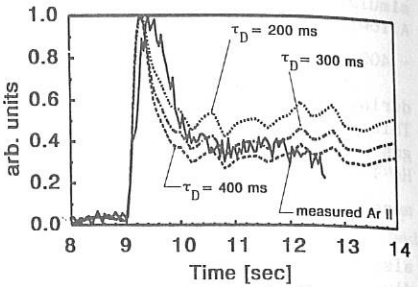

Fig. 2: Comparison of the Ar II signal in the scrape off layer with the calculated neutral Ar influx (applied + recycling flux). The pronounced dependence of the peak to stationary ratio of the calculated Ar flux on τ_D is demonstrated.

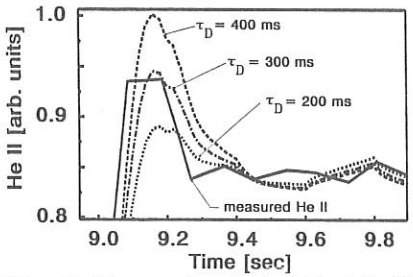

Fig. 3: Measured and simulated He II signals following a He gas puff into an ohmic X- point discharge. The dependence on τ_D of the peak to equilibrium ratio of the calculated He II intensity is shown.

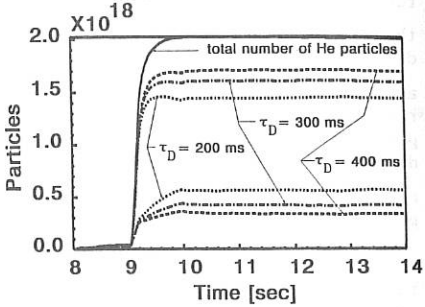

Fig. 4: The solid line represents the total He particle content in the vessel (divertor + plasma). The particle content in the plasma (lower broken lines) and in the divertor reservoir (upper broken lines) are also displayed. Traces with the same line type correspond to the same τ_D.

MODELLING IMPURITY CONTROL IN THE JET PUMPED DIVERTOR

R Simonini, M Keilhacker, A Taroni and M L Watkins

JET Joint Undertaking, Abingdon, OX14 3EA , U.K.

Introduction

For the New Phase of JET, an axisymmetric pumped divertor is proposed (Fig.1) to control the backflow of impurities from the target plates towards the main plasma. The idea is to entrench the impurities in a forced flow of plasma directed along the open magnetic field lines in the scape-off layer and thereby avoid contamination of the bulk plasma. The creation of such a flow can be envisaged by the injection of deuterium gas or pellets into the scrape-off layer; for steady-state operation, a corresponding fraction of the flow has then to be pumped near the targets. Alternatively or concurrently, a fraction of the gas recycled at the targets could be recirculated to the scrape-off layer near the X-point.

Following earlier work [1,2] on modelling these two schemes, we report here on the results obtained for magnetic configurations corresponding to currents up to 6 MA, having improved the impurity model by developing a multistage model where radiation is computed consistently.

We assess the level of flow which is required to entrench impurities near the target plates and the fraction of the deuterium flow at the targets which needs to be recycled near the X-point if this flow must be provided by recirculation. The flow is in the range of $5 \times 10^{23} s^{-1}$, which for the conditions reached at the target plates corresponds to about 90% of the deuterium flow onto the plates. This estimate has been obtained for a configuration where the connection length between the divertor throat and the plates is about 3 m only. By changing the current pattern near the X-point (or by going to lower plasma currents) the connection length could be near 10 m. In this case the flow requirement is eased since it scales roughly inversely linearly with the connection length. We show also that beryllium alone is unlikely to radiate the power required.

Model of the Divertor

For the numerical simulation, a 1-1/2D version of the 2D JET boundary code EDGE2D [3] has been developed. The two-dimensional structure of EDGE2D has been retained and used by the Monte Carlo package NIMBUS [4] which treats the neutral species and computes the sources of deuterium and impurities. The metric coefficients needed for the one-dimensional transport equations are computed from an orthogonal two-dimensional mesh derived from the magnetic flux surfaces obtained from a MHD equilibrium computation.

Fluid equations for the conservation of charged particle density, momentum end energy are solved in the direction parallel to the magnetic field lines. Impurities are represented by either an average species or the full set of ionisation stages. In the former case, the average impurity species is given the charge corresponding to the coronal equilibrium. This is acceptable since, as seen from the momentum equations, to lowest order the ratio of the forces relevant for the retention of impurities is independent of the charge, and

confirmed by calculations with the full model. Parallel transport coefficients, friction, thermal forces and electric fields (not necessarily ambipolar) are classical, following [5] and [6], and allow for arbitrary impurity levels. All ions are assumed to have the same temperature. The electron density is evaluated from quasi-neutrality.

The required boundary conditions at the target plates are subject to a considerable degree of uncertainty having to represent the transition from a fluid to a kinetic description of the flow. We have adopted the widely accepted Bohm conditions, according to which main plasma ions and impurities reach their sound speed at the plates. As for the electron and ion heat fluxes (convection plus conduction) q_e and q_α on the targets, it is assumed that $q_e = \beta_e n_e v_e T_e$ and $q_\alpha = \beta_i n_\alpha v_\alpha T_i$ for all ion species. We consider the coefficients β_e and β_i as parameters and examine the sensitivity of results to their variations ($\beta_e > 5$, $\beta_i > 5/2$).

Transport transverse to the magnetic field is replaced by specified profiles for temperature and density. These are assumed to decay exponentially outwards from the separatrix with given decay lengths. The width of the scrape-off layer plasma is chosen so that the residual perpendicular fluxes are negligible (usually, three times the scrape-off thickness).

Deuterium particles are recycled at the target plates as neutrals. The Monte Carlo code defines the spatial distribution of the ionisation sources in the vicinity of the targets. To enhance the plasma flow in the divertor region, some of the recycled deuterium is removed and recirculated into the scrape-off layer as plasma ions, with assigned spatial distribution along the separatrix (usually, but not necessarily, in the vicinity of the X-point). Those neutrals that escape to the bulk plasma are re-fed as plasma ions uniformly along the separatrix, and this is consistent with maintaining constant the deuterium content.

The Monte Carlo code defines also the spatial distribution of the impurity sources due to erosion at the target plates. A consistent computation of impurity sources is therefore possible. However, since the model for erosion is based, at present, on physical sputtering alone, the absolute concentration of wall impurities in the scrape-off layer turns out to be generally too low and a higher concentration is therefore prescribed.

Details of the model will be found in [7].

Impurity Retention in the Divertor

Of all the forces which act on the impurities, only the friction force with the main plasma ions and the electric field are beneficial for their retention, having to compensate the thermoelectric forces and the impurity pressure gradients which tend to drive impurities out of the divertor into the scrape-off layer and eventually into the bulk plasma. This implies that plasmas with high flow, low T_i, low ∇T_i are desirable.

The magnetic configuration proposed for the pumped divertor is produced by a plasma current of 6 MA, while the divertor coil's current is 800 kA. This gives a connection length in the divertor region just above 3 m. We have assumed an input power of 40 MW into the scrape-off layer, shared equally between electrons and ions. The maximum deuterium density n_i that we have been able to achieve at this level of power is about $10^{20} m^{-3}$ at the separatrix, with an impurity content (beryllium) $n_z \simeq 3\%\ n_i$. To enhance the flow of deuterium in the divertor region, a certain fraction R_H of the gas produced at the targets by recycling is removed and injected in the vicinity of the X-point (recirculation) or can be pumped out and re-fed elsewhere in the scrape-off layer. The performance of the divertor has been assessed in the first instance by considering only

one average impurity species, with constant radiating efficiency $L_R \simeq 10^{-31} Wm^3$. To exemplify the results, we show here three cases corresponding to R_H = 95%, 80%, 20%, respectively, and injected close to the X point. The resulting fluxes Γ_R injected at the X point are $\Gamma_R = 4.6 \times 10^{23}$, 4.3×10^{23} , $1.6 \times 10^{23} s^{-1}$, respectively. The effectiveness of these fluxes in entrenching impurities is shown in Fig. 2, where n_z / n_i is plotted as a function of poloidal distance.

The flows required to entrench impurities could be reduced by increasing the connection length. This can be achieved by either lower plasma and divertor coil currents, as shown in [1] and [2], where the magnetic configuration was produced by about 2.5 MA, or by changing the pattern of the divertor coil currents near the X point. Some calculations have been performed by ad-hoc variations of the poloidal field of the standard magnetic configuration in the divertor region, leading to an increase in the connection length up to about 10 m. The flux required for the retention of impurities falls below $\Gamma_R = 2 \times 10^{23} s^{-1}$, as in the previous low-current case, and this is within the pumping capabilities foreseen.

Impurities which stream out of the divertor region build up until their pressure balances the thermoelectric force in a region, far from the divertor, where no deuterium flow is present to flush them out. Some improvement in the Γ_R and R_H required for perfect entrenchment can be obtained by flushing these impurities out provided a flow of deuterium is present in the whole scrape-off layer. Fig.3 shows n_z / n_i along the separatrix in the case R_H = 80% of Fig.2, for different fractions $\Gamma_X/(\Gamma_X + \Gamma_U)$, where Γ_X is the flux recirculated at the X point and Γ_U is the flux injected uniformly along the separatrix ($\Gamma_R = \Gamma_X + \Gamma_U$): the fraction required is between 70% and 50%, which could be provided perhaps by injecting slow pellets into the scape-off layer. Such a flow in the entire scrape-off region could also flush out the impurities which are likely to be sputtered by the charge-exchange neutrals generated near the X-point by the injected gas. However, a consistent treatment of this problem requires a complete two-dimensional model.

The boundary conditions (the Bohm condition and energy transmission coefficients β_i and β_e) and radiation determine the ion and electron temperatures near the targets. β_i and β_e are subject to large uncertainties, for example β_e depends strongly on the emission of secondary electrons from the targets. We have tested the sensitivity of the results to variations of β_e (from 5 to to 20) and β_i (from 5/2 to 5). The temperature profile T_e is sensitive to β_e only in a thin layer near the plates, and moreover the ion temperature T_i is insensitive to this choice since at the densities obtained in these computations energy equipartition is ineffective in establishing equal ion and electron temperatures (Fig.4). As a consequence, the recirculation flow requirements are unchanged. T_i decreases as β_i increases, thus enhancing friction; however, at the same time the flow of plasma to the targets decreases, the temperature gradients increase and no effective improvement in impurity retention has been observed.

The effect of radiation on T_e in the vicinity of the targets is very similar to that obtained by increasing β_e , so that uncertainties in its evaluation are not expected to play an important role in the range of densities considered.

It is unlikely that beryllium alone radiates sufficiently to keep T_e down and reduce the heat loading on the targets to acceptable levels. Computations performed with the full multi-stage model have shown that with beryllium the radiated power $P_R < 2MW$, even when T_e at the targets becomes as low as 1 eV at high β_e . On the other hand, medium-Z impurities can provide the required P_R . As an example, multi-stage calculations with 3% oxygen show that $P_R \simeq$ 21 MW for an input power of 40 MW.

References

[1] M L Watkins et al, "Modelling the Pumped Divertor" JET-R(89)16.
[2] A Taroni at al, "Simulation of the Boundary Plasma in the Pumped Configuration proposed for JET", 31st APS Meeting, Anaheim, California, USA 1989.
[3] R Simonini F Feneberg A Taroni, 12th European Conference on Controlled Fusion and Plasma Physics II (1985)484.
[4] E Cupini, A DeMatteis, R Simonini, NET Report EUR XII-324/9 (1984).
[5] S I Braginskii, Review of Plasma Physics 1, Consultants Bureau, New York(1965)205.
[6] Yu L Igitkhanov, Contributions to Plasma Physics 28(1988)477.
[7] M Keilhacker et al., to be published

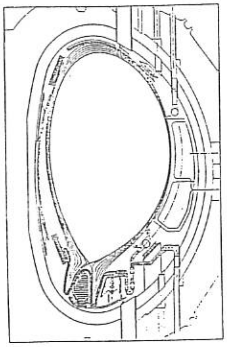

Fig.1 Schematic view of the pumped divertor proposed for JET

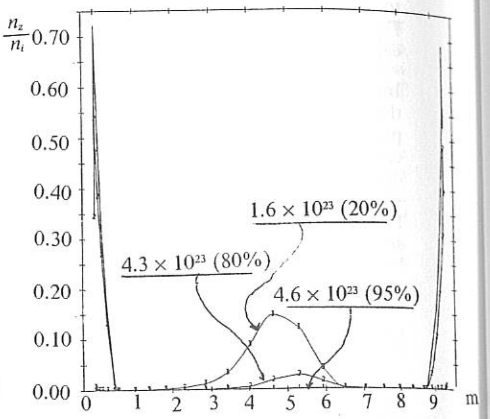

Fig.2 n_z/n_i as function of poloidal distance for different values of Γ_R and R_H

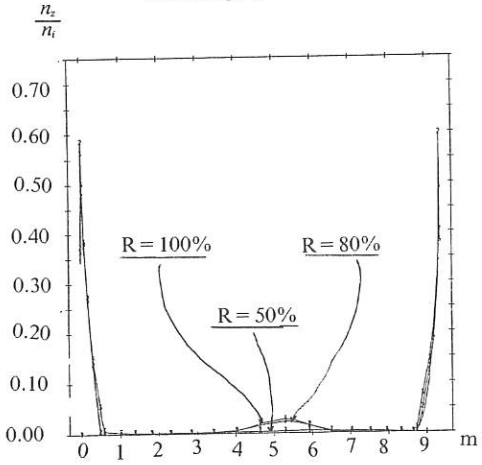

Fig.3 n_z/n_i for different values of $R = \Gamma_X/(\Gamma_X + \Gamma_U)$

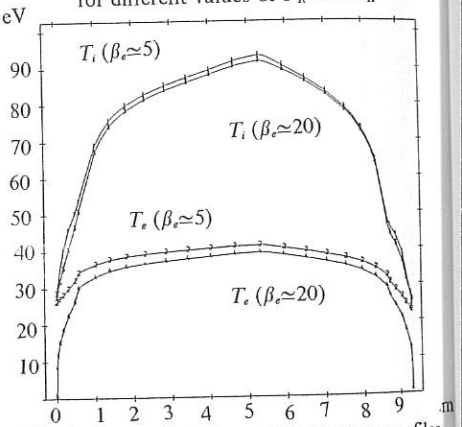

Fig.4 Ion and electron temperature profiles for $\beta_e = 5,20$

SCRAPE-OFF LAYER PARAMETERS AT JET DURING DENSITY LIMIT DISCHARGES

S Clement*, D Campbell,*, S K Erents **, L de Kock, G Saibene, R Sartori and J A Tagle .

JET Joint Undertaking, Abingdon, OXON, OX14 3EA, UK.
*CIEMAT-EURATOM Association, Av. Complutense 22, 28040 Madrid, SPAIN.
**Culham Laboratory, Abingdon, OXON, OX14 3EA, UK.

1.Introduction: During 1989, experiments were performed in JET to investigate the effect of using beryllium as a plasma facing material. Initially, Be was evaporated to form a thin coating ($\simeq$ 100 Å) on the carbon tiles which formed the plasma facing surfaces (Be gettered phase). Later, the carbon tiles of the upper and lower belt limiters were replaced by Be tiles and Be was evaporated onto the remaining plasma facing surfaces. One of the principal beneficial effects was found to be a substantial increase in the density limit and a significant change in the nature of the limit /1/. The most noteworthy changes occured in the Be limiter phase of operation, in which the density limit was increased by a factor of 1.6-2 over the all-carbon phase. In addition, it was found that the limit manifested itself as a MARFE /2,3/, which generally led to a reduction in the plasma density and a return to quiescent operating conditions,rather than a hard disruption as was normal in discharges with carbon plasma facing surfaces /4/.

We have studied the scrape-off layer (SOL) parameters in high density plasmas using Langmuir probes which are located on the belt limiters and which sample the SOL joining the two limiters along the inner wall (where the MARFE usually appears). The data reported here were obtained in limiter discharges at various plasma currents (1 - 4 MA) and with different forms of plasma heating (OH, ICRH, NBI) during the Be limiter phase of operation. An analysis has been made of the edge parameters before and during the MARFE, and a relationship has been found between the edge temperature and density which is valid for all the discharges studied, as long as the power is being convected to the edge.

2.Experimental: Three pairs of Langmuir probes situated in the upper and lower belt limiters have been used. The probes are at different radial positions and allow the measurement of the decay lengths of the SOL parameters. All the edge parameters referred to in the following section have been extrapolated to the last closed flux surface.

3.Results: All the shots studied have been gas fuelled from the edge . Due to the strong D pumping by the beryllium, a high fuelling rate has to be maintained throughout the discharge, (typically around 3 - 4 10^{21} *atoms* s^{-1} in an ohmic discharge). Too high a fuelling rate creates hollow density profiles, and lower density limits are achieved /5/.

The time evolution of the edge parameters is presented for three density limit discharges, which are good examples in the large dataset studied : an ohmic shot with a plasma current $I_p = 4$ MA and a toroidal field $B_T = 2.6$ T which marfed early in the discharge, an ohmic shot ($I_p = 3MA$, $B_T = 2.3T$) where the radiated power increased slowly, and an additionally heated discharge ($I_p = 3MA$, $B_T = 2.6T$,and total input power $P_{in} = 9.5MW$).

- Ohmic, fast edge cooling (shot # 20845) .
  Fig. 1 shows the time evolution of the edge parameters ion saturation current I_{sat} and electron temperature T_e, together with the radiated power P_{rad} and the edge gas fuelling rate F. In a first stage, from 7 to 9 seconds, the fuelling rate is increased and the total

power convected to the edge ($P_{in} - P_{rad}$, not in the figure) is approximately constant, so the increase in fluxes and the decrease of T_e are mostly due to the gas introduction in the edge; T_e reaches a very low value around 10 eV . A first MARFE then occurs ; I_{sat} decreases, but the sampling rate of the probe is too low to make a comparison with the time evolution of P_{rad} . A faster sampling rate has been used at the second MARFE . The maximum in I_{sat} (which had recovered after the first MARFE) occurs at least 0.15 seconds before the maximum in P_{rad}, when P_{rad} is $\simeq$45% P_{in} ; I_{sat} then decreases sharply (90 %) as P_{rad} increases, and recovers fast after the peak. The temperature has not recovered after the first MARFE due the sustained fuelling rate into the edge; it decreases even more during the MARFE.

- Ohmic, slow edge cooling (shot # 20943) .
  The previous shot is characterized by the early edge cooling and marfing. Generally a much steadier behaviour has been achieved in good density limit shots, where edge cooling and radiated power increase are gradual. In shot 20943, the edge temperature decreases slowly between 6 and 12.5 s, from $\simeq$40 eV to $\simeq$10 eV . The density e-folding length λ_{ne} is constant until T_e reaches a value around 20 eV, then decreases. The power convected to the limiters P_{lim}, calculated with SOL parameters, does not vary very much during the last phase of the discharge .

- Additionally heated (shot # 20822)
  Fig. 2 shows the time evolution of several SOL parameters together with some central parameters for comparison. Temperatures around 10 eV are reached again; as in the previous shot, λ_{ne} is constant until $T_e \simeq$ 20 eV and P_{lim} is constant during the last phase of the discharge .

In fig.3, the edge temperature as a function of the edge density is shown for three discharges (shots # 20943, 20822 and 20850, the latter being a 4 MA shot with 15 MW of additional heating). The curves obtained do not constitute a proper scaling, because all the data points are taken with dynamic conditions; however, they summarize the behaviour of the edge parameters observed in a dataset of about 30 high fuelling rate discharges. The points corresponding to additionally heated discharges are displaced towards higher edge densities with respect to the ohmic data, but the shape remains the same. There is a change of slope when the temperature is around 20 eV, where the decrease of T_e with increasing n_e is faster. The parameter which separates the ohmic and additionally heated curves is the average power convected to the edge per particle,

$$P_{part} = \frac{P_{in} - P_{rad}}{n_e V}$$

where n_e is the volume averaged density and V is the plasma volume. In these density limit discharges, p_{part} varies within the same range of values for all the different input powers used (data taken in discharges with 30 MW of additional heating are on the right hand curve) In Fig.4, P_{part} is represented together with the electron temperature versus time for an ohmic and an additionally heated discharge.

4.Discussion: The results obtained are consistent with a similar sequence of events taking place in all the shots which develop a MARFE, independently on whether additional heating is used or not. During a first phase, the total power convected to the edge remains aproximately constant; as the edge fuelling rate is high, a cooling of the edge takes place (the power convected to the edge per particle decreases). Then, when the edge temperature

reaches a certain value (around 20 eV in the present case, where the main radiating impurities are C, Be, and Cl), the radiated power in the edge starts to increase, and self enhanced impurity radiation cooling takes place leading to a MARFE /3/.
Several findings are consistent with previous observations: the decrease in the density scrape-off length around 20 eV agrees with the broadening of central density profiles and hence steep density gradients found near a MARFE /5/; the fact that the first cooling phase depends mainly on the fuelling rate explains why too high fuelling rates lead to lower global density limits /5/. However it must be pointed out that our measurements are taken at the belt limiter, far away from the place where the MARFE is localized, and hence provide no local information, so no insight can be gained as to the mechanisms which quench the MARFE.

References

/1/ C Lowry et al, these proceedings.

/2/ E Stringer et al,12th EPS Conference on Controlled Fusion and Plasma Physics, Europhysical Conference Abstracts 9F, Part I, p86(1985).

/3/ J Neuhauser, W Schneider and R Wunderlich, Nucl. Fus. 26, 1679(1986).

/4/ J Wesson et al, Nucl. Fus. 29, 87(1989).

/5/ D Campbell et al, ITER Workshop on Disruptions, Garching, FRG, 25-27 september 1989.

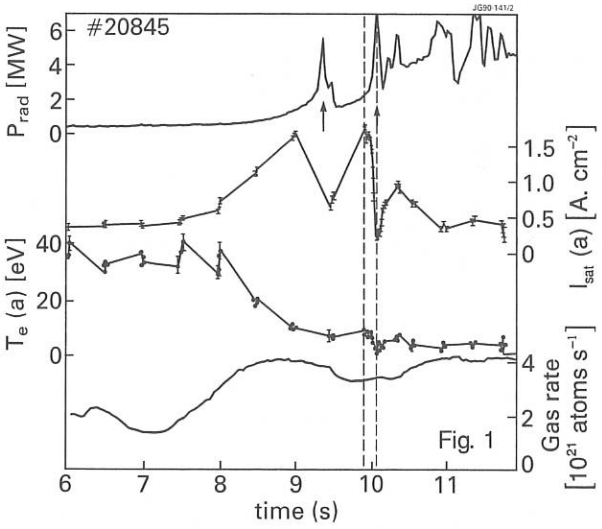

Figure 1. Total radiated power, ion saturation current, electron temperature, and gas fuelling rate, for an ohmic discharge , I_p =4 MA, B_t =2.6 T. The arrows indicate the two first MARFEs.

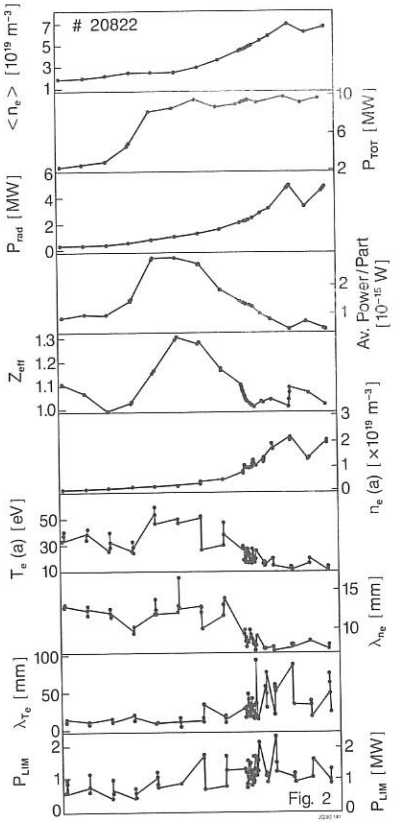

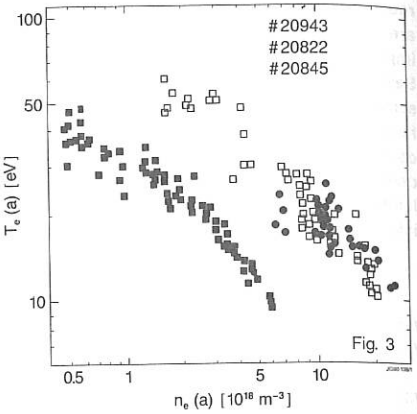

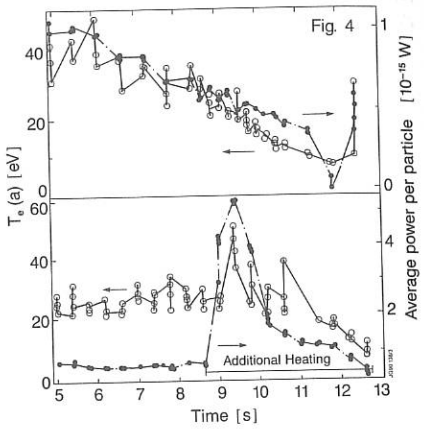

Figure 2. Volume averaged density, total input power, total radiated power, average power convected to the edge per particle, Z effective, edge density, edge temperature, edge density e-folding length, edge temperature e-folding length, and power convected to the limiters, for shot 20822 ($I_p = 3\,MA$, $B_t = 2.6\,T$).

Figure 3. Edge temperature versus edge density for shot 20943 (ohmic, $I_p = 3\,MA$, $B_t = 2.3\,T$), shot 20822 ($I_p = 3\,MA$, $B_t = 2.6\,T$, and 9.5 MW additional heating), and shot 20850 ($I_p = 4\,MA$, $B_t = 2.6\,T$, and 15 MW additional heating).

Figure 4. Edge temperature and average power convected to the edge per particle for the shots 20943 and 20822.

TEMPERATURES AND DENSITIES IN THE JET PLASMA BOUNDARY DEDUCED FROM DEUTERIUM AND BERYLLIUM SPECTRA

M F Stamp and H P Summers

JET Joint Undertaking, Abingdon, Oxon OX14 3EA, U.K.

1. Introduction

The plasma edge is one of the most important regions of a tokamak plasma, since it is the edge parameters that determine the sputtering yields, impurity source rates and ionisation lengths of impurity and fuel species. Knowledge of these edge parameters is often limited; for instance, the electron and ion temperatures are usually assumed to be equal, even though they are clearly different in the plasma centre.

In this paper we describe measurements of edge ion temperature derived from ion Doppler widths, and measurements of the edge electron density from intensity ratios of suitable spectral lines.

2. Experimental Details and Data Analysis

Spectral lines of deuterium (D_α, D_γ), carbon (CII 6578, 6582Å) beryllium (BeI 4407Å and BeII 4361Å), oxygen (OII 4415, 4417Å) and helium (HeI 6678Å) are routinely monitored with the visible wavelength JET survey spectrometer. This is a 1-m Czerny-Turner instrument with an intensified linear diode array detector at its focal plane[1]. Plasma light, emitted from in front of the limiter, is collected by an achromatic lens and fed into the spectrometer via a quartz optical fibre.

The spectral information from the diode array is analysed with a multi-gaussian line fitting routine that deconvolves the instrument function and the Doppler profiles of the spectral lines.

The data presented in this paper are from the last period of machine operation, when JET had a beryllium belt limiter, and the limiter influxes of carbon and oxygen were very low. Consequently, only the analysis of the deuterium and beryllium spectra are presented here.

3. Ion Temperatures

The deuterium influx from the limiter consists of a molecular influx at thermal energies, and a small amount (10-20%) of reflected deuterium. The molecular deuterium fragments into atoms and ions by a variety of reactions [2], some of which produce an excited deuterium atom that subsequently decays radiatively. As they travel into the plasma the deuterium atoms will either emit photons when excited by electron impact, or charge-exchange with plasma ions, or be ionised by electron impact. Since the charge exchange cross-section is similar to the ionisation cross-section in the JET plasma boundary, many atoms will undergo charge-exchange, resulting in a cold deuterium ion and an energetic neutral whose energy is representative of the local ion temperature. The D_α line profile is expected therefore to consist of a broad feature, due to charge-exchange, and a narrow feature due to the slower atoms in the plasma edge.

Fig.1 shows the Doppler ion temperatures that have been measured in ohmic, 3MA, beryllium belt limiter plasmas, as a function of line average

electron density. The deuterium spectral feature requires a two-gaussian fit; where one gaussian ("cold" component) always has a Doppler temperature of ~5eV, and the other ("warm" component) a Doppler temperature of 40-200eV. This "warm" component was emitted by deuterium ions that gained an electron by charge-exchange from a cold neutral and it is therefore a measure of the edge ion temperature.

From fig.1 we can see that the edge ion temperature varies from ~200eV at low density to ~40eV at high density. This is much higher than the measured edge electron temperature, which varies from ~45eV to ~15eV [3]. However, the radial profile of the D_α emission is not known, although we would expect the neutrals to penetrate further, and therefore appear hotter, at lower electron densities. Spatially-resolved measurements in a direction normal to the belt limiter would allow localisation of the D_α emission, but are not possible with the presently-available viewing ports on JET.

The neutral beryllium (BeI) Doppler temperature of 5-15eV indicates that physical sputtering is the dominant source mechanism. The average energy of evaporated atoms would be ~0.1eV, whereas the average energy of atoms produced by physical sputtering is several eV, and is larger for self-sputtering than for D^+ sputtering [4]. The BeII ion temperature is lower than the local ion temperature (from D_α) because the BeII ionisation time is shorter than the energy equipartition time. These beryllium ion temperatures are extremely useful data for the validation of complex impurity sputtering codes [5].

4. Edge Electron Density

Line intensity ratios are sensitive to electron densities in tokamak plasmas when the upper level of one of the transitions is close to the collision limit, and the other not, and the lines share the same excitation mechanism. A collisional-radiative population model is required for interpretation of the line intensities (see for example [6]). For deuterium the line intensity ratio of D_α (n=2-3) to D_γ (n=2-5), and for BeI the line intensity ratio of BeI (8254Å)(2p-3s) to BeI (4407Å)(2p-4s) satisfy the above criteria for density sensitivity.

Experimentally, the 8254Å line is observed with an interference filter-photodiode combination, viewing the other belt limiter to the survey spectrometer. By assuming that the beryllium sputtering yield is the same on both belt limiters (ie normalising to D_α emission) we calculate the ratio of intensities of the 8254Å and 4407Å lines, fig.2. The survey spectrometer also observes the BeII line at 4361Å, so it is straightforward to take the intensity ratio of BeII (4361Å) to BeI (4407Å). This is also a measure of the edge density since the BeII line is a measure of the total BeI influx, but unfortunately the BeI influx is an uncertain mixture of ground state atoms (which are measured from the 8254Å line) and atoms in the $2s2p\ ^3P$ metastable state. The characterisation of the metastable fraction with plasma conditions is in progress so we may be able to use this BeII/BeI line ratio to measure density in the future.

The D_α/D_γ intensity ratio is calculated directly from the calibrated survey spectrometer data, and fig.2 shows the intensity ratios of "total D_α" / "total D_γ" , as well as "cold D_α" / "cold D_γ". The "cold" components of D_α and D_γ measure the electron density close to the plasma edge, while the "warm" components (not plotted because the error bars are larger, ~30%, and the data overlaps the "cold" data) would measure the density deeper in the plasma. An accurate determination of the "warm" D_α/D_γ intensity ratio, combined with a knowledge of the edge density gradient (from Langmuir

probes, for instance) would allow the radial position of the warm D_α and D_γ components to be calculated, and hence the radial position of the D_α Doppler ion temperature.

In the data analysis we are exploiting a new extended collisional-radiative model which handles both hydrogenic ions and non-hydrogenic ions (such as BeI) and includes charge transfer processes. It gives a precise treatment of low levels and levels in the vicinity of the collision limit. Inclusion of up-to-date atomic cross-sections is an essential part of this development which will be reported in detail shortly.

Fig.2 shows the edge electron density calculated from the experimental deuterium line intensity ratios using first results from our collisional-radiative modeling of hydrogen\deuterium. This is in good agreement with the Langmuir probe edge density measurements [3], considering that the probe analysis assumes equal ion and electron temperatures. Our modeling of the BeI line intensities is still in progress and will be completed shortly.

5. Strong Gas Fueling

One plasma shot plotted in fig.1 (#20573, plotted without error bars for clarity) is interesting because the plasma density was raised with gas puffing, then allowed to fall as the limiter and walls pumped, and then raised again with gas puffing. The experimental data (figs.1 and 2) indicate that the edge density is higher (and the ion temperature lower) when the gas puff is raising the average density. This effect can be seen more clearly in fig.3, where the density falls quickly when a string of pellets ends, until it is raised again by a strong gas puff.

6. Conclusions

* Spectroscopic techniques have been used to measure the Doppler ion temperatures of BeI, BeII and neutral deuterium in the plasma edge.
* The warm component in the D_α spectrum gives a measure of the edge ion temperature, although for our viewing geometry the exact radial location of this measurement is not known.
* The BeI Doppler temperature indicates that physical sputtering, rather than evaporation, is the dominant impurity source mechanism.
* The edge ion temperature in JET ohmic plasmas seems to be higher than the edge electron temperature, especially at low electron densities.
* Intensity ratios of spectral lines such as D_α/D_γ or BeI (8254Å) / BeI (4407Å) can be used to measure electron density.
* Electron density profiles can be modified with gas puffing. In particular, with strong puffing, the edge density is raised relative to the central density, resulting in a lower edge temperature. This should have beneficial effects on plasma purity by reducing the impurity sputtering yields.

7. References

[1] M F Stamp et al., J.Nucl.Mat. **162-164** (1989) 404.
[2] A B Erhardt and W D Langer, Report **PPPL**-2477 (1987).
[3] S K Erents et al., this conference.
[4] P C Stangeby, private communication.
[5] P C Stangeby, C Farrell, S Hoskins and L Wood, Nucl.Fus. **28** (1988) 1945
[6] L C Johnson and E Hinnov, J.Quant.Spec.Rad.Trans. **13** (1973) 333.

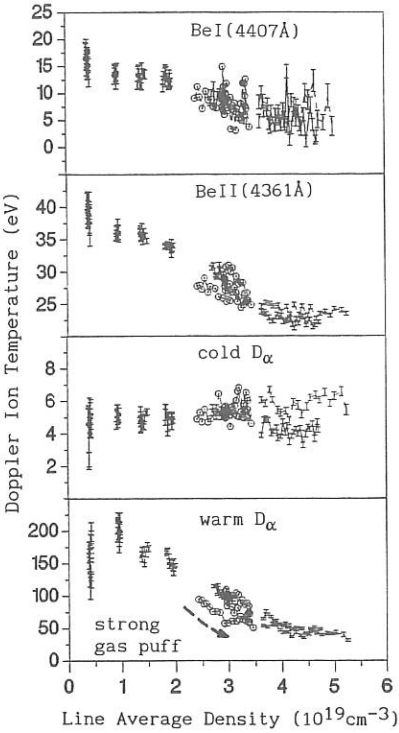

Fig.1 Doppler ion temperatures vs line average density for 3MA ohmic discharges. #20573 is plotted without error bars so that the time evolution of the pulse can be seen. Note that for the same average density, the BeII and warm D_α temperatures are lower with heavy gas puffing.

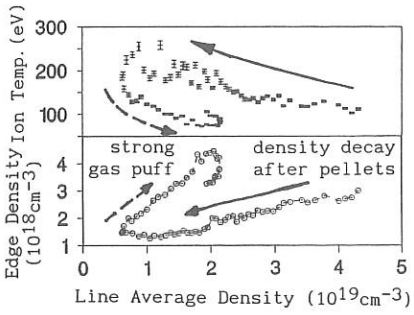

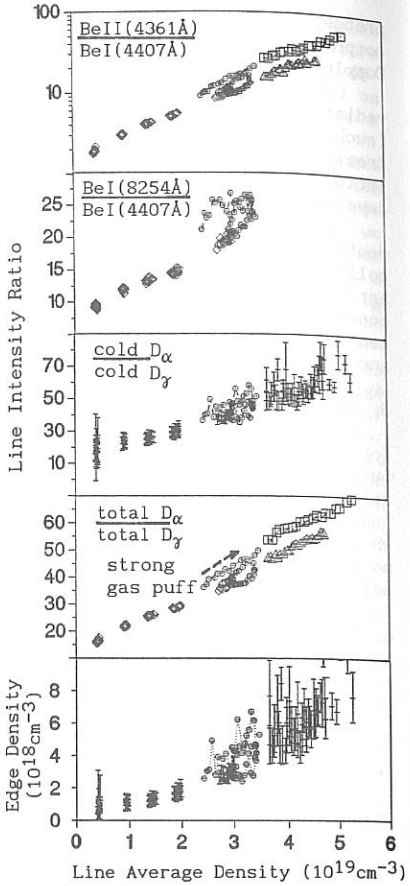

Fig.2 Line intensity ratios, and the edge density, vs line average density ($\bar{n}_e$), for the same data as in fig.1. #20573 shows that for the same $\bar{n}_e$, the edge density is higher with heavy gas puffing.

Fig.3 Edge density and edge ion temperature vs $\bar{n}_e$ for #20949 (3MA, ohmic). Frozen deuterium pellets were used to produce a high density plasma that was then pumped by the limiters and walls. Subsequently, a strong gas puff raised the plasma density. The strong anti-correlation between the edge temperature and the edge density can be clearly seen.

FORMATION OF DETACHED PLASMAS DURING HIGH POWER DISCHARGES IN JET

G M McCracken*, L de Kock, S K Erents*, N Gottardi, P J Harbour, A Hwang*, T T C Jones, K Lawson, P J Lomas, C Lowry, P D Morgan, J O'Rourke, D Pasini, C S Pitcher+, M Stamp, P E Stott, D D R Summers, M Bures, J A Tagle, P Thomas, M von Hellerman

JET Joint Undertaking, Abingdon, UK, OX14 3EA
*Culham Laboratory, UKAEA/Euratom Fusion Association, Oxon, UK
+Canadian Fusion Fuels Technology Project
+Present address: Plasma Physics Laboratory, Princeton, NJ 08544

1. Introduction

Detachment is readily produced in ohmically-heated plasmas by operating near the density limit [1]. As increased additional heating is applied it seems to get progressively more difficult to obtain detachment [2]. Detachment has not previously been attained with heating powers exceeding 9 MW. However, under some circumstances, with very high additional heating power (≥ 20MW) in JET, it has been found that the impurity influx is so large that detachment occurs spontaneously [3]. Most of the power input to the plasma is radiated and the power and particle flux to the limiters is reduced by a factor of 5∿10. We take this as our definition of detachment. A MARFE also forms on the inside mid-plane. This mode of operation is potentially interesting since it is similar in character to the 'cold plasma mantle' [4] proposed for making the power deposition more uniform on the walls of fusion devices.

2. Experimental Conditions

Two groups of discharges have been examined in detail, one in 1988 with a plasma current I_p = 5 MA, using the carbon belt limiters, and the second in 1989 with I_p = 3MA using carbon limiters and beryllium gettering. The distance of the last closed flux surface from the inner wall was typically 50∿100 mm. These specific discharges were chosen because of the extensive edge diagnostics at and near the limiters. In all cases the density is close to the density limit. Both ICRF and NBI heating are used. Plasma detachment occurs when the plasma is resting on the protection tiles of the ICRH antennas, if there is sufficient power reaching the antennas for them to reach some critical temperature. The global parameters, input power P_T, volume-averaged density $\bar{n}_e$ and radiated power P_R are shown in figs 1a, 1b, 1c. The additional heating starts at 6s. A similar discharge in the same series, but with lower input power (18MW), is shown in fig 2. No evidence of detachment or MARFE formation is observed.

3. General features of detachment and MARFE formation

In general there are four phases in the discharges discussed. The first phase (I) is the expected response to the additional heating

power, namely an increase in density and temperature, with a consequent increase in the impurity density and the absolute radiated power [5]. A new equilibrium between input power, radiated power and conducted power can be established as observed in shot 19653, fig 2.

In the second phase (II) the temperature at r/a>0.5 decreases and the current profile begins to peak, as indicated by the second and third Shafranov moments, fig 1d. The ion temperature and the neutron production rate fall by large factors, figs 1 e and f. The most striking change in this phase is the reduction of the interaction at the limiter. The ion flux, measured by the D_α radiation, fig 1h, and the radiation from the low charge states of carbon and beryllium, CI, CII, CIII, BeI, BeII all fall by factors between 5 and 10. These signals are observed both spectroscopically and with CCD cameras. The BeII radiation is shown in fig 1i. The flux reduction occurs at both upper and lower belt limiters, measured spectroscopically, and at the ICRH antennas measured by probes. The reduction of the power and particle flux to the limiters is characteristic of detached plasmas, although in many respects the present conditions are quite different to those in ohmically heated detached plasmas [1]. In particular, the change in temperature profile is much less.

At the beginning of the third phase (III) there is a sudden transition and a MARFE forms on the midplane at the high field side of the plasma. The tomographic reconstruction of the poloidal distribution of the MARFE is shown in fig 3. It is seen to be roughly symmetric about the mid plane. Further evidence of detachment occurs at the transition to the MARFE. The radiation from the outer bolometer channels, viewing the belt limiter region drops, fig 1j, and the coupling resistance of all the 8 ICRF antennas drops indicating a reduction in the local density, fig 1m. While the outer channels of the bolometer array show a fall, indicating detachment, the inner channels viewing the MARFE show a marked rise, fig 1k. During the MARFE the electron density and the carbon density both fall slowly. The near-edge temperature is slowly rising, fig 1n. After about 1s there is a sudden transition back to the attached state.

After the MARFE disappears, phase IV, the particle fluxes to and from the limiters recover to near the pre-detachment values. In a few cases where the additional heating is on for sufficient time, the plasma heats up again and the neutron reaction rate increases, figs 1e, 1f, 1n. This continues for about 0.3s and then the ion temperature and the neutron flux decrease again. This time corresponds to the time required for the impurities to diffuse back into the centre. In one case the detachment and MARFE occurred a second time in the same discharge.

4. Discussion and conclusions

When the power input is initially increased the observed impurity increase and the resulting radiation are to be expected on simple power balance considerations. In the present discharges with very high input powers, there is evidence from the CCD camera observations that edges

of the ICRH antenna tiles are exceeding 1000 K and there is also evidence of the 'carbon bloom' [6]. The heating of the tiles is probably caused by neutral beam particles which are charge-exchanged in the plasma boundary at high $\bar{n}_e$. A qualitative explanation of the behaviour is that, despite the additional heating, the impurity influx is sufficient to cool the edge plasma, the current channel shrinks and detachment ensues. The measured electron temperature at the limiter surface is typically $\sim$ 15 eV. The drop in particle and energy flux to the limiters and the corresponding drop in impurity influx is very striking. However, it is possible that the particle flux arrives at some other surface which is not directly viewed by the diagnostics. The detachment is quite unlike that seen in other ohmically-heated tokamaks [1]. The electron temperature profile changes only very slightly over most of the plasma radius. It should also be made clear that the series of discharges described are not typical of all carbon bloom discharges. If the starting density is lower, at the start of the carbon influx the density and the total radiation simply rise steeply [6]. Only when the density is already near the density limit do the detachment and MARFE formation occur.

During the detached MARFE, phase III, the electron density and the central impurity density decrease slowly. This is a result of the low recycling and low impurity influx. The reduction in density and impurity content eventually leads to the MARFE collapsing and the plasma reattaching. It is to be expected that this cycle would keep on repeating itself if the input power remained high. There is evidence from a series of discharges of increasing power that the length of the detached phase increases as the input power increases.

It is clear that high performance, eg high neutron yield, is limited by a number of factors, of which impurity influx is only one. The neutron flux has reached its maximum well before detachment starts. The detachment and MARFE formation reduce the neutron yield further, but this decrease occurs late in the sequence of events. However, the present discharges are of considerable interest because they exhibit many of the features of the 'cold plasma mantle'. It would clearly be advantageous to produce detachment first and then heat the plasma so that the high impurity flux and damage to the limiters are avoided. This could be done by impurity injection eg with low-z gaseous impurities. The problem of plasma dilution by the impurities is still however unresolved.

5. References

[1] B Lipschultz, J Nucl Mat 145-147 (1987) 15

[2] C E Bush, J D Strachan, J Schivell et al, PPPL 2616 1989

[3] C S Pitcher, G M McCracken et al, Proc 16th EPS Conf Venice 3 (1989) 879

[4] M L Watkins and A Gibson, Proc 8th EPS Conf, Prague 1 (1977) 31

[5] G M McCracken, Plasma Phys and Controlled Fus 29 (1987) 1273

[6] D Pasini et al, Proc 9th PSI Conference Bournemouth, UK, May 1990

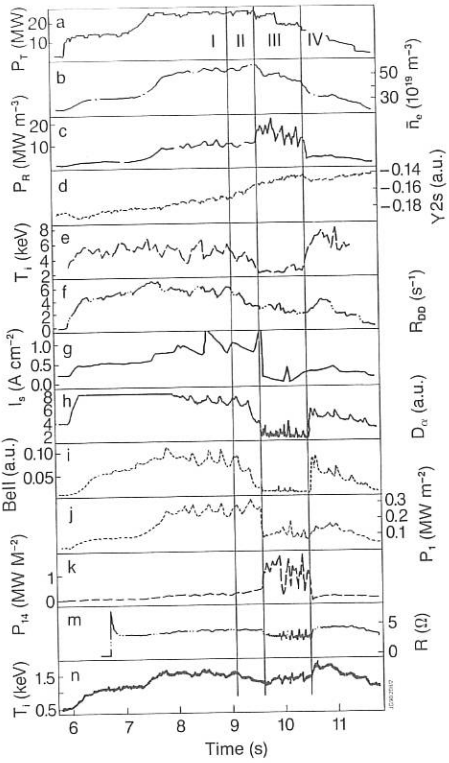

Fig 1

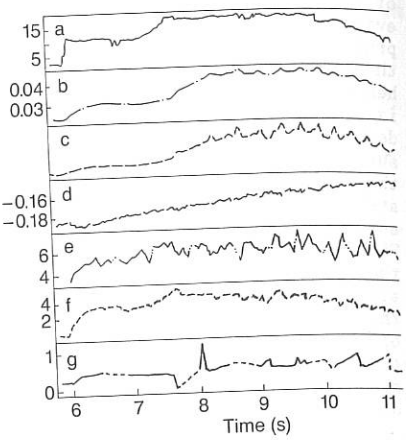

Fig 2

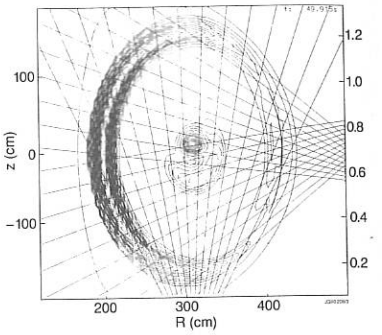

Fig 3

Fig 1. Time dependence of plasma parameters during discharge 19659 showing detachment and MARFE formation. (a) Total input power (b) Volume-averaged density (c) Total radiated power (d) Second Shafranov moment (e) T_i from charge exchange (f) (d,d) reaction rate (g) Ion flux to top limiter (h) D_α intensity (i) BeII intensity (j) Vertical bolometer, channel 1 (k) Vertical bolometer, channel 14 (m) RF2B antenna coupling resistance (n) T_e at R = 3.9m from ECE.

Fig 2a → 2g. As fig 1, but for discharge 19653

Fig 3. Tomographic reconstruction of the radiation from the horizontal and vertical bolometers for discharge 19659 at 10s.

AN INVESTIGATION INTO HIGH ION TEMPERATURES IN THE JET PLASMA BOUNDARY

S K Erents*, S Clement#, P J Harbour, M von Hellerman, L de Kock, G M McCracken*, M F Stamp, P C Stangeby+, D D R Summers, P R Thomas, H Weisen

JET Joint Undertaking, Abingdon, UK, OX14 3EA
*Culham Laboratory, UKAEA/Euratom Fusion Association, Oxon, UK
#Asociacion CIEMAT-EURATOM, Av Computense 22, 28040 Madrid, Spain
+Institute for Aerospace Studies, University of Toronto, Canada,

1. Introduction

It is generally found in Tokamaks that the power to the edge, calculated from langmuir probe data by assuming equal ion and electron temperatures, is less than that measured by thermocouples. This has been found to be true for JET in all phases of operation, and is particularly apparent from recent data taken over a wide range of densities using beryllium limiters. The power to the edge obtained from probes is between 4-5 times too low at low densities, and 1-2 times too low at high densities compared with limiter thermocouple data.

Various reasons for this discrepancy in power can be suggested, but in this paper we investigate the possibility that ion temperature $T_i >> T_e$ in the edge.

2. Experiment

Evidence for high T_i comes from two independent probe measurements. The first uses measured values of T_e and flux density I_{sat} from fixed probes (LIM) in the beryllium belt limiter to calculate the power to the edge, which is then compared with edge power calculated from thermocouples in the limiters. The value of T_i which is required to obtain agreement between the two measurements is then calculated, The second method uses the floating potential $V_f(r)$ measured by a reciprocating probe which moves a distance of up to 20 mm (r) inside the last closed flux surface (LCFS). From $V_f(r)$ and $T_e(r)$ the radial electric field just in front of the limiters is calculated, and the force due to this field on the ions is equated to the ion pressure gradient.

Measurements were made in the plasma current flat top phase of 3MA, 2.2 Tesla ohmic plasmas, when the plasma internal energy was essentially constant, but the volume average density $\langle n_e \rangle$ was unfortunately still changing with time. This varying density gives rise to a scatter in the data for $T_e(a)$ and $n_e(a)$ when plotted as a function of $\langle n_e \rangle$, fig 1. The magnitude of the effect is the subject of a separate paper, (1). A second source of error could be the effective area of the probes in the limiter, which is difficult to calculate because of the glancing angle of field lines. The likely direction of this error would be to raise T_i further.

3. Density and Temperature Scaling

For $\langle n_e \rangle > 2.10^{19}$ m^{-3} the $T_e(a)$ scaling is similar to that observed for carbon belt and discrete limiters, (2), namely $T_e(a) \sim \langle n_e \rangle^{-2}$. For $\langle n_e \rangle < 2.10^{19}$ m^{-3}, $T_e(a)$ becomes almost independent of density at ~ 40eV. This figure is not a limit for the probes - $T_e(a)$ rises with additional heating power to temperatures > 60eV. The edge density rises with a greater than square law dependence on $\langle n_e \rangle$ at high density, (fig 1) primarily as a result of heavy gas puffing into the edge (1).

4. Power Balance

The power to the edge measured using thermocouples is systematically a factor 1.5 less than the difference between input and radiated powers. The error is probably attributable to the toroidal variation of power to the limiters. The power transported to the edge as estimated by the probe data is given by:

$$P_c = \gamma \, I_{sat}(a) \, T_e(a) \quad W.m^{-2} \quad (1)$$

where the power transmission factor γ is usually written as the sum of ion, electron and sheath potential terms

$$\gamma = 2 \, T_i/T_e + 2/(1 - \delta) + V_s \quad (2)$$

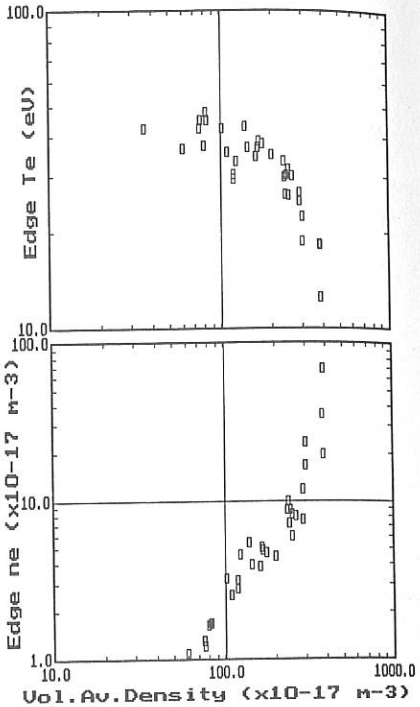

Fig 1 Te(a) and Ne(a) scaling with volume average density

δ is the secondary electron yield and V_s the sheath potential.

$$V_s = -0.5 \ln(2 \pi \, m_e/m_i \; (Z + T_i/T_e) \; (1 - \delta)^{-2}) \quad (3)$$

Values of $\delta(T_e)$ measured for a JET carbon sample can be described empirically by:

$$\delta = (1 - \exp(-0.017 \, T_e)) \qquad 10 < T_e < 120 \text{ eV} \quad (4)$$

The glancing angle (15°) between field lines and limiter may mean that secondaries do not escape, however, ($\delta = 0$). This would imply even higher values for T_i. A good empirical fit to γ from eqns. 2 to 4 for deuterium is:

$$\gamma = 1.88\ T_i/T_e + 7.4\ 10^{-4}\ T_e^2 + 5 \quad 10 < T_e < 120\ \text{eV} \qquad (5)$$

Using eqn. 5 and initially assuming $T_i = T_e$ a value for P_{cT} is obtained by integrating eq 1 across the SOL and around the torus, $P_{cT} = P_c \lambda_p L$ where λ_p is the power e-folding length obtained from the probe radial profiles just outside the LCFS, and L is the total radial length of both limiters in both ion and electron drift directions, (ie $8\pi R_{lim}$). Then from eq. 5:

$$T_i = (T_e(P_{cT}/P_{Th})(6.88 + 7.4\ 10^{-4}\ T_e^2) - 7.4\ 10^{-4}\ T_e^2 - 5)/1.88 \qquad (7)$$

where P_{Th} is the power to the edge estimated from $(P_{in} - P_{rad})$. The results of this calculation are plotted in fig 2. Here $T_i(a)$ is seen to rise to values in excess of 400 eV at low $\langle n_e \rangle$, ($< 10^{19} m^{-3}$) and $n_e(a)$ (corrected for high T_i) is $< 3.10^{17} m^{-3}$ At these very low edge densities the collisionality will be low and we might expect that ions diffusing from the core regions will still be hot at the edge.

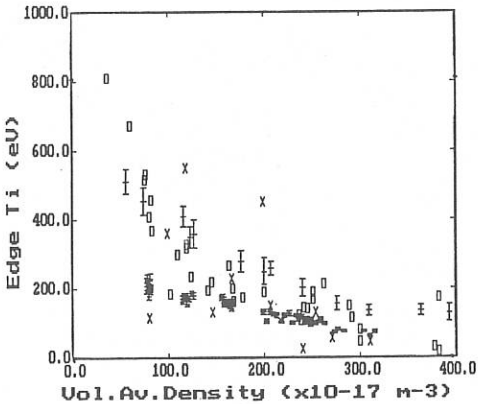

Figure 2. Edge ion temperature from: □ Power Balance, x Electric Field, + Be IV and + D_α Light, plotted as a function of volume average density.

5. T_i from radial electric field

The radial electric field just inside the LCFS is most conveniently obtained from floating potential measurements $V_f(r)$ made by the RCP. The plasma potential V_p is obtained from:

$$V_p = V_s + V_f \qquad (8)$$

and the field: $E_r = dV_p/dr$ (9)

which is usually constant over the first 20 mm inside the LCFS. In this region, the ion pressure gradient dp_i/dr is balanced by E_r, in the absence of rotation. Then

$$dp_i/dr = d(n_e\ (r)kT_i(r))/dr = n_e(r)E_r \qquad (10)$$

Differentiating across the exponential density and temperature profiles in the edge, since $\lambda_{Ti} >> \lambda_{ne}$, we obtain:

$$T_i = E_r \lambda_{ne} \quad (11)$$

Using the above equations, T_i is calculated by an iterative process, choosing a value to calculate V_s (eq 3) and then calculating a new value for eq 11 until a consistent T_i is obtained. The results of this calculation are plotted in fig 2 together with the power balance T_i data. Both methods show that $T_i >> T_e$ at low densities, although there is a larger scatter in the electric field data.

6. Further evidence for high T_i near the edge

Active ion temperature measurements obtained from charge exchanging of Be IV with a diagnostic beam in the main plasma show radial profiles $T_i(r)$ to be very flat, often close to 1keV at the measurement chord which is some 200mm inside the LCFS, in limiter plasmas. Passive charge exchange data, coming from within 200m of the limiter, is plotted as a function of $\langle n_e \rangle$ in fig 2 together with the probe data.

Doppler broadening of the D_α light coming from recycled deuterium (3) is also plotted. This is colder than the Be IV, which is to be expected since it is ionized closer to the limiter. Both measurements show a fall in T_i with increasing $\langle n_e \rangle$, and could marginally overestimate $T_i(a)$ as measured by the probes because light is coming from an undetermined distance just in front of the limiter. The flat radial profiles suggest that this overestimation should not be large, however.

7. Conclusion

Evidence to support the fact that ion temperatures in the range 200-500eV exist in the edge of JET ohmic plasmas at densities $< 2.10^{19} m^{-3}$ has been obtained from four independent diagnostics. Furthermore, the ion temperature has been observed to fall with increasing density, as would be expected from both power balance and increased collisionality. Due to uncertainties in absolute values of flux density, probe data alone could not substantiate these high values of T_i. However, taken together with the evidence from the other diagnostics, there is a strong case for $T_i >> T_e$ at and near to the edge.

8. References

(1) S Clement et al, 9th PSI Conference, 1990 Bournemouth, UK
(2) S K Erents et al, Nuclear Fusion, 28, No 7, 1988, 1209-1221
(3) M F Stamp et al, this conference

EDGE PLASMA BEHAVIOUR IN THE FT TOKAMAK

V. Pericoli Ridolfini

Associazione EURATOM-ENEA sulla Fusione, Centro Ricerche Energia Frascati, C.P. 65 - 00044 Frascati, Rome, Italy

With FT tokamak it is possible to study the scrape-off layer (SOL) plasma with densities and power flux densities which are higher, and therefore more reactor relevant, than in other tokamaks. That is of special importance due to the well established link between the SOL and the main plasma and for other key questions as the wall or limiter power loading and the impurity influx in a reactor. The present study wants to give scaling laws for the principal SOL parameters, density n_{eL} and temperature T_{eL} at the limiter radius, of their e-folding lengths λ_n, λ_T and to describe the response of the SOL plasma to lower hybrid (LH) power injection.

EXPERIMENT

The SOL plasma has been sampled with two 4 probes arrays at two different positions: $\Phi = 90°$, $\theta = 45°$ and $\Phi = 180°$, $\theta = 135°$ where Φ is the toroidal angle starting from the limiter and θ is the poloidal angle. A new assembly of the electrodes in the array allows to test easily their integrity, and avoid misinterpretations of the measurements [1]. The local values of n_e, T_e and the potential ϕ are derived following Stangeby's model [2] through a full non-linear fit of the current-voltage characteristic. Radial plots of these quantities are then obtained gathering data from several similar shots to infer their values at the limiter radius and the e-folding lengths. The space parameter covered in this paper is, for line averaged plasma density $2.5\times10^{13} \leq \bar{n}_e \leq 2.7\times10^{14}$ cm^{-3}, for plasma current $220 \leq I_p \leq 450$ kA, the magnetic field B_T is6 and 8 T, the LH frequencies 2.45 and 8 GHz and LH powers $P_{LH} \leq 350$ kW.

The FT SOL plasma looks very similar within the experimental errors in both locations where it is sampled . Differencies, especially for n_e, are found for non centered plasmas but they can be satisfactorily explained following a code described in [1]. Then in the limit of this spatial sampling the FT SOL plasma is treated as homogeneous. The main results concerning the average properties of the SOL are:

a) the value of the density at the limiter radius cannot be accounted for, over all its variability range $10^{13} \leq n_{eL} \leq 10^{14}$ cm^{-3}, taking $\bar{n}_e$ as the unique free parameter, at least if a simple power law is desired, see Fig. 1a.

b) The temperature T_{eL} shows a clear trend to decrease slowly with $\bar{n}_e$, Fig. 1b. Standard regression analysis gives,the following laws, being q_L the safety factor

$$n_{eL} = 3.54\times10^{-2}\ \bar{n}_e^{1.29} \times q_L^{0.9} \qquad [10^{13}\,\mathrm{cm}^{-3}] \tag{1}$$

$$T_{eL} = 3.7\times10^{2}\ \bar{n}_e^{-0.56} \times q_L^{-1} \quad [\mathrm{eV}, 10^{13}\,\mathrm{cm}^{-3}] \tag{2}$$

Law (2) is satisfactory followed only if $\bar{n}_e \leq 10^{14}$ cm^{-3}.

c) the density e-folding length λ_n decreases with $\bar{n}_e$ see Fig. 2 according to

$$\lambda_n = 1.05\ \bar{n}_e^{-1/4} \qquad [\mathrm{cm}, 10^{13}\,\mathrm{cm}^{-3}] \tag{3}$$

The values obtained for λ_T show much more scattering and no clear trend with $\bar{n}_e$ but they always range between 2.5 and 4 times λ_n values.

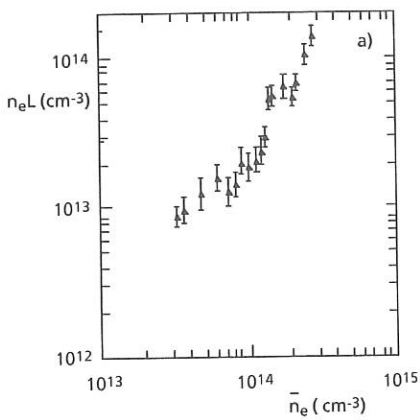

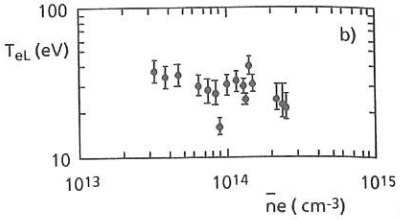

Fig. 1 - Plot of the averaged values of a) density n_{eL} and b) temperature T_{eL} extrapolated to the limiter radius versus the line averaged density $\bar{n}_e$

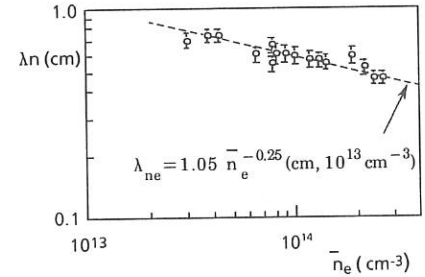

Fig. 2 -Plot of the density e-folding length vs $\bar{n}_e$. The dashed line is the best fit with a law $\lambda_n \propto \bar{n}_e^{-a}$

d) When RF is applied the plasma density drops on every probe location inside the vessel if $\bar{n}_e \leq 4\times10^{13}$cm^{-3}, for both LH frequencies, 2.45 and 8 GHz, though by different amounts, and a hollow density profile develops in the SOL as previously noted [3] . Figure 4 shows the reduction in density measured at r = 20.8 cm as a function of the 2.45 GHz coupled power, and compares it with calculations described below. Temperature is not strongly affected by LH power. D_α brightness always decreases as well, together with n_e in the SOL, and a clear increase in the particle confinement time is observed [4].This effect disappears very rapidely at higher densities, independently of the frequency used. In general, the influence of the LH power on the FT SOL is rather poor for $\bar{n}_e \geq 5\times10^{13}$ cm^{-3}, except a slight increase of the density [3] in presence of strong PDI instabilities.

DISCUSSION

A simple diffusion model [5] can explain satisfactorily the power dependence of n_{eL} on $\bar{n}e$ given in Eq. (1), while it can only provide suggestions for the role played by I_p or the safety factor q_L. The balance of particle and energy fluxes, gives the laws for n_{eL} and T_{eL}

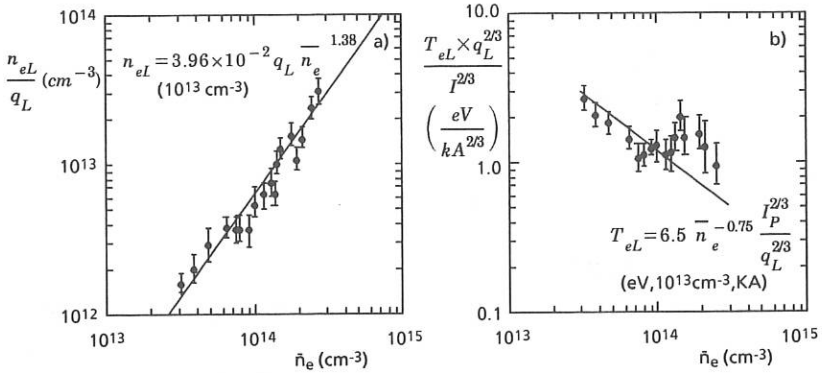

Fig. 3 - Plot vs $\bar{n}_e$ of a) n_{eL}/q_L, b) $T_{eL}(q_2/I_p)^{2/3}$. The Full lines are the best fits for the power laws $\bar{n}_e^{1.38}$ and $\bar{n}_e^{-0.75}$ respectively (see text)

$$n_{eL} = \eta\lambda_n \langle\sigma v_{iz}\rangle \bar{n}_e^2 \tag{4}$$

$$T_{eL} = K(I_P/\lambda_n n_{eL})^{2/3} \tag{5}$$

where η and K can be approximately by constants [5,1]. Considering Eq. (3) and that the mean ionization rate $\langle\sigma v_{iz}\rangle$ is $\propto \sqrt{T_e}$ in the 10-100 eV range, one has

$$n_{eL} = A\, I_P^{1/4}\ \bar{n}_e^{1.38} \tag{6}$$

$$T_{eL} = B\sqrt{I_P}\ \bar{n}_e^{-0.75} \tag{7}$$

A and B are constants. The exponents of $\bar{n}_e$ predicted by the model are satisfactorily near to those from regression analysis, Eq. (1), (2). On the contrary, the exponents of I_P, or q_L in (6), (7), do not reproduce the experimental data, specially for n_{eL}. That can be due to an influence of I_P on the particle inward pinch velocity which is totally neglected by holding η constant in (4). Present data however do not allow to investigate further this point.

Assuming as correct the exponent 1.38 of $\bar{n}_e$ in (6), the best law fitting the n_{eL} data, shown in Fig. 3a, and from this one plus Eqs. (5) and (3) the law for T_{eL} are

$$n_{eL} = 3.96\times10^{-2} q_L\ \bar{n}_e^{1.38} [10^{13}\,\mathrm{cm}^{-3}] \tag{8}$$

$$T_{eL} = K\,(I_P/q_L)^{2/3}\ \bar{n}_e^{-0.75}\ [\mathrm{eV}, \mathrm{kA}, 10^{13}\,\mathrm{cm}^{-3}] \tag{9}$$

The fit of the experimental data gives K = 6.5, see Fig. 3b. The law (9) is followed by the experiment more satisfactorily than law (7) even though it proves valid only for $\bar{n}_e \leq 1.3\times10^{14}$ cm^{-3}. It is an open point whether the higher temperatures are due to the occurrence of gradients along the field lines.

Turbulence in FT SOL can explain qualitatively the scaling of λ_n, Eq. (3). For Boltzmann like fluctuations the perpendicular particle diffusion coefficient is [1] $D_\perp \propto T_e \langle(\delta n_e/n_e)^2\rangle 1/2$. In FT SOL is [1] $\langle(\delta n_e/n_e)^2\rangle 1/2 \propto n_e^{-2/3}$ under a wide range

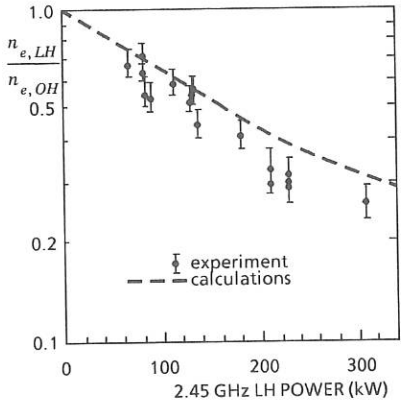

Fig. 4 - Scaling of the SOL density ratio $n_{e,LH}/n_{e,OH}$ with the 2.45 GHz coupled power, at r = 20.8 cm. Full dots: experiment, dashed line: calculation (see text).

of plasma parameters. Thus the usual relationship $\lambda_n = \sqrt{\bar{D}_\perp L_\parallel}/c_s$, where $L_\parallel$ is the field line connection length and c_s the ion sound speed gives $\lambda_n \propto T_e^{1/4} n_e^{-1/3}$. Experimentally no clear dependence is observed on local T_e values. So ,neglecting T_e, assuming $n_e = n_{eL}$ and using (8) one has $\lambda_n \propto \tilde{n}_e^{-0.46}$, compare with (3). It must be noted that essentially non Boltzmann fluctuations, as observed in Text and Pretext tokamaks, would instead predict an increase of λ_n with $\tilde{n}_e$ even though slight [1].

The effect of LH power on the SOL plasma density is tentatively described as the result of the oscillatory energy ε_ω acquired by the edge electrons in the LH field. Indeed, after living the LH resonance cones the electrons maintain, on average, their ε_ω, as for an ensemble of oscillators if the driving force is suddenly switched-off, for approximately a mean free path λ_c. In the LH phase then, the equilibrium in the SOL is assured by the gradient of the pressure plus the kinetic term. Asssuming the ohmic profile as the equilibrium one, and considering that the relative weight of ε_ω is vanishing at less than 2 cm inside the limiter radius the following equation holds

$$P_{OH}(r) = P_{LH}(r) + n_{LH}(r) \cdot \varepsilon_\omega(r) \qquad (10)$$

The numerical solution of (10) for an assigned ohmic density profile gives a hollow LH density profile very similar to the observed one and the scaling with LH power, shown in Fig. 4. The model is satisfactory also for the 8 GHz case.

Density reduction spreads over the whole plasma surface if λ_c is longer than half the torus circumference and half the minor circumference. That is satisfied in FT only for $\tilde{n}_e \leq 4\times10^{13}$ cm^{-3}, and if the total energy thermal + kinetic of an electron is considered in the calculation of λ_c. In addition, the only poloidal velocity, whose magnitude can meet the above requirement for λ_c, is that due to the $E_r \times B$ drift, being E_r the radial component of the limiter sheath electric field [6].

REFERENCES

[1] V. Pericoli-Ridolfini, ENEA Report RT/FUS/89/17 (1989)
[2] P.C. Stangeby, J. Phys. D: Appl. Phys. **15**,1007 (1982)
[3] V. Pericoli-Ridolfini, Plasma Phys. and Controlled Fusion **27**,709 (1985)
[4] R.De Angelis, G. Tonini, Proc. 12th European Conference on Controlled Fusion and Plasma Physics, Vol. 9F, Part II, p. 690 (1989)
[5] P. C. Stangeby, J. Nucl. Mat. **145-147**,105 (1987)
[6] V. Pericoli-Ridolfini, ENEA Report RT/FUS/89/19 (1989)

Scrape-off Layer Based Model for the Disruptive Tokamak Density Limit and Implications for Next-generation Tokamaks

K. Borrass

The NET Team, c/o Max-Planck-Institut für Plasmaphysik, Boltzmannstr. 2, D-8046 Garching b. München

A model based on analysis of the scrape-off layer and divertor regions has been proposed for the disruptive density limit in divertor tokamaks [1]. A threshold condition for the onset of the processes leading to density limit disruptions is derived which is essentially the condition for the existence of a stable thermal equilibrium in front of the divertor plates. The model has been extensively validated against ASDEX results. In this study the impact of the model on next-generation tokamaks, such as NET/ITER, is investigated. The basic features of the model are outlined and the main differences between a medium-size device like ASDEX and NET/ITER are discussed.

Description of Model

A one-dimensional model according to Fig. 1 is used to describe the scrape-off layer and divertor zones. The basic equations are the equations of momentum, energy and particle conservation ($T_e = T_i = T$ and $n_e = n_i = n$ are always assumed):

$$\frac{\partial}{\partial z}(mnV^2 + 2nT) = 0 \,, \tag{1}$$

$$\frac{\partial}{\partial z} q_{\parallel} = Q \,, \tag{2}$$

$$\frac{\partial}{\partial z}(nV) = S \,. \tag{3}$$

Here z is the coordinate along a flux tube and Q and S are source terms for power and particles, respectively. With some additional assumptions a two-temperature global model is obtained from eq.(1) to eq.(3) which contains only the sheath edge temperature T_D and scrape-off layer temperature $T_S (\simeq T(z=0))$ [2] [3]. The main assumptions are: except in the recycling region Spitzer conductivity is the main parallel transport mechanism; perpendicular transport is dominated by Bohm diffusion; the Mach number is $\simeq 1$ at the sheath edge and $<< 1$ at the stagnation point. The model provides a relation between the scrape-off layer density n_S and the divertor temperature T_D which is the basis for the derivation of a density limit (cgs units being used except where otherwise stated):

$$n_S \sim [1 - (\frac{T_D}{T_S})^{7/2}]^{3/8} \; \frac{T_D^{11/32}}{(\xi\beta + 1/c_s(T_D) \int_0^L dz Q_{rad} + \gamma T_D)^{11/16}} \,. \tag{4}$$

Here γ is the sheath energy transfer coefficient [4], ξ is the average ionization energy of a neutral ($\xi \simeq 17.5 + (5 + \frac{37.5}{T_D})\, log_{10}(\frac{10^{15}}{n_D})$; ξ, T_D in eV; n in cm^{-3} [4]), β is the fraction of neutrals that are ionized in the flux tube under consideration and Q_{rad} is the impurity radiation loss term in eq.(2) . The factor of proportionality depends on the device parameters ($a, R, B_t, \kappa, divertor\ geometry$) and discharge parameters ($q, P_{in}, mass\ number, profile$

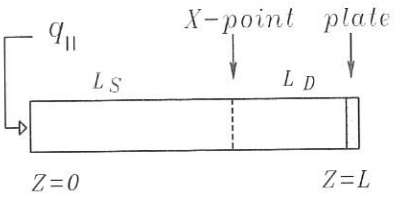

Fig. 1
One-dimensional model of the scrape-off layer. The divertor plate is located at $z = L$.

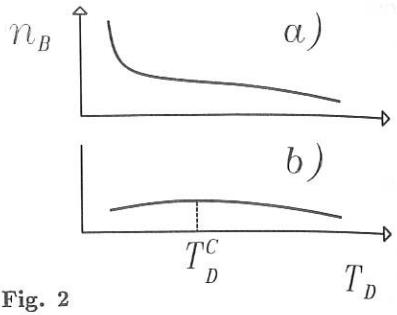

Fig. 2
Schematic behaviour of the right-hand side of eq.(4) .

parameters,..). A density limit is established by the fact that n_S, considered as a function of T_D, may have a maximum, which is interpreted as the critical density. Close to the density limit typically $T_D << T_S$ holds and the T_D-dependence in the first term of eq.(4) can be ignored. Possible shapes of the second term in eq.(4) are indicated in Fig. 2, where type b) would be associated with a density limit. Which of the cases prevails depends on the behaviour of β, ξ and Q_{rad}. ASDEX and NET/ITER are considered as typical examples of medium-size and next-generation tokamaks. Bohm diffusion is adopted for perpendicular transport in order to reproduce the experimentally observed B_t-dependence of the density limit.

ASDEX

ASDEX has a box-type divertor as shown in Fig. 3. A sizable fraction of neutrals which escape from the divertor plasma are pumped [5]. A recycling model, including outward diffusion of neutrals near the plate, inward diffusion into the fan and pumping, has been proposed [1] which predicts that β decreases as T_D. ξ, on the other hand, is nearly constant for typical ASDEX discharges. In the absence of impurity radiation one therefore obtains behaviour according to Fig. 2a (no density limit). If a recycling low-Z impurity is assumed to be the dominant radiator in the divertor, a model according to

$$\int_0^L dz Q_{rad} = C_{rad} \ell f_{imp} n_D^2 \ , \tag{5}$$

($C_{rad} \simeq 1 \cdot 10^{-18}\ erg\ cm^3\ s^{-1}$ corresponding to, for instance, oxygen; f_{imp} the impurity concentration) is appropriate [6]. Note that for given n_S one has approximately $n_D \sim 1/T_D$ [1] . Hence

$$\int_0^L dz Q_{rad} \sim T_D^{-2} \tag{6}$$

holds and impurity radiation losses rapidly increase with decreasing T_D, leading to a behaviour as shown in Fig. 2b. A radiating layer thickness comparable to the scrape-off layer width Δ_D in the divertor ($\ell \simeq \Delta_D B_t / B_p$) together with impurity concentrations of

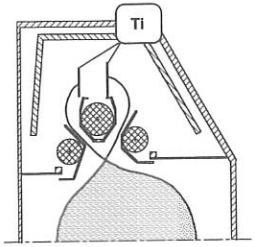

Fig. 3
Illustration of the old ASDEX divertor geometry.

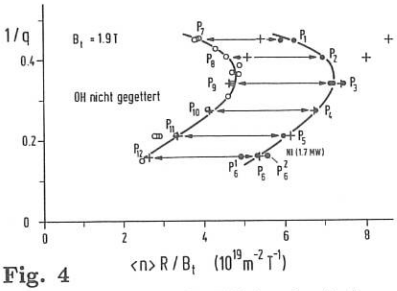

Fig. 4
Comparison with ASDEX density limit for ohmic and neutral injection cases (redrawing of Fig. 1 of [7], except for the calculated points (+)). $f_{imp} = 0.01$.

$f_{imp} \approx 0.01$ is found to give best fits of ASDEX data [7] (see Fig. 4).

NET/ITER

In ITER, since the divertor plasma in an open configuration is wider [8] and the divertor temperature higher (see below), the escape probability of neutrals is very low ($\approx 10^{-3}$) and therefore $\beta \simeq 1$ holds. On the other hand, for ITER-like parameters ξ decreases more strongly with T_D. As a consequence, behaviour as in Fig. 2a is again observed in the absence of impurity radiation even though the reason is quite different from the previously discussed ASDEX case. With impurity radiation, behaviour as in Fig. 2b is again obtained.

General Features

As a consequence of the flat shape of $n_S(T_D)$ according to Fig. 2a of eq.(4) and eq.(6) the following general features of the model are obvious:

i) Impurity radiation is an essential ingredient for the existence of a critical density, but at the limit it provides only a small fraction of the power losses in the divertor.
ii) T_D takes a minimum value T_D^c when the limit is approached.
iii) T_D^c increases with the impurity content.
iv) The critical density depends only weakly on f_{imp}.
v) The power flux on the divertor plates does not vanish when the density limit is approached.

Scalings

For typical ASDEX parameters the model predictions are approximately described by the scaling

$$n_e^{crit} \simeq 15.4 \, \frac{q_\perp^{0.43} \, B_t^{0.31}}{(qR)^{0.45}} \, , \qquad (7)$$

(n_e in $10^{-19} m^{-3}$; B_t in T; $q_\perp$ in MW/m^2, R in m), where $n_e(a)$ is the electron density at the separatrix and $q_\perp$ is the net power flux across the separatrix. Note that eq.(7) applies to

double-null hydrogen discharges in the "old" [9] ASDEX divertor configuration. Slightly different coefficients are obtained for single-null or deuterium discharges. Detailed analysis of experimental data with regard to these aspects remains to be done. The scaling is also affected by the divertor geometry. After reconstruction of the ADEX divertor [9] , for instance, different regimes are found which are no longer described by a single scaling law [1] .

For an ITER-like configuration the critical density behaviour can be approximated by the scaling ($f_{imp} = 0.01$, double-null)

$$n_e^{crit} \simeq 5.0 \, \frac{q_\perp^{0.57} \, B_t^{0.31}}{(qR)^{0.09}} \, , \tag{8}$$

(n_e in $10^{-19} m^{-3}$; B_t in T; $q_\perp$ in MW/m^2, R in m).

Implications on Divertor Design

Critical issues for the divertor design in NET/ITER-like devices are the peak heat loads and erosion [8] . Erosion is largely determined by the sheath edge temperature T_D. Values of up to about 30 eV would be marginally acceptable for graphite or tungsten first walls, considered as candidate materials for the so-called physics and technology phases, respectively, of ITER [8] . From the preceding discussion it follows that T_D^e in NET/ITER should essentially be determined by the impurity content in the divertor region. This is confirmed by numerical studies. Values of $T_D \approx 20-40$ eV are obtained for $f_{imp} \approx 0.005-0.05$ indicating that temperatures lower than about 20 eV may not be possible. Taking into account safety margins for the proximity to the density limit, the divertor temperature therefore might be a matter of concern. In present 2-D modelling of NET/ITER edge conditions impurity radiation is ignored and consequently solutions according to Fig. 2a are obtained, suggesting that arbitrarily low T_D-values can be obtained by increasing the edge density [10]. Improved 2-D modelling is needed for further clarification of this point.

References

[1] K. Borrass, NET Report No. 95, EUR-FU/80/89-95

[2] M. F. A. Harrison, An Analytical Model of the Scrape-off Layer and Divertor Plasma, to be published

[3] J. D. Galambos, Y.-K. M. Peng, Oak Ridge National Laboratory Report ORNL/FEDC-83/14

[4] M. F. A. Harrison, P. J. Harbour and E. S. Hotston, Nucl. Techn./Fus. Vol. 3 (1983) 432

[5] G. Haas, W. Poschenrieder, J. Neuhauser, S. Kaesdorf, Journ. of Nucl. Materials 162-164 (1989) 509-513

[6] M. F. A. Harrison, Atomic Physics, in D. E. Post and R. Behrisch (ed.), NATO ASI Series, Series B: Physics, Vol. 311, Plenum Press, New York 1988

[7] H. Niedermeyer et al., Proc. 12th European Conf. on Contr. Fus. and Plasma Physics, Budapest 1985, contrib. papers, Vol. I, p. 159

[8] ITER Concept Definition, Vol. 2, ITER Documentation Series, No. 3, Internatinal Atomic Energy Agency, Vienna 1989

[9] H. Niedermeyer et al., Plasma Physics and Contr. Fus., Vol. 30, No. 11, pp. 1443-1453, 1988

[10] M. F. A. Harrison, E. S. Hotston, G. P. Maddison, H. D. Pacher, at this conference

SIMULATION OF EDGE PLASMA AND DIVERTOR CONDITIONS IN NET/ITER

M.F.A. Harrison, E.S. Hotston*, G.P. Maddison* and H.D. Pacher

The NET Team
c/o Max-Planck-Institut für Plasmaphysik,
Boltzmannstr. 2, 8046 Garching bei München, FRG.
*Culham Laboratory, AEA Technology,
Oxfordshire OX14 3DB, U.K.

1. INTRODUCTION

Conditions in the scrape-off layer (SOL) and divertor plasma determine divertor plate power loads and erosion rates and hence are critical issues in the conceptual design of NET/ITER. They strongly influence the selection of materials and engineering design of plasma facing components and they constrain the operational scenario of the main plasma. In particular they conflict with the plasma requirements for efficient current drive, e.g. low $<n_e>$ and high $<T>$. Systems code explorations [1] of the acceptable envelope of operational space has led to four typical scenarios:

TABLE 1. Typical Iter Operating Scenarios

	Physics (ignited)	Physics (steady state)		Technology (hybrid)**
	PI	PS1*	PS2	T
Fusion power [MW]	1080	825	1010	870
Current drive power [MW]	0	150	150	76
Pulse length [s]	400	ss	ss	1900
Z_{eff}(core plasma)	1.7	3.8	2.0	1.6
Power entering SOL [MW]	113	84	275	150
$<n_e>$ [$10^{20}/m^3$]	1.2	0.75	0.7	1.45

*Seeded with iron impurities, **15% of I_p is non-inductively driven.

This paper describes the simulation of divertor performance based on two-dimensional fluid modelling of edge plasma.

2.APPLICATION OF TWO-DIMENSIONAL MODELS

The Braams code in its original "along field", two-fluid version [2] is employed for the D/T plasma. Transport of neutral D/T within the divertor chamber is simulated numerically using an analytical model comparable to that outlined in [3,4]. Release of neutral D/T particles at the first-wall is not included but the exhaust of D/T gas is accounted for by assigning to each divertor plate a spatially invariant albedo (>0.995) which is adjusted so that the D/T exhaust rate is about 20 times the rate at which helium is produced by fusion

reactions in the core. Transport of impurity ions (e.g. He^{2+} and sputtered plate material) is not yet included but power losses due to D/T ionisation and radiation are self-consistently determined.

The curvilinear, orthogonal mesh used for the Braams code is derived by the LINDA mesh generating code [5]. Both the inner and outer divertor and SOL plasmas are modelled but only for the bottom half of ITER. Symmetry in the up/down direction is assumed by imposing reflecting boundary conditions at the mid-plane. The null-to-strike-point distance is 1.5m for the outer plates and 0.6m for the inner plates. The plasma transport equations are solved for orthogonal divertor plate surfaces but allowance is made for the effect of plate to separatrix inclination (15^o at the outer and 45^o at the inner plate) upon the distribution of neutral particle source terms by appropriate increase in the neutral ranges along B. The core/edge interface (which forms the inner boundary of the edge model) is assumed to be the flux surface which lies 2.5 cm inboard of the separatrix at the outer mid-plane. The input power per unit area is uniform over this surface but distributed in the ratio 4/1 to the inner and outer regions respectively. The ratio of electron to ion input power is taken to be $P^e_\perp/P^i_\perp = 3/1$. The plasma density at the interface is assumed to be uniform and its magnitude adjusted to give about $<n_e>/3.5$ at the separatrix intercept at the outer mid-plane. Zero radial fluxes of particles and energy are assumed for the boundary conditions at the first-wall. There is no linking of plasma transport between the inner and outer SOL and divertor regions which, in the mesh, are separated by insulating (and reflecting) cells. Transport of electron and ion energy through the sheaths at the divertor targets is treated as described in [4] and the reflection coefficients used to describe the return to the plasma of neutral particles and energy are based upon data given in [6]. Z_{eff} in the SOL and divertor plasmas is based upon the specification given in [7], namely

$$Z_{eff} = 1+0.8[Z_{eff}(\text{core})-1].$$

It is implicit in the "along field" version of the Braams code that $n_e=n_i$ and so in the present calculations Z_{eff} acts only on those plasma parameters which involve collisionality, e.g. parallel electron and ion conductivity, parallel viscosity and electron-ion equipartition frequency.

Cross field anomalous transport is taken as specified in [7], namely:

$$x^e_\perp = 2m^2/s;\ x^i_\perp = D_\perp = 2/3\ m^2/s \text{ and } v_{pinch} = 0$$

These values of $x^e_\perp$, $x^i_\perp$, $D_\perp$ are a factor of 2 larger than those derived from present-day H-mode experiments to account for the effect of Edge Localized Modes (ELM's) on transport. Parallel transport is classical [2] and no parallel thermal flux limiter is available in this version of the code. This omission is likely to be relatively unimportant since $Z_{eff}>1$.

The calculations are performed for graphite divertor plates. Erosion and redepositon are determined using a simple model [8] in which the effective sputtering yield Y_{eff} of the surface intercepted by a divertor plasma channel of radial width δr is expressed as

$$Y_{eff}=\frac{Y_{DT}}{(1-Y_s)}\ \frac{(1-Y_s^n)}{n}$$

where $n = \delta r/\Delta \cos\alpha$. Here Δ is the range (perpendicular to the surface) of released atoms (or hydrocarbon molecules), α is the angle of inclination relative to the magnetic surface) and Y_s the sum of carbon self-sputtering yields, i.e. physical plus radiation enhanced sublimation. The model includes both physical sputtering and radiation enhanced sublimation due to D/T ions as well as chemical erosion. The profile of plate surface temperature is taken to be proportional to the power deposition profile, but with a baseline temperature of 100°C and a peak temperature of 1000°C.

TABLE 2. Performance of the ITER options
(Data in brackets refer to inner SOL and divertor)

	Physics			Technology
	(ignited)		(steady state)	(hybrid)**
	PI	PS1*	PS2	T
Power to divertor [MW]	45.3 (11.3)	33.7 (8.5)	110 (27.5)	60 (15.0)
$<n_e>/3.5$ [$10^{19}/m^3$]	3.4 (3.2)	2.3 (1.9)	2.2 (2.1)	4.0 (3.8)
Peak load on plate[a] [MW/m^2]	5.0 (2.7)	3.3 (1.8)	47 (29)	7.0 (3.8)
Peak T_e at plate [eV]	7.5 (2.3)	5.9 (1.3)	234 (170)	9.1 (3.3)
D/T radiation in divertor [MW]	3.9 (1.7)	3.5 (1.9)	3.3 (1.2)	4.2 (1.8)
Peak net erosion[c] [10^{-3}m/a]	40 (2)	5 (2)	(b) (b)	40 (>1)
Rate of C release [10^{21}/s] at 1000°C peak	67 (18)	56 (13)	(b) (b)	95 (24)

[a] Includes 13.6 eV D^+/T^+ recombination energy
[b] Runaway erosion ($Y_s > 1$) occurs even at assumed plate temperatures
[c] Per integrated burn year - at net erosion peak near strike point; values are very sensitive to temperature

3. RESULTS

Data for the four examples of ITER are given in Table 2 and the profiles of power loads on the plates in Fig.1.The reduction in T_e relative to previous calculations (e.g. Ref. 8, Appendix 4) appears to be due to a combination of improved representation of the magnetic geometry (longer connection length near the separatrix) and the assumption of $Z_{eff} > 1$ in the present analyses. Furthermore, both T_e and the peak power loads decrease with decreasing $P^e_\perp/P^i_\perp$ but at present there are no experimental data which can fix the appropriate value of $P^e_\perp/P^i_\perp$.

The loads for the ignited case appear reasonable, not greater than 15 MW/m^2 when

allowance is made for a) toroidal peaking and b) modelling uncertainties. The hybrid technology case loads are rather high but could be reduced somewhat by seeding with impurities as has been invoked for the steady state option "PS1". Net erosion in these three cases is relatively modest due to the small values of T_e at the plate. However, steady state case "PS2" leads to very large power loads and plasma temperatures (the calculation is in fact not complete because runaway erosion would occur even at the assumed plate temperatures). It is concluded that power load and temperature scenarios within the presently envisaged range of divertor operating conditions are possible for the physics ignited, impurity-seeded steady state, and long-pulse hybrid (15 % current drive) scenarios, but that a pure steady state scenario (low density, no impurity seeding) is not possible within present constraints.

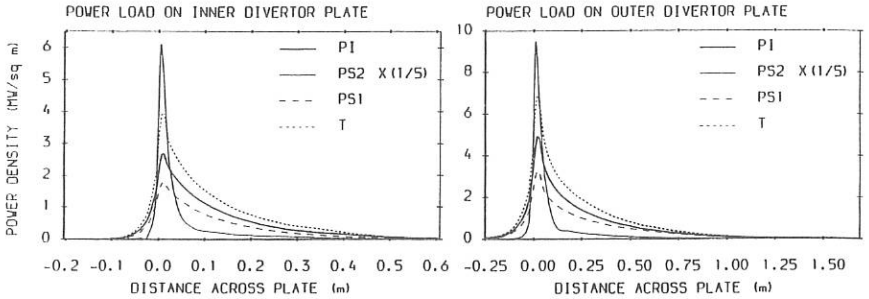

Fig. 1 Profiles of power loads on the inner and outer divertor plates inclined at 45° and 15° to the separatrix.

4. REFERENCES

1. ITER Conceptual Design Interim Report IAEA/ITER/DS/7, IAEA, Vienna 1990.
2. B.J. Braams, M.F.A. Harrison, E.S. Hotston and G. Morgen in "10th Int. Conf. on Plasma Physics and Contr. Nucl. Fusion Research, London, Sept. 1984 IAEA, Vienna, paper E-II-5-2.
3. M.F.A. Harrison, P.J. Harbour and E.S. Hotston, Nuclear Technology/Fusion, 3, 432 (1983).
4. M.F.A. Harrison, E.S. Hotston and A. De Matteis, Commission of the European Communities, NET Report Nr. 50, EUR-FU/XII-361/86/50 (1985)
5. G.P. Maddison, Commission of the European Communities, NET report Nr. 82, EUR-FU/XII-80/87/82 (1987).
6. R. Behrisch and W. Eckstein in "Physics of Plasma-Wall Interactions in Controlled Fusion", Plenum Press, New York and London (1984), p. 413.
7. ITER "Summary Report for the June-October Joint Work Session, 1989", ITER-IL-PH-5-9-81
8. M.F.A. Harrison and E.S. Hotston, Commission of the European Communities, NET Report Nr. 97, EUR-FU/80/90/97 (1990).
9. ITER "Summary Report for the January-March Joint Work Session, 1990", ITER-IL-PH-5-0-42.

COLLECTOR PROBE MEASUREMENTS OF IMPURITY FLUXES IN TEXTOR WITH MOLYBDENUM AND GRAPHITE LIMITERS

M. Rubel[1]*, H. Bergsåker[1], B. Emmoth[1] and P. Wienhold[2]

[1]Manne Siegbahn Institute of Physics, Association Euratom - NFR,
S-104 05 Stockholm, Sweden
[2]Institute of Plasma Physics, Association Euratom - KFA, D-5170 Jülich, FRG

1. INTRODUCTION

Tokamak discharges cause erosion of plasma facing surfaces due to physical and chemical processes which result in a contamination of the plasma by impurity atoms (C, O, metals). This contribution brings a report on an experiment which was carried out in order to study: a) the influence of the limiter composition on the impurity production and transport; b) erosion of carbonization layers deposited on metallic surface. The studies were performed at TEXTOR and part of the measurements was done using a collector probe: Stockholm - TEXTOR probe system which was described in literature earlier /1/. The graphite probe (a rotatable cylinder shielded by a titanium housing with a 2 mm slit which allows plasma ions to reach the collecting surface) was exposed, in a time resolved mode, to the scrape-off layer of the deuterium plasma. Ions drifting in the tokamak current direction (the "ion drift" direction) were collected during four plasma discharges. Three exposures (# 25812, 25815, 25816, time resolution 255 ms) were made in the presence of the carbonized (150 - 180 nm layer) molybdenum limiter at minor radius r = 44 cm, whereas the last one (# 25817, time resolution 510 ms) was performed when the molybdenum piece was retracted to r = 50 cm and graphite poloidal limiters (C-limiter) were used at r = 46 cm. Basic plasma parameters during all shots were similar: maximum plasma current I_p = 348 kA, magnetic field B_T = 2 T, central electron density $n_e(0)$ = (3.38 - 3.47) x 10^{13} cm^{-3}, shot duration 3.2 - 3.5 s. The probe was placed always 30 mm deep in the scrape-off. The night preceding the experiment with the Mo limiter TEXTOR was carbonized. The operation schedule with the Mo-limiter was: a) 54 shots behind the liner at r = 59 cm; b) 6 shots ($\sim$ 17.1 s) at r = 50 cm when the C-limiter was at r = 46 cm; c) 5 ($\sim$ 17.7 s) shots at r = 46 and 8 shots ($\sim$ 19.1 s) at r = 44 cm when the C-limiter was at 50 cm; d) the last shot at r = 50 cm and the C-limiter at 46 cm. The probe exposures started 68 shots after the carbonization, and 4 shots after the location of the Mo-limiter at 44 cm. The exposed probe was analysed at the surface analysis station (Stockholm) by means of high energy ion beam techniques: Rutherford backscattering spectroscopy for the analyses of metals (molybdenum and wall material components :Cr, Ni, Fe) and oxygen impurity atoms, and nuclear reaction analysis to determine the cencentration of deuterium within the near surface region.

---

*permanent address: Space Research Centre, Ordona 21, Pl-01 237 Warsaw, Poland

The main goal of the study was to recognize temporal and spatial behaviour of molybdenum impurity fluxes in the scrape-off layer during consecutive plasma discharges.

RESULTS AND DISCUSSION

Figure 1 shows an evolution of molybdenum and other metallic impurity deposition rates during four exposures of the probe to the plasma. There are also plotted results for deuterium collected on the probe. It is necessary to stress the fact that for deuterium, the deposition rates (collected fluxes) are not identical to the incident fluxes because re-emission of deuterium and chemical $D-C$ reactions (which lead to the formation of gaseous products) reduce the collection efficiency, whereas metals are known to stick ($s \cong 1$) well to carbon surfaces /2/.

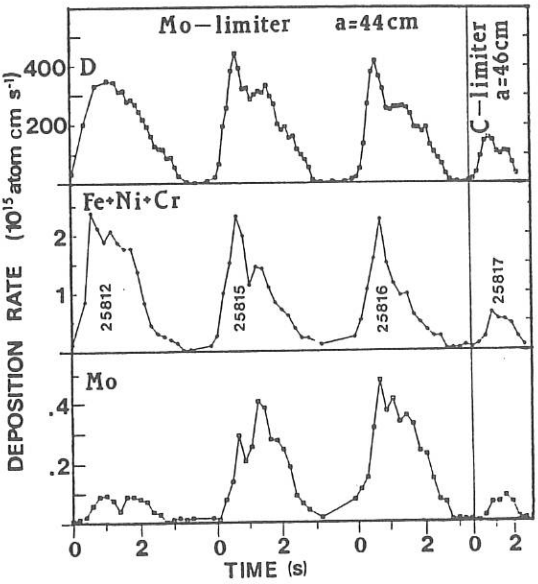

Fig. 1. DEPOSITION RATES OF DEUTERIUM, INCONEL COMPONENTS AND MOLYBDENUM AS A FUNCTION OF THE DISCHARGE TIME.

The shape of the time-resolved plots is similar for all the species analysed, but the amplitudes differ distinctly. Similar measurements were also performed at other radial positions on the probe, showing the same general features. The concentrations increase sharply to some maximum value, at the beginning of the discharge, and later they decay more or less smoothly during following stages of the shot.

Radial distributions of deposition rates for molybdenum and Inconel components have also been investigated showing that they decay exponentially. Characteristic e-folding lengths inferred from these measurements are as follows: $\lambda_{Mo(limiter)} = 26$ - 31 mm; $\lambda_{C(limiter)} \cong 43$ mm. These values are dependent on the limiter in use since the position of the test and the main limiter in the torus is different. However, for a given limiter, the e-folding lengths are the same for all kinds of atoms deposited on the probe.

Time- and space-resolved measurements indicate that in the presence of the Mo limiter, the molybdenum deposition rates and hence the fluxes to the probe increase from shot to shot, whereas the collected fluxes of other species remain on the same level. The molybdenum flux (Φ_{Mo}) increases from $0.9 \cdot 10^{14}$ cm^{-2} s^{-1} for # 25812 to $3.7 \cdot 10^{14}$ cm^{-2} s^{-1} for # 25816 (flat top values), which may indicate a linear increase of the molybdenum influx of $0.7 \cdot 10^{14}$ cm^{-2} s^{-1} per shot, or exponential increase of 40 % per shot. Typical fluxes of other metals (Φ_{Me}) sputtered from walls (Fe, Ni, Cr) are approx. (15 - 17) $\cdot 10^{14}$ cm^{-2} s^{-1}, and for deuterium $3 \cdot 10^{17}$ cm^{-2} s^{-1}.
Another important observation is that the withdrawal (after # 25816) of the Mo limiter to the wall position and the operation with the main poloidal limiters resulted in a significant decrease of all the fluxes collected on the probe surface. This may partly be explained by connection lengths effects which influence the transport of ions to the probe: 50.8 m for the Mo-limiter at 44 cm and the probe at 47 cm, and 25.0 m for the C-limiter at 46 cm and the probe at 49 cm. However, one perceives stronger decrease of the molybdenum fluxes than those measured for other metals and deuterium.
The comparison between fluxes of respective species can be done when the ratio of fluxes (Φ_{Mo}/Φ_{Me} and Φ_D/Φ_{Me}) is considered. Relative variations of the fluxes can be recognized since values of the Φ_{Mo}/Φ_{Me} ratio should mostly be affected by the limiter composition but not by the limiter configuration and relative variations of the fluxes can be recognized. The ratios determined for respective shots, from time-resolved (average for flat top values at $r = 47.5$ cm for the Mo-limiter and $r = 49.5$ cm for the C-limiter) and radial (average for 1.3 s) measurements, are shown in Table 1.

Table 1. RATIOS OF FLUXES DEPOSITED ON THE PROBE

SHOT	TIME AVERAGE		RADIAL AVERAGE		REMARK
	Φ_{Mo}/Φ_{Me}	Φ_D/Φ_{Me}	Φ_{Mo}/Φ_{Me}	Φ_D/Φ_{Me}	
25812	0.032	165			Mo-limiter
25815	0.102	176	0.085	170	Mo-limiter
25816	0.150	175	0.150	179	Mo-limiter
25817	0.059	171	0.058	167	C-limiter

Once again, the results collected in Table 1 confirm the increase of the molybdenum fluxes when the Mo - limiter is in operation, and immediate decrease (by a factor of ~ 3) of these fluxes when the graphite limiter is inserted. Simultaneously, the ratio of Φ_D/Φ_{Me} remains almost constant for all the discharges.

The results allow to formulate the following conclusions: a) the carbonization layer on the Mo-limiter is gradually eroded from shot to shot and molybdenum is sputtered by the plasma; b) atoms once removed from the limiter are transported by the plasma along the torus, later deposited on the surrounding surfaces, and they are removed again from the plasma facing surfaces during following discharges.

One may expect that the production of the molydbenum impurity by the plasma sputtering at the limiter had to be preceded by removal of the carbonization (150 - 180 nm thick $\cong 1.6 \cdot 10^{18}$ C *at* cm^{-2}) layer deposited on the limiter during the carbonization of TEXTOR. Taking into account: a) exposure time of the Mo-limiter at different radial positions (see *Introduction*), b) characteristic e-folding lengths in the presence of the C and Mo limiters, c) possible fluxes of deuterium ($5 \cdot 10^{18}$ cm^{-2} s^{-1} /3/) , carbon ($\sim 1.25 \cdot 10^{17}$ cm^{-2} s^{-1} /4/) and metals ($5 \cdot 10^{15}$ cm^{-2} s^{-1}, these paper) at the limiter , and assuming the electron temperature 20 eV at the limiter one expects (from /5/) following physical sputtering yields: of carbon by deuterium (for 60 eV D^+ $Y_{D/C} = 6 \cdot 10^{-3}$), carbon (for 200 eV $C^{(3+)}$ $Y_{C/C} = 0.2$), nickel (for 300 eV $Ni^{(5+)}$ $Y_{Ni/C} = 0.05$). These values allow to infer that $\sim 0.35 \cdot 10^{18}$ C *at* cm^{-2} was removed when the Mo-limiter was at $r = 50$ cm. Later, when the Mo- limiter was acting as the main limiter at $r = 46$ or 44 cm, the recession rate of carbon from the carbonization layer was $\sim 5.5 \cdot 10^{16}$ cm^{-2} s^{-1} and rest of the carbon layer ($1.25 \cdot 10^{18}$ cm^{-2} could be fully removed after 23 s of the TEXTOR operation. It means that during the last shots (25812 - 25816, when probe exposures were made) performed in the presence of the Mo - limiter bare molybdenum on the limiter surface was exposed to the plasma. Again, taking into account respective fluxes of plasma species (D and impurities) and sputtering yields for D, C, Ni and Mo on molybdenum /5/one may expect that the recession rate of molybdenum was $\sim 1.25 \cdot 10^{16}$ Mo *at* cm^{-2} s^{-1}.

The measurements presented and discussed here are also in agreement with previous observations concerning impurity production in tokamaks /6 /. Moreover, the results obtained by means of the collector probe technique can be considered as complementary ones to spectroscopical data collected during the same experiment /7/.

3. *REFERENCES*

1. H.-E. Sätherblom *et al.*, Nucl. Inst. and Meth. A240 (1985) 171.
2. B. Emmoth and H. Bergsåker, Nucl. Instr. and Meth. B33 (1988) 435.
3. U. Samm *et al.*, Plasma Phys.and Contr. Fusion 29 (1987) 1321.
4. P. Wienhold *et al.*, J. Nucl. Mater. 145 & 147 (1987) 642.
5. N. Matsunami *et al.*, Atomic Data and Nuclear Data Tables 31 (1984) 1.
6. P. Wienhold *et al.*, J. Nucl. Mater. 145 & 147 (1987) 631.
7. J. Winter *et al.*, in press.

ELECTRON EXCITATION COEFFICIENTS FOR THE CONTINUOUS SPECTRUM OF DEUTERIUM

J.Božin*, Z.Stokić, V.Stojanović, Z.Petrović and B.Jelenković

Institute of Physics, POBox 57, 11000 Belgrade Yugoslavia
*Faculty of Physics, Univ. of Belgrade, POBox 550,Yugoslavia

INTRODUCTION

Breakdown of gas in the Tokamak reactor is established at very high values of electric field to gas density ratio (E/N). At moderate values of E/N which are characteristic of most discharges, charge particles are not in thermal equilibrium but there is an equilibrium between the energy gained from the electric field and dissipated in collisions. At high values of E/N such equilibrium can not be established, and nonequilibrium phenomena such as runaway electrons occur. Comparison of experiment and theory under conditions of high E/N can be used to test calculation procedures and cross sections used to model the behavior of electrons in such discharges. Recent measurements have shown the importance of heavy particles (ions and fast neutrals) in such discharges.

In this work the absolute values of electron excitation coefficients of $a^3\Sigma_g$ state of deuterium as a function of electric field to gas density ratio E/N,have been measured. As it is known the radiation from $a^3\Sigma_g$ state to the repulsive $b^3\Sigma_u^+$ state results in the well known UV continuum. Therefore the total light emitted between 200 - 400 nm from a low current ($\simeq$ 1 μA) D_2 discharge at distance of 5 mm from the anode was detected using the monochromator and photon counting chain.

EXPERIMENT AND EXPERIMENTAL PROCEDURE

The electron drift tube for low pressure and low current discharges is shown on Fig.1. The discharge was operated between parallel plane electrodes 80 mm in diameter, and

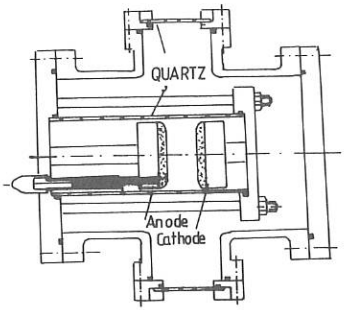

Fig.1. Electron drift tube for high voltage and low pressure gas discharges.

separated by 40 mm. The anode was made from graphite in order to minimize the yield of backscattered and secondary electrons. The electrodes are enclosed in a tightly fitting quartz tube to prevent long path breakdown. Shown on Fig.2 is Paschen curve for deuterium, with points representing the N*d values at which the measurements were taken. After determining the quantum efficiency of the detection system, using the irradiance standard deuterium lamp, Osram Model UV-40, the excitation coefficients were placed on the absolute scale for E/N between 250 Td and 6 kTd using the following equation

$$\alpha/N = \Sigma_\nu (\alpha/N)^\nu = \frac{\Sigma_\nu R^\nu A^\nu (1+N/N_0^\nu)}{j_e N A^{\nu k} Q(\lambda_{\nu k})} \qquad (1)$$

where ν corresponds to different vibrational levels of the upper state, N is the gas density, R is the measured signal for transition ν-k, Q is the factor which includes the quantum efficiency and geometry of detection system, j_e is the local electron current density , e is the electron charge, N_0 is the quenching density, and A_ν and $A_{\nu k}$ are transition probabilities for level ν and it's νk branch, respectively. As for the $a^3\Sigma_g$ state the measured radiation is the sum of a continuous emission from different vibrational levels. Since the populations of the individual vibrational levels are not known, excitation coefficients for these levels can not be evaluated from the measured signal. But, for the transition from bound upper state to the repulsive state, the relation $A^\nu = A^{\nu k}$ holds.

From the comparison of our experimental (shown on Fig.3.)to the calculated spectral dependence of continuous radiation, one can conclude that only first two vibrational levels are dominantly populated. The relation (1) has been used to obtain the excitation coefficients for the $a^3\Sigma_g^+$ state taking in to accountthe value of8.2 10^{-24} m^3 for the product of the collisional quenching rate coefficient and the radiative lifetime[1], e.g. $1/N_0$.

The results for the excitation coefficients of $a^3\Sigma_u^+$ state were compared with the theoretical calculations for hydrogen[2] and are presented in Fig.4. The total uncertainty of the determination of the excitation coefficients, which includes uncertainties of the calibration procedure, measurements of gas pressure, electric fields and discharge currents, was less then 15%.

CONCLUSIONS

Our measurements of the excitation coefficients for UV continuum in D_2 are first absolute measurements at very high E/N. The experimental results were compared with the Boltzmann calculations[2] at moderate E/N and with the beam model[3] at very high E/N. Both spectral and spatial scans of UV continuum shall be presented at the conference. Spatially dependent light emission at high E/N is important for determining the spatial growth of electron density in the anode vicinity.

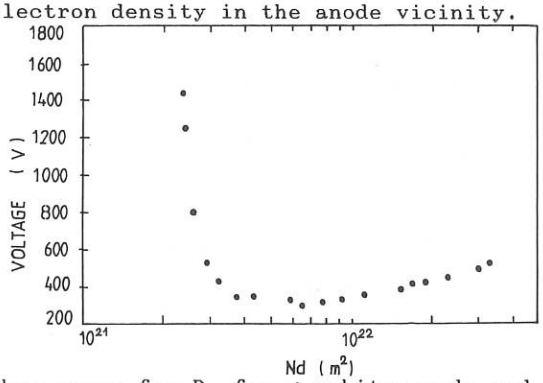

Fig.2. Paschen curve for D_2 for graphite anode and stainless steel cathode.

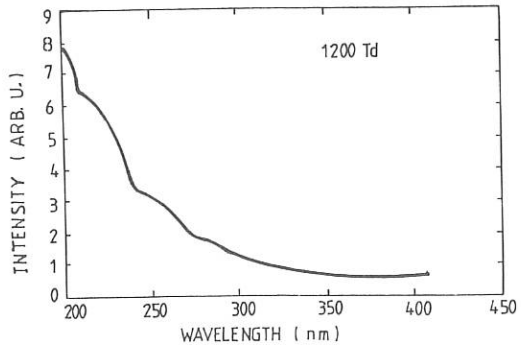

Fig.3. Spectral dependence of continuum radiation between 200 and 400 nm in D_2 discharges at 1200 Td.

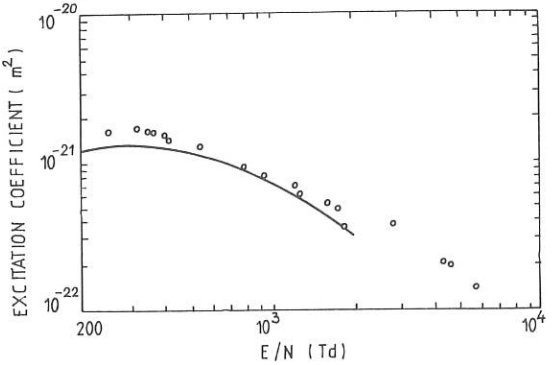

Fig.4. Excitation coefficients for $a^3\Sigma_u^+$ state of D_2 vs E/N. Our measurements are given by points while the solid line represents the calculations[2] for H_2.

References:

1. H.Tischer and A.V.Phelps (unpublished).

2. S.J.Buckman and A.V.Phelps, in Tabulation of cross sections and Calculated Transport and Reaction Coefficients for Electrons in H_2 and D_2, JILA Information Center Report, No.27, (1985).

3. A.V.Phelps, B.M.Jelenković and L.C.Pitchford, Phys.Rev.A 36, 5327 (1987).

3D-MONTE CARLO MODELLING OF THE NEUTRAL GAS TRANSPORT IN PUMP LIMITERS

A. Nicolai

Institut für Plasmaphysik, Forschungszentrum Jülich GmbH,
Association EURATOM-KFA, P.O. Box 1913, D-5170 Jülich, FRG

1. Introduction

Descriptions of the neutral gas transport in poloidal divertors, limiter scrape off regions and in pump limiters were attempted already by means of Monte Carlo methods. In these approaches the confining walls were described by quadratic surfaces /1/ and as estimators the pseudo collision /2/ and the tracklength estimator /3/ combined with nonanalogue methods as generalized splitting and russian roulette (importance sampling) were employed.

In the following a procedure is envisioned which is inherent to general pipe configurations with arbitrary torsion and curvature and resorts to a decomposition into finite plane geometrical elements. For the plasma domain a generalized pseudo collision or "pseudo tracklength" estimator both allowing to score the decisive ionization rate directly, are used, and in the vacuum regions the standard tracklength estimator is employed /4/.

2. Decomposition of the walls maintaining the vacuum and defining the plasma geometry.

As has been demonstrated in case of ALT II /4/ the main parts of the pump limiter assembly may be represented by pipes with circular or rectangular cross-section. General pipes with circular cross-section can be generated by moving a sphere along a threedimensional curve and envisioning the generated enveloping surface. This surface can be approximated by a sequence of prisms with regular polygons determining the respective cross-section. A similar procedure is possible in case of rectangular pipes, which are decomposed into parallelepipeds. The centerline of the pipe surface is approximated by a sequence of straight lines; the inclination and rotation angles of these straight lines with respect to each other stand for the curvature and torsion of the original centerline. Due to the just mentioned approximations of the pipe surfaces natural volume elements occur: prisms, parallelepipeds and frusta of pyramids; by the latter the prisms belonging to circular pipes of different radii may be connected.

3. Neutral plasma interaction, backscattering and estimators

The random walk of the neutral particles is mainly determined by the

density function for the likelihood of absorption given by /4/

$$a(\vec{x}) = \Sigma_t(\vec{x}) \exp\left(-\int_0^s ds' \, \Sigma_t(\vec{x}(s'))\right)$$

s is the length of the particle path, $\vec{x}$ the radius vector of the particle position, and $\Sigma_t(x)$ the total macroscopic attenuation coefficient for neutral particles. In case of the atoms this coefficient is computed from the rates for ionization of H_o^* (n = 1,2,3), charge exchange and multi-step excitation including the rates for the transitions 1s–2s, 1s–2p, 2s–2p, n=1 → n=2 (total), and n=2 → n=3 (total). The (dominant) molecular reactions are described by the rates for dissociation, molecular dissociative ionization, molecular ionization, dissociative recombination, dissociative excitation and molecular ion dissociative ionization.

The backscattering model is that of ref. /5/ which resorts to a three dimensional distribution in the velocity space of the backscattered particles and is aligned with MARLOWE data. The number backscattering coefficient at low energies is $R_{p_o} = 0.6$. The scoop walls consist of carbon, all the other walls of iron.

The scoring of the macroscopic quantities is equivalent to the solution of the Boltzmann equation /1,3/. Here the pseudo collision and the tracklength estimator for the plasma and vacuum region respectively are employed. In case of the pseudo collision estimator the attenuation of the medium is artificially enhanced beyond the maximum attenuation. A sufficient number of events per mesh cell is obtainable only if the mean free pseudo-pathlength is of the order of the extension of the smallest mesh cell. This necessary condition must be supplemented by the requirement that the pseudo collision technique is combined with importance sampling /2,4/. The quantities to be computed by means of the estimators are /4/

$$E_i = \int g_i(\vec{x},\vec{v}) \, \psi(\vec{x},\vec{v}) \, d\vec{x} \, d\vec{v}$$

In this expression

$$\psi(\vec{x},\vec{v}) = |\vec{v}| \, f(\vec{x},\vec{v})$$

is the angular neutral flux density and $g_i(\vec{x},\vec{v})/|\vec{v}|$ is the physical quantity the average of which is to be computed by means of the distribution function $f(\vec{x},\vec{v})$. The unbiased estimators of the ionization losses, density and scalar pressure are summarized in /4/ for the pseudo collision and tracklength estimator. In case of the pseudo tracklength estimator the contributions of the track between two successive pseudo collisions are scored. Thus the sampling of the collision points is alleviated considerably.

4. Results and conclusions

The computations had been based on the ALT II geometrical data /6/ and on parameters belonging to ohmically heated TEXTOR plasmas. The pumping speed of the turbopump is 3000 l/sec.

a) Conductance calculations /4/
The conductance $L(DP \rightarrow TP)$ of the pipe structure between the deflector plates (DP) and the entrance to the turbopump (TP) and the analogous conductance $L(DP \rightarrow TE_i, TE_e)$ between the deflectorplates and the scoop entrances TE_i, TE_e are important for the ALT II performance, since the losses via the scoop entrances compete with the pumping if the neutral-plasma interaction can be neglected. The results $L(DP \rightarrow TP) = 739$ l/s and $L(DP \rightarrow TE_i, TE_e) = 546$ l/s yield the effective pumping speed of the turbopump $V_{eff}(TP) = 594$ l/sec and that of the scoop entrances (simulated with a sticking coefficient st = 1) $V_{eff}(TE_{i,e}) = 468$ l/sec /4/. $V_{eff}(TP)$ is around 25 % larger than $V_{eff}(TE_{i,e})$ in spite of the long vacuum ducting. $V_{eff}(TP)$ agrees reasonably well with the experimental value $V_{eff}(TP) = 650$ l/sec /7/. The deviation might be due to neutral-neutral collisions enhancing the conductance.

b) Trend calculations /4/
The dependence of the pumped fraction (identical with the removal efficiency) the absorbed and escaping fractions on the total plasma current entering the scoops, ϕ, was investigated. The parameter range of the throat plasma is $1A < \phi < 10A$ and $T = 10$ eV; it corresponds to ohmically heated plasmas. Because a direct comparison with experimental data points is not intended, some simplifying assumptions concerning the profile parameters are introduced. The radial decay length of the plasma density in the ion side scoop and in the electron side scoop are $\lambda_i = 1.5$ cm and $\lambda_e = 2$ cm respectively /7/. The temperature was assumed to be constant. Fig. 1 shows the dependence of the pumped (f_p) the ionized (f_i) and escaping (f_e) fraction on the total current intercepted by the scoop entrances. With increasing current, and therefore with increasing plasma density, the ionized fraction increases and the escaping fraction decreases. The pumped fraction decreases somewhat with increasing current. Experimentally, the opposite trend was observed in particular if the high recycling regime is entered by means of additional heating /7/. This trend may be explained by introducing the ad hoc assumption of a constant backstreaming ratio b = 0.8 (Fig. 1) /4/. The thus effected flux enhancement e´ in the region between deflector plates and the flux probes in the scoops has the same tendency as the enhancement e (used in Fig. 1) between the scoop entrances and the deflector plate /4/. The enhancement e´ which might be in spite of the small distance between the deflector plate and the probes important, is much smaller than e. e´ is to be used if f_p is defined by means of the current $\phi´(\phi´ > \phi$ for $b \neq 0)$ at the flux probes. In this case f_p is smaller than f_p shown in Fig. 1, the purpose of which is to show the right trend only. We note that with decreasing density the aforementioned vacuum case is approached and therefore f_p has to increase with decreasing current (Fig. 1). Furthermore a density dependent b might be more realistic than a constant b.

c) Concluding remarks
Although a plasma-dynamics-code (as TORUS IV /4/) was not coupled to the Monte-Carlo code EOS II the results show that the modelling with respect to the prescribed plasma background reproduces the observed trend already if a backstreaming model /4/ is included. The expediency of geometrical part of EOS II is demonstrated by the conductance calculations yielding reasonable results although neutral-neutral collisions are not included. The decisive question concerning the reduction of the Mach number at the scoop entrances because of recycling is not addressed here. Since this

reduction influences the collection efficiency directly, a combination of EOS II with TORUS IV is needed. In this way the flux at the scoop entrance could be computed consistently.

References

/1/ L.L. Carter, E.D. Cashwell, Particle-Transport Simulation with the Monte Carlo Method, Technical Information Center, Office of Public Affairs, U.S. Energy Research and Development Administration (1975) 44.
/2/ D.B. Heifetz, J. Comput. Phys. 46 (1982) 309.
/3/ J. Spanier and E.M. Gelbard, Monte Carlo Principles and Neutron Transport problems, Addison-Wesley Publishing Company, Reading (Massachusetts) Menlo Park (California), London, Don Mills (Ontario).
/4/ A. Nicolai, A Monte-Carlo Code Describing the Neutral Gas Transport in Pipe Configurations with Attenuating Media, to be published in Computer Science Communications.
/5/ A. Nicolai, D. Reiter, J. of Comput. Phys. 55 (1084) 129.
/6/ M. Goebel et al., J. Nucl. Mater. 162-164 (1989) 115-127.
/7/ W.J. Corbett, Ph. D. thesis, University of California, Los Angeles, 1989.
K.H. Dippel, private communication.

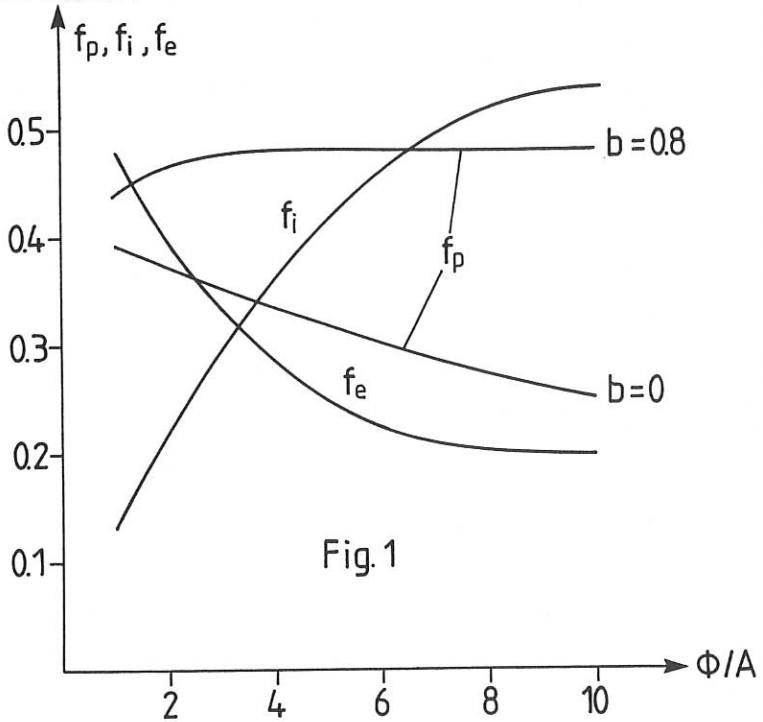

Fig. 1

RADIATION FROM IMPURITIES IN JET LIMITER PLASMAS DURING THE C AND Be PHASES

K D Lawson, R Barnsley*, R Giannella*, N Gottardi*, N C Hawkes, F Mompean*, T K Patel*, N J Peacock

Culham Laboratory, UKAEA/Euratom Fusion Association, Abingdon, Oxon, UK, OX14 3DB
*JET Joint Undertaking, Abingdon, Oxon, UK, OX14 3EA

ABSTRACT

The VUV and XUV emission from JET allows the total radiated power to be analysed in terms of the contributions from individual impurity elements. This division of the radiated power into its elemental components and the analysis of the emission from the separate ion species are valuable diagnostic indicators of the plasma behaviour under different operating conditions.

INTRODUCTION

A technique has been developed to enable the bolometric measurement of the total power radiated from the JET plasma to be divided into components due to the individual impurity elements (Be,C,O,Cl and Ni) found in the plasma. The components are determined by normalising VUV and XUV line intensities to the bolometric data under conditions where a single element happens to dominate the radiation loss. The technique is useful in that it allows the processing of large numbers of JET pulses under a variety of operating conditions. Scaling laws [1] to take into account changes in the n_e and T_e profiles are being evaluated, but for the most part do not appear to result in a significant modification of the present description for determining the radiated power components. Figure 1 illustrates the components calculated for a 3MA discharge. It can be seen that the sum of the calculated components is in satisfactory agreement with the radiated power measured by bolometry.

Be EVAPORATION OPERATIONS

Knowledge of the contributions to the radiated power from individual elements is of especial use when assessing the results of introducing Be into the torus. This was first done by evaporating Be so as to getter O, the C limiters being retained from pre-Be operations. Subsequently, Be limiters have been used. The O content of the plasma is reduced from 0.2-2% of n_e to ~0.1-0.4% of n_e [2] and the low contribution of O to the radiated power can be seen in figure 1, this pulse occurring during the Be evaporation phase.

The introduction of Be into the torus has led to the radiated power becoming a smaller fraction of the total input power, falling from ~50% during the C limiter operations to ~20% with Be limiters. This fraction measured during the ohmic phase is shown in figure 2a for a sequence of pulses during the Be evaporation operations. The low fraction radiated immediately after a Be evaporation rises as the Be layer covering the limiter is eroded over a number of discharges. Be with an initial concentration of up to $0.05n_e$ is replaced by C as the dominant impurity, the C concentration being typically $0.03\text{-}0.10n_e$. Figures 2b and 2c illustrate the powers radiated by C and Be as a fraction of the total input power. The correlation of the C component with the total radiated power fraction is clearly seen, as is the anticorrelation with the Be radiated power component. This is because the Be fractional power peaks between 0.1-0.15, whereas the C fraction is higher lying between 0.15 and 0.3 of the total input power.

Ni RELEASE DURING ICRH

The value of the technique of the VUV and XUV line analysis can be further illustrated by a study of the Ni release during ion cyclotron resonance heating (ICRH) and by a demonstration of the importance of Cl in the 1989 JET discharges. The main source of Ni in JET has been the ICRH antennae screens. Its release into the bulk plasma depends on a number of parameters, the investigation of which requires a series of similar discharges. The sequence of 3MA discharges, pulse numbers 19588-19737 have initial average n_e of ~$2.0 \times 10^{19} m^{-3}$ and average T_e of ~1.0keV. The ratio of a radiated power component to n_e gives a measure of the ion density. The increase in the Ni ion density during the first 2s of ICRH is shown to be linearly dependent on the heating power in figure 3a. The larger increase in the Ni impurity levels with monopole phasing of the antennae [3], which is due to the difference in the electric field structure, is also confirmed for these pulses. Figure 3b shows the corresponding increase in the C ion density. Again the dependence is linear with power, but no distinction can be made between the monopole and dipole phasing, the release of C being dependent chiefly on the heat flux to the C limiters.

In this sequence of pulses, Ni accounts for up to 10% of the total input power, whereas the proportion due to C is larger being typically 15-30%.

Cl IN 1989 JET DISCHARGES

Cl was found to be present in the majority of 1989 JET discharges, but became particularly important during the Be limiter operations. The fraction of the radiated power due to Cl is found to increase with density, from ~0.03 at an average density of ~$1\text{-}1.5 \times 10^{19} m^{-3}$ up to 0.9 as the density limit [4] is approached. Figure 4 illustrates a 4MA density limit discharge to which 11MW of neutral beam heating and 6MW of ICRH are applied. An axial density of $1.1 \times 10^{20} m^{-3}$ is reached in this pulse just before the plasma disrupts.

PLASMA DISRUPTIONS

A final example of the insight derived from an analysis of the VUV emission is illustrated in figure 5 by a comparison of the spectra observed before and during a plasma disruption [5]. At 10.87s, before the disruption, the plasma current is 1.9MA. The second spectrum, with a later time frame of duration 16ms, is recorded at 10.96s during the current run down and corresponds to a current of between 1.3MA and 0.05MA. Immediately prior to the disruption, O and Cl dominate the spectrum. The intense C II lines relative to C III at 10.96s, together with an absence of O II and Cl II, indicates that the disruption terminates with an influx of C, with an associated non-stationary ionisation temperature, T_e, that is probably less than 10eV.

CONCLUSIONS

The analysis of the VUV and XUV line intensities in conjunction with bolometry can provide a measure of the contribution of the different impurity elements to the radiation from the JET plasma. As such, the analysis has wide applications, being crucial whenever radiation plays a part in determining plasma behaviour.

REFERENCES

[1] G Janeschitz et al., Proc. 16th EPS Conference, Venice, 1989, vol 4, p1549
[2] N C Hawkes et al., Bull. A.P.S., 1989, vol 34, p1980
[3] M Bures et al., Proc. of IAEA Tech. Comm. Meeting, Fusion Eng. and Design, Garching,1989
[4] C G Lowry et al., Bull. A.P.S., 1989, vol 34, p2054
[5] J A Wesson et al., Nuclear Fusion, 1989, vol 29, p641

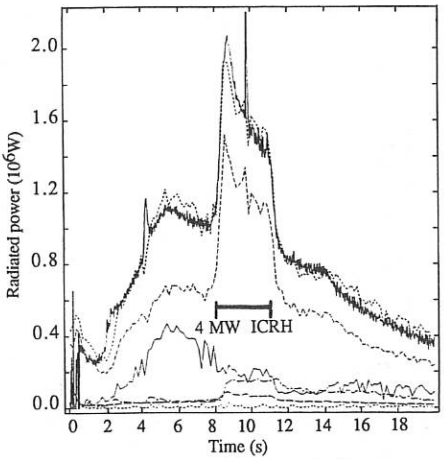

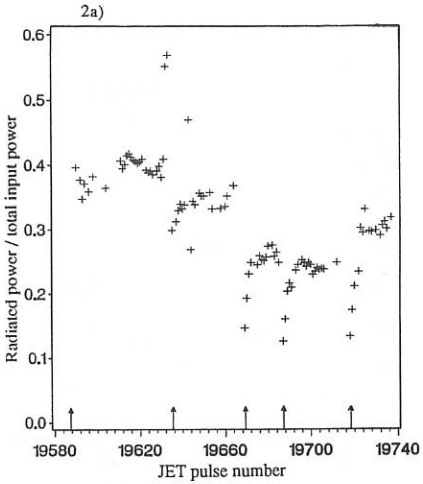

Figure 1. Components of the radiated power, C ---, Be — —, Ni — · —, Cl ——, O ····. The sum of the calculated powers, ----, is compared with the bolometric measurement, ⋀⋀⋀.

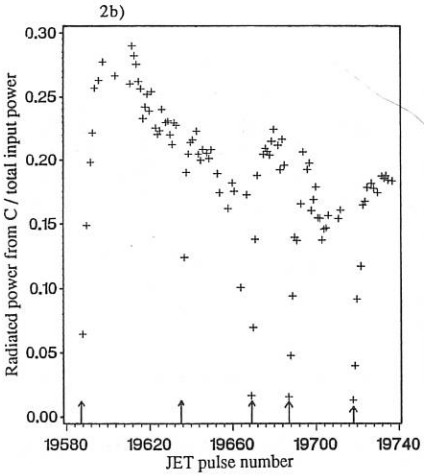

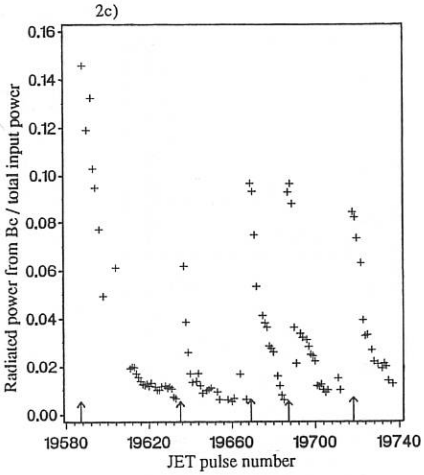

Figure 2. The ratio of a) the total radiated power, b) the radiated power from C, c) the radiated power from Be to the total input power measured during the Ohmic phase for a sequence of pulses during Be evaporation operations. Arrows indicate the first pulse after an evaporation.

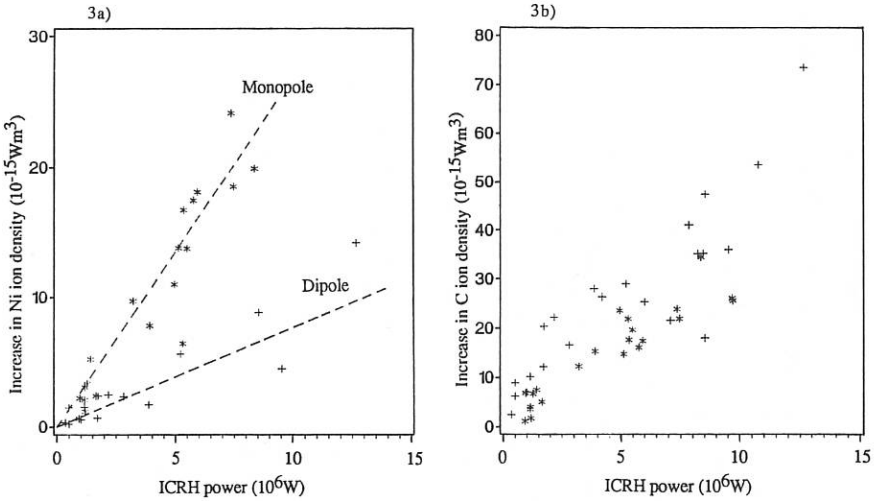

Figure 3. The increase in the a) Ni, b) C ion density during the first 2s of ICRH as a function of heating power. The ion density is the ratio of the elemental radiated power to average n_e and has arbitrary units. * indicates monopole and + dipole phasing of the antennae.

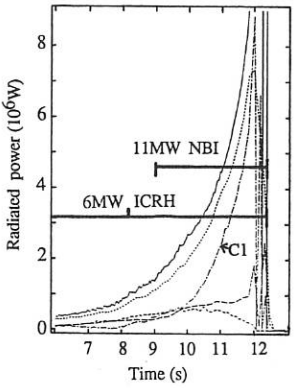

Figure 4. Components of the radiated power: Be — —, Ni – – –, Cl —·. The sum of the calculated powers,·– – –·, is compared with the bolometric measurement, ——.

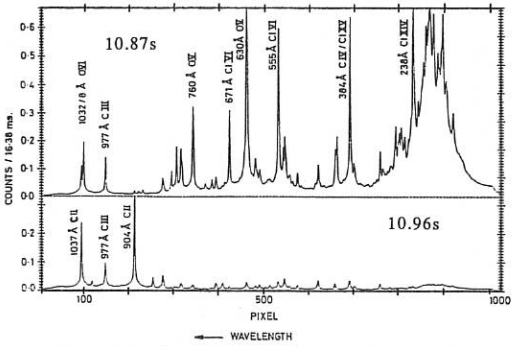

Figure 5. VUV spectra measured before, 10.87s, and during, 10.96s, a plasma disruption.

MODELLING OF CARBON IN THE TFTR EDGE PLASMA

B. J. Braams*, D. P. Coster, A. B. Ehrhardt, C. F. F. Karney,
D. M. Manos, M. Petravic, C. S. Pitcher, A. T. Ramsey,
D. P. Stotler, M. Ulrickson

Princeton Plasma Physics Laboratory, Princeton, NJ 08543-0451
*Courant Institute, 251 Mercer Street, New York, NY 10012

The performance of high power discharges in TFTR is often degraded by a sudden large influx of carbon from the limiter, called a "carbon bloom". We have recently begun an effort to model the TFTR edge plasma and the plasma-wall interaction, with use of the B2 fluid code (Braams, 1986) and the DEGAS neutral gas transport code (Heifetz, 1982). Our aim is to learn about transport properties of the edge plasma, and to understand better the release of carbon from the limiter and its penetration into the main plasma.

The edge plasma diagnostics on TFTR are: (1) A fast probe on the outside midplane, measuring electron density and temperature, floating potential, and parallel power flow, as function of radius. The probe can obtain data up to 2 cm inside the last closed flux surface (lcfs) in OH discharges, and to 5 cm outside lcfs for high power neutral beam discharges. A second, slower moving probe is on the bottom of the device. (2) A visible survey spectrometer, tunable from the near ultraviolet to the red. It has a midplane radial view, and measures H-alpha and lines of C(0+)-C(2+). (3) The H-alpha interference filter array (HAIFA) has five channels viewing a 70° segment of the inner limiter. The channels are fitted with filters to measure H-alpha and C(1+) emission; the detectors are absolutely calibrated. (4) Two periscopes fitted with visible or infrared cameras. The visible light camera has a 60° field of view, from tangential to the inner limiter to almost normal to the limiter, and is filtered to observe H-alpha or C(2+) light. It is relatively calibrated. The IR camera is a single color pyrometer (1.0 to 1.8 μm wavelength band), and measures detailed temperature profiles of the limiter. (5) Thermocouples

attached to the back of the bumper limiter measure the total power deposition. (6) The core plasma profiles of electron temperature and density extend to 5-10 cm inside the lcfs, and Thomson scattering extends to about 1 cm inside lcfs, both with large error bars at the edge.

The B2 code solves a system of fluid equations describing a multispecies plasma in an axisymmetric geometry. The DEGAS code calculates transport of neutral particles (hydrogen and impurities) in the plasma. As part of this work we have developed an interface between the two codes, so that DEGAS provides an ionization source for B2 and B2 provides the plasma background in which DEGAS tracks neutrals. Both codes were used in previous studies mainly to simulate purely hydrogenic plasma. DEGAS has now been upgraded to follow carbon and the breakdown of methane in the edge plasma. We have had difficulty, however, with the B2 calculations when the carbon concentration exceeds the trace impurity level, and are working to improve the ability of B2 to simulate plasmas with high concentrations of carbon.

At present we are using the combination of B2 and DEGAS to model the TFTR plasma without the carbon impurity. By fitting the experimentally determined power flux, edge profiles, and H-alpha signals we can obtain estimates for the electron heat conductivity and the particle diffusivity. The inclusion of carbon in the calculations will allow a detailed comparison to be made with the experiment and will enable us to understand the mechanism by which carbon blooms terminate some TFTR discharges.

This work is supported by DoE contracts DE-AC02-76-CHO-3073 and DE-FG02-86ER53223.

Braams B. J. (1986) "Computational Studies in Tokamak Equilibrium and Transport" (thesis, University of Utrecht, the Netherlands).

Heifetz D., Post D. E., Petravic M., Weisheit J., and Bateman G. (1982) J. Comput. Phys **46**, 309.

FIRST-WALL BEHAVIOR IN TFTR*

C. S. Pitcher,† H. F. Dylla, M. G. Bell, R. V. Budny, R. J. Hawryluk, K. W. Hill, S. J. Kilpatrick, P. H. LaMarche, M. Leonard, D. M. Manos, D. Mueller, D. K. Owens, A. T. Ramsey, G. Schmidt, S. D. Scott, M. Ulrickson, and M. C. Zarnstorff

Plasma Physics Laboratory, Princeton University
P.O. Box 451, Princeton, New Jersey 08543

1. Introduction

First-wall experiments in the last operating campaign of TFTR (August 1989 - February 1990) have concentrated on "carbon blooms" [1] and boronization [2]. The purpose of the present paper is to summarize the experiments performed in these two areas.

2. Carbon Blooms

It has been observed on both TFTR and JET that when excessive localized heating occurs on the graphite limiter, enhanced impurity release results, i.e. above the level associated with physical sputtering by deuterons and carbon ions. This phenomenon has been called the "carbon bloom" and is thought to be due to a thermally activated process (i.e. sublimation) which may be further enhanced by radiation damage associated with the energetic particles striking the limiter [3]. Camera observations on TFTR with CI, CII and CIII filters indicate that the enhancement above the physical sputtering level is detectable at ~1600 C and rapidly increases as the hot spot temperature rises [1]. The hot spots occur at carbon tile edges, where the incident power density from the plasma is large, or at damage sites, where the carbon surface is thermally decoupled from the bulk.

2.1 Results

Figure 1 gives the time traces for a TFTR discharge which had a strong carbon bloom. In this discharge the neutral beam power was P_{NB} = 22.5 MW starting at t = 3.0 s, the plasma current was I_p = 1.6 MA, the toroidal magnetic field B_T = 5T, the major and minor radii R/a = 2.45 m/0.8 m. Shown in the figure are the Z_{eff}, the poloidally-averaged CII emission from the bumper limiter, the D-D neutron rate S_{DD}, the radiated power P_{rad} and the temperature of a hot spot as determined by infrared thermography. This hot spot, which was observed to persist during the entire experimental run, consisted of an area of approximately 3 cm^2 located at the mid-plane of the inner wall bumper limiter [1]. The hot spot location is approximately 125° toroidally away from the CII measurement. Thus, the CII measurement is a global measurement of carbon influx rather than a local measurement of influx from this hot spot.

Before the start of neutral beam injection the Z_{eff} of the ohmic target discharge is high, ~4. This decreases to a value of ~2 by t = 3.4 s due primarily to the diluting effect of the beam ions. Also on the application of power, the CII emission, the neutron rate S_{DD}, and the radiated power P_{rad} all increase and by t = 3.4 s these parameters have all reached approximately steady-state conditions, which in the absence of a carbon bloom would be maintained until the beam power is reduced. This behavior, i.e. increasing carbon influx, radiated power, etc., with increasing beam power, can all be explained using simple power and particle balance considerations assuming only physical sputtering of the graphite limiter by deuterons and carbon ions [4,5]. However, after t = 3.4 s the carbon influx starts to rise again resulting in an increase in the Z_{eff} and the radiated power, and a decrease in the

†Canadian Fusion Fuels Technology Project, Toronto, Canada

neutron rate. The temperature at which this enhanced impurity production occurs is approximately 1600 C, well below the temperature at which regular thermal sublimation is significant. By t = 3.73 s, the temperature of the hot spot has reached ~2500 C and the carbon influx, which had been rising, starts to increase at a faster rate. This increased rate of rise is also noticeable on the radiated power and apparent in the rate of decrease of the neutron rate. By t = 3.9 s, the CII signal and radiated power have peaked. At this time the temperature of the hot spot has also peaked at a value of ~3100 C despite the continued application of beam power. This is probably due to significant edge radiation and normal thermal sublimation.

2.2 Discussion

The enhancement in the carbon influx above the physical sputtering level at a temperature of ~1600 C is not consistent with normal thermal sublimation but may be explained by a radiation damage enhanced process which effectively reduces the sublimation energy of surface carbon atoms. This effect starts to become appreciable in ion beam simulations for incident deuteron and carbon ions at ~1200 C [3]. At a temperature of 1600 C the effective sputtering yields are increased by a factor of ~6 over the room temperature physical sputtering values. In the case of carbon, the self-sputtering yield, Y_C, is enhanced to a level of $Y_C \sim 2$ [6]. Although this enhancement at the hot spot is significant, the area of this particular hot spot is small compared to the total area of the limiter and thus a local factor of six increase cannot explain the global effect on the discharge. It may be that numerous other hot spots on the limiter, although not reaching as high a temperature, may combine to significantly contribute to the global influx. Another possibility is that with the local self-sputtering yield being above unity, a moderated runaway effect is generated.

When the surface temperature reaches ~2500 C the influx due to normal sublimation is expected to be of order $\sim 10^{19}$ C cm^{-2} s^{-1} [7]. This is to be compared with the total carbon influx which is of order $\sim 6 \times 10^{21}$ C s^{-1}, obtained from the CII intensity and the theoretical photon efficiency [8]. Again a single hot spot cannot explain the enhancement in the global carbon influx and thus, either numerous hot spots or some local feedback mechanism is responsible.

It is clear from Fig. 1 that the carbon bloom suppresses the neutron rate which would have otherwise remained constant over the period 3.4 to 4.0 s. The bloom starts after the peak neutron rate, however, and thus does not play a limiting role in the maximum neutron rate in this particular discharge. The importance of blooms in determining the maximum neutron rate is demonstrated in Fig. 2, where the time (from the start of the beams) to reach the peak in the neutron signal and the start of the bloom is plotted versus beam power. Typically the neutron rate peaks ~0.35 s after the start of neutral beam injection and as expected, the time for a bloom to occur deceases as the beam power is increased. The two curves cross at ~25 MW and it is at powers above this level that blooms occur early enough to suppress the peak neutron rate. These results vary depending on the plasma shaping and on the history of damage sites on the bumper limiter.

3. Boronization

Boronization has been carried out twice in the last campaign [2] following the technique developed on TEXTOR [9] and ASDEX [10]. This involved the deposition of a thin (40 - 100 nm) amorphous, carbon/boron film onto first-wall structures using a glow discharge. The boronization had a number of beneficial effects on subsequent tokamak discharges. Comparing reference discharges before and after boronization, the oxygen content dropped by a factor of ~2, the metal concentration decreased by a factor of two to five so that their contribution to Z_{eff} was <0.2 and the carbon influx from the bumper limiter decreased by 1.6 to 3.0. The carbon decrease is consistent with the C/B stoichiometry obtained with SIMS analysis of surface collector probes exposed to the boronization. Figure 3 shows the BII and CII spectroscopic signals from the bumper limiter as a function of discharge number following

a 100 nm boronization. The suppression of the carbon influx was temporary, lasting approximately 10 to 20 discharges with the boron influx being anti-correlated with the carbon. The BII measurement is taken at a different toroidal location than the CII, which was measured at a low point on the bumper limiter (reduced particle flux) and thus, the BII and CII signals do not show perfect anti-correlation. The hydrogen recycling behavior of the carbon/boron film was found to be similar to pure carbon and thus, supershot performance, which is connected to hydrogen recycling, was not enhanced as a result of boronization.

The main benefit of the boronization was in the control of oxygen. This was manifested in two ways. First, in high density discharges the radiated power fraction was reduced significantly resulting in a higher density limit. This is demonstrated in Fig. 4, which compares the radiated power as a function of density for reference discharges (I_p = 1.4 MA, R/a = 2.45 m/0.80 m, B_T = 4T, ohmic heating ~1 MW) before boronization and after. Typically, the radiated power is reduced by 150 kW at moderate density and the density limit extended by 25%. At low density, boronization had little effect, which is to be expected since the dominant impurity in TFTR at low density is carbon rather than oxygen [11]. The second advantage of the boronization was an improvement in the ability to recover from plasma disruptions and loss-of-vacuum incidents. Typically, before boronization, 10 to 20 helium conditioning discharges were required to reduce oxygen levels and re-establish low recycling conditions following a high power disruption. Following boronization, low oxygen levels were re-established in two to three discharges.

4. Conclusions

Carbon blooms have serious consequences for plasma performance on TFTR. At powers as low as 15 MW the discharge can be severely perturbed, the large carbon influx increases the radiated power, the Z_{eff}, and suppresses the neutron rate. However, only at high power (~25 MW) does the bloom occur early enough that the peak neutron rate is affected. Since TFTR can run at significantly higher power (>30 MW) carbon blooms must be controlled before this extended performance can be fully realized. Two steps have recently been taken to reduce carbon blooms. Limiter tile alignment has been improved and critical graphite tiles have been replaced with carbon fiber reinforced graphite [1].

Boronization has reduced the oxygen radiation in TFTR discharges at moderate to high density, resulting in an extension of the density limit. At low density the effect of boronization on reducing carbon impurity levels is transient. Boronization also significantly improves the ability to recover from oxygen incursions from disruptions and loss-of-vacuum incidents.

*This work supported by U.S. Department of Energy Contract No. DE-AC02-76-CHO3073.

References

[1] M. Ulrickson, et al., Proc. of 9th PSI Conf., Bournemouth, U.K., May 1990.
[2] H. F. Dylla et al., Proc. of 9th PSI Conf., Bournemouth, U.K., May 1990.
[3] J. Roth, in "Physics of Plasma-Wall Interactions in Controlled Fusion," ed. D. E. Post and R. Behrish (Plenum, NY 1986).
[4] C. S. Pitcher et al., J. Vac. Sci. Tech. A8 (3), May/June 1990.
[5] C. S. Pitcher, Fus. Eng. Design, in press.
[6] J. Roth et al., private communication.
[7] R. Behrish, J. Nucl. Mat. **93/94** (1980) 498.
[8] K. H. Behringer, J. Nucl. Mat. **145-147** (1987) 145.
[9] J. Winter et al., J. Nucl. Mat. **162-164** (1989) 713.
[10] W. Poschenrieder et al., Proc. of 9th PSI Conf., Bournemouth, U.K., May 1990.
[11] K. W. Hill et al., Proc. 11th Int. Conf. IAEA, Kyoto, 1986, 1 (1987) 207.

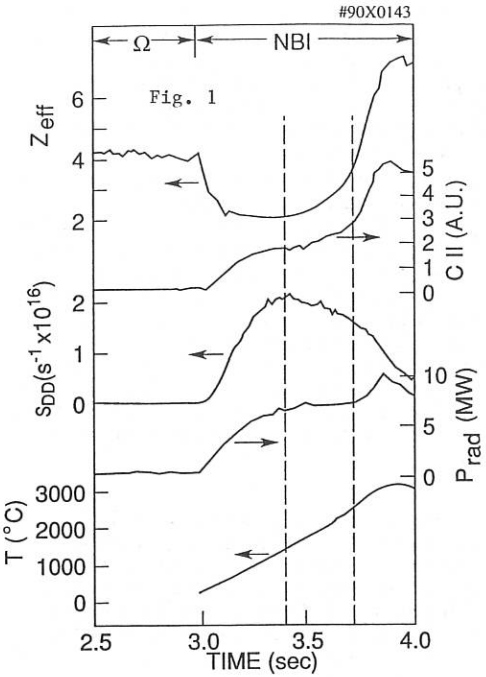

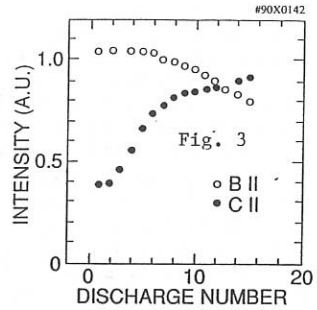

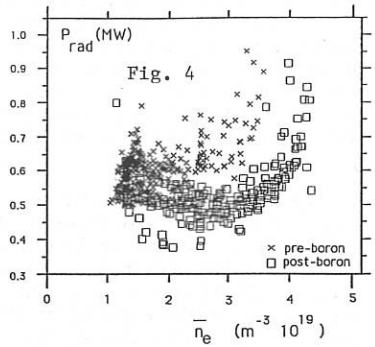

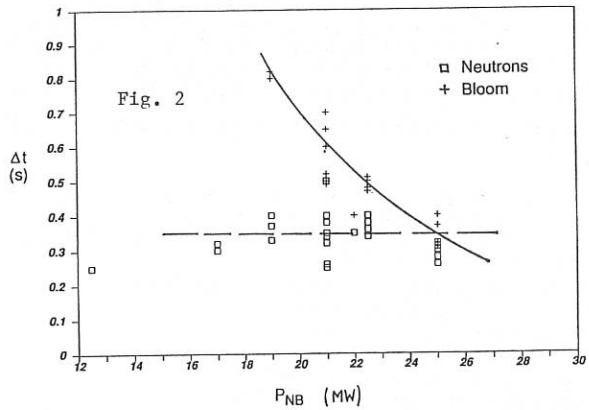

Fig. 1. Z_{eff}, the CII emission, the D-D neutron rate S_{DD}, the radiated power P_{rad} and the temperature of a hot spot for a discharge with a strong carbon bloom.
Fig. 2. The time delay to reach the peak neutron rate and the onset of carbon blooms.
Fig. 3. BII and CII intensities from the limiter following boronization.
Fig. 4. Radiated power versus density in reference discharges before and after boronization.

Multi-Species Impurity Accumulation Phenomena in ASDEX

G. Fussmann, A. Kallenbach, K. Krieger, K.-H. Steuer
Max-Planck-Institut für Plasmaphysik
D-8046 Garching, West Germany

1. Introduction

Accumulation of metallic impurities has been observed in ASDEX in numerous discharges where an improvement of the confinement had been achieved [1]. On the other hand, low-Z - impurities like carbon did not exhibit such a clear tendency of accumulation. In particular, the profiles of Z_{eff} showed only a slight peaking towards the plasma centre. Such observations were made under carbonized as well as non-carbonized wall conditions. More recently we investigated the accumulation processes under boronized conditions during counter NI-heating. This time, markedly peaked Z_{eff} profiles were found and the accumulation of C could be confirmed also by CX-spectroscopy. In addition, gas puffing experiments with Kr, Ar, Ne, N_2, and He showed clear evidence of accumulation for all elements apart from He, the behaviour of which is still uncertain because of difficulties in the interpretation of the CX-spectroscopy data.

When trying to understand the obvious differences between carbonization and boronization one has to realize that, in the case of boronization, O is suppressed and partially replaced by B. Furthermore, copper, the main metallic impurity, has also been reduced. These changes suggested an interpretation in terms of multi-species interaction in such a manner that the heavier elements tend to expel the lighter ones out of the central region. In addition, changes in profiles of density and temperature are also to be considered.

In this paper we concentrate on the question of whether the different behaviour with respect to accumulation can be explained by neoclassical multi-species theory. More experimental observations are reported in another contribution to this conference [2] .

2. Neoclassical Multi-Ion Transport

The general concept of neoclassical theory of more than one impurity species has been worked out in Ref.[3]. More specifically, in [4] the case of one light and one heavy impurity has been treated in the trace approximation for the conditions of Alcator-C and TEXT where the two ions were in different collisional regimes. Such calculations are already rather envolved because of the difficulties that arise if the low-Z particles are in the plateau or banana regime. It is therefore most important to address the question of collisionalities first. For this purpose we discuss the collision-frequency matrix shown below for three ions (assuming $m_1 < m_2 < m_3$).

$$\nu_{ab} = \nu_{11} \begin{pmatrix} 1 & \sqrt{2}\,\frac{Z_2^2}{Z_1^2}\frac{n_2}{n_1} & \sqrt{2}\,\frac{Z_3^2}{Z_1^2}\frac{n_3}{n_1} \\ \sqrt{2}\,\frac{Z_2^2}{Z_1^2}\frac{m_1}{m_2} & \sqrt{\frac{m_1}{m_2}}\,\frac{Z_2^4}{Z_1^4}\frac{n_2}{n_1} & \sqrt{2\,\frac{m_1}{m_2}}\,\frac{Z_2^2 Z_3^2}{Z_1^4}\frac{n_3}{n_1} \\ \sqrt{2}\,\frac{Z_3^2}{Z_1^2}\frac{m_1}{m_3} & \sqrt{\frac{2\,m_1 m_2}{m_3^2}}\,\frac{Z_2^2 Z_3^2}{Z_1^4}\frac{n_2}{n_1} & \sqrt{\frac{m_1}{m_3}}\,\frac{Z_3^4}{Z_1^4}\frac{n_3}{n_1} \end{pmatrix}$$

with

$$\nu_{11} = \frac{4}{3}\sqrt{\frac{\pi}{m_1}}\,\ln\Lambda\, T^{-1.5}\, e^4\, Z_1^4\, n_1$$

The first row of the above matrix describes the interaction of the background ions (here deuterons) with themselves and with the two impurity ions. Similarly, the second row yields the collision-frequencies of the lighter impurity ions with deuterons, themselves, and the heavier ions, respectively. The meaning of the third row and the extension to more than three species is obvious. Analogously, the collisionality-matrix ν^*_{ab} , and the collisionalities of the various ions $\nu^*_a = \Sigma\, \nu^*_{ab}$ are obtained from $\nu^*_{ab} = \nu_{ab}\, R_0\, q\, \varepsilon^{-3/2}\, v_a^{-1}$, where $v_a = (2T_i/m_a)^{1/2}$, $\varepsilon = r/R_0$, and q is the safety factor (assuming all ions at temperature T_i).
For a typical accumulation phase during NI counter heating we have $n_{eo} \approx 5\cdot 10^{13}$ cm^{-3}, $T_{io} \approx 1$ KeV, and the following concentrations on axis : B (1%), C (1.5%), O (1.5%), and Cu (0.2%). The normalized collision matrix under these conditions (in units of 800 s^{-1}) is shown below.

	D^+	B^{+5}	C^{+6}	O^{+8}	Cu^{+20}	α	$\nu^* \varepsilon^{3/2}$
D^+	1	0.4	0.8	1.4	1.1	1	0.06
B^{+5}	7.1	2.8	8.5	15	13	0.25	1.3
C^{+6}	8.5	4.7	7.9	20	17	0.54	1.8
O^{+8}	11	6.3	15	22	26	0.96	2.9
Cu^{+20}	19	11	25	51	58	0.80	11.4

The frequencies for Cu - Cu collisions are seen to be most effective, but the interaction of Cu with O is nearly as strong. Also given in the table are the collision strengths $\alpha = Z^2 n_Z / n_D$ for the four impurities, which with $\alpha \approx 1$ again corroborate the importance of impurity-impurity interactions. Finally, in the last column we have added the quantity $\nu^* \varepsilon^{3/2}$ for all 5 ions which, in case of being larger than unity, indicates that those species are in high collisional Pfirsch- Schlüter regime (PS). Hence, all above impurities are in the PS regime on axis, and moreover, because of $\nu^* \propto T_i^{-2}$, over the whole plasma cross-section.
A rigourous theoretical treatment of the above situation of several impurities with relatively large collision strengths does not seem available at present. Our analysis is therefore to some degree of an exploratory character and, as a first approach, we do not consider additional effects such as toroidal and poloidal rotation .
Before discussing the neoclassical fluxes it appears reasonable to have a look on the classical ones being derived for a straight cylinder. Ignoring the thermal forces these are

$$e_a \Gamma_a = B^{-2} \sum_b m_a n_a \nu_{ab} \left(\frac{p_a'}{e_a n_a} - \frac{p_b'}{e_b n_b} \right)$$

where $p_a' = dp_a/dr$. Toroidal effects lead to the well known enhancement factor $2\, q^2$. Furthermore, the thermal forces can be included - as shown in [5], for impurities in the PS regime and background ions in the banana or plateau regime - by making the following replacements

$$\left(\frac{p_a'}{e_a n_a} - \frac{p_b'}{e_b n_b} \right) \rightarrow T \left\{ K \left(\frac{n_a'}{e_a n_a} - \frac{n_b'}{e_b n_b} \right) + H \frac{T'}{T} \left(\frac{1}{e_a} - \frac{1}{e_b} \right) \right\}$$

The coefficients H and K are, in general, functions of the impurity collision strengths α_Z and the collisionality of the background ions. For H=K=1 the classical result is reproduced. Under the cited conditions with $\nu_{DD}^* \varepsilon^{3/2} \ll 1$, however, we have $H \approx -1/2$ and $K \approx 1$ for all impurities. The negative temperature gradient coefficient, H, is of particular importance since it will lead to impurity screening.
In contrast to [3,4] we have fully retained the last bracket $(1/e_a - 1/e_b)$ with charges e_a, e_b in the replacement above. This factor is found necessary to attain stationary conditions pertaining the principle of detailed balance. This principle can be expressed in the following way : if one

ion is in equilibrium with a second one, then all ions are in equilibrium with each other. Accordingly, each of the above curly brackets must vanish separately. For the same reason the ratio $\beta = H/K$ must be postulated to be independent of the charges too. The stationary solutions are then obtained as : $n_a \propto n_b^{e_a/e_b} T^{\beta(e_a - e_b)}$. Again, owing to the detailed balance, we can express this result in terms of the deuteron density

$$n_z = n_{Z0} \left(n_D / n_{D0}\right)^Z \left(T / T_0\right)^{\beta (Z-1)}$$

3. Comparison with Experiments

The neoclassical formalism was applied to compare especially with Z_{eff} and CX-spectroscopy profiles of O and C during : 1) A counter NI-phase showing pronounced impurity accumulation, and 2) a quiescent H^*-phase (co NI) with practically flat Z_{eff} profiles. Results are presented in Figs. 1a to 3b.

In the Figs. 1a,b we show the normalized profiles of electron density and temperature which differ considerably in shape for the two cases. Also the central values of temperature are quite different (counter NI : $T_{e0} = 0.74$ keV, $n_{e0} = 6.3 \cdot 10^{13}$ cm^{-3}, H^* : $T_{e0} = 2.50$ keV, $n_{e0} = 5.0 \cdot 10^{13}$cm^{-3}). In the counter NI accumulation case the profile is seen to become hollow because of the high central radiation losses. We have calculated the stationary neoclassical density profiles of all ions (without any anomalous contributions) resulting from the measured n_e-profile and the equation of quasi-neutrality $n_e = n_D + Z_B n_B + Z_C n_C + Z_O n_O + Z_{Cu} n_{Cu}$ by specifying the concentrations on axis, and using the last formula of Sec.2 with $\beta = -0.5$. The deuteron density is thus obtained from the zeros of a polynomial at each radius. The central concentrations n_{Z0} / n_{e0} were mainly determined from CX and bolometric (Cu) measurements (H^* : B (1%), C (2%), O (1%), Cu (0.005%), for counter NI see Sec.2). A pronounced dilution of deuterium is to be seen from Figs.2 in both cases.

Finally, we present in Figs. 3 the comparison between calculated and measured Z_{eff}-profiles. In the counter NI case the peaking of the profile is well reproduced. It is essentially produced by Cu and O, whereas the contributions from C and B vary much less over the cross-section.

This reduced peaking of the light elements is enhanced by the expelling effect of the heavier ions. The calculations are also in good agreement with the measured profiles of O and C by CX spectroscopy which cannot be shown here because of lack of space. Due to the slight hollowness of the T_e profile the temperature screening term is enhancing the central peaking of the high-Z elements. On the other hand, the peaking towards the boundary is not reproduced in the calculations shown in Fig.3a. It is to be noted, however, that no sources are considered in these simulations.

The agreement between measurement and calculation in the non- accumulating case shown in Fig.3b is poorer but still satisfactory. Here the theoretical Z_{eff}-profiles are even slightly hollow as a result of impurity screening caused by the strong T_e gradients in the boundary region. A more refined fitting of the radial Z- dependence of Cu and O would to some extent reduce this effect.

4. Conclusions

We find a surprising well agreement between measurements and neoclassical predictions in accumulation and non-accumulation phases. During accumulation the central peaking of the light impurity ions can be reduced on account of interaction with the heavier ions. Most important are the profile shapes of both density and temperature. Under high collisional impurity conditions the accumulation can become unstable due to radiation losses causing a central flattening (or indentation) of the T_i-profile.

References

[1] G. Fussmann, J. Hofmann, G.Janeschitz et al., J. Nucl. Mat. 162-164 (1989),14-13
[2] K.-H. Steuer et al., this conference
[3] S. P. Hirshman and D.J. Sigmar, Nucl. Fus. 21 (1981),1079
[4] K.W. Wenzel and D.J. Sigmar, Nucl. Fus. (to be published)
[5] A. Samain and F. Werkhoff, Nucl. Fus. 17 (1977), 53

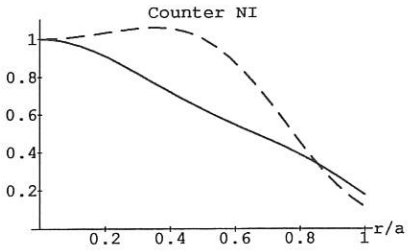

Fig.1a Normalized **Ne** (solid) and **Te** (dashed) during counter NI accumulation phase (#30438)

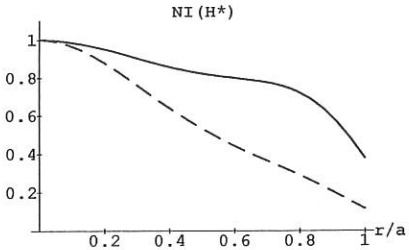

Fig.1b **Ne** (solid) and **Te** (dashed) during H* -phase of NI (#30820)

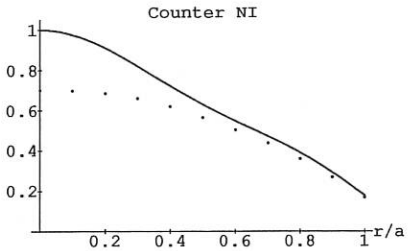

Fig.2a **Electron** (solid) and **deuteron** (dotted) density profiles .

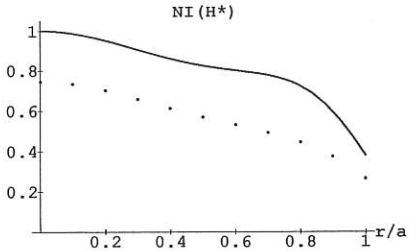

Fig.2b **Electrons & deuterons** (as Fig. 2a)

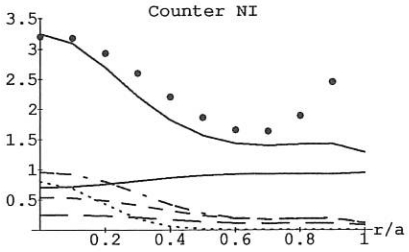

Fig.3a **Zeff-profiles** : measured (points) calcul. : total & deutr. (sol.), O (dot-dashed), C (short dashed), B (long dashed), Cu (dotted)

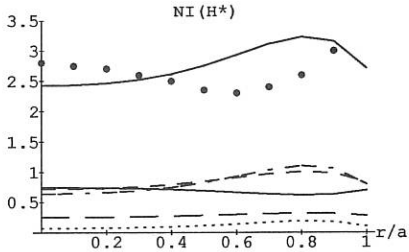

Fig.3b **Zeff-profiles** (as Fig. 3a)

POWER FLOW AND ELECTRIC CURRENT ASYMMETRIES IN THE ASDEX SOL

N.Tsois*,G.Kyriakakis*,E.Kakoulidis*,A.Carlson,J.Neuhauser,W.Feneberg
and the ASDEX team.

Max-Planck Institut fuer Plasmaphysik,EURATOM-Association
Garching b.Muenchen ,F.R.G

I. Introduction : The fast reciprocating Langmuir probe in the ASDEX divertor (fig.1) was used to study the existence of currents in the scrape-off layer.The multiple tip configuration consisted of three tips in triple-probe arrangement /1/ and a fourth tip grounded to measure net currents. The probe sweeping mode of operation allows the acquisition of up to four radial profiles of the electron temperature,plasma density, floating potential and net current of the grounded tip.

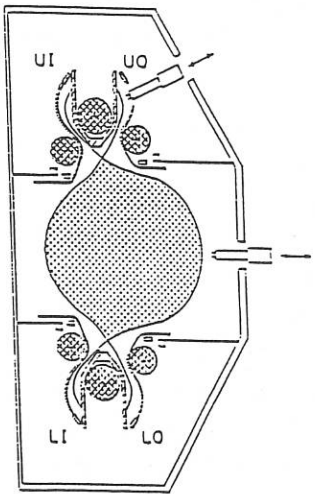

Fig.1 : Langmuir probe arrangement in ASDEX SOL.

Measurements on JET have shown the existence of a current flowing at the divertor target plate /2/ believed to originate from power flow asymmetries /3,4/. The probe in ASDEX is in close proximity to the outer target plate,hence the grounded tip should collect any current flowing to the target.Divertor regions not accessible by the probe were analysed by use of other edge diagnostics, namely microwave interferometry,target plate calorimetry,and bolometry /5/.

II. Experimental results : Radial profiles were acquired for a series of shots with different characteristics; ohmic,neutral injection and lower hybrid heated discharges

with normal and reversed toroidal field polarities. A set of typical profiles during ohmic heating phases ,are shown in fig. 2 for three values of the main plasma density.

It is clearly seen that the radial profiles of the grounded tip current change with plasma density and operating mode (single-null, double-null,auxilliary heating). At low densities the probe tip ,and consequently the target plate,always collects an ion current. This suggests a non-ambipolar enhanced electron transport across the magnetic field. At medium and high densities the radial pattern of the current depends on the operating mode and to some extent on the magnetic field polarity. High currents ,with absolute values reaching 70 - 80% of the ion saturation current (1 - 10 A/cm2) ,have been observed to flow close to the separatrix ,parallel and antiparallel to the main plasma current . During lower hybrid and neutral injection discharges,the known effects on the divertor plasma profiles /5,6/,i.e enhanced power flow,increased Jsat,Te and modulation by ELMs , are also manifested on the current profiles but no obvious qualitative discrepancies with the depicted behaviour were observed.

III. Interpretation - Discussion : The measured current will be interpreted within the context of a parallel current flowing in the scrape-off layer due to the differential power flow on the outer and inner target plates. When the probe collects electrons the direction of current flow is away from the UO target along field lines (fig. 1).

In single-null configurations the ratio of the line densities $N(UO)/N(UI) \sim 1$ and the power flux ratio $P(UO)/P(UI) \sim 3$ as deduced from target calorimetry. With the assumption that the location of the separatrix Rs is accurate to within 1 - 2 mm (fig. 2-b),for $R < Rs + 1cm$ the UO plasma is connected via a flux channel with the UI target,whereas for the profile wing the connection is with the LO target. Assuming uniform density in each connection channel and pressure constancy along field lines we obtain $T(UO)/T(UI) \sim 2$. For these values of temperature and power ratio theory /3,4/ predicts $J_{\parallel} / Jsat \sim 0.50$ which is in agreement with measured values. The same arguments applied for $R > Rs + 1cm$ and for fig. 2-c ,yield the correct direction and magnitudes comparable to theory.

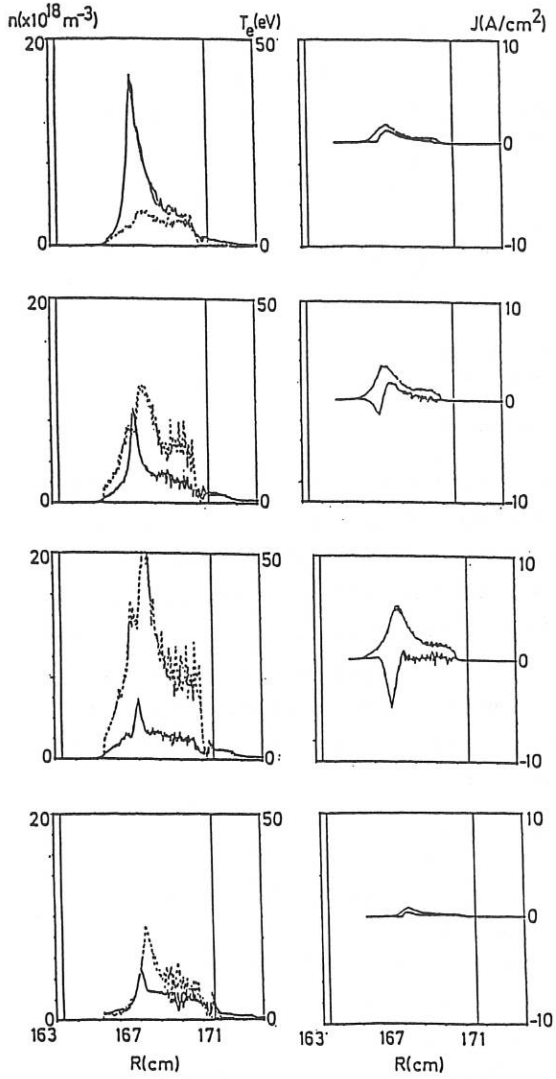

Fig. 2 : Radial profiles of electron temperature, density (left) and probe ion saturation, grounded tip current (right).

(a) $\bar{N}e$ = 1.4x10^{19} m-3
Rs = 167.1 cm
single-null

(b) $\bar{N}e$ = 2.8x10^{19} m-3
Rs = 167.4 cm
single-null

(c) $\bar{N}e$ = 4.2x10^{19} m-3
Rs = 167.4 cm
single-null

(d) $\bar{N}e$ = 3.3x10^{19} m-3
Rs = 167.5 cm
double-null

Rs : magnetically calculated separatrix position.

In additionally heated discharges a localised current close to the separatrix ,parallel to the main current is observed during the onset of the H-mode (fig. 3). Its highly localised nature,although compatible with H-mode characteristics near the separatrix,makes quantitative comparisons difficult.

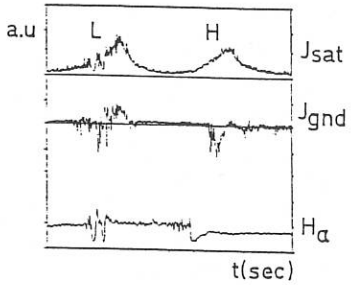

Fig. 3. Ion saturation and grounded tip currents vs time (Shot# 29664).

IV. Conclusions : Evidence seems to suggest that the current flowing in the ASDEX scrape-off is consistent with the thermoelectric current scenario. Its magnitude is comparable to values predicted by theory and its direction of flow agrees with observed power flux asymmetries. The discrepancy observed at low densities may be explanable in terms of other effects, such as positive charging of the edge plasma /2/,or recycling asymmetries. At low densities,however,the electron m.f.p is long and a kinetic description is required /7/.The magnitude of this current renders it significant in edge transport studies.

* NCSR " Demokritos ", Athens, Greece

/1/ Tsois N.,et.al.,(1989) Proc.16th Europ.Conf.on Contr.Fusion and Plasma Physics,Venice,1989,13B,p.907.

/2/ Harbour P.J.,et.al.,J.Nucl.Mater.,162-164 (1989) 236

/3/ Feneberg W.,Zanino R.,(1987) Proc.14th Europ.Conf.on Contr.Fusion and Plasma Physics ,Madrid,1987,11D,p.748

/4/ Staebler G.M.,Hinton F.L.,Nuclear Fusion,29,10 (1989) 1820

/5/ Neuhauser J.,et.al.,(1989) Proc.16th Europ.Conf.on Contr.Fusion and Plasma Physics ,Venice,1989,13B,p.

/6/ Tsois N.,et.al.,(1987) Europhys.Conf.Abstr.1987,11D,p.658

/7/ Chodura R. these proceedings.

DETERMINATION OF IMPURITY TRANSPORT COEFFICIENTS BY SINUSOIDAL MODULATED GAS PUFFING

K. Krieger, G. Fussmann and the ASDEX team

Max-Planck-Institut für Plasmaphysik,
EURATOM-IPP Association D-8046 Garching, FRG

1. Introduction

Impurity transport in tokamaks has been investigated for several reasons. On the one hand, there is the possibility of attaining intolerably large radiation losses and deuterium/tritium dilution in the plasma core region caused by impurities. On the other hand, the behaviour of impurity ions can give valuable information on the physical nature of the underlying transport mechanisms, which is of great interest from a theoretical point of view. Therefore it is desirable to measure as accurately as possible the impurity transport coefficients for various ions under different plasma conditions. In the following we describe a new experimental method — hitherto used to analyze the transport of the background plasma [1,2] — that was recently applied to impurities on ASDEX [3]. The principles of the method are outlined with particular emphasis on the differences that occur in applying the technique to impurity ions instead of the bulk plasma. Experimental results are shown from ASDEX discharges with pure ohmic and with additional NI-heating derived from analysis with a simplified transport model mainly used for less detailed study of the transport quantities as a function of plasma parameters.

2. Experiment

Impurity compounds in gas form are released into the plasma vessel through a piezo-electric valve which allows sinusoidally modulation of the gas flux in time. The amount of gas can be controlled by the valve voltage and the gas pressure at the valve. The impurity radiation is observed in several spectral ranges. The visible light emitted from neutrals or singly ionized atoms at the plasma edge reflects the particle influx, whereas the VUV and X-radiation reflect mainly the impurity density. Because of their strong recycling, rare gases are less useful for sinusoidally modulated gas puffing. Instead we used SiH_4, H_2S and HBr.

Harmonic analysis of the measured signals allows determination of phase relations and Fourier amplitudes at the modulation frequency. Phase shift differences are determined by measuring line intensities from neutrals or low ionization stages, representing the particle source, and signals from higher ionized states emitted from the central plasma region. With absolutely calibrated spectrometers it is also possible to determine the ratio of Fourier amplitudes for the densities of different ionization states which is necessary for measurement of streaming velocities.

Impurity transport in the plasma is described (poloidal and toroidal asymmetries beeing neglected) by the continuity equation

$$\frac{\partial n_z(r,t)}{\partial t} = -\frac{1}{r}\frac{\partial}{\partial r} r\Gamma_z(r,t) + Q_z(r,t), \tag{1}$$

where n_z is the density, Γ_z is the radial flux and Q_z is the effective source of impurity ions in ionization state Z. The latter consists of a sink term from particle losses in the scrape-off layer, a source term from the ionization of neutral atoms and terms from ionization and recombination

between adjacent ionization states. The flux is assumed to consist of diffusive and streaming terms: $\Gamma_z = -D_z\,\partial n_z/\partial r + v_z n_z$. Considerable simplification is achieved by summing Γ_z over all charge states, which leads to an equation for the total impurity density n_I with the effective source now consisting only of ionization of neutral particles and losses in the scrape-off layer and with D and v depending virtually only on the radius [4]. As a useful approximation of the real transport, we assume a simple model with constant diffusion coefficient D and a linearly increasing inward drift $v = -v_a r/a$. Furthermore, we can neglect the sources by concentrating on the plasma interior $r \leq a$ since, in contrast to the analysis of the background plasma, the impurity sources and sinks are essentially located within the scrape-off region. We therefore need only solve the corresponding homogeneous equation. The sinusoidal modulation of the particle source leads to a purely sinusoidal time dependence of the particle density. With the ansatz $n_I(r,t) = n_I(r,\omega)e^{i\omega t}$ we arrive at the equation

$$\frac{1}{r}\frac{\partial}{\partial r} r\left(D\frac{\partial n_I}{\partial r} + v_a \frac{r}{a} n_I\right) - i\omega n_I = 0 \tag{2}$$

with the edge condition $n_I(a,t) = n_I(a,\omega)\sin(\omega t)$. The solution can be expressed as a confluent hypergeometric function with imaginary first parameter:

$$n_I(r,\omega) = -in_I(a,\omega)\,{}_1\mathrm{F}_1\left(i\frac{k^2a^2}{2\alpha}, 1, \frac{\alpha}{2}\frac{r^2}{a^2}\right)e^{-\frac{\alpha}{2}\frac{r^2}{a^2}} / {}_1\mathrm{F}_1\left(i\frac{k^2a^2}{2\alpha}, 1, \frac{\alpha}{2}\right)e^{-\frac{\alpha}{2}}. \tag{3}$$

In the case of $v_a \to 0$ the solution is given in terms of Kelvin functions:

$$n_I(r,\omega) = n_I(a,\omega)(\mathrm{bei}_0(kr) - i\,\mathrm{ber}_0(kr))/(\mathrm{bei}_0(ka) + i\,\mathrm{ber}_0(ka)). \tag{4}$$

For abbreviation we introduced $k = \sqrt{\omega/D}$ and the drift parameter $\alpha = av_a/D$ (defined as positive for inward drifts). From the solution one can calculate the phase shift and Fourier amplitude at a given frequency. Such an evaluation is shown in Fig. 1 for a frequency of $\omega/2\pi = 5\,s^{-1}$ and the ASDEX minor radius $a = 0.4\,m$. The figure shows the contour lines for constant central amplitude $A(0)$ and constant central phase shift $\varphi(0) - \varphi(a)$ of the impurity density. Measuring both quantities in an experiment allows — within the scope of this simplified model — determination of the drift parameter and the diffusion coefficient from the intersection of two levels. One important feature of Fig. 1 is the small dependence of the phase shift on the drift parameter, particularly in the left part of the figure. Owing to this peculiarity the diffusion coefficient can be approximately determined from a measurement of the phase shift alone as mentioned above.

3. Results from ASDEX

Because of the lack of absolute calibration of the available spectrometers we concentrated so far on the analysis of the diffusion coefficient which is mainly determined by the phase shift.The interpretation was based on the simple transport model (D = const., $v \sim r$) described in the previous section. The consistency of this model was checked by comparing the phases of all measured line intensities with those predicted by detailed code calculations using the full system of equations with the measured transport parameters. In the table below, we present results from two discharges with H_2S gas puffing at different electron densities. It turns out, that — within the accuracy achieved — the agreement between the numerical simulation and the measurement is quite satisfactory, showing the usefulness of the transport model for evaluation of experimental results.

$\bar{n}_e(10^{19}m^{-3})$	$D(m^2/s)$	α	Ion	λ(Å)	Measured -	Calc. Phase
2.72	0.45	2	S XIV	417.61	1.04	1.09
			S XVI	4.73	2.24	2.28
3.64	0.36	2	S XIV	417.61	1.17	0.88
			S XV	5.04	2.04	2.11
			S XVI	4.73	2.49	2.49

Impurity diffusion coefficients were determined by means of the described analysis in deuterium discharges for a number of varying plasma parameters. Figure 2a shows results measured as a function of the electron density $\bar{n}_e$ for various impurity species with ion charges of $Z = 13$, 15 and 25. The dependence on the toroidal magnetic field B_t and the plasma current I_p is depicted in Fig. 2b. The error bars denote the uncertainty in the drift parameter $\alpha = a\, v_a/D$, which was assumed to be in the range from 1 to 3 in the data analysis. In that range the resulting peaking of the impurity equilibrium profiles is approximately of the same magnitude as for the background plasma. It is seen that the diffusion shows no obvious dependence on charge (and mass) of the ions. In this context it is to be noted that there is also no Z-dependence for the diffusion coefficients according to neoclassical theory. In this theory the dependence occurs solely in the drift terms, showing a linear increase with Z [6]. On the other hand, we find the diffusion coefficients to decrease with increasing electron density. Furthermore, at fixed density the diffusion coefficient seems to increase nearly linearly with B_t and to increase also with I_p. It should be noted however, that these results were obtained from experiments with HBr gas oscillations, where a detailed analysis with numerical simulations was not possible due to the lack of atomic data for bromine. Therefore it will be necessary to check these results using other impurity gases to exclude effects arising from different temperatures or profile shapes.

For discharges with additional NI-heating, only data from H_2S experiments have been evaluated so far. In a plasma with electron density $\bar{n}_e = 3.63 \cdot 10^{19}m^{-3}$ we obtained $D = 0.8 \pm 0.1\, m^2/s$.

Summarizing, the presented results are in obvious contradiction to the neoclassical theory of impurity transport, which predicts a functional dependence according to $D \sim n_e(1 + 2q^2)B_t^{-2}$, i.e. in the plasma centre where $q \simeq 1$, $D \sim n_e B_t^{-2}$ and in the boundary region where $q \gg 1$, $D \sim n_e I_p^{-2}$. Thus, the results obtained can only be explained by additional anomalous diffusion dominating the transport processes. This behaviour is in striking contrast to the non-stationary accumulation phases found under conditions of improved plasma confinement [6].

As a final remark, we note that the diffusion coefficients presented accord well with earlier results obtained by the laser blow off method [4] and injection of impurity-doped pellets [5].

References

[1] Bagdarasov, A. A., *et al.*, *Nucl. Fusion* Suppl. **1** (1985) 181.

[2] Gentle, K.W., *et al.*, *Plasma Physics and Controlled Fusion* **29** (1987) 1077.

[3] Krieger, K., G. Fussmann, submitted to Nuclear Fusion.

[4] Fussmann, G., *Nucl. Fusion* **26** (1986) 983.

[5] Behringer, K.H., Büchl, K., *Nucl. Fusion* **29** (1989) 415.

[6] Fussmann G., *et al.*, *J. Nucl. Materials* **162-164** (1989) 14.

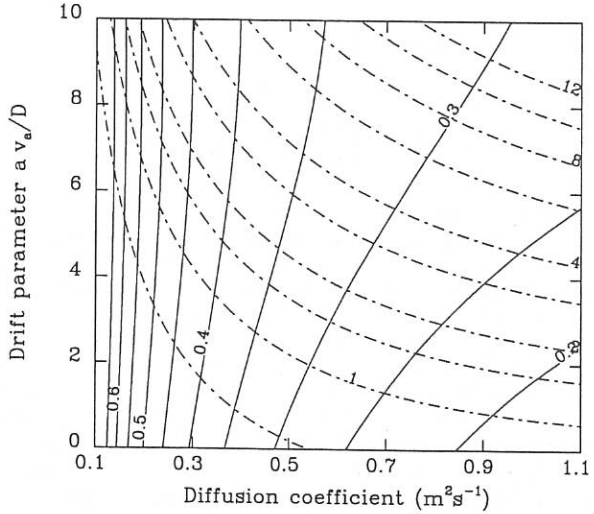

Figure 1: *Contours of constant Fourier amplitude (dashed) and phase shift (solid) in the plasma centre for* $\omega = 10\pi\ s^{-1}$ *and* $a = 0.4\ m$.

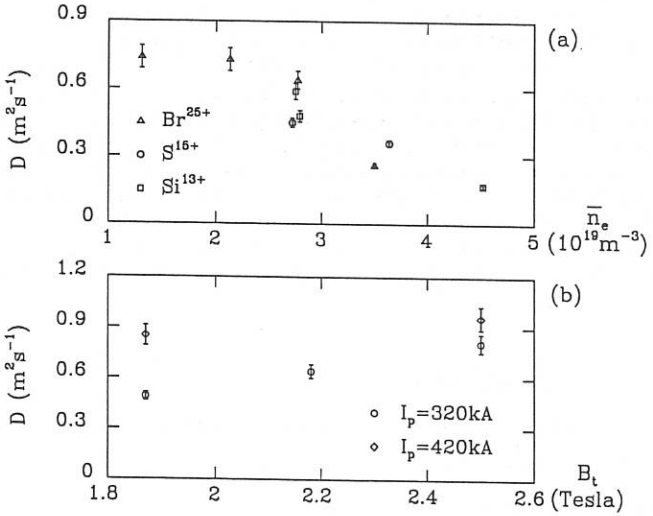

Figure 2: *Diffusion coefficient as a function of line-averaged electron density for various impurity species (a), and as a function of the magnetic field for two plasma currents (b).*

IMPURITY TRANSPORT AND PRODUCTION IN LOWER HYBRID DISCHARGES IN ASDEX

R. De Angelis

Associazione EURATOM-ENEA sulla Fusione, Centro Ricerche Energia Frascati, C.P. 65 - 00044 Frascati, Rome, Italy

G. Fussmann, J.V.Hofmann, K. Krieger and the ASDEX Team

Max-Planck-Inst.f. Plasmaphysik, D-8046 Garching, FRG, EURATOM-Association

INTRODUCTION

During lower hybrid (LH) heating and current drive (CD) operation in ASDEX we have examined experimentally how the wave injection affected impurity production in different base plasmas and coupling regimes. In particular we studied the scaling with power and with the wave spectrum, the comparison with other heating methods used on ASDEX and the possibility that the large number of fast electrons involved in LH operation could have some influence on the impurity release from the wall.

EXPERIMENTAL OBSERVATIONS

The LH power injected ranged from 0 to 1.2 MW, thus providing substantial changes of the power input to the plasma; moreover in the current drive regime full current drive operation was achieved with vanishing and negative loop voltage. Large modifications of the ohmic input power and the profiles of current, temperature and density and sawtooth suppression have been documented [1].

Experimental determinations of Z_{eff} (deduced by infrared bremsstrahlung) show that it could change,at low density, from a base value of 3 to 5-6 for an injected 1 MW power.

The line emissions were observed in the soft x-rays, ultraviolet and visible regions of the spectrum on the main impurities present in ASDEX. Observations include O, C, Fe and Cr originating from the vacuum vessel and Cu which is the constituent of the divertor plates.

Cu was generally the dominating impurity with respect to radiation and Z_{eff} during LH at low density, appreciable variations of the oxygen content were detectable only at the highest densities.

In this paper the lines of CuXX (λ=12.57), and of OVIII (λ=18.98 Å) (ions located around 0.75 of the minor radius) were considered as representatives of the impurity fluxes; they show a qualitative agreement with lower ionization lines seen in the visible range.

A comparison of the line intensities with the Z_{eff} measurements revealed that the power dependence of Z_{eff} was similar to that of the Cu signals at low densities. At high density Z_{eff} increased only slightly with power in accordance with a reduced Cu contribution and a weaker dependence of O on power.

IMPURITY PRODUCTION AS FUNCTION OF LH POWER AND SPECTRUM

The lower hybrid wave was usually launched in two steps of power of typically 500 ms duration; the observed fluxes , in the majority of cases after a few tens of ms,

reached a new stationary level from which the increment over the ohmic phase could be estimated. Under similar conditions the new flux value depends only on the final LH power reached and not on the previous power step.

In the following the results will be mainly expressed as Cu XX percentage variations $\Delta I/I$ over the initial Ohmic value.

At high density ($n_e \geq 3\times10^{13}$ cm^{-3}), $\Delta I/I$ increases roughly linearly with the total power (ohmic + LH) injected into the plasma (Fig. 1). This result was also found (Fig. 2) in discharges where LH and neutral beams were injected simultaneously or alone. This suggests the conclusion that impurity production is tied only to the power given to the plasma by any of the sources used.

At lower density ($n_e \leq 2\times10^{13}$ cm^{-3}), we found a number of new features which required some more detailed investigation.

First, when the LH power was below a threshold value, dependent on the grill phasing, the impurity flux was reduced to values well below those of the ohmic phase; this is reasonable because the reduction in the loop voltage and consequently in the ohmic input to the plasma will also result in a reduction of the total energy input to the plasma when not balanced by a sufficiently high LH power (Fig. 3).

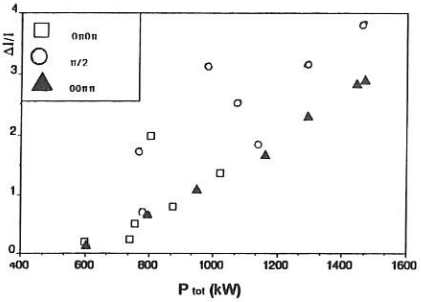

Fig. 1 - Relative CuXX variations vs P_{tot} in LH operation $n_e = 5.4\times10^{13}$ cm^{-3}

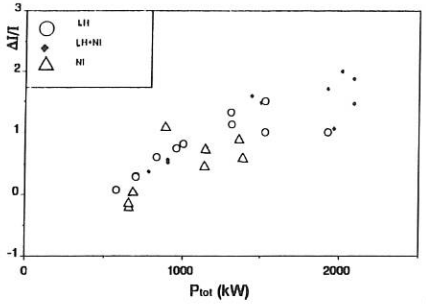

Fig. 2 - Relative CuXX variations vs P_{tot} in mixed LH, NI operation $n_e = 3.4\times10^{13}$ cm^{-3}

Unexpectedly nevertheless, the $\Delta I/I = 0$ value (i.e. same flux as in the ohmic phase) corresponds now to a value of the total input power greater than the initial ohmic value.

This is found to be accompanied by a reduction of the floating potential near the divertor plates, (the main source for the Cu production in ASDEX) (Fig. 4); similar observations have been reported in [2].

However, absolute measurements of the Cu flux sputtered in the divertor (Fig. 4) do not show deviations from the ohmic value and from a simple linear dependence on P_{tot}. The decrease of the Cu content in the discharge appears so as due to a different screening of the impurities by the plasma .

The absolute sputtered fluxes are about a factor 4 lower than in a deuterium beam heated discharge with similar characteristics ([3]).

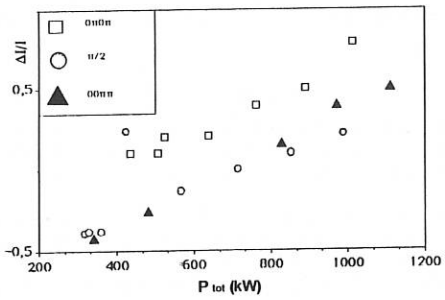

Fig. 3 - Relative CuXX variations vs P_{tot} in LH operation $n_e = 1.35 \times 10^{13}$ cm^{-3}

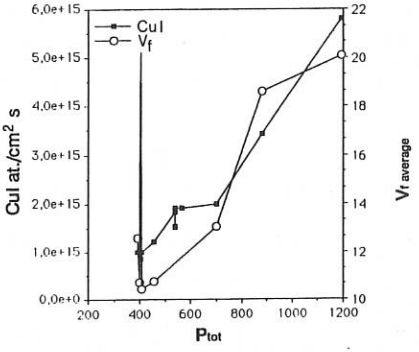

Fig. 4 - Sputtered Cu flux and floating potential in the divertor region.

IMPURITY CONFINEMENT TIME

In order to clarify to what extent the variations of the impurity content were due to changes in their production rate or of their transport, some measurements of their confinement time have been made by the laser blow off method.

The confinement of impurities was estimated, for a current driven discharge at 1.2 MW input LH power, by measuring the exponential decay time of the injected titanium, via observation of lines of ions from the inner half radius of the discharge (TiXIX, TiXX, TiXXI, TiXXII).

From these a doubling of the confinement time (e.g. from 49 ms in the ohmic discharge to 95 ms for LHCD) is inferrred.

By comparing with numerical model calculations a reduction of the diffusion coefficient from 7500 cm^2/s (ohmic) to 5000 cm^2/s is inferred.

The injected impurity atoms which penetrate into the plasma induced also marked density perturbation. These perturbations were by a factor 2.5 smaller in LH operation than in ohmic discharges, thus confirming the improved screening of the impurities.

CONCLUSIONS

The impurity content during LH operation has an almost linear dependence on the total power given to the plasma. In the case of low density, current drive operation the impurity signals resulted smaller than in ohmic discharges with equal input power.

In this regime also an improvement of the particle confinement times was observed both for impurity and background species and was accompanied by increased electron density and broader density profiles [4].

This appears consistent with variations of the time averaged central diffusion coefficient associated with increased sawtooth periods (or sawtooth suppression) due to the modifications of the current density profiles.

A similar influence of sawteeth on impurity confinement time was also reported in FT ([5, 6, 7]).

The higher impurity confinement time with the same measured sputtering fluxes would imply an enhanced impurity content in LH discharges, this not observed because of a smaller penetration of the incoming impurities.

Finally the large slideaway production observed in current driven plasmas at low LH power, was not accompanied by an increase of impurity signals. From this observations we concluded that there is no significant impurity production concomitant with slideaway electron bombardment of the neutralizer plate or wall material.

REFERENCES

[1] F. Leuterer et al., 8th Topical Conference on Radio Frequency Power in Plasmas, Irvine (1989)
[2] J. Tachon, Physics of Plasma Wall Interactions in Controlled Fusion, Nato Course, Val Morin, 1984
[3] G. Fussmann et al., IPP Internal Report III/153, (1989)
[4] Gehre, K.W. Gentle, this Conference
[5] R. De Angelis et al., Proc. EPS Conf. Dubrovnik, 1988, pag. 179
[6] R. De Angelis, G.Tonini, Proc. EPS Conf. Budapest 1985, pag. 690
[7] FT group, Proc. EPS Conf. AAchen 1983, pag. 31

PLASMA EDGE BEHAVIOR ON THE WAY TO AND AT THE DENSITY LIMIT

K. McCormick, A. Hyatt,** G. Kyriakakis*, E. R. Müller, H. Niedermeyer, A. Stäbler, D. Thomas**, N. Tsois*, ASDEX- and NI-Teams

Max-Planck-Institut für Plasmaphysik, 8046 Garching bei München, Federal Republic of Germany, EURATOM-Association

1. Introduction: Previous studies of the density limit (DL) on ASDEX have indicated that the DL is associated with an edge density limit/1/. An extensive density limit campaign in deuterium plasmas with both OH- and NI-heating (P_{NI}=1.15 MW, H^0) has been used to systematically document plasma edge properties over the entire density ramp leading up to the density limit.

The temperature T_{es} near the plasma separatrix was measured by the YAG Thomson scattering system. Densities at the separatrix n_{es} from Thomson scattering are corroborated by the lithium beam diagnostic. Langmuir probes in the divertor deliver n_{ed}- and T_{ed}-values. These results are examined within the overall context of ASDEX plasma edge physics. For doubly-null diverted discharges, and boronized wall conditions, I_p and B_t were varied simultaneously ($230 \le I_p \le 460$ kA; $1.8 \le B_t \le 2.8$ T) in the relationship $B_t \approx I_p^{-0.64}$ yielding q_a(cylindrical) $\doteq 0.52 \times I_p^{-1.635}$ (MA). A companion paper /2/ juxtaposes global results for these discharge series against earlier findings for other divertor configurations and wall conditions.

2.1 Experimental Results and Discussion - OH: Figure 1 summarizes experimental observations made before and at the density limit. Three distinct operational regimes may be discerned: (1) $I_p \le 310$ kA (q_a ~3.8-5.9), where Marfes are formed and the ratio $(n_{es} / \bar{n}_e)_{DL}$ at the DL is small (Fig.1e), (2) $320 \le I_p \le 390$ kA (q_a ~3.8 - 2.4), where $(\bar{n}_e)_{DL}$ continues to rise smoothly with I_p, and (3) $I_p > 390$ (q_a ~ 2.3 -1.9), where $(\bar{n}_e)_{DL}$ initially suffers a gradual decrease as $q_a = 2$ is approached, and increases again for $q_a \le 2$. The latter regime is also characterized by higher T_{es} at the DL (Fig.1c), but otherwise the electron pressure at the separatrix $P_{es} = n_{es}T_{es}$ (Fig.1f) roughly follows the trend established for lower I_p.

The power flow P_{sol} to the scrape-off-layer (SOL) is an important parameter in determining the plasma edge pressure /3/. Figure 1b illustrates that P_{OH} at the DL generally increases with I_p. A regression analysis including values leading up to the DL reveals $P_{OH} \approx \bar{n}_e^{0.49} \times I_p^{1.13}$ (Regression coefficient R = 0.99. B_t is not included since it is has a fixed relationship to I_p.) This is in accordance with a generalized scaling law $P_{OH} \approx \bar{n}_e^{0.26} B_t^{-0.35} I_p^{1.13}$ (R=0.995) far from the DL, gained from an extensive OH campaign under steady-state, boronized wall conditions. Agreement is also found for P_{sol}: $P_{sol} = P_{OH} - P_{RAD,main}$ is approximately proportional to P_{OH} for steady-state conditions, and increases somewhat faster than P_{OH} during the density ramp. The exception to this P_{sol} scaling seen in the region I_p = 400-440kA is correlated with the density dependence of $P_{RAD,main}$ on $\bar{n}_e$ near the DL: $(P_{RAD,main})_{DL} \approx \bar{n}_e^{1.4}$. Thus, the lower DL leads to a dramatically lower $P_{RAD,main}$, thereby causing P_{sol} to continue increasing with I_p. For the power flow to the target plate $P_{div} = P_{sol} - P_{RAD,div}$, the steady-state scaling is $P_{div} \approx \bar{n}_e^{-0.51} P_{sol}^{1.37}$ (R=0.96). For the density ramp, one finds $P_{div} \approx P_{OH}^{0.94}$, with a much weaker dependence near the DL as evident in Fig.1b. This is due to the rapid increase in $P_{RAD,div}$ with I_p.

About 60% of the input power is radiated irrespective of the proximity to the DL. During a Marfe most of the radiative loss occurs in the main chamber. Otherwise, the divertor radiation becomes dominant at high I_p. The direct values of $P_{RAD,main}$ and $P_{RAD,div}$ may be read from Fig. 1b using $P_{RAD,main} = P_{OH} - P_{sol}$, and $P_{RAD,div} = P_{sol} - P_{div}$.

*NRS Demokritos, Attiki, Greece **GA Technologies, San Diego, USA

$n_{es} / \bar{n}_e$ far away from the DL (Fig.1e) increases gradually ($n_{es} / \bar{n}_e \approx 0.2$-$0.24$) with I_p, in keeping with the normally observed broading of the density profile as q_a becomes smaller. Excluding the Marfe region, $n_{es} / \bar{n}_e$ remains constant up to the density limit at the highest currents, and for $I_p \sim 320$ kA decreases about 10% during the $\bar{n}_e$-ramp.

For non-Marfing cases, the SOL density falloff length λ_n increases only very moderately with density. Certainly within the last 50mS before a disruption there is no change in λ_n. The DL itself is accompanied by a very appreciable flattening of the SOL density profile.

2.1.1 The Edge Density Limit Regime ($320 \le I_p \le 390$ kA, $3.8 \le q_a \le 2.4$): For these parameters the DL can be quite convincingly correlated with an edge - (divertor -) temperature limit. Fig.1c illustrates that $(T_{es})_{DL}$ lies between 30-40 eV. The development of T_{es} during the density ramp for I_p=350, 370 and 390 kA is depicted in Fig.2. T_{es} becomes smaller with larger n_{es}. The non-hyperbolic shape of the T_{es}-n_{es} characteristic arises as P_{es} decreases somewhat during the density ramp at the lower currents (Fig.1f). The shift of the curves to the right for each successive I_p simply reflects the scaling of P_{es} with P_{sol} discussed below.

As mentioned, n_{es} is related linearly to $\bar{n}_e$ with a maximum deviation of 10% to the lower side for all n_e. Langmuir probe measurements in the divertor near the separatrix find n_{ed} to be proportional to n_{es} within a particular shot. However, the constant of proportionality and the offset change from shot-to-shot. This is probably due to the probe sampling a different plasma region with respect to the separatrix. In any case, n_{ed} tracks with n_{es}, thereby leading to a decrease in T_{ed} - typically from 9 down to 4 eV. The T_{ed} vs. n_{ed} characteristic mirrors the midplane behavior, i.e. the 370 kA case exhibits a sharp linear drop in T_{ed} with n_{ed}, whereas for 390 kA the change is more hyperbolic.

2.1.2 The Density Limit Regime for Ip>390kA ($q_a \le 2.3$): A DL mechanism other than a *global* edge temperture limit is functional. The lower density limits are accompanied by a lower edge density (Fig.1d). Since P_{es} continues to increase with I_p(Fig.1f), T_{es} is automatically larger at the disruption (Fig.1c).

Figure 3 examines P_{es} as a function of P_{sol} (no Marfes) with $\bar{n}_e$ as a parameter. At low P_{sol} (low I_p) , the edge pressure augments weakly with P_{sol}. Above $P_{sol} \approx 0.35$ MW, the operational curve steepens. The important aspect is that all density limit points lie roughly on the same curve, indicating no abrupt change in plasma edge phenomena throughout the region.

Below $q_a \approx 2.4$ strong toroidal asymmetries are observed in the divertor target plate loading. One can speculate whether or not the divertor temperature might locally fall to a critical level sufficient to provoke a disruption. Refer to /2/ for more discussion on this topic.

2.1.3 The Marfe Density Limit Regime: The appearance of a Marfe is signaled by an increase in $P_{RAD,main}$ by a least a factor of two, a similar reduction in $P_{RAD,div}$, and virtually no change in T_{ed} (~5-6eV). n_{ed} and n_{es} drop around 40% and 25% respectively, and remain approximately constant while n_e is ramped up. Hence, at the DL the density profile exhibits strong peaking (Fig.1e). λ_n in the midplane typically goes from 3.5 cm (pre-Marfe) to 7.5 cm. No T_{es} values are available.

The P_{sol} and P_{div} values of Fig.1b for this region are questionable. $P_{RAD,main}$ is gained under the assumption of poloidal symmetry. A Marfe radically violates this premise. Since $P_{RAD,div}$ is normally proportional to P_{sol}, the decrease in $P_{RAD,div}$ during the Marfe by a factor of two implies a similar reduction in P_{sol}. This is not seen using the formalism of $P_{sol} = P_{OH}$-$P_{RAD,main}$; rather, P_{sol} is found to remain constant. As a consequence, the total amount of power radiated during the Marfe phase is quite likely higher than the indicated 60%. Nevertheless, 100% radiation levels do not exist: Enough power flow into the SOL exists to maintain the divertor plasma parameters quoted above, with $P_{RAD,div} \approx 50$ kW.

2.2 NI-Heating: Figure 4 summarizes density-limit, edge-related quantities. The general OH phenomenology - Marfes for $q_a > 3.6$, a (now only slight) dip in $\bar{n}_e$ at the DL for $q_a < 2.4$ - is also present with NI. On the average, P_{sol} is a factor of 2.3 higher than for OH alone (Fig.4b). This leads to an approximate 20% increase in the DL (Fig.4a), and as well, increases the ratio $n_{es}/\bar{n}_e$ by 25-50%, dependent on I_p, but independent of the temporal position within the density ramp. T_{es} at the DL lies around 50-60eV. T_{ed} values at the DL are not available.

The rather modest increase in $\bar{n}_e$ with P_{sol} may be qualitatively understood within the framework of the scaling law /3/: $T_{es} = 92 nes^{-0.77} x P_{sol}^{0.65}$ (eV, $10^{13}/cm^3$, MW) (R=0.94), under the suppositions that (a) the DL occurs at the same divertor temperature T_{ed} and (b) T_{es} is related to T_{ed} by classical heat conductivity along field lines in the SOL. To conduct a factor of 2.3 more heat into the divertor requires an increase in T_{es} of about 25% over OH conditions, accounting in a first approximation for the observed T_{es}. Using the experimental values of P_{sol} from Fig.4b, and n_{es} from Figures 4c,a the scaling law predicts values for T_{es} close to those measured. Nonetheless, the universality of such simple considerations for predicting the DL remains to be demonstrated.

3. Summary and Conclusions: For both Ohmic- and NI-heated density limit discharges, three distinct operational regimes have been identified: (1) At high q_a, where Marfes appear, (2) $2.4 \leq q_a \leq 3.8$, where the DL can be correlated with a low edge (divertor) temperature, and (3) $q_a \leq 2.3$, where the DL is not related to a low *global* edge temperature. For the latter two regimes no signifigant change in the SOL density falloff length is observed up to the DL. Within 10%, $n_{es}/\bar{n}_e$ remains constant throughout the ramp up to the density limit for both OH and NI (excluding Marfes). However, $n_{es}/\bar{n}_e$ ranges over 0.2-0.25 (OH) and 0.27-0.32 (NI) as a function of q_a. This OH-NI difference may be understood by considering the fact that P_{es} is generally observed to increase with P_{sol}. Hence, higher heating powers imply a higher P_{sol} and concommittantly higher edge densities and temperatures. The small increase observed in the line density limit with NI-heating is consistent with the edge parameter scaling $T_{es} \approx n_{es}^{-0.77} x P_{sol}^{0.65}$ under the stipulations that (a) the disruption occurs at approximately the same divertor temperature, and (b) T_{ed} and T_{es} are interdependent via something like classical heat conductivity. Thus, a sizeable fraction of the additional heating is used to simply support the higher edge densities and temperatures for the same line density. From these considerations it is clear that discharges which do not exhibit a global density profile broadening upon application of NI (ctr-NI, pellet injection /1/) will yield a higher line density limit.

/1/ A. Stäbler et al., Proc. 16th EPS Conf. Contr. Fus. and Plasma Phys. I(Venice 1989)23
/2/ A. Stäbler et al., this conference
/3/ M. Bessenrodt-Weberpals, K.McCormick, F.X.Söldner, F.Wagner et al., submitted to Nuclear Fusion for publication.

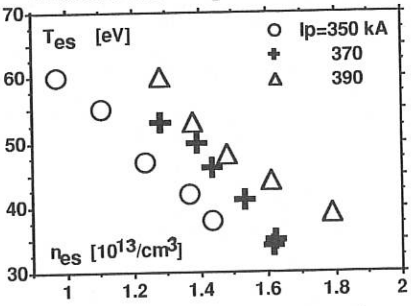

Fig.2 T_{es} vs. n_{es} during the ramp to the DL for I_p=350,370,390 kA. The lowest T_{es} values are taken within 50 mS of the DL.

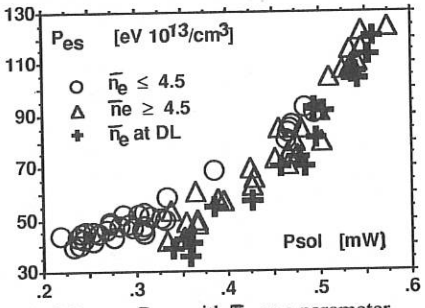

Fig.3 P_{es} vs. P_{sol} with $\bar{n}_e$ as a parameter. Typical values of P_{es} up to the DL are given. Higher I_p are associated with larger P_{sol}.

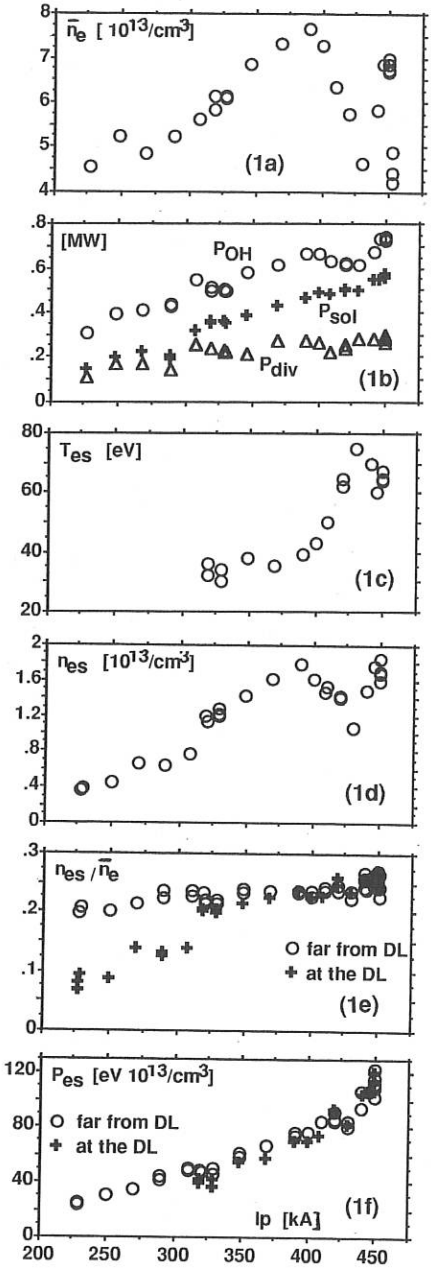

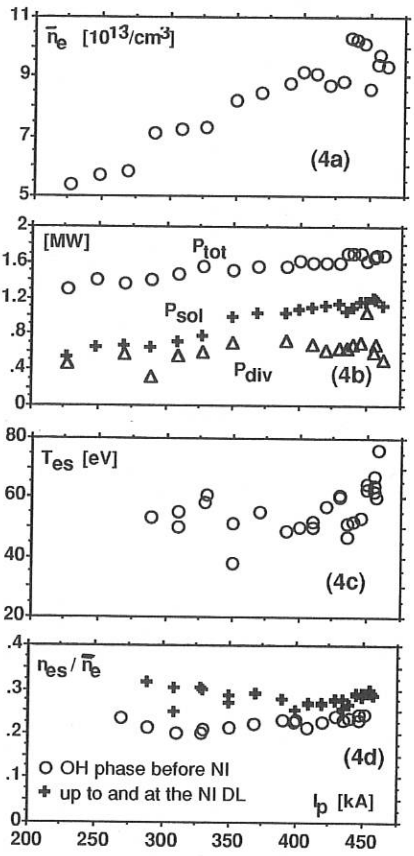

Fig.1 LEFT Edge parameters for OH vs. I_p:
(a) line density $\bar{n}_e$ at the DL,
(b) P_{OH}, the power flow into the SOL P_{sol}, and the power flow to the divertor target plate P_{div}. All at the density limit,
(c) edge temperature within 50 mS of the DL,
(d) edge density n_{es} at the DL,
(e) $n_{es}/\bar{n}_e$ at the start of the density ramp and at the DL,
(f) electron pressure P_{es} at the beginning of the density ramp, and at the DL.

Fig.4 ABOVE Parameters for NI-Heating:
(a) $\bar{n}_e$ at the DL, (b) P_{tot}, P_{sol} and P_{div} at the DL, (c) T_{es} near the DL,
(d) $n_{es}/\bar{n}_e$ for OH, and for NI during the density ramp, including the DL.

THERMOELECTRIC CURRENTS IN THE SCRAPE-OFF LAYER

R. Chodura

Max-Planck-Institut für Plasmaphysik, EURATOM Association
D-8046 Garching, Fed. Rep. Germany

Abstract

Poloidal asymmetry of the energy flux across the separatrix into the scrape-off layer of a divertor tokamak leads to different temperatures at the target plates. This temperature difference drives an electric current along field lines through the scrape-off layer which may change the equilibrium and transport properties of the configuration. A particle code in a simplified 1D geometry is used to simulate the thermoelectric current generation. The code includes the electrostatic sheath formation and recycling at the plates as well as electrical and heat conduction along field lines for arbitrary collisionality. Results of model calculations are shown for varying energy input.

1. Introduction

Particle flow in the scrape-off layer (SOL) along magnetic field lines is ambipolar only if the particle and energy input is completely symmetric. Obviously, this is not the case in many toroidal devices [1, 2]. Radial energy fluxes from the core are larger at the outer part of the poloidal cross-section than at the inner one, possibly caused by a higher level of fluctuations at regions of bad curvature. In a single-null divertor configuration this poloidal asymmetry leads to different temperatures of the two limiting target plates and thus to different sheath potentials at these plates. The different sheath potentials in turn drive a thermo-electric current along the magnetic field through the layer [3, 4, 5]. Field-parallel currents in the SOL change the equilibrium field configuration at the separatrix and the radial transport [6].

It is the purpose of this paper to study the generation of the thermo-electric current in a more realistic model than [4, 5], i.e. including finite pressure gradients, magnetic field, recycling at the plates and long mean-free-path lengths up to the collisionless limit.

2. Model

Figure 1a shows a schematic view of the poloidal cross-section of an axisymmetric single-null divertor configuration. Field lines external to the separatrix end on two target plates. In the model these field lines are straightened and hit the plates under a fixed angle ψ to the normal. The SOL plasma is assumed to be 1D in the coordinate x perpendicular to the plates. Figure 1b shows a cross-section along the (x, B) plane through this simplified geometry.

The plasma within the two target plates is represented by a number of discrete simulation ions and electrons. The electric field is calculated self-consistently from their density distribution. Thus, the electrostatic sheaths in front of the target plates are resolved in the model but their widths relative to the connection length $L_\parallel$ is artificially enlarged. Coulomb collisions between plasma particles, on the other hand, are included

in the model with realistic mean free path lengths [7]. They represent classical transport properties such as current and heat conductivity for arbitrary large mean-free-path lengths as compared to gradient lengths.

The two limiting target plates at $x = 0$ and $x = L$ are assumed to neutralise the incoming plasma ions and to absorb the incoming electrons. The neutralised ions are recycled into the plasma as neutrals with a recycling coefficient R and are assumed to be ionized within an e-folding length d ahead of the plates consuming an energy W per reionized particle.

The particle losses at the target plates are replenished by particles diffusing into the SOL across the separatrix from the bulk plasma. In the 1D model these particles are described by an ambipolar particle source $S^n(x)$. Energy is fed into the SOL plasma partly by convection

$$S^q_{conv} = 2S^n T_e$$

and partly by heat conduction from the bulk

$$S^q_{cond} = \nu n(T_b - T)$$

where T_b represents the bulk temperature, n and T the local density and temperature in the SOL and $\nu(x)$ an x-dependent transfer rate.

3. Results

Calculations were done for the following set of parameters: $L_\parallel = 42m, \phi = 0$, reference density and temperature $n_o = 1 \cdot 10^{19} m^{-3}$ and $T_o = 70$ eV, mean free path length for electron-electron collsions $\lambda_o = t_{ce}(n_o, T_o)v_o = 4.9m$, where t_{ce} is the electron self-collision time and $v_o = (T_o/m_e)^{1/2}$, complete recycling, i.e. $R = 1, S^n = 0$, effective ionization energy $W = 28$ eV, transfer rate $\nu \propto sin(\pi x/L)exp(2\pi x/L)$. The target plates were kept at equal potential.

In Fig. 2 x profiles of density n, electron temperature T_e, particle and energy flux Γ and Q are plotted for $T_b = T_o$ and $\psi = 0$. $Q(x)$ shows the asymmetric energy input into the SOL resulting in a higher electron temperature at the sheath edge in front of the r.h.s. target plate. Keeping both target plates at equal potential electrons preferentially flow to the hot plate and ions to the cold plate, i.e. a current through the plasma arises from the right to the left plate. Density adjusts to the temperature profiles in order to satisfy pressure balance.

Figure 3 shows the dependence of the thermoelectric current J on the bulk temperature T_b, i.e. on the energy input. For decreasing T_b, the SOL temperature decreases as well and the electric resistivity increases. But at the same time, also parallel heat conduction in the SOL is reduced and thus the temperature difference in front of the plates increases so that, altogether, a higher thermoelectric current results.

References

[1] F. Wagner, M. Keilhacker, ASDEX and NI Teams, J. Nucl.Mat. **121** (1984), 103;

[2] S.L. Allen et al., J. Nucl.Mat. **162–164** (1989), 80;

[3] P.J. Harbour et al., J. Nucl.Mat. **162–164** (1989), 236;

[4] P.J. Harbour, Contrib. Plasma Phys. **28** (1988), 415;

[5] G.M. Staebler, F.L. Hinton, Nucl. Fusion **29** (1989), 1820;

[6] F.L. Hinton, G.M. Staebler, Nucl. Fusion **29** (1989), 405;

[7] R. Chodura, 8th Europ. Conf. on Comput. Physics, Garmisch, 1986, Europhysics Conf. Abstracts 10D, 97.

Figure Captions

Fig.1: Scrape-off layer and model geometry.

Fig.2: Density n, electron temperature T_e, particle and energy fluxes Γ and Q along the scrape-off layer for $\psi = 0$.

Fig.3: Thermoelectric current J, normalized by $J_s = 2en_o(T_b/m_i)^{1/2}$, for different bulk temperatures T_b.

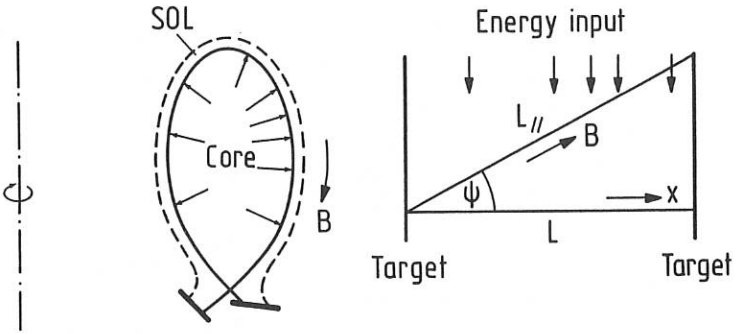

Fig. 1

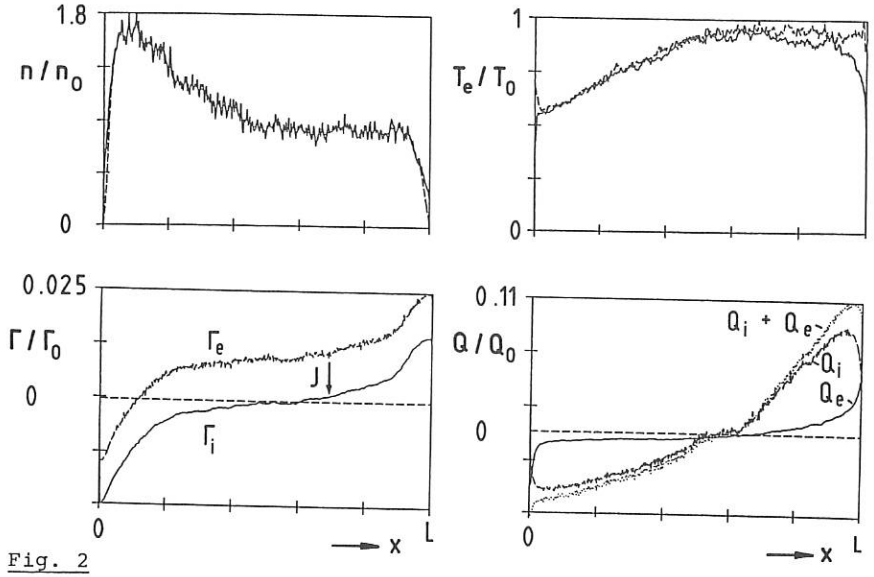
1.8
n / n0
0
1
Te / T0
0
0.025
Γ / Γ0
0
Γe
J
Γi
0
x
L
0.11
Q / Q0
0
Qi + Qe
Qi
Qe
0
x
L

Fig. 2

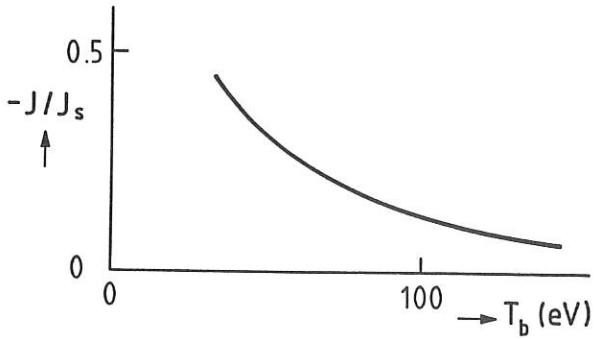
0.5
-J / Js
0
0
100
Tb (eV)

Fig. 3

INFLUENCE OF PLASMA-NEUTRAL INTERACTIONS ON ALT-II PUMP LIMITER PERFORMANCE DURING NI HEATING AT TEXTOR

R.A.Moyer[1], K.H. Finken[2], D. Reiter[2], C.C. Klepper[3], R.W. Conn[1], K.H. Dippel[2], D. Gray[1], D.L. Hillis[3], A. Pospieszczyk[2], G.H. Wolf[2], the TEXTOR Team[2], and the NI Team[2]

[1]Institute of Plasma and Fusion Research and Mechanical, Acrospace, and Nuclear Engineering Department, University of California, Los Angeles, CA 90024, U.S.A.†

[2]Institut für Plasmaphysik, Forschungszentrum Jülich, Association Euratom-KFA, FRG

[3]Oak Ridge National Laboratory, Oak Ridge, Tennessee, 37831 U.S.A.*

Measurements of the particle exhaust by the ALT-II toroidal belt pump limiter during neutral beam injection (NI) on the TEXTOR tokamak have demonstrated the influence of plasma-neutral interactions on the particle exhaust efficiency of the pump limiter. During NI, the plasma flow into the pump limiter throat increases 3-5 times. This increase is due nearly entirely to an increase in the plasma density, while the electron temperature remains nearly constant. Localized recycling at the neutralizer plates has been seen with both Langmuir probes and a fiber optic for viewing H_α light from the neutralizer plate. This H_α light increases a factor 3 over OH levels for 1.5 MW of NI heating, while Langmuir probe measurements show a buildup of plasma flux and density at the neutralizer plate. The buildup factor is well modeled with the Monte Carlo neutral particle code EIRENE.

The experimentally measured removal efficiency, defined here as the particle flux removed by the pumps normalized to the ion flux at the neutralizer plate, increases from 20-25% in OH discharges to as high as 45% in NI heated discharges as the incident ion flux increases from 0.1A/cm^2 to 1.0 A/cm^2. The corresponding exhaust efficiencies, defined as the fraction of the core efflux pumped by the limiter, reach 10%. Such large exhaust efficiencies are favorable for density control during NI and helium "ash" removal. To study the influence of plasma-neutral interactions on the removal efficiency, changes in the backconductance for neutral gas in the pump limiter throat as a function of the incoming plasma conditions have been studied by injecting helium gas into the plenum and monitoring the partial pressure in the plenum with an absolutely calibrated Penning discharge. The results are compared with similar experiments on the ALT-I modular pump limiter and with simulations using the EIRENE code. Plasma-neutral interactions significantly influence the removal and exhaust efficiencies of the pump limiter for the range of throat plasma parameters encountered during NI, and affect the ability of pump limiters to meet particle and helium exhaust requirements in larger devices.

† research supported by U.S.D.O.E. Contract #DE-FG03-85 ER 51069

* reseach supported by U.S.D.O.E. Contract #DE-AC05-84OR21400

AN ANALYTICAL MODEL FOR NEUTRAL AND CHARCHED PARTICLES IN CLOSED PUMP LIMITER

M.Z.Tokar'

Institute for High Temperatures of the USSR Academy of Sciences, Moscow, USSR

Introduction. In number of modern tokamaks pump limiters are used for control of the edge plasma parameters /1-3/. In thermonuclear reactor projects /4/ pump limiters are considered as a possible alternative or additional for divertor configuration of magnetic field method for unburnt fuel, helium ash and other impurity exhaust. From the point of view of limiter operation efficiency the dependence of neutral particle pressure P_g in pumping system on the plasma parameters in the scrape-off layer (SOL) is of importance since an increase of P_g will permit to decrease needed pump rate and facilitate solution of reactor technological problems. In connection with this the experimentally observed /3/ mode of closed pump limiter operation with strong neutral compression is of great interest. In such a mode P_g sharply grows up when the SOL plasma density n_s exceeds some critical level.

Modelling of neutral behaviour in the limiter channel (Fig.1) carried out in Ref./3/ on the base of Monte-Carlo method has given a good agreement with experimental data. But for analysis of reasons and conditions of the transition to the compression mode an elaboration of relatively simple analytical models of charged and neutral particles is reasonable. One of such approaches has been proposed in Ref./5/, where the hydrogen neutrals are described in hydrodynamic approximation. It is correct if the atom path length between charge-exchanges with ions $s_c=v_i/(k_c n)$, where v_i is the thermal velocity of ions, k_c is the constant of charge-exchange and n is the plasma density in the channel, is smaller than the channel width d. This is equivalent to condition $nd \gtrsim 10^{14}cm^{-2}$, which doesn't hold for experiments described in Ref./3/. In such a situation a kinetic description of neutrals in the pump limiter channel is needed. In the given paper a model including kinetic description of neutrals is presented.

Model and basic equations. In a closed pump limiter case (Fig.1) the surface mainly perceiving the heat flux from the discharge and the neutralizing surface creating the flux of neutrals into pumped volume are separated. The processes in the limiter channel weakly influence on the SOL plasma parameters and their values at the channel entrance - n_s, T_s - are determined by recycling on the surface faced to the discharge. The neutrals coming from the neutralizing plate, about which we assume that they are atoms with the wall temperature T_w, are ionized by electrons and charge-exchanged with ions in the channel. As a result the hot atoms with $T_i \gg T_w$ are appearing for which the plasma in the channel is transparent. Cold and hot atoms are reflected diffusively from the channel walls with isotropic distribution function over the velocity along

the magnetic field direction l, g_o. Such a behaviour can be described by the kinetic equation:

$$v_l \partial f_o/\partial l + v_x \partial f_o/\partial x = -(k_i + k_c)nf_o \qquad (1)$$

where $f_o(l,x,v_l,v_x)$ is the cold atom distribution function, k_i is the constant of ionization.

Eq.(1) let's integrate over v_x and the channel width assuming that n weakly depends on x. As a result one obtains the equation for function $F_o=1/d \int_o^d dx \int_{-\infty}^{\infty} f_o dv_x$:

$$v_l \partial F_o/\partial l = -(k_i + k_c)nF_o - j_o^w/d \qquad (2)$$

The cold atom flux at the channel walls $j_o^w = \int_{-\infty}^{\infty} v_x f_o dv_x/_{x=0}^{x=d}$ consists of two parts:

$$j_o^w = F_o v_o - (N_o v_o + n_* v_i)g_o$$

The first part corresponds to the cold atoms leaving the plasma, the second one is entering of atoms diffusively reflected from the wall with distribution function $g_o(v_l) = [\delta(v_l - v_o) + \delta(v_l+v_o)]/2$, $v_o = \sqrt{2T_w/m_a}$, N_o and n_* are the densities of cold and charge-exchanged atoms, respectively, in the channel.

During charge-exchange the atoms acquire the plasma flow velocity along the magnetic field V_l and consequently n_* satisfies the following continuity equation:

$$d(n_* V_l)/dl = k_c n N_o - n_* v_i/d \qquad (3)$$

We also take into account that these atoms appearing at the point with co-ordinate l hit the wall at an average closer to the neutralizing plate at $l'=l+d\, V_l/(2v_i)$ $(V_l < 0)$. Using Eq.(3) and assuming that the characteristic dimension of the parameter changes along l is large in comparison with d one can obtain from Eq.(2) the equations for N_o and the cold atom flux density along the channel $j_o = \int_{-\infty}^{\infty} F_o v_l dv_l$:

$$dj_o/dl = -k_i n N_o, \quad j_o = -D_a dN_o/dl + V_a N_o \qquad (4)$$

Here $D_a = dv_o/(1+d_c/l_o)$ is the diffusivity due to the atom velocity chaotization during collisions with the channel walls; $V_a = dk_c n V_l/v_i$ is the effective velocity of the cold atom convection due to that the charge-exchanged neutrals have a velocity v_l along the magnetic field; $l_o^{-1} = l_i^{-1} + l_c^{-1}$, $l_c = v_o/(k_c n)$, $l_i = v_o/(k_i n)$.

As a first approximation we use one-fluid hydrodynamic equations for description of the plasma in the pump limiter channel. With neglect of charged particle transport across the magnetic field the equations of continuity and motion along the lines of forces are following /6/:

$$d(nV_l)/dl = k_i n N_o, \quad d(m_i n V_l^2 + 2nT)/dl = -k_c n N_o m_i V_l \qquad (5)$$

The plasma temperature is leveled along the channel by the electron heat conduction.

Very rough but qualitatively reflected substance of the matter solution of Eq-s (4),(5) one can obtain if assume that with the distance from the plate N_o and particle fluxes decrease with some characteristic length L. Under boundary condition $V_1(0)=-V_s=-\sqrt{2T/m_i}$ and with taking into account that $k_i < k_c$ this gives:

$$N_o(0) \cong \frac{V_s}{L\sqrt{k_i k_c}}, \quad L \cong d_c\sqrt{\frac{l_i}{l_c}}\left(\sqrt{1+\frac{l_c^2}{d_c(l_c+d)}}-1\right) \qquad (6)$$

These relationships are correct if L doesn't exceed the channel length.

From Ex.(6) it follows that with $n_s \simeq n_s^c = v_o/(k_c d)$ the character of the neutral density dependence on the SOL plasma parameters is changed:

$$N_o(0) = \frac{V_s\sqrt{n_s}}{\sqrt{d\ v_o k_c}} \quad \text{with } n_s \ll n_s^c \qquad (7a)$$

$$N_o(0) = \frac{2dk_c V_s n_s^2}{v_o^2} \quad \text{with } n_s \gg n_s^c \qquad (7b)$$

It's clear from n_s^c view that the reason of this transition into the state with neutral compression is an increase of the charge-exchange influence.

Comparison with experiment. In experiments with closed pump limiter on T-10 tokamak /3/ the dependence of the gas pressure in the pumped volume (without pumping) on saturated ion current density, $j_s = n_s v_s$, on probes located near the channel entrance has been measured. This dependence is shown on Fig.2 by points. Here the results of neutral component modelling by Monte-Carlo method are also presented by curve 1. The results of calculations on the base of the model presented in this paper are shown by curve 2. It's assumed that $P_g = N_o(0)T_w$. Since without pumping the neutral flux into volume is balanced by the return flux and hence their density in the volume is closed to $N_o(0)$. For calculations it was taken $T_w = 500°K$; the heat balance of the SOL plasma isn't exactly consided and according to the current notions it's assumed $T_s \sim j_s^{-1}$ and $T_s = 25$ ev with $j_s = 10^{19}$ cm^{-2}s^{-1}.

The transition to the compression state is observed with $j_s \simeq j_s^c = 10^{19}$cm^{-2}s^{-1} which corresponds to $n_s = 2\cdot10^{12}$ cm^{-3}. This value is closed to n_s^c if one takes $v_o=1{,}6\cdot10^5$cm/s, d=2cm, $k_c=3\cdot10^{-8}$cm^3/c; $n_s^c = 2{,}7\cdot10^{-12}$cm^{-3}. It follows from Ex.(7) that $P_g \sim j_s^{1/4}$ with $n_s \ll n_s^c$ and $P_g \sim j_s^{5/2}$ with $n_s \gg n_s^c$.

Conclusion. Thus the model proposed explaines the reasons and conditions of the transition to the closed pump limiter mode operation with the neutral compression: the transition is stipulated by the increase of the cold atom charge-

exchange on the ions, which prevents the neutral spreading along the channel and results in their accumulation near the limiter neutralizing plate; the transition takes place when the cold neutral path length before charge-exchange becomes smaller than the channel width. The model gives satisfactory agreement with experimental results and it's relative simplicity is attractive from the point of view of introduction of helium and other impurities description.

References

1. Mioduszewski P., J.Nucl.Mater. 111-112 (1982) 253.
2. Pontau A.E. e.a., J.Nucl.Mater 128-129 (1984).
3. Alexander K.F. e.a. Plasma Phys. and Contr.Nucl.Fus.Res., Vienna, IAEA, 1987, v.1, p.237.
4. INTOR Phase Two A Part II, Vienna, IAEA, 1986.
5. Ghendrih Ph. e.a., Contr.Fus. and Plasma Phys., Venice, 1989, Pt.3, p.1023.
6. Nedospasov A.V., Tokar' M.Z. Contr.Fus. and Plasma Phys., Moscow, 1981, v.1, p.J10.

Figure captions

Fig.1. Closed pump limiter: 1 - neutralizing plate, 2 - channel, 3 - pumped volume.

Fig.2. The dependence of the neutral pressure on j_s: points - experimental data of Ref./3/, curve 1 - results of calculation by Monte-Carlo method in Ref./3/, curve 2 - results of the present paper.

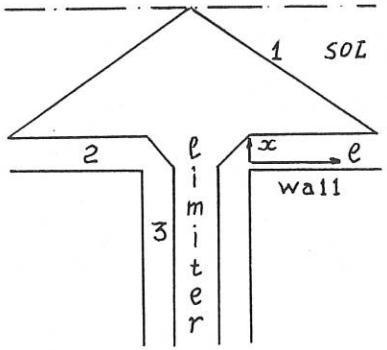

Fig. 1

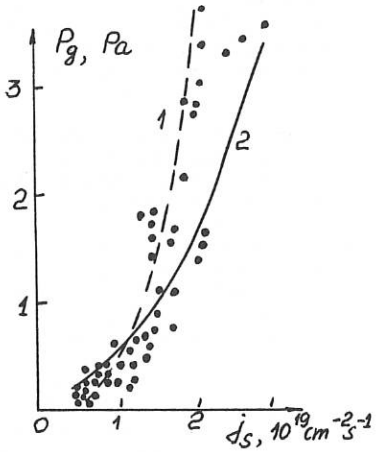

Fig. 2

ERGODIZED EDGE EXPERIMENTS IN JFT-2M TOKAMAK

T.Shoji, T.Fujita[a], M.Mori, A.M.Howald[b], A.W.Leonard[b], N.Ohyabu[c], H.Tamai, H.Aikawa, K.Hoshino, K.Ida[c], S.Kasai, T.Kawakami, H.Kawashima, H.Maeda, T.Matsuda, Y.Miura, K.Odajima, H.Ogawa, S.Sengoku, N.Suzuki, T.Yamamoto, T.Yamauchi, T.Hamano, K.Hasegawa, A.Honda, I.Ishibori, M.Kazawa, Y.Kashiwa, K.Kikuchi, F.Okano, T.Shibata, T.Shiina, K.Suzuki, S.Suzuki, T.Tokutake and S.Uno

Japan Atomic Energy Research Institute
Naka-machi, Naka-gun, Ibaraki-ken, JAPAN

ABSTRACT The effects of the ergodic magnetic structure (generated by a localized EML coil system) on the ohmic and the H-mode plasma in JFT-2M limiter and single-null open divertor configurations have been investigated. It is observed that the maximum density (stored energy) of the limiter ohmic plasma is improved by about 25% and the steady state H-mode of NB-heated divertor plasma is realized by application of EML fields.

1. INTRODUCTION

Recently, externally applied magnetic fields, resonant with the normally occurring equilibrium fields, have been investigated as means of controlling the particle and heat fluxes at the edge of tokamaks in TEXT [1] and others. The characteristics of our EML experiments in JFT-2M [2] are to investigate the effects on (1) non-circular limiter/divertor plasma, (2) L-/H-modes with additional heating, (3) due to EML fields with broad mode spectrum. Especially, our efforts are devoted to control the particle transport in H-mode. The co- and counter-injections of hydrogen neutral beam with each maximum power of 0.8MW are used, estimated net input powers are 90% of torus input for co-injection and 70% for counter-injection.

2. EML COIL AND CALCULATION OF MAGNETIC FIELD STRUCTURE

The resonant helical fields are produced by two local coil sets installed outside the vacuum vessel (Fig.1). Selection of high m/low m and even n/odd n modes can be done by the change of coil current direction. The magnetic field structures were studied by the Fourier analysis and the field line tracing. The poloidal mode spectrum is broad due to the locality of EML coils and has its peak at m=5 and 11 near the plasma surface (r=30cm) for low m and high m cases, respectively (Fig.2). By the island width calculations, it is found that many high-m small islands are involved in the ergodized region in "high m" mode, while a few, low-m large islands are dominant in "low m" mode, in which the overlapping of islands reaches q=2 surface at relatively small current (2kA). The maximum current of EML coil is 5kA (40kAT) and the transport coefficient estimated by the calculation of stochastic magnetic diffusion ($Dm=\langle dr^2/2l\rangle \sim 9\times10^{-7}$m, [3]) is about $3m^2/s$ for high m/odd n case.

3. EXPERIMENTAL RESULTS

(1) Improvement of maximum density (Limiter/Ohmic)

As EML fields (Low m/even n, 1.7kA) are applied to the D-

shaped limiter ohmic plasma (235kA, 1.2T), it is observed that the growth of magnetic fluctuation (m/n=2/1 mode) is suppresed (Fig.1) and the maximum density is improved about 25% (Fig.5). The Energy confinement time increases with density without saturation. Also, the radiation loss and impurity line intensity decrease, especially, the radiation from inner side part, at which plasma contacts to limiter, becomes small substancially (Fig.4), which means the relaxation of the plasma-wall interaction. As EML current is risen up to 2kA, plasma is disrupted in accordance with the calculaion of islands width.

(2) Steady state H-mode by EML (Divertor/NB-heating)

For the divertor H-mode cases(Ip=225kA,Bt=1.27T(CCW)) with NB-heating, the increases of density and radiation loss are suppressed by EML (high m/odd n, 3.9kA) and the steady state H-mode can be realized with $D\alpha$ burst (Fig.6). As seen in Fig.7, the edge electron density is suppressed at the lower level and goes to the steady state point without the transition to L-mode. And also the relaxation of the edge electron temperature gradient (from 90eV/cm to 68eV/cm), measured by the electron cyclotron emission, is observed (Fig.8). The dependece of stored energy on electron density for EML-on case is almost the same with EML-off case (for the higher NB-power case, the improvements of stored energy is obseraved). The profiles of main plasma density and temperature are also almost the same for both cases with the same mean density. But the profile of the toroidal rotation measured by charge exchange recombination spectroscopy is shifted about the order of 10~15km/s to the electron drift direction, which corresponds to the direction of L-mode profile, holding the edge pedestals of ion temperature and toroidal rotation (Fig.9). The property of $D\alpha$-burst depends on the direction of toroidal field and for the case of CW-Bt, it does not appear, but the magnetic fluctuation, which maybe has effects on particle flux, increases by EML.

The asymmetry of particle flux (measured by ion saturation current of Langmuir probe) to inner (ion side) and outer (electron side) divertor plates during H-mode [4] is decreased at higher electron density due to application of EML fields (Fig. 10), but is not changed at lower electrondensity. The electron temperature is hardly changed and therefore the reduction of particle flux by EML with the high heating power leads to the reduction of heat flux. It seems that the particle and heat fluxes corresponding to this reduction must flow onto the wall or onto the unmeasured part of divertor plates.

ACKNOWLEDGEMENTS

The authors are grateful to Drs. S.Shimamoto, M.Tanaka, T. Iijima and M.Yoshikawa for continuous encouragement.

REFERENCES

[1]S.C.Mccool et al,Nuclear Fusion, 29 (1989) 547.
[2]T.Shoji et al,11th EPS conf.,Achen, Part I(1983) p55.
[3]A.B.Rechester et al,Phys. Rev. Lett. 40 (1978) 38.
[4]I.Nakazawa et al,16th EPS conf.,Venice, Part III(1989) 887.

a) On leave from Tokyo University, Tokyo, Japan.
b) On leave from General Atomics, San Diego, California.
c) National Institute of Fusion Science, Nagoya, Japan.

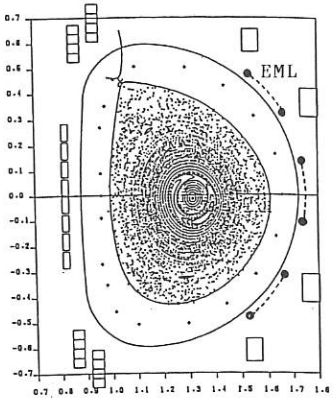

Fig.1 The poloidal position of EML coils and magnetic field puncture plot(High m/ even n, 4.9kA; Div.q-fit=3.6).

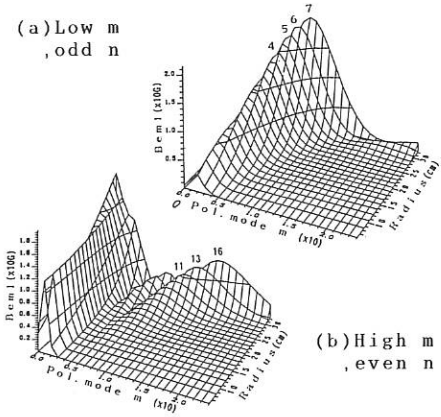

Fig.2 Fourier spectrum profiles of EML field; (a)Low m/odd n, (b)High m /even n.

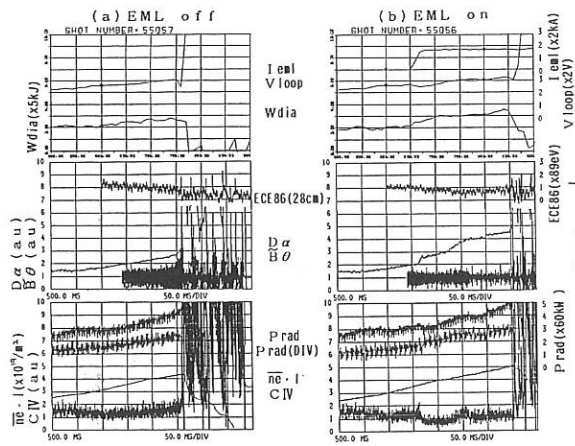

Fig.3 Time evolutions of improvement of maximum density by EML(low m/even n, 1.7kA; Lim.OH); (a)EML off, (b)EML on.

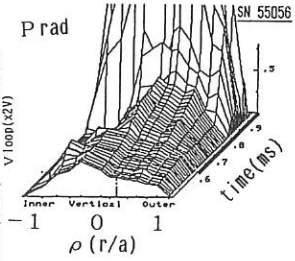

Fig.4 Time evolution of radiation profile (chord integral). EML is applied from 650ms

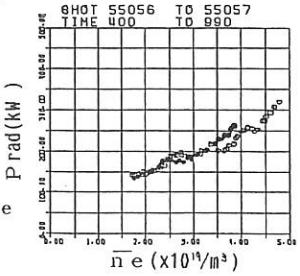

Fig.5 Density dependence of total radiation for EML off and on cases.

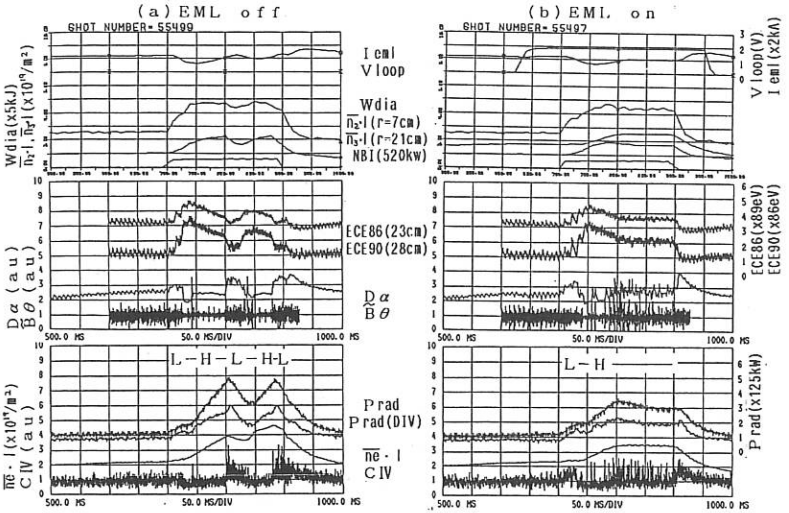

Fig.6 Steady state H-mode by EML; time evolutions of (a)EML off and (b)EML on cases(high m/odd n; Div.)

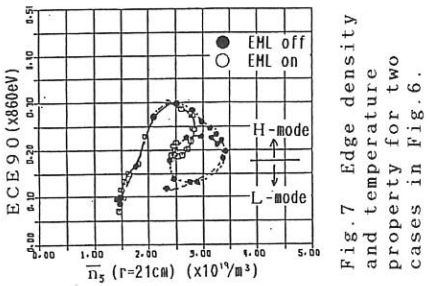

Fig.7 Edge density and temperature property for two cases in Fig.6.

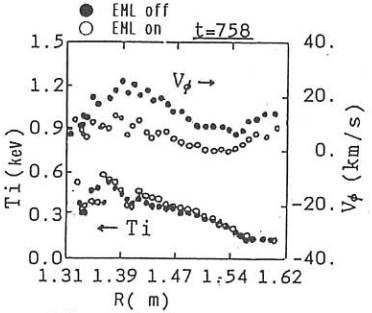

Fig.9 Ion temperature and toroidal rotation profiles(high m/odd n).

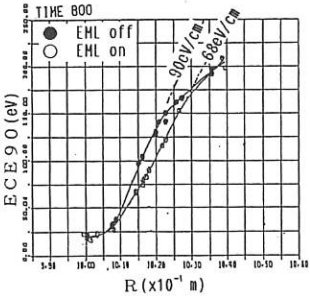

Fig.8 Effect of EML on edge temperature gradient measured by ECE diagnostics.

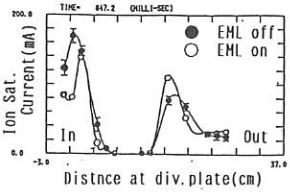

Fig.10 Ion saturation current profiles at divertor plates measured by Langmuir probes (In; ion side), (NBI; 1.3MW).

Edge turbulence and its possible suppression by velocity shear in TEXT

Ch.P. Ritz, H. Lin, Roger D. Bengtson,
S.C. McCool, T.L. Rhodes, A.J.Wootton
Fusion Research Center, The University of Texas,
Austin, Texas 78712, USA

Electrostatic turbulence is known to account for much of the particle and heat transport in the edge of TEXT ohmically heated plasmas.[1,2] Recently it has been proposed that this turbulence should be stabilized by velocity shear, which fissures the fluid elements.[3,4] This stabilization mechanism has been suggested to explain the confinement improvement during H mode. In the plasma edge there is a naturally occuring velocity shear region in the neighborhood of the last closed flux surface, and this can be used to investigate shear effects. Here we present an experimental study of this effect and how the shear layer can be affected by stochastic magnetic field lines.

The mean velocity of the fluctuations, v_{ph}, perpendicular to B is dominated by $v_E = E_r/B$ effects, as shown in Fig. 1(a). The contribution to v_E from the pressure gradient, v_{de}, is small and varies slowly with radius. The density profile is slightly steepened in the region of maximal velocity shear, as shown in Fig. 3. The density and potential fluctuations, $\tilde{n}$ and $\tilde{\varphi}$, are suppressed in a region slightly shifted to larger r/a, Fig. 2(a). The correlation time τ_c^{lab} is reduced in the shear layer with respect to either side, as shown by the cross hatched rectangles in Fig. 4. This is theoretically predicted due to a fissuring of fluid elements in the velocity shear: a nonuniform radial electric field $E_r' = \partial E_r/\partial r \neq 0$ causes in cylindrical geometry a velocity difference Δv_E over a radially correlated structure of correlation length σ_r of

$$\Delta v_E = \left(\frac{\partial v_E}{\partial r} - \frac{v_E}{r} \right) \sigma_r \, .$$

A shear decorrelation time $\tau_{E'}$ can now be defined as the time, in which the correlation volume is stretched apart by v_E by a correlation length $\sigma_\perp = \sigma_{\|v_E}$,

$$\tau_{E'} = \frac{\sigma_\perp}{|\Delta v_E|} = \frac{\sigma_\perp}{\sigma_r} \left(\left| \frac{\partial v_E}{\partial r} - \frac{v_E}{r} \right| \right)^{-1} \qquad (1)$$

Note, the turbulence is also suppressed by $\tau_E = (\sigma_\perp/\sigma_r)|r/v_E|$ in the absence of the velocity shear in a cylindrical or toroidal plasma.

To compute the correlation times $\tau_{E'}$ and τ_E we assume that the ambient turbulence has the same characteristics in the region of high velocity shear as on either side (i.e. no Kelvin-Helmholtz instability effects). We thus use the correlation length of the turbulence measured at a location in the bulk plasma past the shear layer ($\sigma_r \simeq 0.5$ cm, $\sigma_\perp \simeq \sigma_\theta \simeq 1$ cm). The predictions for the decorrelation by a velocity shear, $\tau_{E'}$, and by a constant velocity, τ_E, are shown in Fig. 4. For a comparison with the predicted shear decorrelation times due to electric field effects we need the correlation time τ_c in the frame of reference of the bulk rotation, and not in the laboratory frame τ_c^{lab}. No correction is necessary in the shear layer where $v_E \simeq 0$. Outside of the shear region $\tau_c = \sigma_r/v_{drift}$ can be much larger than τ_c^{lab}, as the measured total phase velocity v_{ph} is similar to v_E within experimental errors (v_E is obtained from the derivative of the measured radial profile and thus can contain large, but unknown errors). The transform from τ_c^{lab} to τ_c is indicated in Fig. 4 by arrows. We find that the experimental correlation time is predicted by the theoretical shear decorrelation time in the velocity shear region. Furthermore the correlation lengths in the shear region are decreased as well and become the same in the radial and poloidal directions. Outside of the shear region the correlation time of the turbulence is not well known due to the uncertainty in the diamagnetic drift velocity of the turbulence and electric field effects on the saturation level of the edge turbulence can not be excluded with certainty. In the naturally occuring shear layer in the edge of tokamaks, however, shear decorrelation and resulting turbulence stabilization are probably an important mechanism .

When a stochastic magnetic field is present in the edge then the radial electric field is substantially modified,[6] and can change from $E_r < 0$ to $E_r > 0$. We have varied the field line stochasticity with an ergodic magnetic limiter[7] (EML) and studied its effects on the velocity shear. We find that the *naturally* occurring positive peak[8] in the potential profile does not move its position with respect to the outermost closed flux surface. It appears that the stochastic field causes an *additional* DC-potential perturbation which is superimposed on the unperturbed profile. For sufficiently stochastic magnetic fields the perturbation produced by the EML has[9] $E_r \simeq T_e[\lambda_n^{-1} + 0.5\lambda_{T_e}^{-1}]$, and this can dominate the naturally occuring E_r profile, as shown in Fig. 1(b). This result connects with the potential profile measurements with the heavy ion beam probe,[6] which show a gradually increasing broad positive shoulder with maximum around $r/a \simeq 0.8$ for large applied magnetic field perturbations. The basic results found for the naturally occurring velocity shear layer are confirmed with the applied stochastic magnetic fields: the $E_r \times B$ velocity dominates the total velocity v_{ph} in the laboratory frame of reference, as shown in Fig. 1(b). No suppressed fluctuation level is observed anymore, when the stochastic field is applied, as shown in Fig. 2(b). The suppression of the fluctuation

levels observed slightly outside of the velocity shear is thus related to the velocity shear.

In conclusion we find that electrostatic fluctuations can be suppressed by a naturally occuring velocity shear close to the outermost closed flux surface. The density profile is slightly steepened in the region of maximal shear. This effect is consistent with shear stabilization models and could be relevant to describe the improved confinement in H-mode discharges. The velocity shear can be modified by stochastic magnetic fields.

References

[1]W.L. Rowan, C.C. Klepper, Ch.P. Ritz, et al., *Nuclear Fusion*, **27**, 1105, (1987).

[2]Ch.P. Ritz, R.V. Bravenec, P.M. Schoch, et al., *Phys. Rev. Lett.*, **62**, 1844, (1989).

[3]K.C. Shaing, G.S. Lee, et al., In *12th IAEA Conf. on Plasma Physics and Controlled Nuclear Fusion Research, Nice,*, volume II, page 13, (1988).

[4]H. Biglari, P.H. Diamond, P.W. Terry, *Phys. Fluids*, **B 2**, 1, (1990).

[5]Ch.P. Ritz, R.D. Bengtson, S.J. Levinson and E.J. Powers, *Phys. Fluids*, **27**, 2956, (1984).

[6]P.M. Schoch, J.S. DeGrassie, et al., In *EPS, Dubrovnik, 16-20 May*, page 191, (1988).

[7]S.C. McCool, A.J. Wootton, et al., *Nucl. Fusion*, **29**, 547, (1989).

[8]R.D. Hazeltine, *Phys. Fluids*, **B 1**, 2031, (1989).

[9]R.W. Harvey, M.G. McCoy, J.Y. Hsu and A.A. Micin, *Phys. Rev. Lett.* **47**, 102, (1981).

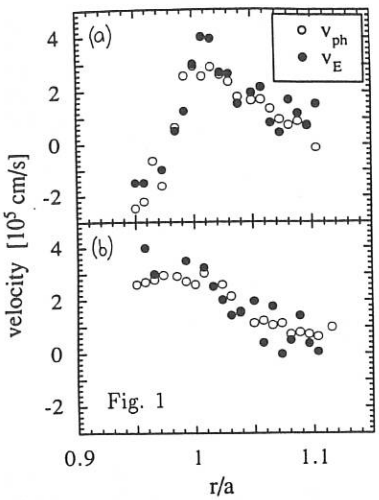

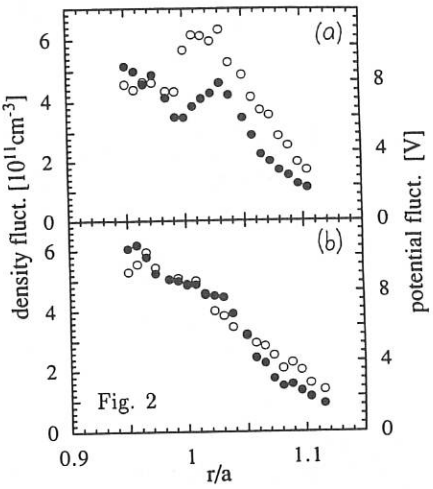

FIG. 1. Radial profiles of the poloidal velocities (a) without, and (b) with applied stochastic magnetic field for a discharges with $B_\phi = 2$ Tesla, plasma current of 200 kA and chord averaged density of $n_{chord} = 2 \times 10^{13}$ cm^{-3}.

FIG. 2. Fluctuation levels for the same data as in Fig. 1. (a) without and (b) with applied stochastic magnetic field.

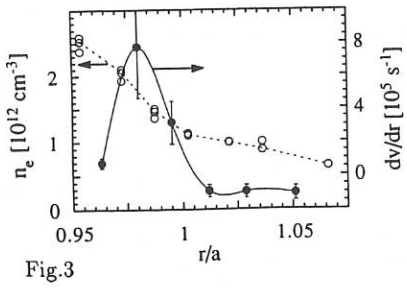

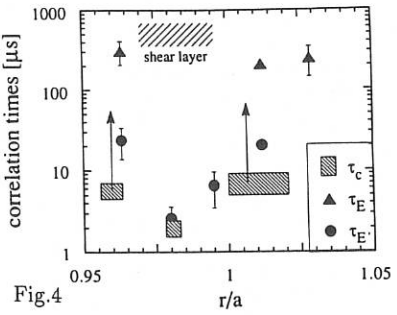

FIG. 3. Density and poloidal velocity shear $\partial v_{ph}/\partial r$ profiles for a similar discharge as in the above figures (a).

FIG. 4. Turbulent decorrelation times due to a constant radial electric field τ_E and due to the nonuniform electric field $\tau_{E'}$ compared with the auto-correlation time of the fluctuations τ_c^{lab} (same data as used in Fig. 3(a,b)). Arrows indicate the change expected by a transform of τ_c^{lab} into the moving frame of reference (τ_c).

A COMPARISON OF FLUCTUATIONS AND TRANSPORT IN THE SCRAPE-OFF LAYER OF A LIMITER [TEXT] AND DIVERTOR TOKAMAK [ASDEX]

Roger D. Bengtson[1], M. Bessenrodt-Weberpals[2], A. Carlson[2], K. W. Gentle[1], L. Giannone[2], Y. J. Kim[1], H. Lin[1], J. Neuhauser[2], H. Niedermeyer[2], T. L. Rhodes[1], Ch. P. Ritz[1], A. Rudyj[2], N. Tsois[2], and A. J. Wootton[1]

[1]Fusion Research Center and Physics Department
University of Texas at Austin, Austin, Texas 78712 USA
and
[2]Max-Planck-Institut fur Plasmaphysik, EURATOM Association,
D-8046 Garching, FDR

Introduction

In the scrape off layer (SOL) of some tokamaks, the detailed measurements of the many quantities necessary to directly determine the fluctuation driven transport are available. We compare the edge fluctuations and transport on two tokamaks, ASDEX, and TEXT, with the objectives of finding any differences which might lead to further understanding of the nature of edge turbulence for ohmically heated tokamaks.

ASDEX [R=1.65 m, a = 0.4 m] is a tokamak operating with a poloidal divertor and copper target plates while TEXT [R = 1.0 m, a = 0.26 m] has a circular poloidal titanium carbide coated carbon limiter. From the point of view of edge transport, the primary differences in ASDEX and TEXT are 1) a separatrix in ASDEX where q becomes large, 2) a factor of 2-3 longer distance to reach a material wall in ASDEX, either through parallel transport to the divertor or perpendicular transport to a wall, and 3) generally a lower level of impurities in ASDEX as compared to TEXT.

Fluctuations and Transport

In Fig. 1 we compare edge conditions, fluctuations and transport under similar ohmic plasma conditions on TEXT [B_T= 2 T, I = 200 kA, $n_e = 4 \times 10^{13}$ cm^{-3}] and ASDEX [2.2 T, 460 kA, 4×10^{13} cm^{-3}]. For these conditions, the Langmuir probe data was interpreted with the assumption of no temperature fluctuations. The most apparent difference in the two conditions is a higher edge temperature, primarily because of the higher current or lower q-value for the ASDEX discharge. The fluctuations in plasma potential have the opposite scaling with radius which is probably due to differences in the local level of impurities. Experiments in TEXT[1] have shown that the level of potential fluctuations can be changed by the injection of impurities. Scale lengths and plasma conditions are quite similar even though the two tokamaks are different in size, and in the distance to a material wall. In both tokamaks, the phase velocity of the turbulence is in the ion diamagnetic direction in the scrape off layer and makes a transition to propagation in the electron diamagnetic direction in a distance of order one cm at the last closed flux surface. The

phase angle between density and potential fluctuations changes sign at the shear layer and the fluctuation driven particle flux is always outwards. The power spectra of density and potential fluctuations are nearly identical. There was no apparent change in the fluctuation spectra at the innermost point on the ASDEX data, indicating that free energy sources involving the derivative of q are not dominant. In both experiments the level of magnetic fluctuations is low and does not contribute to the global energy balance in the edge.

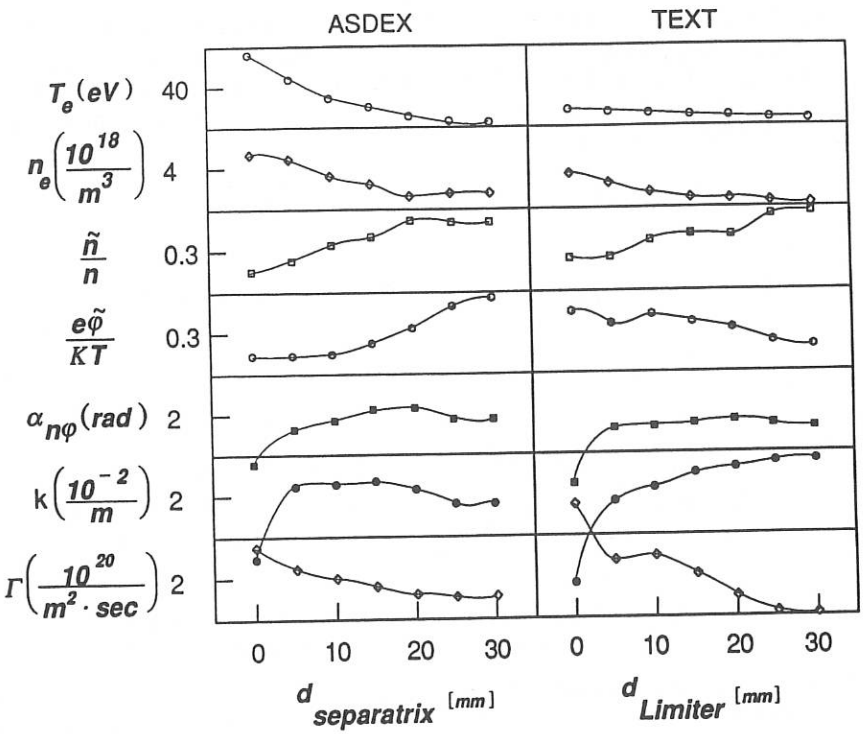

Figure 1. Edge conditions, fluctuations, and fluctuation induced transport in ASDEX and TEXT.

Temperature Fluctuations

We have measured temperature fluctuations in the two experiments using a curve fitting technique[2,3] which assumes an ideal double probe characteristic and fits a curve with six functions and six adjustable parameters to give a best fit to the amplitude of current fluctuations as a function of bias voltage. The fitting parameters are the fluctuation levels, $\tilde{n}/n$, $\tilde{T}/T$, $e\tilde{\phi}/kT$, and their correlations $\langle \tilde{n}\tilde{E} \rangle$, $\langle \tilde{n}\,\tilde{T} \rangle$, and

$<\tilde{n}\tilde{E}>$. A convenient form for understanding the correlation terms is the normalized coherence, for example, $\gamma^2_{nT} = <\tilde{n}\tilde{T}>/<\tilde{n}><\tilde{T}>$. The double probes on TEXT were located at the top of the tokamak and had a probe separation of 2 mm. On ASDEX the double probes were mounted radially with a poloidal probe to probe separation of 3 mm. Figure 2 shows typical current fluctuation data and the associated best fit data for the two machines. There is a significant difference in the data and the best fit even though the plasma conditions are nearly identical [T_e ~ 15 eV, n_e ~ 2 x $10^{13}cm^{-3}$] . The primary difference is in the level of temperature fluctuations where ASDEX has approximately a factor of two higher fluctuations. In TEXT we find $\tilde{T}/T$ ~ 0.4 $\tilde{n}/n$ as compared to $\tilde{T}/T$ ~ 1.0$\tilde{n}/n$ in ASDEX. The higher level of temperature fluctuations can be important in the interpretation of Langmuir probe data, and in estimates of heat flux. The correlation factors, $<\tilde{n}\tilde{E}>$, $<\tilde{n}\tilde{T}>$, and $<\tilde{T}\tilde{E}>$, were generally smaller in the ASDEX data.

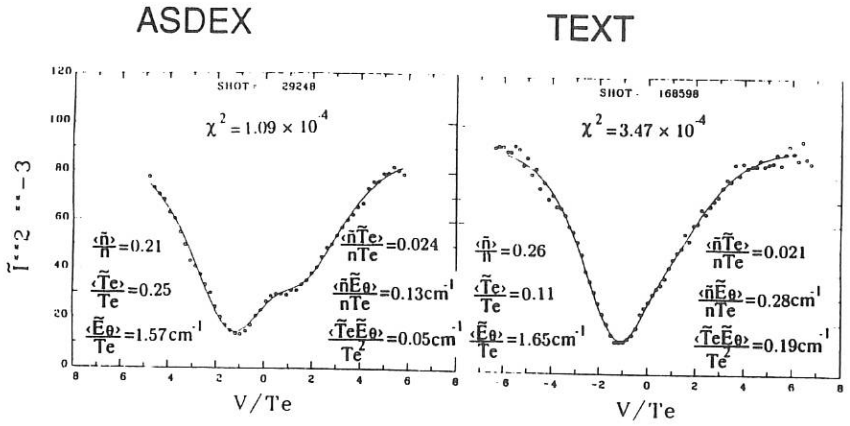

Figure 2. Current fluctuations as a function of bias voltage. The solid line is the best fit to the experimental data.

To substantiate the measurements of a non zero level of temperature fluctuations, we note that the fluctuations are necessary to explain some of the observed scale lengths in the scrape off layer. The fluctuation driven particle flux is $\Gamma_\perp = <\tilde{n}\tilde{E}>/B$ and the fluctuation driven energy flux is $Q_\perp = 3/2(nk<\tilde{E}\tilde{T}>/B) + 3/2(kT<\tilde{n}\tilde{E}>/B)$. With the assumption that most of the energy loss is due to fluctuation driven turbulent processes, we can write

$$\frac{Q_{e\perp}}{\Gamma_\perp} = \gamma_\perp kT \qquad (1)$$

where $\gamma_\perp = 1.5\left[1+\left(\gamma_{ET}^2/\gamma_{En}^2\right)\left(\frac{\tilde{T}}{T}\right)/\left(\frac{\tilde{n}}{n}\right)\right]$. The quantities in parenthesis are experimentally measured quantities from temperature fluctuation measurements.

Differentiating Eqn. 1 with respect to r, and substituting $\frac{Q_\parallel}{\Gamma_\parallel} = \gamma_\parallel kT$, $\frac{\partial Q_\parallel}{\partial r} = \frac{Q_\parallel}{L_\parallel}$, $\frac{\partial \Gamma_\perp}{\partial r} = \frac{\Gamma_\parallel}{L_\parallel}$ we find the ratio of scale lengths to be given by

$$\frac{\lambda_{Te}}{\lambda_\Gamma} = \frac{\gamma_\perp}{\gamma_\parallel - \gamma_\perp}.$$

In the limit where $\tilde{T}/T = 0$ and taking[4] $\gamma_\parallel$ in the range 4.5-6.0 , the ratio $\lambda_T/\lambda_\Gamma \sim 0.33$-0.5. Experimentally we observe λ_T/λ_Γ in range .8-1.2 in TEXT and λ_T/λ_Γ in the range 0.8-1.0 on ASDEX. Under no conditions in either tokamak have we observed the ratio of scale lengths to approach the zero temperature fluctuation limit. The comparison of scale lengths is valid only when fluctuation driven energy flux is the primary energy loss in the edge. Under most operating conditions this comparison is valid.

Using the definitions of Ross[5] *et al* the fluctuation driven convected energy flux $q_{conv} = 5/2kT\Gamma$ and the conducted energy flux is given by $q_{cond} = 3/2k\langle TE\rangle/B - kT\Gamma$. In the TEXT scrape off layer we find $q_{conv}/q_{cond} = 6.0\pm3$ and in ASDEX $q_{conv}/q_{cond} \sim 6$. In both experiments, the fluctuation driven energy flux is consistent[6,7] with power balance measurements. The higher level of temperature fluctuations on ASDEX is compensated by lower correlations between $\tilde{n}$, $\tilde{\phi}$, and $\tilde{T}$.

A comparison of edge conditions of two ohmically heated tokamaks cannot be done to high accuracy, but to the level of comparison possible, the edge turbulence and transport in TEXT and ASDEX are quite similar and seem to be independent of magnetic configuration.

References

1. C. Hidalgo, *et al.* Bull. Am. Phys. Soc. 34, 9 2154 (1989), and to be published.
2. D. C. Robinson and M. G. Rusbridge, Plasma Phys, **11**, 73, (1969).
3. H. Lin, R. D. Bengtson, and Ch. P. Ritz, Phys. Fluids B**1**, 2027 (1989).
4. P. C. Stangeby, Phys Fluids, **27**, 682 (1984).
5. D. W. Ross, Plasma Phys, Controlled Fusion **12**, 155 (1989).
6. M. Bessenrodt-Weberpals, *et. al.* IPP 1/248 (1989).
7. Ch. P. Ritz, *et. al.* Phys. Rev. Lett. **62**, 1844 (1989).

Structure of Density Fluctuations in the Edge Plasma of ASDEX

A.Rudyj, A.Carlson, M.Endler, L.Giannone, H.Niedermeyer, G.Theimer
and the ASDEX-Team

Max-Planck-Institut für Plasmaphysik, EURATOM Association,
D-8046 Garching, Fed. Rep. of Germany

Introduction

It is now generally believed that the anomalous particle and energy transport in tokamaks is caused by turbulent fluctuations. The physical nature of these fluctuations (mode type, the driving mechanism) have still to be identified experimentally before a self consistent transport theory can be developed. In contrast to the confinement region the plasma edge can be well diagnosed. H_α-light , which is emitted at the edge, reacts to density and to some extent to temperature fluctuations. It delivers information about radially integrated spectra and correlations. Langmuir probes measure density and potential fluctuations with good spatial resolution. The edge transport governs the physics in the scrape-off layer and in the divertor which is extremely important for a reactor and therefore deserves a major experimental effort. In this paper we report on an attempt to gain detailed information about the spatial and temporal structure of the edge turbulence hoping to reduce the degrees of freedom for theoretical models to a manageable number.

General properties of edge fluctuations

Previous results from ASDEX and a reference to work done elsewhere can be found in /1/ and /2/. The most important features found on ASDEX are:

- Density and potential fluctuations are observed.
- The mean particle flux calculated from the fluctuation measurements can account for the estimated particle confinement time.
- Frequency spectra are smooth and decay monotonically to higher frequencies.
- The main contribution to $\tilde{n}$ comes from the frequency range below 50 kHz.
- Typical correlation lengths perpendicular and parallel to B are in the order of 1 cm or 10 m respectively.
- The fluctuations propagate in the ion diamagnetic drift direction outside, in the opposite direction inside the separatrix.
- In double-null discharges the fluctuations appear only on the outer (low-field side) edge of the plasma.

Correlations along B

In an earlier measurement a high correlation was found along a magnetic field line over a distance of about 10 m between a probe in the midplane and in the divertor. Because calculated magnetic fields are not accurate enough, the probe position for maximum correlation had to be found experimentally in a two-dimensional scan. As in the earlier measurement the probe in the divertor was fixed slightly outside the calculated separatrix. The probe in the midplane was now

moved slowly in the radial direction during the plateau phase of Ohmic discharges. By changing q_a from shot to shot in very small steps the poloidal scan was performed. Fig. 1 shows a contour plot of the maximum of the cross-correlation functions and the corresponding time delay between the ion saturation currents of the two probes. We observe a maximum correlation of 82 % with zero time delay. The corresponding coherence spectrum decays from 90 % around frequency zero to half of this value at 40 kHz and to the insignificant level of 20 % at 55 kHz. The phase shift is zero within the range of significant coherence. The power spectrum decays from zero to 40 kHz by one order of magnitude.

The results indicate that at least the major part of the fluctuations outside the separatrix is strongly coherent and in phase along the magnetic field. It is not possible to determine the exact angle between the direction of maximum correlation and the magnetic field. Because there is no argument for any non-zero angle we have to assume that the fluctuations are correlated along the magnetic field.

Poloidal structure

To determine the spatial structure of the fluctuations we extended both the H_α-diagnostics and the Langmuir probes to poloidal arrays with 16 observation points. The width of the arrays, which determines the smallest detectable k, is 10 cm for the H_α diagnostics and 3 cm for the probe array. From the signals one calculates wavenumber-frequency-spectra

$$S(k,\omega) = \langle F_s^*(k,\omega) F_s(k,\omega) \rangle$$

(F_s is the complex Fourier transform in time and space) and space-time-cross-correlation functions.

$$\varphi(d,\tau) = \int s(x=0,t)\, s(d,t+\tau)\, dt \;/\; \int s(x=0,t)^2\, dt$$

Fig. 2 shows k-ω-spectra for the Ohmic phase, the L-mode phase and the H-mode phase of a discharge, Fig. 3 shows the corresponding correlation functions.

From the area of high correlation we can read average correlation length and time of the fluctuations, from its slope their poloidal propagation velocity. It is evident from Fig. 3 that in the H-phase there exist structures correlated over a longer time than in Ohmic or L phase. The observed poloidal projection of the propagation velocity is (570 ± 40) m/s in the ohmic phase, (625 ± 25) m/s in the L and (850 ± 25) m/s in the H phase in the ion diamagnetic drift direction for the ASDEX shot #30437 presented here. Since the correlation along the magnetic field lines is very high (see above) and the lines are tilted against the horizontal plane by an angle α, the observed velocity differences could be a result of the toroidal rotation of the plasma with a velocity higher by a factor $1/\sin(\alpha)$ during neutral beam injection. The above velocity differences, especially between L and H phase, are consistent with the measurements by A. Kallenbach of Doppler shifts in resonant charge exchange spectroscopy /3/.

The same poloidal velocities explain the inclination of the strongest contributions to the k-ω-spectra (darkest areas in Fig. 2). The frequency width of the spectra corresponds to a correlation time which might be interpreted as a statistical lifetime of structures. In any of the three types of discharges the frequency width increases as |k| becomes larger. This is consistent with the idea that the mean times for formation and decay of structures is the shorter the smaller the size of the structure. The asymmetry of the frequency-spectra in the high-k range (apart from the poloidal rotation) is another remarkable feature observed in all spectra.

In the H-phase we also observe a structure at a frequency of about 200 kHz propagating in the opposite direction with a velocity of (8700 ± 1000) m/s. The oscillatory nature of this feature can be well seen from the correlation function. The nearly horizontal lobes of the k-ω-spectra at low k suggest that a similar mode exists also in the L-mode and in ohmic discharges.

The frequency integrated k-spectra from H_α and from probes decay with k^{-2} in the range $k > 0.3\ cm^{-1}$. In the longer-wavelength range the spectra from H_α are nearly flat. This range is not accessible by the smaller probe array.

Conclusions

For the major part of the frequency spectrum the coherence length along the magnetic field is by far larger than the connection length between the divertor plates. Therefore the physics in front of the plates has to be taken into account if one tries to understand the edge turbulence. Heat and particle losses to the plates as well as the parallel pressure gradient near the plates might contribute significantly to the physics of the edge turbulence. The radial T_e gradient in the scrape-off layer leads to a gradient of the sheath potential at the plate probably determining the radial electric field and the poloidal velocity via E×B-drift. The transition from the flat to the decaying part of the spectrum defines the only spatial scale length found up to now. It corresponds roughly to the width of the scrape-off layer. A Bohm-like diffusion law with T_e taken at the surface of the plates could result from the absence of any intrinsic scale length. The fact that in double-null discharges the fluctuations appear only on the outer edge suggests that the pressure gradient in the bad curvature region drives the turbulence.

References

1. A.Rudyj et al., 16th Europ. Conf. on Controlled Fusion and Plasma Phys., Venice 1989, Vol. 13B, part 1, p. 27-30.
2. A. Rudyj, PhD thesis, Technical University Munich (1990)
3. ASDEX-Team, Nucl. Fusion 29, 1959 (1989)

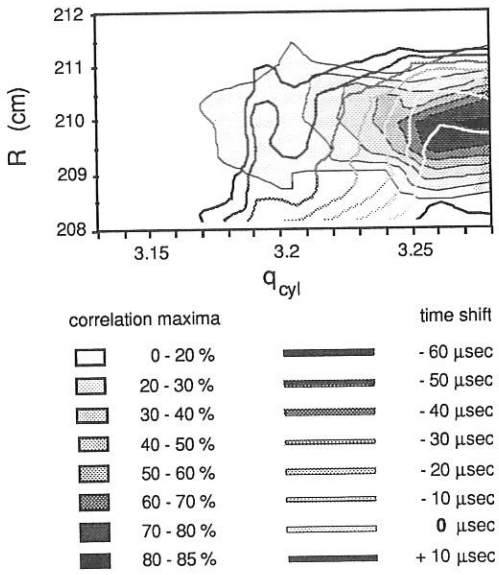

Fig. 1. Correlation between a fixed probe in the divertor and a probe at radius R in the midplane. The contours filled in gray show the value of the maximum of the cross-correlation function $\varphi(\tau)$. The open contours show the time delay τ of the maximum. The variation of q_{cyl} corresponds to a vertical displacement of the probe.

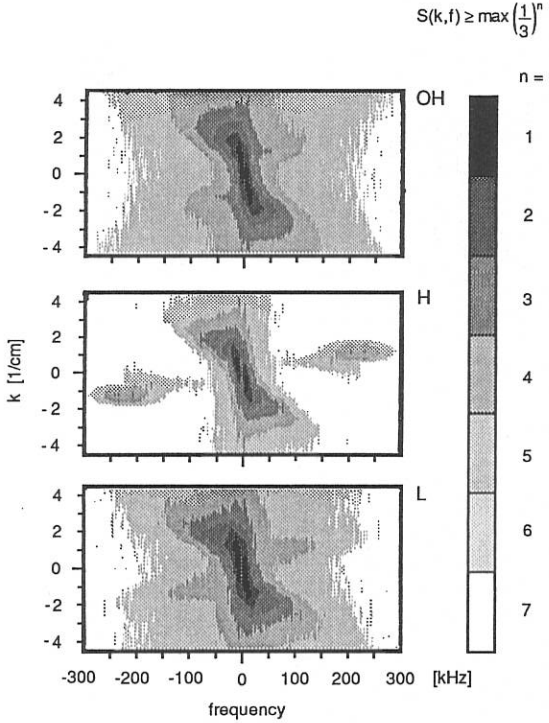

Fig. 2: k-ω-spectra from the H_α diagnostics for Ohmic (OH), H and L-phase of ASDEX shot no. 30437.

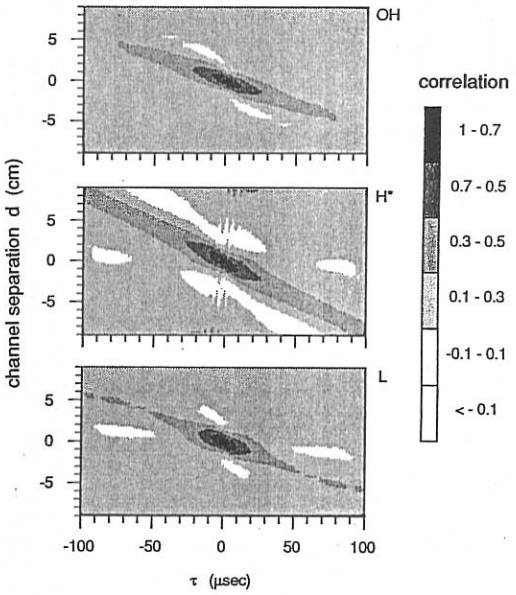

Fig.3: Correlation between different channels poloidally separated by d of the H_α diagnostics for Ohmic (OH), H and L-phase. Same data as used in Fig. 2.

EVALUATION OF NEUTRAL GAS FLUX MEASUREMENTS IN THE ASDEX-DIVERTOR WITH RESPECT TO DIVERTOR-GEOMETRY AND RECYCLING.

D.MEISEL, G.HAAS, R.ARATARI and ASDEX-Team.
Max-Planck-Inst.f.Plasmaphysik, D-8046 Garching, FRG.
EURATOM Association.

INTRODUCTION

Several ionisation-gauges are installed at different locations in the ASDEX-divertor. In principle these gauges are measuring neutral gas fluxes with time resolution of about 1 ms. In most cases the measured flux-values can be expressed as neutral gas density. The neutral gas pressure in the divertor chambers is normally relative high in comparison to the pressure in the main chamber: the gas accumulates in the divertor. Thereby, the absolute energy flux to the target plates, the energy per particle and consequently also the target impurity production is reduced [1].The absolute value of the neutral gas density in a divertor chamber can be regarded as a measure of the ´quality´ of the divertor performance.

In the following we compare the measured neutral gas densities in the different divertor chambers with respect to different magnetic configurations (single-null and double-null) and divertor geometry (symmetric and asymmetric). We discuss the experimental results with the aim to get an improved knowledge how the closed divertor in ASDEX is working. Comparisons with the open Divertor configuration (up to 1986) are made earlier [2][3]. So we restrict the discussion to the results of 1988-90.

The high neutral gas density in the divertor can be a dominant source of gas reflux to the main chamber. We tried to evaluate the contribution of this divertor recycling to the refuelling during ohmic discharges. The result can be expressed as an effective width of the divertor slits. By including the external particle sources (gaspuff, pellet injection, neutral beam injection) this measurement allows us to determine the total particle source, which governs the refueling of the plasma, and a time-constant with the meaning of a particle replacement time.

DIVERTOR GEOMETRY :

The geometry of the ASDEX-divertor chambers were changed several times during the past years. In 1986 water cooled target-plates were installed in both divertors. Each divertor chamber was divided in three sub-chambers a,b,c (Fig.1). The width of the divertor slits decreased from 6 cm to 3.6 cm. Besides these divertor slits additional by-passes to the main chamber were present. The by-passes were closed in 1988 in the upper divertor; the lower divertor stayed unchanged (asymmetric configuration). Since summer 89 the lower chamber is closed, too (symmetric configuration). In the upper divertor ionization gauges are installed in all sub-chambers Ia,Ib,Ic. In the chambers Ia and Ib the gauges can see the divertor plasma; in Ic no view to the plasma is possible. In the lower divertor gauges are installed only in IIa and IIc.

EXPERIMENTAL RESULTS

Non-symmetric Configuration:

By shifting the main plasma column a few cm up and down, the ASDEX-plasma can be coupled either to the upper divertor (Δz=+4cm) or the lower divertor (Δz=-4cm). This is called single-null operation up and down. In the double-null operation (Δz=0cm) the plasma is connected to both divertors. The single-null operation shows normally more

favorable plasma parameters than double-null operation [4]. Fig. 2 compares the measured neutral gas fluxes in Ia and IIa (Fig.1) during the same discharges at three different times (0.9, 1.2 and 1.8 s). The transmission is made from single-null-down to single-null-up by changing the vertical position Δz of the main plasma in a series of discharges. The discharge at 0.9 s is still an ohmic one, at 1.2 sec the density of the main plasma is unchanged with respect to .9 s, but a neutral injection power of 1.4 MW is added. At 1.8 s the NI-power is still the same but the density is further increased. If we compare the measurements at these three times, we compare relatively different plasma conditions at the same machine conditions.

A first result, seen in Fig.2, is the tendency of the neutral gas density to increase with NI-power and with increasing density of the main plasma. This is valid for the neutral density in the different divertor chambers and for the main plasma chamber as well. In order to get the neutral density of the main chamber, we assume, that at single-null operation the ionization gauges in the non-working divertor chambers are measuring the density in the main plasma chamber. Thus, we can evaluate the accumulation factors of the neutral gas density in the divertor chambers with respect to the main chamber for the single-null-up and -down cases.These values are higher in the upper divertor because in contrast to the lower divertor all by-passes to the main chamber are closed (asymmetric geometry).

A further result is clearly seen in Fig.2: the relations between the values of the neutral gas densities in the different chambers (including the main chamber) seem to be nearly the same under the same wall and discharge conditions. By this fact, we assume that divertor and main chamber are strongly coupled by recycling of neutral gas. Taking into account the accumulation of neutral gas in the divertor, we can say, that a strong reflux of gas out of the divertor must exist.

Comparison symmetric-asymmetric:

The by-passes of the lower divertor were closed in summer 1989. After this time, the divertor geometry is symmetric. Fig.3 shows the neutral gas pressure as a function of Δz in this symmetric case. The density, however, is still asymmetric: the lower divertor chamber shows densities which now are 20-50% higher than the upper chamber. This is true in all kinds of plasma discharges (ohmic, additional heating). We have good reasons to assume that this effect is caused by the ExB-drift.

Comparison inside-outside:

Only one ionization gauge exists in an inner divertor chamber (Ib). The measured signals at this location show relatively large deviations in comparison to the other locations (Ia,Ic,IIa,IIc). An example is shown in Fig.4. Calibration errors can be excluded because we observe the same values in both chambers (Ia,Ib) in the single-null-down case (Fig.4).

An explanation for this discrepancy of the measured values in the single-null-up case may be the fact, that ionization gauges measure primarily gas flux. This is supported by comparing chamber Ia and Ic showing always nearly the same values. The same is true for chamber IIa and IIc. Furthermore we have strong indications by interferometric density measurements that the density of the divertor plasma in Ib is much higher than in Ia.

Effective Conductance:

High neutral gas pressure in the divertor chambers affect the main plasma discharge by a particle reflux through the divertor slits. We expect that this is in some cases the main contribution to the recycling in ASDEX inspite of possible wall contact of the scrape-off-layer on the divertor slits.

The estimate of an effective conductance between divertor and main chamber starts with the assumption of a steady state plasma discharge. The particle confinement time t_p is defined as quotient of particles in the main plasma N to the sum of all gas fluxes to the main chamber ΣQ:

$$t_p = N / (\Sigma Q) \quad (1)$$

$$\Sigma Q = Q_{GP} + Q_{NI} + ... + (F_{Div} * 2\pi R) * q_{Div} \quad (2)$$

Q_{GP} is the flux due to gaspuffing ($\int Q_{GP} * dt$ is measured in ASDEX by the gas-puffing diagnostic). Neutral injection can be a source of particles, too. The flux coming from the divertor can be written as the product of an effective divertor slit-width F_{Div} and the flux q_{Div} measured with the ionization gauges.

In a steady state ΣQ=const. The corresponding condition d/dt (ΣQ)=0 allows us to estimate the effective slit-width:

$$F_{Div} = \dot{Q} / (2\pi R * \dot{q}_{Div}) \quad (3)$$

F_{Div} can be inserted into relation (1) in order to estimate t_p.

We show the result (Fig.5) of such an estimate for a so-called standard-discharge in ASDEX (symmetric divertor geometry) in comparison to a similar discharge (open divertor, 6 cm slit-width). For F_{Div} we estimate a width of about 10 cm, which is somewhat larger than the geometric value of 2*3.6 cm.

CONCLUSION:

The measurements with ionization gauges in the different ASDEX divertor chambers have shown, that relatively small changes in geometry (closing of by-passes) can improve divertor operation by a factor of 2. Best results are obtained when only one divertor chamber is active (single-null configuration). In the symmetric configuration the divertor operation is nevertheless asymmetric: the lower divertor neutral gas pressure in single-null-down configuration is typically 20-50% higher than the pressure in the upper chamber in the single-null-up case. The large asymmetry in the measured values between inner and outer divertor chamber in the single-null case is yet not understood. In this case the plasma scrape-off-layers which enter the chambers are connected around the main plasma. The simplest model of divertor operation would predict similar pressures for both chambers. The rough estimates of the effective slit conductance of the divertors indicate the somehow surprising result, that the effective slit-width in the narrow divertor geomety without by-passes is larger than in the case of a relative open geometry with by-passes.

REFERENCES

[1] R.Aratari et al., 9th PSI Conference to be published (1990)
[2] G.Haas,W.Poschenrieder,J.Neuhauser,S.Kaesdorf,The ASDEX Team and the NI Team, Journal of Nuclear Materials 162-164 (1989) 509-513
[3] H.Niedermeyer et al., Plasma Phys. and Contr. Nucl. Fusion 30 (11) (1988) 1443-1453
[4] ASDEX Team, Nuclear Fusion Vol.29, No. 11 (1989)

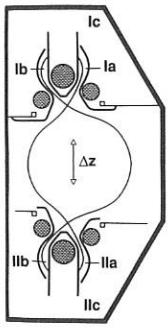

Fig.1 Divertor Geometry (asymmetric)

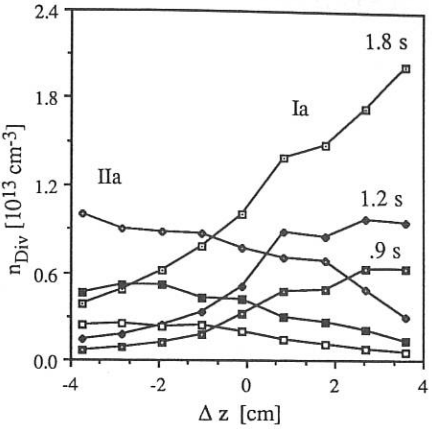

Fig.2 Neutral Density in asymmetric configuration.

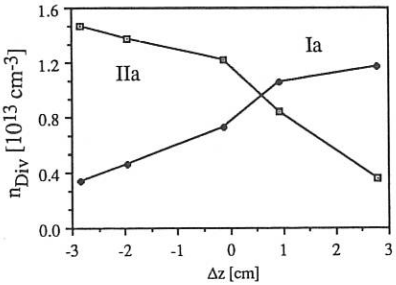

Fig.3 Neutral density in symmetric configuration.

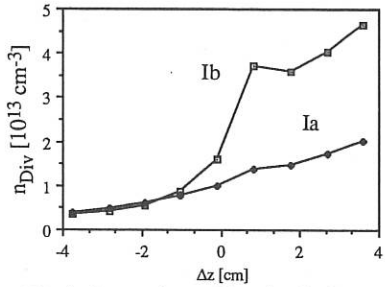

Fig.4 Comparison of density in the inner (Ib) and outer (Ia) chamber

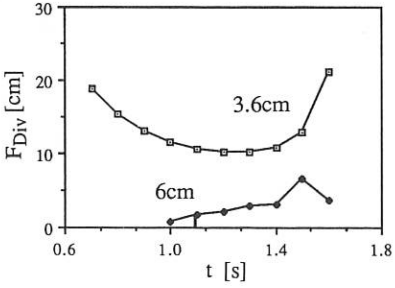

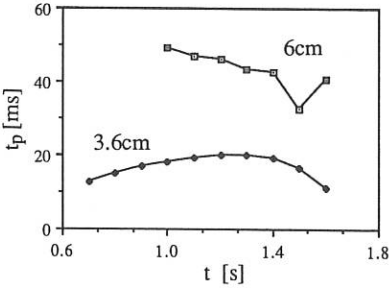

Fig.5a,b Estimation of the effective divertor slit-width F_{Div} in two cases: real slit-width 6cm and real slit-width 3.6cm. 5b shows the corresponding estimate of the particle replacement time.

A STUDY OF IMPURITY TRANSPORT IN THE TEXTOR PLASMA BOUNDARY

S. J. Fielding, *G. M. McCracken*, *R. A. Pitts*, *D. Rusbüldt*[+], *U. Samm*[+], *P. C. Stangeby*[*]

Culham Laboratory, Abingdon, Oxon OX14 3DB, UK
(Euratom/UKAEA Fusion Association)

[+] Institut fur Plasmaphysik, Kernforschungsanlage Julich, Gmbh, Association Euratom Kfa, D–5170 Julich, Fed Rep Germany

[*] JET Joint Undertaking, Abingdon, Oxon OX14 3EA, UK
and University of Toronto, Institute for Aerospace Studies

INTRODUCTION

Impurity transport in the boundary layer of tokamaks may be crucially important in determining the impurity concentrations in the plasma core. Impurity atoms or molecules released from a surface enter the plasma, are rapidly ionised and heated and at the same time undergo transport along and across the magnetic field. Because of the localisation of sources and sinks the problem is inherently 3-dimensional. A number of initial experimental investigations addressing boundary layer impurity transport have been reported [1–3] and a 2-D/3-D Monte Carlo code [4] has been developed. In the present study, we have used a system of gas–puffing through a Test Limiter to introduce impurities into the plasma boundary of TEXTOR and detailed spectroscopic measurements have been made to characterize the impurity behaviour.

EXPERIMENT

Fig 1 shows schematically the experimental arrangement of the Test Limiter and spectroscopic diagnostics. The ALT II belt limiter and the poloidal rail limiters were at a minor radius of 46cm. The radial position of the tip of the Test Limiter could be varied between 45 and 50cm and impurity gas injected through an orifice in the limiter tip. Typically a 1s gas pulse length was used at ~0.6s into the discharge, when plasma conditions had reached constant values. Two impurity gases CO and CH_4 were studied, with the majority of data from CO. Typical operating conditions of TEXTOR for these experiments were $I_p = 340kA, B_T = 2.0 -> 2.28T, \overline{n_e} = 2 \times 10^{19} m^{-3}, Te(0) \sim 1.2keV$, with 2MW of neutral beam heating in a limited number of discharges.

A CCD camera and interference filter were used to give 2-D images of the toroidal and poloidal distributions of the injected impurities. CCD observations were made in CI(909.5nm), CII(657.8nm), OI(844.6nm), OII(441.5nm) and H_α light, the filters being changed between successive discharges.

A high resolution visible spectrometer provided repeated spectral scans of ~ 1nm width, at 50Hz. An oscillating external mirror permitted toroidal spatial scans with the spectrometer at 5Hz, over a range of $\pm 15cm$. In 3rd order at 460nm the spectrometer has a resolution of 0.012nm. The π components of the Zeeman split emission lines were selected for all shots,

except for one or two where the σ components were used to check the analysis. Impurity ion temperatures were derived from the measured Doppler–broadened line profiles by a non-linear least squares fit to modelled line shapes, constructed from the convolution of the measured instrument profile with Gaussian intensity distributions calculated from the spectroscopic term configurations. Error bars on the temperatures represent the range over which the the residuals in the least squares fit double in value.

In addition, the full range of TEXTOR edge diagnostics was used to provide plasma data in the boundary region.

RESULTS

With the Test Limiter at 46cm the toroidal distributions of OI and OII resulting from CO puffing are shown in Figs 2. As has been observed previously [1], the neutral atoms are well confined to the source region, consistent with rapid dissociation and ionisation of the molecule. The OII is significantly broader, due to heating of the ions by the background plasma and streaming along the field lines. The results for CI and CII are similar to oxygen, OII being somewhat narrower than CII. CIII is observed to be much broader still. For methane puffing the CI, CII and CIII results are very similar to those for CO, indicating either that the dissociative kinetic energy of the carbon atom is similar for the two molecules or that the toroidal distributions are relatively insensitive to this.

The spatial distribution of the individual charge states varies significantly with the radial position of the gas puff. When the limiter tip is moved out to $\sim$ 4cm beyond the last closed flux surface the OI and OII distributions are much broader.

Impurity ion temperatures derived from the line profile measurements provide further information on the detailed kinetics of the gas–puffed impurities. Fig 3 shows data from OII, for CO injection, where the good fit to the modelled Gaussian profile, typical of the majority of the data indicates that the C^+ energy distribution corresponds closely to a Maxwellian. Fig 4 shows ion temperature data from OII and CIII for CO injection, as a function of Test Limiter radial position. For OII there is a decrease in temperature as the gas is injected into hotter, denser plasmas at smaller radius. This effect is even more marked for CIII, where it is also seen that the measured temperatures are strongly influenced by the gas puff strength, unlike for OII. Data for CII is only available for 50cm limiter radius and weak gas puff when a temperature of 4$\pm$2 eV is measured.

DISCUSSION AND MODELLING

The 2-D/3-D Monte–Carlo code LIM [3] has been used to model the CO gas puff. LIM follows the trajectories of individual neutrals, launched with specified spatial, angular and velocity distributions, until ionisation. The ion is then followed in its parallel(assumed classical) and cross field diffusion(anomalous, specified $D_\perp$ and v_{pinch}) with further ionisation and recombination/loss. Code output includes 2–D or 3–D plots of the impurity density and temperature of each charge state, spectroscopic distributions (weighted by the appropriate photon efficiency), Zeff, Prad etc.

The CO puffing was modelled assuming the first reaction to be e + CO -> CO^+ + 2e followed by electron impact dissociation of the CO^+. The experimentally observed strong localisation of both OI and CI suggests not only rapid ionisation and dissociation of CO, but also a very

low dissociation energy. Using an energy of 0.05eV in LIM ($D_\perp=2m^2s^{-1}$,v_{pinch} = 0)for both C and O products gives the spatial variation shown in Fig 2, in quite good agreement with experiment. Both the code and the experimental data show a narrower OII distribution than CII. CO puffing experiments have also been carried out on DITE [1] where radial profiles of OI, OII, CI and CII were measured. In that work it was assumed that the CO was dissociated prior to ionisation and it was concluded that the fragment energies were higher, of order 1eV.

Fig 4 shows the variation in temperature of OII and CIII as a function of limiter tip minor radius for two values of gas–puff. The trend of increasing impurity temperature with limiter radius can be explained qualitatively by the associated decrease in ionisation and increase in thermalisation rates in the cooler region of the plasma. The effect is more severe for CIII because of its higher ionisation energy, and hence much more rapidly varying ionisation rate with local electron temperature. This may also explain why the CIII temperature is more strongly affected than for OII when the local plasma temperature is reduced by strong gas puffing.

The change in temperature of low ionisation stage impurities with plasma temperature has been simulated using a simple analytic model. It can be shown that in a uniform plasma with T_e=T_i, an impurity ion of initial temperature $T_{imp}(0)$ will attain an average temperature $<T_{imp}> = (T_i \times \tau_{iz} + T_{imp}(0) \times \tau_{th})/(\tau_{iz} + \tau_{th})$ where τ_{iz} is the ionisation time and τ_{th} is the thermalisation time. Note that $<T_{imp}>$ is independent of density. Using published ionisation rates [5] for τ_{iz}, Spitzer for τ_{th} and measured values of T_e, ~40eV at 46cm and ~10eV at 50cm, the model predicts an increase in OII temperature from 3eV to 8eV for $T_{imp}(0)$=0.05eV, but a decrease for CIII from 25eV to 10eV for $T_{imp}(0)$=2eV. Hence this simple model agrees with the trend of the OII data but strongly disagrees with the CIII results. However, if we assume T_i constant at 40eV then both OII and CIII temperatures increase with radius.

It should be noted that the temperature data given in Fig 4 were obtained with the line of sight of the spectrometer viewing the limiter tip, as shown in Fig 1. In recent helium puffing experiments, spatially resolved measurements have been made which show a large toroidal temperature variation, the temperature of HeII rapidly increasing away from the gas inlet orifice. Such measurements have not yet been made for CO or CH_4 but, if similar toroidal variation were observed for the OII and CIII temperatures, then a radial scan at other fixed toroidal positions might lead to better agreement with the simple model. Future experiments are planned using a new, fully instrumented Test Limiter in which the toroidal variation of T_{imp} will be investigated, in combination with local measurements of the background electron and ion temperatures.

REFERENCES

1. C. S. Pitcher et al, Nucl Fus 29, (1989), 1919
2. D. H. J. Goodall et al, J. Nucl Mat 145–147, (1987), 596
3 C. S. Pitcher et al, J. Nucl Mat 162–164, (1989), 337
4 P. C. Stangeby et al, Nucl Fus 28, (1988), 1975
5 K. L. Bell et al, CLM R216, (1982)

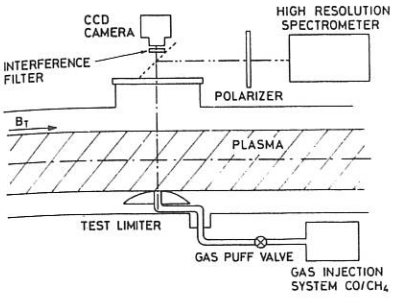

Fig 1. Schematic of impurity gas–puff experimental arrangement on TEXTOR.

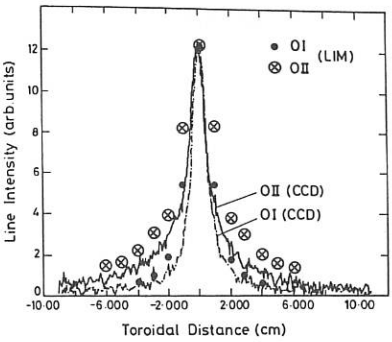

Fig 2. CCD measurements of toroidal distributions of OI and OII line emission from CO puffing. Also shown are the results from LIM simulations, normalised to the peak experimental values.

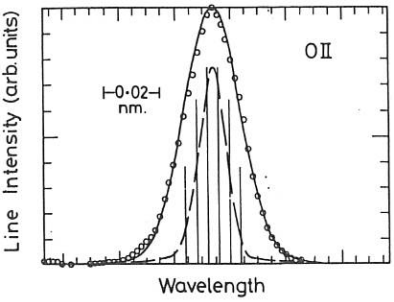

Fig 3. OII line emission profile from CO puffing: o experimental points, full curve fit to data for Timp = 2eV, dashed curve instrument function. Also shown are the π Zeeman components.

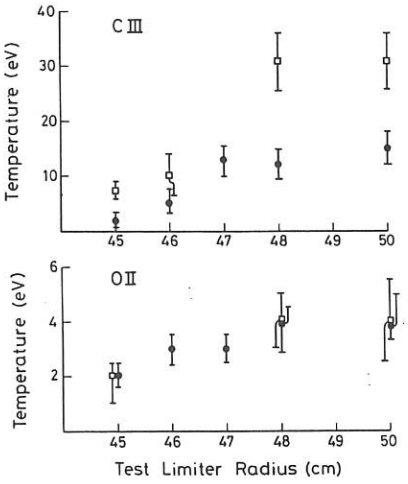

Fig 4. OII and CIII impurity temperatures derived from line profile measurements as a function of test limiter radius; open points gas puff pressure 10mb, filled–in points 20mb.

EFFECTS OF BORONISATION ON THE PLASMA PARAMETERS IN TCA

Th. Dudok de Wit, B.P Duval, Ch. Hollenstein, B. Joye

Centre de Recherches en physique des plasmas
Association Euratom-Confédération Suisse
Ecole Polytechnique Fédérale de Lausanne
21, Av. des Bains, CH-1007 Lausanne Switzerland

INTRODUCTION Wall conditioning and deposition of low Z materials on the first wall and limiters play an important role in plasma impurity control. Carbon film deposition (carbonisation) is already used on many Tokamaks. As proposed by Veprek [1], a film containing boron and carbon would be more resistant to chemical erosion and could also getter the oxygen. This procedure (boronisation) has been tried on Textor [2], Asdex [3] and recently on TCA. The TCA vacuum vessel, the 8 rf antenna groups and 4 antenna screens are stainless steel and there are 4 carbon limiters placed in one poloidal plane.

FILM DEPOSITION AND COMPOSITION Boronisation was achieved with a four hour glow discharge at room temperature. A single antenna without rf assistance produced the discharge in a gas mixture of 80% He, 10% CH_4 and 10% B_2H_6 at a pressure of 5 10^{-3} mbar. A discharge current of 1 A was maintained by an antenna voltage of 400 V (current density 10 $\mu A/cm^2$). A film thickness between 30 and 70 nm [4] was determined from surface analysis of germanium and silicon samples exposed to the boronisation glow. The boron concentration in the film was twice the value of carbon, as in the working gas. A high oxygen concentration (18%) was measured, which was not observed to enter the plasma during tokamak operation. In a second boronisation, the oxygen concentration in the film fell to 7%.

PLASMA PARAMETERS 1) Impurities: After boronisation, the vacuum vessel base pressure decreased, the main improvement being a reduction of 5 in the partial pressure of water and a large reduction in the partial pressures of the hydrocarbons. It should be noted that TCA was not as *clean* as has previously been obtained after several months of uninterrupted operation. Thus, the conditions before boronisation should not be considered as the best achieved on TCA. The impurity content of the tokamak plasma is illustrated by the evolution of the radiated power profile measured with a 16

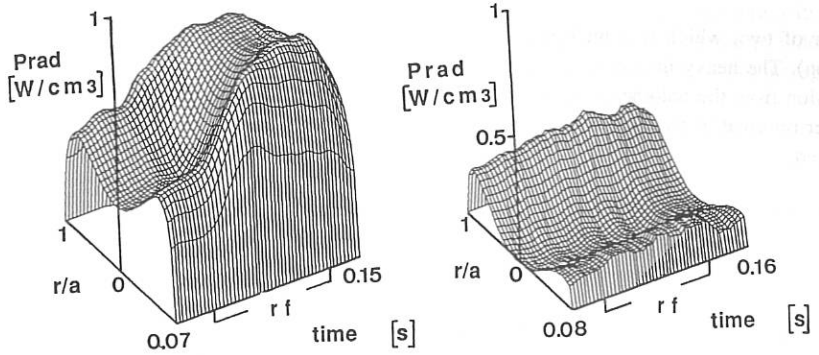

Fig 1 *Evolution of the radiated power profile before (left) and after boronisation (right)*

channel bolometer array (Fig.1). Before boronisation the profile was slightly hollow with 0.25 W/cm^3 on axis indicating that heavy impurities were present in the discharge. The increase in radiated power during the Alfvén Wave rf pulse is in part due to the increase in plasma density, but also to impurities. After boronisation, the core radiated power dropped to an unmeasurable level, indicating that the plasma was free of heavy impurities and the edge power radiation, representative of the light impurities, decreased by a factor of 4. The increase during the rf pulse is now fully explained by the electron density. The ratio of total radiated power to the input power dropped from 65-70% before boronisation to 25% after, modifying the global power balance. An increase of the electron thermal conductivity of 50% was measured from heat pulse propagation analysis during the sawteeth. Other evidence of the reduction of all impurities was the decrease of a factor of 40 of the soft X- ray fluxes measured through a 7 μm Be filter. The sawteeth inversion radius did not change, but the relative amplitude of the sawteeth and their period both increased by a factor of 2.

Spectral line analysis was performed by VUV and Visible spectrometers. The VUV observations of CIV and OVI line emission indicated a reduction of ~5 and ~20 in the impurity content normalised to plasma density (Fig 2). Spectral features from Cr I (not ionised) were observed on the outer carbon limiter, but disappeared immediately after the boronisation. We concluded that the TCA limiters were contaminated with heavy metal impurities, but that the boronisation film effectively shielded the old limiter surface from the plasma. Together with the bolometer data we conclude that the heavy metal plasma content was reduced to extremely low levels.

The improved plasma purity reduced the plasma loop voltage from 1.8 to 1.3 V resulting in an increase of the discharge current flat top of 60% (Fig 3). This figure also shows the evolution of the plasma resistance and the electron density during the rf pulse. The excellent conditions obtained with boronisation degraded slightly, and also differently for the light and heavy impurities. After ~500 discharges, with no glow discharges to clean the walls and limiters, the total radiated power increased by a

factor of two, which was well explained by increases in the light impurities (mostly carbon). The heavy impurities monitored by the soft X-ray emission and central power emission from the bolometer significantly increased. The Cr I spectral lines on the outer limiter returned to their pre-boronisation levels indicating that the limiter was no longer covered.

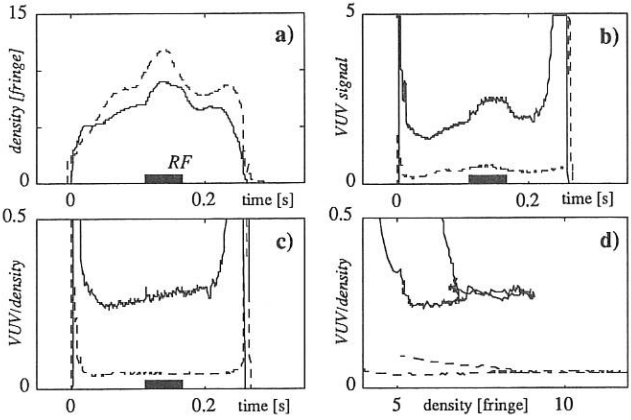

Example of impurity reduction resulting from Boronisation for Carbon

——— Before Boronisation
- - - - - After Boronisation

a) *Plasma line integrated density against time*

b) *VUV signal for CIV at 1548Å against time*

c) *VUV signal normalised to plasma density against time*

d) *Normalised VUV signal against density*

Fig 2: *From the raw traces of plasma density a) and CIV line intensity b), c) shows the CIV line intensity normalised to the plasma density through the plasma discharge. We see that the impurity increase during the RF pulse is accounted for by the increased plasma density, and that the small impurity accumulation before Boronisation is removed by Boronisation. In d) the locus of the normalised CIV line intensity is plotted against plasma density from which we deduced a reduction of ~5 in the Carbon content. A similar result was obtained with a CIII line and a reduction of ~20 from observations of OV and OVI spectral features*

Several hours of glow discharge in hydrogen restored most of the conditions following boronisation and even further reduced the carbon impurity level, although the heavy metal content was not greatly affected. Even after ~900 discharges, the plasma performance was still much better than before boronisation.

2) Density and recycling: At low to moderate densities, the plasma density control was possible except during the Alfvén Wave rf pulse where the unavoidable density increase remained a function of the rf power [5]. The recycling coefficient increased at high density impeding a rapid decrease of the plasma density. Due to the presence of hydrogen in the film, the plasma isotope mixture could not be chosen arbitrarily. Immediately after the boronisation, the ratio of D/H with a deuterium filling gas decreased through the discharge to ~1 at the end. After further discharges in deuterium, spectroscopic measurements indicated that the hydrogen concentration dropped to <5%. Extensive glow discharges in hydrogen reduced the deuterium concentration to nearly zero. This was confirmed by the measurement of the effective mass of the plasma core using the Discrete Alfvén Waves [6]. A lowest value of 1.05 was

achieved indicating that not only the deuterium concentration but also the impurity concentration were reduced to a very low level. The boronised vessel seems to hold more gas and to change working gas it is necessary to empty the stored gas using helium glows or to replace the working gas using a hydrogen or deuterium glow.

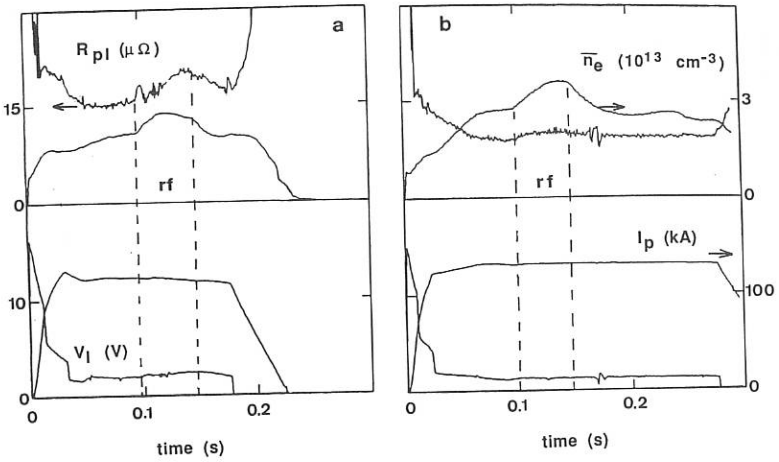

Fig 3 *Time evolution of the plasma current, loop voltage, plasma resistance and electron density: a) before, b) after boronisation*

CONCLUSION Boronisation in TCA has led to a large decrease in the level of all observed impurities (except boron !) by a factor of 5 or more. The smaller loop voltage allowed a gain of 60% of the current flap top length. Despite the high gas content in the coating, clean deuterium and hydrogen plasmas were obtained following different glow discharge cleaning. The boronisation film holds more working gas than the unboronised plasma vessel.

Acknowledgements: This work was partly funded by the Fonds National Suisse de la Recherche Scientifique.

References:

[1] Veprek S. et al. J. nucl Mater. **63** (1976) 405
[2] Waelbroeck F. et al. Plasma Physics and Controlled Fusion **31** (1989) 185
[3] Asdex team, Paper presented at the 9th Plasma Surface Interaction Conf.(1990)
[4] Hollenstein Ch. et al. ibid
[5] Collins G.A. et al. Proc. of the 12th European Conf. on Contr. Fusion and Plasma Physics, Budapest, Vol 9, p. 248 (1985)
[6] Dudok de Wit Th. et al. Particle transport studies on TCA using the dynamical response of the effective mass; presented at this conference.

PUMP LIMITER INFLUENCE ON THE HELIUM DISCHARGE PARAMETERS IN TUMAN-3 TOKAMAK

V.I.Afanasiev, V.E.Golant, A.B.Izvozchikov, V.G.Kiptilyj, A.A.Korotkov, A.N.Novokhatskij, K.A.Podushnikova, G.T.Razdobarin, V.V.Rozhdestvenskij, N.V.Sakharov, A.I.Smirnov, A.S.Tukachinskij, A.A.Fedorov, A.V.Khudoleev, K.G.Shakhovets, S.P.Yaroshevich

Ioffe Physico-Technical Institute,
Academy of Sciences USSR, Leningrad

The ohmic discharge in helium has been investigated to study the helium ion transport in plasma. In the first experiments the stable discharge was obtained only with substantially reduced gas puff ($\bar{n}_e \leqslant 6\ 10^{12} cm^{-3}$). Therefore the pump limiter was installed on the outer part of the torus for recycling control and optimization of the discharge parameters/1/. The mushroom like limiter of the closed type collected particles on the ion drift side. Its single throat head is made of stainless steel. The radial thickness of the head is 0.3 cm at the leading edge and 1.3 cm in the middle. The entrance throat is 4 cm long and 2 cm wide. The limiter was located at r=22 cm.

The pump limiter has allowed to obtain a stable helium discharge with parameters: I_p= 100 kA, B_t= 0.4 T , $\bar{n}_e$ = (1-3) $10^{13} cm^{-3}$, $T_e(0)$= 350 eV (Fig.1).

The behaviour of the main and impurity ions in the discharge was studied by spectroscopic methods. The concentration of He^{2+} and O^{6+} ions in the plasma core were measured by charge-exchange spectroscopy (CHES) using He^+(4685 Å, n= 4-3) and O^{5+}(1125 Å, 5f ^{2}F-4d ^{2}D, 5291 Å, 8h^{2}H-7g ^{2}G) charge-exchange excited line radiation. DINA-4A diagnostical hydrogen-atom beam injector was utilized /2/ with an equivalent

beam current density of 100 mA/cm^2 in the plasma. The energy of the hydrogen atoms was 15 keV and the injection time was 100 μsec. The line intensities were measured by means of two calibrated vacuum-ultraviolet (vuv) and visible-range spectrometers viewing the hydrogen beam at an angle of 14°. The spatial resolution was 12 cm and 4 cm for vuv- and visible-range spectrometers respectively. The intensities of He^+ and O^{5+} lines mentioned above were being compared with that of H_β and L_α lines of the diagnostical beam atoms to obtain better accuracy /3/.

The concentration of O^{6+} ions measured by CHES in the plasma centre is represented in Fig.2. The other oxygen ions densities were restored by simulation taking into account the experimentally determined radial distributions of the electron density and of the electron temperature. The oxygen flux at the plasma edge was determined from O^{5+}(1032 Å) line intensity. The diffusion lifetime of oxygen ions τ_z= 25 ms was derived to obtain the experimental O^{6+} ions concentration.

Since the effective charge in the plasma core due to oxygen corresponded to that obtained from the plasma conductivity (Fig.1d) we were able to determine He^{2+} ions concentration from the neutrality: $2 \cdot n[He^{2+}] = n_e - \Sigma Z_i n_i$ taking into consideration $\Sigma Z_i n_i$ of oxygen impurity. The radial distribution of He^{2+} ions density is shown in Fig.3b. The result of the direct measurement by CHES is also represented taking into account the effective emission cross-section of He^+(4685 Å) line from calculations /4/

Assuming the value of the effective lifetime $\tau = n[He^{2+}]/\mathrm{div}\Gamma[He^{2+}]$ to be independent of r we determined He^+ ions density corresponding to measured chord intensity of the natural plasma luminescence of He^+(4685 Å) line from the ionization- balance equation. The level of He^+ ions density corresponds to a value τ = 6 - 8 ms. The global helium confinement time τ_p obtained from helium flux Φ into plasma (Fig.1e) is nearly equal to the value of τ indicating weak dependence of the confinement time on plasma radius.

Helium recycling was studied in the discharge stage where the gas puff was switched off. There were the discharges in which the electron density decreased after that. But more typical were the discharges in which the electron density remained the same or even increased due to oxygen impurity accumulation (as in Fig.1b). Taking that into consideration we determined helium recycling coefficient:

$$R = 2\pi a\Phi/(2\pi a\Phi - dN/dt), \quad N = \int_0^a 2\pi r \cdot n[He^{2+}] \cdot dr$$

Minimum value of R =0.94 corresponds to a pump limiter efficiency $\varepsilon \simeq 6\%$.

References:

/1/ Mioduszewski P., J.Nucl.Mat. 112 (1982) 253.

/2/ Roslyakov G.V., Diagnostics for fusion reactor conditions. EUR 8351-I EN, Varenna, 1 (1982) 311-323.

/3/ Korotkov A.A., Zinoviev A.N., Afanasiev V.I., Shakhovets, Fiz. Plazmy 15 (1989) 118-120.

/4/ Zinoviev A.N., Korotkov A.A., Pis'ma Zh. Ehksp. Teor. Fiz. 50 (1989) 276-279.

Figure Captions:

1: The characteristics of helium discharge under study. Fig.1b represents also the gas valve impulse. Curves 1 and 2 in Fig.1d represent, respectively, Z_{eff} due to oxygen density in the centre of plasma and average Z_{eff} measured from the plasma conductivity. $\bar{N}_{He}$ - average helium ions density, τ_p - global confinement time of helium ions, R -helium recycling coefficient.

2: Evolution of oxygen ions concentrations in the central part of the plasma (r <12 cm). Triangles represent the O^{6+} ions density measured by CHES.

3: a) He^+(4685 Å) line profile due to charge-exchange excitation by hydrogen beam (active), the same line in the natural plasma luminescence (passive),
b) Radial distributions of helium ions densities obtained from $n_e(r)$ and $\Sigma Z_i n_i$ of oxygen impurity. The experimental point indicates the direct measurement by CHES.

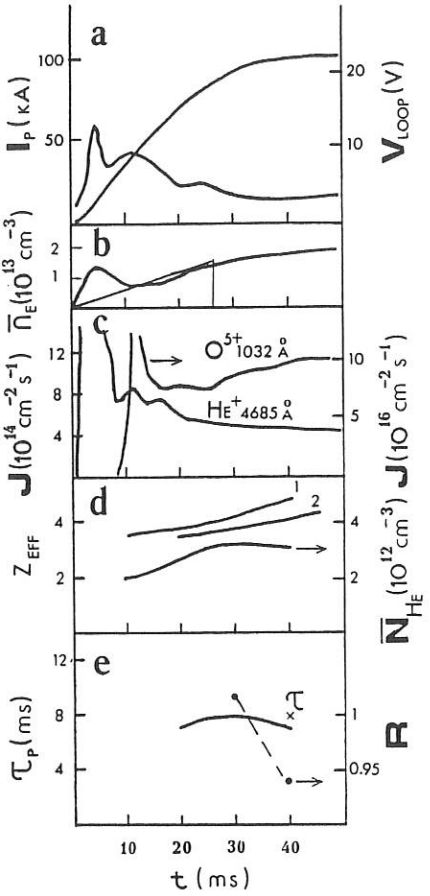

Fig. 1

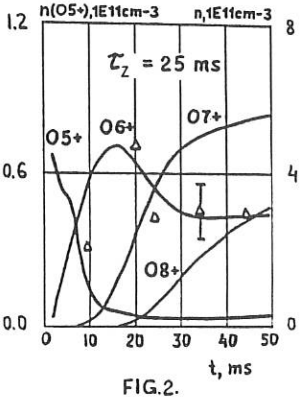

FIG.2.

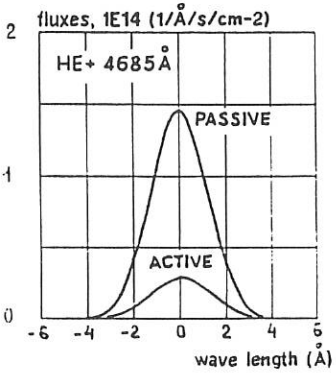

FIG.3a.

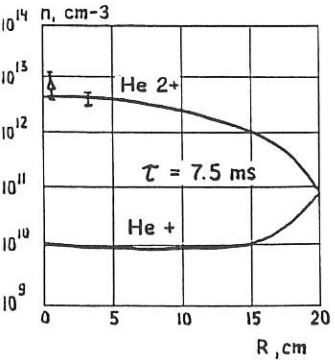

FIG.3b.

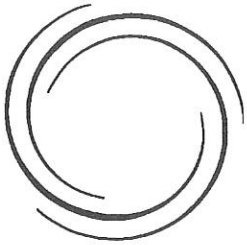

INDEX OF ALL AUTHORS

INDEX

Abe M. I-351
Abramyam L.A. IV-1844
Adams J.M. I-1,323,331
Adati K. I-34
Afanasjev V.I. I-82,299,III-1480
Afshar-rad T. IV-1864
Agarwal A.K. II-966
Agostini E. IV-1701
Aikawa H. III-1452
Airoldi A. II-813,III-1108, IV-1709
Akaoka N. IV-1508
Akatova T.Yu. I-411,III-1125, IV-1684
Akiyama R. I-34
Akulina D.K. II-431
Alava M.J. III-1003
Alcock M.W. III-1283
Alejaldre C. II-489,497,509, III-1255
Alikaev V.V. III-1076,1080, 1084
Alladio F. II-765
Alper B. II-557,565
Alport M.J. IV-1794
Amano T. II-451
Anabitarte E. IV-1492,1572
Andel R. van III-1121
Anderegg F. IV-1811
Anderson W.A. II-931
Anderson D. II-817
Ando A. I-34
Andreeva E.V. II-894
Andryukhina Eh.D. II-463
Angelis R. De III-1435
Aramaki E.A. II-601
Aranchuk L.E. II-651
Aratari R. I-291,295,III-1468
Arbuzov A.I. I-299
Argenti L. III-1112
Arnold R.C. IV-1860
Arsenin V.V. II-589
Arshad S. III-1267,1283
Arutiunov A.B. II-671,777,893
Asakura N. I-283,375
ASDEX-Team I-54,62,70,94,110, 151,207,239,291, 295,391,395,III-1052,1092,1167, 1171,1215,1263, 1287,1291,1323, 1427,1431,1435, 1439,1464,1468, IV-1552,1556,1676
Assis A.S. de II-861,IV-1786
Askinasi L.G. I-299,411
ATF Group II-443
Attenberger S. I-1,5,9
Austin M.E. I-26,150,174, III-1133
Awano M. II-541
Azarenkov N.A. IV-1848
Azevedo C.A. De II-861
Azizov E.A. I-14
Azumi M. III-1011,1307
Baboolal S. IV-1750
Babykin V.M. II-651
Baek W.Y. I-403
Bagdasarov A.A. I-195,231,III-1076, 1080,1084
Bagdoo J. III-1195
Baity F.W. III-1311
Balet B. I-1,5,106,162, 259,323
Bamford R.A. II-553,557
Barbato E. III-1163
Barbian E.P. IV-1528
Barnes C.W. I-114,146
Barnsley R. I-247, III-1365,1413, IV-1608
Barocio-Delgado S. I-30
Barth C.J. IV-1600
Bartiromo R. III-1092,1287, 1291,1323
Bartlett D.V. I-162,259,III-1150, IV-1504,1709
Bastistoni P. II-765
Batani D. IV-1876
Batanov G.M. II-467
Batchelor D.B. III-1311
Bateman G. I-134
Batishchev O.V. IV-1840
Baty H. II-889
Bätzner R. IV-1520
Bayley J. II-663
Becker G. II-826, 833
Beer M. III-1048
Behn R. I-78,IV-1680
Behrisch R. III-1357
Beidler C.D. II-513,517
Belavin M.I. II-593
Belikov V.S. III-1199
Belitz H.-J. IV-1568
Bell G.L. II-439,443,455
Bell J.D. III-1353, IV-1492
Bell M.G. I-114,134,

Bell M.G. 146,387, III-1048,1419
Bell R. I-146,283,375
Belle P. van I-1,331,III-1015,IV-1496
Bengston R.D. III-1456,1460
Berezovskij E.L. I-13, II-785, IV-1488
Berger-By G. III-1231
Bergsaker H. III-1401
Bernabei S. III-1287,1291, 1323
Berni L. II-601
Bertrand P. III-1299
Bessenrodt-Weberpals M. I-58,III-1460
Besshou S. II-459
Besson G. III-1175
Betello G. IV-1717
Beulens J.J. III-983
Bharuthramt R. IV-1750
Bhatnagar V.P. I-255,III-1015, 1019,1150
Bhattacharyya S.N. II-966
Biancalana V. IV-1876
Bianconi F. IV-1876
Bibeau C. IV-1861
Bibet P. III-1231
Bickerton R. I-134
Bieger W. IV-1568
Bigelow T.S. II-443,455
Bishop C.M. I-178
Bitter M. I-114,III-1048
Bittoni E. II-687
Bizarro J.P. III-1231
Blackwell B.D. II-435,521
Blank H.J. de II-919
Blokland A.A.E. van IV-1528
Blum J. II-872
Bobrovskij G.A. IV-1484
Bobylev A.V. II-877
Bogolyubskij S.L. II-609
Boileau A. IV-1664
Boivin R. III-1048
Bomba B. IV-1516,1520
Bombarda F. IV-1713
Bondeson A. II-906,954,962
Bongers W.A. III-1117
Bonicelli T. I-419
Bonoli P.T. III-1100
Bora D. I-287,III-1068
Borg G.G. III-1175,1179
Borie E. IV-1803
Bornatici M. IV-1832
Borozenets A.M. III-1060
Borrass K. III-1393
Borschegovskij A.A. I-195,III-1080,1084
Bosch H.S. II-873,III-1215
Bosch S. IV-1520
Bose M. II-684
Bosman R. III-1117,1121
Boyd D.A. IV-1624,1668
Boyev A.G. IV-1725
Bozin J. III-1405
Braams B.J. III-1417
Bracco G. I-118,IV-1717
Brakel R. II-479
Brambilla M. III-1056
Branas B. IV-1592
Braun F. III-1052,IV-1552
Bretz N.L. I-42,146,387, III-1048,IV-1544
Briguglio S. II-707
Brink A.M. van den I-199
Brower D.L. I-26,150,174, III-1133
Browning B. II-622
Browning P.K. II-577,622
Bruhms H. III-1223
Bruneau J.L. III-1231
Brunsell P. II-573,610
Brusati M. II-719,IV-1709,1713
Bruschi A. I-170,III-1112
Brzosko J.S. IV-1520
Brzozowskij J. II-573,655
Büchl K. I-235
Büchse R. I-66,239,291,391
Bud'ko A.B. II-639
Budny R.V. I-387,III-1419
Bugarya V.I. I-231
Bulyginskij D.G. III-1125,IV-1684
Bunting C. II-553,557,561,565, 573
Buratti P. I-118
Burdakov A.V. II-614
Bures M. I-255,III-1015,1019, 1381
Burhenn R. II-479
Burrell K.H. I-203,271,275,279, IV-1604
Bush C.E. I-114,146,III-1048
Bussac M.N. II-889
Cable M. IV-1861
Cadez V.M. IV-1737
Cai R. III-1341
Cains R.A. III-1035
Caldas I.L. II-675,III-1349
Calker C. van IV-1520
Callen J.D. I-142,II-853

Camargo S.J. II-675
Campbell D.J. I-5,255,323,327,339, III-1015,1019,1150, 1373
Campbell M. IV-1861
Canobbio E. III-1207
Capes H. II-845
Capitain J.J. III-1231
Cardinali A. III-1159,1203
Carlson A. III-1167,1427, 1460,1464,IV-1676
Carlstrom T.N. I-203,271,279
Carolan P.G. II-553,557,561,565, 569,IV-1564
Caron X. IV-1705
Carrao L. II-533,537
Carrera R. II-970
Carreras B.A. II-443,497,509, III-1353
Carter K. III-1353
Cartwright D.C. IV-1875
Castejón F. II-489,III-1255
Castle G. I-174
Cavallo A. I-46,146,III-1048
Cekic M. III-1137
Cenacchi G. II-813
Cercek M. IV-1815
Cesario R. III-1159,1203
Challis C.D. III-1150
Chan V.S. III-1031
Chance M.S. I-367,387
Chang C.S. III-1027
Chang Z. I-142,II-853
Chaniotakis E.A. I-134
Chankin A.V. III-1076,1080
Chaudron G.A. III-1195
Chávez-Alarcón E. I-30
Cheetham A. I-219,323,331,III-1150
Chen J.Y. I-26,III-1133
Chen L. II-707
Cheng C.Z. II-910
Chernenko A.S. II-651
Chernyshev F.V. I-82,411
Chies T. IV-1701
Chistyakov V.V. I-231,III-1076,1080, IV-1536,1616
Chittenden J.P. II-663
Chiu S.C. III-1031
Chodura R. III-1443
Choi D.-I. II-663,752,III-1027
Christiansen J.P. I-5,9, II-797,III-1015
Chu M.S. I-371
Chudin N.V. III-1327
Chudnovski A.N. II-781
Chugunov I.N. IV-1688
Chuvatin A.S. II-651
Cima G. I-174,III-1133
Cirant S. III-1108,1112
Ciric D. III-978
Clement S. I-255,III-1373,1385
Coad J.P. III-1357
Coe S. IV-1864
Cohn D.R. I-134
Colchin R.J. I-439
Coleman L. IV-1861
Colestock P.L. I-134,III-1048
Colunga-Sánchez S. I-30
Compass Group IV-1564
Conn R.W. III-1447
Connor J.W. I-130,178,II-695
Conrads H. I-383
Conroy S. I-98,331
Conway G.D. II-435,521
Cook D.R. III-999
Cooper W.A. II-931
Coppi B. II-793
Coppins M. II-663
Cordey J.G. I-1,106,110,162, II-797,III-1015
Core W.G.F. I-251,331, III-1015,1019
Cornelissen P. I-383
Correll D. IV-1861
Corrigan G. I-263, II-801,805
Corti S. I-323,III-1150
Coster D.P. III-1417
Costley A.E. IV-1500,1504
Cottrell G.A. I-5,9,III-1015,1019
Coulon J.P. III-1365
Cox M. I-130,178, III-1019,1219,1267
Crisanti F. II-765
Croci R. III-1207
Crume E.C. Jr. II-447,455
Cruz Jr. D.F. da III-1121
Culverwell I.D. II-663
Cunningham G. II-622
Cupido L. IV-1560
D'haeseleer W.D. II-748
Dahmani F. IV-1856
Dahyia R.P. III-983
Dam J.W. van II-970
Damstra R.D. III-1117,1121
Dan'ko S.A. II-609
Dangor A.E. II-663
Daniele R. IV-1790
Darrow C. IV-1861
Davis J.I. IV-1861

DeBoo J.C. I-126,275
Décoste R. III-1195
Deha I. IV-1876
Deliyanakis N. I-178,III-1267
Dellis A.N. III-1267
Delvigne T. I-287,III-1040
Demchenko V. IV-1741
Demers Y. III-1195
DeMichelis C. III-1231
Deng C. I-363
Desselberger M. IV-1864
Devos J. I-287
Dewar R.L. II-521
Diachenko W.D. I-327
Dicken D. IV-1680
Diesso M. IV-1548
DIII-D Research Team I-203,275, IV-1596,1604
Ding X. I-307,III-1341
Dippel K.H. I-287,403, III-1447
Dmitrieva M.V. III-1295
Dnestrovskij A.Yu. II-789
Dnestrovskij Yu.N. II-785,894, III-1239 IV-1616,1620
Dodel G. I-207
Dodhy A. II-471,475
Dokuka V.N. I-14
Domier C.W. IV-1798
Domínguez N. II-497,509
Dong J. I-154
Donné A.J.H. IV-1656
Dooling P.J. II-622
Doyle E.J. I-203,279, IV-1596,1604
Drake J.R. II-573
Druetta M. IV-1580
Du T. I-415
Duan X. III-1341
Düchs D.F. II-691, 801
Dudok de Wit Th. I-74,187,III-1476
Dunlap J.L. III-1353,IV-1492
Durodié F. I-287
Durst R.D. IV-1564
Duval B.P. I-74,III-1476, IV-1680
Dyabilin K.S. II-463
Dyer G.R. II-443,III-1353
Dylla H.F. III-1419
Eberhagen A. I-151,III-1263
Eckhartt D. III-1336
ECRH -Team II-471,475, 479,483,484,
ECRH -Team III-1275, IV-1572,1576
Edenstrasser J.W. II-881
Edery D. II-938
Edlington T. III-1267
Edwards A.W. I-5,323,335,III-1150
Efthimion P.C. I-42,50
Egorov S.M. I-231,IV-1536
Ehrenberg J. III-1357
Ehrhardt A.B. III-1417
Ehrlich R. IV-1861
Ejiri A. II-541,549
Elevant T. II-817,IV-1496
Elfimov A.G. III-1064,1141,1315
Elisavetin A.A. I-195
Elizavetin D.Yu. III-1080,1084
Elliott J.A. IV-1778
Ellis J.J. IV-1608
Emmoth B. III-1401
Endler M.A. III-1464
Engelhardt W. I-62
Englade R.C. III-1100
England A.C. II-439,443,455
Erckmann V. III-1271,1275
Erents K. I-219
Erents S.K. III-1373,1381,1385
Eriksson L.-G. I-327,III-1015,1019, 1150
Esch H.P.L. de I-90
Esipchuk Yu.V. III-1080,1084
Est Q.C. van IV-1600
Estrada T. IV-1592
Evdokimov D.B. III-1080,1084
Evrard M.P. III-1019
Fahrbach H.-U. III-1171
Fajemirokun H. IV-1692
Fall T. III-1231,IV-1580
Famà F. IV-1871
Farina D. III-1088
Fasoli A. IV-1807,1811
Federov A.A. I-299,411,III-1480
Federov S.V. III-1295
Fedyanin O.I. II-463
Feix M. III-1299
Feneberg W. II-773,III-1427
Fernández J.C. II-643
Ferrante G. IV-1790
Ferron J.R. I-275,371,427
Fessey J.A. IV-1500
Fidone I. III-1129,1279, IV-1705
Field A.R. IV-1556
Fielding S.J. III-1267,1283,1472
Figueira J.F. IV-1875

Fijalkow E. III-1299
Finken K.H. I-403,III-1447
Fishpool G.M. I-347,III-1283
Fitzpatrick R. I-130,379,II-923
Fletcher J.D. I-355,359
Fonck R.J. I-50
Forrest C. III-1287
Foster M.S. I-150
Fowler R.H. II-439
Frank N.A. II-773
Fredrickson E. I-114,387,III-1048
Fried B.D. I-138
Frieling G.J. IV-1664
Fu B. I-154
Fu G.Y. II-970
Fuchs V. III-1195
Fujii T. III-1007,1011
Fujisawa A. II-541,549
Fujita T. III-1452
Fujiwara M. II-451
Fukumoto H. I-351
Fukuyama A. II-809,III-1011, 1251,1307
Fussmann G. I-62,183,III-1423, 1431,1435,IV-1556
Fyaretdinov A. III-1259
Gabellieri L. III-1335
Gaigneaux M. I-287
Galbiati S. IV-1636
Gandy R.F. I-150,174,III-1133
Gao Q. I-154,311
Garbet X. II-728,736,938, IV-1588
Garcia L. II-493,501
Gardner H.J. II-521
Garina S. III-1064,III-1141
Garribba M. I-419
Gasparino U. III-1271,1275
Gaunt R. IV-1794
Gebhardt U. I-868
Gee S.J. II-622
Gehre O. I-70
Gentille B. de III-1231,1259
Gentle K.W. I-70,174, III-1133,1460
Gernhardt J. I-207,IV-1552
Gervais F. IV-1588
Ghendrih Ph. II-845
Ghizzo A. III-1299
Giannella R. I-9,247,263, III-1365,1413, IV-1608,1713
Giannone L. I-58,151,207, III-1460,1464
Gibson K.J. II-557,561
Giesen B. I-287
Giles P. IV-1584
Gill C. III-1231
Gill R.D. I-335,III-1150
Giruzzi G. III-1129,1259, 1279,IV-1705
Giulietti A. IV-1864,1876
Giulietti D. IV-1876
Gizzi L. IV-1864
Gladush G.G. I-14
Glaude V. III-1195
Glendinning G. IV-1861
Glowienka J.C. II-443,455
Goedbloed J.P. I-399
Gohil P. I-279
Golant V.E. I-82,299,411, III-1480
Golberg S.M. II-659
Goldston R.J. I-134,146
Gondhalekar A. I-219
Goniche M. III-1231
Good T.N. IV-1807,1811
Gordeev E.M. II-609
Gorelenkov N.N. II-914
Gorelov Yu. III-1259
Gorini G. I-170,III-1112, IV-1652
Gossett J.M. II-439
Gott Yu.V. IV-1612
Gottardi N. I-247,259,263,323, 339,III-1019,1150, 1381,1413
Goulding R.H. III-1311
Gowers C.W. I-162,259,323, IV-1504,1692
Graaf M.J. de III-983
Granucci G. III-1112
Grashin S.A. III-1076
Gray D. I-403,III-1447
Greene G.J. III-1048,IV-1540
Grek B. I-42,114,146
Grekov D.L. II-529
Grésillon D. IV-1588,1721
Grimbergen T.W.M. IV-1528
Grisham L.R. I-146
Grishanov N.I. III-1141
Groebner R.J. I-203,271,275,279, IV-1604
Groot B. de III-11121
Gross R.A. I-387
Grua P. II-732
Gruber O. I-94,151,183,182, II-841

Gruber R. II-931
Grunov C. IV-1488
Gryaznevich M.P. I-411,III-1327
Guha S. IV-1758
Guilhem D. III-1231,IV-1580
Guldbakke S. IV-1520
Guo D. I-363
Guo G. I-154,311
Guo Z. II-970
Gurov A.A. III-1080
Gusev V.K. I-299,411
Gyergyek T. IV-1815
Haas F.A. II-942
Haas G. III-1365,1468
Haas J.C.M. de I-158
Hacker H. II-479
Hackmann J. IV-1680
Haegi M. II-687
Haendler B. IV-1861
Haines M.G. II-663
Hale G.M. II-873
Hamada Y. I-34
Hamamatsu K. III-1011,1307
Hamano T. III-1452
Hamberger S.M. II-521
Hammel B. IV-1861
Hammet G.H. I-146,III-1048
Hammett G.W. I-162
Hamnen H. II-817,III-1019
Han S. III-1154
Hanatani K. II-459
Handley M.J. II-773
Hansen P.M. I-166
Hanson G.R. IV-1492
Harada M. II-459
Harbour P.J. I-259,III-1365,1381, 1385
Harmeyer E. II-517
Harris D.B. IV-1875
Harris J.H. III-1353,IV-1492
Harrison M.F.A. III-1397
Hartfuss H.J. IV-1572,1576
Harvey B.M. III-1035
Harvey R.W. III-1259,1323
Hasan Z. IV-1758
Hasegawa K. III-1452
Hastie R.J. I-130
Hatayama A. I-255,III-1211
Hatcher R. I-283,367
Hatcher W. IV-1861
Hattori K. II-545
Hauer A. IV-1875
Hawkes N.C. I-247,III-1365,1413
Hawryluk R.J. I-387,III-1419
Haynes P.S. I-379
Heer F.J. de IV-1664
Heeren R.M.A. III-978
Heikkinen J.A. III-1003
Heindler M. II-638
Hellberg M.A. II-773,IV-1750,1754
Hellblom G. II-573,610
Hellermann M. von I-9,162,III-1150, 1361,1381,1385, IV-1496,1608,1664
Hellsten T. III-1003,1015,1019, 1150
Helton F.J. I-371,427
Hender T.C. I-130,323,379,399, II-923,927,III-1283
Henesian M. IV-1861
Henins I. II-643
Hennequin P. IV-1588
Herrmann W. I-66,III-1171, IV-1672
Hess W. III-1231,IV-1580
Hesse M. IV-1697
Hickok R.L. I-26,38,III-1133
Hidalgo C. III-1353,IV-1492
Hidekuma S. I-34,267
Hill D.N. I-134
Hill K.W. I-42,114,146, III-1048,1419
Hillis D.L. III-1447
Hirano Y. II-545
Hirayama T. I-223
Hiroe S. II-443
Hirokura S. I-34,227
Hirota I. II-545
Hirsch K. IV-1692
Hirshman S.P. II-505
Hively L.M. II-970
Hoang G.T. III-1231
Hoekstra R. IV-1664
Hoenen F. III-1040
Hoffman D.J. III-1048,1311
Hofmann J.V. III-1435,IV-1556
Hofmeister F. III-1052,IV-1552
Hogan J.T. II-825
Hogewey G.M.D. I-158
Hollenstein Ch. III-1476
Holzhauer E. I-207
Honda A. III-1452
Honda R.Y. II-601
Hong B.G. II-711
Honma T. II-585,III-1039
Hoog F.J. de III-983
Hopman H.J. III-978,983
Horton L.D. II-439,447,455

Hosea J. III-1048
Hoshino K. III-1340,1452
Hosokawa M. II-451
Höthker K. IV-1568
Hotston E.S. III-1397
Hou J. I-154
Houlberg W.A. I-134
Houtte D. Van III-1231
Howald A.M. III-1452
Howard J. II-521
Howe H.C. II-443,451
Howell B. I-46
Howl W. I-371
Hsuan H. I-114
HT-6B Group I-363
Huang K. I-311
Huang R. I-363
Hubbard A. III-1195
Hübner K. IV-1516,1520
Hugenholtz C.A.J. III-1121
Hughes T.P. II-553
Hugill J. I-379,III-1267,1283
Hugon M. II-703,962
Hulse R.A. I-46,50
Hutter T. III-1231
Huysmans G.T.A. I-323,399
Hwang A. III-1381
Hyatt A. III-1439
Ichiguchi K. II-459
ICRH-Team I-239,II-479, III-1052
Ida K. I-34,267, II-451, III-1452
Idei H. II-451
Igarashi H. II-585 III-1039
Iguchi H. II-451
Ikeda Y. III-1183
Ikegami H. I-34
Imai T. III-1183
Ingraham J.C. II-581
Ingrosso L. IV-1520
Innocente P. II-533
Irie M. II-626
Ishibori I. III-1452
Isichenko M.B. II-667
Isler R.C. II-439,447,455
Itoh K. I-267,II-740,809, III-1307
Itoh S.I. I-267,II-740,809, III-1307
Itoh T. IV-1508
Its E.R. I-82,299,411
Ivanov A.A. III-1064
Ivanov N.V. III-1080
Izvozchikov A.B. I-82,411,III-1480
Jacchia A. I-166,170
Jackson G.L. I-275
Jacquinot J. I-255,259,323,327, III-1015,1019,1150
Jadoul M. I-319
Jaeckel H.J. III-1365
Jaeger E.F. III-1311
James R.A. III-1259
Jan G.-D. IV-1824
Janeschitz G. III-1365
Janos A. I-146,387,III-1048
Janz S. III-1259
Jardin S.C. I-134,387,III-1191
Jarmén A. II-723
Jarvis O.N. I-1,98,331,III-1015
Jassby D. III-1048
Jelenković B. III-1405
Jelić N. IV-1815
Jernigan T.C. II-443,447,455
JET Team I-110
JFT-2M Group III-1340
Ji H. II-541,549
JIPP T-IIU Group I-227
Jobes F. I-146,III-1048
Joffrin E. I-323
John P.I. IV-1745
Johnson D.W. I-42,46,50,114,146, III-1048
Johnson M.F. I-259
Johnson P.C. III-1267,1283
Johnston T.W. III-1299
Jones T.T.C. I-1,5,9,III-1381
Joye B. I-74,187,III-1179, 1476,IV-1680
Joyer P. I-303,IV-1584
JT-60 Team I-223,III-1183, IV-1508
Kaita R. III-1048
Kajiwara T. II-459
Kakoulidis E. III-1427
Kakurin A.M. III-1080
Kalda J.L. II-667,IV-1820
Kalinin Yu.G. II-609
Kallenbach A. I-58,62,182,183, III-1423
Källne E. II-573,655,IV-1652
Kalyushnij V.N. II-525
Kamada Y. I-223
Kamelander G. II-685
Kamenets F.F. II-639
Kaneko H. II-459
Kaneko O. I-34, II-451

Kania D. IV-1861
Kantor M.Yu. III-1125,IV-1684
Karas' V.I. IV-1840
Kardaun O. I-110, II-797
Karita A. I-34
Karlsson P. II-610
Karney C.F.F. III-1417
Karttunen S.J. III-1303
Karyukin A.V. II-614
Kasai S. III-1452
Kashiwa Y. III-1452
Kasparek W. III-1271
Kauffman R. IV-1861
Kauffmann M. I-215
Kaufman A.N. III-999
Kaw P.K. II-966,IV-1745
Kawahata K. I-34,227
Kawakami T. III-1452
Kawano Y. I-223
Kawashima H. III-1340,1452
Kawasumi Y. I-34
Kayama M.E. II-605
Kaye S.M. I-283,367,375
Kazawa M. III-1452
Keane C. IV-1861
Keilhacker M. III-1369
Kellman A.G. I-275,371,427
Kerdja T. IV-1856
Kernbichler W. II-638
Kesner J. I-387
Kessel C. I-367,375
Kever H. I-383
Khairutdinov R.R. I-14
Khalil Sh.M. IV-1774
Khattak F. IV-1864
Khudoleev A.V. I-82,III-1480
Kiessling M. I-868
Kikuchi K. III-1452
Kilkenny J. IV-1861
Kilpatrick S.J. III-1048,1419
Kim J.Y. II-752,III-1460
Kim S.K. I-150,IV-1656
Kimura H. III-1007,1011
Kingsep A.S. IV-1820
Kiptilyj V.G. I-82,III-1480,IV-1688
Kirov A.G. III-1319
Kislov A.Ya. III-1080,1084
Kislov D.A. I-315,III-1080, IV-1484
Kislyakov A.I. I-82
Kisslinger J. II-517
Kitson D.A. II-577,622
Klein H. IV-1520
Klepper C.C. III-1447,IV-1580
Kleyn A.W. III-978
Klüber O. II-291,837,III-1223
Knight A. I-78
Koch R. III-1044
Kochanov A.E. IV-1733
Kocherga O.D. IV-1819
Kock L. de I-9,III-1357,1373, 1381,1385
Koh W.-H. III-1027
Koidan V.S. II-614
Koide Y. I-223,IV-1508
Kolesnichenko Ya. III-1199
Kolik L.V. II-467
Komori A. II-459
Kondo K. II-459,IV-1524
Koning J.J. III-1121
Konyukhov V.V. II-614
Kooijman W. III-1121
Korelev V.D. II-609
Kornblum H IV-1861
Kornherr M. I-291,391
Korotkov A.A. I-82,299,III-1480
Kostomarov D.P. II-894,III-1239
Kovan I.A. III-991
Kovanen M.A. I-251,III-1019
Kovrov P.E. III-991
Krämer M. III-1167
Krasheninnikov S.I. II-671,777, 789,893
Krieger K. I-66,III-1423,1431, 1435
Krikunov S.V. I-299,411
Kritz A.H. III-1100,1191
Krivenski V. IV-1648
Krivitaky V.S. III-1187
Kruyt O.G. III-1117,1121
Kubo H. I-223,IV-1508
Kubo S. II-451
Kucinski J. IV-1520
Kugel H. I-283,375
Kuhn S. II-715, IV-1782,1786
Kühner G. II-471,475, 484
Kuksov P.V. II-609
Kukushkin A.B. IV-1632
Kumazawa R. I-34
Kunkel W.B. III-979
Kupschus P. I-1,5,9
Kurki-Suonio T. I-271
Kuroda T. I-34
Kurzan B. I-62
Kusama H. II-626
Kusama Y. III-1183
Kuteev B.V. I-231,IV-1536

Kuz'min S.V. II-618
Kuznetsova L.K. III-1247
Kwon M. II-439
Kwon O.J. I-323,399,927
Kyrazis D. IV-1861
Kyriakakis G. III-1427,1439
LH-Team I-70, III-1092, 1171,1215, 1291,1323
Lackner K. II-841
Lallia P. III-1015
Lam N.T. III-1023
Lama F. III-1357
LaMarche P.H. III-1419
Lammeren A.C.A.P. van IV-1600,1656
Lamoureux M. IV-1697
Landen N. IV-1861
Lane S. IV-1861
Lang R. I-215,235, 239,III-1215
Langley R.A. II-455
Lao L.L. I-371,427
Larionov M.M. III-1125
Lasalle J. III-1231, IV-1701
Lashkul S.I. III-1125
Lau Y.T. I-375
Laumann C. IV-1861
Laundy B. I-1
Laurent L. II-728, IV-1693,1721
Laviron C. IV-1588
Lawson J. IV-1861
Lawson K.D. I-247,339, III-1381,1413
Lazaros A. II-479
Lazarus E.A. I-371,427
Lazzaro E. I-251,259, 323,343,399
Lean H. III-1019
Lebeau D. III-1044
Lebedev S.V. I-299,411, II-614
LeBlanc B. I-283,367, 375,III-1048
Lecousty P. III-1231
Lee D.K. II-443
Lee J.K. I-371
Leenstra E.J. IV-1628,1852
Lehecka T. I-203,279, IV-1596
Lehner T. IV-1693,1721
Lehnert B. II-647
Leitao J. IV-1560
Lengyel L.L. I-243
Leonard A.W. III-1452
Leonard M. III-1419
Lerbinger K. II-935
Lerche R. IV-1861
Leuer J.A. I-427
Leung K.N. III-979
Leuterer F. III-1092,1215,1223, 1287,1291,1323, IV-1552
Levin L.S. I-327,III-1125, IV-1684
Levinton F. I-375
Li F. I-311
Li G. I-363
LI J. IV-1836
Li L. I-363
LI W.L. I-150,174,III-1133
Liberman M.A. II-639,659
Lie Y.T. I-287
Lietzke A.F. III-979
Liew S.L. IV-1548
Likin K.M. II-467
Liljeström M. II-756
Lin H. III-1456,1460
Lipin B.M. I-299,411
Lippmann S. I-275
Lisak M. II-817
Lister J.B. I-74,187,III-1175, IV-1680
Litaudon X. III-1231
Litvak A.G. IV-1844
Liu W. III-1154
Lloyd B. III-1267,1283
Loch R. I-215,235,239,III-1215
Lohr J. I-271,III-1259
Lok J. III-1121
Lomas P.J. I-1,5,9,III-1015,1381
Longinov A.V. III-1331
Lontano M. IV-1636,1762
Lopes Cardozo N. I-170,IV-1660
López Fraguas A. II-489,497,501,509
López-Callejas R. I-30
Lorenzen J. II-817
Loughlin M.J. I-1,331
Lowry C.G. I-9,339, III-1015,1381
Lucca F. De I-166,170, III-1112
Luce T.C. III-1259
Luciani J.F. II-889,935
Luckhardt S.C. IV-1624
Luhmann N.C. Jr. I-150,174,203,279,

Luhmann N.C. Jr. III-1133,IV-1596,1604, 1798
Lukash V.E. I-14
Lukin A.A. II-609
Lukinov V.A. III-1331
Lukyanov M.Yu. IV-1725
Lunin N. IV-1762
Lütjens H. II-906
Lyadina E.S. I-315,IV-1484,1616, 1620
Lynch V.E. II-443,497,509
Lyon J.F. II-439,455
Lysenko S.E. II-785
Lysyansky P.B. II-618
Maassberg H. II-484,III-1271,1275
Mace R.L. IV-1750,1754
Machida M. II-601
Maddison G.P. I-130,III-1397
Maeda H. III-1452
Maejima Y. II-545
Magne R. III-1231
Mahdavi M.A. I-279
Mancuso S. II-765
Mandl W. III-1361,IV-1496,1608, 1664
Manhood S.J. III-1267,1283
Manickam J. I-367,375
Manos D.M. III-1417,1419
Mansfield D.K. I-42,50,114,146, III-1048
Manso M.E. II-837,IV-1560
Mantica P. I-166,170,III-1112
Marco F. De III-1159
Marcus F.B. I-1,323,331
Marklin G.J. II-643
Marmar E. I-46,387
Marmillod Ph. III-1175
Martin G. I-303,III-1231,IV-1584
Martin-Solis J.R. I-219
Martinelli A.P. III-1357
Martini S. II-533
Masai K. II-451
Masai M. I-34
Masoud M.M. II-630
Mast K.F. I-263
Mata J. IV-1560
Matias J. II-837,IV-1560
Matjukov A.V. IV-1688
Matsuda K. III-1259
Matsuda T. III-1452
Matsumoto H. I-203,271, 279,IV-1604
Matsuo K. II-459,IV-1524
Matsuoka K. II-451
Matsuura H. II-459
Matthews G.F. III-1283
Mattioli M. III-1231,IV-1580
Mattor N. II-695
Mauel M.E. I-387
Maximov Yu.S. III-1080
Mayanagi K. II-541,549
Mayberry M.J. III-1150,1311
Mayer H.M. I-183
Mayo R.M. II-643
Mazur S. II-573,610
McCool S.C. I-150,174,III-1456
McCormick K. I-58,395,III-1323, 1439
McCracken G.M. I-9,III-1381,1385,1472
McCuire K. I-387,III-1048
McCune D. I-42,387
McDonald T.E. IV-1875
McKenzie J.S. III-1219
Medley S.S. I-134,III-1048
Medvedev A.A. I-13,III-1080,IV-1488
Meigs A.G. I-26
Meisel D. III-1468
Mekler K.I. II-614
Mel'nik V.N. IV-1729
Mélendez-Lugo L. I-30
Mendonça J.T. II-918
II-719, 837
Mennella A. III-1104
Merazzi S. II-931
Merkel R. I-215
Mertens V. I-151,215,235,239, III-1215,1263
Messiaen A.M. I-383,287,III-1040
Messina G. IV-1790
Meyer R.L. IV-1705
Micozzi P. I-122
Migliuolo S. II-898
Miley G.H. II-970
Miller G. II-581
Milligen B.Ph. van III-1121,IV-1660
Minagawa H. II-459
Minardi E. II-857
Minenko V.P. III-1145
Mioduszewski P.K. II-455
Miramar Blásquez J.F. II-488
Mirensky V.Yu. III-1080,1084, IV-1488
Mirnov S.V. I-14
Mironov V.A. IV-1844
Miroshnikov I.V. I-231,IV-1536
Mishin A.S. IV-1688

Mitchell I. II-663
Miura Y. III-1452
Miyamoto K. II-541,549
Mizuuchi T. II-459
Mohamed B.F. IV-1774
Moleti A. IV-1717
Mompean F. I-247,III-1413
Monaco F. III-1287
Monakhov I.A. III-9
Mondt J.P. II-769
Monier P. III-1231
Montalvo E. II-970
Montgomery D. IV-1861
Montvai A. II-691
Morales G.J. I-138,III-995
Moreau D. III-1150,1231
Morera J.P. II-845
Moret J.-M. I-187
Morgan P.D. I-162,259,323, III-1361,1381,IV-1496
Mori M. III-1452
Morita S. II-443,447,451,455
Morotov D.K. II-764
Morotov N.N. II-764
Morris A.W. I-347,379,III-1283
Morris R.N. II-439
Morsi H.W. I-247,IV-1608
Moser F. IV-1803
Moulin B. III-1231,IV-1701
Mourgues F. II-736
Moyer R.A. I-287,403,III-1447
Moyseenko V.E. III-1060
Mu J.-L. II-727,728
Mueller D. I-146,387, III-1048,1419
Müller E.R. I-395,III-1439
Müller G.A. III-1271
Müller R.W. IV-1860
Münich M. III-1287,IV-1552
Munson C.P. II-581
Murakami M. II-443,455
Muraoka K. II-459,IV-1524
Muratov V.I. IV-1880
Murmann H.D. I-54,62,III-1092,1323
Murphy J.A. I-146
Muzzolon A. II-537
Myors D.J. III-974
Nagasaki K. II-809
Nagashima K. I-223
Nagatsu M. I-150,IV-1524
Nagayama Y. I-146,III-1048
Naito O. III-1183
Najdenov V.O. IV-1688
Nakamura Y. II-459
Nakasuga M. III-459
Nardone C. I-166
Narihara K. I-34
Navarro A.P. IV-1572,1592
Nave M.F.F. I-335
Nave F. I-323
Navratil G.A. I-387
Nazikian R. IV-1544
NBI-Team IV-1572,1576
Nefedov V.V. II-894
Neilson G.H. I-134
Nelson B.A. II-605,III-1137
Nemoto M. III-1011,1183
Nemov V.V. II-525
NET-Team III-1397
Neudatchin S.V. I-195
Neuhauser J. I-395,III-1427,1460
Neves J. IV-1560
NI-Team I-54,62,94,295,395, II-479,483,III-1291, 1323,1439,1447
Nicolai A. II-825,III-1409
Niedermeyer H. I-207,395,III-1439, 1460,1464
Nielsen P. I-5,9,162,323, III-1015,IV-1692
Nieswand C. I-78,IV-1680
Nieuwenhove R. Van I-287,III-1068
Nishimura K. II-451
Nishino N. I-223,IV-1508
Nishitani T. I-223
Nocentini A. II-801, 849
Noda N. II-451,459
Noll P. I-419
Nordlund P. II-573,610
Nordman H. II-723
Noterdaeme J.-M. I-239,III-1052,1056, IV-1552
Nothnagel G. I-355,359
Notkin G.E. III-1080,1084
Novokhatskij A.N. III-1480
Nowak S. III-1108,IV-1709
Nunes F. IV-1560
O'Brien D.P. I-251,323,399
O'Brien M.R. III-1019,1219,1267
O'Rourke J. I-5,158,162,323, 343,III-1015,1019, 1150,1381
Obiki T. II-459,IV-1524
Ochirov B.D. II-467
Oda T. II-459
Odajima K. III-1452
Ogawa T. III-1452
Ogawa Y. I-34,227

Oh Y.-H. II-752
Ohdachi S. II-541,549
Ohkubo K. I-34
Ohyabu N. III-1452
Oka Y. I-34
Okabayashi M. I-283,367
Okada T. II-459,IV-1524
Okajima S. I-227,IV-1524
Okamura S. II-451
Okano H. III-1452
Okano K. III-1211
Okretic V.K. IV-1737
Oks E. IV-1644
Olivian J. IV-1588
Olsson M. I-1,331,IV-1496
Ongena J. I-383,III-1040,IV-1532
Oomens A.A.M. III-1121
Oost G. Van I-287,III-1068,IV-1532
Orefice A. IV-1709
Orsitto F. I-118,IV-1640
Ortolani S. II-533
Os C.F.A. van III-979
Osborne T.H. I-203,279,371
Osipenko M.V. III-987
Ostrikov K.N. IV-1848
Otsuka M. I-351
Ott W. II-483
Ottaviani M. II-711
Owens D.K. I-42,387,III-1419
Owens K. III-1048
Oyevaar T. IV-1528
Ozaki T. I-34, II-451
Pacher G.W. I-423
Pacher H.D. I-423,III-1397
Palleschi V. IV-1867,1871
Pan C.-H. IV-1824
Paoletti F. III-1203
Parail V.V. III-1243,1247
Parham B.J. III-1267,IV-1564
Paris P.J. IV-1807,1811
Park C.-H. III-1027
Park H.K. I-42,46,50,114,146, III-1048
Parker R. II-962
Parlange F. III-1231
Partridge J. III-1357
Pasini D. I-5,9,247,III-1361,1381
Patel A. II-557,565,569
Patel T.K. III-1413
Patterson D.M. I-174
Pättikangas T.J.H. III-1003,1303
Paul S. I-283,375
Paume M. IV-1721
Pavlov Yu.D. III-1080
Peacock N.J. III-1413
Pecquet A.L. III-1231
Pedit H. IV-1782
Pedorenko A.V. II-894
Peebles W.A. I-134,150,174, 203,279,III-1133, IV-1596,1604,1798
Pegoraro F. II-793,898,946
Pégourié B. III-1227
Pellet Injection Team I-239, II-479,483, III-1215,1287
Peng Y.-K.M. II-825
Penningsveld F.-P. II-483
Pereira J. IV-1560
Pericoli Ridolfini V. III-1203,1389
Perkins F.W. I-134,III-1031
Persson H. II-817
Pesic S. III-1116
Petravic M. III-1417
Petrie T.W. I-275
Petrov A.Ye. II-467
Petrov S.Ya. I-82
Petrov Yu.V. IV-1684
Petrovic Z. III-1405
Peysson Y. III-1227,1231
Philipona R. I-203,279, IV-1604
Phillion D. IV-1861
Phillips C.K. III-1048
Phillips P.E. I-26,174, III-1133
Pietrzyk Z.A. I-78
Pigarov A.Yu. I-13
Pilipenko V.V. III-1060
Pillon M. I-98
Pimenov A.B. III-1080,1084, IV-1488
Pitcher C.S. III-1381,1417, 1419
Pitts R.A. III-1283,1472
Pivinskij A.A. II-785
Platz P. III-1231, IV-1697,1701
Pochelon A. I-78,IV-1680
Podushnikova K.A. I-299,411, III-1480
Polevoj A.R. I-195
Politzer P. III-1259
Polman R.W. III-1121
Pomphrey N. I-134
Popel S.I. III-1190
Popov A.M. II-894
Porcelli F. I-259,323,

Porcelli F. 327,II-898, 918,946
Porkolab M. I-134,III-1100
Porte L. I-323,IV-1504
Porto P. II-601
Pospieszczyk A III-1447
Postupaev V.V. II-614
Potapenko I.F. II-877, III-1064
Power A. II-663
Pozzoli R. III-1088,1104
Prater R. III-1259
Prentice R. I-5,9,IV-1500
Prokhorov D.Yu. II-777
Pu Z.-Y. II-727,728
Puiatti M.E. II-533,537
Puri S. III-1031,1158, 1315,IV-1770
Qin Pinjian I-363
Qiu X.-M. IV-1824
Quemeneur A. IV-1588
Ramponi G. IV-1709
Ramsey A.T. I-42,46,114, 146,III-1048, 1417,1419
Ran L. I-311
Rasmussen D.A. II-439,443, 455
Rassadin L.A. IV-1688
Rau F. II-517
Rax J.-M. II-938, III-1231, IV-1693
Rayburn T.M. II-439
Razdobarin G.T. I-299,411, III-1125,1480, IV-1684
Razumova K.A. I-315, III-1080,1084
Rebut P.H. II-703
Reichle R. I-251
Reiter D. III-1447
Remkes G.J.J. I-199,407
Renner H. III-1271
Ress D. IV-1861
Rettig C. IV-1604
Rey G. III-1231
Reznichenko P.V. IV-1536
Rhodes T.L. III-1353,1456, 1460
Ribe F.L. II-605, III-1137
Ribeiro C. III-1349
Richards B. I-26,174,
Richards B. III-1133
Riedel K. I-151
Rieser H. II-715
Rij W.I. van II-505
Rimini F. III-1015,1150, IV-1709,1713
Ringler H. II-471,475,484
Ritz Ch.P. I-150,II-581, III-1353,1456,1460
Riviere A.C. III-1267,1283
Roberts D.E. I-355,359
Roberts J. IV-1548
Robinson D.C. I-130,178,s211, III-1267,1283
Robouch B.V. IV-1520
Roccella M. I-122
Rodriguez L. I-22,III-1231
Rodriguez R. III-1259
Rodriguez Yunta A. II-505
Rogdestvensky V.V. I-82
Roger D. III-1456
Röhr H. I-62
Rollet S. IV-1652
Romanelli F. II-707,711
Romannikov A.N. II-914
Romero H. III-995
Ronzio D. III-1104
Roquemore A.L. IV-1548
Rosa M. De IV-1871
Rosenbluth M.N. I-126,II-970
Roubin J.-P. II-728,732
Rowan W.L. I-26,174
Roy A. II-958
Roy I.N. I-195,II-954, III-1080,1084
Rozhansky V. II-744
Rozhdestvensky V.V. I-299,411,III-1480
Ruan L. I-154
Rubel M. III-1401
Rudakov D.L. III-1076
Rudakov L.I. II-609
Rudyj A. III-1460,1464, IV-1676
Rusbridge M.G. II-561,622
Rusbüldt D. III-1472
Russo A.J. I-403
Ryan P.M. III-1311
Rynn N. IV-1811
Ryter F. I-94,239,295, III-1052
Sabbagh S.A. I-387
Sack C. I-263,II-691,801
Sack H.C. I-259
Sadler G. I-1,5,9,98,

Sadler G. 162,323,331, III-1015, IV-1496,1608
Sadowski M. II-634
Sagara A. II-451
Sager G. I-271
Saibene G. III-1357,1373
Saito K. II-545
Saitou N. II-626
Sakamoto M. I-34,227
Sakanaka P.H. II-861
Sakasai A. I-223,IV-1508
Sakharov N.V. I-82,299,III-1480
Salas A. II-501
Salmon N.A. III-1150
Salomaa R.R.E. III-1303
Salvetti A. IV-1871
Salzmann H. IV-1692
Samain A. II-728,736, 845,938
Samm U. I-287,III-1472
Sanchez J. IV-1572,1592
Sandeman J.C. IV-1778
Sandmann W. I-215,235,239
Sano F. II-459
Santi D. I-118
Santiago M.A.M. IV-1786
Sanuki H. II-451
Sapozhnikov A.V. II-467
Sardei F. II-471,475
Sarksyan K.A. II-467
Sartori R. III-1357,1373
Sasao M. I-34
Sato M. II-459
Sato K.N. I-34,227
Sato K. I-34
Savrukhin P.V. I-195,315,III-1080, IV-1484,1620
Saxena Y.C. IV-1749
Sayal V.K. IV-1828
Scarin P. II-533,537
Scharer J.E. III-1023
Scharp L.E. II-521
Scheffel J. II-610,IV-1836
Schep T.J. II-946
Scherbakov A.G. III-1072
Schiffel J. III-1048
Schissel D.P. I-271,275
Schivell J. I-146
Schmidt G.L. I-5,42,46,259, III-1048,1419
Schmidt J.A. I-134
Schneider W. II-841
Schoenberg K.F. II-581
Schooch P.M. I-26,38,174,III-1133
Schoon N. IV-1532
Schorn R.P. I-287
Schram D.C. III-983
Schubert R. IV-1552
Schüller F.C. I-199,407,III-1121
Schüller P.G. III-1271
Schultz G. II-954,III-1133
Schupfer N. IV-1786
Schwartz J. IV-1532
Schweer B.F. I-287
Schwenn U. II-931
Scott S.D. I-50,114,146, III-1419
Seki T. I-34
Sen A. II-966
Sengoku S. III-1452
Seraydarian R.P. I-271
Sergeev V.Yu. I-231,IV-1536
Serra F. II-837,IV-1560
Sesnic S. I-367,375
Sevastyanov A.A. IV-1820
Shakhovets K.G. I-82,411,III-1480
Sharma S.R. IV-1828
Sharma S.K. II-684
Shashkov A.Yu. II-609
Shats M.G. II-467
Shcheglov M.A. II-614
Sheffield J. I-102
Shepard T.D. II-439
Sherwell D. I-355,359
Shibata T. III-1452
Shigueoka H. II-861
Shiina S. II-545
Shiina T. III-1452
Shimada T. II-545
Shimazu Y. II-541,549
Shimpo F. I-34
Shinohara S. II-541,549
Shirai A. II-541,549
Shishkin A.A. II-529
Shishkin A.G. III-1239,1243,1247
Shkarofsky I.P. III-1191,1195
Shoji T. II-451,III-1452
Shoucri M. III-1191,1299
Shukla P.K. II-760,IV-1766
Shuklin A.P. IV-1880
Shurygin R.V. III-987
Shurygin V.A. IV-1612
Shustova N.V. III-1125,IV-1684
Sidle J.B. II-553
Sidorov V.P. III-1145
Siegrist M. IV-1680
Sigmar D.J. I-134
Sigov Yu.S. IV-1840

Silaev I.I. IV-1840
Silari M. III-1112
Silivra O.A. III-1199
Siller G. IV-1560
Silva A. II-837,IV-1560
Silva R.P. Da III-1349
Silvester C. I-379,III-1283
Simmet E. I-182
Simonetto A. III-1112
Simonini R. III-1369
Simpkins J.E. II-455
Simpson J.C.B. III-1357
Simpson P.R. III-1283
Singh A.K. IV-1749
Singh D.C. I-174,III-1133
Singh D.P. IV-1867,1871
Sinman A. II-597
Sinman S. II-597
Sips A.C.C. I-158,199,323, IV-1500
Sitenko A.G. IV-1802
Skiff F. IV-1624,1807,1811
Skovoroda A.A. II-593,III-1072
Smeets P.H.M. III-1121
Smeulders P. I-323,331,III-1150
Smirnov A.I. III-1239,1243,1247, 1480
Smirnova E.A. II-609
Smith B.A. I-150,174
Smith G.R. III-1096
Smith R.J. IV-1628
Smits F.M.A. III-1121
Snider R. III-1259
Sobhanian S. II-451
Solari G. III-1112
Söldner F.X. I-58, II-837, III-1092,1171, 1215,1223,1287, 1291,1323,IV-1560
Soliman H.M. II-630
Soltwisch H. IV-1660
Sosenko P.P. II-686,IV-1802
Soumagne G. IV-1680
Speck R. IV-1861
Spineau F. II-902
Springmann E. II-801
St. John H. I-271
Stäbler A. I-395,III-1439
Stakenborg J. III-1117,1121
Stambaugh R.D. I-134,371
Stamp M.F. I-9,III-1357,1361, 1365,1377,1381, 1385
Stangeby P.C. III-1385,1472
Start D.F.H. I-1,255,323,327, III-1015,1019,1150
Stearns J.W. III-979
Stepanenko M.M. III-1080
Stephan Y. II-872
Stern R. IV-1811
Steuer K.-H. I-62,182,295, III-1052,1423
Stevens J. III-1048
Stickelmann C. I-287
Stojanovic V. III-1405
Stojic A. III-1116
Stokic Z. III-1405
Stork D. I-90,247,255,259
Storm E. IV-1861
Stotland M.A. III-1319
Stotler D.P. I-134,III-1417
Stott P.E. III-1381
Strachan J.D. III-1048,IV-1548
Strait E.J. I-275,371,427
Stratton B.C. I-42,46,50,114, 146,III-1048
Streikov V.S. III-1080
Stringer T.E. II-801,805
Stroth U. I-58,66,151,183
Stubberfield P.M. I-1,5,106,162
Subbotin A.A. III-1327
Sudo S. II-459,IV-1524
Suematsu H. IV-1524
Sugama H. II-459
Sugie T. I-223,IV-1508
Sukachov A.V. III-1319
Summers D.D.R. I-9,251,III-1357, 1377,1381,1385
Summers H.P. III-1361, IV-1496,1664
Sund R.S. III-1023
Sünder D. II-764
Sushkov A.V. III-1076,1080
Suzuki K. III-1452
Suzuki N. III-1452
Suzuki S. III-1452
Synakowski E.J. I-42,46,50,114, 146,III-1048
Szydlowski A. II-634
Tagle J.A. III-1373,1381
Takahashi C. II-451
Takahashi H. I-283,367,375
Takase H. III-1211
Takeiri Y. II-451
Takeuchi H. I-223,III-1183, IV-1508
Takeuchi K. I-351
Takita Y. II-451

Takizuka T. III-1007
Talvard M. III-1231
Tamai H. III-1452
Tamor S. II-970
Tan M. I-311
Tanahashi S. I-34
Tang L. I-311
Tanga A. I-1,255,259,323, III-1015
Taniguchi Y. I-34
Tarasyan K.N. II-785
Taroni A. I-5,327, II-801, II-1365,1369
Taroni L.L. I-247
Tartari U. IV-1636
Taylor G. I-42,46,114,146, III-1048
Taylor R.J. I-138, 287
Taylor T.S. I-251,371,427
TBR-1 Team III-1349
Teichmann J. II-864
Telesca G. IV-1532
Tendler M. II-744
Terry J. I-46,387
Tessema G.Y. IV-1778
TEXTOR Team III-1447
TFTR Group III-1048,IV-1540
Theimer G. III-1464
Thoe R. IV-1861
Thomas C.E. II-439,IV-1492
Thomas D. III-1439
Thomas P.R. I-1,263,III-1015, 1019,1381,1385
Thomsen K. I-110,166,259, II-797,III-1015
Thumm M. III-1271
Thyagaraja A. II-942
Tibone F. I-5,255, II-801,805
Tielemans A.J.H. III-1121
Tilia B. IV-1717
Tisma R. I-215
Titishov K.B. III-1080
Tito C.J. III-1121
TJ-I Team I-18,IV-1512
Tobita K. III-1011,1183
Todd T.N. I-130,379
Toffol Ph. De III-1044
Toi K. I-34
Tokar' M.Z. III-1345,1448
Tokunov A.I. III-1125,IV-1684
Tokutake T. III-1452
Tollivier J.S. II-443
Tonon G. III-1231
TORE SUPRA Team I-86
Towner E.H. I-114
Towner H.H. I-146
Toyama H. II-541,549
Tran M.Q. IV-1807,1811
Trebes J. IV-1861
Tribaldos V. IV-1648
Troyon F. II-954,958
Truc A. IV-1588
Trukhin V. III-1259
Tsai S.-T. II-727,728
Tsois N. I-395,III-1427,1439, 1460
Tsuchimoto M. III-1039
Tsui H.Y.W. II-581
Tsukahara Y. IV-1508
Tsukishima T. IV-1524
Tsunawaki Y. IV-1524
Tsuzuki K. II-451
Tsuzuki T. I-34
Tsypin V.S. III-1145
Tsytovich V.N. III-1190
Tubbing B.J.D. I-1,255,259,III-1015
Tuccillo A.A. III-1287,1335
Tukachinskij A.S. I-299,411,III-1480
Turnbull A.D. I-371,427
Turner M.F. I-130
Turner R. IV-1861
Tutter M. III-1271,IV-1576
Uchino K. II-459
Uckan T. III-1353,IV-1492
Ueda I. II-541
Ueda N. II-809
Ueeda T. III-1251
Uesugi Y. III-1340
Ulrickson M. I-134,III-1417,1419
Uno S. III-1452
Ushakov S.N. I-231,IV-1536
Ushigusa K. III-1183
Vakulenko M.O. II-686
Valencia-Alvarado R. I-30
Valisa M. II-533,537
Vallet J.C. I-86,III-1231
Vallinga P.M. III-983
Vandenplas P.E. I-287
Varela P. IV-1560
Varias A. II-497,509
Vaselli M. IV-1867,1871
Vasin N.L. I-195,231,III-1076,1080,1084, IV-1536
Vayakis G. I-211,III-1283
Vdovin V.L. III-1295
Vega J.A. I-22
Velikovich A.L. II-659

Vergamota S. IV-1560
Verhoeven A.G.A. III-1117,1121
Vershkov V.A. III-1076,1080
Villiers J.A.M. De I-355,359
Vlad G. II-906
Vlad M. II-902
Vladimirov S.V. III-1187
Vlases G. I-339
Vlasov V.P. IV-1488
Voge A. II-950
Volkov V.P. III-1080
Vollmer O. I-94,183,295
VonGoeler S. III-1048
Voropaev S.G. II-614
Voytenko D.A. III-1319
Wade M.R. II-439,443
Wagner F. I-58,94,110,295
Wagner R. IV-1520
Waidmann G. I-319
Wakatani M. II-459
Wallace R. IV-1861
Walsh M.J. II-557,565,569
Waltz R.E. I-126,134
Wan S. III-1154
Wang J.P. II-853
Wang L. III-1149
Ward D. I-323
Warrick C.D. III-1283
Wassenhove G. Van III-1040
Watari T. I-34
Watkins J.G. I-403
Watkins M.L. III-1369
Watkins N. I-331
Weber P.G. II-581
Wegner P. IV-1861
Wégrowe J.-G. III-1235
Weiland J. II-769
Weisen H. I-5,9,90,162,259, 323,III-1361,1385, IV-1496,1608
Weller A. II-479
Wen Y. III-1154
Wenzel K.W. I-150
Wenzel U. IV-1488
Werthmann H. II-715
Wesner F. I-239,III-1052, IV-1552
Wesson J.A. I-335,III-1015
Westerhof E. II-821,III-1121
Weynants R.R. I-383,287,III-1040
Wieland R.M. I-114,146,387
Wienhold P. III-1401
Wilgen J.B. II-443,455,IV-1492
Wilhelmsson H. II-885
Willen U. III-1019
Willi O. IV-1864
Wilson J.R. III-1048
Wing W.R. II-443,455
Winter J. I-275
Wintermeyer G. IV-1794
Winternitz P. II-864
Wira K. III-1263
Wobig H. II-517
Wolf G.H. I-287,III-1447
Wolfe S.M. I-271
Wolfe S.W. I-335
Wolle B. IV-1516
Wong K.L. III-1048,IV-1544
Wootton A.J. I-38,174,III-1133, 1353,1456,1460
WVII-AS Team II-471,475,479,483, 484,517,III-1271, 1275,IV-1572,1576
Wysocki F.J. II-643
Xang X.Z. III-1133
Xiang Z. III-1154
Xie J. I-363
Xu D. I-307
Xu G. I-154
Yagi Y. II-545
Yagura S. III-978
Yakashima T. II-459
Yakovenko Yu.V. II-699
Yamada H. II-451
Yamada M. IV-1811
Yamagishi K. II-541,549
Yamagiwa M. III-1007
Yamamoto T. III-1340,1452
Yamauchi T. III-1452
Yan L. I-311
Yan Y. I-307
Yang J.-G. II-752
Yang J.W. I-287,III-1040
Yang Q. III-1341
Yang S. III-1341
Yang X.Z. I-26
Yaramyshev G.S. III-1080
Yaroshevich S.P. I-82,299,411, III-1480
Yavorsky V.A. II-699
Ye H. III-999
Yin Y. II-679
Yoneta A. III-1039
Yoshida H. I-223
Yoshino R. I-223
Young K.M. I-134
Young P. IV-1861
Yu C. I-150,174,

Yu C.	III-1133,1154
Yu G.Y.	I-415
Yu M.Y.	II-760
Yuan D.	III-1149
Yuan D.C.	IV-1680
Yushmanov P.N.	II-781, 789,III-1080
Zaitsev F.S.	III-1247
Zakharov L.E.	III-1327
Zambotti G.	III-1235
Zamkov V.I.	III-1060
Zang X.Z.	I-38
Zanza V.	IV-1717
Zao J.	I-307
Zarnstorff M.C.	I-42,114,146,387, III-1419
Zastrow K.-D.	II-655,IV-1608
Zavadsky V.M.	IV-1684
Zavala G.	I-243
Zaveri P.	IV-1745
Ze F.	IV-1861
Zebrowski J.	II-634
Zhang D.	III-1149
Zhang H.	I-307
Zhang Z.M.	I-26
Zhao H.	I-311
Zheng S.	III-1149
Zheng Y.	I-154,307,311, III-1341
Zhil'tsov V.A.	II-593,III-1072
Zhong Y.	I-154
Zhu S.	III-1154
Zohm H.	I-54,291,II-837, III-1223
Zolotukhin A.V.	II-529
Zou X.L.	II-736 IV-1693,1721
Zouhar M.	III-1287
Zukakishvili G.G.	III-1060
Zurro B.	I-18,IV-1512
Zushi H.	II-459,IV-1524
Zweben S.	III-1048